The Higgs boson

Gadatsch, S.

Publication date
2015
Document Version
Final published version

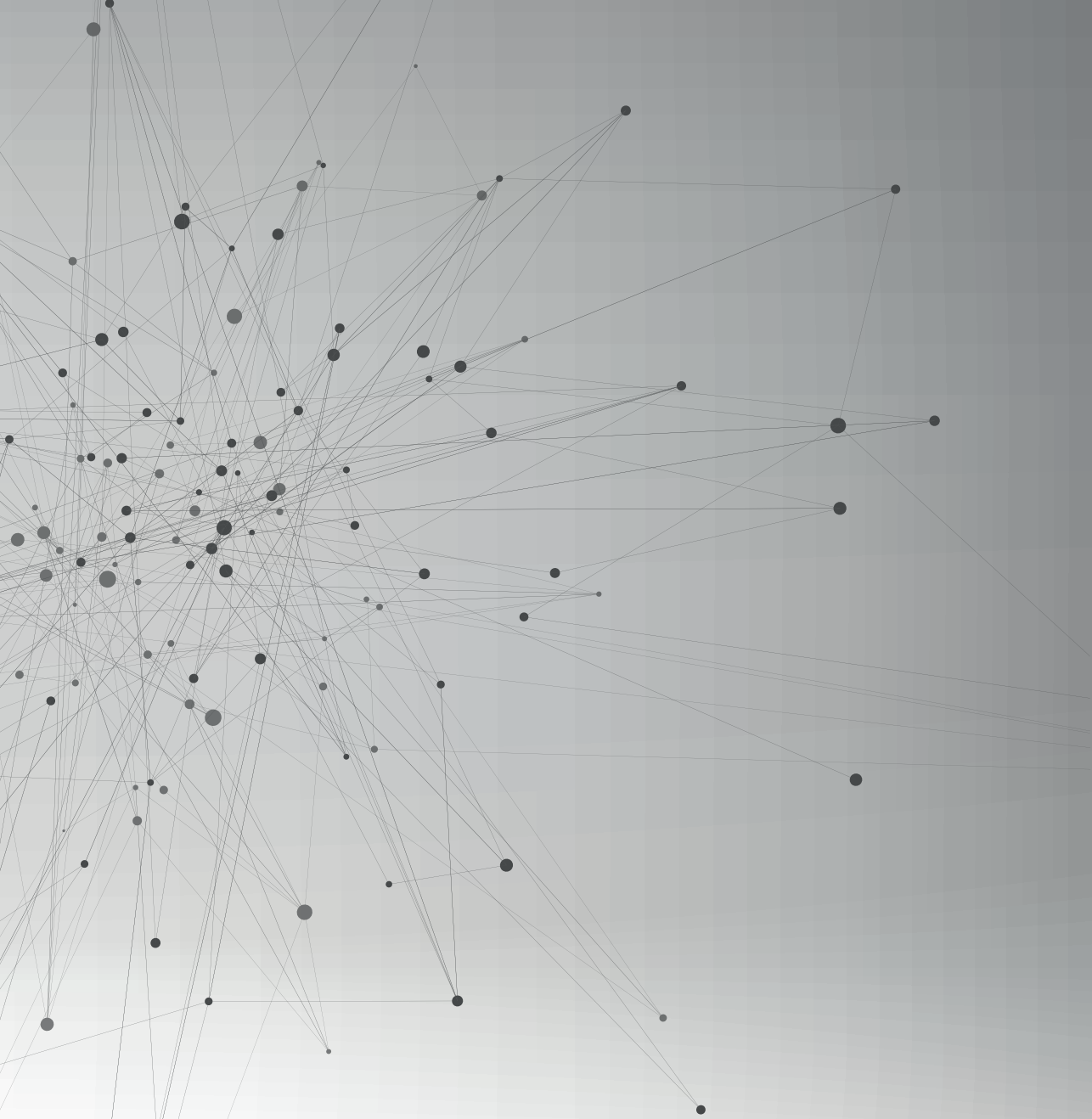

The Higgs Boson

Stefan Gadatsch

Stefan Gadatsch

The Higgs Boson

The Higgs Boson

ACADEMISCH PROEFSCHRIFT

ter verkrijging van de graad van doctor
aan de Universiteit van Amsterdam
op gezag van de Rector Magnificus
prof. dr. D.C. van den Boom
ten overstaan van een door het College voor Promoties ingestelde
commissie, in het openbaar te verdedigen in de Aula der Universiteit
op vrijdag 26 juni 2015, te 11:00 uur

door

Stefan Gadatsch

geboren te Hachenburg, Duitsland

Promotiecommissie:

Promotor:	prof. dr. S.C.M. Bentvelsen (Universiteit van Amsterdam)
Copromotor:	dr. W. Verkerke (Nikhef)
Overige leden:	prof. dr. W.J.P. Beenakker (Universiteit van Amsterdam)
	prof. dr. H.G. Raven (Vrije Universiteit)
	dr. M.M. Kado (LAL Orsay)
	prof. dr. ir. P.J. de Jong (Universiteit van Amsterdam)
	prof. dr. J.J. Engelen (Universiteit van Amsterdam)
	prof. dr. S.J. de Jong (Radboud Universiteit Nijmegen)
	dr. A.P. Colijn (Universiteit van Amsterdam)

Faculteit der Natuurwetenschappen, Wiskunde en Informatica

The Higgs Boson
Set in XCharter, Open Sans, and Source™ Code Pro using LuaLaTeX
Cover art by deomis/Shutterstock.com
Printed in the Netherlands by Ipskamp Drukkers

This work is part of the research program of the *Stichting voor Fundamenteel onderzoek der Materie (FOM)*, which is part of the *Nederlandse organisatie voor Wetenschappelijk Onderzoek (NWO)*. It was carried out at the *Nationaal Instituut voor Subatomaire Fysica (Nikhef)* in Amsterdam, the Netherlands.

Contents

Introduction

The Standard Model of Elementary Particle Physics (SM) provides a fundamental description of all established elementary particles, their dynamics and interactions, except gravity. Fermions of half-integer spin form all matter in nature. The interactions between the fermions are interpreted as exchange of force-mediating bosons of integer spin. Symmetries play an essential role in constructing the SM, making it an remarkably elegant theory. However, the particles embedded into the theory are a priori massless, unlike the observed particles. Thus, a mechanism must be introduced to give the particles mass in the theory.

The W and Z gauge bosons can acquire their mass through breaking of the electroweak (EW) symmetry, referred to as electroweak symmetry breaking (EWSB). In the SM, the complex Higgs scalar field induces a spontaneous breaking of the EW gauge group when it acquires a non-vanishing vacuum expectation value (VEV). The mechanism is commonly referred to as the Brout-Englert-Higgs mechanism. It ensures that the structure of the gauge interactions do not change and the theory remains a viable perturbative description of the established physics phenomena up to the Planck scale. The Higgs field picked up its VEV through the so-called EW phase transition when the early universe cooled down and expanded after the Big Bang. The underlying dynamics of this process are not known. Spontaneous symmetry breaking also gives mass to the fermions, yet the concept differs from the mechanism gauge bosons acquire their mass. The fermion mass terms are generated in the SM by gauge invariant Yukawa interactions between the Higgs field and the fermion fields. Elucidating the mechanism of EWSB and the origin of elementary particle masses is among the principal quests of the CERN Large Hadron Collider (LHC) physics program.

The Brout-Englert-Higgs mechanism postulates the existence of one real scalar field, identified as the Higgs boson. However, its mass is not predicted by the theory. Instead, it must be determined experimentally. Prior to the turn-on of the LHC, Higgs boson masses below 114 GeV and in the range of 158 GeV to 175 GeV have been excluded by direct searches at Large Electron-Positron Collider (LEP) [1] and Tevatron [2], respectively. Global fits to precision EW data implied an upper limit on the Higgs boson mass of 158 GeV [3]. It was not until 2012 that the discovery of a new particle with a mass near 125 GeV in the search for the SM Higgs boson was announced by the ATLAS [4] and CMS [5, 6] collaborations at the LHC.

Measurements of Higgs boson properties start with the identification of collisions with a recognizable signature of Higgs boson decay products. For some decay modes, the mass

of the Higgs boson can be explicitly reconstructed from its decay products, independent of assumptions on other properties of the Higgs boson. With the Higgs boson mass known, all properties of the SM Higgs boson, such as its production cross section and partial decay widths, are predicted by the SM. This then allows to test the predictions against the recorded collision data. Every theoretical extension of the SM alters the scalar sector of nature and exhibits distinct features that probe specific aspects of the SM. Only combined measurements of all Higgs boson properties fully reveal its rich phenomenology, which is comparable with the complexity of the phenomenology of flavor physics. The salient feature of the Brout-Englert-Higgs mechanism is the prediction that the coupling strengths of particles to the Higgs boson are proportional to the observed masses of these particles. Any deviation of this scaling behavior may indicate fundamental physics beyond the SM. Thus, measuring the Higgs boson couplings is the ultimate test of Brout-Englert-Higgs mechanism and the scalar sector of the SM.

However, in its current form, the SM can not be regarded as a complete theory of nature. The model does not answer several fundamental questions satisfyingly. Among these are for example the hierarchy problem regarding the naturalness of the Higgs boson mass, the nature of Dark Matter (DM), or the dynamical origin of EWSB. Many of the proposed solutions for these open questions have implications at the current energy frontier and predict modifications or extensions of the minimal scalar sector that is embedded in the SM. Some of the promising scenarios with fundamental physics beyond the SM are composite Higgs models, theories with two Higgs doublets, Supersymmetry (SUSY), and other models with a dark matter candidate. All these models make explicit predictions how the couplings of the observed 125 GeV Higgs boson deviate from the SM expectation. From a comparison against the recorded collision data, statements about these beyond Standard Model (BSM) theories can be made.

Organization of the manuscript and original contributions

The manuscript is organized as follows. Chapter 1 presents a comprehensive introduction to the SM, in particular to the phenomenology of the scalar sector. Many of the concepts reviewed in this chapter refer to textbooks [7–10] for further detail. The chapter concludes with a concise review of possible extensions and modifications of the SM.

Chapter 2 describes the technical design of the ATLAS and CMS experiments at the LHC as well as their performance during LHC Run 1. The chapter is based on the Technical Design Reports (TDRs) of either experiment [11–18], originally published by CERN and the ATLAS and CMS collaborations.

Chapter 3 reviews the event reconstruction with the ATLAS detector in the high pile-up LHC environment and highlights the performance of the Inner Detector (ID) in Sec. 3.1. I contributed to the optimization of the track and vertex reconstruction algorithms and studied their computational performance in high occupancy conditions. These performance studies

have also been published by the ATLAS collaboration as Ref. [19]. The remainder of the chapter presents a concise review of the reconstruction and calibration techniques for the physics objects used in the physics analyses to which I contributed.

Chapter 4 summarizes the general concepts of statistical data analysis. An important aspect of statistical data analysis that is not well covered in text books is the variety of practical and conceptual techniques that are used to construct probability models that are the basis of statistical inference. I review in this chapter the relevant techniques for model building and describe in detail the newly developed technique of moment morphing. The work presented in this thesis on moment morphing was previously published as Ref. [20].

Chapter 5 focuses on the identification of the sequential Higgs boson decay $H \to WW^* \to \ell\nu\ell\nu$, with the Higgs boson produced through gluon fusion (ggF) or vector boson fusion (VBF). In the analysis team for $H \to WW^* \to \ell\nu\ell\nu$ decays, I was responsible for the design of the statistical analysis model and the statistical interpretation of the data, starting with the 2012 analysis that was part of the Higgs boson discovery publication [4]. I was exceptionally awarded authorship of this discovery paper ahead of the normal ATLAS qualification period owing to my contributions to the $H \to WW^* \to \ell\nu\ell\nu$ analysis. Since the Higgs boson discovery analysis I have contributed to improvements in the signal acceptance and extraction, and to a better understanding of the dominant background processes, in particular of the background from non-resonant W boson pair production and the Drell-Yan (DY) process. Analysis techniques that I developed for this analysis have been widely adopted within the ATLAS collaboration, e. g. [21–29]. I have also been editor of the ATLAS internal documentation that is the basis for the reviewed analysis and supports it. Most results presented in this chapter have been previously published in Ref. [30].

Chapter 6 presents combined measurements of the Higgs boson production and decay rates and coupling strengths with the ATLAS detector, published as Ref. [31]. I performed all Higgs coupling strength measurements presented in this chapter, and as presented in Ref. [31], and performed the cross-check analysis for all signal rate measurements. The software framework that I developed that handles the technical aspects of building the joint likelihood functions for these coupling measurements has been adopted by other physics working groups within the ATLAS collaboration and by other collaborations, e. g. [22, 32–35]. I was editor of Ref. [31] and for its predecessor [36], as well as editor of the internal supporting documentation [37] for these publications. The text of Cha. 6 largely follows that of Ref. [31].

Chapter 7 studies the implications of the measured Higgs boson coupling strengths for selected scenarios with fundamental physics beyond the SM. I constructed the statistical models that implement coupling strength models that correspond to various BSM physics theories and performed all measurements presented in this chapter in collaboration with a small analysis team. The results shown in this chapter have been published in Ref. [38].

Chapter 8 describes the measurement of the Higgs boson mass using the full LHC Run 1 collision data sets of the ATLAS and CMS experiments. I contributed to the nominal mass measurement and to the understanding of the systematic uncertainties and their correlations. The combined mass measurement has been published as Ref. [22], and the text of Cha. 8 largely follows that of the paper.

Chapter 9 presents the physics potential of future facilities, e. g. the High-Luminosity LHC (HL-LHC) and International Linear Collider (ILC), for Higgs boson precision measurements. The description of the facilities and their envisioned upgrades is based on the respective TDRs [11–13, 39] (HL-LHC), [40–46] (ATLAS), and [47–51] (ILC). The projections for Higgs boson signal strength and coupling strength measurements with ATLAS at the HL-LHC in Sec. 9.2 are based on Ref. [52]. I performed all measurements in collaboration with a small analysis team. The phenomenology of Higgs physics at the ILC and the prospects for these measurements have been reviewed in Ref. [53] and are summarized here for convenience only. The combination of prospective HL-LHC and ILC measurements are exclusively my own work and have not been published elsewhere. Finally, Sec. 9.3 discusses the implications of the measured Higgs boson coupling strengths for selected scenarios with fundamental physics beyond the SM. I performed all interpretations in collaboration with a small analysis team and was one of the editors of the original publication (cf. Ref. [54]).

The final chapter concludes the manuscript with a discussion of the results.

The Standard Model and beyond

1

Over the past decades the SM has become textbook material. The theory is covered in all its elegance in the literature, e.g. Refs. [7–9], and review articles, e.g. Ref. [10], which serve as an excellent introduction to the topics discussed in this chapter. Hence, the emphasis is put on a phenomenological introduction to the scalar sector of the SM and possible extensions thereof, e.g. the Two Higgs Doublet Model (2HDM) or the Higgs portal model to DM.

1.1 Symmetries of the Standard Model

The SM is a non-abelian gauge theory, also called Yang-Mills theory [55], with the gauge group

$$\mathcal{G}_{\text{SM}} = SU(3)_C \otimes SU(2)_L \otimes U(1)_Y, \tag{1.1}$$

describing all known elementary particles, their dynamics and interactions, except gravity[1], which is covered by General Relativity (GR) [56]. Figure 1.1 shows an overview of the various particles. For each of them exists an antiparticle with the same mass but opposite inner quantum numbers. The interactions between fermions of half-integer spin are interpreted as exchange of force-mediating bosons of integer spin. As for other Quantum Field Theorys (QFTs), the equations of motion (e.o.m.) follow from a Lagrangian density, which is constructed entirely from the SM gauge group (1.1) following symmetry principles. In contrast, the fermions are a priori an empirical input to the theory, rather than following from fundamental principles.

The local $SU(2)_L \otimes U(1)_Y$ symmetry corresponds to the EW interaction described by the Glashow-Salam-Weinberg model (GSW model) [59–61], combining the electromagnetic and weak interactions, although not introducing a unification scale. The remaining $SU(3)_C$ reflects the symmetry of the strong interaction, namely an exact symmetry of three colors of the six quarks [62–64]. Even though EW theory and Quantum Chromodynamics (QCD), the theory of the strong force, form the SM in terms of a quantized gauge theory, they are not (yet) combined like the electromagnetic and the weak force. In the following the fermions are categorized according to their behavior under these symmetries by assigning the particles intrinsic quantum numbers and properties like masses.

[1] Owing to its exiguous relative strength, gravitation can be safely neglected when studying the other fundamental forces.

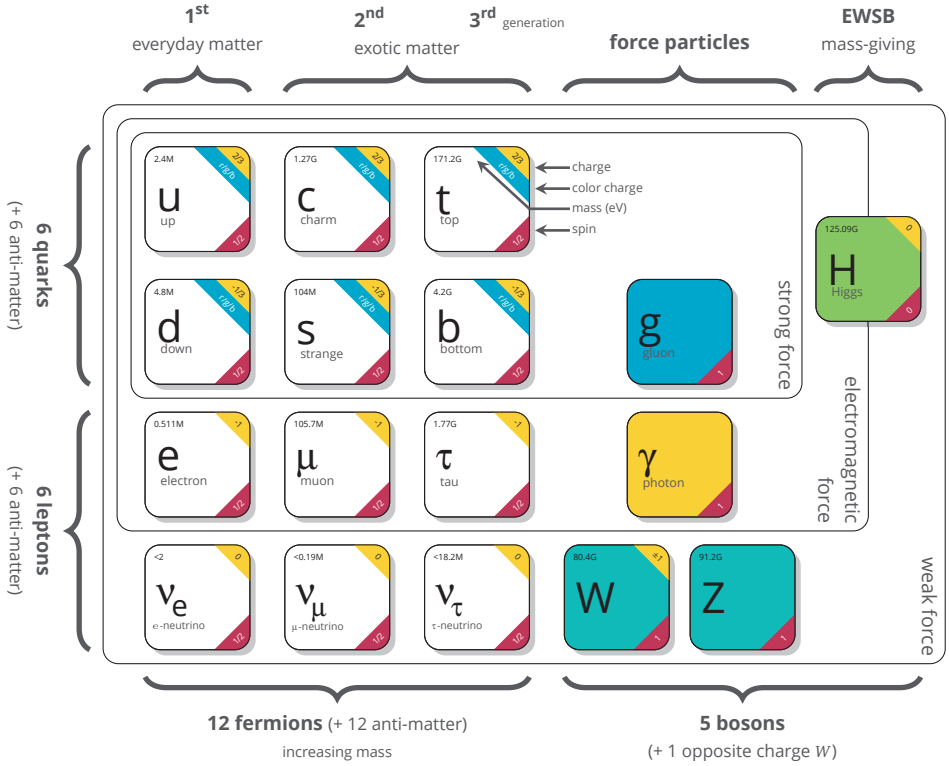

Figure 1.1: Particles of the SM. The particles are arranged according to the symmetries described in Sec. 1.1. Their charge, color charge, spin and mass are indicated. Graphic adapted from Ref. [57], values (other than the Higgs boson mass) taken from Ref. [58].

Established by their transformation properties under $SU(3)_C$, fermions can be arranged in two groups, namely quarks carrying three possible color charges, red, green or blue (r, g, b), and thus transforming as a triplet, and colorless leptons not interacting strongly, i.e. transforming as a singlet. Due to confinement, quarks occur only in colorless bound states called hadrons, and, like the colors, are not observed directly in nature. Regarding those bound states, one distinguishes between mesons, built up of a quark and an antiquark, and baryons, built up of three quarks. Hence, the quark masses cannot be defined in a conventional way and one needs an effective theory to describe weak decays of the heavy quarks at high energies.

The charge associated with the weak interaction $SU(2)_L$ is the weak isospin T, of which the third component T_3 is conserved in weak interactions. Only the fermions left-handed chirality eigenstates ψ_L,

$$\psi = P_L\psi + P_R\psi = \psi_L + \psi_R, \tag{1.2}$$

with the left- and right-handed projection operators P_L and P_R,

$$P_L = \frac{1-\gamma^5}{2} \quad \text{and} \quad P_R = \frac{1+\gamma^5}{2}, \tag{1.3}$$

transform non-trivially under the weak isospin $SU(2)_L$. Hence, left-handed fermion fields with $T_3 = \pm 1/2$ appear as doublets while their right handed counterparts with $T_3 = 0$ are singlets. Last, $U(1)_Y$ transformations conserve the weak hypercharge Y_W,

$$Y_W = 2(Q - T_3), \tag{1.4}$$

a combination of the weak isospin and the electric charge Q of a particle.

The quantum numbers of fermions in the EW sector are summarized in Table 1.1, introducing the convenient notation

$$\begin{aligned} \boldsymbol{Q}_L &= \left(\begin{pmatrix} u_L \\ d_L \end{pmatrix}, \begin{pmatrix} c_L \\ s_L \end{pmatrix}, \begin{pmatrix} t_L \\ b_L \end{pmatrix}\right) \\ \boldsymbol{u}_R &= \left(u_R, c_R, t_R\right) \\ \boldsymbol{d}_R &= \left(d_R, s_R, b_R\right) \end{aligned} \quad \text{and} \quad \begin{aligned} \boldsymbol{L}_L &= \left(\begin{pmatrix} \nu_{eL} \\ e_L \end{pmatrix}, \begin{pmatrix} \nu_{\mu L} \\ \mu_L \end{pmatrix}, \begin{pmatrix} \nu_{\tau L} \\ \tau_L \end{pmatrix}\right) \\ \boldsymbol{\ell}_R &= \left(e_R, \mu_R, \tau_R\right) \end{aligned} \tag{1.5}$$

for quarks and leptons respectively, assuming that the generations of quarks and leptons behave in the same way under gauge transformations and differ only by their masses.

Table 1.1: Electric charge Q, weak isospin T_3 and weak hypercharge Y_W of the fundamental fermions.

		particle type	Q	I_3	Y_W
$\boldsymbol{Q}_L$	-	left-handed quarks	$2/3$ $-1/3$	$1/2$ $-1/2$	$1/3$
$\boldsymbol{u}_R$	-	right-handed up-type quarks	$2/3$	0	$4/3$
$\boldsymbol{d}_R$	-	right-handed down-type quarks	$-1/3$	0	$-2/3$
$\boldsymbol{L}_L$	-	left-handed leptons	0 -1	$1/2$ $-1/2$	-1
$\boldsymbol{\ell}_R$	-	right-handed leptons	-1	0	-2

1.2 Electroweak interactions and the Brout-Englert-Higgs mechanism

1.2.1 The electroweak Lagrangian

The gauge invariant GSW Lagrange density describing EW interactions of the known particles introduced in Sec. 1.1 is constructed entirely from the $SU(2)_L \otimes U(1)_Y$ symmetry group.

Fermion kinetic terms

The free Lagrangian, summing over the left-handed weak isodoublets ψ_L and right-handed weak isosinglets ψ_R,

$$\mathscr{L} = \sum_{\psi_L} \bar{\psi}_L(x)(i\partial\!\!\!/)\psi_L(x) + \sum_{\psi_R} \bar{\psi}_R(x)(i\partial\!\!\!/)\psi_R(x) \tag{1.6}$$

is invariant under global $SU(2)_L \otimes U(1)_Y$ transformations in flavor space,

$$\psi_L(x) \mapsto \psi'_L(x) \equiv \exp\left(iY_W\beta\right) U_L \psi_L(x) \tag{1.7}$$

$$\psi_R(x) \mapsto \psi'_R(x) \equiv \exp\left(iY_W\beta\right) \psi_R(x) \tag{1.8}$$

with the weak hypercharge Y_W associated with the field transforming and the non-abelian $SU(2)_L$ transformation

$$U_L \equiv \exp\left(i\frac{\tau_i}{2}\alpha^i\right), \tag{1.9}$$

which acts only on the left-handed doublet fields ψ_L as discussed in Sec. 1.1. Hence, the global flavor symmetry of the matter Lagrangian is $[U(3)]^5$. The Lagrangian (1.6) becomes invariant under local $SU(2)_L \otimes U(1)_Y$ gauge transformations, i.e. $\alpha^i = \alpha^i(x)$ and $\beta = \beta(x)$, by replacing the derivatives with covariant objects, containing in total four different gauge bosons, one per gauge parameter. Since the right-handed particles do not couple to weak isospin, their covariant derivative takes the simple form

$$D_\mu\psi_R(x) \equiv \left(\partial_\mu + ig_1\frac{Y_W}{2}B_\mu(x)\right)\psi_R(x) \tag{1.10}$$

which serves to define the $U(1)_Y$ coupling g_1. The corresponding covariant derivative for the $SU(2)_L$ doublet is given by

$$D_\mu\psi_L(x) \equiv \left(\boldsymbol{I}\left(\partial_\mu + ig_1\frac{Y_W}{2}B_\mu(x)\right) + ig_2\frac{1}{2}\boldsymbol{\tau}\cdot\boldsymbol{W}_\mu(x)\right)\psi_L(x), \tag{1.11}$$

where g_2 represents the $SU(2)_L$ gauge coupling constant, $\boldsymbol{I}$ denotes the 2×2 unit matrix and the vector $\boldsymbol{\tau} = (\tau_1, \tau_2, \tau_3)$ contains the Pauli matrices. The gauge fields' transformation prop-

erties are fixed from requiring the same behaviour of the fermion fields and their covariant derivatives under these transformations,

$$B_\mu(x) \mapsto B'_\mu(x) \equiv B_\mu(x) - \frac{1}{g_1}\partial_\mu \beta(x), \tag{1.12}$$

$$\boldsymbol{W}_\mu(x) \mapsto \boldsymbol{W}'_\mu(x) \equiv U_L(x)\boldsymbol{W}_\mu(x)U_L^\dagger(x) + \frac{i}{g_2}\partial_\mu U_L(x)U_L^\dagger(x). \tag{1.13}$$

The coupling g_1 of fermion fields to B_μ is free and depends on the convention for the weak hypercharge Y_W. In contrast, there is a unique $SU(2)_L$ coupling g_2 to W_μ^i. Thus, the fermionic kinetic Lagrangian reads

$$\begin{aligned}\mathscr{L}_{\text{fermion kinetic}} =& \bar{\boldsymbol{Q}}_L(x)(i\not{\partial})\boldsymbol{Q}_L(x) + \bar{\boldsymbol{u}}_R(x)(i\not{\partial})\boldsymbol{u}_R(x) + \bar{\boldsymbol{d}}_R(x)(i\not{\partial})\boldsymbol{d}_R(x) \\ &+ \bar{\boldsymbol{L}}_L(x)(i\not{\partial})\boldsymbol{L}_L(x) + \bar{\boldsymbol{\ell}}_R(x)(i\not{\partial})\boldsymbol{\ell}_R(x),\end{aligned} \tag{1.14}$$

treating the neutrinos as massless, i.e. right handed neutrino fields are left out.

Gauge field kinetic terms

The gauge kinetic terms for the SM gauge bosons are constructed from the field strengths, which are defined from the commutator of two covariant derivatives,

$$B_{\mu\nu}(x) = \partial_\mu B_\nu(x) - \partial_\nu B_\mu(x), \tag{1.15}$$

$$W^i_{\mu\nu}(x) = \partial_\mu W^i_\nu(x) - \partial_\nu W^i_\mu(x) - g_2\varepsilon^{ijk}W^j_\mu(x)W^k_\nu(x). \tag{1.16}$$

The $U(1)_Y$ field strength $B_{\mu\nu}$ is gauge variant under $SU(2)_L \otimes U(1)_Y$ transformations, unlike the $SU(2)_L$ field strength $W^i_{\mu\nu}$,

$$\boldsymbol{W}_{\mu\nu}(x) \mapsto \boldsymbol{W}'_{\mu\nu}(x) \equiv U_L \boldsymbol{W}_{\mu\nu}(x)U_L^\dagger \quad \text{and} \quad B_{\mu\nu}(x) \mapsto B'_{\mu\nu}(x) \equiv B_{\mu\nu}(x). \tag{1.17}$$

Hence, the gauge invariant kinetic Lagrangian for gauge fields reads

$$\mathscr{L}_{\text{gauge kinetic}} = -\frac{1}{4}W_i^{\mu\nu}(x)W^i_{\mu\nu}(x) - \frac{1}{4}B^{\mu\nu}(x)B_{\mu\nu}(x), \tag{1.18}$$

where the trace i is taken in the $SU(2)_L$ space. The Lagrangian (1.18) is not only quadratic in the derivatives of the gauge boson fields but contains as well three- and four-point self-interaction terms, proportional to the $SU(2)_L$ coupling g_2, like already given in the fermion kinetic Lagrangian.

Scalar sector

Although the theory describes at this point mathematically consistent weak isospin and weak hypercharge, all fermions and gauge bosons are, in contrast to our experimental observa-

tions, massless. In particular the low strength and limited range of the weak interaction are explained by mediating massive gauge bosons $W^{\pm}$ and Z^0. This is solved by the Brout-Englert-Higgs mechanism of EWSB [65–71], which spontaneously breaks the $SU(2)_L \otimes U(1)_Y$ symmetry into the electromagnetic gauge group $U(1)_Q$ through the introduction of scalar fields. The technical details of the Brout-Englert-Higgs mechanism will be worked out in section 1.2.2 after having constructed the Lagrangian density. Since one physical Higgs boson is observed [4–6] and in total three symmetries get broken by the Brout-Englert-Higgs mechanism, the minimal field content needed is a complex $SU(2)_L$ doublet Φ made of two complex Higgs fields ϕ^+ and ϕ^0, each carrying one unit of hypercharge, $\Phi = (\phi^+, \phi^0)^T$.

The most general, but minimal, Lagrangian invariant under $SU(2)_L \otimes U(1)_Y$ transformations and describing the required scalar fields, is given by

$$\mathscr{L}_{\text{scalar}} = (D_\mu \Phi)^\dagger (D^\mu \Phi) - V(\Phi) \tag{1.19}$$

with the gauge covariant derivative acting on the doublet

$$D_\mu \Phi = \left(\boldsymbol{I} \left(\partial_\mu + i \frac{g_1}{2} B_\mu \right) + i g_2 \frac{\boldsymbol{\tau}}{2} \boldsymbol{W}_\mu \right) \Phi \tag{1.20}$$

and the Higgs self interaction

$$V(\Phi) = -\mu^2 \Phi^\dagger \Phi + \lambda (\Phi^\dagger \Phi)^2 \quad \text{with} \quad \mu^2, \lambda > 0, \tag{1.21}$$

described by the most general fourth-order polynomial in Φ and $\Phi^\dagger$ not violating gauge invariance.

Yukawa interactions

Dirac mass terms for the quarks and electrons are forbidden, since they would mix left- and right-handed states, but are assigned to different weak $SU(2)_L$ multiplets and thus none transforms under the complex-conjugate representation of another fermion, breaking the gauge symmetry. Since all fermions carry hypercharge, they also cannot acquire Majorana masses. However, with the previously introduced scalar field, a gauge invariant Yukawa interaction, coupling the Higgs and fermion fields, can be written as

$$-\mathscr{L}_{\text{Yukawa}} = \bar{L}_L^i Y_{ij}^\ell \Phi \ell_R^j + \bar{Q}_L^i Y_{ij}^u \tilde{\Phi} u_R^j + \bar{Q}_L^i Y_{ij}^d \Phi d_R^j + \text{h.c.} \tag{1.22}$$

with the Yukawa coupling constants Y_{ij}^ℓ, Y_{ij}^u and Y_{ij}^d and the charge conjugated Higgs doublet, $\tilde{\Phi} = i\tau_2 \Phi^* = (\phi^{0*}, -\phi^-)^T$. After EWSB, this interaction will look like mass terms. Equation (1.22) does explicitly not include right-handed neutrinos, as they are assumed to be massless. The global $[U(3)]^5$ flavor symmetry, up to a subgroup corresponding to baryon and lepton number, is violated by the Yukawa couplings of the fermions to the Higgs field.

1.2.2 Spontaneous symmetry breaking and the Brout-Englert-Higgs mechanism

Gauge boson masses

The potential (1.21), shown in Fig. 1.2, has an infinite set of degenerate Higgs ground state configurations, satisfying

$$\langle \Phi^\dagger \Phi \rangle_0 = \frac{v^2}{2} \quad \text{with} \quad v \equiv \sqrt{\frac{\mu^2}{\lambda}}, \tag{1.23}$$

where v is the VEV corresponding to the ground state of Φ. Only the neutral scalar field can acquire a VEV,

$$Q\langle \Phi \rangle_0 = \left(\frac{\tau_3}{2} + \frac{1}{2} Y_W \right) \langle \Phi \rangle_0 = 0 \quad \overset{(1.23)}{\Longleftrightarrow} \quad \langle \Phi \rangle_0 = \frac{1}{\sqrt{2}} \begin{pmatrix} 0 \\ v \end{pmatrix}, \tag{1.24}$$

such that the remaining unbroken symmetry is the electromagnetic gauge group $U(1)_Q$, although $\langle \Phi \rangle_0$ is neither invariant under $SU(2)_L$ nor under $U(1)_Y$.

To expand the Lagrangian (1.19) around the classical ground state the scalar is expressed as its radial degree of freedom times an exponential containing the generators of the broken gauge symmetry,

$$\Phi = \frac{1}{\sqrt{2}} \exp\left(i \frac{\tau_i}{2} \theta^i(x) \right) \begin{pmatrix} 0 \\ v + h(x) \end{pmatrix} \tag{1.25}$$

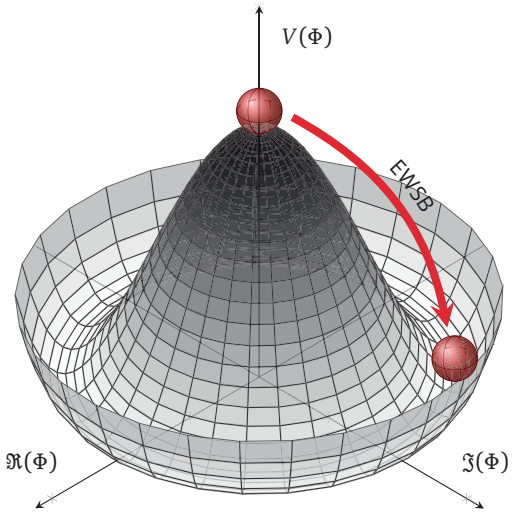

Figure 1.2: Illustration of the Higgs potential and EWSB.

with four real scalar fields $\theta^i(x)$ and $h(x)$. The fields $\theta^i(x)$ describe massless particles, so-called Goldstone bosons, arising when a global symmetry is broken spontaneously. In unitary gauge, $\theta^i(x) = 0$, these unphysical degrees of freedom become longitudinal modes of the massive gauge bosons. Hence, the Higgs-gauge interactions reads

$$\begin{aligned}\mathscr{L}_{\text{scalar}} = &\frac{1}{2}\left(\partial^\mu h(x)\right)\left(\partial_\mu h(x)\right) - \lambda v^2 h^2(x) - \lambda v h^3(x) - \frac{\lambda}{4}h^4(x) \\ &+ \frac{1}{2}\frac{g_2^2 v^2}{4}\left(\left|W_\mu^+\right|^2 + \left|W_\mu^-\right|^2\right) + \frac{1}{2}\frac{g_2^2 v^2}{4\cos^2\theta_W}\left|Z_\mu\right|^2 + 0 A_\mu A^\mu\end{aligned} \tag{1.26}$$

where the mass matrix of the gauge fields is diagonalized by mixing the vector fields,

$$W_\mu^\pm = \frac{1}{\sqrt{2}}\left(W_\mu^1 \mp i W_\mu^2\right), \tag{1.27}$$

$$\begin{pmatrix} Z_\mu \\ A_\mu \end{pmatrix} = \begin{pmatrix} \cos\theta_W & -\sin\theta_W \\ \sin\theta_W & \cos\theta_W \end{pmatrix}\begin{pmatrix} W_\mu^3 \\ B_\mu \end{pmatrix}. \tag{1.28}$$

The Weinberg angle θ_W is defined by

$$\sin\theta_W = \frac{g_1}{\sqrt{g_1^2 + g_2^2}} = \frac{e}{g_2} \quad \text{and} \quad \cos\theta_W = \frac{g_2}{\sqrt{g_1^2 + g_2^2}}, \tag{1.29}$$

such that the coupling strength of the electromagnetic interaction is the electron charge e. In addition to scalar three and four point self interactions, the boson masses can be read off the Lagrangian (1.26): the photon field A_μ stays massless, as required by the unbroken $U(1)_Q$, while other gauge boson mass terms are related through the weak mixing angle θ_W,

$$m_{W^\pm} = \frac{1}{2}g_2 v \quad \text{and} \quad m_Z = \frac{1}{2}\frac{g_2 v}{\cos\theta_W} = \frac{m_{W^\pm}}{\cos\theta_W}. \tag{1.30}$$

The real scalar field, identified as the Higgs boson, is invariant under $U(1)_Q$, i.e. neutral, with the mass

$$m_H = \sqrt{2\lambda v^2} \quad \text{and} \quad v = \frac{2m_W}{g_2} = 246\,\text{GeV}. \tag{1.31}$$

Custodial symmetry

The Higgs Lagrangian is not only invariant under $SU(2)_L \otimes U(1)_Y$, but also has an accidental approximate global symmetry $SO(4) = SU(2)_L \otimes SU(2)_R$ before EWSB[2], which manifests itself in the limit of a vanishing $U(1)_Y$ coupling, $g_1 \to 0$. When the Higgs field acquires a non-zero VEV, the symmetry is broken spontaneously to $SO(3) = SU(2)_{L+R}$, the diagonal subgroup of $SU(2)_L \otimes SU(2)_R$, called the custodial symmetry [72, 73]. For vanishing hypercharge coupling, the B_μ field is zero and the symmetry becomes exact, i.e. the $SU(2)_L$ gauge fields

[2] $SO(4)$ is isomorphic to $SU(2)_L \otimes SU(2)_R$ because they share the same Lie algebra.

W_μ^i transform as a triplet under the unbroken global $SU(2)_{L+R}$, resulting in equal gauge boson masses at tree level, $m_{W^\pm} = m_Z$, i.e.

$$\frac{m_{W^\pm}}{m_Z} = \cos^2\theta_W = 1 \quad \text{or} \quad \rho \equiv \frac{m_{W^\pm}^2}{m_Z^2 \cos\theta_W} = 1. \tag{1.32}$$

Radiative corrections to the gauge boson masses beyond tree level will violate custodial symmetry softly and show up as deviations of the ρ parameter from one. The leading order correction from Higgs bosons at one-loop depends logarithmically on the Higgs boson mass m_H [74–76],

$$(\Delta\rho)^{\text{1-Higgs}} = -\frac{11 m_Z^2 \sin^2\theta_W}{48 v^2 \pi^2} \ln\frac{m_H^2}{m_Z^2}, \tag{1.33}$$

in the limit of heavy Higgs, $m_H \gg m_{W^\pm}$, yet higher orders have been computed up to three-loop level [77]. The dominant corrections due to massive fermions are contributions of virtual top and bottom quark loops to the W and Z boson propagators, and have been calculated up to three loops [78, 79]. The leading order correction [80]

$$(\Delta\rho)^{\text{1-fermion}} = \frac{3}{16 v^2 \pi^2}\left(m_t^2 + m_b^2 - 2\frac{m_t^2 m_b^2}{m_t^2 - m_b^2}\ln\frac{m_t^2}{m_b^2}\right) \tag{1.34}$$

allowed to predict the top quark mass from EW precision measurements before its discovery by both the Collider Detector at Fermilab (CDF) and DØ collaborations at the Tevatron at the Fermi National Accelerator Laboratory (Fermilab) [81, 82].

Fermion masses

Fermion masses are generated by the Yukawa interaction term of the SM Lagrangian when the Higgs field acquires a VEV and breaks $SU(2)_L$ spontaneously. The mass matrices for leptons, down-type and up-type quarks are

$$m_{ij}^{\ell,u,d} = \frac{1}{\sqrt{2}} Y_{ij}^{\ell,u,d} v \tag{1.35}$$

with the corresponding Yukawa coupling matrices $Y_{ij}^{\ell,u,d}$. However, they are not necessarily diagonal in the fermion generations, meaning that the states of the gauge invariant Lagrangian are not mass eigenstates and the mass matrices need to be diagonalized. Assuming massless neutrinos[3], the mass eigenstates for the charged leptons are obtained by unitary transformations $\mathscr{U}_L$ and $\mathscr{U}_R$ of the corresponding fields,

$$m_{ij}^\ell \bar{\ell}_L^i \ell_R^j \mapsto \bar{\ell}_L^k \underbrace{\mathscr{U}_L^{\dagger ik} m_{ij}^\ell \mathscr{U}_R^{jl}}_{\delta^{kl} m_\ell} \ell_R^l. \tag{1.36}$$

[3] The observation of neutrino oscillations [83] indicates that neutrinos are not massless, but rather have a finite mass term much smaller than the quarks and charged leptons. Since right-handed neutrinos transform as a singlet under the SM symmetry group, a Majorana mass term is allowed.

In the quark sector bi-unitary transformations need to be used to realize mass eigenstates, since up-type quarks need to acquire a mass term in contrast to neutrinos, and a simultaneous diagonalization of m^u_{ij} and m^d_{ij} would modify the weak charged currents. Hence, in the mass basis, the quark fields read

$$u_{L,R} \to \mathcal{V}_{u_{L,R}} u_{L,R} \quad \text{and} \quad d_{L,R} \to \mathcal{V}_{d_{L,R}} d_{L,R}, \tag{1.37}$$

satisfying

$$\mathcal{V}^\dagger_{u_L} m_u \mathcal{V}_{u_R} = \text{diag}(m_u, m_c, m_t) \quad \text{and} \quad \mathcal{V}^\dagger_{d_L} m_d \mathcal{V}_{d_R} = \text{diag}(m_d, m_s, m_b) \tag{1.38}$$

with real entries m_i, which are proportional to the Yukawa couplings. The mismatch between $\mathcal{V}^\dagger_{u_L}$ and $\mathcal{V}_{d_L}$ defines the unitary, not necessary diagonal, Cabibbo-Kobayashi-Maskawa matrix (CKM matrix) [84, 85]

$$\mathcal{V}^\dagger_{u_L} \mathcal{V}_{d_L} \equiv V_{\text{CKM}}. \tag{1.39}$$

It induces charged flavor transitions between u_L and d_L, while flavor changing neutral currents (FCNCs) are absent at the tree level, as neutral current interactions neither mix left- and right-handed fields, nor up- and down-type quarks. Historically, the suppression of FCNCs is referred to as the Glashow-Iliopoulos-Maiani mechanism (GIM mechanism) [86]. The unitarity of the CKM matrix expresses the universality of the weak interaction in the quark sector. Further, the quark mixing matrix is the source of all known CP violation in the SM.

1.3 Quantum Chromodynamics

The strong force is described by QCD through a non-abelian gauge theory with the gauge group $SU(3)_C$, where the subscript indicates the conserved quantum number under the groups symmetry transformations. This section introduces the fundamentals of the theory, relevant to the physics at the LHC at CERN. A more complete review can be found e.g. in Refs. [87–89]. Particular emphasis is put on the discussion of the rich structure of events at hadron colliders, involving not only the primary hard process, but also parton showers (PSs) associated colored participating partons, hadronization as well as the underlying event (UE), following e.g. Ref. [90].

In color space, a quark field of flavor f and color j transforms as a triplet under global $SU(3)_C$ transformations,

$$q^f_j \mapsto q'^f_j \equiv U_j{}^i q^f_i \quad \text{with} \quad U = \exp\left(iT^a\theta_a\right) \tag{1.40}$$

where the generators of the fundamental representation of the $SU(3)_C$, $T^a = \lambda^a/2$, $(a = 1, \ldots 8)$, are the Gell-Mann matrices λ^a, obeying the non-trivial commutation relation $\left[\lambda_a, \lambda_b\right] = 2if_{abc}\lambda_c$. Hence, the choice of the gauge group, $SU(3)$ rather than $U(3)$, prohibits the existence of a single gauge boson which couples to hadrons and transforms as a singlet under

the color symmetry. Neglecting non-perturbative QCD effects, breaking CP-symmetry[4], the gauge invariant QCD Lagrangian reads

$$\mathscr{L}_{\text{QCD}} = -\frac{1}{4} G_a^{\mu\nu} G^a_{\mu\nu} + \bar{q}_j^f \left(i \not{D}_{jk} - m_q^f \delta_{jk} \right) q_k^f \quad \text{with} \quad D_\mu q^f = \left(\partial_\mu + i g_s G_\mu^a T^a \right) q^f , \tag{1.41}$$

the field strength tensor of the gluon fields G_μ^a,

$$G^a_{\mu\nu} = \partial_\mu G^a_\nu - \partial_\nu G^a_\mu - g_s f^{abc} G^b_\mu G^c_\nu, \tag{1.42}$$

and the strong coupling constant g_s. The force mediating gauge bosons transform non-trivially themselves, meaning that the non-abelian structure of the kinetic term of the Lagrangian (1.41) generates three- and four-point self-interactions of the gluons.

1.3.1 Perturbative QCD and its renormalization

The calculation of cross sections of physics processes, such as the scattering of two quarks shown in Fig. 1.4a, using Feynman diagrams [94] typically leads to an infinite power series in the coupling strength of the underlying interaction, where the dominant contribution emanates from the tree level, yet higher order corrections from loop diagrams need to be considered. Often it is sufficient to only examine QCD corrections to a given process, arising from quark and gluon loops, such as the ones shown in Fig. 1.4b and 1.4c, owing to the high relative strength of the strong force compared to the others.

However, the higher order calculations diverge due to quantum loop corrections to the Green functions, so that they, after parametrizing the arising singularities, have to be canceled. Several methods preserving Lorentz and gauge invariance exist for the first step, e.g. dimensional regularization [95–99], which continues the calculations to $D = 4 - 2\epsilon$ space-time dimensions. The divergences will appear as poles in ϵ in the limit $\epsilon \to 0$ and can be removed by renormalization, e.g. by subtracting them in the minimal subtraction scheme (MS) [100] or the modified minimal subtraction scheme ($\overline{MS}$) [101], or they will drop out in the physical observable.

The dependence of renormalized parameters, such as the coupling constant, and Green functions on the renormalization scale μ_R in perturbative QCD is described by the renormalization group equation (RGE), which can be directly computed from the ϵ poles of the renormalization constants [102–104]. The running of the strong coupling constant, in terms

[4] The term $\mathscr{L}_{\theta_{\text{QCD}}} = \frac{\theta_{\text{QCD}}}{32\pi^2} \tilde{G}^a_{\mu\nu} G^{\mu\nu a}$ is experimentally constrained to be $\theta_{\text{QCD}} < 10^{-9}$ [91], though naturally θ_{QCD} is expected to be of natural size. One proposed dynamical solution of this fine tuning problem is the so-called Peccei-Quinn-mechanism [92, 93], which gives rise to axions.

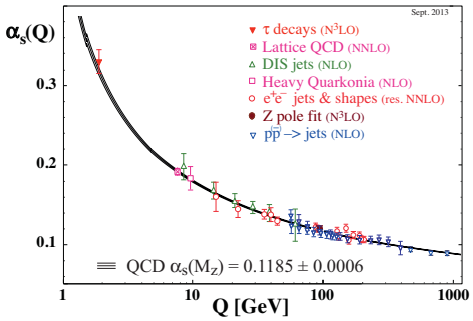

Figure 1.3: Summary of measurements of α_s as a function of the energy scale Q. The respective degree of QCD perturbation theory used in the extraction of α_s is indicated in brackets (NLO; NNLO; res. NNLO; N^{3}LO). Figure taken from Ref. [58].

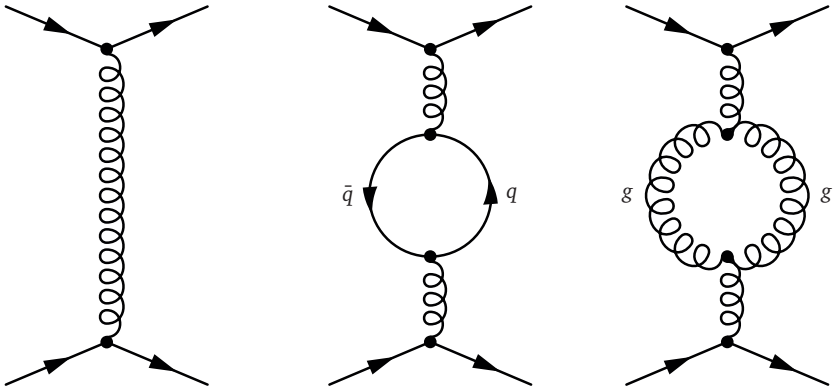

Figure 1.4: Scattering of two quarks at (a) tree level and with (b) quark-antiquark and (c) gluon loop corrections. Quark-antiquark loops lead to a screening of the color, $\alpha_s^{q\bar{q}}(|q^2|) = \alpha_s(\mu^2)\left(1 + 2n_f \frac{\alpha_s(\mu^2)}{12\pi} \ln \frac{|q^2|}{\mu^2}\right)$. However, the gluon contribution effects the opposite direction, $\alpha_s^{gg}(|q^2|) = \alpha_s(\mu^2)\left(1 - 11n_c \frac{\alpha_s(\mu^2)}{12\pi} \ln \frac{|q^2|}{\mu^2}\right)$. Summing up both contributions to all orders, one finds the running coupling $\alpha_s(|q^2|) = \alpha_s(\mu^2)\left(1 + (11n_c - 2n_f)\frac{\alpha_s(\mu^2)}{12\pi} \ln \frac{|q^2|}{\mu^2}\right)^{-1}$.

of $\alpha_s \equiv g_s^2/4\pi$, is shown in Fig. 1.3 and for the example constructed in Fig. 1.4, i.e. including leading order corrections only, given by

$$\alpha_s(\mu_R^2) = \frac{12\pi}{(11n_c - 2n_f)\ln \dfrac{\mu_R^2}{\Lambda_{\text{QCD}}^2}}, \tag{1.43}$$

where n_c is the number of colors and n_f the number of quark flavors. The coupling strength vanishes for increasing energies, $\mu_R/\Lambda_{\text{QCD}} \to \infty$, owing to asymptotic freedom [64, 105]. The screening effect of color charge, similar to the screening of electric charge in Quantum Electrodynamics (QED), from $q\bar{q}$ pair induced corrections is compensated by contributions from virtual gluon fields in the SM. However, for soft QCD, i.e. at low energies, the coupling diverges, causing quarks and gluons to form hadronic color singlets, which is called color confinement.

1.3.2 Factorization and parton distribution functions

Hadronic interactions

The LHC does not collide free quarks, but protons, i.e. complex composite bound states of three strongly interaction valence quarks (uud), gluons, and sea quarks ($q\bar{q}$ pairs), each carrying a fraction $x_i = 0, \ldots, 1$ of the proton's total momentum, $\boldsymbol{p}_i = x_i \boldsymbol{p}_h$, assuming that the partons move collinear with the surrounding proton. Revisiting the previous section, the soft structure of a hadron is characterized by the confinement scale Λ_{QCD}, at which the strong coupling constant in perturbative QCD would diverge, the so-called Landau pole, and thus is subject to non-perturbative QCD. A hard-scatter process, on the other hand, typically takes place at high energies above the QCD scale and can be computed in perturbative QCD.

The factorization theorem [106] allows the cross section of a general hadron-hadron process, $h_1 + h_2 \to f$, to be expressed as the convolution of a non-perturbative, but universal, parton distribution function (PDF) $f_{i/h}(x_i, Q^2)$, describing the probability for finding a parton i with longitudinal momentum fraction x_i inside a hadron h at a given energy scale Q, and the partonic cross section of the hard-scatter process, $\hat{\sigma}_{i+j\to f}$, calculated perturbatively,

$$\sigma_{h_1+h_2\to f} = \sum_{i,j} \int \mathrm{d}x_1 \, \mathrm{d}x_2 f_{i/h_1}(x_1, \mu_F^2) f_{j/h_2}(x_2, \mu_F^2) \hat{\sigma}_{i+j\to f}. \tag{1.44}$$

The factorization scale μ_F arises from infrared (IR) regularization of the integral over the Lorentz-invariant phase space, Φ_f, accessible by the possible partonic final states f, and thus separates the hard and soft processes.

Parton distribution functions

The PDFs are not a priori calculable in QCD, but can be measured at an arbitrary scale μ_0 in well-understood processes, such as deep inelastic scattering (DIS) [107, 108], DY [109] and $pp \to$ jets [110], and, owing to their universality, extrapolated to other scales as a function

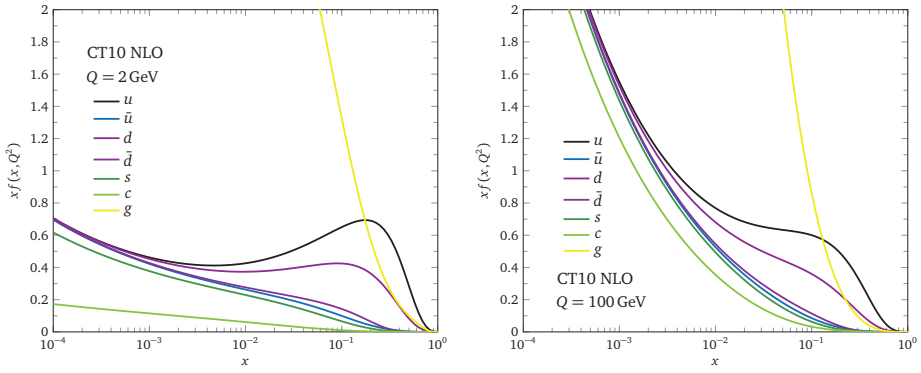

Figure 1.5: Distributions of the PDFs $xf(x,Q^2)$ for the lightest quarks and the gluon using the CT10 NLO PDF set [116] as a function of the partonic momentum x at (a) $Q = 2\,\text{GeV}$ and (b) $Q = 100\,\text{GeV}$. The plots are made using data from the HEPDATA online tool [121].

of the factorization scale. The RGE evolution is given by the Dokshitzer-Gribov-Lipatov-Altarelli-Parisi equations (DGLAP equations) [111–113], a set of coupled integro-differential equations,

$$\mu_F^2 \frac{\mathrm{d}f_{i/h}(x_i,\mu_F^2)}{\mathrm{d}\mu_F^2} = \frac{\alpha_s(\mu_F^2)}{2\pi} \sum_j \int_{x_i}^1 \frac{\mathrm{d}x_j}{x_j} P_{i\leftarrow j}\left(\frac{x_i}{x_j}\right) f_{j/h}(x_j,\mu_F^2), \tag{1.45}$$

where $P_{i\leftarrow j}$ describes the splitting of parton j into parton i in the collinear limit. Several collaborations, such as MSTW [114], Coordinated Theoretical-Experimental Project on QCD (CTEQ) [115, 116], HERAPDF [117], and NNPDF [118, 119], provide PDF sets at different orders, recommended in the PDF4LHC prescription [120] for the computation of central values and uncertainty bands for processes at the LHC. Figure 1.5 shows the RGE evolution of the CT10 NLO PDFs set [116] as a function of the partonic momentum for the lightest quarks and the gluon from a factorization scale of 2 GeV to 100 GeV. The resonance of a few hard light quarks at high values of the parton momentum fraction at low factorization scales indicates that the hadron, and in particular the proton, structure is dominated by these valence quarks. At higher scales, the valence quark resonance broadens due to increasing contributions from gluons and sea quarks.

Parton showers and soft QCD processes

As mentioned already in the context of the DGLAP equation, scattered, annihilated, and created partons can split and loose energy radiating additional gluons or $q\bar{q}$ pairs, that are either collinear with the outgoing partons or are soft, and thus generate showers which need to be simulated universally as the description using leading order (LO) matrix elements (MEs)

or even higher fixed order MEs lacks information about the substructure of the emerging particles. Hence, a PS describes the evolution of an event in momentum transfer from ultraviolet (UV) scales, defined by the hard process, down to a IR cut-off scale at which the partons form color singlets under $SU(3)_C$ due to non-perturbative confinement, called hadronization. It is intuitive to iteratively describe the evolution of a PS using step-wise Markov chains with the Sudakov form factor defining the probability of not observing parton splittings above a given scale.

PSs can be initiated by the hard process, or hard partons originating from partons radiated before or after the hard scattering process, i.e. initial state radiation (ISR) or final state radiation (FSR). The energy of the PS is localized in narrow cones of collinearly traversing partons, called jets [122]. It is preserved by the hadronization mechanism, which is described using fragmentation models as a computation from first principles is not possible. Typical models are for example string fragmentation [123] and cluster fragmentation [124, 125]. Jets are not fundamental objects defined by QCD, but rather reconstructed by jet clustering algorithms [126], such as the k_t [127–129] and anti-k_t [130] algorithms, or the Camebridge/Aachen algorithm (C/A algorithm) [131, 132], which are described in more detail in Sec. 3.3.1.

The total cross section of hadron-hadron interactions is 101.7 ± 2.9 mb at LHC energies of 8 TeV [133]. The main contributions arise from soft QCD processes, e.g. inelastic, non-diffractive processes (minimum bias), or the UE. In particular through the UE, the topology of a hard parton-parton interaction can change: additional soft jets or multiple parton interactions (MPIs) can arise from the hadronization process of beam remnants, i.e. the partonic substructure of the incoming hadrons, which do not participate in the hard scattering [90, 134].

1.4 Higgs production and decays at the LHC

The study of the Higgs boson properties is key to the LHC, ATLAS and CMS physics programs. This section summarizes the production and decay of SM Higgs bosons at hadron colliders, described in more detail for example in Refs. [10, 135] and references therein.

1.4.1 Production modes

The Higgs boson production in proton-proton collisions at the LHC is dominated by processes involving couplings of the Higgs boson to heavy particles, i.e. the massive gauge bosons and the top and bottom quarks. The main production mechanisms, shown in Fig. 1.6, are ggF [136] through a heavy quark loop ($gg \to H$), Fig. 1.6a, VBF [137–141] ($qq' \to qq'H$), Fig. 1.6b, the associated production with a W or Z boson, also called Higgs-strahlung [142, 143] ($q\bar{q} \to WH, ZH$), Fig. 1.6c, and production in association with heavy top [144–146]

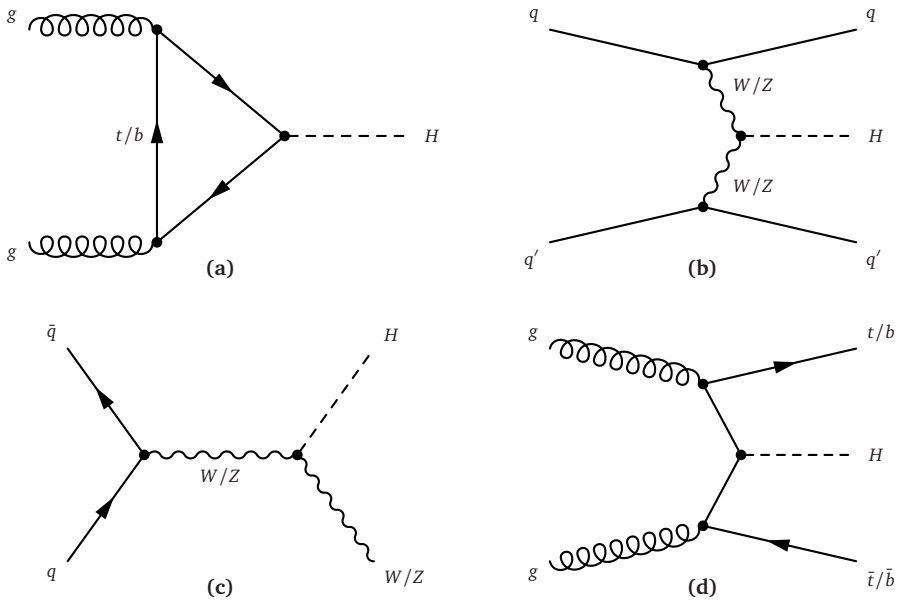

Figure 1.6: Feynman diagrams showing the main production mechanisms of the SM Higgs boson at hadron colliders: (a) ggF, (b) VBF, (c) Higgs-strahlung, and (d) associated production with heavy quarks.

or bottom [147–149] quark pair ($q\bar{q}/gg \to t\bar{t}H, b\bar{b}H$), Fig. 1.6d, or a single top quark (tH) [150–154], Fig. 1.7. Although the Higgs-strahlung process is dominated by quark-initiated subprocesses, the gluon-initiated contribution [155–159], shown in Fig. 1.8, constitutes a non-negligible higher order correction.

Pair production of Higgs particles, e.g. Refs. [160–164], is suppressed by powers of additionally arising EW couplings, leading to a much reduced production cross section, compared to the single Higgs production mechanisms. In the remainder of this section the various production modes for the Higgs boson at the LHC are discussed in more detail. The following chapters will guide the reader through the measurement of the Higgs Boson's properties and the implications for the SM and BSM scenarios.

Gluon fusion

The cross section for the ggF production mode is at LO quadratically proportional to the strong coupling constant α_s [136]. At NLO, QCD radiative corrections to the total cross section involve real corrections and virtual corrections of the form $gg \to Hg$, $gq \to Hq$ and $q\bar{q} \to Hg$, which contain an extra factor α_s, like the Higgs boson production in gluon-quark collisions and in annihilations of quark-antiquark pairs. These have been computed in Refs. [166–168],

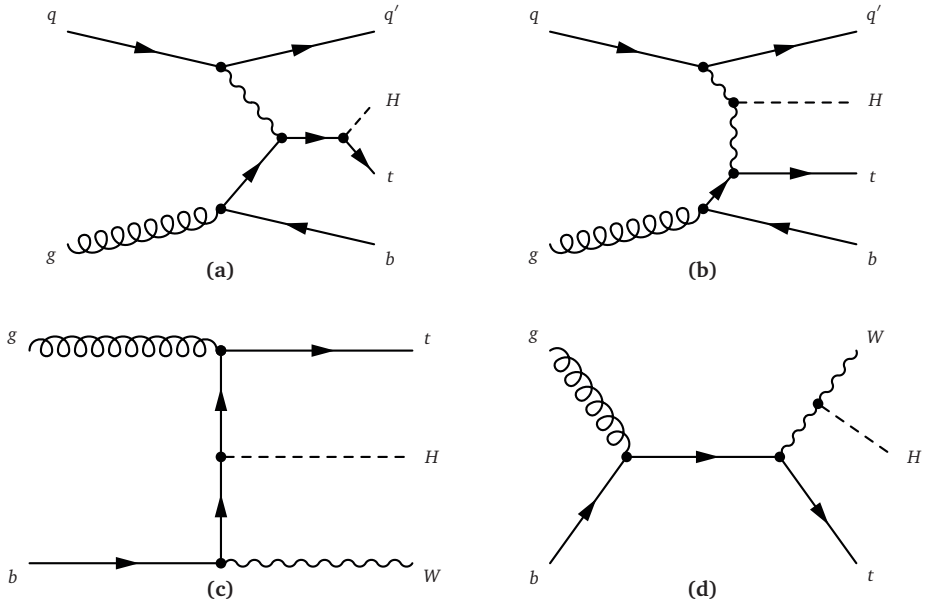

Figure 1.7: Representative Feynman diagrams showing the Higgs boson production in association with a single top quark through (a) (b) the t-channel, $qg \to tHq'b$, in the four-flavor scheme [165], or (c) (d) through WtH production, $gb \to WtH$.

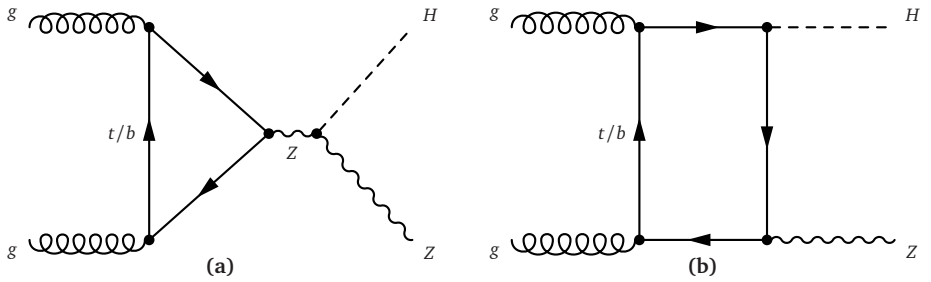

Figure 1.8: Feynman diagrams showing the $gg \to ZH$ production mechanism of the SM Higgs boson at hadron colliders.

leading to corrections of the central value of the LO cross section of 70%. Three-loop NNLO corrections [169–171] have been computed using heavy quark effective theory (HQET) [172–175][5]. The correction is more modest, though the cross section is increasing by 30%. QCD soft gluon corrections are re-summed at up to next-to-next-to-leading logarithm (NNLL) [176, 177], leading to a 5% increase of the cross section at NNLO. EW corrections are assumed to

[5]Long-distance and short-distance effects associated with the QCD scale Λ_{QCD} and the mass of the heavy quark respectively, separate naturally into an effective coupling constant arising from integrating out the heavy quark and effects that can be computed analytically, assuming massless gluons and light quarks.

factorize from the QCD corrections and have been computed up to NLO [178, 179]. Taking all previously described corrections into account [180–183], the cross section for Higgs boson production through ggF is $\sigma(gg \to H) = 19.2 \pm 2.0\,\text{pb}$ [135] for a Higgs boson mass of $m_H = 125.36\,\text{GeV}$ at a centre-of-mass energy of 8 TeV.

Weak vector boson fusion

The Feynman diagram for VBF production is shown Fig. 1.6b and alludes to rich kinematics, which can be exploited in this production mode. This makes it particularly suitable for the identification in proton-proton collisions at the LHC [184]. The cross section for VBF is dominated by the fusion of two W bosons, $\sigma(WW \to H) \approx 3\sigma(ZZ \to H)$, since the W boson couplings to fermions exceed the ones of the Z boson. Following the equivalent vector boson approximation (EVBA) [185–187], which is valid in the high energy regime of the LHC, the gauge bosons exchanged in the three-body process carry just enough energy to produce a Higgs boson, while the quarks which emitted them have large energies but small transverse momenta of the order of the weak boson mass. This gives rise to two forward tagging jets separated by a large gap in pseudorapidity, defining a central region, in which the Higgs is produced and its decay products tend to be. In the central region the hadronic activity, characterized by additional jets in the final state, is expected to be low, since the quark lines in the VBF process do not exchange color. Hence, forward jet-tagging and central jet-vetoing serve as powerful experimental techniques in the search for Higgs bosons produced via VBF. EW and QCD corrections to the VBF process, i.e. virtual quark self energies and vertex corrections as well as real ISR and FSR, have been computed at NLO [188–190] and up to NNLO for QCD [191], leading to corrections of the LO [138] cross section of up to 10%, resulting in a cross section for Higgs boson production through VBF of $\sigma(qq' \to qq'H) = 1.57 \pm 0.04\,\text{pb}$ [135] for a Higgs boson mass of $m_H = 125.36\,\text{GeV}$ at a centre-of-mass energy of 8 TeV.

Higgs-strahlung

The associated production of a Higgs boson with a weak gauge boson can be viewed as a virtual vector boson created in a DY process [192], splitting into the real final state particles. Thus, taking into account the charge of the W boson, the QCD corrections, calculated up to NNLO [142, 193, 194], are the ones of the DY process [195, 196] and lead to corrections of the cross section of about 30%. The gluon-initiated subprocess is the most prominent QCD correction beyond NLO of non-DY type. Naively, its cross section is suppressed by approximately one order of magnitude compared to the quark-initiated ZH production process. At NNLO, it adds approximately 3% to the total cross section [194]. In particular in boosted environments, the $gg \to ZH$ production mode becomes relevant. EW corrections at NLO [197] contribute with a 20% increase of the LO cross section. These include photon exchange between the initial state $q\bar{q}$ pair, bremsstrahlung, collinear photon emission, and

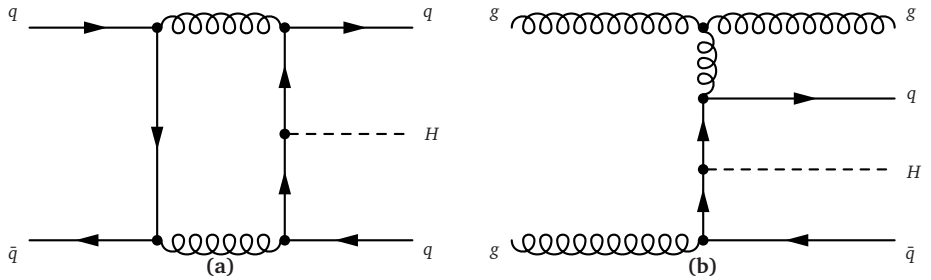

Figure 1.9: Representative Feynman diagrams for QCD corrections to the associated Higgs production with heavy top or bottom quarks arising from (a) pentagonal $q\bar{q}$ and gg initiated processes and (b) real corrections with additional gluons in the final state. Many more diagrams with the same topology can be drawn.

bosonic one-loop corrections to vertices and self-energies. The resulting cross section for Higgs strahlung is $\sigma(q\bar{q} \to WH) = 0.698 \pm 0.018\,\text{pb}$, $\sigma(q\bar{q} \to ZH) = 0.412 \pm 0.013\,\text{pb}$ [135] for a Higgs boson mass of $m_H = 125.36\,\text{GeV}$ at a centre-of-mass energy of 8 TeV. The final states of VH-like events are characterized by the decay products of the produced W or Z boson in addition to the Higgs boson decay products, i.e. additional charged leptons, missing transverse energy arising from neutrinos, or two additional jets, which, in contrast to the ones produced in VBF, have a low invariant mass.

Associated Higgs production with heavy top or bottom quarks

Even though the Feynman diagram shown in Fig. 1.6d dominates the cross section of the associated Higgs production with heavy top or bottom quarks at the current centre-of-mass energy at the LHC, other diagrams such as gluon fusion, with the Higgs boson radiated from an external heavy quark line, are possible, all leading to final states with three massive particles. At NLO several involved QCD corrections arise, for example through pentagonal $q\bar{q}$ and gg initiated processes, c.f. Fig. 1.9a, or real corrections leading to an additional gluon in the final state, c.f. Fig. 1.9b. These corrections have been computed up to NLO QCD for the $q\bar{q}/gg \to t\bar{t}H$ process [145, 198–201] and up to NNLO QCD in the five-flavor scheme [202] and up to NLO QCD in the four-flavor scheme [203, 204] for the $q\bar{q}/gg \to b\bar{b}H$ process. Their size depends strongly on the choice of renormalization and factorization scale. The cross section of Higgs boson production in association with top quarks is at $\sigma(q\bar{q}/gg \to t\bar{t}H) = 0.128 \pm 0.014\,\text{pb}$ [135] and goes to $\sigma(q\bar{q}/gg \to b\bar{b}H) = 0.202 \pm 0.028\,\text{pb}$ for bottom quarks [205] for a Higgs boson mass of $m_H = 125.36\,\text{GeV}$ at a centre-of-mass energy of 8 TeV. Higgs boson production in association with a single top quark proceeds through the t-channel, $qg \to tHq'b$, or through WtH production, $gb \to WtH$. The s-channel production is neglected due to its exiguous cross section compared to the other tH production processes. In the SM the tH production cross section is suppressed by the destructive interference at the tree level between diagrams where the Higgs boson is radiated from W boson and

Table 1.2: (a) cross sections (in pb) for the production of a Higgs boson with $m_H = 125.36\,\text{GeV}$ in the different modes at $\sqrt{s} = 7\,\text{TeV}$ and $\sqrt{s} = 8\,\text{TeV}$. (b) Branching ratios (BRs) for the various decay modes of a Higgs boson with $m_H = 125.36\,\text{GeV}$. Values obtained by linear interpolation between the ones for 125.3 GeV and 125.4 GeV from Ref. [135], except for the tH production cross section which is taken from Ref. [206]. The uncertainties on the cross sections are the quadratic sum of the uncertainties on the QCD scales, PDFs and α_s. The uncertainty on the tH cross section is calculated following the procedure of Ref. [135].

Production process	Cross section (pb) $\sqrt{s} = 7\,\text{TeV}$			$\sqrt{s} = 8\,\text{TeV}$		
$gg \to H$	15.0	±	1.6	19.2	±	2.0
$qq' \to qq'H$	1.22	±	0.03	1.57	±	0.04
$q\bar{q} \to WH$	0.573	±	0.016	0.698	±	0.018
$q\bar{q}/gg \to ZH$	0.332	±	0.013	0.412	±	0.013
$q\bar{q}/gg \to b\bar{b}H$	0.155	±	0.021	0.202	±	0.028
$q\bar{q}/gg \to t\bar{t}H$	0.086	±	0.009	0.128	±	0.014
tH	0.012	±	0.001	0.018	±	0.001
Total	17.4	±	1.6	22.1	±	2.0

(a)

Decay mode	Branching ratio (%)		
$H \to b\bar{b}$	57.1	±	1.9
$H \to WW^*$	22.0	±	0.9
$H \to gg$	8.53	±	0.85
$H \to \tau\tau$	6.26	±	0.35
$H \to c\bar{c}$	2.88	±	0.35
$H \to ZZ^*$	2.73	±	0.11
$H \to \gamma\gamma$	0.228	±	0.011
$H \to Z\gamma$	0.157	±	0.014
$H \to \mu\mu$	0.022	±	0.001

(b)

top quark lines. Consequently, its production cross section is small compared to the cross section for ttH production, $\sigma(tH) = 0.018 \pm 0.001\,\text{pb}$ [206] for a Higgs boson mass of $m_H = 125.36\,\text{GeV}$ at a centre-of-mass energy of 8 TeV. However, in BSM theories [151–154], the interference becomes constructive and the tH production cross section may exceed the ttH one.

Summary

The total cross section for SM Higgs boson production at the LHC with $m_H = 125.36\,\text{GeV}$ are predicted to be $17.4 \pm 1.6\,\text{pb}$ at a centre-of-mass energy of 7 TeV and $22.3 \pm 2.0\,\text{pb}$ at a centre-of-mass energy of 8 TeV [135]. Table 1.2a recaps the cross sections for the production of a Higgs boson with $m_H = 125.36\,\text{GeV}$ in the different modes at $\sqrt{s} = 7\,\text{TeV}$ and $\sqrt{s} = 8\,\text{TeV}$. The cross sections of the main production mechanisms are summarized in Fig. 1.10a as a function of the Higgs boson mass. Figure 1.10c shows a summary of several SM total and fiducial production cross section measurements, corrected for leptonic branching fractions, compared to the corresponding theoretical expectations [207], which are background processes for the Higgs boson property measurements, but exhibit several orders of magnitude higher production rates than the Higgs boson at the LHC.

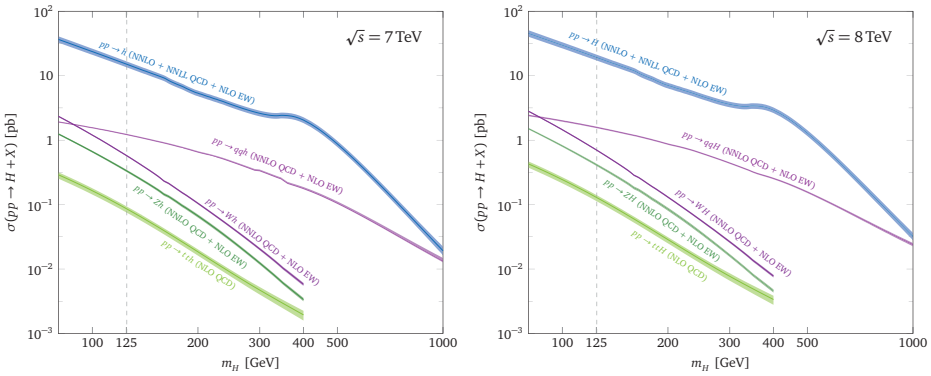

(a) (b)

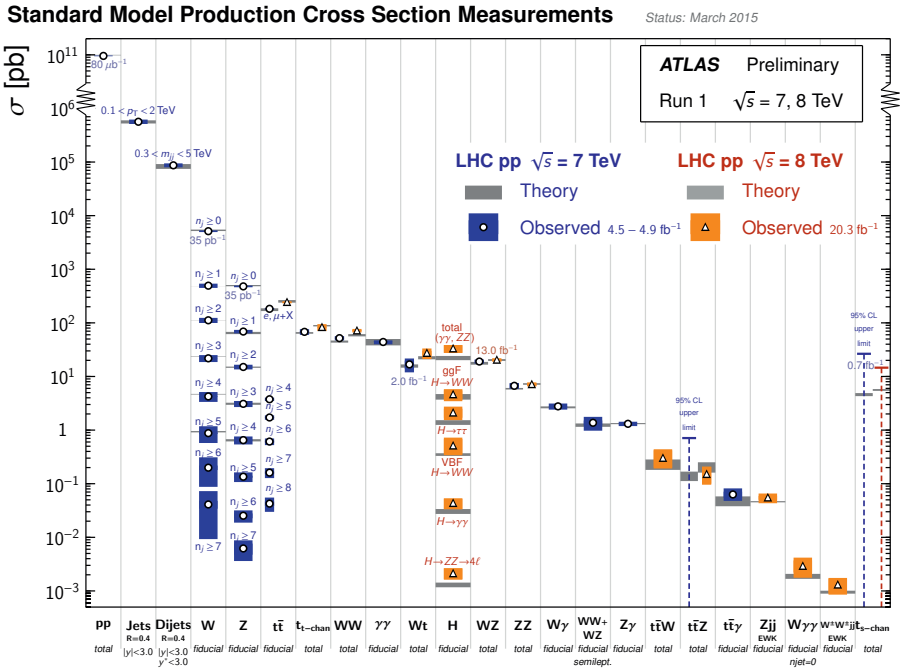

(c)

Figure 1.10: SM Higgs boson production cross section [135] at (a) $\sqrt{s} = 7$ TeV and (b) $\sqrt{s} = 8$ TeV, compared to (c) the total and fiducial production cross section measurements of several SM background processes [207].

1.4.2 Decay modes

The Higgs boson mass m_H is the only parameter not predicted by the theory in the scalar sector of the SM. Once it is fixed, the BRs of the Higgs boson into massive particles, i.e. fermions and vector bosons, defined as

$$\mathrm{BR}(H \to X) = \frac{\Gamma(H \to X)}{\sum_Y \Gamma(H \to Y)} \tag{1.46}$$

can be computed, since each partial width depends only on kinematic factors and the square of the Higgs coupling to the decay products, which are directly proportional to their (pole) masses. In particular the relations

$$g_{HVV} \propto \frac{m_V^2}{v} \quad \text{and} \quad g_{Hff} \propto \frac{m_f}{v} \tag{1.47}$$

hold. Thus, the partial decay width into the heaviest particle allowed by phase space will be largest. The corresponding Feynman diagrams are shown in Fig. 1.11.

At leading order, the partial width of the Higgs boson decaying into fermions is given by the Born approximation [208]

$$\Gamma(H \to f\bar{f}) = \frac{n_c}{8v^2\pi} m_H m_f^2 \beta_f^3 \quad \text{with} \quad \beta_f = \sqrt{1 - \frac{4m_f^2}{m_H^2}} \tag{1.48}$$

and the color factor $n_c = 3$ (1) for quarks (leptons). The decays are strongly suppressed for $m_H \approx 2m_f$. For hadronic decays QCD corrections are taken into account up to NLO, e.g. [209–213]. Since the observed Higgs boson mass is below the kinematical threshold to decay into two real massive EW gauge bosons, $m_H \leq 2m_V$, at least one of them must be off-shell and partial width for three and four body decays have been computed in Refs. [214–217].

Massless particles, such as photons and gluons, do not couple directly to the Higgs boson, but contribute to the total decay width of the Higgs boson via loop induced decays involving heavy, colored or charged, particles. Figure 1.12 shows the decay of the SM Higgs boson into two photons or $Z\gamma$, mediated by W boson and heavy charged fermion loops. These decays are suppressed by additional powers of the EW or strong coupling constant, rendering them only relevant at Higgs masses below 130 GeV [208], even when taking into account two-loop virtual corrections, e.g. Refs. [168, 218–220].

Figure 1.13a summarizes the Higgs BRs as a function of the Higgs boson mass. A wide range of decay modes of the Higgs boson is accessible at the observed mass of 125.36 GeV, dominated by the decay into two bottom quarks and followed by the decay into a pair of W bosons. Table 1.2b summarizes the BRs for the various decay modes of a Higgs boson with $m_H = 125.36$ GeV. Nevertheless, the total decay width, Fig. 1.13b, is very narrow in that

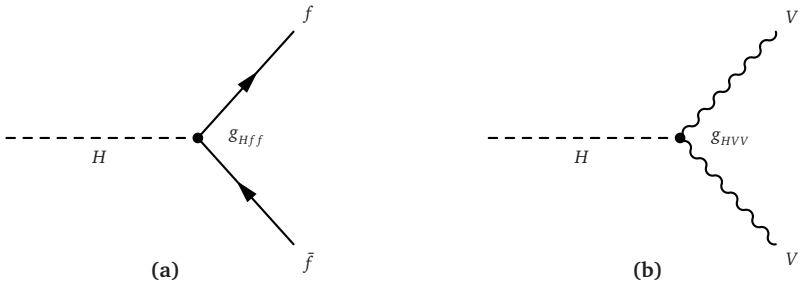

Figure 1.11: Feynman diagrams showing the decay modes of the SM Higgs boson in a pair of (a) fermions and (b) vector bosons.

range. Every decay channel exhibits distinctive signatures, for example isolated leptons or missing transverse energy (MET), which are exploited by various measurements of the Higgs boson properties, described in Cha. 5 and 6. The uncertainties on the BRs largely reflect the experimental uncertainties of the input parameters, i.e. the strong coupling constant α_s and the quark masses, but also missing higher order contributions in the perturbation theory. Hence, the uncertainties on the BRs are correlated two-fold: on one hand through the variations of the input parameters, and on the other hand trivially because they have to add up to one, explicitly

$$\frac{\delta \mathrm{BR}(H \to X)}{\mathrm{BR}(H \to X)} = (1 - \mathrm{BR}(H \to X)) \frac{\delta \Gamma(H \to X)}{\Gamma(H \to X)} + \sum_{Y \neq X} \mathrm{BR}(H \to Y) \frac{\delta \Gamma(H \to Y)}{\Gamma(H \to Y)}, \tag{1.49}$$

leading primarily to a suppression of the uncertainty on $\mathrm{BR}(H \to X)$ at low masses.

1.5 Beyond a minimal scalar sector

While all measurements of the discovered Higgs particle's properties, i.e. its mass [21, 22, 221], spin and parity [33, 222] and combined coupling measurements of the observed production and decay rates [31, 221], are compatible with the SM predictions, the crucial question arises whether the scalar sector is indeed minimal as postulated by the SM, or extended by means of BSM theories.

1.5.1 Puzzles faced by the Standard Model

Even though the SM in its current form seems to give a valid perturbative description of physics phenomena up to the Planck scale, it comes with intrinsic problems and cannot answer several fundamental questions satisfyingly. The reader is introduced to some of these problems in the following paragraphs. Figure 1.15 illustrates the big questions and some of the ideas to answer them.

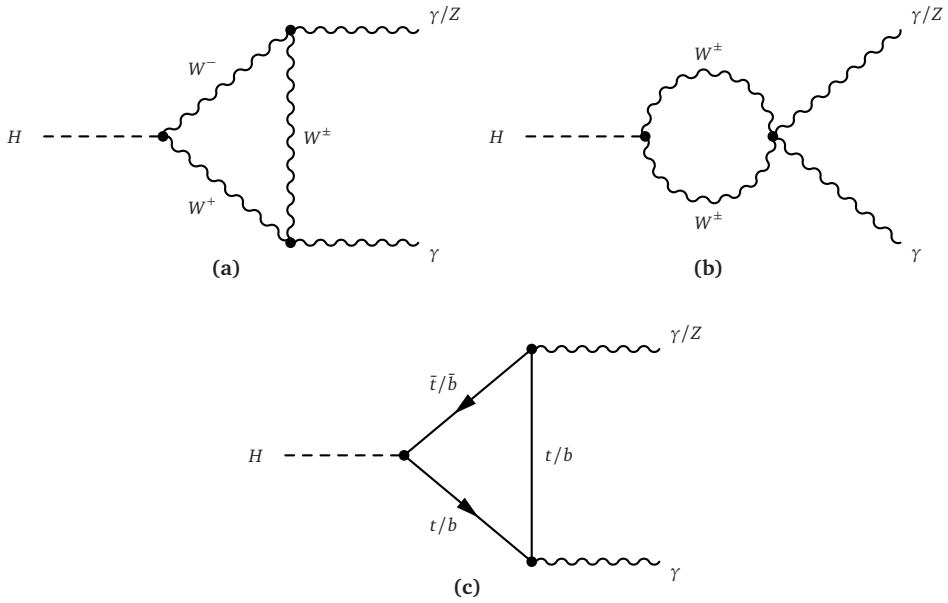

Figure 1.12: Feynman diagrams showing the decay of a SM Higgs boson into two photons or $Z\gamma$, mediated by (a) and (b) W boson and (c) heavy charged fermion loops.

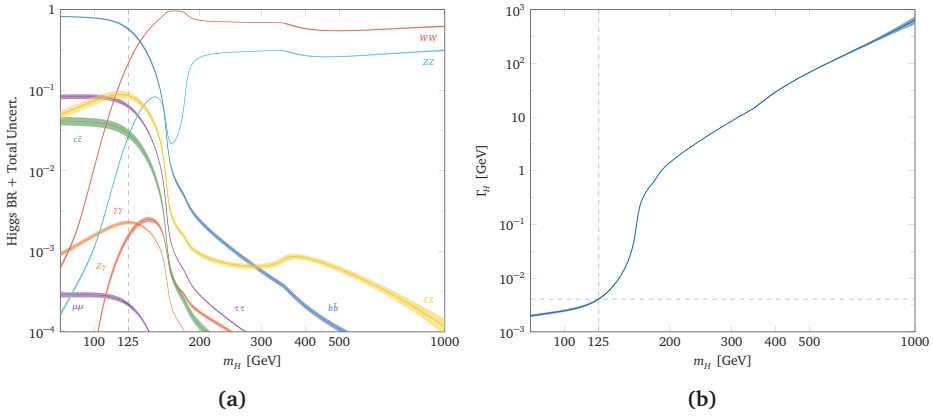

Figure 1.13: (a) SM Higgs boson BR and (b) total decay width as a function of the Higgs boson mass m_H. Values taken from Ref. [135].

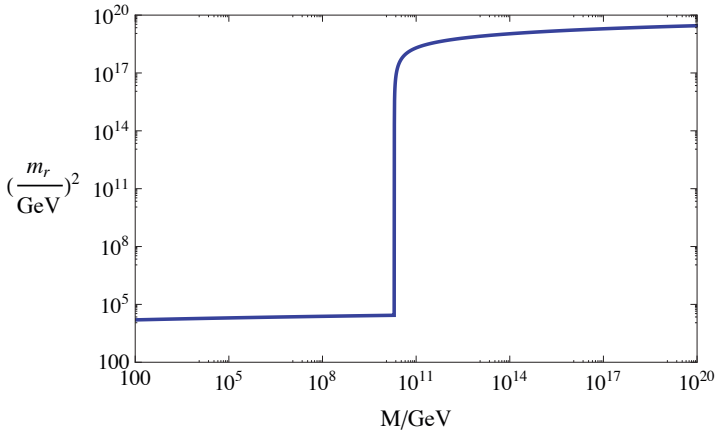

Figure 1.14: The renormalized running Higgs boson mass squared, m_r^2, as function of the scale M in the SM with NP emerging at the scale $\Lambda_{\text{NP}} = 10^{10}$ GeV coupling to the Higgs boson with a strength of approximately unity. Figure taken from Ref. [227].

The SM with the Higgs boson introduced in the previous section, in particular the Higgs potential, is fully renormalizeable. In case New Physics (NP) emerges at a certain scale Λ_{NP}, the renormalized running Higgs boson mass squared exhibits a jump at the NP scale as shown in Fig. 1.14. Below and above Λ_{NP} the behaviour is locarithmic. The size of the jump depends quadratically on the scale of NP and on the NP's coupling to the Higgs boson. If the scale of NP is high, i.e. there is a hierarchy, then a fine tuning is required. The theory needs to be tuned to a relative accuracy of possibly several orders of magnitude [223–226], namely $m_H^2/\Lambda_{\text{NP}}^2$, to reproduce the observed physical Higgs boson mass at the Fermi scale. However, if the theory is natural, i.e. constants are of similar order of magnitude, the jump is small and does not present a problem. Many models and mechanisms have been proposed to protect the Higgs boson mass against the physics details at shorter distances, e.g. the Minimal Supersymmetric Standard Model (MSSM) and models in which the Higgs boson itself is a composite state with a finite size. It should be noted that in the absence of NP there is no hierarchy problem.

Various astrophysical measurements, e.g. of temperature fluctuations of the cosmic microwave background (CMB) [228], indicate that today's Baryon density in the Lambda Cold Dark Matter model (ΛCDM model) is $\Omega_b = 4.9\%$, while the cold DM density is $\Omega_c = 26.7\%$ and the Dark Energy density is $\Omega_\Lambda = 68.3\%$. All quoted densities are normalized to the critical density. The nature of DM cannot be explained in the SM and motivates the existence of additional new particles and interactions, which potentially can be probed through studying Higgs boson properties.

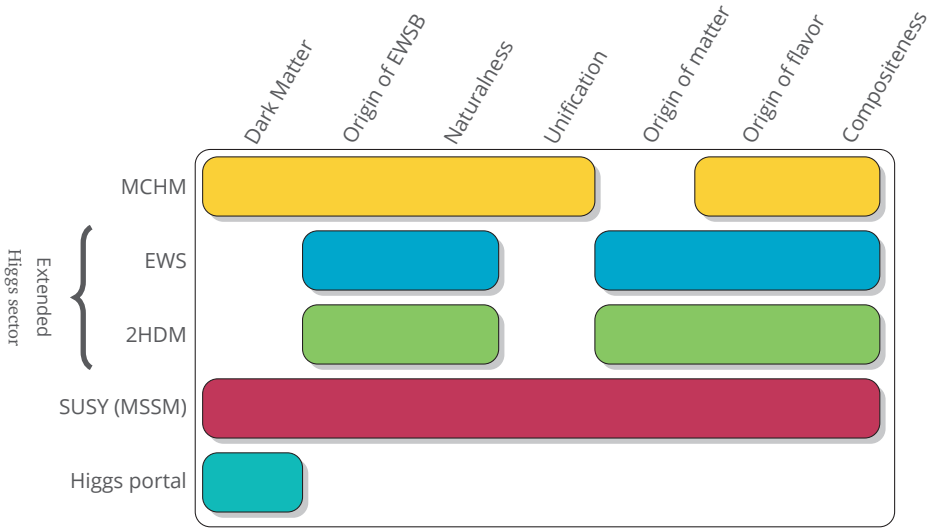

Figure 1.15: BSM scenarios discussed in this work and the big questions they could answer. Graphic adapted from Ref. [229].

Even though a non-zero VEV of a Higgs doublet seems to be responsible for EWSB, its dynamical origin is not known. EWSB in the SM is induced by manually forcing the lowest order of the Higgs self interaction to be negative. In supersymmetric models EWSB is promoted radiatively through the sizable top quark-Higgs coupling, which was mentioned already in the context of the naturalness problem. A wholly composite or partially composite Higgs boson could induce EWSB through strong dynamics around the weak scale and give hints about new forces in nature.

The origin of flavor, i.e. quarks, leptons, neutrinos and their mass hierarchies and mixing angles, is now known in the SM. Many scenarios of physics beyond the SM predict a flavor structure with implications for flavor-changing couplings, in particular flavor-changing neutral current decays. The direct or indirect evidence of such models would provide important insight into some of the most fundamental parameters of particle physics.

1.5.2 Minimal Composite Higgs Model

The SM scalar naturalness problem would be solved by the light Higgs boson being a composite pseudo Nambu-Goldstone (pNG) boson rather than an elementary particle as virtual quantum corrections to its mass become saturated at the compositeness scale in the same way as the mass of the QCD pion does not receive corrections from the Planck scale. [230]. This section introduces one explicit example of such theories, the Minimal

Composite Higgs Model (MCHM) [231–233][6], which is an interpolation between the EWSB mechanism introduced previously and strongly coupled technicolor (TC) [236]. The model can be derived entirely from symmetry considerations on a slice of anti-de Sitter (AdS) spacetime.

A five-dimensional strongly coupled Conformal Field Theory (CFT) with a global $\mathscr{G} = SO(5) \otimes U(1)_X$ gauge symmetry in the bulk is compactified by the IR and UV boundaries, i.e. it has a four-dimensional holographic representation [237]. On the IR boundary, $\mathscr{G}$ is dynamically broken down to $\mathscr{H}_1 = SO(4) \otimes U(1)_X$ with $SO(4)$ being isomorphic to the custodial symmetry $SU(2)_L \otimes SU(2)_R$ introduced in Sec. 1.2.2. On the UV boundary, the gauge symmetry in the bulk reduces to the SM EW gauge group $SU(2)_L \otimes U(1)_Y = \mathscr{G}_{\text{SM}} \subset \mathscr{G}$. The gauge bosons of the EW symmetry group remain external to the CFT. The SM EW group must be embedded in the unbroken subgroup $\mathscr{H}_1$ so that $\mathscr{H} = \mathscr{H}_1 \cap \mathscr{G}_{\text{SM}}$ is the unbroken gauge group and hypercharge is realized as $Y = T_3^R + X$. Hence, there are four real pNG bosons h^a $(a = 1, 2, 3, 4)$, i.e. a composite state of the CFT corresponding to the $SO(5)/SO(4)$ degrees of freedom of the fifth component of the five-dimensional gauge field, transforming as fundamentals under $SO(4)$, or equivalently as a real bi-doublet under $SU(2)_L \otimes SU(2)_R$, which can be identified with the Higgs boson.

The global symmetry in the bulk, $\mathscr{G}$, is explicitly broken by interactions between the SM fields and the CFT and dynamically generates, at the one-loop level, a Higgs potential, which, together with contributions coming from the fermions, notably the top quark, breaks the EW symmetry $\mathscr{G}_{\text{SM}}$. The Higgs VEV can be different by a scaling factor ξ from the sigma-model [238] scale f,

$$v^2 \equiv \xi f^2 = f^2 \sin^2 \frac{\langle h \rangle}{f} \quad \text{with} \quad h \equiv \sqrt{(h^a)^2} \quad \text{and} \quad f = \frac{1}{L_1} \frac{2}{\sqrt{g_5^2 k}} \tag{1.50}$$

and depends on the $SO(5)$ gauge coupling in the bulk g_5, the AdS_5 curvature radius $1/k$ as well as the position of the IR boundary in conformal coordinates L_1, which relates to the mass of the lightest gauge boson Kaluza-Klein (KK) resonance as $m_\rho \simeq 3\pi/4L_1$.

Finally, the trilinear couplings of the physical Higgs boson to the gauge fields follow from expanding the associated effective action around the VEV of the Higgs field $\langle h \rangle$,

$$g_{hVV} = g_{hVV}^{\text{SM}} \sqrt{1 - \xi}. \tag{1.51}$$

The form of the Yukawa interaction, and thus the fermion masses as well as the Higgs boson couplings to fermions, depends on the representation chosen for embedding the SM fermions in the $SO(5)$ bulk representation. Possible choices include the spinorial representation of $SO(5)$, containing two complex doublets, transforming under $SU(2)_L$ and $SU(2)_R$ respectively,

[6] Other approaches like Little Higgs (LH) models [234] or warped extra-dimensional field theories, e.g. Ref. [235], are documented in the literature, but shall not be discussed here.

and referred to as MCHM_4 [231], and the fundamental representation of $SO(5)$, given in Refs. [232, 233], and referred to as MCHM_5,

$$m_{u,d}^{\mathrm{MCHM}_4} \propto \sin\frac{\langle h\rangle}{f} \quad \text{and} \quad m_{u,d}^{\mathrm{MCHM}_5} \propto \sin\frac{\langle h\rangle}{f}\cos\frac{\langle h\rangle}{f}. \tag{1.52}$$

Thus, from the expansion around the Higgs VEV follow the Higgs fermion couplings

$$g_{hff}^{\mathrm{MCHM}_4} = g_{hff}^{\mathrm{SM}}\sqrt{1-\xi} \quad \text{and} \quad g_{hff}^{\mathrm{MCHM}_5} = g_{hff}^{\mathrm{SM}}\frac{1-2\xi}{\sqrt{1-\xi}}, \tag{1.53}$$

such that in the limit $\xi \to 0$ the SM is recovered and the resonances of the CFT decouple, $f \to \infty$, while the Higgs couplings vanish for $\xi \to 1$.

1.5.3 Additional electroweak singlet

The SM contains in its minimal version one complex Higgs doublet field, leading to a single physical Higgs boson after EWSB, as discussed in Sec. 1.2.2. The simplest extension of the SM leading to a more involved scalar sector is the addition of a real field X, which transforms as a singlet under the SM gauge group and thus is a possible candidate for solving the DM problem [135, 239–243]. The most general gauge-invariant and renormalizeable Lagrangian for this model follows from its SM counterpart (1.19) by adding kinetic terms for the new scalar field,

$$\mathscr{L}_{\mathrm{scalar}} = (D_\mu\Phi)^\dagger(D^\mu\Phi) + (D_\mu X)(D^\mu X) - V(\Phi, X) \tag{1.54}$$

and modifying the scalar potential (1.21) such that

$$V(\Phi, X) = -\mu_1^2\Phi^\dagger\Phi - \mu_2^2X^2 + \lambda_1(\Phi^\dagger\Phi)^2 + \lambda_2X^4 + \lambda_3\Phi^\dagger\Phi X^2. \tag{1.55}$$

The Potential is bounded from below for the quartic couplings satisfying

$$\lambda_1, \lambda_2 > 0 \quad \text{and} \quad \lambda_3 > -2\sqrt{\lambda_1\lambda_2}, \tag{1.56}$$

while μ_1^2 and μ_2^2 are chosen to be positive. The Higgs doublet field Φ as well as the electroweak singlet (EWS) field X acquire a non-zero VEV, v and x respectively. Spontaneous symmetry breaking is completely analogous to the SM calculation and leads to mixing between the singlet state and the surviving state of the doublet field,

$$\begin{pmatrix} h \\ H \end{pmatrix} = \begin{pmatrix} \cos\alpha & -\sin\alpha \\ \sin\alpha & \cos\alpha \end{pmatrix}\begin{pmatrix} \tilde{h} \\ \tilde{H} \end{pmatrix} \tag{1.57}$$

parametrized by the mixing angle α,

$$\tan\alpha = \frac{\lambda_3 vx}{-\lambda_1 v^2 + \lambda_2 x^2 + \sqrt{(\lambda_1 v^2 - \lambda_2 x^2)^2 + (\lambda_3 vx)^2}}. \tag{1.58}$$

The mass eigenvalues of the two CP-even Higgs bosons are

$$m^2_{h,H} = \lambda_1 v^2 + \lambda_2 x^2 \mp \sqrt{(\lambda_1 v^2 - \lambda_2 x^2)^2 + (\lambda_3 v x)^2}, \tag{1.59}$$

where h (H) denotes the lighter (heavier) mass eigenstate, assumed to be non-degenerate.

Mixing of the EW states further implies that the couplings of h to vector bosons V and fermions f are suppressed by $\kappa \equiv \kappa_V = \kappa_f = \cos\alpha$ compared to the SM, and similarly for the heavy state H by $\kappa' \equiv \kappa'_V = \kappa'_f = \sin\alpha$. Therefore, the production cross sections of the Higgs bosons relate to the SM according to

$$\sigma_h = \kappa^2 \times \sigma_{h,\mathrm{SM}} \quad \text{and} \quad \sigma_H = \kappa'^2 \times \sigma_{H,\mathrm{SM}}. \tag{1.60}$$

In case of no new states light enough for the lighter state to decay into, i.e. it is assumed to have identical decay modes to those of the SM Higgs boson, the BR for a given final state i is that of the SM, while the total decay width is reduced by κ^2,

$$\Gamma_h = \kappa^2 \times \Gamma_{h,\mathrm{SM}} \quad \text{and} \quad \mathrm{BR}_{h,i} = \mathrm{BR}_{h,\mathrm{SM},i}. \tag{1.61}$$

For the heavier Higgs boson H, if kinematically accessible, novel decay channels such as Higgs-to-Higgs decays $H \to hh$ are possible. Thus, the total decay width is composed of SM final states, suppressed by κ'^2, and invisible and di-Higgs final states, $\Gamma_H = \kappa'^2 \Gamma_{H,\mathrm{SM}} + \Gamma_{H,\mathrm{new}}$, such that

$$\Gamma_H = \frac{\kappa'^2}{1 - \mathrm{BR}_{H,\mathrm{new}}} \times \Gamma_{H,\mathrm{SM}} \quad \text{and} \quad \mathrm{BR}_{H,i} = (1 - \mathrm{BR}_{H,\mathrm{new}}) \times \mathrm{BR}_{H,\mathrm{SM},i}, \tag{1.62}$$

predicted for a SM Higgs boson with mass m_H. Hence, these Higgs states, h and H, fully unitarize the high-energy scattering amplitudes for longitudinal gauge boson scattering, $V_L V_L \to V_L V_L$ and $V_L V_L \to f\bar{f}$ with $V = W, Z$ and f being a fermion[7].

1.5.4 The Two Higgs Doublet Model

Another class of BSM models, termed 2HDMs, is constructed by adding a second complex isodoublet scalar field with weak hypercharge one to the SM scalar sector [135, 244–246]. These models capable of describing the phenomenon of CP violation, related to rare FCNC effects, which was one of the earliest reasons for them to be introduced. However, they also form the basis for a wide range of concrete examples, such as the MSSM, described in Sec. 1.5.5.

Typically, CP violating Higgs boson couplings, making it impossible to distinguish between scalars and pseudoscalars, as well as tree level FCNCs, which are strongly constrained by

[7] At the tree level, the Higgs boson production cross section and partial widths are proportional to the gauge boson and fermion couplings of the Higgs fields, relative to the corresponding SM couplings. Hence, assuming a common scaling factor, the constraint of unitarity implies that $\kappa^2 + \kappa'^2 = 1$.

existing data, are eliminated from the potential by additional discrete symmetries, such as the Paschos-Glashow-Weinberg condition [247, 248][8]. Under these assumptions, the most general gauge invariant scalar Higgs potential formed by the doublets Φ_1 and Φ_2, which allows a soft violation of the imposed requirements by dimension two terms, is given by

$$\begin{aligned} V(\Phi_1,\Phi_2) =& m_{11}^2\Phi_1^\dagger\Phi_1 + m_{22}^2\Phi_2^\dagger\Phi_2 - \left[m_{12}^2\Phi_1^\dagger\Phi_2 + \text{h.c.}\right] + \frac{1}{2}\lambda_1(\Phi_1^\dagger\Phi_1)^2 + \frac{1}{2}\lambda_2(\Phi_2^\dagger\Phi_2)^2 \\ &+ \lambda_3(\Phi_1^\dagger\Phi_1)(\Phi_2^\dagger\Phi_2) + \lambda_4(\Phi_1^\dagger\Phi_2)(\Phi_2^\dagger\Phi_1) + \left[\frac{1}{2}\lambda_5(\Phi_1^\dagger\Phi_2)^2 + \text{h.c.}\right], \end{aligned} \tag{1.63}$$

with all parameters being real and containing eight real scalar fields:

$$\Phi_a(x) = \frac{1}{\sqrt{2}}\begin{pmatrix} \phi_a^+(x) \\ v_a + \eta_a(x) + i\chi_a(x) \end{pmatrix} \quad \text{with} \quad \langle\Phi_a\rangle_0 = \frac{1}{\sqrt{2}}\begin{pmatrix} 0 \\ v_a \end{pmatrix} \quad \text{and} \quad a = 1,2 \tag{1.64}$$

Of these eight degrees of freedom, three massless Goldstone bosons become the longitudinal polarizations of the $W^\pm$ and Z bosons when acquiring mass, leaving five physical Higgs bosons: two neutral CP-even bosons h and H, one neutral CP-odd boson A, and a pair of charged scalars $H^\pm$. The angle β,

$$\tan\beta \equiv \frac{v_2}{v_1} \quad \text{with} \quad v^2 \equiv v_1^2 + v_2^2 = \frac{4m_W^2}{g_2^2} = (246\,\text{GeV})^2 \tag{1.65}$$

diagonalizes the mass-squared matrices of the charged scalars and the pseudoscalars, while the mass-squared matrix of the scalars, i.e. the two neutral, CP-even Higgs states, is diagonalized by the mixing angle α. These parameters fully determine the couplings of the various Higgs fields to the vector bosons and fermions.

In light of the discovered Higgs boson only the couplings of the light neutral scalar h to fermions and gauge bosons will be discussed in the following paragraph. Two discrete symmetries,

$$\Phi_1 \to -\Phi_1 \quad \text{and} \quad \Phi_1 \to -\Phi_1,\ \boldsymbol{d}_R \to -\boldsymbol{d}_R \tag{1.66}$$

ensure that the Paschos-Glashow–Weinberg condition is satisfied and in return define two types of 2HDMs, Type I and Type II respectively. Conventionally, in these models all right handed fermions transform in the same way under the imposed Z_2 symmetry and thus couple to the same Higgs doublet, making one doublet in the Type I model fermiophobic in the limit of no mixing. However, other conventions leading to natural flavor conservation, the lepton-specific and flipped 2HDMs, accommodate for different couplings, are summarized in Table 1.3. In the former the right handed quarks couple to Φ_2 and the right handed leptons to Φ_1, while in the latter the couplings of the quark sector are the same as in the Type II

[8] The Paschos-Glashow–Weinberg theorem states that "a necessary and suffcient condition for the absence of FCNC at tree level is that all fermions of a given charge and helicity transform according to the same irreducible representation of $SU(2)$, correspond to the same eigenvalue of T_3 and that a basis exists in which they receive their contributions in the mass matrix from a single source." [246]

Table 1.3: Yukawa couplings of the light Higgs boson h to up-type quarks (κ_u), down-type quarks (κ_d) and leptons (κ_ℓ), expressed as ratios of the corresponding SM predictions in 2HDMs of various types.

Coupling	Type I	Type II	Lepton specific	Flipped
κ_u	$\cos\alpha/\sin\beta$	$\cos\alpha/\sin\beta$	$\cos\alpha/\sin\beta$	$\cos\alpha/\sin\beta$
κ_d	$\cos\alpha/\sin\beta$	$-\sin\alpha/\cos\beta$	$\cos\alpha/\sin\beta$	$-\sin\alpha/\cos\beta$
κ_ℓ	$\cos\alpha/\sin\beta$	$-\sin\alpha/\cos\beta$	$-\sin\alpha/\cos\beta$	$\cos\alpha/\sin\beta$

model and the lepton sector is identical to Type I. All models have in common the coupling of the right handed up type quarks to Φ_2 and the couplings of h to vector bosons, fixed by gauge invariance,

$$\kappa_V \equiv \frac{g_{hVV}^{\text{2HDM}}}{g_{hVV}^{\text{SM}}} = \sin(\beta-\alpha). \tag{1.67}$$

Thus, in the limit $\sin(\beta-\alpha)\to 1$, termed SM alignment limit, the SM is recovered for h. The introduced couplings unitarize the longitudinal gauge boson scattering amplitudes.

1.5.5 The Minimal Supersymmetric Standard Model

SUSY [249–257], the first non-trivial extension of the Poincaré group in QFT, postulates the existence of superpartners, differing by spin $1/2$ from the SM particles. The presence of softly broken SUSY is motivated by phenomenological arguments, as it provides, if realized at low energies, means to simultaneously solve the naturalness and hierarchy problems by canceling divergent loop contributions of the heavy SM particles to the Higgs boson mass by those of the corresponding SUSY partners [258–263], as well as a candidate for a DM particle, e.g. through enforcing lepton and baryon number conservation through introducing a discrete symmetry, R-parity [264, 265], in the MSSM [258, 266–269].

The MSSM is a concrete realization of a 2HDM of Type II with a strict upper bound on the mass of the lightest Higgs boson h, $m_h < m_Z$ at tree level, which however is broken by higher order radiative corrections. An extensive review of the rich phenomenology of its scalar sector can be found in Ref. [270], however, in the following the focus will be put on the scalar sector of a simplified MSSM model, the hMSSM, in which the discovered Higgs boson is identified with the light CP-even state h [271, 272]. In this model the mass squared mixing matrix of the neutral, CP even Higgs bosons reads

$$\begin{aligned}\mathscr{M}_S^2 = (m_Z^2+\delta_1)&\begin{pmatrix}\cos^2\beta & -\cos\beta\sin\beta\\ -\cos\beta\sin\beta & \sin^2\beta\end{pmatrix}\\ &+m_A^2\begin{pmatrix}\sin^2\beta & -\cos\beta\sin\beta\\ -\cos\beta\sin\beta & \cos^2\beta\end{pmatrix}+\begin{pmatrix}0 & 0\\ 0 & \frac{\delta}{\sin^2\beta}\end{pmatrix}\end{aligned} \tag{1.68}$$

where δ_1 and δ are radiative corrections arising primarily from top quark and top squark loops and are given as a function of m_A and the ratio of the VEVs of the two doublet fields $\tan\beta$ [273]. Neglecting the subdominant correction $|\delta_1/\delta| \leq 0.25$ at low SUSY breaking scales, the MSSM sacalar sector is entirely described by the mass of the CP-odd boson A, m_A, and $\tan\beta$ at the light Higgs boson mass m_h, which fixes the dominant radiative corrections involving SUSY parameters, in particular

$$\frac{\delta}{\sin^2\beta} = \frac{(m_A^2 - m_h^2)(m_h^2 - m_Z^2) + m_A^2 m_Z^2 \sin^2 2\beta}{\sin^2\beta\, m_A^2 - (m_h^2 - m_Z^2 + \sin^2\beta\, m_Z^2)} \tag{1.69}$$

Hence, the mass matrix is diagonalized to find the eigenvectors corresponding to the physical states and thus the Higgs boson couplings to vector bosons (κ_V), up-type fermions (κ_u) and down-type fermions (κ_d), expressed as ratios to the corresponding SM predictions,

$$\kappa_V = s_d(m_A, \tan\beta)\frac{1}{\sqrt{1+\tan^2\beta}} + s_u(m_A, \tan\beta)\frac{\tan\beta}{\sqrt{1+\tan^2\beta}}, \tag{1.70}$$

$$\kappa_u = s_u(m_A, \tan\beta)\frac{\sqrt{1+\tan^2\beta}}{\tan\beta} \quad \text{and} \quad \kappa_d = s_d(m_A, \tan\beta)\sqrt{1+\tan^2\beta}. \tag{1.71}$$

The functions $s_u = \sin\alpha$ and $s_d = \cos\alpha$ diagonalize the CP-even neutral states,

$$s_u = \frac{1}{\sqrt{1 + \frac{\left(m_A^2+m_Z^2\right)^2\tan^2\beta}{\left(m_Z^2+m_A^2\tan^2\beta - m_h^2\left(1+\tan^2\beta\right)\right)^2}}} \quad \text{and} \quad s_d = \frac{\left(m_A^2+m_Z^2\right)\tan\beta}{m_Z^2 + m_A^2\tan^2\beta - m_h^2\left(1+\tan^2\beta\right)} s_u. \tag{1.72}$$

Additional corrections which arise in the MSSM can lead to a breaking of the universality of down-type fermion couplings, such that for example $\kappa_b \neq \kappa_\tau$, though it has been shown that these are generally subdominant [272] and thus not included in the studied model. Also, production cross sections and decay rates of the light Higgs boson are subject to corrections, such as top squark contributions to the ggF process, e.g. Refs. [274–276], Higgs boson decays to SUSY particles, Higgs-to-Higgs decays, or other effects from light SUSY particles [277], which are neglected in light of current experimental results.

1.5.6 Dark Matter and the Higgs portal model

Many BSM scenarios postulate a weakly interacting massive particle (WIMP) as DM candidate. Even though it generally interacts very weakly with the SM particles, a portal to DM opens through the gauge invariant interaction of the DM candidate with the scalar sector such that the SM fields could interact elastically with the hidden sector by Higgs boson exchange, terming these models Higgs portal to DM [243, 278–282].

The Higgs-WIMP interactions depend on the spin of the DM candidate and read for real scalars S, vectors V, or Majorana fermions f, which are motivated by neutralinos in SUSY,

$$\mathscr{L}_{hSS} = -\frac{1}{2}m_S^2 S^2 - \frac{1}{4}\lambda_S S^4 - \frac{1}{4}\lambda_{hSS}\Phi^\dagger\Phi S^2 \tag{1.73}$$

$$\mathscr{L}_{hVV} = \frac{1}{2}m_V^2 V_\mu V^\mu + \frac{1}{4}\lambda_V (V_\mu V^\mu)^2 + \frac{1}{4}\lambda_{hVV}\Phi^\dagger\Phi V_\mu V^\mu \tag{1.74}$$

$$\mathscr{L}_{hff} = -\frac{1}{2}m_f \bar{f} f - \frac{1}{4}\frac{\lambda_{hff}}{\Lambda}\Phi^\dagger\Phi \bar{f} f \tag{1.75}$$

where λ_{hSS}, λ_{hVV} and λ_{hff} are the couplings of the Higgs boson to the DM candidates of the indicated spin and the mass scale Λ is of the same size as the mass of the mediator, assuming a coupling of $\mathcal{O}(1)$ [280].

Spin dependent, discrete Z_2 symmetries ensure the stability of the DM particles, while the Higgs boson could decay into light DM states, that is assuming the WIMP mass to be less than half the Higgs boson mass, shown in Fig. 1.16a, which escape detection and thus are invisible [283]. Measuring the Higgs partial decay widths into a pair of DM particles are given by [280]

$$\Gamma^{\text{inv}}(h \to SS) = \lambda_{hSS}^2 \frac{v^2 \beta_S}{128\pi m_h} \tag{1.76}$$

$$\Gamma^{\text{inv}}(h \to VV) = \lambda_{hVV}^2 \frac{v^2 \beta_V m_h^3}{512\pi m_V^4}\left(1 - 4\frac{m_V^2}{m_h^2} + 12\frac{m_V^4}{m_h^4}\right) \tag{1.77}$$

$$\Gamma^{\text{inv}}(h \to ff) = \frac{\lambda_{hff}^2}{\Lambda^2}\frac{v^2 \beta_f^3 m_h}{64\pi} \tag{1.78}$$

with the kinematic factor $\beta_\chi = \sqrt{1 - 4m_\chi^2/m_h^2}$ associated with the two-body $h \to \chi\chi$ decay and the m_χ being the physical masses of the DM particles after EWSB, allows to deduce the coupling scale factor $\lambda_{h\chi\chi}$ for each of the possible models.

Hence, the properties of the WIMP candidates, i.e. its mass and the cross section for WIMP-nucleon scattering via Higgs boson exchange, $\sigma_{\chi-N}$, shown in Fig. 1.16b, can be probed indirectly, and thus complementary to direct detection experiments [284–290], by

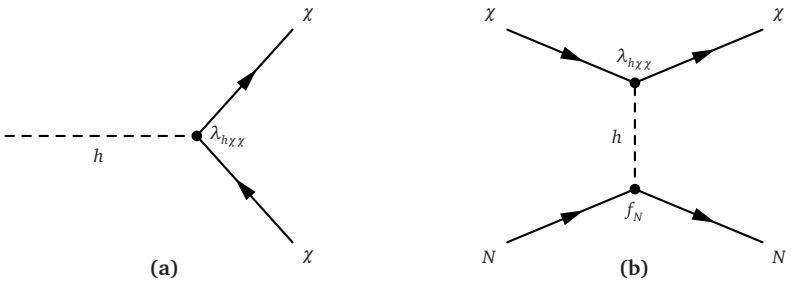

Figure 1.16: Feynman diagrams showing (a) the decay of a SM Higgs boson into light DM states and (b) WIMP-nucleon scattering via Higgs boson exchange.

re-interpreting the measured couplings of the Higgs boson to the DM candidates [278]. The cross section is given by

$$\sigma_{S-N} = \lambda_{hSS}^2 \frac{m_N^4 f_N^2}{16\pi m_h^4 (m_S + m_N)^2} \tag{1.79}$$

$$\sigma_{V-N} = \lambda_{hVV}^2 \frac{m_N^4 f_N^2}{16\pi m_h^4 (m_V + m_N)^2} \tag{1.80}$$

$$\sigma_{f-N} = \frac{\lambda_{hff}^2}{\Lambda^2} \frac{m_N^4 f_N^2 m_f^2}{4\pi m_h^4 (m_f + m_N)^2} \tag{1.81}$$

with m_N being the nucleon mass and $f_N = \sum f_L + 3 \times \frac{2}{27} f_H$ parametrising the Higgs-nucleon coupling in terms of contributions of light quarks, f_L, and heavy quarks, f_H, that are estimated using lattice QCD [291, 292].

1.5.7 Effective field theory

The various models discussed in the previous sections predict observables that can directly be compared with experimental data in order to search for NP beyond the SM. The number of the arising degrees of freedoms can become enormously large and a priori it is not clear how to search for these models or even which of them are correct. All measurements performed by the LHC experiments are in remarkable agreement with the SM prediction. This calls for a model independent parametrization of any possible deviation from the predicted EW sector in terms of an effective Lagrangian for the light Higgs doublet. Such an effective description is valid as long as any effect of the NP states is (up to logarithmic contributions) suppressed by inverse powers of the heavy scale Λ at which they appear [293–297].

The construction of effective theories has become a standard tool in particle physics and is applied for example to the description of heavy quarks in flavor physics [298–300]. The

effective Lagrangian is expanded into a sum of local operators O_i, which contain the long-distance contributions from scales below Λ, multiplied with Wilson coefficients $C_i(\Lambda)$, which contain the short-distance contributions above the scale Λ:

$$\mathscr{L} = \mathscr{L}_{\mathrm{SM}} + \sum_k \frac{1}{\Lambda^k} \sum_i C_{ik}(\Lambda) O_{ik}. \tag{1.82}$$

Only one dimension-5 operator is compatible with the SM (gauge) symmetry and generates a Majorana mass for the left-handed neutrinos. Most next-to-leading terms in the Λ^{-k} expansion are given by dimension-6 operators[9]. They have been systematically classified in Refs. [301, 302]. References [303, 304] work towards an exhaustive list of the constraints on the various Wilson coefficients and the effect of the various operators on production and decay rates and other physical observables relevant to Higgs physics. Employing a model independent framework for measuring the Higgs boson couplings is a key aspect in the Higgs physics pursued during Run 2 of the LHC.

[9] The mass dimension of fields can be calculated from the requirement that the action in D space-time dimensions $S = \int \mathrm{d}^{\mathrm{D}} x \mathscr{L}(x)$ should be dimensionless. For $D = 4$ the mass dimensions of quark fields, covariant derivatives, Higgs fields and field strengths are $\dim[\mathrm{q}] = 3/2$, $\dim[\mathrm{iD}_\mu] = 1$, $\dim[\Phi] = 1$, and $\dim[\mathrm{W}_{\mu\nu}] = \dim[\mathrm{B}_{\mu\nu}] = \dim[\mathrm{G}^{\mathrm{a}}_{\mu\nu}] = 2$ respectively.

The LHC and the ATLAS and CMS detectors

2

The elucidation of the mechanism of EWSB through measuring the properties of the discovered Higgs boson, i.e. its mass and couplings to SM particles in addition to the spin and CP properties, and the search for BSM phenomena in the scalar sector, is a highlight of the experiment's extensive physics programs at the LHC [11–13, 16] at CERN. For this purpose the particle collisions provided by the LHC are recorded by various detectors, notably the 4π general purpose experiments ATLAS [14, 17, 305] and CMS [15, 18, 306], but also the ALICE [307] and LHCb [308] detectors, devoted to the study of heavy ion collisions, in particular the quark-gluon plasma, and flavor physics, respectively, and the smaller experiments LHCf [309], MoEDAL [310] and TOTEM [311]. This chapter summarizes at first the technical design and performance of the LHC accelerator complex, before subsequently discussing the multipurpose detector systems ATLAS and CMS relevant to the Higgs analyses described in the following chapters.

2.1 The Large Hadron Collider

2.1.1 The CERN accelerator complex

The LHC is a circular, two-ring-superconducting hadron-hadron, accelerator and collider. In this document recorded data from proton-proton collisions is interpreted. The LHC is hosted in the 27 km former LEP [313, 314] underground tunnel which is situated at CERN, near the city of Geneva, Lac Léman and the Jura mountains between 45 m and 170 m below soil. It shares the geometry of the LEP collider with eight arcs and eight straight sections. The LHC is designed to operate at centre-of-mass collision energies of up to $\sqrt{s} = 14\,\text{TeV}$, though the delivered centre-of-mass energy was $\sqrt{s} = 7\,\text{TeV}$ during 2010 and 2011 and $\sqrt{s} = 8\,\text{TeV}$ in 2012 for proton-proton collisions. The reason to run at a lower energy than the design value is an accident during the initial start-up in September 2008. The increase of the centre-of-mass energy from $\sqrt{s} = 7\,\text{TeV}$ to $\sqrt{s} = 8\,\text{TeV}$ is motivated by the increasing production cross sections for signal processes, e.g. for the Higgs boson, relative to the increase of the background rates.

The colliding hadrons traverse a chain of pre-accelerators, which is shown in Fig. 2.1. Hydrogen atoms have their valence electron stripped off so that the remaining protons can be accelerated to 50 MeV in the Linear accelerator 2 (LINAC2). They are injected into the Proton

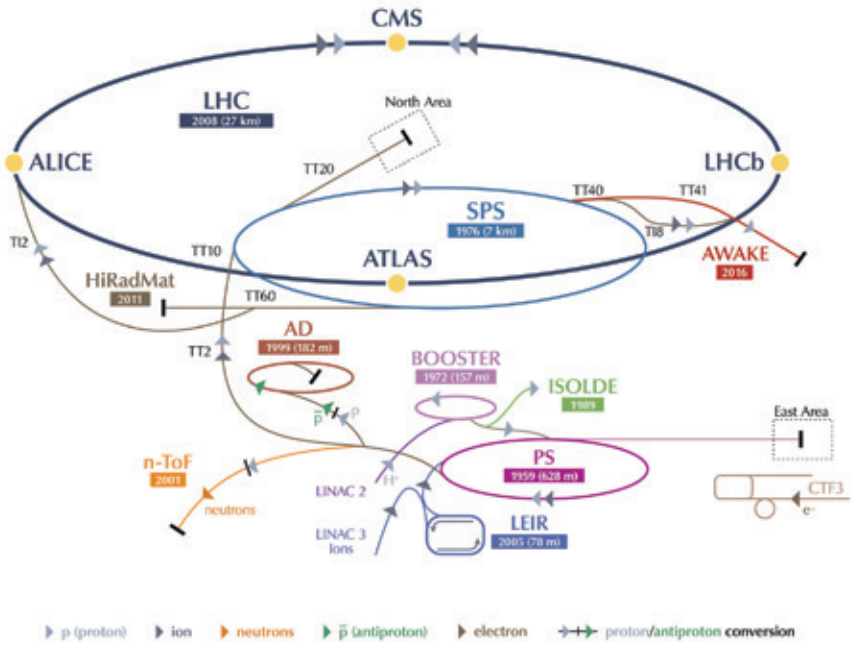

Figure 2.1: The CERN accelerator complex. The injection chain traversed by protons colliding in the LHC is described in the body. Figure adapted from Ref. [312].

Synchrotron Booster (PSB), the first circular pre-accelerator in a series of three, increasing the energy further to 1.4 GeV. The remaining two, i.e. the Proton Synchrotron (PS) and the Super Proton Synchrotron (SPS), accelerate the protons to energies of 25 GeV and 450 GeV respectively. Eventually they are arranged in bunches of nominally 1.1×10^{11} protons and injected into the LHC with a bunch spacing of down to 25 ns. Each beam is composed of up to 2808 bunches. The beams, will be captured, accelerated to the designated centre-of-mass energy, and stored using a 400 MHz superconducting Radio Frequency (RF) cavity system. Beyond this, the system is also used for damping longitudinal injection errors. It is composed of eight cavities per beam, which are operated at 4.5 K and deliver 2 MV each. The accelerating field is 5 MV/m.

The use of two counter-rotating particle beams, instead of colliding particles with their anti-particles, is motivated by the high beam intensity required to achieve the performance goals, in particular the design luminosity, and requires their phase space to be separated. However, the limited physical space in the former LEP tunnel demands the use of a two-in-one or twin-bore design, pioneered at Brookhaven National Laboratory (BNL), which couples the rings both magnetically and mechanically. The 1232 dipole magnets have two apertures, i.e. one for each particle beam. They are operated at temperatures below 2 K and with a

current of 11700 A to maximize the magnetic field strength, which is 8.33 T in the peak. The high magnetic field bends the paths of the particle beams.. Complementary to the dipole magnets, 392 quadrupole magnets are installed which stabilize the particle beams and focus them.

Four of the straight sections serve as experimental insertion, i.e. the proton beams cross each other at these locations, allowing particle detectors to study the collisions. The ATLAS and CMS detectors are located at diametrically opposite sections of the accelerator, which they share with LHCf and TOTEM respectively. The two experiments operating at lower luminosity, ALICE and LHCb, sharing the cavern with MoEDAL, are located at Point 3 and Point 8. The remainder of this chapter is dedicated to the description of the two high luminosity experiments ATLAS and CMS.

2.1.2 Luminosity and pile-up

The LHC is designed to have a nominal instantaneous luminosity of $L = 10^{34}\,\mathrm{cm}^{-2}\mathrm{s}^{-1}$, which depends only on the beam parameters and, assuming a Gaussian beam distribution and equal beam parameters for both beams, reads [16]

$$L = \frac{N_b^2 n_b f_{\mathrm{rev}}}{4\pi\sigma^{*2}} F \quad \text{with} \quad F = \left(1 + \left(\frac{\theta_c \sigma_z}{2\sigma^*}\right)^2\right)^{-\frac{1}{2}} \tag{2.1}$$

where N_b is the number of particles per bunch, n_b the number of bunches per beam, f_{rev} the revolution frequency[1], $\sigma^*_{x,y}$ the transverse root mean square (RMS) beam size at the interaction point, and F the geometric luminosity reduction factor due to the crossing angle at the interaction point, which depends on θ_c being the full crossing angle at the interaction point, σ_z the RMS bunch length, and σ^*. The beta function at the collision point, defined as $\beta^* = \pi\sigma^{*2}/\varepsilon_n$, with the transverse beam emittance ε, is a measure of the beam's squeezing. The total number of events generated in collisions is then given by

$$N_{\mathrm{event}} = \mathscr{L}\sigma_{\mathrm{event}} \quad \text{with} \quad \mathscr{L} = \int L\,\mathrm{d}t \tag{2.2}$$

and depends on the integrated luminosity $\mathscr{L}$ measured in units of inverse barns, where $1\,\mathrm{b} = 10^{-28}\,\mathrm{m}^2$, and the cross section σ_{event} of the process under study. Figures 2.2a and 2.2c show the cumulative luminosity versus day delivered to ATLAS and CMS respectively during stable beam conditions and for proton-proton collisions in 2010, 2011 and 2012.

The number of inelastic proton-proton interactions per bunch crossing, termed pile-up events, follows a Poisson distribution with mean value μ, which is proportional to the beam intensity,

[1] The revolution frequency $f_{\mathrm{rev}} = \beta c/2\pi R$, with R being the machine radius, defines also the RF frequency $f_{\mathrm{RF}} = h f_{\mathrm{rev}}$ of the cavity system, which must be an integer multiple of the revolution frequency. The harmonic number h is limited to 35640 at the LHC.

inversily proportional to the emittance, and also varies between colliding bunches. Hence, the average over all bunch crossings and the integrated luminosity is typically referred to as $\langle\mu\rangle$. In data, μ is calculated from the instantaneous luminosity L, the number of colliding bunches n_b and the revolution frequency f_{rev}, all introduced previously, as well as the total inelastic cross section σ_{inel}, which is taken from PYTHIA [315] to be 71.5 mb for 7 TeV collisions and 73.0 mb for 8 TeV collisions,

$$\mu = \frac{L\sigma_{\text{inel}}}{n_b f_{\text{rev}}}. \tag{2.3}$$

Hence, the uncertainty on μ depends predominantly on the uncertainty of the luminosity measurement, 1.8 % for 7 TeV [316] and 2.8 % for 8 TeV, which is derived, following the same methodology as that detailed in Ref. [316], from a preliminary calibration of the luminosity scale derived from beam-separation scans performed in November 2012, and the total inelastic cross section, independently, and complementary to the used simulations, estimated by TOTEM [133, 317] and ATLAS [318] by extrapolating the measured cross section for events in the acceptance of scintillators in the forward region. Similar analyses have been performed by the CMS collaboration [319, 320] and reveal a luminosity uncertainty of 2.2 % and 2.6 % in the signal yield in the data recorded at 7 TeV and 8 TeV, respectively. The uncertainties in the measured integrated luminosities are partially correlated between the two experiments.

In addition to the previously described in-time pile-up, so called out-of-time pile-up, i.e. interactions from neighboring bunch crossings, can occupy detector sub-systems during read out. The luminosity-weighted distributions of the mean number of interactions per crossing measured by ATLAS and CMS are shown in Fig. 2.2b and Fig. 2.2d respectively. A detailed description of the performance of the ATLAS detector, in particular the ID, in high-occupancy scenarios will be given in Cha. 3. Table 2.1 summarizes the main beam and machine parameters as well as the performance of the LHC during the first years of data taking and compares it to the design values.

2.2 The ATLAS detector

The ATLAS detector, shown in Fig. 2.3, is a general purpose detector designed in particular for the search for NP phenomena at the TeV scale, but also for precision measurements of SM parameters. It covers almost hermetically the detection of particle collisions provided by the LHC in the full 4π solid angle by combining several sub-detector systems installed in layers around the interaction point. Each of them serves a particular purpose in the study of the collisions, which will be detailed in the remainder of this section, focusing on the requirements dictated by search for Higgs physics and measurements of the Higgs boson properties in the various production and decay modes, while a more extensive review is given in Ref. [17] and references therein.

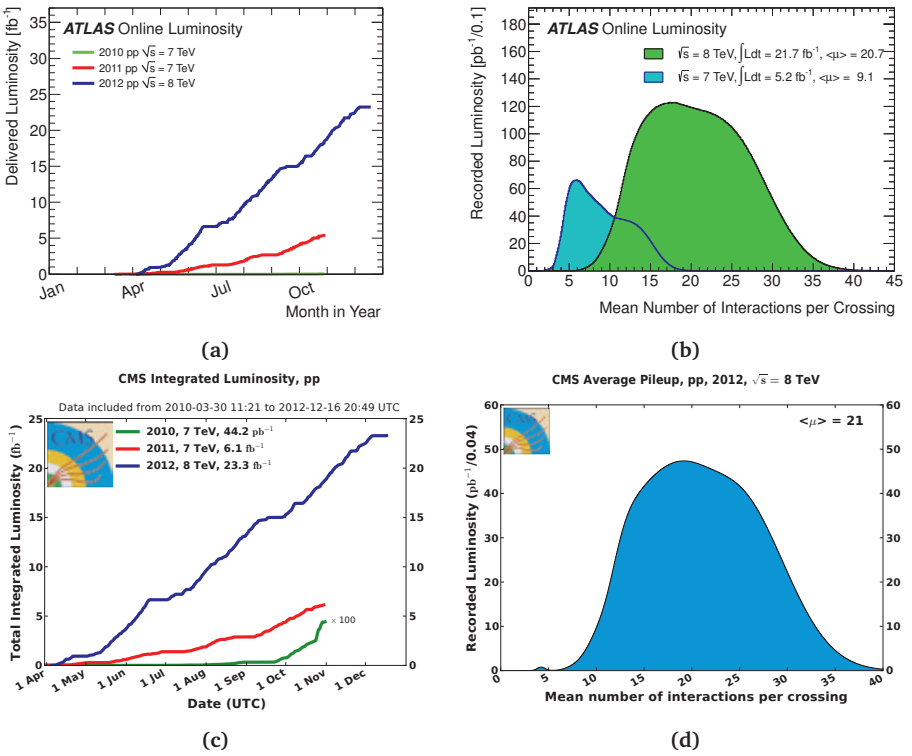

Figure 2.2: Cumulative luminosity versus day delivered to (a) ATLAS and (c) CMS during stable beam conditions and for proton-proton collisions. This is shown for 2010 (green), 2011 (red) and 2012 (blue) data-taking and luminosity-weighted distribution of the mean number of interactions per crossing for (b) the full 2011 (green) and 2012 (blue) dataset of ATLAS and (d) the full 2012 dataset of CMS. The integrated luminosities and the mean μ values are given in the figures. The mean number of interactions per crossing corresponds the mean of the poisson distribution on the number of interactions per crossing calculated for each bunch.

Processes involving a SM or BSM Higgs boson as introduced in Cha. 1 played a crucial role in the design of the ATLAS detector. After the discovery of the Higgs boson, the study of its properties exploits the full performance of the ATLAS detector. At the measured mass value of about 125 GeV most couplings of the Higgs are directly accessible through its various production and decay modes.

Coordinate system

The ATLAS barrel is invariant under discrete rotations around the beam axis and the two circular end-caps, closing off the sides of the barrel, guarantee forward-backward symme-

Table 2.1: Main beam and machine parameters as well as performance of the LHC during the first years of data taking during proton-proton collisions. For the ATLAS specific rows exist similar values from the CMS experiment. Parameters shown are the best achieved for that year in normal physics operations. The values for 2010, 2011 and 2012 data have been extracted from the ATLAS Data Summary pages [321], and the design values are taken from [11].

Parameter	2010	2011	2012	design
Centre-of-mass energy $\sqrt{s}$ [TeV]	7	7	8	14
Maximum number of bunch pairs colliding	348	1854	1380	2808
Minimum bunch spacing for physics [ns]	150	50	50	25
Typical bunch population $\left[10^{11}\,\text{protons}\right]$	0.9	1.2	1.6	1.15
Peak instantaneous luminosity $\left[10^{33}\,\text{cm}^{-2}\text{s}^{-1}\right]$	0.21	3.65	7.73	10
Delivered integrated luminosity $\left[\text{fb}^{-1}/\text{year}\right]$	0.049	5.6	23.1	80 - 120
ATLAS recorded integrated luminosity $\left[\text{fb}^{-1}/\text{year}\right]$	0.045	5.3	21.7	–
Average number of interactions $\langle\mu\rangle$	–	9.1	20.7	19.02
Maximum inelastic interactions per crossing	3.8	32.2	69.5	–

try with respect to the nominal interaction point which defines the center of the detector. Motivated by this geometry, typically a cylindrical coordinate system is used to describe the ATLAS experiment itself as well as its recorded data. The azimuthal angle $\phi \in [-\pi, \pi]$ is measured around the beam axis z and the pseudorapidity $\eta = -\ln\tan(\theta/2)$, invariant under longitudinal boosts in z-direction, with the polar angle $\theta \in [0, \pi]$ is the angle from the beam axis[2]. Hence, the conditions $\phi = 0$ along the x-axis, which is pointing radially inward to the center of the LHC ring, and $\theta = 0$ in positive z-direction define a right-handed coordinate system with the x-y plane being transverse to the beam axis and the y-axis pointing upwards. Thus, the momentum and energy transverse to the beam direction, denoted by p_{T} and E_{T}, respectively, are computed in the x-y plane.

2.2.1 Particle detection and identification

Figure 2.4 shows an illustration of the signatures of different particles in the ATLAS detector as they occur in the rich set of physics processes studied at the LHC. Each particle leaves a unique fingerprint in one or more of the detector sub-systems. The information needed for their identification can be classified into position and energy measurements. A detailed review of particle detection is for example given in Ref. [322].

Charged particles deposit energy along their path through the detector. These energy deposits, in the following referred to as hits, are used to build a distinct trajectory, which is associated with a charged particle. Trajectories are reconstructed using a high-resolution tracking device close to the interaction point and the muon spectrometer surrounding all

[2] In case of massive objects, e.g. jets, the rapidity $y = 1/2\ln\left[(E + p_z)/(E - p_z)\right]$ is used instead of the pseudorapidity.

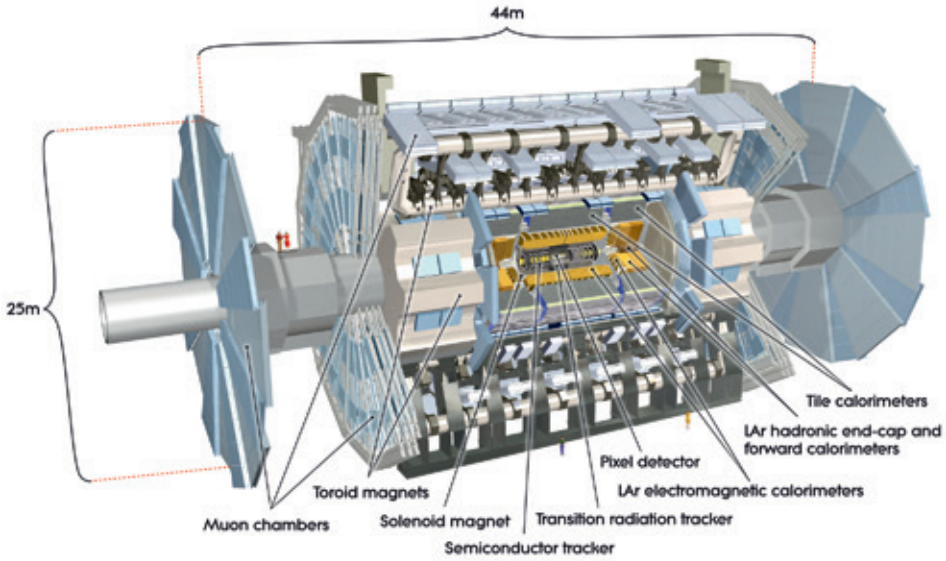

Figure 2.3: Cut-away view of the ATLAS detector. The various detector sub-systems are indicated and labeled. The humans shown on the left of detector indicate the size of the apparatus, 44 m in length, 25 m in height, and weight of approximately 7000 t. Figure taken from Ref. [17].

other sub-detectors. In the very center of the detector semiconductor track detectors are used, i.e. solid state detectors with a high-density doped material in which charged particles produce electron–hole pairs that can be collected. Additionally transition radiation below the Cherenkov threshold, i.e. the electromagnetic radiation emitted when a charged particle traverses an inhomogeneous medium, e.g. the boundary between a dielectric and a gas, is used for particle identification. The charge and mass of the particle can be reconstructed by measuring the curvature of the helix in a magnetic field. The interaction point of a collision, i.e. the vertex, can be inferred by tracing all reconstructed tracks back to a common region in the center of the detector.

Calorimeters measure the energy of both charged and neutral particles traversing the detector through their interactions with the dense absorbing material. The dominant processes for high-energy charged particles are photon emission, i.e. bremsstrahlung, and ionisation. High-energy photons produce predominantly e^+e^- pairs. The particles will lose their energy in a cascade of additional electromagnetic or hadronic particles, called shower. The number of produced shower particles is subsequently measured in thin layers of an active medium, from which the energy of the initial particle can be deduced. The calorimater in ATLAS are sampling calorimeters, i.e. they are constructed of several alternating layers of absorber

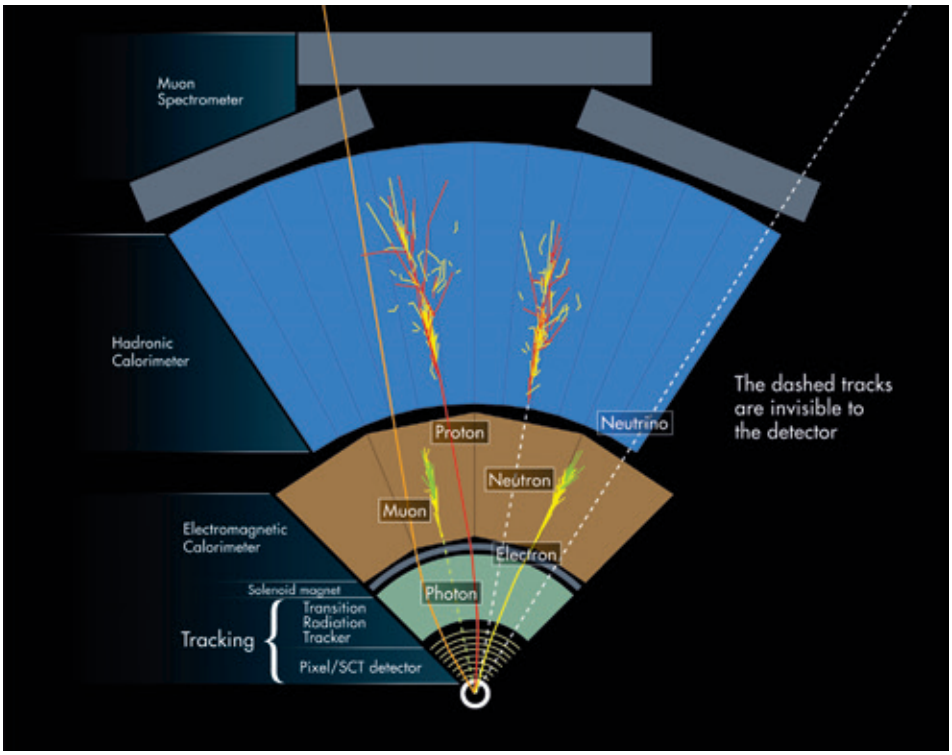

Figure 2.4: Illustration of signatures of different particles in the ATLAS detector as they occur in the rich set of SM and BSM Higgs boson decays, each leaving a unique fingerprint in one or more of the detector sub-systems. Figure taken from Ref. [323].

material and active material. The longitudinal and lateral shower profile and its penetration depth into the calorimeter system are additional useful information to distinguish different particle types. Showers originating from electromagnetic particles are characterized by a dense narrow profile contained in the electromangnetic calorimeter (ECAL). Strongly interacting particles will produce broader showers that deeply penetrate the hadronic calorimeter (HCAL).

The combination of these information is sufficient to identify any particle produced in a particle collisions: muons i.e. minimum ionizing particles, typically leave only little energy in the calorimeters and do not initiate a shower. They can be identified by a track in the muon spectrometer, since all other detectable particles are stopped before reaching this sub-detector. Matching this track to a trajectory in the center of the detector further enhances the identification of muons. Electrons are characterized by a track in the inner tracking system associated with the primary collision vertex and matched to a shower contained

in the ECAL. If the track of such a shower is associated with a displaced vertex in the ID, the incident particle is a converted photon. Similarly, if no track can be matched to an electromagnetic shower, it was initiated by an unconverted photon. A broad shower in the HCAL associated with a reconstructed track indicates a charged hadron, e.g. a proton or charged pion. In case no track matches with the shower, it is initiated by a neutral hadron, e.g. a neutron or neutral pion. τ-leptons have a too short decay length to reach the detector and can only be identified through the reconstruction of their decay products, i.e. electrons, muons and hadrons. High-momentum neutrinos interact only weakly with the detector and escape without being detected, but their presence can be inferred from MET in the event, c.f. Sec. 3.3. The performance of the reconstruction algorithms for the various physics objects is discussed in more detail in Cha. 3.

2.2.2 Inner Detector

The ID tracking system consists of three independent sub-detectors: two silicon-based detectors in the inner part of the tracking volume, i.e. Pixel and Semiconductor Tracker (SCT), and the Transition Radiation Tracker (TRT) in the systems outer part. The ID provides hermetic, efficient and robust pattern recognition to measure the trajectories of charged particles, precise impact parameter measurements as well as primary and secondary vertex identification. Pixel and SCT detector use complementary technologies, pixels and microstrips respectively, with a coverage in $|\eta|$ that is limited to 2.5. The TRT is made from polyimide drift tube elements filled with a xenon-based gas mixture. It detects the transition radiation photons generated by traversing particles and covers the pseudorapidity range up to $|\eta| < 2.1$.

The performance of the inner detector and tracking is vital for several aspects of the Higgs boson studies performed by the ATLAS collaboration and presented here. Measurements involving leptons, e.g. in the $H \to ZZ^* \to 4\ell$ and $H \to WW^* \to \ell\nu\ell\nu$ channels, require a robust identification of electrons and high p_{T} muons and accurate measurement of their momentum. Muons from Higgs boson decays have to be distinguished from charged hadron decays. The $H \to \gamma\gamma$ decay mode can only be exploited by efficiently separating electrons from photon conversions. Jets are an important signature of e.g. the Higgs production through VBF, but also of heavy flavor decays. Hence, it is important to identify showers initiated by b-quarks, as they appear both in signal processes, e.g. in the $H \to b\bar{b}$ decay, and in many reducible and irreducible background processes to the studied Higgs signals, e.g. $t\bar{t}$ production competing with the ttH process or $H \to WW^* \to \ell\nu\ell\nu$ decays. The ID is designed to cope with these tasks. Chapter 3 discusses the the performance of the ID and its role in reconstructing physics objects.

The layout of the ID is illustrated in Fig. 2.5 and consists of a barrel part and two end-caps within a superconducting solenoidal coil that provides a 2 T axial magnetic field. The barrel is composed of several cylindrical layers of sensors arranged concentrically around the beam

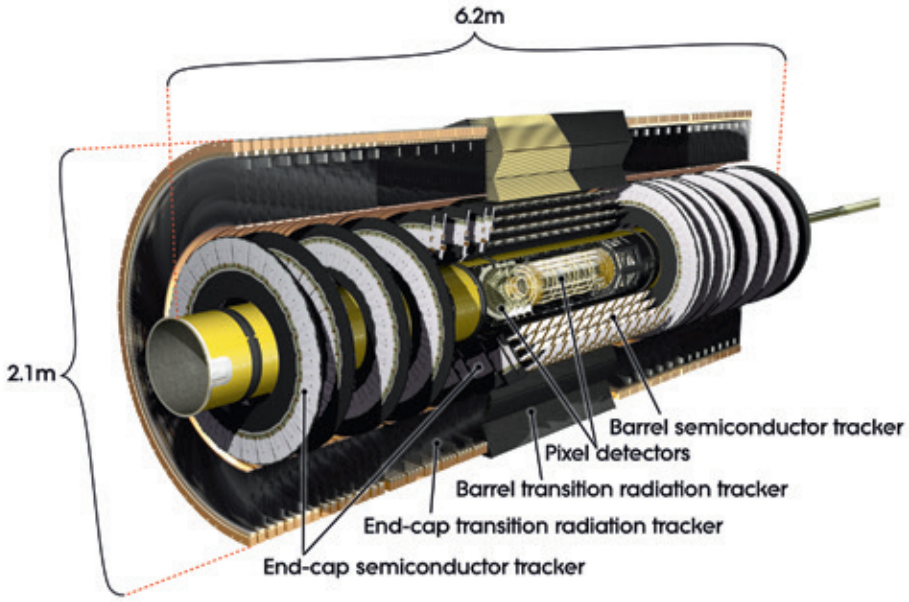

Figure 2.5: Cut-away view of the ATLAS ID. Figure taken from Ref. [17].

Table 2.2: Main characteristics of the three ATLAS ID detector components and the intrinsic accuracy of single modules. Values extracted from Ref. [17].

Detector	Element size	Resolution in $R-\phi \times z$	Hits/track in the barrel	Radius of barrel layers [mm]
Pixel	$50 \times 400\,\mu\text{m}^2$	$10\,\mu\text{m} \times 115\,\mu\text{m}$	3	50.5, 88.5, 122.5
SCT	$80\,\mu\text{m}$	$17\,\mu\text{m} \times 580\,\mu\text{m}$	4	299, 371, 443, 514
TRT	4 mm	$130\,\mu\text{m}$	36	from 554 to 1082

axis, c.f. Fig. 2.6a, whilst the end-caps are composed of a series of disks or wheels of sensors perpendicular to the beam axis, c.f. 2.6b. Table 2.2 summarizes the main characteristics and the intrinsic accuracy of the aforementioned three ATLAS ID sub-detectors, which is needed to achieve the designed resolution of $\sigma_{p_\text{T}}/p_\text{T} = 0.05\,\% \, p_\text{T}[\text{GeV}] \oplus 1\,\%$. The ID's performance in Run 1 as well as the used algorithms in the event reconstruction are reviewed in greater detail in Cha. 3 in the light of the high pile-up LHC environment.

Pixel detector

Approximately 80.4 million readout channels of the Pixel detector are distributed over 1744 Pixel modules, which are segmented in $R-\phi$ and z. The modules are arranged in three layers around the interaction point and house 16 front-end electronics chips with 2880 electronics channels each. The sensor tile area is $63.4 \times 24.4\,\text{mm}^2$ in the transverse plane, i.e. $R-\phi$, and is composed of $250\,\mu$m thick n-type silicon wafer readout pixels with a size of $50 \times 400\,\mu\text{m}^2$. The chosen configuration comes with an intrinsic accuracy of $10\,\mu$m in transverse direction, and $115\,\mu$m in the longitudinal direction, i.e. z in the barrel and R in the end-cap region.

Semiconductor Tracker

The second high resolution tracker, the SCT, contributes approximately 6.3 million readout channels, distributed over 4088 modules. In the barrel, a module consists of $64.0 \times 63.6\,\text{mm}^2$ sensors with a strip-pitch of $80\,\mu$m made from a total of 768 active strips of $285\,\mu$m thick silicon wafers each, and tiles four coaxial cylindrical layers. The sensors mounted on the nine disks perpendicular to the beam axis in either of the end-caps are trapezoid shaped with a strip-pitch ranging from $54\,\mu$m to $90\,\mu$m, and thus add four space-points for track candidates in the intermediate radial range. The usage of back-to-back stereo sensors at an angle of 40 mrad allows to establish a measurement of the z-coordinate along the strip length and improves spatial resolution in conjunction with the $R-\phi$ measurement from a set of strips in each layer parallel to the beam direction. The intrinsic accuracy per module, defined by the used strip pitch, is $17\,\mu$m in transverse direction, $R-\phi$, and $580\,\mu$m in the longitudinal direction, z in the barrel and R in the end-cap region.

Transition Radiation Tracker

The last, and outermost, component of the ID is the TRT, contributing approximately 351000 readout channels with an intrinsic accuracy of $130\,\mu$m per straw. The number of channels is low in comparison with other tracking devices, but the TRT is capable of compensating this by measuring long trajectories with a large number of hits in the drift tubes. The information passed to the reconstruction algorithms is substantial, though limited to the $R-\phi$ plane. The tubes are 4 mm in diameter with a $31\,\mu$m gold plated tungsten anode wire. They are arranged in 73 layers of length 144 cm and interleaved with fibres in the barrel, and 160 layers of length 37 cm and interleaved with foils in the end-caps. The dielectric material used to interleave the straw tubes provides transition radiation for traversing relativistic charged particles, that can be used to distinguish electrons from pions based on their energy deposition.

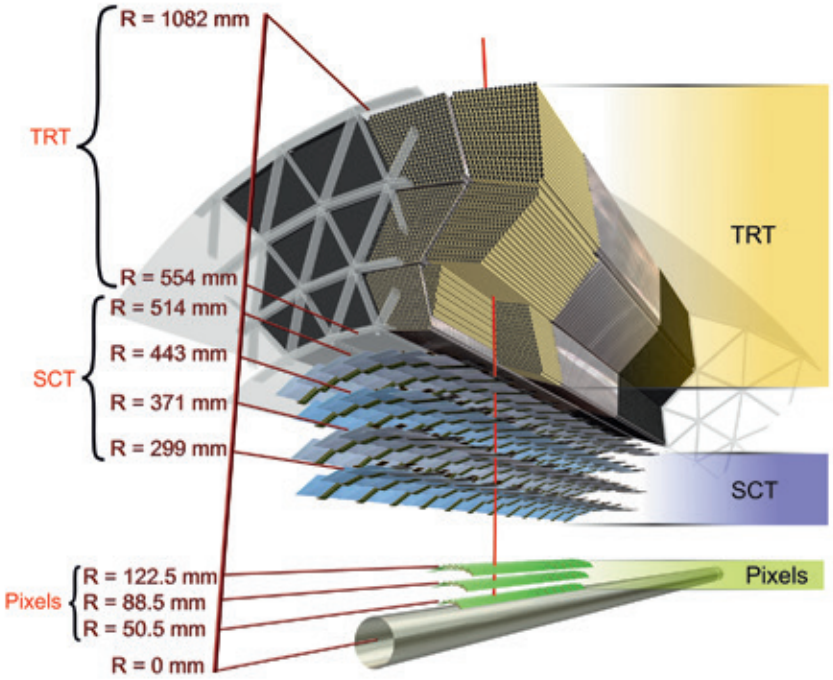

(a)

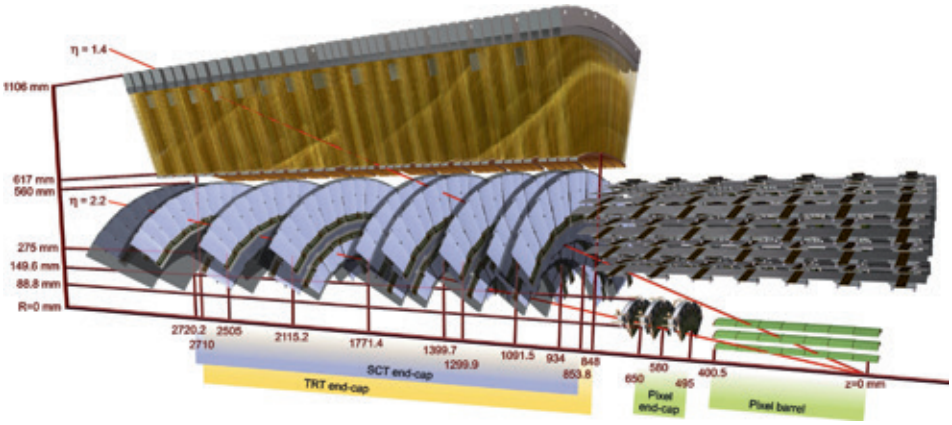

(b)

Figure 2.6: Drawings showing the sensors and structural elements in the (a) barrel and (b) end-cap of the ATLAS ID: beryllium beam-pipe, silicon Pixel layers, SCT, and polyimide drift tube elements of the TRT. Figures taken from Ref. [17].

2.2.3 The calorimeter system

At larger distances from the interaction point high granularity liquid-argon (LAr) electromagnetic (EM) and hadronic sampling calorimeter are installed, shown in Fig. 2.7. The ECAL and HCAL provides EM energy measurements in the pseudorapidity range $|\eta| < 3.2$ with a transition region between $1.37 < |\eta| < 1.52$. The HCAL ensures that not only electrons and photons are absorbed, but also hadrons lose their energy through particle showers. These are detected using scintillating tiles and LAr as active material in the barrel, $|\eta| < 1.7$, and in the forward direction, $1.5 < |\eta| < 4.9$. The design resolution is $\sigma_E/E = 10\,\%/\sqrt{E[\mathrm{GeV}]} \oplus 0.7\,\%$ for EM calorimetry. To achieve the physics goals hadronic calorimetry requires a resolution of $\sigma_E/E = 50\,\%/\sqrt{E[\mathrm{GeV}]} \oplus 3\,\%$ for the barrel and end-cap, $|\eta| < 3.2$, , while it can degrade to $\sigma_E/E = 100\,\%/\sqrt{E[\mathrm{GeV}]} \oplus 10\,\%$ in the forward direction, $3.1 < |\eta| < 4.9$.

Electromagnetic calorimeter

The ECAL is a lead-LAr detector with an accordion geometry, i.e. accordion-shaped kapton electrodes and lead absorber plates with varying size in different regions of the detector. The design provides full, azimuthal crack-less coverage in ϕ and fast read-out. It is divided into a barrel and two end-cap components. The former consists of two two identical half-barrels, separated by a 4 mm gap at $z = 0$ and centered around the beam axis. Each of them is 3.2 m long with an inner and outer radius of 2.8 m and 4 m respectively. Similarly, each end-cap calorimeter is mechanically divided into two coaxial wheels. These are 63 cm thick and have external and internal radii at ambient temperature of 2098 mm and 330 mm, respectively.

At various regions of the detector, LAr presampler detectors are implemented to determine the energy loss upstream of the calorimeter and thus to improve the energy measurements in these regions. Each barrel module, depicted in Fig. 2.8a, has three layers in depth. The front layer has a depth of only 4.3 radiation lengths (X_0), but a fine granularity of $\Delta\eta \times \Delta\phi = 0.003 \times 0.1$ allowing precision measurements of the energy deposits of EM showers initiated by electrons and photons through bremsstrahlung and e^+e^- pair production. The middle layer has a depth of $16X_0$ and absorbs most of the energy of the EM shower. The back layer has a depth of $2X_0$ and collects only the tails to distinguish EM and hadronic showers and therefore can be less segmented in η. The end-cap wheels are divided into eight wedge-shaped modules and share the accordion geometry with the barrel. Each module is subdivided into three longitudinal layers of similar depths as in the barrel. The total thickness of the ECAL amounts to more than $22X_0$ in the barrel and more than $24X_0$ in the end-caps, while being transparent for hadronic objects such as jets, i.e. the ECAL is approximately 1.5 nuclear interaction lengths λ deep.

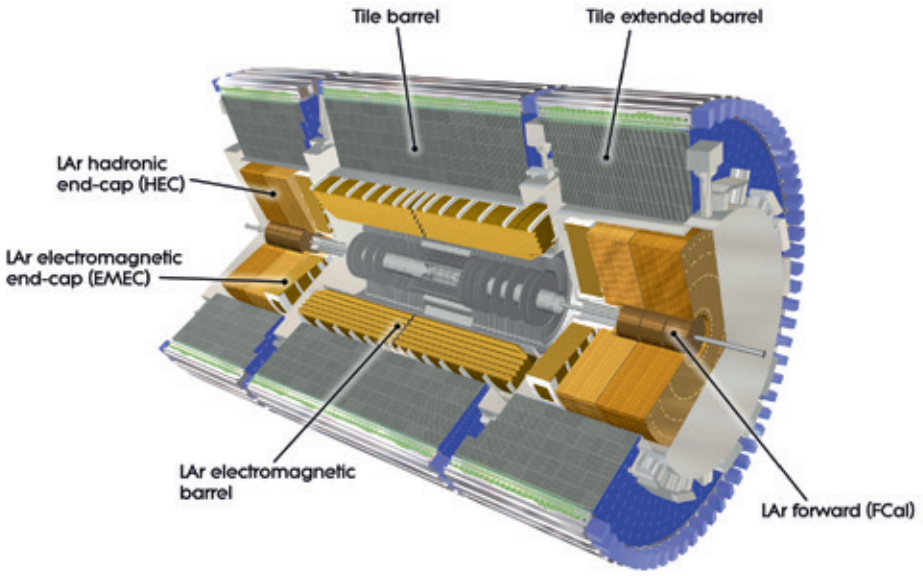

Figure 2.7: Cut-away view of the ATLAS calorimeter system. The various components are indicated using color-coding and labels. Figure taken from Ref. [17].

Hadronic calorimeter

The ATLAS HCAL is located directly outside of the ECAL and consists of the tile calorimeter, the LAr hadronic end-cap calorimeter (HEC) and the LAr forward calorimeter (FCal). It is of particular importance for the measurement of the energy deposit of hadronic showers and jets.

The tile sampling calorimeter is composed of a central barrel in the region $|\eta| < 1.0$ and two extended barrels covering the range $0.8 < |\eta| < 1.7$. The dimensions of the barrels are 5.8 m and 2.6 m in length respectively, spanning radii from 2.28 m to 4.25 m. The HCAL uses steel as absorber and scintillating tiles as active material, azimuthally distributed over 64 modules of size $\Delta\phi = 0.1$, each subtending 5.625 degrees in azimuth, c.f. Fig. 2.8b. Similar to the ECAL, the tile calorimeter's barrel and extended barrels are segmented in depth in three layers with thickness of approximately 1.5, 4.1, and 1.8λ, and 1.5, 2.6, and 3.3λ respectively. The innermost readout cells obey the highest granularity, $\Delta\eta \times \Delta\phi = 0.1 \times 0.1$ and the total nuclear interaction length at the outer edge of the tile-instrumented region is 9.7λ at $\eta = 0$.

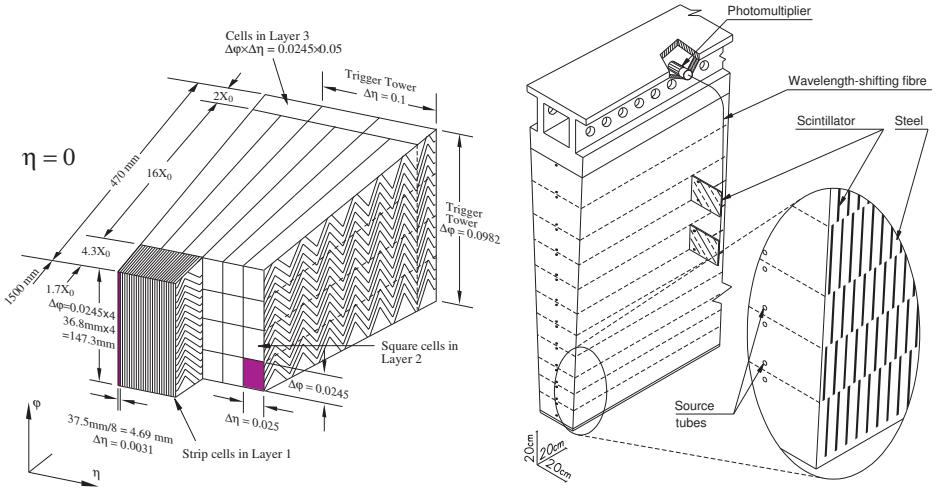

Figure 2.8: Schematic view of (a) an ECAL barrel module where the different layers are indicated as well as the accordion-shaped lead absorber plates and (b) a tile calorimeter module, also showing the layers of steel absorber and active scintillator materials as well as the optical readout using a photomultiplier. The granularity in η and ϕ of the ECAL's cells of each of the three layers with varying depth is displayed, too. Figures taken from Ref [17].

The HEC consists of two independent wheels with a total of four layers in depth per end-cap and is composed of 32 identical wedge-shaped modules with copper absorber material. They are interleaved with LAr gaps with readout cells of the size $\Delta\eta \times \Delta\phi = 0.1 \times 0.1$ in the central region and lower granularity further outside. It is placed directly behind the ECAL end-cap components, extending over a range of $1.5 < |\eta| < 3.2$. Thus it overlaps with both the tile calorimeter and the FCal to minimize crack-regions by reducing the drop in material density in the overlapping region.

The FCal consists of three 45 cm deep modules in each end-cap, all using LAr as active medium. The absorber material is different for the modules. The first uses copper and is optimized for EM measurements, while the other two, made of tungsten, measure predominantly the energy of hadronic interactions and contribute significantly to the total depth of approximately 10 nuclear interaction lengths.

2.2.4 Muon spectrometer

The surrounding muon spectrometer (MS) is shown in Fig. 2.9 for a quarter-section in a plane containing the beam axis. In particular its air-core toroid system defines the overall dimensions of the ATLAS detector. The toroid system comprises a long barrel and two inserted end-cap magnets, providing approximately 1.0 to 7.5 Tm of bending power in a large volume within a light and open structure.

The MS uses three layers of high precision tracking chambers, i.e. Monitored Drift Tubes (MDTs) and Cathode Strip Chamberss (CSCs), for detecting muon candidates in the bending plane of the magnetic field, i.e. in the $R-z$ plane, and fast triggering chambers, Resistive Plate Chambers (RPCs) and Thin Gap Chambers (TGCs). The stand-alone, muon momentum resolution, i.e. without using information from the ID, is designed to be $\sigma_{p_T}/p_T = 10\,\%$ at $p_T = 1\,\text{TeV}$ in the range $|\eta| < 2.7$. This can be achieved owing to the reduced amount of material traversed by candidates after the calorimeters, which minimizes multiple-scattering effects. It is possible to detect muon candidates with a momentum between 3 GeV and 3 TeV. In particular the $H \to ZZ^* \to 4\mu$ channel benefits from a highly efficient and pure reconstruction of muons, the only charged particles not stopped by the calorimeter system or interactions with the detector material.

Precision tracking

In the barrel region, $|\eta| < 2.0$, three layers of 16 slightly overlapping MDTs are installed between and on the eight coils of the superconducting barrel toroid magnet at radii of approximately 5 m, 7.5 m, and 10 m around the beam axis. This implies that the chamber sizes increase in proportion of their distance from the interaction point. In the end-cap regions,

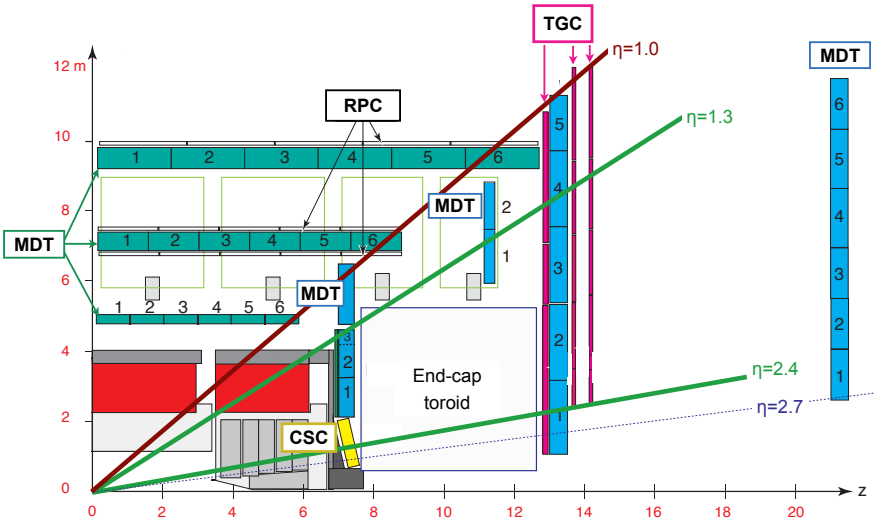

Figure 2.9: Schematic view of a quarter-section of the ATLAS MS in a plane containing the beam axis. The different sub-detectors are colored and labeled. Figure taken from Ref. [324].

$2.0 < |\eta| < 2.7$, MDT chambers have been mounted on two large wheels perpendicular to the beam axis, located at distances of 14 m and 21.5 m from the nominal interaction point. The innermost layer, a wheel located at a distance of $|z| = 7.4$ m, is equipped with CSCs owing to their higher rate capability and time resolution, which allow to measure both track coordinates simultaneously from the induced-charge distribution.

The MDT chambers consist of three to eight layers of 30 mm wide and 1 m to 6 m long pressurized aluminum drift tubes filled with Ar/CO_2 gas with a tungsten-rhenium anode. They achieve an average intrinsic resolution of 80 μm each, resulting in a resolution of 35 μm per chamber. In contrast, CSCs are trapezium shaped multiwire proportional chambers with two cathode strips per plane. They are installed perpendicular to each other, yielding a resolution of 40 μm in the bending plane and about 5 mm in the transverse plane due to a coarser cathode segmentation. The locations and deformations of the MDT chambers and CSCs are known to a precision below 30 μm, monitored by a high-precision optical alignment system of RASNIKs [325, 326], BCAMs, and SaCams, complemented by track-based alignment algorithms.

Trigger chambers

Muon tracks are triggered by a system of fast trigger chambers complementing the precision tracking chambers. The system is composed of three stations of two layers of gaseous parallel electrode-plate detectors, namely RPCs, in the barrel region, $|\eta| < 1.05$, and four TGC stations in the end-caps, $1.05 < |\eta| < 2.4$. The RPCs are placed below and above the middle MDT layer and outside of the precision tracking system. The configuration of TGC stations amounts to nine layers of multiwire proportional chambers, located in front of the innermost tracking layer and arranged into one triplet and two doublets surrounding the second largest MDT wheel. Beyond the primary requirement of providing fast and coarse tracking information to be used in the high-level trigger, described in the following section, the chambers provide means to measure the second track coordinate in the non-bending azimuthal projection, which is matched to the MDT hits in the bending plane.

2.2.5 Trigger system

As previously alluded to, the detector is operated in a high occupancy environment of more than 20 inelastic proton-proton interactions per bunch crossing. This translates into an interaction rate of approximately 400 MHz at a bunch spacing of 50 ns, making it impossible to entirely record every event. Hence, an online event selection, i.e. a trigger system, is employed in order to reject minimum bias events while maintaining the highest efficiency possible for all physics searches and analyses performed. The decision chain contains three distinct levels, i.e. Level-1, Level-2 and the event filter. The latter two are collectively termed high-level trigger. Each trigger level refines the decisions made at the previous

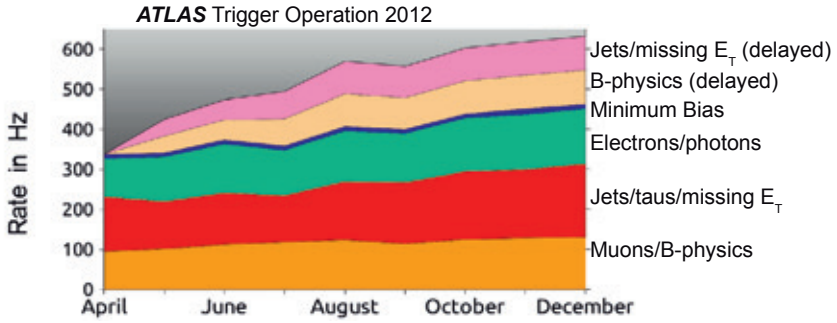

Figure 2.10: Event Filter stream recording rates per month for stable beam conditions in 2012. Figure taken from Ref. [327].

level by employing additional selection criteria to gradually reduce the interaction rate to approximately 600 Hz suitable for physics analyses, c.f. Fig. 2.10, which is possible to write on disk at a data storage rate of approximately 900 MB/s.

The Level-1 fast triggering system is hardware-implemented and reduces the incoming bunch crossing rate to 75 kHz. It uses reduced granularity calorimetry and MS information to search for charged leptons, photons, and jets, as well as large missing and total transverse energy, i.e. the key signatures of the physics ATLAS is designed to study. The Level-2 selection is software-implemented and seeded by Region-of-Interest (RoI) information defined by the Level-1 trigger on an event-by-event basis. It uses full granularity information and precision for all detector sub-systems in the identified locations, i.e. the regions of the detector with coordinates η and ϕ which obey interesting features. Finally, the event filter uses offline reconstruction algorithms, described in more detail in Cha. 3, to implement its selection criteria.

2.3 The CMS detector

The analysis presented in Cha. 8 combines ATLAS and CMS measurements to compute the world average of the Higgs boson mass. The correlations of experimental systematic uncertainties between the analyses performed by the two collaborations depend on the different technologies used by the detectors. This section will briefly introduce the reader to the CMS experiment at CERN.

The CMS detector, shown in Fig. 2.11, is, just like the previously described ATLAS detector, a multipurpose apparatus designed to study the particle collisions provided by the LHC. It follows a similar physics program as ATLAS, notably the study of the nature of EWSB, for

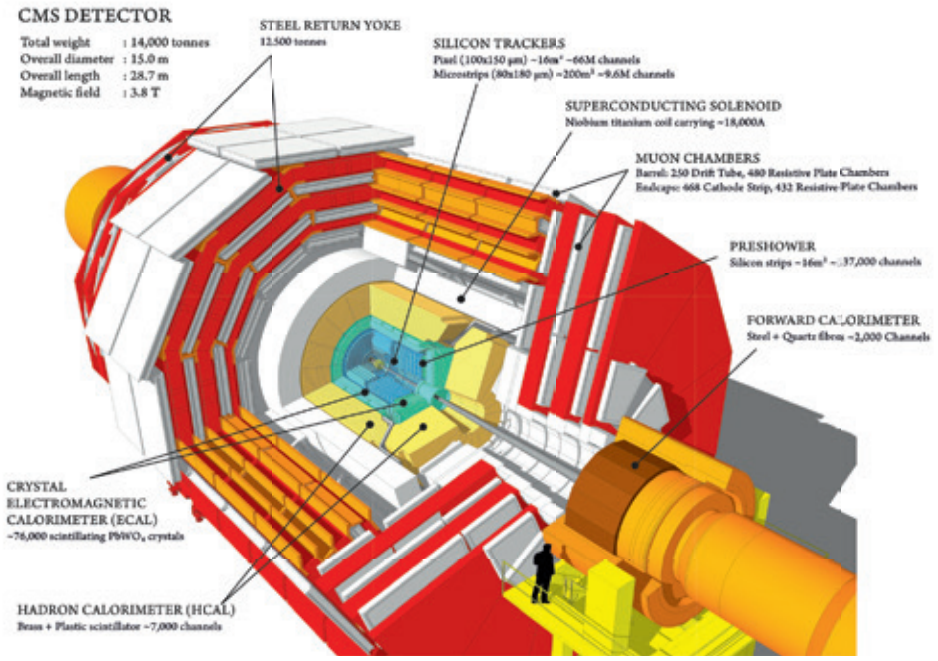

Figure 2.11: Sectional view of the CMS detector. The various detector sub-systems are indicated and labeled. Figure taken from [328].

which the Brout-Englert-Higgs mechanism is presumed to be responsible. The two detectors employ different designs and technologies to match the detector requirements imposed by the LHC environment. Hence, the two experiments operate independently and cross-check each other. The design of CMS, in particular its main distinguishing features, i.e. a high-field solenoid, a full-silicon-based inner tracking system, and a homogeneous scintillating-crystals-based ECAL, are briefly described in the remainder of this section, though for a more detailed view, the reader is referred to Ref. [18] and references therein.

The CMS detector is of cylindrical shape with a forward-backward symmetry with respect to the nominal interaction point in the center of the detector. It is 21.6 m long with an outer radius of 7.3 m and has a weight of 12500 t. The apparatus is divided into a barrel region, $|\eta| < 1.2$, with sub-detectors installed on concentric layers of increasing distance from the beam axis, and the end-caps, $|\eta| > 1.2$, where the sub-systems are mounted on wheels perpendicular to the z-axis[3].

[3] ATLAS and CMS use the same cylindrical coordinate system with the z-axis along the beam line, x pointing inwards to the center of the LHC ring, and the y-axis pointing upwards. Hence, for the CMS detector pseudorapidity is defined as well as $\eta = -\ln\tan(\theta/2)$ with the polar angle θ measured from the z-axis.

The design of CMS is driven by its 13 m long 3.8 T superconducting solenoid magnet with a 6.3 m cold bore, providing a bending power of 12 Tm. The solenoid can saturate 1.5 m of iron, which is needed to measure precisely the momentum of high-energy charged particles, in particular muons. To ensure full geometric coverage up to $|\eta| < 2.4$ with no acceptance gaps, a total of four muon stations are installed in the steel flux-return yoke of the magnet, each consisting of several layers of aluminium drift tubes (DTs) in the barrel region and CSCs in the end-cap region, complemented by RPCs. The stand-alone momentum resolution of the MS is about 9 % for small values of the pseudorapidity and for transverse momenta below 200 GeV, which degrades to values between 15 % and 40 % depending on η at 1 TeV due to multiple-scattering in the detector material.

Inner tracker and calorimetry are housed inside the cold bore of the magnet, immersed in its uniform magnetic field. The tracking volume is given by a cylinder of 5.8 m length and 1.3 m radius, extending the coverage up to $|\eta| < 2.5$. It is equipped with three barrel layers and two endcap disks of silicon pixel detectors with an intrinsic resolution of $100 \times 150\,\mu\text{m}^2$ close to the interaction point and ten barrel layers and twelve end-cap disks of silicon microstrip detectors further out to provide the required granularity and precision to cope with the immense track multiplicities in the LHC high pile-up environment. These strips are arranged in parallel to the beam axis in the barrel, while being along the transverse dimension in the end-caps, each with an intrinsic accuracy of $20 \times 50\,\mu\text{m}^2$. The transverse momentum resolution for high momentum tracks of the order 100 GeV is between 1 % and 2 % in the central region up to $|\eta| < 1.6$, beyond which it degrades. The hermetic homogeneous ECAL, using lead tungstate crystals, and the brass/scintillator sampling HCAL are placed between the tracker and solenoid. They have a coverage in pseudorapidity up to $|\eta| < 3.0$. The scintillation light of the ECAL is detected by silicon avalanche photodiodes (APDs) and vacuum phototriodes (VPTs) in the barral and end-cap regions, respectively. For the HCAL wavelength-shifting fibres embedded in the scintillator tiles are used in combination with hybrid photodiodes (HPDs) capable of operating in high axial magnetic fields.

The calorimeter system is complemented by a silicon strip preshower system installed in front of the end-cap ECAL, covering $1.6 < |\eta| < 2.6$, a tail-catcher in the barrel region, and a iron/quartz-fibre calorimeter that ensures full geometric coverage and extends the coverage in pseudorapidity in the region $3.0 < |\eta| < 5.0$. The thickness of the ECAL is larger than $25X_0$, while the HCAL thickness varies between 10 and 15 nuclear interaction lengths, depending on η. In a test beam, for the ECAL the typical energy resolution was found to be

$$\left(\frac{\sigma}{E}\right)^2 = \left(\frac{2.8\,\%}{\sqrt{E}}\right)^2 + \left(\frac{0.12}{E}\right)^2 + (0.30\,\%)^2 \tag{2.4}$$

where E is measured in GeV and the three terms correspond to the stochastic term, the noise term, and the constant term, respectively. The jet transverse energy resolution, determined by the resolution of the HCAL, improves with the jet transverse energy. Typical

values are between 15 % and 30 % at 30 GeV and about 10 % at 300 GeV depending on the pseudorapidity.

CMS uses a two-level online event selection, namely the Level-1 hardware trigger based on electronic implementations and a software based High-Level Trigger (HLT), to reduce the event rate to 300 Hz. The Level-1 trigger uses information from the calorimeters and MS to select potentially interesting events, whereas the HLT takes advantage of the software framework also used for offline reconstruction, notably the Particle Flow event description algorithm [329, 330]. The Particle Flow algorithm is used to reconstruct and identify each single particle, i.e. electrons, muons, photons, charged hadrons and neutral hadrons, with an optimized combination of all sub-detector information.

Event reconstruction in the high pile-up LHC environment

3

To utilize the ATLAS detector's full potential, information from all detector sub-systems must be combined when analyzing the recorded collision data. Only then it is possible to accurately reconstruct the full event topology except for weakly interacting particles such as neutrinos, and identify the particles produced in the pp collisions. Undetectable particles on the other hand cause a momentum imbalance in the transverse plane referred to as MET, under the assumption that their mass is negligible. The following sections describe the algorithms used to perform the reconstruction of the collected collision data, their performance in the presence of pile-up, and the definition of the objects used by the physics analyses described in the remainder of this dissertation, in particular by the $H \to WW^* \to \ell\nu\ell\nu$ analysis, which is detailed in Cha. 5.

Understanding the (high) pile-up LHC environment deserves special attention and requires taking the perspective of both accelerator physicists and detector physicists. Pile-up interactions present a fantastic, yet simple, opportunity to increase the data statistics available for physics analyses, but also a serious challenge to maintain the high quality of the recorded data. Recalling the previous chapter, the average number of inelastic proton-proton interactions per bunch crossing is directly proportional to the total inelastic cross section, the instantaneous luminosity, and the bunch spacing.

In 2011, the LHC was operated at $\sqrt{s} = 7\,\text{TeV}$ with a peak instantaneous luminosity of $3.65 \cdot 10^{33}\,\text{cm}^{-2}\text{s}^{-1}$ and a bunch spacing of 50 ns. In 2012, the centre-of-mass energy was increased to 8 TeV, leading to an increase of approximately 2% of the total inelastic cross section. However, the peak instantaneous luminosity increased approximately by a factor of 2, owing to reducing the beta function at the collision point. In order to control the stored beam energy and prevent electron cloud instabilities, the bunch spacing was not adapted to the changes of the other beam and machine parameters, leading to an significant increase in the number of pile-up interactions, even beyond the design values, cf. Tab. 2.1. Over time, the improved understanding of the machine will allow to operate it at the designed bunch spacing, 25 ns, which is necessary to mitigate the effect of reaching the design values of the LHC for the centre-of-mass energy and the instantaneous luminosity.

In the detector, pile-up events lead to an increased particle multiplicity, challenging all detector sub-systems. The limited data storage rate implies a hard limit on the number of events that can be recorded. To maintain the rate, more stringent selection criteria have to be employed already at every level of the trigger system. The increasing per-event detector occupancy requires fast read-out electronics, and becomes relevant in particular for the

sub-detectors with a sensitivity window longer than the bunch spacing. In an environment with a high density of read-out channels above the noise threshold, the resolution for the reconstruction of physics objects is degraded. The signals from multiple objects are identified as coming from a single object. Thus, the reconstruction efficiencies degrade and reliably identifying all produced particles becomes impossible. A high occupancy environment even increases the probability to reconstruct fake objects due to random combinations of unrelated channels. In particular the ID, being closest to the interaction point, suffers from the high track multiplicity. Not only the quality of the physics objects is also, affected the computing resources for the event reconstruction must be considered. The reconstruction time and memory consumption grow progressively due to additional genuine objects, but also due to more expensive pattern recognition and ambiguity solving.

3.1 Inner Detector performance in pile-up

All Higgs analyses presented in this work rely directly or indirectly on leptons, heavy flavor tagging, or the identification of charged hadrons. The ATLAS ID tracking system, detailed in Sec. 2.2.2, detects charged particles and measures their momentum through the bending of the trajectories in an axial magnetic field. Information from the ID is used together with the ECAL and MS to determine the momentum of electrons and high-p_{T} muons, respectively as well as measuring their impact parameter, indicating prompt production in a single interaction. Hence, robust reconstruction algorithms are crucial to maintain a good performance of the ID in a high per-event occupancy environment of a large number of inelastic interactions per bunch crossing. This section is largely based on work presented previously in Ref. [19] and summarizes the changes in the track and vertex algorithms required to maximize the performance of the ID in a high density environment.

The occupancy of each sub-detector is shown in Fig. 3.1a as a function of the number of reconstructed vertices. It is defined as the fraction of channels read out and therefore is directly proportional to the charged-particle multiplicity, up to corrections for detector noise and track overlap. The Pixel detector, having the highest granularity of the components of the ID, has the lowest occupancy, even though it is closest to the interaction point and has the highest particle flux. The highest occupancy in the silicon detectors is found in the first layers of the SCT, having a lower granularity than the Pixel detector. The TRT occupancy, calculated from all straws passing the out-of-time rejection requirement [331], is even higher.

Figure 3.1b compares the occupancy of the Pixel detectors with that of the TRT using collision data samples with medium and high pile-up, taken during two fills with high intensity bunches delivered in October 2011. Comparing the distribution obtained from the data sample containing no effects from out-of-time pile-up with the one that includes out-of-time pile-up effects, it is found that out-of-time pile-up has a small impact on the occupancy of the Pixel detector, while a 3 % difference is found for the TRT at fixed Pixel occupancy. Thus, with increasing TRT occupancy, the signal from two or more particles can overlap in the same straw, accumulating to 10 % of all hits at a 20 % detector occupancy.

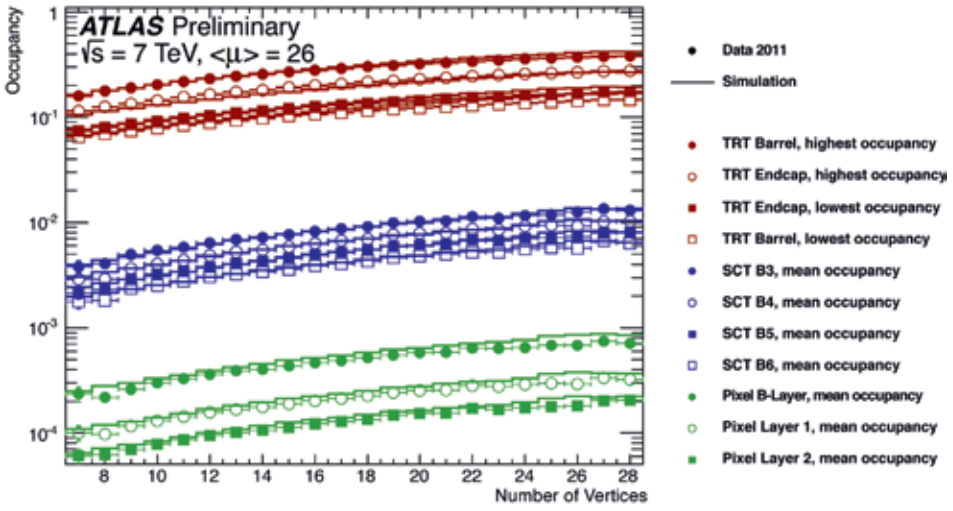

(a)

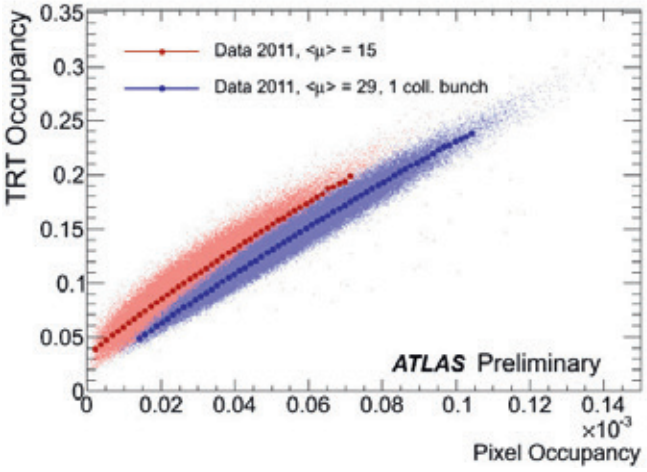

(b)

Figure 3.1: (a) The occupancy of the ID as a function of the number of reconstructed vertices in data and simulation with $\langle\mu\rangle = 26$ and $\mu^{\text{peak}} = 30$ for each layer in the barrels of the silicon detectors and the TRT straw tube layers with the highest and lowest occupancy. (b) Correlation of the Pixel detector and TRT occupancy measured in two data sets A and C. The former uses the beginning of the fill with highest intensity and a bunch spacing such that there were no effects from out-of-time pile-up, while the latter includes out-of-time pile-up effects. Data set A has $\langle\mu\rangle = 29$ and $\mu^{\text{peak}} = 30$. Data set C has $\langle\mu\rangle = 15$ and $\mu^{\text{peak}} = 21$.

3.1.1 Track reconstruction

Tracks in the ID are parametrised by helices [332],

$$\boldsymbol{\tau} = \boldsymbol{\tau}(d_0, z_0, \phi_0, \theta, q/p), \tag{3.1}$$

with the transverse impact parameter d_0 defined as the distance of closest approach in the transverse plane of the track candidate to the primary vertex and the longitudinal impact parameter z_0, i.e. the z-coordinate of the perigee point. Similarly, ϕ_0 and θ are the azimuthal and polar angle of the track candidate at its perigee, respectively. Finally, the helix is a function of the ratio of the particle's charge to its momentum, q/p. Helices are reconstructed using the New Tracking (NEWT) algorithm [333], which consists of multiple sequences of algorithms to efficiently identify the trajectories of primary charged particles, i.e. either particles with a mean lifetime greater than 3×10^{-11} s directly originating from a proton-proton interaction, or from the subsequent decays or interactions of particles with a shorter lifetime, and secondaries or conversions, produced in the interactions of primaries. Common to all stages are the steps of seeding, pattern recognition and final fit.

Trajectories of primaries are reconstructed using an inside-out algorithm starting from seeds composed of triplets of space points in the silicon layers. Pixel clusters provide a three-dimensional position and thus map directly into space points, while pairs of SCT clusters are combined to form a single space point, taking advantage of the angle between the sensors. It is natural to classify the seeds according to their sub-detector location: PPP and SSS seeds have all space points in the Pixel detector or SCT respectively, while PPS seeds use two space points in the Pixel detector and one in the SCT. PSS seeds are not included in the tracking as they suffer from a large fake rate.

Pattern recognition is necessary to enhance the hit collection efficiency with respect to plain seeding. The benefit is twofold: the estimate of the trajectory parameters from primaries is refined; and the reconstruction of detached tracks from photon conversions, decays of long lived particles, and material interactions becomes feasible. The seeds are propagated layer by layer through the ID, moving away from the interaction point and adding hits using a Combinatorial Kalman filter (CKF) [334, 335] combining forward filtering, backward smoothing and an outlier rejection. At each step ambiguities from track candidates with shared hits, incomplete track candidates, or fake track candidates not originating from one single particle are solved using a track scoring strategy, penalizing less precise track candidates [336]. A position measurement might also be associated to multiple track candidates, in particular in a high-occupancy environment, and compromise the track reconstruction efficiency and resolution. These merged clusters in the Pixel detector are identified and split using a set of artificial neural networks (NNs) [337]. Figure 3.2 illustrates the different stages of the track pattern recognition of the inside-out algorithm.

Once a (primary) track is completed, an attempt is made to reconstruct the trajectories of secondaries or conversions. To that end, the inside-out algorithm is followed by a track

search starting from segments reconstructed in the TRT using a global pattern search and a local pattern recognition in the Hough space [338]. The segments are successively extended inwards by adding silicon hits, referred to as back-tracking.

The main challenges to overcome for track reconstruction in high pile-up conditions are a degraded track parameter resolution due to incorrect hit assignment and decreased efficiency and fake tracks from random hit combinations, i.e. reconstructed tracks which could neither be matched to a primary nor to a secondary particle. The number of fake tracks can be minimized by employing robust quality requirements on reconstructed tracks. Selected trajectories must be reconstructed from at least nine space point measurements ("hits") in the Pixel and SCT detectors. In addition, in the Pixel detector must not be any hit missing that would be expected for a valid track candidate ("hole"). Intersections of trajectories with inactive or faulty readout channels are counted as hit, rather than vetoing the candidate by adding a hole. In the less dense $\sqrt{s} = 7\,\text{TeV}$ environment during 2011 data taking, track candidates are required to match the default requirements, i.e. at least seven silicon hits and up to two holes in the Pixel detector, and were optimised for high tracking efficiency at low pile-up [339]. After collecting all hits of a track candidate, its transverse and longitudinal impact parameters, are estimated from a global fit to all assigned hits. The quality of the tracks meeting the robust requirements has been validated in data using samples with different amounts of pile-up [19]. The silicon hit distributions are stable as a function of the number of pile-up interactions, whereas the number of TRT hits shifts marginally and the number of SCT holes increases at the sub-percent level due to the higher detector occupancy.

Figure 3.3 compares the efficiency of the NEWT algorithm, defined as the fraction of reconstructed tracks corresponding to simulated particles with $p_{\text{T}} > 400\,\text{MeV}$ and $|\eta| < 2.5$, as a function of the track p_{T} and η for three Monte Carlo (MC) samples generated using PYTHIA8 [341] with the ATLAS minimum bias tune 4C [342], one containing a single inelastic collision event and the others overlaid with an average of 20 and 40 additional collisions following a Poisson distribution. The comparison is done for tracks passing the default and robust requirements. Despite the large increase in detector occupancy, the track reconstruction efficiency for primaries is stable and decreases for secondaries in the forward region at most by 1 % with increasing pile-up. The increased hit requirements, however, reduce the primary and secondary efficiency globally and independent of the track p_{T} and η by 5 % and at most 2 %, respectively, as tracks that are subject to hadronic interactions might not be identified, compromising the reconstruction of electrons, taus and jets with p_{T} below 1 GeV.

The fraction of non-primary tracks[1], shown in Fig. 3.4, increases by a factor of 3-5 in a high occupancy environment due to an increase in the number of reconstructed combinatorical fake tracks at low and high transverse momentum, while it is minimal around 2 GeV. Em-

[1] Non-primary tracks denote both, secondary tracks and combinatorical fakes.

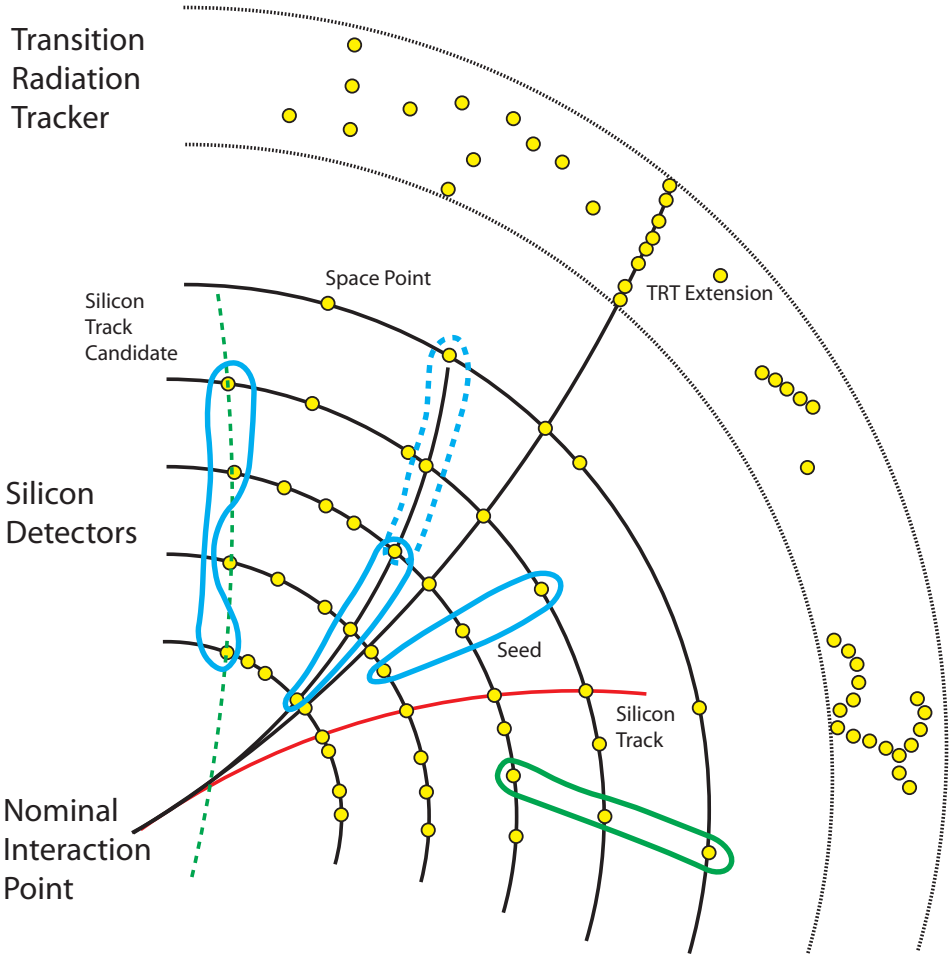

Figure 3.2: Illustration of the track pattern recognition in a simplified model of the ID. Triplets of the measured space points, shown in yellow, form seeds, indicated in blue. Track candidates are represented by lines. The seed marked by the dashed blue curve illustrates a case where two seeds correspond to the trajectory of the same charged particle. The seed shown in green is rejected by the requirement that the seed must be consistent with a particle from the nominal interaction point. The track candidate represented by the green dashed line is rejected because of the same reason. The red track candidate is a fully reconstructed silicon track with no TRT extension while the black candidate corresponds to a track reconstructed using information from all three sub-detectors. Figure courtesy of Ref. [340].

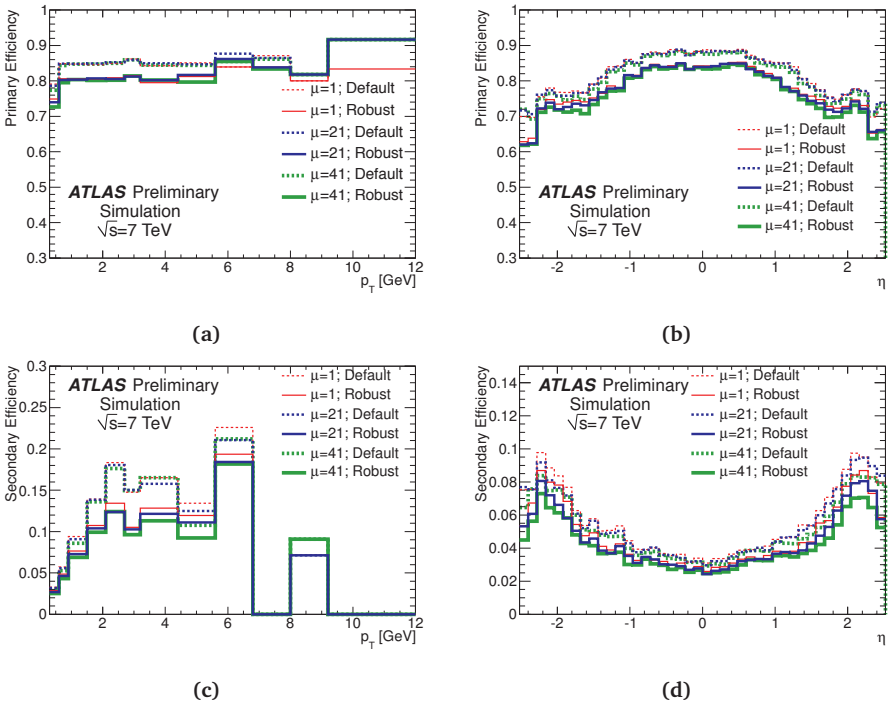

Figure 3.3: The primary (top) and secondary (bottom) track reconstruction efficiency in minimum bias MC samples containing exactly one and on average 21 or 41 interactions as function of the track p_{T} (left) and η (right). The distributions are shown for tracks passing the default (dashed) and robust (solid) requirements. Statistical uncertainties are not shown, but become significant at higher p_{T} as there are few secondary particles.

ploying the robust requirements introduced before, the non-primary rate becomes largely independent of the number of inelastic interactions per bunch crossing over the full p_{T} spectrum and up to a small increase in the forward regions, resulting in a stable average number of reconstructed tracks per interaction, summarized in Tab. 3.1.

3.1.2 Momentum scale and resolution

In particular measurements in the $H \to ZZ^* \to 4\ell$ channel and the ones using low-p_{T} leptons in the $H \to WW^* \to \ell\nu\ell\nu$ channel profit from a good ID momentum resolution. The ID momentum scale and resolution are studied using a tag-and-probe method: pairs of isolated, oppositely charged muons from Z decays, each with a transverse momentum of at least 25 GeV in the central region $|\eta| < 2.5$ are identified by matching independently reconstructed ID and MS tracks, described in more detail in Sec. 3.2.1. Then, the fractional ID momentum resolution $\sigma(1/p)/(1/p)$ is measured using an unbinned maximum likelihood fit of a parametric

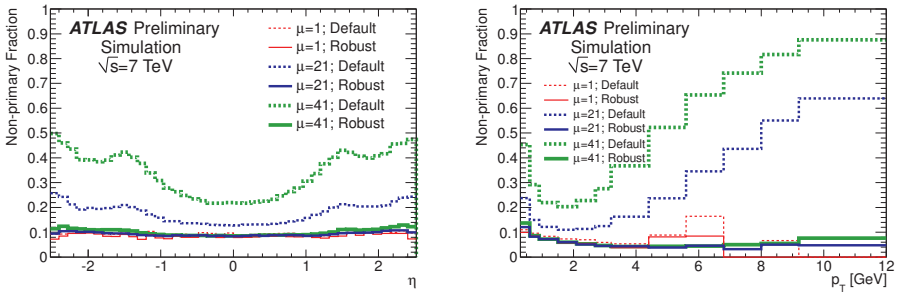

(a) (b)

Figure 3.4: The non-primary fraction in minimum bias MC samples containing exactly one and on average 21 or 41 interactions as function of the track (a) p_{T} and (b) η. The distributions are shown for tracks passing the default (dashed) and robust (solid) requirements. Statistical uncertainties are not shown, but become significant at higher p_{T} as there are few non-primaries, particularly with the robust requirements.

Table 3.1: Average number of default and robust tracks per interaction in data with different amounts of pile-up.

$\langle\mu\rangle$	Default Tracks/$\langle\mu\rangle$	Robust Tracks/$\langle\mu\rangle$
15	11.8	10.3
29	12.8	10.2
32	13.2	10.3

function describing the Z boson line-shape, its intrinsic spatial resolution, and multiple scattering effects in the traversed material, to the invariant mass distribution of the Z boson in the range $70\,\mathrm{GeV} < m_{\mu\mu} < 110\,\mathrm{GeV}$, reconstructed with ID tracks only. Figure 3.5 shows the results as a function of pseudorapidity obtained in four p_{T} intervals

The impact parameter resolution is of particular importance for controlling non-prompt background processes and processes relying on heavy flavor tagging, such as single top quark and top quark pair production as well as associated Higgs production with heavy top or bottom quarks and the Higgs decay to bottom quark pairs. The tails of the transverse impact parameter distribution are dominated by secondary tracks and found to be stable under increasing pile-up interactions owing to the small lateral size of the beam spot. However, the beam spot extends to a few centimeters in the longitudinal direction, causing an increase of the tails of the modified longitudinal impact parameter distribution due to tracks from additional interactions. Figure 3.6 shows the core widths of the transverse and modified longitudinal impact parameters d_0 and $z_0 \sin\theta$ respectively as a function of pseudorapidity for two different regions in $p_{\mathrm{T}}\sqrt{\sin\theta}$, which is directly proportional to multiple scattering effects degrading the impact parameter resolution [343]. Observed discrepancies between data

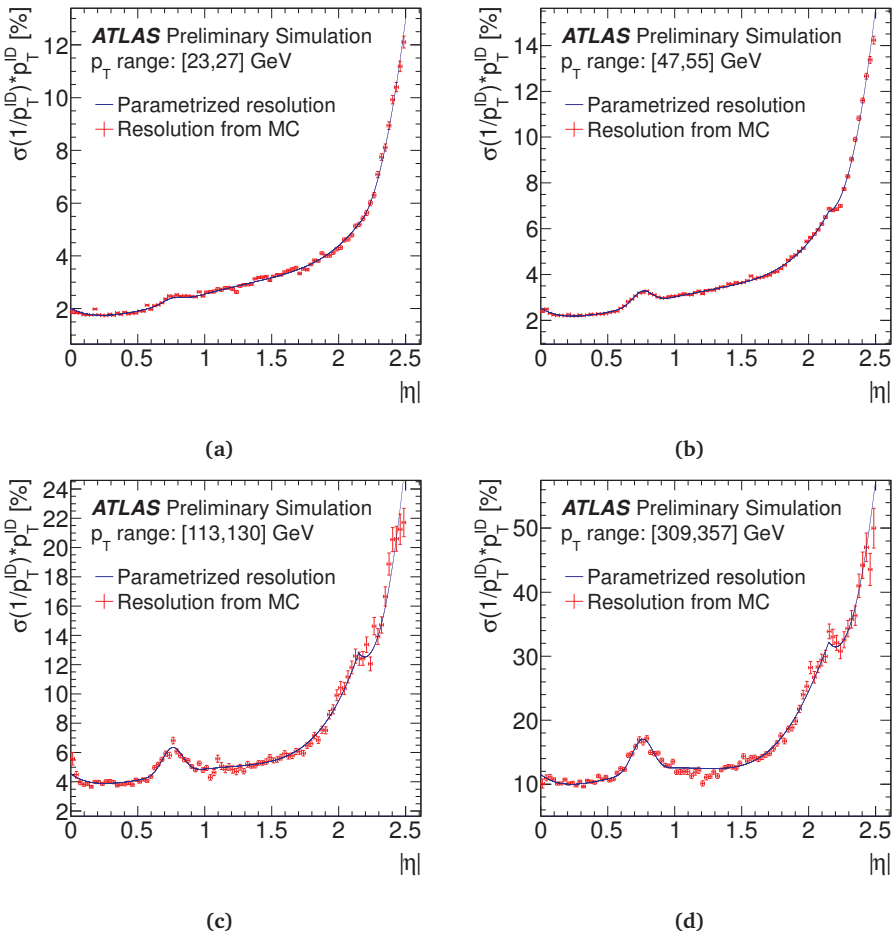

Figure 3.5: Fractional ID momentum resolution $\sigma(1/p)/(1/p)$ as a function of pseudorapidity in four p_{T} intervals using the method described in the text. Figures taken from Ref. [343].

and simulation can be caused by residual misalignments in the detector and an insufficient modeling of the intrinsic detector resolution.

3.1.3 Primary vertex reconstruction

Primary vertices from proton-proton interactions in the ATLAS ID are reconstructed using an iterative search strategy composed of two stages [344]: Vertex seeds are obtained from the highest density reconstructed charged particle tracks in z-direction computed at the

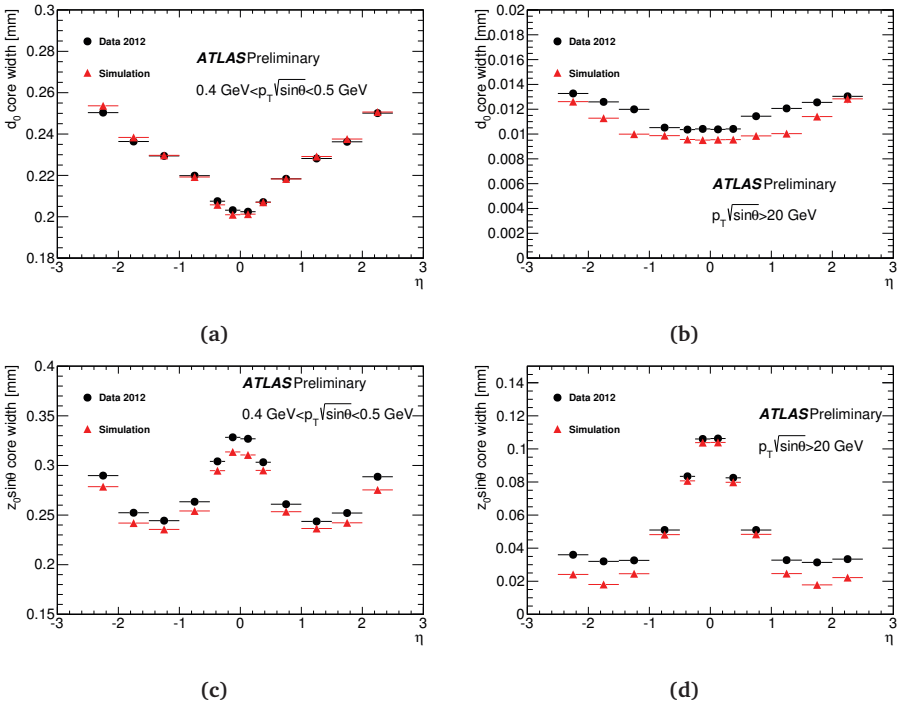

Figure 3.6: Core widths of the transverse (top) and modified longitudinal (bottom) impact parameters d_0 and $z_0 \sin\theta$ respectively as a function of pseudorapidity for two different regions in $p_T\sqrt{\sin\theta}$ (left and right). Figures taken from Ref. [343].

point of closest approach to the beam spot center. In a second step the seed and nearby tracks are fitted using an adaptive χ^2 fitting algorithm to precisely estimate the true vertex position [345]. Deterministic annealing [345, 346] is used to establish the matching of tracks to the vertex candidate and cope with outlying track measurements. Tracks less than approximately 7σ, using a χ^2 probability with two degrees of freedom, compatible with the reconstructed vertex position seed the next iteration of the vertex finding algorithm. The algorithm terminates when all reconstructed tracks in the event have been associated with vertices, or when no additional vertex can be found. The vertex with the highest sum of squared momenta of the tracks associated with it, is labeled as the primary vertex, whereas the remaining ones are referred to as pile-up vertices. Figure 3.7 shows the vertex position resolution without beam constraints as function of the number of tracks associated with the vertex candidate.

Figure 3.8 shows, as a function of the average number of inelastic interactions per bunch crossing, the vertex reconstruction efficiency for the hard scattering process in MC simulations

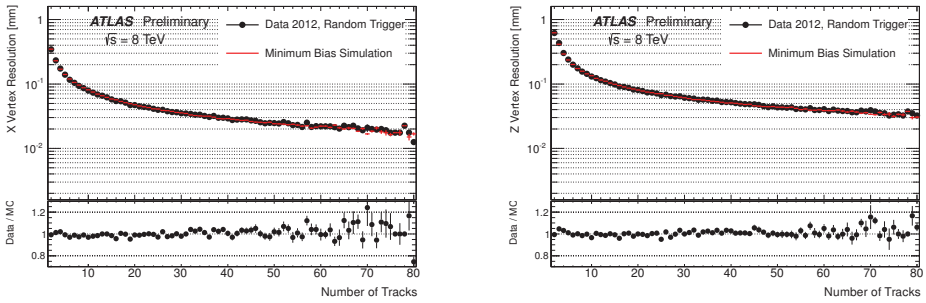

(a) (b)

Figure 3.7: Vertex position resolution without beam constraint in data (black) and MC simulation (red) for the (a) transverse and (b) longitudinal coordinates as function of the number of tracks associated with the vertex candidate. Figures taken from Ref. [347].

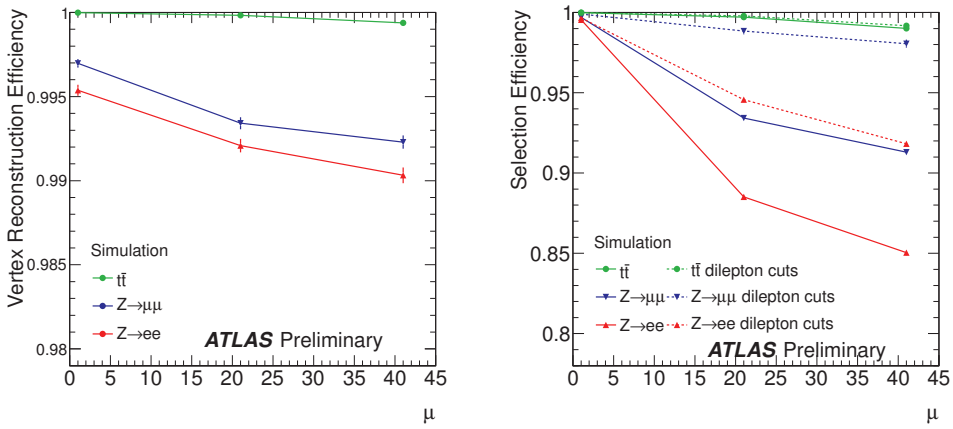

(a) (b)

Figure 3.8: (a) Vertex reconstruction efficiency for the hard scattering process in MC simulations of top quark pair production (green) and the decay of Z bosons into leptons (muons and electrons, blue and red, respectively) as well as (b) the efficiency to reconstruct and select it as the primary vertex with (dashed) and without (solid) selecting dilepton candidates. Figures taken from [347].

of top quark pair production and the decay of Z bosons into leptons as well as the efficiency to reconstruct and select it as the primary vertex with and without selecting dilepton candidates using default tracking cuts in the event reconstruction.

The effect of a high occupancy detector environment on the vertex reconstruction is two-fold. The increasing density of collisions directly degrades the vertex resolution when a nearby track is included in a vertex or two nearby vertices are merged into a single reconstructed vertex. The limited intrinsic resolution of the detector, secondary interactions, or the presence of jets can lead to an opposite effect, namely splitting of one interaction into multiple distinct vertices. The vertex reconstruction is affected also indirectly by a degradation of the track reconstruction quality, resulting in a lower efficiency and an increased fake rate. Figure 3.9 shows the vertex reconstruction efficiency and fake probability as a function of the pile-up interactions in minimum bias MC simulation for reconstructed tracks passing the default and robust requirements outlined in the previous section. The efficiency to reconstruct a single interaction of reconstructable interactions, i.e. interactions with sufficiently hard p_{T} spectrum and large particle multiplicity, is approximately 90 %. With increasing occupancy of the ID, the efficiency decreases to approximately 50 % and the fraction of vertices with dominant contributions from fake tracks increases from less than 0.1 % to approximately 7 % due to the aforementioned reasons. The increased rate of fake vertices can be controlled by requiring reconstructed tracks matching the robust requirements, at the cost of a reduced vertex reconstruction efficiency at low pile-up.

Using the default tracking requirements, the adaptive vertex fitting algorithm with deterministic annealing scheme is stable and preserves the linear dependence of the average number of reconstructed primary vertices on the average number of interactions per beam crossing up to approximately 15 pile-up interactions as shown in Fig. 3.10a. In the high pile-up regime a degradation of the vertex reconstruction efficiency becomes visible. The average number of tracks per event, on the other hand, increases non-linearly and with a higher gradient using the default requirements than with the robust requirements, indicating an increasing fake fraction, both in data and simulation, c.f. Fig. 3.10b.

3.1.4 Computing performance

Another important aspect to consider beyond the detector performance is the event reconstruction time, dominated by the time required to reconstruct the ID, which naturally increases with a higher particle multiplicity through more inelastic interactions per bunch crossing. The exponential scaling is driven by extra combinatorics, affecting the track finding algorithms and the ambiguity solving, due to additional hits in both the silicon detectors and the TRT. Most other algorithms used in the reconstruction process scale proportional to the number of tracks in the event. Hence, the tracking requirements listed in Sec. 3.1.1 are also tuned to optimize the CPU time spent on this task, while not compromising the physics performance.

Central to these requirements is an optimization of the early stages of the pattern recognition to reject seeds not becoming track candidates as the execution time of any algorithm is proportional to the number of its inputs, produced at the previous stage. In a first step

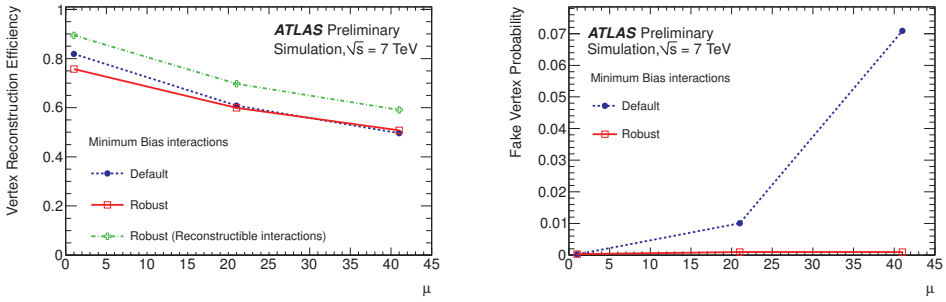

(a) (b)

Figure 3.9: (a) Vertex reconstruction efficiency and (b) fake vertex probability as a function of the average number of interactions in minimum bias MC simulation. The results are shown for tracks passing the default (blue, dashed) and robust (red, solid) track requirements. The vertex reconstruction efficiency is also shown for reconstructable interactions as defined in the text (green, dot-dashed).

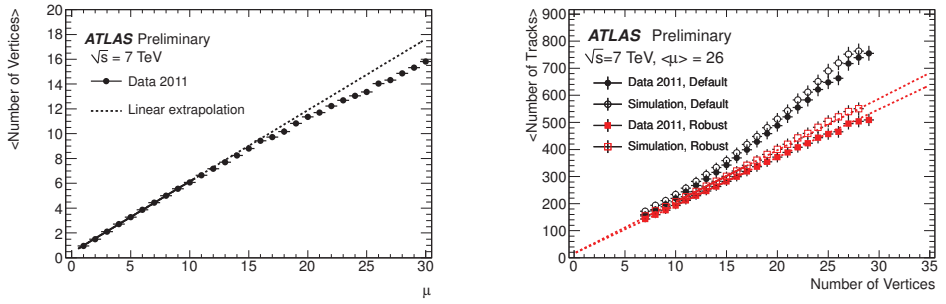

(a) (b)

Figure 3.10: (a) Average number of reconstructed primary vertices as a function of the pile-up interactions in data collected through 2011 at $\sqrt{s} = 7\,\text{TeV}$. The vertices are reconstructed using the default track requirements. A linear fit is performed for events with up to 10 additional pile-up interactions (solid) and extrapolated to higher μ values (dashed). (b) Average number of tracks per event as a function of the number of reconstructed vertices using default (black) and robust (red) tracking requirements in data (closed) and simulation (open) with $\langle\mu\rangle = 30$ and $\mu^{\text{peak}} = 26$. The red, solid lines are linear fits to the track multiplicity with the robust requirements for events with 10 to 17 reconstructed vertices, extrapolated to lower and higher track multiplicities (red, dashed).

SCT-only seeds with large transverse impact parameter that do not become track candidates are removed by requiring the d_0 to be less than 20 cm. Figure 3.11 illustrates an even tighter requirement: Using the default strategy, shown on the left, seeds are rejected only if *all* of their measurement points have been used by another previously reconstructed seed. The requirement is tightened to decrease the seed multiplicity significantly by rejecting seeds if

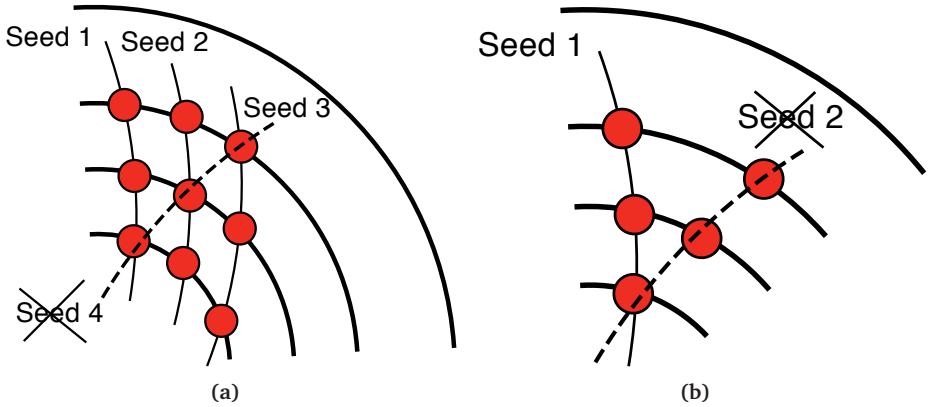

Figure 3.11: Illustration of the two different strategies used to produce seeds. In (a) seed 4 is rejected because all of its measurement points overlap with seeds 1, 2 and 3. For (b) the requirement has been tightened to reject seed 2 as one of its measurement points overlaps with another seed. Figures courtesy of Ref. [348].

any of their space points has been used previously, as illustrated on the right. The order in which seeds are rejected depends on the order in which they are formed, i.e. by increasing impact parameter.

To quantify the improvement on the computational performance, a minimum bias signal sample overlaid with up to 30 additional pile-up interactions, is reconstructed. At $\mu = 1$ the signal contributes significantly to the overall reconstruction time, while at $\mu = 31$, the reconstruction time is dominated by pile-up interactions. It is found, that the ID reconstruction proceeds faster by approximately 30 %, using the CPU mentioned in the caption of Fig. 3.12. The impact of the developed requirements on the physics objects is found to be well below the sub-percent level. In particular the primary efficiency is not reduced, owing to the partial combinatorial filter considering nearby seeds.

3.1.5 Flavor tagging

The jet parton flavor, either b, c, or uds/g (denoted light flavor in the following), is inferred using information from reconstructed tracks and vertices in the ID only, limiting the identification to the acceptance of the ID, i.e. $|\eta| < 2.5$. In this section the algorithms used for the identification of heavy flavors and their calibration is summarized, based on performance studies presented previously in Refs. [349, 350]. Section 3.3.1 then summarizes universally the reconstruction algorithms for the jet direction and the calibration to various energy scales using measurements from the whole detector.

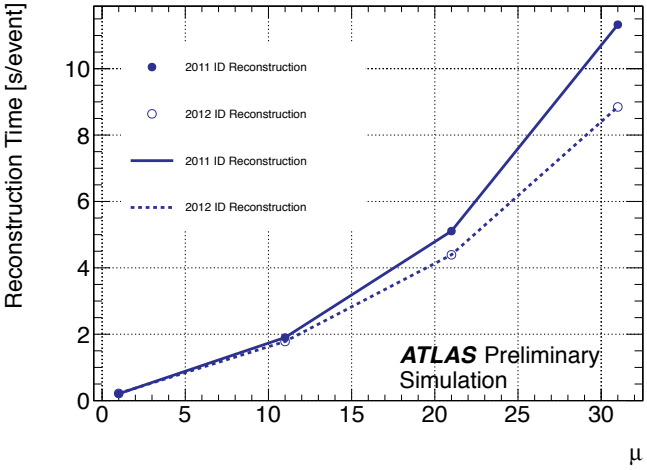

Figure 3.12: The CPU reconstruction time per event for ID reconstruction as a function of the number of interactions for the requirements used in 2011 data-taking and the requirements developed for 2012 data-taking. This was measured on an Intel® Core™2 Duo CPU E8500 @ 3.16 GHz with 3881832 kB of memory.

Several flavor tagging algorithms exploit topologies with displaced vertices originating from long-living hadrons containing heavy quarks, documented in [351]. The charged-particle tracks in a jet from heavy flavor decays have a larger impact parameter than the trajectories associated with the primary vertex, used e.g. by IP3D high-performance flavor tagging algorithm. To further separate between different flavors and reduce the mistag rates, Secondary Vertex (SV) algorithms attempt to reconstruct the displaced vertex associated with a b-jet and uses properties like the decay length significance measured in all space dimensions, and the invariant mass and the sum of energies of the tracks at the secondary vertex. The JetFitter algorithm uses a Kalman filter to reconstruct the full decay chain of the decaying hadron.

To benefit from the advantages of the individual techniques, the most discriminating variables between the various flavors are combined e.g. by the MV1 tagger, in artificial NNs, trained to separate heavy flavor jets and light flavor jets. The MV1 algorithm is calibrated independently for jets originating from b-quarks, from c-quarks, or from light-flavor quarks and gluons. The efficiency for identifying jets originating from b-quarks is measured using di-leptonic $t\bar{t}$ pair candidates in a combinatorial likelihood approach and calibrated for various target identification efficiencies [349]. The main systematic uncertainties affecting the calibration and the flavor composition originate from the modelling of the top and background processes. For the calibration of jets originating from c-quarks or light-flavor, $D^{*+} \to D^0\pi^+$ decays with $D^0 \to K^-\pi^+$ are used [350]. The main systematic uncertainties in this measurement are

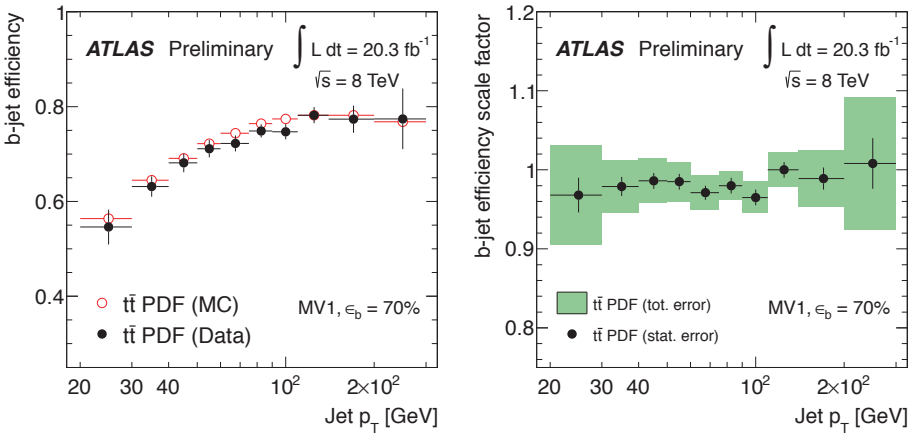

(a) (b)

Figure 3.13: (a) The b-jet efficiencies including the total statistical and systematic uncertainties and (b) the b-jet efficiency scale factors measured using di-leptonic $t\bar{t}$ pair candidates at the 70 % b-jet efficiency working point as a function of the jet transverse momentum. Figures taken from Ref. [349].

related to the D^{*+} mass fit, background parametrisation, the beauty fraction fit, and the extrapolation to an inclusive c-jet sample. The systematic uncertainties on the heavy flavor tagging efficiencies propagate to the measurement of the mistag rate, together with other uncertainties, for example on the heavy flavor fractions. Figure 3.13 shows exemplarily the b-jet efficiencies and the b-jet efficiency scale factors measured using di-leptonic $t\bar{t}$ pair candidates at the 70 % b-jet efficiency working point as a function of the jet transverse momentum.

3.2 Lepton identification and reconstruction

3.2.1 Muons

All analyses presented in the following chapters rely directly or indirectly on an efficient identification and reconstruction of muon candidates. Different reconstruction criteria exist to optimally combine the available information from the various sub-detectors and allow defining four different muon types. Their performance during run 1 data-taking is presented in Ref. [352] and summarized in this section. The most widely used type with the highest purity are combined muon candidates, which are identified by matching a ID muon track candidate, reconstructed using the previously described inside-out algorithm, with a complete track in the MS. Two independent approaches, named chains, are used to combine the information of the ID track and the MS track. The first chain uses the covariance matrices of

the ID and MS muon track candidates to statistically combine their track parameters [353]. The second chain performs a global Kalman Filter fit to the hits from both sub-detectors [354]. In the following results will be shown for chain 1 only.

The reconstruction of segment-tagged muons increases the acceptance for muons with low transverse momentum by matching a muon track candidate with at least one local track segment in the MDT or CSC chambers. Standalone muons can be used to extend the acceptance for muons beyond the coverage of the ID by extrapolating a trajectory measured in the MS back to the interaction region, taking into account the muon's energy loss in the calorimeters and multiple scattering effects. In uninstrumented regions of the MS in the center of the barrel calorimeter-tagged muons, i.e. ID muon track candidates matched to a energy deposit in the calorimeter compatible with a minimally ionizing particle, recover acceptance losses. The $H \to WW^* \to \ell\nu\ell\nu$ analysis presented in Cha. 5 uses combined muon candidates, required to have $|\eta| < 2.5$.

Reconstruction efficiency

The muon reconstruction efficiency for muons of each type is measured using a tag-and-probe method in di-muons from J/Ψ and Z decays complementing each other, i.e. the muon candidates are reconstructed by either the ID or the MS to test the efficiency of the other system, such that the reconstruction efficiency for any type is approximated by

$$\varepsilon(\text{Type}) \approx \varepsilon(\text{Type}|\text{ID}) \cdot \varepsilon(\text{MS}|\text{ID}). \tag{3.2}$$

Differences between the muon reconstruction efficiency measured in MC simulation and data are expressed in terms of an efficiency scale factor. Systematic uncertainties affecting the measurement of the efficiency scale factors in the phase space used by physics analyses originate from several effects: the tag-and-probe method itself is affected by the matching of tag and probe objects and the approximation of the probability of a muon being reconstructed by the ID. Additional uncertainties arise from the data-driven background estimate and background model and the modeling of the kinematic distributions of the probe objects. Furthermore, residual misalignment of detector components need to be considered. Their combined effect is found to be at the sub-percent level for muons with $p_{\mathrm{T}} > 10\,\text{GeV}$ in the range $|\eta| < 2.5$ [352]. Figure 3.14 shows the measured muon reconstruction efficiency for different muon types as a function of the pseudorapidity and the average number of inelastic interactions per bunch crossing for muons with $p_{\mathrm{T}} > 10\,\text{GeV}$ from $Z \to \mu\mu$ decays.

Mass scale and resolution

The di-muon mass scale and resolution is studied in $J/\Psi \to \mu\mu$, $\Upsilon \to \mu\mu$, and $Z \to \mu\mu$ decays in MC simulation and collision data. To reduce the momentum scale uncertainties for muons

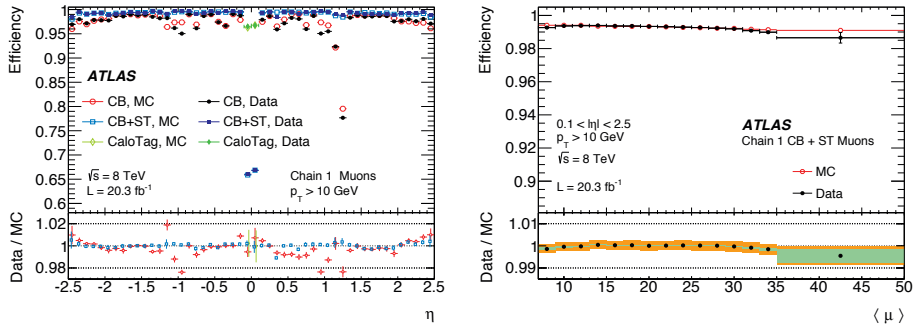

(a) **(b)**

Figure 3.14: Measured muon reconstruction efficiency for different muon types as a function of the (a) pseudorapidity and (b) the average number of inelastic interactions per bunch crossing for muons with $p_{\mathrm{T}} > 10\,\mathrm{GeV}$ from $Z \to \mu\mu$ decays. The statistical and systematic uncertainties are indicated. Figures taken from [352].

the simulated muon transverse momentum is corrected to match the momentum scale and resolution measured from collision data using a template fit to the invariant di-muon mass distribution in bins of η and p_{T} as described in detail in Ref. [352]. Residual systematic uncertainties on these corrections arise from the background estimation and the chosen templates fitted to the resonances and their kinematic distributions, but are generally at the sub-percent level over the full phase space. Typical values of the momentum scale correction for combined muons are below 0.1%. Systematic uncertainties on the momentum scale are about 0.035% in the barrel region and about 0.2% for $|\eta| > 2$. Figure 3.15 shows the comparison of the reconstructed di-muon invariant mass from the studied decays in collision data and in corrected MC simulation as a function of the pseudorapidity of the muon with higher transverse momentum. The relative momentum resolution $\sigma(p)/p$ ranges approximately from 1.7% to 4% for increasing values of pseudorapidity and transverse momentum.

3.2.2 Electrons and photons

Efficient reconstruction and identification of electrons and photons and a precise and robust measurement of their energy is imperative for all measurements presented in the following chapters. The probed phase space from many analyses is increased by combining electrons from $W \to e\nu$, $Z \to ee$, or $\tau \to e\nu\bar{\nu}$ decays with the corresponding final states with muons, for example in the $H \to WW^* \to \ell\nu\ell\nu$ and $H \to ZZ^* \to 4\ell$ decay modes where $\ell = e, \mu$. Clearly, also the $H \to \gamma\gamma$ decay relies on an accurate calibration of the energy measurement of converted and unconverted photons. The reconstruction, identification and calibration strategy for the energy measurement of electrons and photons is described in detail in Refs. [355–357] and repeated here for convenience and completeness.

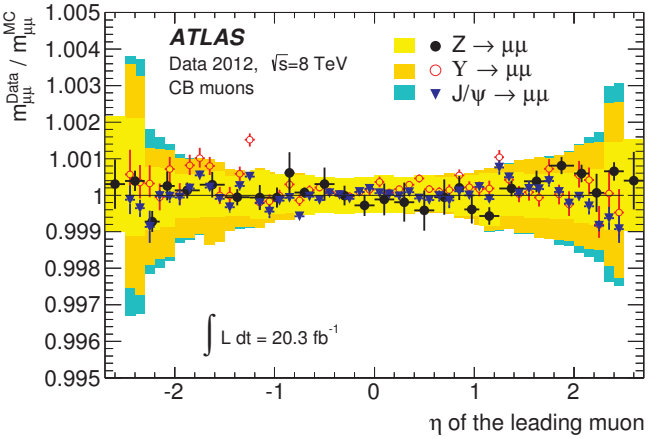

Figure 3.15: Comparison of the reconstructed di-muon invariant mass from $J/\Psi \to \mu\mu$, $\Upsilon \to \mu\mu$, and $Z \to \mu\mu$ decays in collision data and in corrected MC simulation as a function of the pseudorapidity of the muon with higher transverse momentum. The systematic uncertainty on the applied corrections to the MC simulations for each of the three samples is indicated by shaded areas. The error bars on the data represent the combined statistical and systematic uncertainty on the fit. Figure taken from [21].

Reconstruction and identification

Both electrons and photons develop similarly shaped EM showers in the LAr sampling calorimeter and deposit their energy in so called clusters. The reconstruction of these energy clusters is seeded by towers of size $\Delta\eta \times \Delta\phi = 0.025 \times 0.025$ that have a total transverse energy of at least 2.5 GeV. The search is performed using a sliding-window algorithm with a window size of 3×5 towers [358].

The distinguishing feature between electron and photon candidates are reconstructed tracks and interaction vertices in the ID that can be matched to an energy deposit. For both electron and photon candidate tracks are fitted with a Gaussian-sum filter (GSF) to account for radiative energy losses, i.e. bremsstrahlung,and large angle scatterings in the detector material to improve the estimated track parameters [359]. In case a candidate can be associated with a ID track originating from a vertex in the beam interaction region, it is classified as electron. Similarly, if a photon conversion vertex is reconstructed and the candidate matches with a ID track consistent with originating from a photon conversion, it is classified as converted photon. Remaining clusters without matching tracks or reconstructed conversion vertex in the ID are classified as unconverted photons [360].

To ensure that all clusters build by the reconstruction algorithms originate from electrons or photons, their longitudinal and transverse shower profile has to be consistent with those

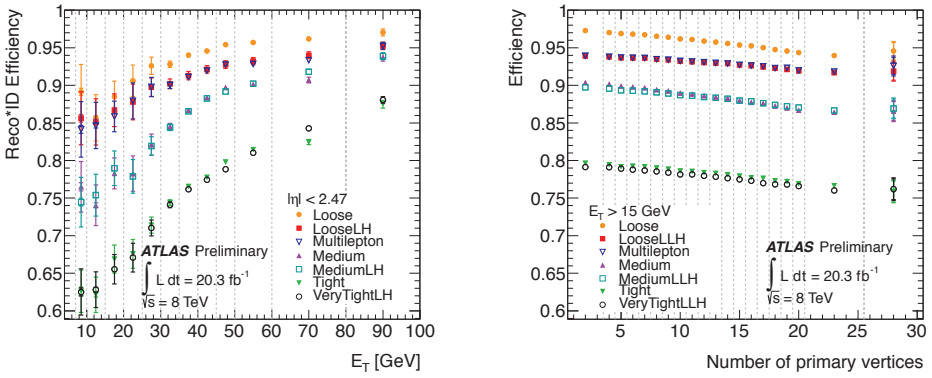

(a) **(b)**

Figure 3.16: (a) Measured combined reconstruction and identification efficiency for electrons for different cut-based and likelihood selections as a function of the transverse energy from $Z \to ee$ decays. (b) Measured identification efficiency for the different cut-based and likelihood selections as a function of the number of reconstructed primary vertices for electrons with $E_{\mathrm{T}} > 15\,\mathrm{GeV}$ from $Z \to ee$ decays. The statistical and systematic uncertainties are indicated. Figures taken from Ref. [356].

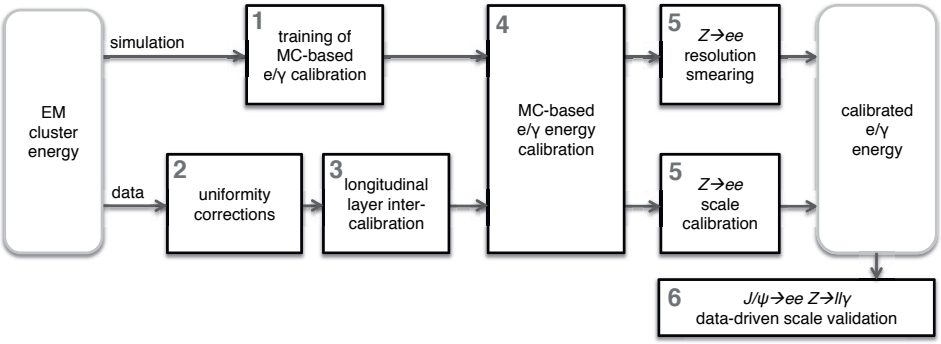

Figure 3.17: Schematic overview of the multivariate regression algorithm used to calibrate the energy measurement of electrons and photons. Figure taken from Ref. [357].

expected for EM showers. For electron candidates both sequential cut-based and, to cope with additional pile-up interactions, likelihood criteria, labelled loose, medium and (very) tight, have been defined with increasing background rejection power [355, 356]. Electrons used in the $H \to WW^* \to \ell\nu\ell\nu$ analysis presented in Cha. 5 have to satisfy the very tight likelihood requirement if $10 < E_{\mathrm{T}} < 25\,\mathrm{GeV}$ and the medium cut-based requirement for $E_{\mathrm{T}} > 25\,\mathrm{GeV}$. Photon candidates can be identified by imposing additional requirements on the shower shapes measured in the first two longitudinal layers of the ECAL and on the leakage into the HCAL [361].

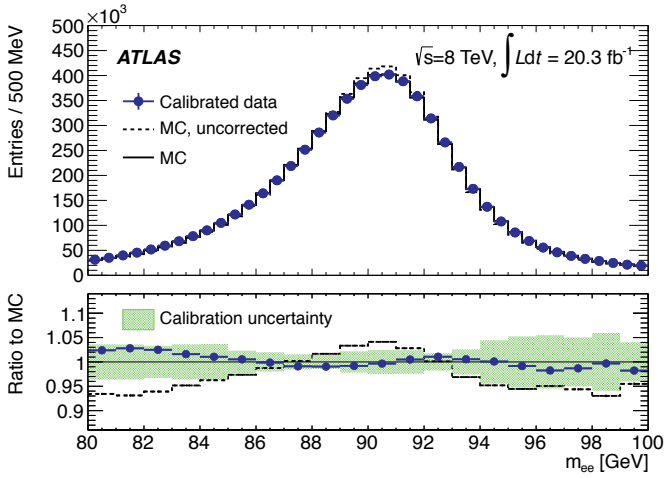

Figure 3.18: Di-electron invariant mass distribution for $Z \to ee$ decays in collision data and MC simulation and the final calibration uncertainty. The former is corrected with the derived energy scale factors and the latter is shown with and without the resolution corrections applied. Figure taken from Ref. [357].

The efficiency to detect an electron is measured independently for the reconstruction with respect to clusters reconstructed in the ECAL and the identification with respect to reconstructed electrons using tag-and-probe methods with electrons from $Z \to ee$ and $J/\Psi \to ee$ decays [355, 356]. The method is corrected for differences of the tracking properties and the shower shapes in the calorimeters between MC simulation and collision data in bins of the transverse energy and pseudorapidity, with the correction factors being at most 1-2 % different from unity. Figure 3.16 shows the measured combined reconstruction and identification efficiency for electrons as a function of the transverse energy and the measured identification efficiency for electrons as a function of the number of reconstructed primary vertices, both for different cut-based and likelihood selections. The overall electron reconstruction efficiency is stable with an increasing number of inelastic interactions per bunch crossing. It rises as a function of E_{T} owing to a better separation of these candidates from backgrounds in many of the discriminating variables used for the cut-based and likelihood selections. The uncertainty on the reconstruction efficiency is approximately 0.5-1.5 % at lower transverse energies and reduces to values below 0.5 % for increasing transverse energies.

Electromagnetic energy calibration

The measurement of the electromagnetic energy deposited in the ECAL by electrons and photons is based on the energy collected in calorimeter cells of varying size in $\Delta\eta \times \Delta\phi$ depending on the candidate type and the detector region, due to the deflection of charged

particles in the magnetic field and bremsstrahlung in upstream detector material. In the barrel 3×7 towers are used for electrons and converted photons and 3×5 towers for unconverted photons. In the end-caps 5×5 towers are used for both electrons and photons. Figure 3.17 shows a schematic overview of the multivariate regression algorithm used to calibrate the energy measurements of electrons and photons. The calibration takes into account corrections for the detector material budget as well as linearity corrections for the energy response, and intercalibrates the LAr calorimeter layers, which are considered as systematic uncertainties. In addition, the energy measurement of electrons and photons is directly affected by the uncertainties in the reconstruction of photon conversions and in the modeling of the lateral shower shape. Figure 3.18 shows the di-electron invariant mass distribution for $Z \to ee$ decays in collision data and MC simulation and the final calibration uncertainty. The former is corrected with the derived energy scale factors and the latter is shown with and without the resolution corrections applied.

3.3 Jets and missing transverse momentum

3.3.1 Jet clustering and calibration

Jets, introduced in Sec. 1.3 from a theoretical perspective as narrow cones of collinearly traversing partons in PSs, are a prominent feature observed at high energy hadron colliders like the LHC at CERN. They are key signatures of many SM and BSM processes, e.g. the Higgs boson production through VBF, c.f. Sec. 1.4, which requires robust algorithms to identify these objects. Experimentally, jets are observed as clusters of topologically related energy deposits in the calorimeter system, associated with tracks of charged particles reconstructed in ID. As such, they cannot be uniquely matched to the source of the PS. In the following the reconstruction of jets and their calibration is summarized, while a detailed description of the methods is given in Refs. [362, 363].

Jet reconstruction

Calorimeter jets[2] are reconstructed from topo-clusters using collinear and infrared safe clustering algorithms, i.e. from energy deposits in topologically connected calorimeter cells with significant signal above a threshold to suppress electronic noise and noise from pile-up interactions [362, 364, 365]. Collinear safe algorithms are insensitive to collinear splitting of partons, i.e. to the distribution of the PS's transverse momentum among decay products. Clustering algorithms are infrared safe if they are not sensitive to extra radiation of soft particles not originating from the fragmentation of the hard scatter process.

[2] Track jets are built from charged particle tracks originating from the primary interaction vertex using the same jet clustering algorithms [362].

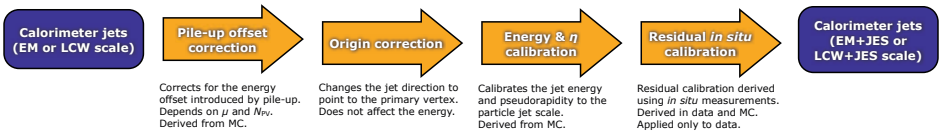

Figure 3.19: Illustration of the calibration scheme for calorimeter jets. Figure taken from Ref. [363].

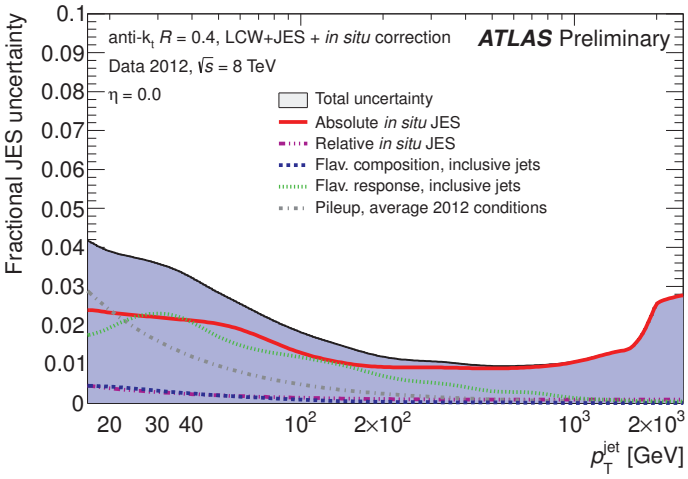

Figure 3.20: Fractional jet energy scale systematic uncertainty as a function of the jet transverse momentum for central anti-k_t jets with radius parameter $R = 0.4$ calibrated with the local cell signal weighting (LCW)+jet energy scale (JES) scheme. Figure taken from Ref. [366].

The most widely used ones are sequential recombination algorithms, which cluster objects hierarchically depending on their respective distance,

$$d_{ij} = \min\left(p_{\mathrm{T}i}^{2p}, p_{\mathrm{T}j}^{2p}\right) \frac{(\eta_i - \eta_j)^2 + (\phi_i - \phi_j)^2}{R^2}, \tag{3.3}$$

starting from the pair with minimal distance. Clusters i are promoted to jets when no remaining d_{ij} is smaller than the distance between i and the beam, $d_{iB} = p_{\mathrm{T}i}^{2p}$. p and R are constants of the algorithm, which define its clustering behavior and the structure of the final jets. The analyses presented in the following chapters use the anti-k_t algorithm [130] utilising the FASTJET software package [367, 368]. The anti-k_t algorithm is characterized by the choice $p = -1$, which ensures that soft radiations will cluster with hard objects before they cluster among themselves, and thus produces, in the absence of close-by hard objects, perfectly conical jets of radius R. Other choices include $p = 1$ (k_t algorithm [127–129]) or $p = 0$ (C/A algorithm [131, 132]), which are not discussed further.

Both the number of reconstructed jet candidates from energy deposits in the calorimeter and their kinematics are sensitive to pile-up effects. To control the contribution additional jets originating from pile-up vertices and stochastic fluctuations of soft activity a requirement is imposed on the jet vertex fraction (JVF), i.e. the fraction of the reconstructed jet energy associated with a particular primary vertex [369].

Calibration and systematic uncertainties

Figure 3.19 illustrates the calibration scheme used for calorimeter jets. Topo-clusters are initially calibrated to the energy scale of EM showers [363, 364] and references therein. In a second step LCW is used to calibrate the jets to the hadronic energy scale by classifying topo-clusters as either electromagnetic or hadronic based on the shower development, i.e. the energy density and the longitudinal shower depth. The reconstructed calorimeter jets are corrected for in-time and out-of-time pile-up, for its geometrical origin in the detector, and for the jet kinematics and direction with respect to single charged and neutral pion MC simulations and residual effects [362, 363]. The jet energy calibration uses in situ techniques that exploit the balance between the jet transverse momenta and the transverse momenta of reference objects, e.g. e^+e^- pairs or photons, in Z-jet, γ-jet or multijet events. Figure 3.20 shows the fractional jet energy scale systematic uncertainty as a function of the jet transverse momentum for central anti-k_t jets with radius parameter $R = 0.4$ calibrated with the LCW+JES scheme, i.e. the jet collection used in the $H \to WW^* \to \ell\nu\ell\nu$ analysis. The in situ calibration techniques obey systematic uncertainties from various sources, classified into detector description, physics modeling, statistics and method, and mixed detector and modeling effects [363]. These are added in quadrature to the systematic uncertainties arising from the flavor composition and response, pile-up effects, and close-by jet effects in order to derive the total uncertainty on the JES.

3.3.2 τ-leptons

τ-leptons decay with a BR of 35 % into electrons or muons and neutrinos, which are indistinguishable from prompt electron and muon candidates, and thus not used for tau identification. The remaining 65 % of the τ-leptons decay into an undetectable neutrino in association with pairs of charged and neutral pions, or rarely kaons, which are identified as jets in the detector. This section summarizes the reconstruction and identification of hadronic tau decays, presented in detail in Ref. [370].

For the reconstruction of hadronic tau decays information from the ID and the calorimeters is combined in a multivariate discriminant, evaluated in the following at Loose, medium, and tight working points that are defined corresponding to different target identification efficiencies for hadronic tau candidates. In particular quantities describing the shower shape in the calorimeters and the ID are used to distinguish between hadronically decaying τ-leptons

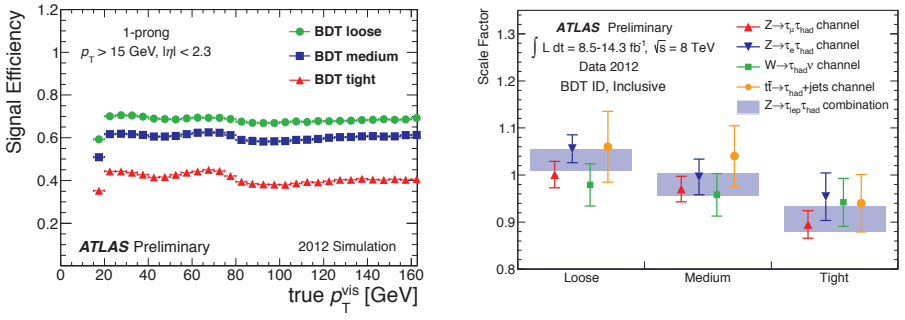

(a) (b)

Figure 3.21: (a) The one prong tau identification efficiency for the three working points of the Boosted Decision Tree (BDT) tau identification as a function of true visible tau transverse momentum for simulated signal candidates from $Z \to \tau\tau$, $Z' \to \tau\tau$, and $W \to \tau\nu_\tau$ decays. (b) Summary of the inclusive hadronic tau identification efficiency scale factors measured in $Z \to \tau_{\text{lep}}\tau_{\text{had}}$, $W \to \tau_{\text{had}}\nu_\tau$, and $t\bar{t} \to \tau_{\text{had}}$ + jets decays for all working points. Figures taken from Ref. [370].

and quark- or gluon-initiated jets. Electrons faking a τ-lepton can be rejected by imposing a veto based on the emission of transition radiation and by the measured shower shape in the calorimeter. Muons, i.e. minimum ionizing particles, typically do not deposit enough energy in the calorimeter system to seed the jet clustering algorithm and thus are unlikely to be misidentified as a τ-lepton. To cope with inefficiencies of the MS and low energy muons the electromagnetic fraction and the track momentum in connection with the calorimeter energy are used to discriminate hadronic tau decay candidates and reconstructed muons in addition to a veto on their geometrical overlap. As an example, Fig. 3.21a shows the one prong tau identification efficiency for the three working points of the BDT tau identification as a function of true visible tau transverse momentum for simulated signal candidates from $Z \to \tau\tau$, $Z' \to \tau\tau$, and $W \to \tau\nu_\tau$ decays. The $H \to \tau\tau$ analysis entering the Higgs coupling combination uses the medium identification criterium, which has a misidentification probability of 1-2 % for hadronic tau decay candidates with $p_T > 20$ GeV. Hadronic tau identification efficiency scale factors are measured using a tag-and-probe method in three different final states, $Z \to \tau_{\text{lep}}\tau_{\text{had}}$, $W \to \tau_{\text{had}}\nu_\tau$, and $t\bar{t} \to \tau_{\text{had}}$ + jets, summarized for all working points in Fig. 3.21b. The calibration of the tau energy scale and the associated systematic uncertainty is beyond the scope of this work, but can be found in Ref. [371]. Typical values for the systematic uncertainty for hadronic tau decay modes with one (at least two) reconstructed track(s) are at most 3 % (4 %) in the phase space covered by the ID.

3.3.3 Missing transverse momentum

The interaction cross section of neutrinos, WIMPs, and other weakly interacting particles, is exiguous. Thus, the detection would typically be indirectly through (inelastic) interactions with a large-volume or massive detector. Examples of such experimental setups are Super-Kamiokande [372], Antares [373]/KM3NeT [374], IceCube [375], SuperCDMS [376], the XENON program [377–379], and LUX [380]. The ATLAS detector is neither designed, nor equipped with detectors that would allow measuring the trajectories of these particles. Thus, in practice, all weakly interacting particles escape the ATLAS detector undetected.

However, the transverse momentum of the colliding partons in the initial state of events at a collider like the LHC at CERN is zero[3]. Hence, the transverse momentum of the undetected particles can be inferred from the momentum imbalance in the plane transverse to the beam axis in the final state. It is obtained from the negative vector sum of the momenta of the selected particles and soft objects in a collision,

$$\boldsymbol{E}_{\mathrm{T}}^{\mathrm{miss}} = \left(\sum_{\text{selected}} \boldsymbol{E}_{\mathrm{T}} + \sum_{\text{soft}} \boldsymbol{E}_{\mathrm{T}} \right). \tag{3.4}$$

Here, soft objects are characterized by a transverse energy that is below selection cuts for the hard objects. In the following different methods of reconstructing missing transverse energy (MET), defined by the choice of selected objects and the measurement strategy of soft objects, are presented. Their performance and calibration is extensively discussed in Refs. [381, 382].

Calorimeter based MET reconstruction, in the following denoted by $E_{\mathrm{T}}^{\mathrm{miss}}$, takes into account energy deposits in ECAL and HCAL, calibrated according to the reconstructed and identified high-p_{T} associated with the topo-cluster. Besides reconstructed electrons, photons, hadronically decaying τ-leptons, jets, and muons, also topo-cluster not associated with any such object are considered for the calculation of the $E_{\mathrm{T}}^{\mathrm{miss}}$ calorimeter term.

The $E_{\mathrm{T}}^{\mathrm{miss}}$ reconstruction, response, and resolution are directly affected by pile-up interactions degrading the performance of the reconstruction algorithms for all objects entering the calculation, mainly through the jet and soft terms. Several methods have been exploited to suppress pile-up contributions to these terms, the jet area method [382, 383], a requirement based on the JVF, and scaling the soft terms with the soft term vertex fraction (STVF), i.e. the fraction of momenta of tracks matched to the soft term, which are associated with the hard scattering vertex [382].

A significant improvement of the resolution can be achieved by guiding the momentum measurement of soft objects using tracking information from selected leptons and jets asso-

[3] Note that the momentum along the beam direction is distributed over all partons moving collinear with the surrounding proton and thus not necessarily balanced.

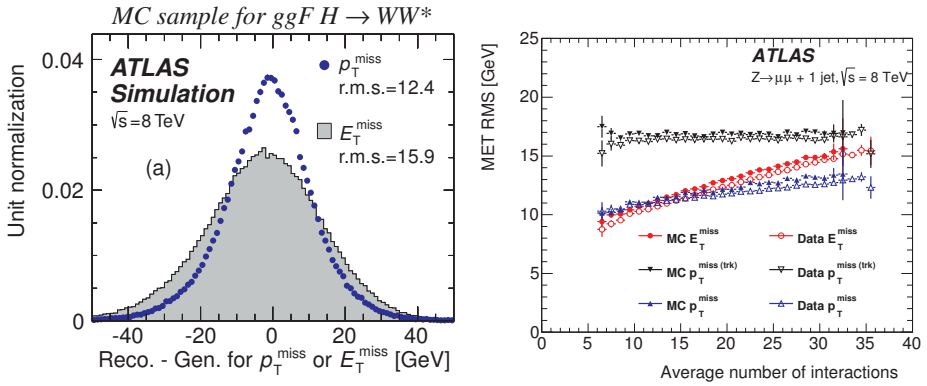

(a) **(b)**

Figure 3.22: (a) Comparison between the MET resolution for the calorimeter based (E_T^{miss}) and the track based (p_T^{miss}) reconstruction of soft objects, using simulated Higgs boson events produced via gluon-fusion, no associated jet, and with a $H \to WW^*$ decay topology. (b) MET resolution as function of the average number of interactions per bunch crossing for $Z \to \mu\mu$ events produced with one associated jet for various MET flavors, E_T^{miss}, $p_T^{miss\,(trk)}$, and p_T^{miss}. The $\mu\mu$ events are selected from Z mass window in the $n_j = 1$ category of the $H \to WW^* \to \ell\nu\ell\nu$ analysis, cf. Cha. 5. The resolution of $p_T^{miss\,(trk)}$ is very stable under pile-up, but degraded due to missing the neutrals from the hard jet. Figures taken from Ref. [30].

ciated to the primary vertex. This track-based reconstruction, denoted p_T^{miss}, is used in the $H \to WW^* \to \ell\nu\ell\nu$ analysis in the calculation of the transverse mass. The improvement is illustrated in Fig. 3.22a using simulated Higgs boson events produced via gluon-fusion, no associated jet, and with a $H \to WW^*$ decay topology. It should be noted explicitly, that the reconstructed transverse mass benefits from the enhanced MET resolution.

A simplified variant of p_T^{miss} not including the jets in the sum over selected objects in (3.4), denoted $p_T^{miss\,(trk)}$, is used in the $H \to WW^* \to \ell\nu\ell\nu$ analysis to reject DY events. The relative directions of reconstructed MET with respect to other objects is defined for example as

$$p_{T,rel}^{miss} = \begin{cases} p_T^{miss} \sin\Delta\phi_{near} & \text{if } \Delta\phi_{near} < \pi/2 \\ p_T^{miss} & \text{otherwise,} \end{cases} \tag{3.5}$$

with $\Delta\phi_{near}$ being the difference in azimuth between p_T^{miss} and the closest high-p_T object.

The E_T^{miss} performance is studied in different event topologies, namely $Z \to \ell\ell$, $W \to \ell\nu$, and Higgs boson decays, as well as in SUSY processes. As an example, Fig. 3.22b shows the MET resolution as function of the average number of interactions per bunch crossing for $Z \to \mu\mu$ events produced with one associated jet for various MET flavors. The $\mu\mu$ events are selected from the Z mass window in the $n_j = 1$ category of the $H \to WW^* \to \ell\nu\ell\nu$ analysis, cf. Cha. 5.

Statistics and moment morphing

4

This chapter is intended to introduce the reader to the statistical model, notations and conventions used by the LHC experiments, in particular for the analyses presented in the following chapters. To interpret a measurement x, one must define a probability model $f(x|\boldsymbol{\alpha})$ that defines the probability of a measurement x under the hypothesis $\boldsymbol{\alpha}$ of this model, characterized by one or more observables x. A second section of this chapter discusses statistical methods used in the frequentist approach to make inferences on the probability model, i. e. statements on $\boldsymbol{\alpha}$. More details on the statistical treatment of the data, in particular in parameterized likelihood analyses, are given in Refs. [58, 384–386].

4.1 Statistical modeling

4.1.1 Likelihood functions

Given a set of measurements x, and a hypothesis $\boldsymbol{\alpha}$, the likelihood $L(x|\boldsymbol{\alpha}) = L(\boldsymbol{\alpha})$ is defined as the probability of the data under this hypothesis, formulated as a probability density function (p.d.f.), $f(x|\boldsymbol{\alpha})$. The measurement x can be a single number, or one or more continuously distributed and repeatedly measured independent and identically distributed observables. Here, $\boldsymbol{\alpha} = (\mu, \boldsymbol{\theta})$ represents both theoretical parameters such as the Higgs boson mass m_H or signal rates, and nuisance parameters parametrizing the effect of systematic uncertainties on the predicted distributions of the various signal and background processes, correcting the probability model. Generically, μ denotes the parameter of interest (POI) of the tested model and indicates a continuous set of hypotheses, and $\boldsymbol{\theta}$ represents the nuisance parameters. For NP searches at the LHC, a common choice is $\mu = \sigma_{\text{obs}}/\sigma_{\text{SM}}$, i. e. the inclusive signal strength parameter defined as the ratio of the measured cross section and the predicted cross section of the nominal signal model, e. g. the SM. In this convention, the nominal hypothesis is given by $\mu = 1$, while the null hypothesis is typically given by $\mu = 0$. Other choices used in the following chapters also include the Higgs boson mass m_H, scale factors for the various Higgs boson coupling strength parameters, or model parameters of BSM models. The likelihood function itself is invariant under reparametrizations, $L(\boldsymbol{\alpha}) = L(\eta(\boldsymbol{\alpha}))$.

For a cut-and-count analysis the observable x corresponds to the observed count n, and the corresponding data set is denoted $\mathscr{D} = \{n\}$. Given an expected count $\nu(\boldsymbol{\alpha})$, the likelihood is given by a Poisson distribution,

$$L(\mathscr{D}|\boldsymbol{\alpha}) = \text{Poisson}(n|\nu(\boldsymbol{\alpha})). \tag{4.1}$$

In a typical search for NP on top of a SM background, the expected count comprises the rates for all signal and background scattering processes contributing to the total yield,

$$\nu(\boldsymbol{\alpha}) = \sum_{k\in\text{processes}} \nu_k(\boldsymbol{\alpha}). \tag{4.2}$$

Disjoint selections of the data, $\mathscr{D} = \{\mathscr{D}_1, \ldots \mathscr{D}_{c_{\text{max}}}\}$, e. g. selection criteria imposed to enhance the contribution of a physical process in a channel $c = \{c_1, \ldots, c_{\text{max}}\}$, are simultaneously described by a product over the respective likelihood functions $L(\boldsymbol{\alpha})$,

$$L(\boldsymbol{\alpha}) = \prod_{c=1}^{c_{\text{max}}} L(\boldsymbol{\alpha}). \tag{4.3}$$

If there exists a discriminating observable x in the event selection, the observed data can be augmented from the event count n to the data set $\mathscr{D} = \{x_1, \ldots, x_n\}$. Each component x_e of this extended data set follows the p.d.f. $f(x_e|\boldsymbol{\alpha})$. The probability to observe n events given $\nu(\boldsymbol{\alpha})$ can be described by a Poisson term, and should be included in the likelihood. The likelihood function for this extended data set is then

$$L(\mathscr{D}|\boldsymbol{\alpha}) = \text{Poisson}(n|\nu(\boldsymbol{\alpha})) \prod_{e=1}^{n} f(x_e|\boldsymbol{\alpha}), \tag{4.4}$$

referred to as an extended likelihood or marked Poisson model [384]. Similar to the counting case (4.2), the p.d.f. $f(x|\boldsymbol{\alpha})$ is the weighted sum of the templates for each process contributing to the total rate,

$$f(x|\boldsymbol{\alpha}) = \frac{1}{\nu(\boldsymbol{\alpha})} \sum_{k\in\text{processes}} \nu_k(\boldsymbol{\alpha}) f_k(x|\boldsymbol{\alpha}). \tag{4.5}$$

At the LHC analytical predictions for $f_k(x|\boldsymbol{\alpha})$ are generally not available. Instead the distributions are estimated from MC simulation. In such case, the data is customarily divided into "data classes" based on ranges in x, so that only histograms of the predictions $f_k(x|\boldsymbol{\alpha})$ are required as input. The likelihood function simplifies to a product over the n_{bins} Poisson terms, cf. Eqn. (4.3),

$$L(\mathscr{D}|\boldsymbol{\alpha}) = \prod_{i=1}^{n_{\text{bins}}} \text{Poisson}(n_i|\nu_i(\boldsymbol{\alpha})). \tag{4.6}$$

For the presented analyses ROOT [387] and in particular the RooFit toolkit [388] are used to model the data and to construct probability densities.

4.1.2 Subsidiary measurements and systematic uncertainties

Systematic uncertainties arise from many sources, some of which have been introduced in Cha. 3. They make the relation between the data and the POI less certain. Hence, they need to be incorporated in the statistical model of a physics measurement. Their effect on the predicted counts and distributions is often captured by the introduction of additional model parameters, whose value is considered to be unknown. These additional nuisance parameters $\boldsymbol{\theta}$ enlarge the parameter space. Nuisance parameters are often estimated from subsidiary measurements $f_{\text{subs},p}(\mathscr{D}_{\text{subs}}|\theta_p, \boldsymbol{\alpha}_{\text{other}})$ for all $\theta_p \in \boldsymbol{\theta}$. For example the calibration of the JES is measured from dedicated JES data samples $\mathscr{D}_{\text{JES}}$ with a dedicated analysis. Including systematic uncertainties into the model for physics measurement using nuisance parameters effectively allows to jointly measure $\boldsymbol{\alpha} = (\mu, \boldsymbol{\theta})$, which may result in a stronger constraint on the systematic uncertainties than the subsidiary measurement provides.

If we suppose $\mathscr{D}_{\text{subs}}$ is statistically independent from $\mathscr{D}$, e.g. if the subsidiary measurements are defined by event selection criteria orthogonal to the requirements employed for the physics measurement, then the full information of the subsidiary measurement, i.e. the likelihood $L_{\text{subs},p}(\theta_p, \boldsymbol{\alpha}_{\text{other}}|\mathscr{D}_{\text{subs}})$, can be included in the joint model according to the prescription given in Eqn. (4.3). This is typically the case for control regions or sidebands used to normalize a background process.

In most cases, e.g. for uncertainties estimated from dedicated calibration measurements performed by performance groups, only a maximum likelihood estimate for the nuisance parameter θ_p, and a standard error, is available, $\tilde{\theta}_p \pm \sigma_p$, i.e. the probability model for such an subsidiary measurement is approximated by an idealized model,

$$f_{\text{subs},p}(\mathscr{D}_{\text{subs}}|\theta_p, \boldsymbol{\alpha}_{\text{other}}) \to f_p(\tilde{\theta}_p|\theta_p, \sigma_p), \tag{4.7}$$

referred to as a constraint term. While the effect of each individual systematic uncertainty on the distribution of the observable x of the physics measurement can be determined from the provided information, $f(x|\theta = \tilde{\theta})$ and $f(x|\theta = \tilde{\theta} \pm \sigma)$, it is not sufficient to construct the full probability model. In case of multiple systematic uncertainties approximated by idealized measurements, correlated effects of nuisance parameters are left unspecified, i.e. both the likelihood of the subsidiary measurements and the effect of systematic uncertainties in the physics measurement are assumed to factorize. Section 4.3 will return to the effect of correlated estimates of systematic uncertainties. Including the constraint terms explicitly, the full likelihood can be written as

$$L(\mathscr{D}, \mathscr{G}|\boldsymbol{\alpha}) = \prod_{c=1}^{c_{\max}} \left[\text{Poisson}(n_c|\nu_c(\boldsymbol{\alpha})) \prod_{e=1}^{n_c} f_c(x_{ce}|\boldsymbol{\alpha}) \right] \times \prod_{p \in \mathbb{S}} f_p(\tilde{\theta}_p|\theta_p, \sigma_p), \tag{4.8}$$

where $\mathscr{G} = \{\tilde{\theta}_p\}$ denotes the global observables for the set of nuisance parameters $\mathbb{S}$ that are constrained by subsidiary measurements.

The functional form of the subsidiary measurement $f(\tilde{\theta}|\theta,\sigma)$ as well as the response of the expected rate $\nu(\theta)$ to changes in the magnitude of the systematic effect and the template $f(x|\theta)$ depend on the source of the uncertainty modeled by the nuisance parameter θ. A continuous parametrization of the model for varying nuisance parameter values is approximated based on the available information from a simplified measurement, i.e. the nominal model and its "up" and "down" variations. The remainder of this section discusses the explicit forms used for different sources of systematic uncertainties.

Subsidiary measurements and response functions

Statistical uncertainties on the number of selected events in channel follow a Poisson distribution. Hence, for nuisance parameters describing the finite MC template statistics in a counting measurement a Poisson is chosen as subsidiary measurement,

$$f(\tilde{\theta}|\theta,\sigma) = \text{Poisson}(\tilde{\theta}|\theta\tau)) \quad \text{with} \quad \tilde{\theta} = \left(\frac{\sigma}{\nu^{\text{MC}}}\right)^2 \quad \text{and} \quad \tau = \left(\frac{\nu^{\text{MC}}}{\sigma}\right)^2, \tag{4.9}$$

with ν^{MC} being the number of events estimated using MC techniques and σ being the total statistical uncertainty. Hence, $\tilde{\theta}$ corresponds to the total MC sample and τ is simply the luminosity ratio for an estimate from MC, or the ratio between the counts in signal and control selections. The nominal value of θ is 1 such that $\tilde{\theta}$ would fluctuate about $\theta\tau$. For stacked histogram templates Barlow and Beeston proposed to implement one nuisance parameter per bin for every component to model the effect of template statistical uncertainties [389]. Alternatively, a more lightweight approach approximates the effect of finite template statistics by associating a single nuisance parameter with the total prediction and statistical uncertainty for each bin [390]. Suppose that in a data class b the expected count not subject to MC statistical uncertainties is given by $\nu_b^{\text{data}}(\boldsymbol{\alpha})$, e. g. because the estimate is data driven. Similarly, $\nu_b^{\text{MC}}(\boldsymbol{\alpha})$ is the count expected in b for which MC statistical uncertainties need to be included. The total expected count in this data class is then given by

$$\nu_b(\boldsymbol{\alpha}) = \nu_b^{\text{data}}(\boldsymbol{\alpha}) + \theta\,\nu_b^{\text{MC}}(\boldsymbol{\alpha}). \tag{4.10}$$

Conventionally, in all other cases Gaussian subsidiary measurements are used,

$$f(\tilde{\theta}|\theta,\sigma) = \text{Gaussian}(\tilde{\theta}'|\theta',\sigma'). \tag{4.11}$$

The effect of a variation of a nuisance parameter is parametrized such that the transformed nuisance parameters θ' and the global observables $\tilde{\theta}'$ are dimensionless, the value of the global observables is $\tilde{\theta}' = 0$, and the variance of the Gaussian constraint is $\sigma' = 1$.

A common choice is $\theta' = \ln\theta$ so that θ follows a log-normal distribution,

$$f(\tilde{\theta}|\theta) = \frac{1}{\sqrt{2\pi}\ln\kappa}\frac{1}{\theta}\exp\left(-\frac{(\ln(\theta/\tilde{\theta}))}{2(\ln\kappa)^2}\right). \tag{4.12}$$

In this case the (positive definite) rates respond to nuisance parameter variations as

$$\nu(\theta') = \nu(\theta'=0)\kappa_{\pm}^{\theta'} \quad \text{with} \quad \kappa_{+} = \frac{\nu(\theta'=1)}{\nu(\theta'=0)} \text{ and } \kappa_{-} = \frac{\nu(\theta'=0)}{\nu(\theta'=-1)}. \tag{4.13}$$

The condition $\kappa_{+} \neq \kappa_{-}$ represents an asymmetric uncertainty, which can be implemented in a bifurcated way that ensures a continuous parametrization of the response function, e.g. using a higher order polynomial or a exponential function. Henceforth, the prime will be suppressed and θ will refer to the transformed nuisance parameter.

Shape variations

The effect of a systematic uncertainty on the shape of the distribution of an observable x, $f(x|\theta)$ is treated factorized from its effect on the count. To approximate the effect of a systematic uncertainty on $f(x|\theta)$ is constructed from $f(x|\theta = 0)$ and the alternate distributions $f(x|\theta = \pm 1)$ using template morphing techniques, i.e. by an interpolation between the provided templates,

$$f(x|\theta)\big|_{\theta=0,\pm1} \mapsto f(x|\theta)\ \forall\theta \tag{4.14}$$

Several algorithms have been developed over the past years: vertical morphing [390] interpolates the contents of each bin in a piecewise way using a higher order polynomial or a exponential function of the nuisance parameter θ. Integral morphing [391] interpolates the cumulative distribution function (c.d.f.) and thus models shifting peaked distributions more accurately than vertical morphing. Another approach is moment morphing [20], which non-linearly interpolates the moments of the templates and is capable of modeling coherent effects of systematic uncertainties, described in detail in Sec. 4.3.

4.2 Statistical inference

This section summarizes the frequentist methods used in the context of Higgs physics to make inferences about the POI of a likelihood model, constructed as described in the previous section using a sample of data, e.g. the collision data recorded by the ATLAS and CMS experiments during Run 1 of the LHC [386, 392]. The frequentist treatment suggests to interpret probability as asymptotic frequency of the outcome of a repeatable experiment. Bayesian statistics gives another interpretation of probability, which shall not be discussed in this section. A comprehensive summary of statistics concepts and suggestions for further reading can be found e.g. in Ref. [58].

4.2.1 Parameter estimation

The estimates of parameters from data presented in the remainder of the thesis are obtained maximizing a likelihood function $L(\boldsymbol{\alpha}) = L(\mathscr{D}, \mathscr{G}|\boldsymbol{\alpha})$ with respect to the parameters $\boldsymbol{\alpha}$, c.f. Eqn. (4.8), where henceforth the shorthand notation of the likelihood will be used. For a description of the method of least squares the reader is referred to the literature, e.g. [384]. The maximum likelihood estimators (MLEs) for $\boldsymbol{\alpha}$, denoted as $\hat{\boldsymbol{\alpha}}$, i.e. the values that maximize $L(\boldsymbol{\alpha})$, or, equivalently, minimize $-\ln L(\boldsymbol{\alpha})$, are the solutions of the likelihood equations

$$\frac{\partial \ln L(\boldsymbol{\alpha})}{\partial \alpha_i} = 0 \quad \text{for all} \quad \alpha_i \in \boldsymbol{\alpha}. \tag{4.15}$$

Similarly, the conditional maximum likelihood estimators (CMLEs) $\hat{\hat{\boldsymbol{\theta}}}$ maximize the likelihood function $L(\boldsymbol{\alpha}) = L(\mu, \boldsymbol{\theta})$ conditional on a fixed value of the POI, μ. Both the MLEs and the CMLEs depend implicitly on the data of the measurement $\mathscr{D}$ and the data of the subsidiary measurement $\mathscr{G}$. For complex probability models such as the ones used throughout the document, the solution to Eqn. (4.15) can not be found analytically and it needs to be calculated numerically, e.g. using MINUIT [393].

The MLEs $\hat{\boldsymbol{\alpha}}$ are asymptotically unbiased, i.e. the estimate converges to the true value, and efficient for large data samples. The variance of any parameter α can be read off from the variance-covariance matrix $V_{ij} = \mathrm{cov}(\hat{\alpha}_i, \hat{\alpha}_j)$, which incorporates the effect of all systematic uncertainties that are correlated with α. The variance is the second moment of a distribution and does not guarantee a probability interpretation unless the distribution is known to be Gaussian, which is the asympotic distribution of any measurement in the limit of infinite statistics (central limit theorem (CLT)). For a statement with guaranteed probability interpretation for measurements with low statistics, frequentist confidence intervals need to be constructed, cf. Sec. 4.2.4.

The HESSE algorithm in MINUIT measures the Hessian matrix from finite steps in the likelihood function to obtain the variance-covariance matrix, approximated for a set of MLEs by

$$H_{ij}(\hat{\boldsymbol{\alpha}}) = -(V)^{-1}_{ij}(\hat{\boldsymbol{\alpha}}) = \left.\frac{\partial^2 \ln L(\boldsymbol{\alpha})}{\partial \alpha_i \partial \alpha_j}\right|_{\hat{\boldsymbol{\alpha}}}. \tag{4.16}$$

The approximation becomes exact for a linear model with Gaussian distributions. The vertical distance $d(\hat{\boldsymbol{\alpha}}, \boldsymbol{\alpha}_{\text{true}})$ between the estimated and the true values of the parameters $\boldsymbol{\alpha}$ can be calculated using the gradient of the log-likelihood at the estimated values, $\mathrm{grad}(\ln L(\hat{\boldsymbol{\alpha}}))$, assuming a quadratic function with variance-covariance $V(\hat{\boldsymbol{\alpha}})$:

$$d(\hat{\boldsymbol{\alpha}}, \boldsymbol{\alpha}_{\text{true}}) = 0.5 \times \sum_{i,j} \left.\frac{\partial \ln L(\boldsymbol{\alpha})}{\partial \alpha_i}\right|_{\hat{\alpha}_i} H_{ij}(\hat{\boldsymbol{\alpha}}) \left.\frac{\partial \ln L(\boldsymbol{\alpha})}{\partial \alpha_j}\right|_{\hat{\alpha}_j}. \tag{4.17}$$

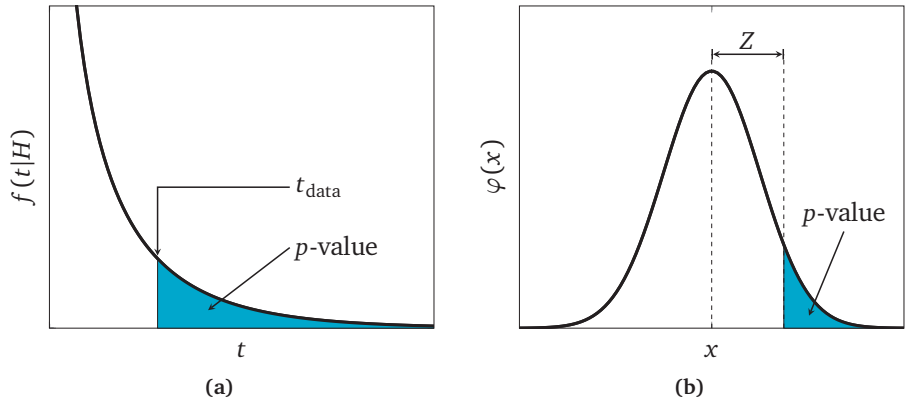

Figure 4.1: Illustration of (a) the construction of p-values from the observed value of the test statistic and (b) the relation to the significance obtained from a standard normal distribution $\varphi(x) = (1/\sqrt{2\pi})\exp(-x^2/2)$. Figures adapted from Ref. [396].

The MIGRAD algorithm in MINUIT combines this metric with a stable variation of the Davidon-Fletcher-Powell variable-metric algorithm [394, 395], i.e. a quasi-Newton method, to realize a maximum likelihood fit that converges along the steepest descent.

4.2.2 Hypothesis testing

Beyond parameter estimation that rely on assumed Gaussian distributions, the level agreement of the data with a given (null) hypothesis H_0 can be quantified without such assumptions, taking into account that an alternative hypothesis H_1 or set of alternative hypotheses may describe the underlying distribution of the data more accurately. Many of the statistical tests described in this section have been implemented by the RooStats project [397]. In frequentist statistical tests this statement is based on a test statistic, e.g. $t = -2\ln\lambda(H_0, H_1)$, which compares the likelihoods of the different hypotheses and thus reflects the level of agreement between the data and the tested hypothesis, H_0. The Neyman-Pearson lemma [398] states that in the absence of undetermined parameters the likelihood ratio

$$\lambda(H_0, H_1) = \frac{L(H_1)}{L(H_0)} \tag{4.18}$$

maximizes the statistical power of the test of H_0 with respect to H_1, i.e. the probability of rejecting the null hypothesis in case the alternative hypothesis is true. The sampling distribution of the test statistic, i.e. the ensemble of all possible values the test statistic can take under the given hypothesis, is interpreted as a p.d.f. of the test statistic, $f(t|H_0)$. In general, the sampling distribution has to be obtained from ensembles of randomized data sets, though under certain general conditions, an asymptotic distribution of the test statistic

may be derived, c.f. Sec. 4.2.3. The probability for finding a value of t that is equal or greater than the value t_{data}, i.e. the probability for finding data that is less compatible with the predictions of H_0 than a given dataset is, is given by

$$p = \int_{t_{\text{data}}}^{\infty} f(t|H_0)\,\mathrm{d}t \tag{4.19}$$

referred to as p-value. Throughout the document, when not stated otherwise, p-values are converted into an equivalent normal significance Z,

$$Z = \Phi^{-1}(1 - n_{\text{side}}p), \tag{4.20}$$

where Φ^{-1} is the quantile of the standard normal distribution, i.e. the inverse of its c.d.f., illustrated in Fig. 4.1. Deviations of the data from the tested hypothesis may only be allowed for one direction, $n_{\text{side}} = 1$, or in either direction, $n_{\text{side}} = 2$.

In the following the hypothesis H is defined by the value of a single POI μ. The extension to more than one POI is trivial. In general the distribution $f(t|H) = f(t_\mu|\mu, \boldsymbol{\theta})$, and thus also the associated p-values, depend explicitly on the values of the nuisance parameters $\boldsymbol{\theta}$. The dependence is dissolved in the limit of large data samples when constructing the test statistic from the profile likelihood ratio (PLR),

$$t_\mu = -2\ln\lambda(\mu) \quad \text{with} \quad \lambda(\mu) = \frac{L(\mu, \hat{\hat{\boldsymbol{\theta}}}(\mu))}{L(\hat{\mu}, \hat{\boldsymbol{\theta}})}, \tag{4.21}$$

owing to the features of the MLEs and CMLEs discussed in the previous section, in particular their bias and efficiency. The subscript μ indicates the value of the POI, which characterizes the hypothesis H. The test statistic t_μ is asymptotically independent of the true values of $\boldsymbol{\theta}$. The p-value for testing a particular value of μ is based on the sampling distribution of t_μ constructed at the values of the nuisance parameters profiled using the observed data under the assumption of the given POI:

$$p_{\mu,\text{obs}} = \int_{t_{\mu,\text{obs}}}^{\infty} f(t_\mu|\mu, \hat{\hat{\boldsymbol{\theta}}}(\mu, \text{obs}))\,\mathrm{d}t_\mu. \tag{4.22}$$

Median experimental sensitivity

The median expected probability to reject a hypothesis μ assuming that the alternative hypothesis μ' were true depends on the assumed values of the nuisance parameters of the model. The common choice is to take the nuisance parameters at their values estimated from data, while assuming the hypothesized value μ' for the POI when estimating the median $t_{\mu,\text{median}}$ of the distribution $f(t_\mu|\mu = \mu', \hat{\hat{\boldsymbol{\theta}}}(\mu = \mu', \text{obs}))$. Similarly to Eqn. (4.22) the

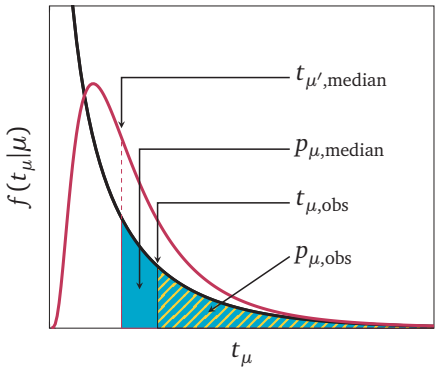

Figure 4.2: Illustration of the construction of the observed and the median expected p-value under the assumption of $\mu = \mu'$. Figure adapted from Ref. [396].

median expected p-value is given by the integral over the sampling distribution of the statistic t_μ,

$$p_{\mu,\text{median}} = \int_{t_{\mu',\text{median}}}^{\infty} f(t_\mu|\mu, \hat{\hat{\boldsymbol{\theta}}}(\mu,\text{obs}))\,\mathrm{d}t_\mu. \tag{4.23}$$

Figure 4.2 illustrates the construction of the observed and the median expected p-value under the assumption of $\mu = \mu'$.

Hypothesis testing with parameters with boundaries

If the parameter μ is associated with a (physically) positive definite quantity, e.g. the rate of signal events, it has a boundary $\mu \geq 0$. Statistically, its estimator $\hat{\mu}$ may take negative values to maximize the likelihood provided that the deficit of events with respect to the background prediction does not lead to a negative probability density. The constraint $\mu \geq 0$ is included in the definition of the alternative test statistic $\tilde{t}_\mu$ rather than in the maximum likelihood estimation procedure of $\hat{\mu}$,

$$\tilde{t}_\mu = -2\ln\tilde{\lambda}(\mu) \quad \text{with} \quad \tilde{\lambda}(\mu) = \begin{cases} \frac{L(\mu,\hat{\hat{\boldsymbol{\theta}}}(\mu))}{L(\hat{\mu},\hat{\boldsymbol{\theta}})} & \hat{\mu} \geq 0 \\ \frac{L(\mu,\hat{\hat{\boldsymbol{\theta}}}(\mu))}{L(0,\hat{\hat{\boldsymbol{\theta}}}(0))} & \hat{\mu} < 0 \end{cases}, \tag{4.24}$$

i.e. for a non-physical estimate of μ, the hypothesis $\mu = 0$ is assumed to represent the best level of agreement with the data. The computation of p-values follows along the same lines as presented for the PLR. It can be shown that using the sampling distribution of t_μ to calculate a p-value for $\tilde{t}_\mu$ is always conservative [399], cf. Sec. 4.2.3.

Discovery test statistic

The discovery test statistic q_0 is a special case of the statistic $\tilde{t}_\mu$ and is used to test, and possibly reject, the null hypothesis $\mu = 0$ to establish the discovery of a positive signal:

$$q_0 = \tilde{t}_0 = \begin{cases} -2\ln\lambda(0) & \hat{\mu} \geq 0 \\ 0 & \hat{\mu} < 0 \end{cases}. \tag{4.25}$$

Here, negative fluctuations of the data are taken as maximally compatible with the null hypothesis. However, in order to probe p-values larger than 50 % arising if $\hat{\mu} \ll 0$, the statistic can be modified to explicitly populate the negative side of the test statistic's ensemble,

$$q_0 = \begin{cases} -2\ln\lambda(0) & \hat{\mu} \geq 0 \\ +2\ln\lambda(0) & \hat{\mu} < 0 \end{cases}. \tag{4.26}$$

This procedure is informally referred to as "uncapping".

Test statistics for upper limits

For establishing an upper limit on the parameter μ, c.f. Sec. 4.2.4, two test statistics can be constructed for models without (q_μ) and with ($\tilde{q}_\mu$) restriction on the POI respectively,

$$q_\mu = \begin{cases} -2\ln\lambda(\mu) & \hat{\mu} \leq \mu \\ 0 & \hat{\mu} > \mu \end{cases} \quad \text{and} \quad \tilde{q}_\mu = \begin{cases} -2\ln\tilde{\lambda}(\mu) & \hat{\mu} \leq \mu \\ 0 & \hat{\mu} > \mu \end{cases}. \tag{4.27}$$

This definition ensures that the case $\hat{\mu} > \mu$ is not considered evidence against the hypothesized value of μ. To probe p-values larger than 50 % the statistics can be uncapped,

$$q_\mu = \begin{cases} -2\ln\lambda(\mu) & \hat{\mu} \leq \mu \\ +2\ln\lambda(\mu) & \hat{\mu} > \mu \end{cases} \quad \text{and} \quad \tilde{q}_\mu = \begin{cases} -2\ln\tilde{\lambda}(\mu) & \hat{\mu} \leq \mu \\ +2\ln\tilde{\lambda}(\mu) & \hat{\mu} > \mu \end{cases}. \tag{4.28}$$

4.2.3 Asymptotic formulae and Asimov data

In the limit of large statistics both the sampling distributions for the various test statistics introduced in the previous section and the significance for a given dataset under different hypotheses can be approximated analytically, described in detail in Ref. [396]. This section summarizes the derivation for the asymptotic formula for the PLR t_μ and the alternative PLR $\tilde{t}_\mu$ to illustrate the method's fundamental principles and states the results for convenience. The approximate sampling distributions and cumulative functions for the remaining test statistics follow trivially and can be found in Ref. [396].

Wald has shown [400] that for large samples of the size N the statistic constructed from the PLR and the alternative PLR are parabolic and can be approximated by

$$t_\mu = -2\ln\lambda(\mu) \approx \frac{(\mu-\hat{\mu})^2}{\sigma^2} \quad \text{and} \quad \tilde{t}_\mu = -2\ln\tilde{\lambda}(\mu) \approx \begin{cases} \frac{(\mu-\hat{\mu})^2}{\sigma^2} & \hat{\mu} \geq 0 \\ \frac{\mu^2}{\sigma^2} - \frac{2\mu\hat{\mu}}{\sigma^2} & \hat{\mu} < 0 \end{cases}, \tag{4.29}$$

up to higher order corrections $\mathcal{O}(1/\sqrt{N})$.

In Eqn. (4.29) $\hat{\mu}$ follows a normal distribution with mean μ', i.e. the hypothesized value, and standard deviation σ, which can be obtained from the Fisher information matrix, c.f. Eqn. (4.16), or more practical an Asimov data set, discussed in detail below. Explicitly the sampling distribution of $\hat{\mu}$ then reads

$$f(\hat{\mu}|\mu') = \frac{1}{\sqrt{2\pi}\sigma}\exp\left(-\frac{(\hat{\mu}-\mu')^2}{\sigma^2}\right). \tag{4.30}$$

Since the test statistic t_μ is monotonic in μ, its sampling distribution follows from a change of variables to be a non-central χ^2 distribution,

$$f(t_\mu|\mu') = \frac{1}{2\sqrt{t_\mu}}\frac{1}{\sqrt{2\pi}}\left[\exp\left(-\frac{1}{2}\left(\sqrt{t_\mu}+\frac{\mu-\mu'}{\sigma}\right)^2\right)+\exp\left(-\frac{1}{2}\left(\sqrt{t_\mu}-\frac{\mu-\mu'}{\sigma}\right)^2\right)\right], \tag{4.31}$$

which reduces to χ^2 distribution for one degree of freedom in case the hypothesis $\mu = \mu'$ is true [401]. The sampling distribution of $\tilde{t}_\mu$ follows along the same lines:

$$\begin{aligned} f(\tilde{t}_\mu|\mu') = {} & \frac{1}{2}\frac{1}{\sqrt{2\pi}}\frac{1}{\sqrt{\tilde{t}_\mu}}\exp\left[-\frac{1}{2}\left(\sqrt{\tilde{t}_\mu}+\frac{\mu-\mu'}{\sigma}\right)^2\right] \\ & + \begin{cases} \frac{1}{\sqrt{2\pi}(2\mu/\sigma)}\exp\left[-\frac{1}{2}\frac{\left(\tilde{t}_\mu-\frac{\mu^2-2\mu\mu'}{\sigma^2}\right)^2}{(2\mu/\sigma)^2}\right] & \tilde{t}_\mu > \mu^2/\sigma^2 \\ \frac{1}{2}\frac{1}{\sqrt{2\pi}}\frac{1}{\sqrt{\tilde{t}_\mu}}\exp\left[-\frac{1}{2}\left(\sqrt{\tilde{t}_\mu}-\frac{\mu-\mu'}{\sigma}\right)^2\right] & \tilde{t}_\mu \leq \mu^2/\sigma^2 \end{cases}. \end{aligned} \tag{4.32}$$

The c.d.f.s of t_μ and $\tilde{t}_\mu$ assuming μ' follow from integration,

$$F(t_\mu|\mu') = \Phi\left(\sqrt{t_\mu}+\frac{\mu-\mu'}{\sigma}\right)+\Phi\left(\sqrt{t_\mu}-\frac{\mu-\mu'}{\sigma}\right)-1 \tag{4.33}$$

$$F(\tilde{t}_\mu|\mu') = \Phi\left(\sqrt{\tilde{t}_\mu}+\frac{\mu-\mu'}{\sigma}\right)+\begin{cases} \Phi\left(\frac{\tilde{t}_\mu-(\mu^2-2\mu\mu')/\sigma^2}{2\mu/\sigma}\right)-1 & \tilde{t}_\mu > \mu^2/\sigma^2 \\ \Phi\left(\sqrt{\tilde{t}_\mu}-\frac{\mu-\mu'}{\sigma}\right)-1 & \tilde{t}_\mu \leq \mu^2/\sigma^2. \end{cases} \tag{4.34}$$

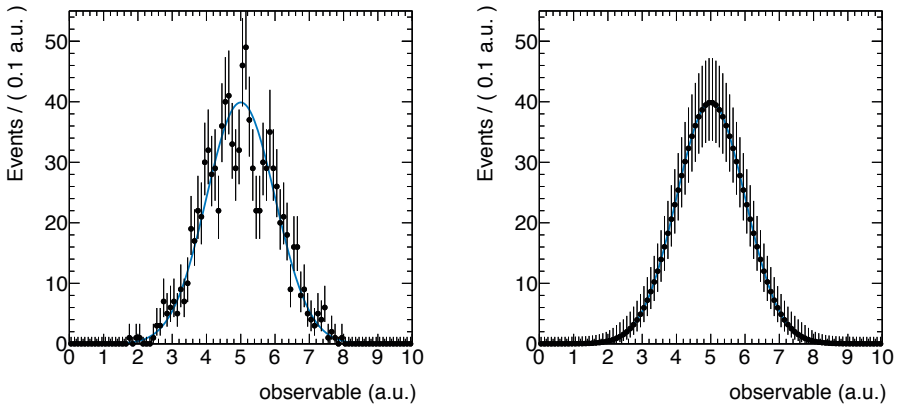

(a) **(b)**

Figure 4.3: Illustration of the difference between (a) a random pseudo-data set and (b) Asimov data set generated from the same normal distribution, overlaid in blue. The asymmetric Poisson confidence intervals are shown for each dataset.

with the previously introduced c.d.f. of the standard normal distribution. Hence, p-values for the hypothesized $\mu' = \mu$ for an observed value $t_{\mu,\text{obs}}$ or $\tilde{t}_{\mu,\text{obs}}$ respectively are given by

$$p_{\mu,\text{obs}} = 1 - F(t_\mu|\mu) \quad \text{and} \quad p_{\mu,\text{obs}} = 1 - F(\tilde{t}_\mu|\mu). \tag{4.35}$$

The median expected sensitivity as well as the fluctuations about this expectation, i.e. the previously introduced standard deviation σ of $\hat{\mu}$, can be obtained using a Asimov data set, i.e. an artificial, binned, representative data set, which is defined such that the estimators for all parameters are consistent when using it to evaluate the likelihood function. In practice, this can either be realized by generating a large ensemble of pseudo-experiments, one of which is shown in Fig. 4.3a, or rather a single data set generated from the CMLEs with all statistical fluctuations suppressed, shown in Fig. 4.3b. Following the Wald approximation, the variance of the distribution of μ' is estimated as

$$\sigma^2_{\text{Asimov}} \approx \frac{(\mu-\mu')^2}{t_{\mu,\text{Asimov}}} \quad \text{or} \quad \sigma^2_{\text{Asimov}} \approx \begin{cases} \frac{(\mu-\mu')^2}{\tilde{t}_{\mu,\text{Asimov}}} & \mu' \geq 0 \\ \frac{\mu^2}{\tilde{t}_{\mu,\text{Asimov}}} - \frac{2\mu\mu'}{\tilde{t}_{\mu,\text{Asimov}}} & \mu' < 0 \end{cases}, \tag{4.36}$$

for the two test statistics considered in this section. The subscript indicates that the test statistic is evaluated using the Asimov data set.

4.2.4 Confidence intervals

The point estimate of a parameter μ of Sec. 4.2.1 is typically complemented by an objective confidence interval, which covers the true value of the POI with a previously specified coverage probability, and builds on the concept of hypothesis testing introduced in the preceding section. In the frequentist paradigm the coverage probability is the asymptotic frequency of the intervals constructed in a repeatable experiment, to contain the true parameter value. Historically, the construction of a confidence interval follows a procedure due to Neyman [402].

In practice, a confidence interval can be constructed from an (inverted) hypothesis test by testing the compatibility of the true value of the POI μ with all hypothesized physical values μ', which the POI may take, c.f. Sec. 4.2.2. The confidence interval at a specified confidence level (CL) $\mathrm{CL} = 1 - p_\mu$ contains all values of μ with a p-value greater than or equal to the chosen p_μ. The p-value can be computed using the analytic prescription given in the previous section, i.e. using the p.d.f.s of the sampling distributions. Hence, one can set both central and one-sided (upper and lower) limits on the POI by varying the ordering rule and thus choosing the upper and lower tail areas. The upper limit yields the largest value of the POI which is not excluded. It is intuitive to consider an example to visualize the concept of constructing confidence intervals, e.g. a single random variable x that follows a standard normal distribution,

$$\varphi(x, \mu, \sigma) = \frac{1}{\sigma\sqrt{2\pi}} \exp\left(-\frac{(x-\mu)^2}{2\sigma^2}\right). \tag{4.37}$$

Figure 4.4a illustrates the construction of central confidence intervals for the measurement of a normally distributed random variable using the t_μ test statistic. The green and yellow shaded areas correspond to probabilities of 68.27 % and 95.45 % respectively, derived from the c.d.f. of the asymptotic sampling distribution of the test statistic, i.e. a χ^2 distribution with one degree of freedom.

Measurements of parameters with boundaries

Suppose the measured parameter is near a physical boundary, e.g. a BR, which is positive definite, cf. Sec. 7.6. In this case the parameter has to be restricted to the physically allowed region, as first described by Feldman and Cousins for cases without nuisance parameters [403], cf. Sec. 4.2.2. The case where a parameter has both upper and lower boundaries is treated similarly, as described in [404]. In the presence of nuisance parameters in the likelihood, the boundary is included in the definition of the (alternative) test statistic $\tilde{t}_\mu$ and the the asympotic formalism can be followed. Figure 4.4b shows the one-sided 95 % confidence intervals constructed from various test statistics using different asymptotic distributions for the previously introduced example imposing a boundary $\mu \geq 0$. It is obvious that t_μ does

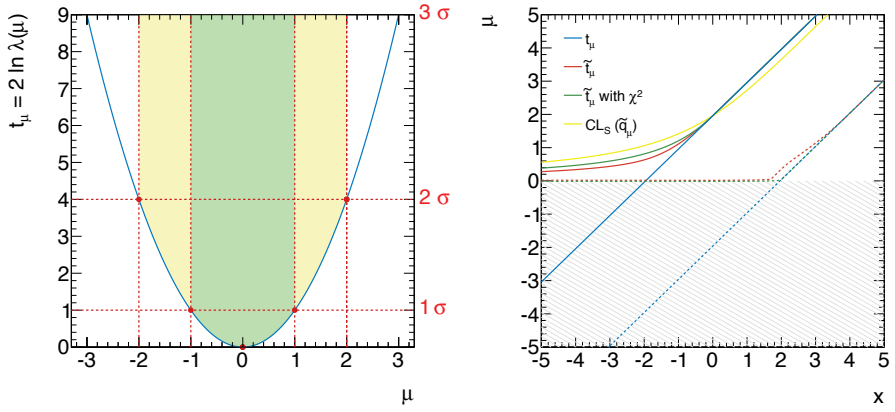

Figure 4.4: (a) Construction of different symmetric confidence intervals for the measurement of a normally distributed random variable using the t_μ test statistic. (b) Comparison of various 95 % confidence intervals constructed from different test statistics using different asymptotic distributions for a normally distributed random variable imposing a boundary $\mu \geq 0$ with the one-sided CL_S upper limit. Solid lines indicate an upper limit, dashed lines indicate a lower limit. Figure adapted from Ref. [399].

not account for the boundary and serves for measurements only. The asymptotic distribution of $\tilde{t}_\mu$ includes the corrections due to the presence of the boundary and leads to a more steeply falling distribution compared to a χ^2 distribution, i.e. the asymptotic distribution of t_μ. Hence, the Feldman-Cousins style limit provides less over-coverage near the boundary compared to the more conservative χ^2 cutoff.

For comparison, the one-sided CL_S upper limit [405] based on $\tilde{q}_\mu$ has been constructed by solving

$$CL_S(\mu) = \frac{p_\mu}{1 - p_b} \leq 5\,\%, \tag{4.38}$$

where p_b is the p-value derived from the same test statistic under the null hypothesis, which is situated at the boundary, i.e. the background-only hypothesis when searching for a signal. Traditionally the formalism has been used to avoid spurious exclusion of signal models due to low sensitivity, e.g. in the case of sizable downward fluctuations in the data. Figure 4.4b shows that the Feldman-Cousins style confidence interval provides a similar protection for the sensitivity problem, albeit less then CL_S for large negative fluctuations. In light of the Higgs boson discovery and the search for new physics in the scalar sector, the SM serves as null hypothesis in measurements of properties of the Higgs particle, whereas before the discovery the SM without the Higgs boson was the null hypothesis. CL_S upper limits are

constructed to make statements about signal strengths, whereas $\tilde{t}_\mu$ is used for measuring properties.

The construction of a confidence interval for a single POI with a physics boundary can be generalized to a n parameter case with a potentially non-trivial boundary shape in the n-dimensional parameter space by restricting the alternative PLR test statistic to the physically allowed region of the parameter space. Employing a standard χ^2_n cut leads to some over-coverage near the boundaries, similar to the one-dimensional case. However, in a higher dimensional space, boundaries may take non-trivial shapes, so that a general asymptotic prescription can not be derived, cf. Cha. 7.

4.3 Moment morphing

The importance of continuous and smooth parametric models was emphasized already in Sec. 4.1 in the context of the modeling of systematic uncertainties by nuisance parameters. Beyond this, the POIs, e.g. the Higgs boson mass or parameters that characterize a SUSY model, require a continuous and smooth parametric description in case their values are estimated using a profile likelihood technique and their confidence intervals are constructed, since the computation relies on calculating the derivatives of the likelihood with respect to the model parameters. It is not practical to simulate MC templates with sufficiently large statistics for the various combinations of model parameters so that typically a p.d.f. $f(x|\alpha_i)$ for an observable x is constructed by interpolating between a nominal prediction $f(x|\alpha_i = \tilde{\alpha}_i)$ and the alternate distributions $f(x|\alpha_i = \alpha_i')$ using template morphing techniques.

Several algorithms exist that can be used to interpolate between MC sample distributions [390, 391]. Interpolation techniques have been used on multiple occasions in particle physics, for example to predict kinematic distributions for intermediate values of a model parameter, e. g. the simulated Higgs boson, W boson or top quark mass, or to describe the impact of systematic uncertainties, which are often modeled as shape or rate variations about a nominal template of a kinematic distribution.

Additional subtleties arise if the likelihood does not factorize, i.e. when

$$L(\alpha_i, \alpha_j) \neq L(\alpha_i) \times L(\alpha_j) \quad \text{with} \quad \alpha_i, \alpha_j \in \boldsymbol{\alpha}, \tag{4.39}$$

which leads to a correlated estimate of two or more model parameters. Correlated estimates of nuisance parameters in subsidiary measurements can be incorporated by using a multivariate normal distribution for the constraint term, rather than factorizing normal distributions. The non-factorizable response of model parameters in the physics measurement must be implemented in the template morphing algorithm to simultaneously describe coherent changes in the affected parameters.

In the remainder of this section a new morphing technique, moment morphing [20], is presented, which has the advantage over existing methods in that it is fast, numerically stable, allows for both binned histogram and continuous templates, has proper handling of both horizontal as well as vertical shifting distributions (explained in Sec. 4.3.1), and is not restricted in the number of input templates, the number of model parameters or the number of input observables. In particular, the latter feature allows the moment morphing technique to model the impact of a non-factorizable response between different model parameters, where varying one model parameter at a time is insufficient to capture the full response function.

4.3.1 Construction of the morphing p.d.f.

This section details the construction of the moment morphing p.d.f.. The method proposed here is based on the linear combination of input templates. The dependency on the morphing parameter(s) can be non-linear, and is captured in multiplicative coefficients and a transformation of the template observables. Interpolation using a single morphing parameter is described in the following section. Then, the interpolation using multiple morphing parameters is described, showing that dependencies between morphing parameters can be readily modeled. Other choices of basis functions for the construction of the morphing p.d.f. are considered afterwards.

Interpolation with a single morphing parameter

Consider an arbitrary p.d.f. $f(\boldsymbol{x}|m)$, where f depends on the single morphing parameter m and describes the observables $\boldsymbol{x}$. The true dependency on m is not known or difficult to obtain. Instead, the p.d.f. f has been sampled at n different values of m, with each $f(\boldsymbol{x}|m_i)$ representing a known input template shape for a single value of the morphing parameter, labeled m_i. In the following the goal is to construct a parametric approximation of $f(\boldsymbol{x}|m)$ for arbitrary m, which is continuous and smooth in the model parameter, as required for example by the statistical tests used in particle physics alluded to in Sec. 4.2. There are two steps to this.

First, given the sampling points, $f(\boldsymbol{x}|m)$ can be expanded in a Taylor series up to order $n-1$ around reference value m_0,

$$f(\boldsymbol{x}|m) \approx \sum_{j=0}^{n-1} \frac{\mathrm{d}^{(j)} f(\boldsymbol{x}|m_0)}{\mathrm{d}m^{(j)}} \frac{(m-m_0)^j}{j!} = \sum_{j=0}^{n-1} f_j'(\boldsymbol{x}|m_0)(m-m_0)^j, \tag{4.40}$$

where the second equality defines $f'(\boldsymbol{x}|m)$. For the n given values of m follows the vector equation:

$$f(\boldsymbol{x}|m_i) \approx \sum_{j=0}^{n-1}(m_i - m_0)^j f'_j(\boldsymbol{x}|m_0) = \sum_{j=0}^{n-1} M_{ij} f'_j(\boldsymbol{x}|m_0), \tag{4.41}$$

where $M_{ij} = (m_i - m_0)^j$ defines a $n \times n$ transformation matrix. Inverting Eqn. (4.41) gives

$$f'_j(\boldsymbol{x}|m_0) = \sum_{i=0}^{n-1} \left(M^{-1}\right)_{ji} f(\boldsymbol{x}|m_i) \tag{4.42}$$

which allows to determine the n values $f'_j(\boldsymbol{x}|m_0)$. Substituting this in Eqn. (4.40), $f(\boldsymbol{x}|m)$ reads

$$f(\boldsymbol{x}|m) \approx \sum_{i,j=0}^{n-1}(m - m_0)^j \left(M^{-1}\right)_{ji} f(\boldsymbol{x}|m_i), \tag{4.43}$$

which can be used to predict the template shape at any new value of the morphing parameter given by m',

$$f_{\text{pred}}(\boldsymbol{x}|m') = \sum_{i=0}^{n-1} c_i(m') f(\boldsymbol{x}|m_i), \tag{4.44}$$

which is a linear combination of the input templates $f(\boldsymbol{x}|m_i)$, each multiplied by a coefficient $c_i(m')$,

$$c_i(m') = \sum_{j=0}^{n-1}(m' - m_0)^j \left(M^{-1}\right)_{ji}, \tag{4.45}$$

which themselves are non-linear and depend only on the distance to the reference points. This approach of weighting the input templates is also known as vertical morphing. Note that the coefficients c_i are independent of the derivatives of $\boldsymbol{f}$ with respect to morphing parameters or to the observable set $\boldsymbol{x}$, making their computation easy.

The coefficient for a point included in the set of input templates is one, i. e.

$$c_i(m_j) = \delta_{ij}, \tag{4.46}$$

and by construction the sum of all coefficients c_i equals one:

$$\sum_i c_i(m) = 1. \tag{4.47}$$

This turns out to be a useful normalization, as will be seen below.

To illustrate, one can consider a morphed p.d.f. using only input templates at two values of the morphing parameter, m_{min} and m_{max}. The coefficients $c_i(m)$ become linear in m and reduce to the simple fractions:

$$c_{i_{\text{min}}} = 1 - m_{\text{frac}} \tag{4.48}$$

$$c_{i_{\text{max}}} = m_{\text{frac}}, \tag{4.49}$$

where $m_{\text{frac}} = (m - m_{\text{min}})/(m_{\text{max}} - m_{\text{min}})$, $c_{i_{\text{min}}}$ and $c_{i_{\text{max}}}$ sum up to one, and all other coefficients are zero.

Second, it may be that the sampled input p.d.f.s f_i describe distributions in $\boldsymbol{x}$ that vary strongly as a function of m in shape and location. This is equivalent to the first and second moments (i. e. the means and variances) of the input distributions having a dependence on the morphing parameter m.

Since the input p.d.f.s in Eqn. (4.44) are summed linearly, it is imperative to translate all input distributions $f_i(\boldsymbol{x})$ in the sum before combining in the morphed p.d.f. such that their locations match up. The process of translating the input observables (but not scaling; see below) is also called horizontal morphing. In addition it is necessary to take in account the change in the width of the input distributions as a function of the morphing parameter.

To achieve this, the mean μ_{ij} and width σ_{ij} of each input distribution i and observable x_j are shifted to the common values of $\mu'_j(m)$ and $\sigma'_j(m)$. These are obtained by multiplying the underlying means and widths with the coefficients $c_i(m)$ of Eqn. (4.45)

$$\mu'_j(m) = \sum_i c_i(m) \cdot \mu_{ij} \tag{4.50}$$

$$\sigma'_j(m) = \sum_i c_i(m) \cdot \sigma_{ij} \tag{4.51}$$

In order to shift the input p.d.f.s a linear transformation of each observable is applied. For each p.d.f. i and observable j define

$$x'_{ij} = a_{ij} x_j + b_{ij}, \tag{4.52}$$

with slope

$$a_{ij} = \frac{\sigma_{ij}}{\sigma'_j} \tag{4.53}$$

and offset

$$b_{ij} = \mu_{ij} - \mu'_j a_{ij}. \tag{4.54}$$

to replace the original observables x_j in the input p.d.f.s

$$f(\boldsymbol{x}|m_i) \to f(\boldsymbol{x}'|m_i). \tag{4.55}$$

Since only a linear transformation is applied to each observable, i. e. only the first two moments of the input p.d.f.s are modified, the normalization of the scaled input template is analytically related to the normalization of the original template as

$$\int_{-\infty}^{+\infty} f(\boldsymbol{x}'|m_i)d\boldsymbol{x} = \frac{1}{\prod_j a_j(m)} \int_{-\infty}^{+\infty} f(\boldsymbol{x}|m_i)d\boldsymbol{x}, \tag{4.56}$$

with the slope $a_j = \sigma_j/\sigma'_j$, where j refers to the observable x_j. The construction of the complete morphed p.d.f. as the sum of the transformed input p.d.f.s then gives

$$p(\boldsymbol{x}|m') = \sum_i c_i(m') f(\boldsymbol{x}', m_i) \prod_j a_j(m'). \tag{4.57}$$

As the coefficients c_i add up to 1 by construction, the morphed p.d.f. of Eqn. (4.57) is unit-normalized as well for normalized input templates.

This leads to an important computational advantage and novelty: for models where the input templates are constant, such as histogram-based templates, no normalization integrals need to be recalculated during the minimization of the likelihood function, which is often a bottle-neck when using morphed p.d.f.s. As a result, the number of input templates is generally increasable without significant performance loss.

Note that the self-normalization of Eqn. (4.56) remains valid when applying a rotation to the set of (multiple) observables, which would introduce covariance moments to the modified input p.d.f.s. Though technically possible, such rotations are avoided here as they obscure the physical interpretation of the observable set. A consequence of this on the accuracy of the morphed p.d.f. to model changing correlations between observables is discussed in Sec. 4.3.3.

The processes of vertical and horizontal morphing (i. e. summing and translating) and of scaling the input morphed p.d.f.s are illustrated in Fig. 4.5a, which morphs between two normal distributions. The technique proposed also accurately models the evolution of rapidly changing distributions as illustrated in Fig. 4.5b. In the sample, the application of moment morphing is used to describe the non-linear transition of a Cauchy distribution via a Crystal Ball line shape into a normal distribution. The parameters of the used p.d.f.s are chosen such that the positions of their means as well as their shapes vary substantially as a function of the morphing parameter α, in particular in the tails of the distributions which change dynamically along the morphing path.

Figure 4.6 shows an application of the technique described in this section to a complex physics and detector simulation. The reconstructed invariant mass distribution for a Standard Model Higgs boson with mass 125 GeV decaying to four leptons is described by non-linearly interpolating between a series of templates corresponding to simulation response estimates for four assumed Higgs boson masses, at 123, 124, 126 and 127 GeV. As reference templates kernel estimation p.d.f.s modeling events simulated with MADGRAPH [206] and an

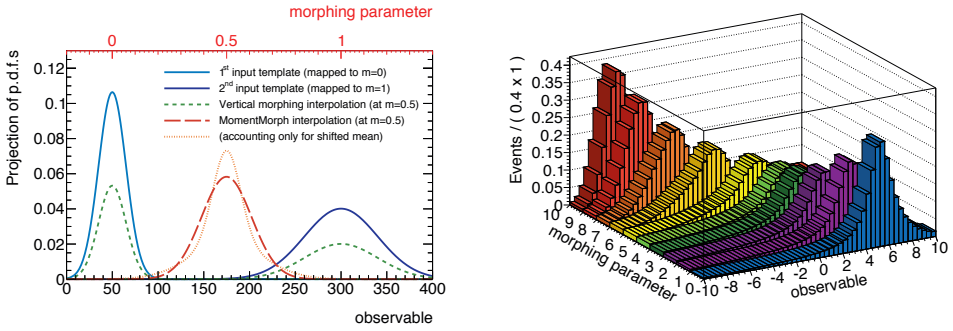

(a) (b)

Figure 4.5: Two examples of moment morphing. (a) Construction of the morphed p.d.f. The interpolation is done between two normal distributions, shown as solid lines, corresponding to values 0 and 1 of the morphing parameter. After vertical morphing, the mean of the templates is shifted to the common value and their widths are adjusted accordingly. The dashed p.d.f. shows the morphed p.d.f., which is a linear combination of the modified inputs. (b) Non-linear morphing of a Cauchy distribution ($m = 0$) via a Crystal Ball line shape ($m = 5$) into a normal distribution ($m = 10$).

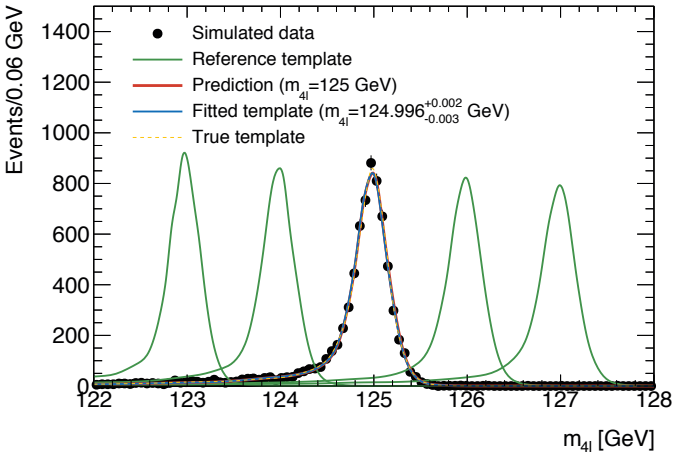

Figure 4.6: Example of p.d.f. interpolation. The reconstructed invariant mass distribution for a 125 GeV Standard Model Higgs boson decaying to four leptons (solid, red) has been predicted by non-linearly interpolating between the reference distributions for surrounding mass hypotheses (solid, green), as described in the text. The prediction is compared to the true 125 GeV template (dashed, yellow) derived from the simulated data for this hypothesis and a fit of the morphed p.d.f. to this dataset (solid, blue).

ATLAS-type PGS [406] simulation are used. Despite rapidly evolving features, the template predicted by the morphing technique reproduces the true template at 125 GeV. The resulting morphed p.d.f. is parametrized in terms of the "true" Higgs boson mass, as opposed to the reconstructed invariant mass, and a fit of the morphed p.d.f. to a dataset with an assumed true Higgs boson of 125 GeV directly and accurately measures that true Higgs boson mass.

Interpolation with multiple morphing parameters

The non-linear implementation of multiple morphing parameters is analogous to the single parameter case of Sec. 4.3.1. We illustrate here the expansion to two parameters, including correlated effects in the template distribution caused by changing of two or more morphing parameters simultaneously, before generalizing the approach to an arbitrary number of parameters.

The general Taylor series expansion of $f(\boldsymbol{x}|m_1, m_2)$, depending on parameters m_1 and m_2, around (m_{1_0}, m_{2_0}) reads:

$$\begin{aligned} f(\boldsymbol{x}|m_1, m_2) = {} & f(\boldsymbol{x}|m_{1_0}, m_{2_0}) \\ & + \frac{1}{1!}\left[(\Delta m_1)\frac{\partial}{\partial m_1} f(\boldsymbol{x}|m_{1_0}, m_{2_0}) + (\Delta m_2)\frac{\partial}{\partial m_2} f(\boldsymbol{x}|m_{1_0}, m_{2_0})\right] \\ & + \frac{1}{2!}\left[(\Delta m_1)^2\frac{\partial^2}{\partial m_1^2} f(\boldsymbol{x}|m_{1_0}, m_{2_0}) + 2(\Delta m_1)(\Delta m_2)\frac{\partial^2}{\partial m_1 \partial m_2} f(\boldsymbol{x}|m_{1_0}, m_{2_0})\right. \\ & \left. + (\Delta m_2)^2\frac{\partial^2}{\partial m_2^2} f(\boldsymbol{x}|m_{1_0}, m_{2_0})\right] + \ldots, \end{aligned} \tag{4.58}$$

which, for a 2×2 square grid with reference points surrounding (m_1, m_2), is approximated by:

$$\begin{aligned} f(\boldsymbol{x}|m_1, m_2) = {} & f(\boldsymbol{x}|m_{1_0}, m_{2_0}) \\ & + (\Delta m_1)\frac{\partial}{\partial m_1} f(\boldsymbol{x}|m_{1_0}, m_{2_0}) + (\Delta m_2)\frac{\partial}{\partial m_2} f(\boldsymbol{x}|m_{1_0}, m_{2_0}) \\ & + (\Delta m_1)(\Delta m_2)\frac{\partial^2}{\partial m_1 \partial m_2} f(\boldsymbol{x}|m_{1_0}, m_{2_0}). \end{aligned} \tag{4.59}$$

Here the middle two terms are the linear expansions along m_1 and m_2, and the last term represents the expansion along both m_1 and m_2 simultaneously. The addition of the fourth "corner" point allows one to model functions that cannot be factorized into functions depending only on m_1 or m_2.

Repeating the Taylor series expansion for a grid of $k \times l$ reference points, and again writing the truncated series as a vectorial equation, leads to Eqn. (4.41) with additional mixed terms in the transformation matrix M and the derivatives f'_j. The transformation matrix M now reads

$$M = \begin{pmatrix} 1 & 0 & \cdots & 0 & 0 & \cdots & 0 & \cdots & 0 \\ 1 & (\Delta m_{2_{10}}) & \cdots & (\Delta m_{2_{10}})^{k-1} & (\Delta m_{1_{10}}) & \cdots & (\Delta m_{1_{10}})(\Delta m_{2_{10}})^{k-1} & \cdots & (\Delta m_{1_{10}})^{l-1}(\Delta m_{2_{10}})^{k-1} \\ \vdots & \vdots & \cdots & \vdots & \vdots & \cdots & \vdots & \cdots & \vdots \\ 1 & (\Delta m_{2_{n0}}) & \cdots & (\Delta m_{2_{n0}})^{k-1} & (\Delta m_{1_{n0}}) & \cdots & (\Delta m_{1_{n0}})(\Delta m_{2_{n0}})^{k-1} & \cdots & (\Delta m_{1_{n0}})^{l-1}(\Delta m_{2_{n0}})^{k-1} \end{pmatrix}, \tag{4.60}$$

where $\Delta m_{i_{n0}} = m_{i_n} - m_{i_0}$ is a short notation for the distance between reference point n and reference point 0 in the ith dimension of the parameter space. The distance vector $\mathbf{\Delta m}$ is in multiple dimensions defined as

$$\mathbf{\Delta m} = \begin{pmatrix} 1 & (\Delta m_{2_{l0}}) & \cdots & (\Delta m_{2_{l0}})^{k-1} & (\Delta m_{1_{l0}}) & \cdots & (\Delta m_{1_{l0}})(\Delta m_{2_{l0}})^{k-1} & \cdots & (\Delta m_{2_{l0}})^{l-1}(\Delta m_{2_{l0}})^{k-1} \end{pmatrix}^T. \tag{4.61}$$

Following Eqn. (4.44), the coefficients c_i for a new point $(m'_1, m'_2) = (m_{1_q}, m_{2_q})$ are now given by

$$c_i(m'_1, m'_2) = \sum_{j=0}^{(k\times l)-1} \left(M^{-1}\right)_{ji} \cdot (\Delta m)_j. \tag{4.62}$$

The construction of the morphed p.d.f. $p(\boldsymbol{x}|m_1, m_2)$ using these coefficients is as in Eqn. (4.57).

The extension to an arbitrary number of morphing parameters, n, is a matter of using an n-dimensional grid of input p.d.f.s, with $k \times l \times \ldots$ grid points, and consistently expanding the transformation matrix M with the additional higher order terms.

Returning to the 2×2 square grid of input p.d.f.s with reference values surrounding (m_1, m_2), the coefficients in (m_1, m_2) reduce to

$$c_{00}(m_1, m_2) = (1 - m_{1,\text{frac}}) \cdot (1 - m_{2,\text{frac}}) \tag{4.63}$$
$$c_{10}(m_1, m_2) = m_{1,\text{frac}} \cdot (1 - m_{2,\text{frac}}) \tag{4.64}$$
$$c_{01}(m_1, m_2) = (1 - m_{1,\text{frac}}) \cdot m_{2,\text{frac}} \tag{4.65}$$
$$c_{11}(m_1, m_2) = m_{1,\text{frac}} \cdot m_{2,\text{frac}}, \tag{4.66}$$

with $m_{1,\text{frac}} = (m_1 - m_{1_{00}})/(m_{1_{10}} - m_{1_{00}})$ and $m_{1,\text{frac}} = (m_2 - m_{2_{00}})/(m_{2_{01}} - m_{2_{00}})$. Note that the coefficients are all positive when staying within the boundaries of the grid, and add up to 1. Towards the corner point $(m_{1_{11}}, m_{2_{11}})$, the nominal coefficient c_{00} and linear-expansion coefficients c_{10} and c_{01} are turned off, and the quadratic term $m_{1,\text{frac}} \cdot m_{2,\text{frac}}$ in c_{11} is turned on in full, describing the change caused by changing m_1 and m_2 simultaneously.

Shown in Fig. 4.7 is an illustration of a multivariate normal distribution modeling the dependency between two observables. The covariance matrix as well as the mean change as a function of two parameters α_1 and α_2. In the given example the distributions are known for 2×2 grid points fulfilling $\alpha_i = \{0, 1\},\ i = 1, 2$. The information is used to linearly interpolate the p.d.f. to any desired point in the two-dimensional parameter space. The yellow contours

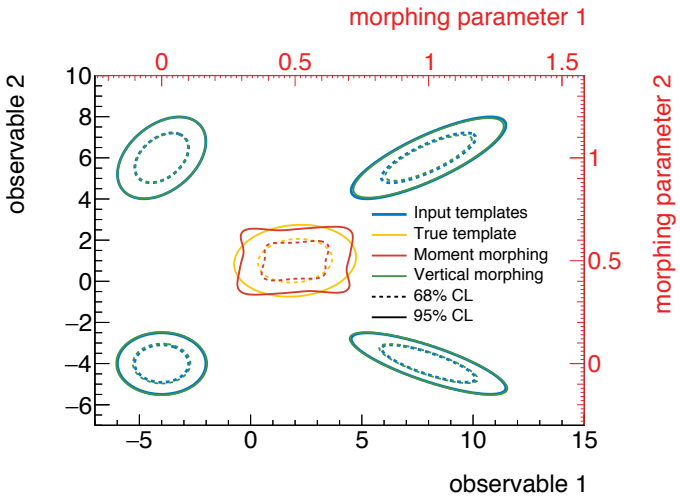

Figure 4.7: Example of multi-dimensional moment morphing. Linear interpolation between multivariate normal distributions in a multi-dimensional parameter space. For illustration purposes only, the plot has a 1-to-1 mapping between the corners of the morphing parameter and observable space. The example is constructed such that mean and covariance of the multivariate normal distributions follow an analytic description, in particular the variation of Pearson's correlation coefficient can be described bi-linearly. The corner contours (blue) of the grid represent the input templates to the morphing algorithm. Dashed and solid contours indicate one and two standard deviations from the mean respectively. The true template in the center of the grid, i. e. at $(0.5, 0.5)$, is shown in yellow. The prediction of the morphed p.d.f. for the central point is shown in red. The green contours represent the prediction from vertical interpolation.

in the center of the grid, i. e. at $(\alpha_1, \alpha_2) = (0.5, 0.5)$, represent the true template, which is compared with the prediction by the moment morphed p.d.f. (red) and the prediction by vertical morphing only (green). Similar to the example presented in Fig. 4.5a, vertical morphing only does not yield a central template with shifted mean. The difference between the moment morphed template and the true template is induced by the change of the correlation between the two observables with varying morphing parameter values. In case of constant correlation between the observables of the input templates, the prediction of the moment morphed p.d.f. is exact. More discussion on this follows in Sec. 4.3.3.

Other choices of basis functions

Finally, having derived the morphed p.d.f. using a Taylor series expansion, the dependency on a morphing parameter m can be easily re-expressed in any orthonormal basis $\{\Psi_0, \ldots, \Psi_{n-1}\} = \{\Psi_i\}_{i=0,\ldots,n-1}$. The choice of the basis functions can simplify the studied problem and thus lead to a better approximation, even to an exact description. For example, if the dependency

on model parameters is expected to be periodic, it can be expressed in Fourier space as a linear combination of the eigenvectors Ψ_i:

$$p(\boldsymbol{x}|m) = \sum_{i=0}^{n-1} d_i(\boldsymbol{x})\Psi_i(m), \tag{4.67}$$

where the coefficients d_i read

$$d_i(\boldsymbol{x}) = \int p(\boldsymbol{x}|m)\Psi_i(m)\mathrm{d}m. \tag{4.68}$$

Thus, the dependency of the morphed p.d.f. on the observables enters through the coefficients $d_i(\boldsymbol{x})$ only, while the basis functions are independent of $\boldsymbol{x}$.

Note that the number of sampling points limits the number of utilizable basis functions $\Psi_i(m)$. Analogously to Eqn. (4.44), p can then be predicted at any new point m',

$$p_{\text{pred}}(\boldsymbol{x}|m') = \sum_{i,j=0}^{n-1} \Psi_j(m')\left(M^{-1}\right)_{ji} p(\boldsymbol{x}|m_i), \tag{4.69}$$

with the modified $n \times n$ transformation matrix $M_{ij} = \Psi_j(m_i)$.

4.3.2 A p.d.f. for modeling systematic uncertainties

In a typical analysis performed in a particle physics experiment, the impact of systematic uncertainties is typically quantified by varying one-by-one the model parameters relating to detector modeling and physics models (e. g. energy calibrations, factorization scales) and to record the template distribution with these modified settings. The resulting pairs of alternate templates, corresponding to "up" and "down" variations of the uncertain model parameters, must then be incorporated in the likelihood model of the physics analysis, in the form of a model nuisance parameter that causes the template distribution to deform as prescribed by the pair of "alternate" templates.

For the most widely-used statistical test at the LHC, the profile likelihood ratio, it is required that the modeling of the systematic uncertainty in terms of a nuisance parameters is done in a continuous way. In particular, the maximization of the likelihood function, as needed (twice) in the profile likelihood ratio, requires continuous and smooth parametric models to describe the signal and background processes present in the data[1].

[1] Specifically, the likelihood for a physics measurement, $L(\mu, \boldsymbol{\theta})$, where μ is the physics parameter of interest and $\boldsymbol{\theta}$ are the nuisance parameters that parametrize the impact of systematic uncertainties on the signal and background predictions, must be defined for all values of μ and $\boldsymbol{\theta}$. The profile likelihood ratio is given by

$$\lambda(\mu) = \frac{L(\mu, \hat{\hat{\boldsymbol{\theta}}})}{L(\hat{\mu}, \hat{\boldsymbol{\theta}})}, \tag{4.70}$$

This section builds a parametrized p.d.f. describing a set of systematic variations about the nominal prediction for a signal or background process, using the morphing technique of Sec. 4.3.1. Each systematic uncertainty i is described with a nuisance parameter, θ_i, that continuously morphs between the variation and nominal templates such that $\theta_i = \pm 1$ corresponds to the $\pm 1\sigma$ ($1\sigma = 1$ standard deviation) variations, and $\theta_i = 0$ corresponds to the nominal template[2]. Additional variation templates may be added for different values of θ_i.

The response of the likelihood function to changes in the nuisance parameters is here assumed to be factorized, *i. e.* it is assumed that the effect of a simultaneous change in two or more nuisance parameters can be described as a superposition of the effects of changing each nuisance parameter individually. (Unfactorizable uncertainties are not discussed here; their treatment is handled following the recipe of Sec. 4.3.1.) Where n unfactorizable uncertainties would require a full n-dimensional grid of input templates, this assumption reduces the number of required inputs to a set of n one-dimensional variations, with only the nominal template in common – a "star" shape in the nuisance parameter space.

The construction of the morphed p.d.f. as the sum of the input templates becomes

$$p_{\text{pred}}(\boldsymbol{x}|\boldsymbol{\theta}) = (1 - \sum_{i=1} \sum_{j=\pm 1,\pm m} c_{ij}(\theta_i)) \cdot p(\boldsymbol{x}, 0) + \sum_{i=1} \sum_{j=\pm 1,\pm m} c_{ij}(\theta_i) \cdot p_{ij}(\boldsymbol{x}|\theta_i = j), \qquad (4.71)$$

where the double-sum runs over the implemented systematic uncertainties and their available $\pm 1 \ldots \pm m\sigma$ variations. The morphed p.d.f. is self-normalized, as by construction all coefficients add up to one.

In the publicly available implementation, detailed in Sec. 4.3.4, the coefficients $c_{ij}(\theta_i)$ are linear, and depend only the two closest input points surrounding θ_i, as in Eqn. (4.48). Also, the linear transformation of the observables $\boldsymbol{x} \to \boldsymbol{x}'$, responsible for scaling and horizontal morphing, can be turned on or off. (By default it is off.) Henceforth this p.d.f. is called the star-morphed p.d.f.

This type of star-morphed p.d.f. has been used in the analysis of Higgs decay to 4 leptons ($H \to ZZ^* \to 4\ell$) by the ATLAS experiment [24] to describe the various background components contributing the ZZ mass spectrum, each including the variations of all relevant systematic uncertainties.

Figure 4.8 shows an example application of the star-morphed p.d.f., used to describe the dominant background process for a typical $H \to 4\ell$ analysis, labeled $q\bar{q} \to ZZ$. As in Sec. 4.3.1,

where $\hat{\mu}$ and $\hat{\boldsymbol{\theta}}$ represent the unconditional maximum likelihood estimates of μ and $\boldsymbol{\theta}$, and $\hat{\hat{\boldsymbol{\theta}}}$ represents the conditional maximum likelihood estimate for the chosen value of μ. Therefore λ is a function of μ. (Note that the data is omitted in the short hand notation of L.) For a more detailed discussion on the profile likelihood ratio test statistic, see Ref. [396] and the previous sections.

[2] A Gaussian constraint is applied separately for each systematic uncertainty to account for uncertainty in the external measurement. This constraint preferably centers each systematic variation around the nominal prediction, with a reduced likelihood for potential shifts; however, a combined fit to the observed data may of course prefer shifts in the nuisance parameters.

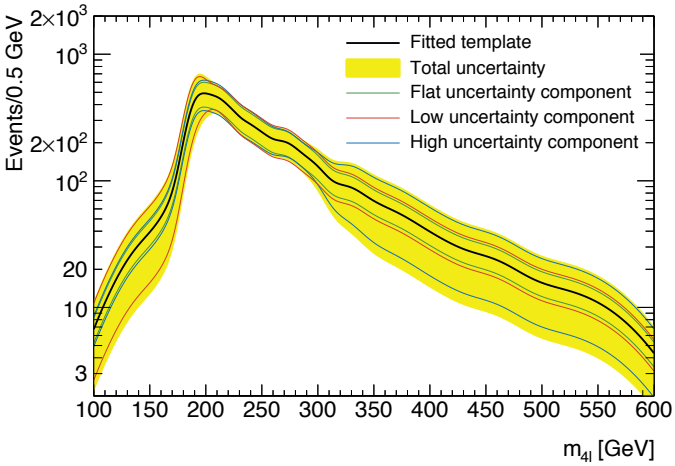

Figure 4.8: Example application of the star-morphed p.d.f. to describe the effect of different uncertainties. Three example uncertainties affecting different regions of the shown spectrum have been added to the star-morphed p.d.f. The black curve shows the fitted template for the $q\bar{q} \to ZZ$ process along with the total uncertainty derived from all included sources indicated by the yellow band. The green, red and blue curves show the partial uncertainties corresponding to a flat, low mass and high mass effect, respectively.

this background prediction has been obtained from events simulated with MADGRAPH [206] and PGS [406]. For illustration, three non-physical systematic uncertainties have been added to the star-morphed p.d.f.. One is a shape variation in the low mass region, the second is a shape variation in the high mass region, and the third is an overall normalization uncertainty that affects the entire mass region. The effects of these systematic uncertainties on the template distribution are shown in Fig. 4.8.

4.3.3 Accuracy of moment morphing and comparison to alternative morphing algorithms

The accuracy of a moment morphing function $f_{\text{pred}}(\boldsymbol{x}|\alpha)$ is assessed here using a series of benchmark models for which the true distribution $f_{\text{true}}(\boldsymbol{x}|\alpha)$ is defined.

A priori one can demonstrate that moment morphing provides an exact solution for any set of true distributions in which the first and second moment (i. e. the mean and width) of $f_{\text{true}}(\boldsymbol{x}|\alpha)$ change linearly with the morphing parameter α and all other moments are constant (i. e. the shape of the distribution does not change other than through its first and second moment). The simplest example of such a distribution is a Gaussian distribution with a linearly changing mean and width. However, the class of true distributions that are exactly reproduced by moment morphing is not restricted to this example: any distribution with linearly changing

first and second moments and fixed higher-order moments is exactly described. In particular, when considering use cases in particle physics, the physics parameters of interest (particle masses, resonance widths, etc.) are often related to the first and second moments; hence a correct description of these is most critical.

Deviations from the exact solution can occur in two ways: a) the dependence of the first and second moment of $f_{\text{true}}(\boldsymbol{x}|\alpha)$ become non-linear in α, or b) higher moments of the shape of the distribution depend on α, either linearly or non-linearly. The magnitude of both types of deviations are under explicit control of the user, as the moment morphing algorithm allows templates to be specified at any number of freely choosable values of α.

Deviations of the first type are generally unproblematic as it is always possible to construct a configuration of templates in which: a) the dependence of the first and second moments between any pair of adjacent templates is sufficiently close to linear (when choosing the piece-wise linear interpolation option), or b) where the dependence of the moments over the entire domain of α is well approximated by a n^{th}-order polynomial for n templates (when choosing the non-linear interpolation option). For this reason, no attempt is made here to quantify the accuracy of moment morphing due to (local) non-linearity of the first and second moment of $f_{\text{true}}(\boldsymbol{x}|\alpha)$.

Deviations of the second type, introduced by changing higher-order moments, may be more limiting in cases where higher-order moments of the true distribution change rapidly as a function of α. It should be noted that changes in the truth distribution related to higher-order moments are empirically accounted for in the morphing algorithm, by gradually changing the weight of moment-adjusted input templates as a function of α. However, the morphed distribution does not guarantee a linear change in these higher-order moments as a function of α, as is done for the first and second moments.

The impact of this empirical modelling of changes in higher-order moments is quantified in the following paragraphs.

Performance on benchmark models

The accuracy of moment morphing is evaluated here on nine analytical benchmark models that are similar to various particle physics use cases, and the accuracy is compared to two other morphing algorithms that have historically been used in particle physics: vertical morphing and "integral morphing".

In the vertical morphing approach[3] templates are interpolated with a simple weighting strategy:

$$V(x|\alpha) = (1-\alpha)/2 \cdot T_L(x) + (\alpha+1)/2 \cdot T_R(x) \tag{4.72}$$

[3] Note that the moment morphing algorithm reduces to vertical morphing strategy if the adjustment step of the first and second moments of the input templates is omitted.

Table 4.1: Benchmark models used to quantify accuracy of moment morphing and alternative morphing algorithms.

Name	Model description	Dependence on morphing parameters	
N_μ	Gaussian$(x\|\mu, \sigma = 1)$	$\mu = 2 \cdot \alpha$	
N_σ	Gaussian$(x\|\mu = 0, \sigma)$	$\sigma = 1 + 0.5 \cdot \alpha$	
$N_{\mu\sigma}$	Gaussian$(x\|\mu, \sigma)$	$\mu = 2 \cdot \alpha$	$\sigma = 1 + 0.5 \cdot \alpha$
Γ_k	GammaDist$(x\|k, \theta = 1)$	$k = 3 + 0.7 \cdot \alpha$	
Γ_θ	GammaDist$(x\|k = 3, \theta)$	$\theta = 1 + 0.7 \cdot \alpha$	
$\Gamma_{k\theta}$	GammaDist$(x\|k, \theta)$	$k = 3 + 0.7 \cdot \alpha$	$\theta = 1 + 0.7 \cdot \alpha$
C_1	Chebychev$(x\|a_1, a_2 = 0)$	$a_1 = 0.5 + 0.4 \cdot \alpha$	
C_2	Chebychev$(x\|a_1 = 0.5, a_2)$	$a_2 = 0.4 \cdot \alpha$	
C_{12}	Chebychev$(x\|a_1, a_2)$	$a_1 = 0.5 + 0.4 \cdot \alpha$	$a_2 = 0.4 \cdot \alpha$

where $T_{L/R}$ are the left and right template models corresponding to $\alpha = \pm 1$. The vertical morphing approach is widely used in LHC physics analyses, notably in the modeling of distributions in the discovery analysis of the Higgs boson. In contrast, in the integral morphing approach [391] interpolation occurs between the cumulative distribution functions of the templates $T_{L/R}$. The integral morphing approach is more suited to models with rapidly shifting means, like moment morphing and unlike vertical morphing, but is computationally intensive due to (numeric) integration and root-finding steps, and is restricted to the description of one-dimensional distributions. The integral morphing approach has been used, among others, in physics analyses published by the DØ and CDF collaborations.

The nine analytical benchmark models tested here are detailed in Tab. 4.1. For the first three benchmark models N_μ, N_σ and $N_{\mu\sigma}$, based on the normal distribution, moment morphing provides an exact solution, and these models are included in the benchmark to facilitate accuracy performance comparisons with the other morphing approaches. The second set of benchmark models is based on the Gamma distribution:

$$\Gamma(x|k,\theta) = \frac{x^{k-1}e^{-x/\theta}}{\theta^k \Gamma(k)}, \tag{4.73}$$

and are included as an example of a distribution where also higher-order moments of the true distribution changes as a function of the morphing parameter. The last set of three benchmark models is based on the 2$^{\text{nd}}$-order Chebychev polynomials:

$$C(x|a_1,a_2) = 1 + a_1 x + a_2(2x^2 - 1), \tag{4.74}$$

as a distribution that is representative of typical background distributions.

Given a pair of input templates positioned at $\alpha = \pm 1$, the accuracy of the morphing methods is quantified using the Kolmogorov-Smirnov (KS) distance. This is the largest distance between

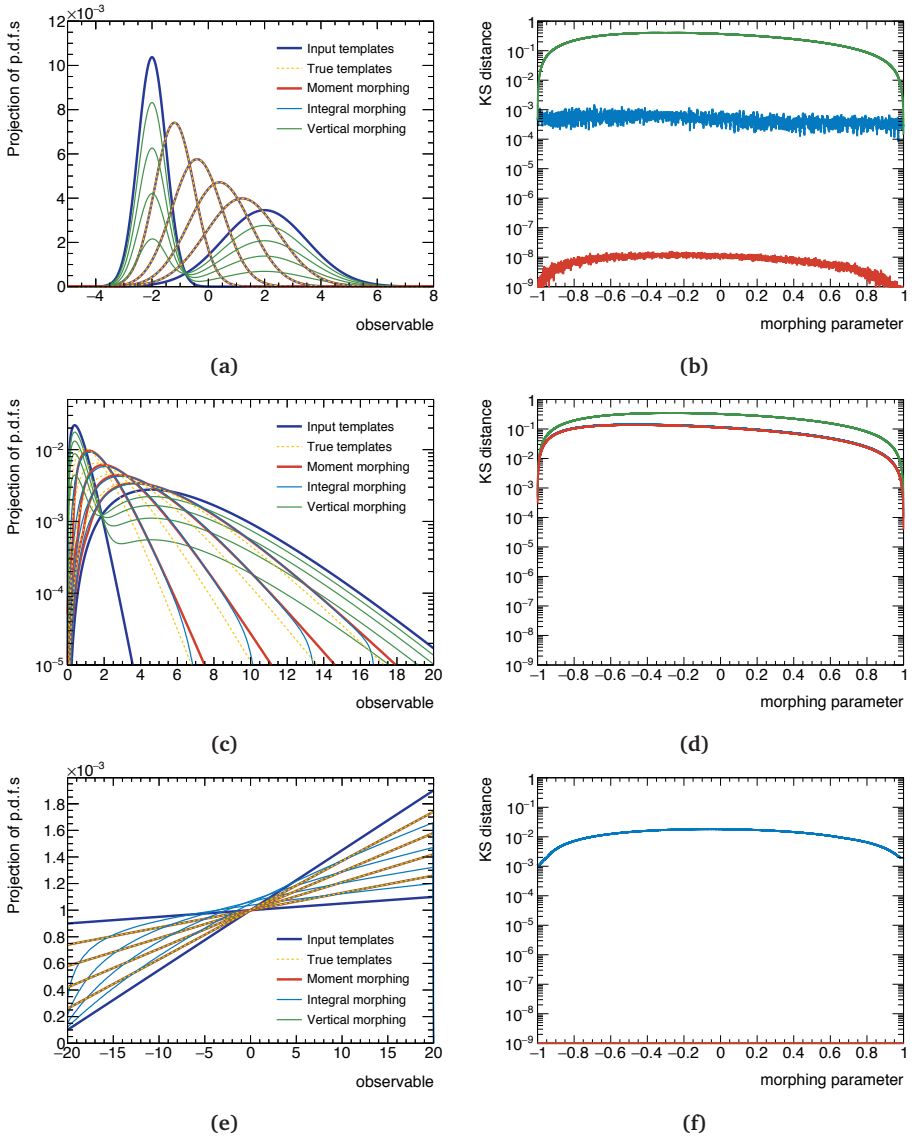

Figure 4.9: Accuracy of the moment morphing, vertical morphing and integral morphing algorithms on three of the benchmark models defined in Table 4.1. Top row: the $G_{\mu\sigma}$ model, center row: the Γ_k model, bottom row: the C_1 model. The plots in the left column overlay the truth model distributions for various values of the morphing parameter α ($\alpha = \pm 1$ shown in dark blue, which also serve as templates for the morphing algorithms, other values of α shown in yellow dashed) on the predicted distribution by moment morphing (red), vertical morphing (green) and integral morphing (light blue). To quantify the level of agreement between truth and morphing predictions, the right column shows the KS distance between the truth model and predicted distributions as a function of the morphing parameter α by the three types of morphing models, using the same colour codings as the left column plots.

Table 4.2: Accuracy of the moment morphing, vertical morphing and integral morphing algorithms on the nine benchmark models defined in Tab. 4.1, expressed in the KS distance at $\alpha = 0$ and the largest KS distance that occurs in the range $-1 < \alpha < 1$.

Name	Moment morphing		Vertical morphing		Integral morphing	
	$KS(\alpha = 0)$	$KS_{\max}$	$KS(\alpha = 0)$	$KS_{\max}$	$KS(\alpha = 0)$	$KS_{\max}$
N_μ	0	0	0.28	0.28	4.8×10^{-4}	8.1×10^{-4}
N_σ	3.7×10^{-9}	5.3×10^{-9}	0.044	0.046	2.8×10^{-4}	9.1×10^{-4}
$N_{\mu\sigma}$	1.1×10^{-8}	1.3×10^{-8}	0.36	0.40	4.4×10^{-4}	9.2×10^{-4}
Γ_k	0.0064	0.0069	0.032	0.032	0.0033	0.0036
Γ_θ	9.2×10^{-4}	1.1×10^{-3}	0.28	0.32	5.4×10^{-4}	6.9×10^{-4}
$\Gamma_{k\theta}$	0.11	0.14	0.32	0.35	0.11	0.14
C_1	0	0	0	0	0.018	0.018
C_2	0.0086	0.0086	0.0086	0.0086	0.013	0.013
C_{12}	0.020	0.020	0.020	0.020	0.040	0.040

the cumulative distribution functions of the truth model and the cumulative distribution function of the morphing interpolation model for any value of x, as a function of the morphing parameter α. The KS distance values range between zero (perfect agreement between the two distributions) and one (complete spatial separation of the distributions in x). Figure 4.9 illustrates the accuracy of the three morphing approaches on the $N_{\mu\sigma}, \Gamma_{k\theta}$ and C_1 models, along with the KS statistic as a function of α for all morphing approaches.

Accuracy metrics for all nine benchmark models are given in Tab. 4.2, which summarizes for each benchmark model and each morphing strategy the KS distance at $\alpha = 0$ (the morphing mid-point), and the worst KS distance that occurs in the morphing range $\alpha \in [-1, 1]$.

As expected, the moment morphing approach exactly replicates the $N_{\mu\sigma}$ benchmark model, unlike the vertical morphing approach. The integral morphing algorithm can also exactly replicate the $N_{\mu\sigma}$ model, but is limited to an accuracy of about 0.001 due to numerical precision limitations, related to integration and root-finding in the algorithm's implementation. For the $\Gamma_{k\theta}$ benchmark model, no morphing algorithm can exactly reproduce the truth model due to changing higher-order moments, but the moment and integral morphing algorithms perform about equally, and significantly better than the vertical morphing algorithm. For the C_1 benchmark model both the moment morphing and vertical morphing perform identically, as the first and second moment of the true distribution do not depend on α, hence both approaches reduce to the same algorithm, which happens to describe the C_1 model perfectly[4].

In summary, in these tests the moment morphing approach is as good as and usually better than the two alternative morphing methods.

[4]This perfect performance is specific to the C_1 benchmark that changes the first Chebychev coefficient only. Truth models that change high-order coefficients are imperfectly described by all morphing algorithms, as detailed in Table 4.2.

Accuracy for multi-dimensional distributions and multi-parameter morphing

For morphing models with multiple morphing parameters, and/or with input distributions with multiple observables, it is challenging to capture the accuracy with a limited set of benchmark models as KS tests have no simple equivalent for multidimensional distributions, and the number of benchmark permutations to test becomes large with multiple morphing parameters.

Nevertheless, one can illustrate the challenges of morphing and the performance of moment morphing with a single simple yet challenging two-parameter benchmark model for two-dimensional distributions: a multivariate normal distribution:

$$f_{\text{true}}(\boldsymbol{x}|\alpha,\beta) = \text{Gaussian}(\boldsymbol{x}|\boldsymbol{\mu},\mathbf{V}),$$

for which all five degrees of freedom, $\mu_x, \mu_y, \sigma_x \equiv V_{xx}, \sigma_y \equiv V_{yy}$ and $\rho \equiv V_{xy}/\sqrt{V_{xx}V_{yy}}$ depend linearly on two morphing parameters α, β.

In the case where the correlation coefficient ρ is independent of α, β, moment morphing provides the exact solution for this multi-variate Gaussian model, similar to the one-dimensional case, even if the dependence of $\mu_x, \mu_y, \sigma_x, \sigma_y$ is strong, as long as it is linear. Conversely, vertical morphing will perform poorly, especially if μ_x or μ_y depend strongly on α, β, while integral morphing is not available for multi-dimensional distributions.

The more challenging scenario where also ρ depends on α, β is visualized in Fig. 4.7. Moment morphing will not provide an exact solution for this class of models as the covariance moments are not explicitly corrected for, nevertheless the covariance of the interpolated shape at $(\alpha, \beta) = (0.5, 0.5)$ reasonably matches the covariance of the true model, although the shape is no longer perfectly Gaussian.

4.3.4 Implementation

This section discusses the publicly available morph classes, and is followed by details of the chosen extrapolation approach of a morph parameter beyond the provided input range.

Available morph classes

Moment morphing has been implemented in C++ for the RooFit toolkit [388]. As of ROOT release 5.34.22, the morphing features described in this document are available in the RooFit models library. Common to all classes is the ability to handle one or multiple observables, as well as the implementation of a cache that stores pre-calculated expensive components such as numerically computed moments, e. g. the means and widths of each input template, required for the translation of the corresponding observables.

The following moment morph classes are available in RooFit.

- The `RooMomentMorph` p.d.f. can be used to interpolate between an arbitrary number of reference distributions using a single morphing parameter. The algorithms settings described in this paper, e. g. linear or truly non-linear, can be used.

  Furthermore, a sine-linear variant transforms m_{frac} to $\sin(\pi/2 \cdot m_{\text{frac}})$ before calculating the coefficients, thus ensuring a continuous and differentiable transition when crossing between two adjacent sets of enclosing grid points. In addition, non-linear coefficients for adjusting the moments of the p.d.f.s can be mixed with linear coefficients when constructing the morph p.d.f., and an option is available to select positive non-linear coefficients only.

- `RooStarMomentMorph` is the natural extension for combining multiple one-dimensional `RooMomentMorph` p.d.f.s with one common sampling point. The class supports linear and sine-linear interpolation. The transformation of the template observables can be turned on or off.

- `RooMomentMorphND` allows the parametrization of a n-dimensional parameter space, interpolating linearly or sine-linearly between reference points sitting on a hyper-cube of arbitrary size.

- `RooMomentMorphFunc` and `RooMomentMorphFuncND` are similar to the top moment morph p.d.f.s, but can be used to interpolate between functions, not p.d.f.s.

Example code of how to use the moment morph p.d.f. is given below.

```
// This example builds two normal distributions and uses moment morphing to
// interpolate between the templates using RooFit.
using namespace RooFit;

// Create a persistable container for RooFit projects, allowing to use a simplified
// scripting language to build the p.d.f.s needed in this example
RooWorkspace w("w", 1);

// Build two normal distributions, corresponding to different values in the morph
// parameter space. They share the same observable, but have otherwise different
// moments, i.e. mean and width.
w.factory("RooGaussian::gaussian1(obs[0,400],50,15)");
w.factory("RooGaussian::gaussian2(obs,300,40)");

// Build a RooMomentMorph p.d.f. which interpolates between the normal distributions
// created before. The interpolation is parametrized by the parameter alpha and the
// reference templates map to alpha=0 and alpha=1 respectively.
w.factory("RooMomentMorph::morphpdf(alpha[0,1],obs,{gaussian1,gaussian2},{0,1})");

// Set the morphing parameter alpha explicitly to 0.5.
w::alpha->setVal(0.5);

// Create a frame to draw the p.d.f. from before and show the input templates as
// solid blue curves and the moment morph p.d.f. at alpha=0.5 in dashed red.
```

```
RooPlot* frame = w::obs->frame();
w::gaussian1->plotOn(frame, LineColor(kBlue), LineStyle(kSolid));
w::gaussian2->plotOn(frame, LineColor(kBlue), LineStyle(kSolid));
w::morphpdf->plotOn(frame, LineColor(kRed), LineStyle(kDashed));
frame->Draw();
```

Listing 4.1: Sample code to build the model shown in Fig. 4.5a.

Extrapolation beyond input boundaries

By construction, the validity of the morph p.d.f. of Eqn. (4.57) is highest when interpolating its morph parameter(s) within the provided range(s) of input values. Beyond these the predictive power is a priori unknown, but of course can be interesting to investigate. Some ad hoc choices need to be made for extrapolation cases, which were not covered by the description of the algorithm so far.

As apparent from Eqn. (4.45), when extrapolating m beyond the input boundary values m_{min} and m_{max}, the coefficients $c_i(m)$ increase in size and may become highly negative. In this situation the morph p.d.f. can become smaller than zero, and as such ill-defined. To prevent this, the following extrapolation approach is implemented.

- Whenever one of the morph parameters extends beyond the input range, i. e. $m < m_{\text{min}}$ or $m > m_{\text{max}}$, the coefficient multiplied with the nearest input p.d.f. is forced to one, and all other coefficients are set to zero.
- The same is done for the transformed width of Eqn. (4.50), which is to remain greater than zero.
- Beyond the input boundaries, the transformed mean of Eqn. (4.50) does remain well-defined, and uses the coefficients of either Eqn. (4.45) or Eqn. (4.48), depending on the linearity setting used.

Computational performance of moment morphing

Template morphing is one of the computationally limiting factors in current High Energy Physics (HEP) analyses, which makes understanding the performance of the algorithm at hand crucial. Figure 4.10 compares the performance of the linear and non-linear algorithms settings in terms of average CPU time needed for the evaluation of the morph p.d.f. as a function of the used reference templates. The benchmark makes use of the caching described in Sec. 4.3.4. It excludes the computation time needed for the calculation of the moment integrals over the input templates, which is a one-time calculation, the result of which can be cached in the RooFit workspace file along with the model if desired by the user. Details of the setup are described in the caption of the figure.

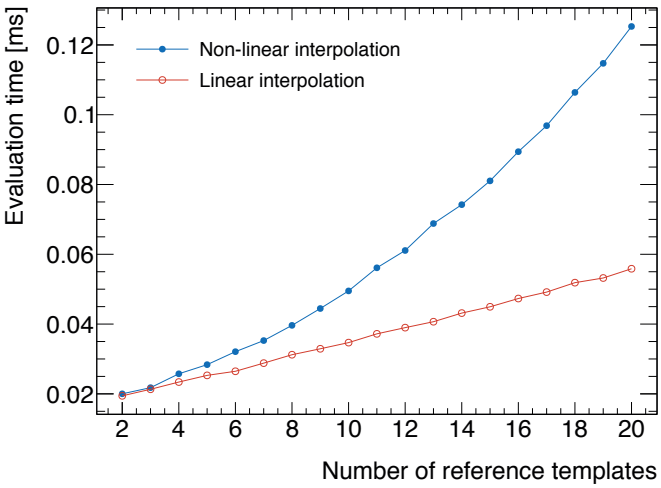

Figure 4.10: Benchmark results for `RooMomentMorph`. The figure shows the average CPU time for the evaluation of the morph p.d.f. as a function of the reference templates used for the interpolation for linear (red) and non-linear (blue) algorithms settings. This was measured on an Intel(R) Xeon(R) CPU E5-2450 @ 2.10 GHz with 2 GB of memory per core. As reference p.d.f.s normal distributions with varying mean are used.

For the interpretation of performance numbers it should be noted that the evaluation time for non-linear morphing models depends quadratically on the number of reference templates n, as for every template the associated coefficient is a product of n distances. In the linear case, the evaluation time is driven by the efficiency of the algorithm finding the two closest reference points surrounding the point at which the p.d.f. is evaluated. For 10 (20) reference templates, the ratio of non-linear over linear evaluation time is 1.4 (2.2).

Higgs boson decays to WW^*

5

This chapter summarizes the measurement of Higgs boson decays to W boson pairs, which subsequently decay leptonically into electrons or muons, and neutrinos, $H \to WW^* \to \ell\nu\ell\nu$. As the mass of the Higgs boson is low, at least one W boson is produced off shell. The analysis has previously been presented in full detail in Ref. [30]. This chapter focuses on the description of the measurements using the 8 TeV data set recorded by the ATLAS experiment, in particular on the statistical data analysis, but contains the necessary information to follow the analysis. The modifications required for the analysis of the 7 TeV data set are marginal and motivated by the lower integrated luminosity. Thus, the reader is referred to Ref. [30] for the modifications of the object and event selections, and of the background estimate, as well as for a more detailed review.

5.1 Analysis overview

The analysis exploits $H \to WW^*$ final states containing neutrinos and a pair of opposite-charge, isolated leptons, i.e. one electron and muon, respectively, two electrons, or two muons. The number of jets, n_j, is used for further classification. Exclusive $n_j = 0$ and $n_j = 1$ categories target the ggF production mode, while the inclusive $n_j \geq 2$ category is naturally sensitive to the VBF process. The same final state can originate from non-resonant W boson pair production and other di-boson processes, top quark pair and single-top quark production, from DY processes, and due to jets misidentified as lepton. An overview of all processes is presented in Tab. 5.1.

The signal processes and most background processes are modeled using MC simulation and normalized to data in an area of the phase space that is enriched in one or more process, achieved by kinematic selection requirements. Exceptions from this strategy are the background from W bosons produced in association with a jet, and the QCD multijet production, which both are estimated entirely from data. For minor backgrounds, e.g. backgrounds produced by double parton interactions, the theoretically predicted cross section is used. Table 5.2 lists the generator and cross section used for each process at 8 TeV.

When possible, QCD corrections at NLO are included in the matrix-element-level MC calculations through the POWHEG event generator [407–411]. ALPGEN [412] or SHERPA [413] are used to simulate processes with higher parton multiplicities at LO. For some processes only LO simulations are available, such as for $tq\bar{b}$ production (ACERMC [414]) or $gg \to WW$ (GG2VV [415]). The POWHEG and SHERPA samples use input PDFs from CT10 [116] and

Table 5.1: Overview of the background processes considered for the $H \to WW^* \to \ell\nu\ell\nu$ measurement. Background processes may have the same final state, i.e. they are irreducible, or are reconstructed to have a final state with two charged leptons, moderate MET, and no jets tagged as containing a b-quark due to distinct features.

Name	Process	Feature(s)
WW	WW	Irreducible
Top quarks		
$t\bar{t}$	$t\bar{t} \to Wb\,W\bar{b}$	Unidentified b quarks
t	tW	Unidentified b quark
	$t\bar{b}$, $tq\bar{b}$	q or b misidentified as ℓ; unidentified b quarks
Misidentified leptons (Misid.)		
Wj	W + jet(s)	j misidentified as ℓ
jj	Multijet production	jj misidentified as $\ell\ell$; misidentified neutrinos
Other dibosons		
VV	$W\gamma$	γ misidentified as e
	$W\gamma^*$, WZ, $ZZ \to \ell\ell\,\ell\ell$	Unidentified lepton(s)
	$ZZ \to \ell\ell\,\nu\nu$	Irreducible
	$Z\gamma$	γ misidentified as e; unidentified lepton
Drell-Yan (DY)		
$ee/\mu\mu$	$Z/\gamma^* \to ee$, $\mu\mu$	Misidentified neutrinos
$\tau\tau$	$Z/\gamma^* \to \tau\tau \to \ell\nu\nu\ell\,\nu\nu$	Irreducible

the ALPGEN+HERWIG and ACERMC samples use the CTEQ6L1 PDF set [416]. The Z/γ^* sample is reweighted to the MRSTmcal PDF set [417]. The matrix-element calculation is matched to a UE/PS model, e.g. PYTHIA6 [315], PYTHIA8 [341], HERWIG+JIMMY [418, 419], or SHERPA. The modeling of pile-up interactions follows the same approach as introduced in Cha. 3, i.e. using PYTHIA8. Acceptances and efficiencies of the ATLAS detector are obtained from a simulation [420] of its response based on GEANT4 [421]. For the top quark samples, the model uses a parametrized GEANT4-based calorimeter simulation [422]. The cross section calculations use, amongst others, MCFM [423], TOP++2.0 [424], and DYNNLO [425, 426].

The background from non-resonant W boson pair production is irreducible. However, it can be suppressed by exploiting the kinematic distributions and angular information of the decay products, which exhibit the characteristic properties of the parent boson [427–429]. Charged leptons originating from opposite spin W bosons, i.e. the ones produced in the decay of a spin-0 Higgs boson, have aligned spins. Thus, the opening angle between the two charged leptons in the transverse plane, $\Delta\phi_{\ell\ell}$, is small, and the invariant mass of the

Table 5.2: Overview of the MC generators used to model the signal and background processes. The corresponding cross sections times branching fractions, $\sigma \cdot \mathrm{BR}$, are quoted at $\sqrt{s} = 8\,\mathrm{TeV}$. The reader is referred to [30] and references therein for details on the calculation.

Process		MC generator	$\sigma \cdot \mathrm{BR}$ (pb)
Signal			
ggF	$H \to WW^*$	POWHEG+PYTHIA8	0.435
VBF	$H \to WW^*$	POWHEG+PYTHIA8	0.0356
VH	$H \to WW^*$	PYTHIA8	0.0253
WW			
$q\bar{q} \to WW$ and $qg \to WW$		POWHEG+PYTHIA6	5.68
$gg \to WW$		GG2VV+HERWIG	0.196
$(q\bar{q} \to W) + (q\bar{q} \to W)$		PYTHIA8	0.480
$q\bar{q} \to WW$		SHERPA	5.68
VBS $WW + 2$ jets		SHERPA	0.0397
Top quarks			
$t\bar{t}$		POWHEG+PYTHIA6	26.6
Wt		POWHEG+PYTHIA6	2.35
$tq\bar{b}$		ACERMC+PYTHIA6	28.4
$t\bar{b}$		POWHEG+PYTHIA6	1.82
Other dibosons (VV)			
$W\gamma$	($p_{\mathrm{T}}^{\gamma} > 8\,\mathrm{GeV}$)	ALPGEN+HERWIG	369
$W\gamma^*$	($m_{\ell\ell} \leq 7\,\mathrm{GeV}$)	SHERPA	12.2
WZ	($m_{\ell\ell} > 7\,\mathrm{GeV}$)	POWHEG+PYTHIA8	12.7
VBS $WZ + 2$ jets	($m_{\ell\ell} > 7\,\mathrm{GeV}$)	SHERPA	0.0126
$Z\gamma$	($p_{\mathrm{T}}^{\gamma} > 8\,\mathrm{GeV}$)	SHERPA	163
$Z\gamma^*$	(min. $m_{\ell\ell} \leq 4\,\mathrm{GeV}$)	SHERPA	7.31
ZZ	($m_{\ell\ell} > 4\,\mathrm{GeV}$)	POWHEG+PYTHIA8	0.733
$ZZ \to \ell\ell\,\nu\nu$	($m_{\ell\ell} > 4\,\mathrm{GeV}$)	POWHEG+PYTHIA8	0.504
Drell-Yan			
Z	($m_{\ell\ell} > 10\,\mathrm{GeV}$)	ALPGEN+HERWIG	16500
VBF $Z + 2$ jets	($m_{\ell\ell} > 7\,\mathrm{GeV}$)	SHERPA	5.36

dilepton system, $m_{\ell\ell}$, is low but broadly distributed in the range below $m_H/2$. The charged leptons from non-resonant W boson pair production, on the other hand, are well separated, and tend to have a larger invariant mass.

Events originating from top quark decays are typically accompanied by high-momentum jets containing a b-hadron decay. If they are tagged as such, c.f. Sec. 3.1.5, the events are not selected. Inefficiencies in the flavor tagging algorithms lead to unidentified b-jets in the

final state. The contribution of top quark pair and single-top quark production to the total background increases with the number of jets in the final state, n_j.

The analysis uses event categories based on the lepton flavor, i.e. different flavor final states ($e\mu$) and same flavor final states ($ee/\mu\mu$), due to the different contributions to these categories from the DY process. The $Z/\gamma^* \to \tau\tau$ background is irreducible in the $e\mu$ categories and enters due to neutrinos produced in subsequent leptonic τ-lepton decays. The $ee/\mu\mu$ sample contains a significant number of $Z/\gamma^* \to ee, \mu\mu$ events, selected due a mismeasurement of the MET caused as a result of the degraded detector resolution at high pile-up, c.f. Sec. 3.3.3, or due to neutrinos produced in b-hadron or c-hadron decays contained in jets produced in association with the Z boson.

Backgrounds with misidentified or unidentified leptons, are suppressed by the identification and isolation requirements on electrons and muons, c.f. Sec. 5.2.1. The sources of this background are in particular hadrons or jets from W+jets and QCD multijet production that are misidentified as leptons, or real or virtual photons converting in the detector material to e^+e^- pairs, which may be asymmetric in p_{T}. Hence, events with this topology can be distinguished further from the signal processes by the magnitude of the transverse momentum of the lower-p_{T} lepton in the event, $p_{\mathrm{T}}^{\ell 2}$. The $p_{\mathrm{T}}^{\ell 2}$ distribution of the non-prompt lepton background falls rapidly with increasing p_{T}, while it peaks near half the difference between the Higgs boson and W boson mass for the signal, since one of the W bosons from the Higgs boson decay is off its mass shell. Further details on the background modeling and estimation are given in Sec. 5.3.

The presence of the neutrinos in the final state prohibits fully reconstructing its invariant mass. However, a transverse mass, m_{T}, can be calculated for the system of the two leptons and the MET [430], i.e. excluding the unknown longitudinal neutrino momenta,

$$m_{\mathrm{T}} = \sqrt{\left(E_{\mathrm{T}}^{\ell\ell} + p_{\mathrm{T}}^{\nu\nu}\right)^2 - \left|\boldsymbol{p}_{\mathrm{T}}^{\ell\ell} + \boldsymbol{p}_{\mathrm{T}}^{\nu\nu}\right|^2}, \tag{5.1}$$

with $E_{\mathrm{T}}^{\ell\ell} = \sqrt{(p_{\mathrm{T}}^{\ell\ell})^2 + (m_{\ell\ell})^2}$ and the vector sum of the neutrino (lepton) transverse momenta, $\boldsymbol{p}_{\mathrm{T}}^{\nu\nu}$ ($\boldsymbol{p}_{\mathrm{T}}^{\ell\ell}$). The kinematic upper bound of the transverse mass scales with the Higgs boson mass. Hence, the m_{T} distribution can be used to discriminate Higgs boson production and the dominant non-resonant WW and top quark backgrounds across all jet bins. Further details on the signal selection is provided in Sec. 5.2.

5.2 Object and event selection

5.2.1 Physics objects

Events used in $H \to WW^* \to \ell\nu\ell\nu$ analysis are selected with triggers that require either a single lepton or two leptons, summarized in Tab. 5.3 with the minimum p_{T} requirements imposed

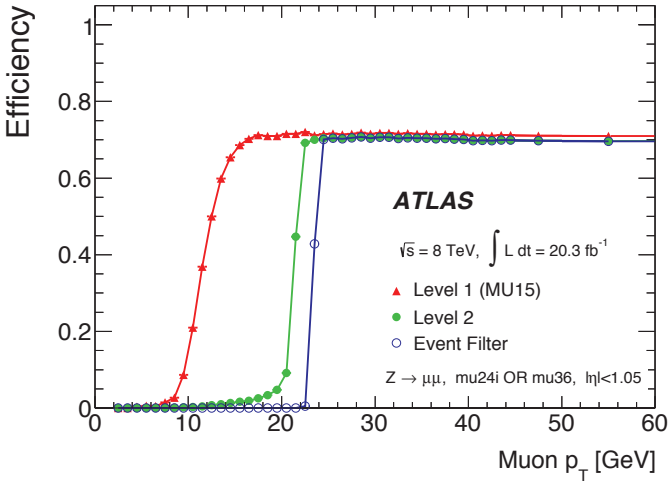

Figure 5.1: The measured efficiency of the two single muon triggers used in the $H \to WW^* \to \ell\nu\ell\nu$ analysis convolved as an "or" between the two, with respect to the offline reconstructed muons in the barrel region. Figure taken from Ref. [324].

by the Level-1 trigger and the high-level trigger for 2012 collision data. The efficiency of the triggers is measured using a tag-and-probe method with lepton candidates from $Z \to ee$ and $Z \to \mu\mu$ decays. Figure 5.1 shows, exemplarily, the measured efficiency of the two used single muon triggers convolved as an "or" between the two, with respect to the offline reconstructed muons in the barrel region.

Table 5.3: The minimum p_{T} requirements imposed by the Level-1 trigger and the high-level trigger for 2012 collision data as they are used in the $H \to WW^* \to \ell\nu\ell\nu$ analysis. Triggers with the indicated "i" use an isolation criterion made with ID tracks. For di-lepton triggers the minimum p_{T} requirements for leading and sub-leading lepton are indicated. The "and" and "or" are logical.

Name	Level-1 trigger	High-level trigger
Single lepton		
e	18 or 30	24i or 60
μ	15	24i or 36
Di-lepton		
e, e	10 and 10	12 and 12
μ, μ	15	18 and 8
e, μ	10 and 6	12 and 8

The selected events are reconstructed following the algorithms presented in Cha. 3. The primary vertex is required to have at least three tracks with $p_{\mathrm{T}} > 400\,\mathrm{MeV}$. The analysis uses combined muon candidates with $|\eta| < 2.5$, reconstructed from matching a MS track with a reconstructed ID track, c.f. Sec. 3.2.1. Electrons are reconstructed in the pseudorapidity range $|\eta| < 2.47$, but excluding $1.37 < |\eta| < 1.52$, i.e. the transition region between barrel and end-cap ECAL. They must satisfy the "very tight" and "medium" likelihood requirements for electrons with $10 < E_{\mathrm{T}} < 25\,\mathrm{GeV}$ and $E_{\mathrm{T}} > 25\,\mathrm{GeV}$ respectively, c.f. Sec. 3.2.2.

In order to distinguish leptons produced in boson decays from the ones produced in QCD processes, and thus to reduce the backgrounds from non-prompt leptons, additional quality requirements are imposed on the lepton's impact parameter and isolation. The significance of the transverse impact parameter, i.e. the ratio of the measured transverse impact parameter d_0 to its estimated uncertainty σ_{d_0}, is required to be smaller than 3.0 for both electrons and muons. The longitudinal impact parameter z_0 is required to satisfy $z_0 \sin\theta < 0.4\,\mathrm{mm}$ and $1.0\,\mathrm{mm}$ for selected electrons and muons, respectively.

To ensure that the energy flow in the vicinity of electrons and muons is small, both track-based and calorimeter based requirements are employed. The track isolation is based on the scalar sum of the transverse momenta, $\sum p_{\mathrm{T}}$, of all reconstructed tracks in the vicinity of the lepton with $p_{\mathrm{T}} > 400\,\mathrm{MeV}$ in a cone in the η-ϕ space, i.e. $\sqrt{\Delta\eta^2 + \Delta\phi^2} \leq \Delta R$. The cone size varies from $\Delta R = 0.4$ for low transverse momenta below $p_{\mathrm{T}} < 15\,\mathrm{GeV}$ to $\Delta R = 0.3$ for higher values above $p_{\mathrm{T}} > 15\,\mathrm{GeV}$. For electron (muon) candidates $\sum p_{\mathrm{T}}$ is required to be less than 6% of the electron E_{T} (muon p_{T}) at low E_{T} (p_{T}), loosened to 10% (12%) at high E_{T} (p_{T}). The calorimetric isolation for electrons requires the topological calorimetric isolation energy, i.e. the sum of the cluster transverse energies, $\sum E_{\mathrm{T}}$, to be less than 20% of the electron E_{T} for candidates with $10 < E_{\mathrm{T}} < 15\,\mathrm{GeV}$, monotonically relaxed to 28% of the electron E_{T} for candidates with $E_{\mathrm{T}} > 25\,\mathrm{GeV}$. The requirement for muons is similar: the sum of the energy deposited in calorimeter cells, $\sum E_{\mathrm{T}}$, must be less than 6% of the muon p_{T} for candidates with $10 < p_{\mathrm{T}} < 15\,\mathrm{GeV}$, which is monotonically relaxed to 28% of the muon p_{T} for candidates with $E_{\mathrm{T}} > 25\,\mathrm{GeV}$.

The computation of $\sum E_{\mathrm{T}}$ is different for electron and muon candidates: for the former $\sum E_{\mathrm{T}}$ is computed from the energy deposited in the ECAL and HCAL inside a cone of $\Delta R = 0.3$ around the candidate electron cluster, but excluding the 5×7 towers in $\eta \times \phi$ around the electron barycenter to not include the electron energy itself. The isolation energy is corrected event-by-event for pile-up and UE contributions [431] and leakage outside the selected candidate electron cluster. The latter uses all calorimeter cells above a noise threshold inside a conical shell with $0.05 \leq \Delta R \leq 0.3$ centered on the muon trajectory. A correction for extra energy and reduced vertex efficiency due to pile-up interactions is applied.

Lepton candidates may be close in $\eta - \phi$ space and their overlap has to be removed. Electron candidates with tracks extending to the MS are removed. A separation of less than $\Delta R < 0.1$

between electron and muon candidates indicates a muon that has undergone bremsstrahlung in the ID material or the calorimeter. Hence, the muon candidate is retained and the electron candidate is removed.

The jets used in the $H \to WW^* \to \ell\nu\ell\nu$ analysis, are reconstructed using the anti-k_t algorithm with radius parameter $R = 0.4$ and calibrated using the LCW+JES scheme, c.f. Sec. 3.3.1. They are, independent of their origin, required to have $p_{\mathrm{T}}^j > 25\,\mathrm{GeV}$ within the ID acceptance, $|\eta| < 2.4$, and a JVF of at least 50 %. Jets in the region $2.4 \leq |\eta| < 4.5$ are required to have an increased threshold of $p_{\mathrm{T}}^j > 30\,\mathrm{GeV}$ to suppress jets originating from pile-up interactions. The reconstructed objects are ordered by their transverse momentum.

Lepton and jet candidates may be close in $\eta - \phi$ space and their overlap has to be removed. If a high-p_{T} electron and a jet candidate are separated by less than $\Delta R = 0.3$, the jet is removed, since the electron is always reconstructed as a jet. In contrast, if a high-p_{T} muon and a jet candidate are separated by less than $\Delta R = 0.3$, the jet is retained in favor of the muon candidate as it indicates a non-prompt muon from a heavy flavor decay.

5.2.2 Signal modeling and associated uncertainties

The theoretical aspects of the Higgs boson production and decay processes are described in detail in Sec. 1.4. The $H \to WW^*$ and other decay partial widths used in this analysis are computed by the PROPHECY4f [432] and HDECAY [433] tools, respectively. The relative uncertainty on the predicted $H \to WW^*$ BR is 4.2%, assuming a Higgs boson with a mass of 125.36 GeV [135].

The templates for the Higgs boson production mode via gluon fusion used in this analysis are determined from simulating events using the POWHEG MC generator interfaced with PYTHIA8. The scale for matching the resummation of higher order terms to the matrix-element calculation is tuned to reproduce the NNLO+next-to-leading logarithm (NLL) calculation of the Higgs boson transverse momentum [205]. The p_{T} spectrum for events produced in association with zero or one jet is reweighted to reproduce the prediction of the NNLO+NNLL dynamic-scale calculation from HRES2.1 [434]. The p_{T} spectrum for events comprising two or more jets is reweighted to reproduce the NLO prediction from POWHEG for the associated production of a Higgs boson and two jets [435].

The effect of missing higher-order perturbative corrections in the calculation of the ggF production process is threefold. Naturally, it gives rise to an uncertainty of approximately 7.5% on the total inclusive cross section of the ggF process at $m_H = 125.36\,\mathrm{GeV}$. Typically, these uncertainties are assessed by varying the renormalization and factorization scales in the MC simulation around the nominal scale (m_H). However, in case an analysis exploits the production cross section of a process as a function of the exclusive number of jets in the event, the nominal procedure may incidentally lead to cancellations between the scale dependence of the perturbative series and subleading Sudakov logarithms from jet binning or veto. The

effect of jet binning or veto on the the predicted distribution of the ggF signal among the exclusive jet bins is evaluated using the jet-veto-efficiency method (JVE method) [205, 436–438] for the ggF-enriched categories and the Stewart-Tackmann method (ST method) [439] for the VBF-enriched category, respectively. A major benefit of choosing the JVE method in the most sensitive categories is owing to the simplicity of including the most recent developments in perturbative calculations in the evaluation of the uncertainties. However, due to the central jet veto the JVE method cannot be used in the $n_j \geq 2$ category. The estimated uncertainties are 11%, 25%, 33%, and 29% in the $n_j = 0$, $n_j = 1$, ggF-enriched $n_j \geq 2$, and VBF-enriched $n_j \geq 2$ categories, and take into account the possibility of events migrating between categories. Thirdly, the signal acceptance in the selected area of phase space is subject to systematic uncertainties due to missing higher-order QCD and EW corrections, too. The effect is estimated to be of the size of a few percent across all categories.

Differences between PDF parametrisations and models are evaluated at the generator level and lead to a uncertainty of 7.2% on the total inclusive cross section for the gluon fusion process. The uncertainty on the signal acceptance in the various categories is approximately 3% across all categories and includes the uncertainty due to jet veto or binning. The matching of the hard-scatter matrix element and the UE/PS model is validated by studying differences between POWHEG+HERWIG and aMC@NLO [206]+HERWIG. The uncertainties on the signal acceptance due to the UE, hadronization, and PS models are assessed by comparing predictions from POWHEG+HERWIG and POWHEG+PYTHIA8. Uncertainties on the jet binning or veto due to the PS model are assumed to be included in the methods outlined in the previous paragraph, and uncertainties due to the hadronization and UE models are found to be small and thus neglected. Each of the effects also induces an uncertainty on the distribution of the reconstructed transverse mass, m_{T}, which is considered in the statistical analysis.

Higgs boson production via VBF is simulated and modeled using POWHEG+PYTHIA8. The uncertainty on the total cross section of the VBF process is 2.7% and almost entirely due to PDF modeling. Additional uncertainties on the signal acceptance are evaluated to be of the size of a few percent, similar to the procedure followed for the ggF process.

5.2.3 Signal selection

This remainder of this section describes in detail the criteria employed to control the extensive backgrounds to the studied process by exploiting its distinct decay topology, aiming at selecting a sample enriched in $H \to WW^* \to \ell\nu\ell\nu$ events.

Preselection

The final state is characterized by two identified leptons with opposite electric charge. The selected trigger, c.f. Sec. 5.2.1, require the transverse momenta of the leading lepton ℓ_1

and subleading lepton ℓ_2 to satisfy $p_{\mathrm{T}}^{\ell 1} > 22\,\mathrm{GeV}$ and $p_{\mathrm{T}}^{\ell 2} > 10\,\mathrm{GeV}$, respectively. Events from $Z/\gamma^* \to ee$, $\mu\mu$ production are rejected by the condition $|m_{\ell\ell} - m_Z| > 15\,\mathrm{GeV}$. Low-mass meson resonances and DY events are removed by requiring $m_{\ell\ell} > 10\,\mathrm{GeV}$ (12 GeV) for the $e\mu$ ($ee/\mu\mu$) final state.

The contributions from the DY process, the production of a W boson in association with jets, or from multijet production are suppressed further by employing requirements on the MET in the event, as shown in Fig. 5.2. The $n_j \leq 1$ and $n_j \geq 2$ ggF-enriched categories with $e\mu$ final states are dominated by the $Z/\gamma^* \to \tau\tau$ and multijet backgrounds, i.e. processes with real MET from neutrinos or fake MET due to misidentified leptons. $Z/\gamma^* \to ee$, $\mu\mu$ production, on the other hand, dominates the $n_j \leq 1$ $ee/\mu\mu$ sample. These backgrounds are reduced by selecting events with $E_{\mathrm{T,rel}}^{\mathrm{miss}} > 40\,\mathrm{GeV}$ and $p_{\mathrm{T}}^{\mathrm{miss}} > 20\,\mathrm{GeV}$, respectively. In the $n_j \geq 2$ VBF-enriched $e\mu$ category no MET requirement is employed to recover signal acceptance for the statistically-limited VBF measurement. However, in the $ee/\mu\mu$ category the requirements $p_{\mathrm{T}}^{\mathrm{miss}} > 40\,\mathrm{GeV}$ and $E_{\mathrm{T}}^{\mathrm{miss}} > 45\,\mathrm{GeV}$ must be imposed due to the large $Z/\gamma^* \to ee$, $\mu\mu$ contamination. Table 5.4 summarizes the pre-selection criteria as well as the additional requirements in each n_j and lepton-flavor category.

The $n_j = 0$ category

A jet veto effectively suppresses the rate of the top background processes. In the absence of a reconstructed jet, the MET is expected to balance the dilepton system. Hence, $\boldsymbol{p}_{\mathrm{T}}^{\mathrm{miss}}$ points away from the dilepton transverse momentum, $\Delta\phi_{\ell\ell,\mathrm{MET}} > \pi/2$, and the magnitude of the dilepton momentum $p_{\mathrm{T}}^{\ell\ell}$ is small in DY events, $p_{\mathrm{T}}^{\ell\ell} < 30\,\mathrm{GeV}$. To further reduce the DY background in the $ee/\mu\mu$ category, events have to satisfy $p_{\mathrm{T,rel}}^{\mathrm{miss\,(trk)}} > 40\,\mathrm{GeV}$.

The residual DY contribution in the $ee/\mu\mu$ category is characterized by an imbalance of transverse momentum in the selected events, caused by a mismeasurement of the energy associated with partons from ISR, c.f. 1.3.2. These events can be suppressed by exploiting the fractional jet recoil relative to the dilepton transverse momentum,

$$f_{\mathrm{recoil}} = \left| \sum_{\text{jets } j \text{ in } \wedge} \mathrm{JVF}_j \cdot \boldsymbol{p}_{\mathrm{T}}^{\,j} \right| \Big/ p_{\mathrm{T}}^{\ell\ell}. \tag{5.2}$$

This definition uses soft jets, i.e. objects with a lower threshold of $p_{\mathrm{T}}^{j} > 10\,\mathrm{GeV}$, within a $\pi/2$ wedge in ϕ ($\wedge$) centered on $-\boldsymbol{p}_{\mathrm{T}}^{\ell\ell}$, i.e. balancing the dilepton system. These objects are weighted by the fraction of the reconstructed jet energy associated with the reconstructed primary vertex of the event. Figure 5.3d shows the differences in the f_{recoil} distribution between DY and non-DY processes in the $ee/\mu\mu$ sample. The simultaneous optimization of the partially correlated f_{recoil} and $p_{\mathrm{T}}^{\ell\ell}$ requirements using the Poisson significance of a cut-and-count experiment with accurately estimated background cross sections, c.f. Sec. 5.3, suggests a tight selection criterion of $f_{\mathrm{recoil}} < 0.1$. The optimization considers systematic uncertainties on the

Table 5.4: Summary of the event selection requirements for the $e\mu$ and $ee/\mu\mu$ lepton-flavor samples in the n_j categories of the 8 TeV data set. All energy-related quantities are given in units of GeV.

Objective		ggF-enriched			VBF-enriched
		$n_j = 0$	$n_j = 1$	$n_j \geq 2$ ggF	$n_j \geq 2$ VBF
Pre-selection	All n_j	$p_{\mathrm{T}}^{\ell 1} > 22$ for the leading lepton ℓ_1 $p_{\mathrm{T}}^{\ell 2} > 10$ for the subleading lepton ℓ_2 Opposite charge leptons $m_{\ell\ell} > 10$ for the $e\mu$ sample $m_{\ell\ell} > 12$ for the $ee/\mu\mu$ sample $\lvert m_{\ell\ell} - m_Z \rvert > 15$ for the $ee/\mu\mu$ sample			
		$p_{\mathrm{T}}^{\mathrm{miss}} > 20$ for $e\mu$ $E_{\mathrm{T,rel}}^{\mathrm{miss}} > 40$ for $ee/\mu\mu$	$p_{\mathrm{T}}^{\mathrm{miss}} > 20$ for $e\mu$ $E_{\mathrm{T,rel}}^{\mathrm{miss}} > 40$ for $ee/\mu\mu$	$p_{\mathrm{T}}^{\mathrm{miss}} > 20$ for $e\mu$ -	No MET requirement for $e\mu$ -
Reject backgrounds	DY	$p_{\mathrm{T,rel}}^{\mathrm{miss\,(trk)}} > 40$ for $ee/\mu\mu$ $f_{\mathrm{recoil}} < 0.1$ for $ee/\mu\mu$ $p_{\mathrm{T}}^{\ell\ell} > 30$ $\Delta\phi_{\ell\ell,\mathrm{MET}} > \pi/2$	$p_{\mathrm{T,rel}}^{\mathrm{miss\,(trk)}} > 35$ for $ee/\mu\mu$ $f_{\mathrm{recoil}} < 0.1$ for $ee/\mu\mu$ $m_{\tau\tau} < m_Z - 25$ -	- - $m_{\tau\tau} < m_Z - 25$ -	$p_{\mathrm{T}}^{\mathrm{miss}} > 40$ for $ee/\mu\mu$ $E_{\mathrm{T}}^{\mathrm{miss}} > 45$ for $ee/\mu\mu$ $m_{\tau\tau} < m_Z - 25$ -
	Misid.	-	$m_{\mathrm{T}}^{\ell} > 50$ for $e\mu$	-	-
	Top	$n_j = 0$ - -	$n_b = 0$ - -	$n_b = 0$ - -	$n_b = 0$ $p_{\mathrm{T}}^{\mathrm{sum}}$ inputs to BDT $\Sigma m_{\ell j}$ inputs to BDT
VBF topology		-	-	See Sec. 5.2.3 for rejection of VBF & VH ($W, Z \to jj$), where $H \to WW^*$	m_{jj} inputs to BDT Δy_{jj} inputs to BDT ΣC_{ℓ} inputs to BDT $C_{\ell 1} < 1$ and $C_{\ell 2} < 1$ $C_{j3} > 1$ for j_3 with $p_{\mathrm{T}}^{j3} > 20$ $O_{\mathrm{BDT}} \geq -0.48$
$H \to WW^* \to \ell\nu\ell\nu$ decay topology		$m_{\ell\ell} < 55$ $\Delta\phi_{\ell\ell} < 1.8$ No m_{T} requirement	$m_{\ell\ell} < 55$ $\Delta\phi_{\ell\ell} < 1.8$ No m_{T} requirement	$m_{\ell\ell} < 55$ $\Delta\phi_{\ell\ell} < 1.8$ No m_{T} requirement	$m_{\ell\ell}$ inputs to BDT $\Delta\phi_{\ell\ell}$ inputs to BDT m_{T} inputs to BDT

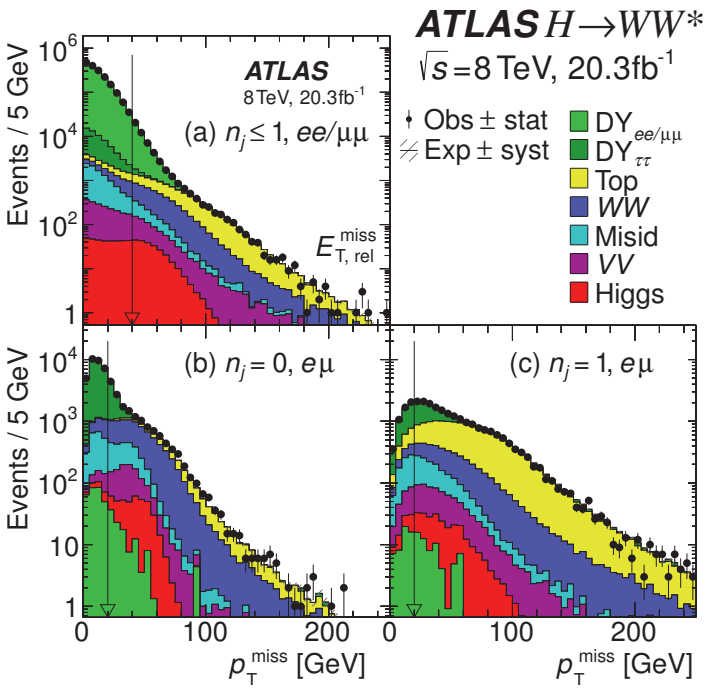

Figure 5.2: Distributions of the $E_{\mathrm{T}}^{\mathrm{miss}}$ and $p_{\mathrm{T}}^{\mathrm{miss}}$ after applying the preselection criteria common to all n_j categories, c.f. Tab. 5.4. The statistical uncertainty is indicated by vertical error bars on the observed data points. The predicted distributions are shown with the cumulative experimental and theoretical uncertainties represented by the shaded band. The stacking order of the histograms depends on the relative contributions of the physics processes in the shown categories. The arrows mark values of selection requirements.

$Z/\gamma^* \to ee, \mu\mu$ production estimated from a previous iteration of the analysis [440], and the total uncertainties on the rates of all other backgrounds, c.f. Sec. 5.3

The decay topology of the SM Higgs boson decay is exploited to separate the resonant Higgs boson production from the non-resonant WW production, $\Delta\phi_{\ell\ell} < 1.8$ and $m_{\ell\ell} < 55\,\mathrm{GeV}$. For an overview of the expected yields for each signal and background process and the observed rate at every stage of the selection, the reader is referred to Ref. [30].

The $n_j = 1$ category

Before applying further selection criteria, the top-quark background dominates the $n_j = 1$ category. It is effectively controlled by rejecting events involving jets with $p_{\mathrm{T}} > 20\,\mathrm{GeV}$ and tagged as containing a b-quark, c.f. Sec. 3.1.5. The multijet background enters the $e\mu$ category due to jets misidentified as leptons measured with a low energy. This topology is

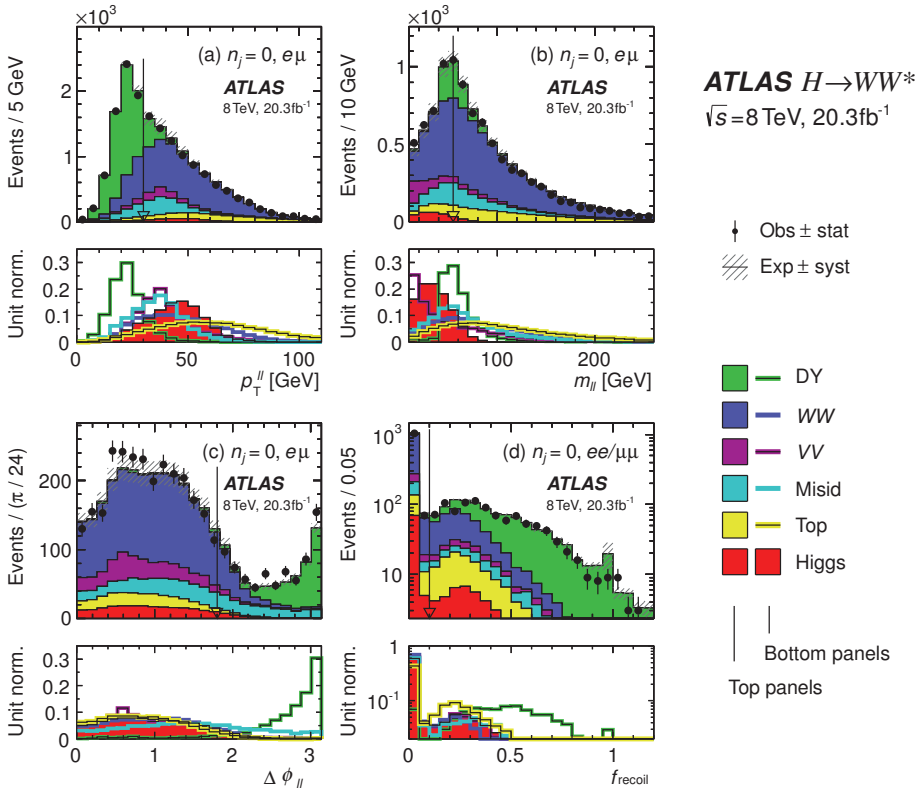

Figure 5.3: Distributions of (a) $p_T^{\ell\ell}$, (b) $m_{\ell\ell}$, (c) $\Delta\phi_{\ell\ell}$, and (d) f_{recoil}, for events in the $n_j = 0$ category of the 8 TeV data set, satisfying all selection criteria up to the one on the shown distribution, respectively. For each observable, the top panel compares the modeling of the cumulative predicted distribution to collision data. The bottom panel emphasizes differences in the shapes of the distributions of the individual expected contributions by normalizing them to a unit area. See Fig. 5.2 for plotting details.

controlled by requiring the transverse mass calculated with the leading or subleading lepton, ℓ_i, to satisfy $m_T^{\ell 1}$ or $m_T^{\ell 2} > 50$ GeV. It is defined as

$$m_T^{\ell_i} = \sqrt{2 p_T^{\ell_i} \cdot p_T^{\text{miss}} \cdot \left(1 - \cos\Delta\phi\right)}, \tag{5.3}$$

with the angle between the lepton transverse momentum and $\boldsymbol{p}_T^{\text{miss}}$, $\Delta\phi$.

This requirement rejects a significant amount of the DY background, too. To further reduce $Z/\gamma^* \to \tau\tau$ background, the mass of the τ-lepton pair is required to be low, $m_{\tau\tau} < m_Z - 25\,\text{GeV}$. In this analysis $m_{\tau\tau}$ is constructed using the collinear approximation [441–443],

$$m_{\tau\tau} = \frac{m_{\ell\ell}}{\sqrt{x_1 x_2}} \quad \text{with} \quad x_i = \frac{p_{\ell,i}}{p_{\tau,i}} > 0, \quad i = 1,2, \tag{5.4}$$

where x_i is the fractional momentum of the charged lepton from a given τ-lepton decay. $\boldsymbol{p}_{\tau,i} = \boldsymbol{p}_{\ell,i} + \boldsymbol{p}_{\text{miss}}$ uses the direction of the measured MET.

The definition of the fractional jet recoil relative to the dilepton transverse momentum is modified from the definition for $n_j = 0$ to use the magnitude of $\boldsymbol{p}_{\text{T}}^{\ell\ell j} = \boldsymbol{p}_{\text{T}}^{\ell\ell} + \boldsymbol{p}_{\text{T}}^{j}$. It is used to reduce the DY background in the $ee/\mu\mu$ categories, $f_{\text{recoil}} < 0.1$, following a similar optimization as described earlier. The $p_{\text{T,rel}}^{\text{miss (trk)}}$ threshold, employed for further suppressing $Z/\gamma^* \to ee, \mu\mu$ events, is lowered to 35 GeV.

As before, the decay topology of the SM Higgs boson decay is used to isolate Higgs boson production and non-resonant WW production, $\Delta\phi_{\ell\ell} < 1.8$ and $m_{\ell\ell} < 55\,\text{GeV}$. The distributions of the variables discussed in this paragraph are shown in Fig. 5.4. For the expected yields for each signal and background process as well as the observed rate at every stage of the selection, the reader is referred to Ref. [30].

The VBF-enriched $n_j \geq 2$ category

The two-jet sample is primarily used to measure Higgs boson production via the VBF mechanism. A BDT multivariate method [444, 445] making use of stochastic gradient boosting [446] as implemented in the TMVA package [447, 448], is used to separate the VBF Higgs boson production from other production modes, such as production via gluon-fusion, and the background processes. The classifier grows 1000 trees with a maximal depth of 5 at a learning rate of 0.125, using a random sample of 25% of the available events. A cross-check analysis is described in Ref. [30].

After applying the common pre-selection criteria, and following the discussion of the kinematics of the VBF process in Sec. 1.4.1, the rapidity gap between the two tagging jets j_1 and j_2 and their invariant mass,

$$\Delta y_{jj} = |\, y_{j1} - y_{j2}\,| \quad \text{and} \quad m_{jj} \approx \sqrt{p_{\text{T}}^{j1} \cdot p_{\text{T}}^{j2}}\, e^{\Delta y_{jj}/2} \tag{5.5}$$

are input variables to the BDT

A central-jet veto [449] is used to suppress the QCD multijet background. The jet centrality with respect to the tagging jets is defined as

$$C_{j3} = \left| \eta_{j3} - \frac{\Sigma\,\eta_{jj}}{2} \right| \Big/ \frac{\Delta\eta_{jj}}{2} \quad \text{with} \quad \Sigma\,\eta_{jj} = \eta_{j1} + \eta_{j2} \quad \text{and} \quad \Delta\eta_{jj} = |\,\eta_{j1} - \eta_{j2}\,|, \tag{5.6}$$

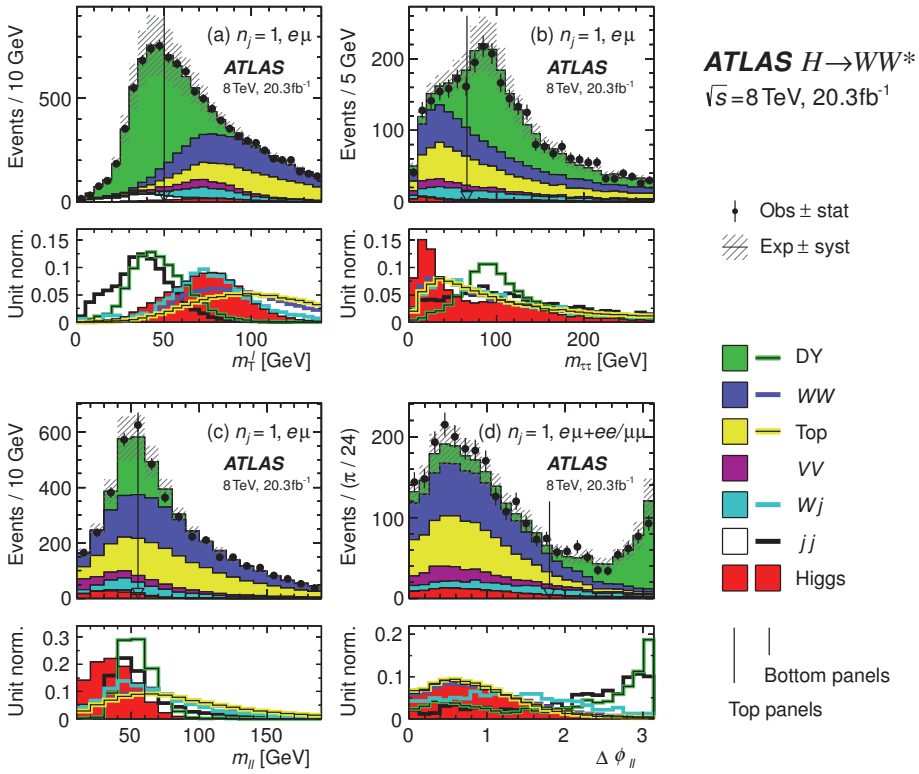

Figure 5.4: Distributions of (a) m_T^ℓ, (b) $m_{\tau\tau}$, (c) $m_{\ell\ell}$, and (d) $\Delta\phi_{\ell\ell}$, for events in the $n_j = 1$ category of the 8 TeV data set, satisfying all selection criteria up to the one on the shown distribution, respectively. See Figs. 5.2 and 5.3 for plotting details.

for jets with $p_T > 20$ GeV, and where η_{j3} is the pseudorapidity of an extra jet j_3. Similarly, the Higgs boson decay products are required to be in the central rapidity regions, i.e. the centrality of each lepton has to satisfy $C_\ell < 1$. The sum of lepton centralities

$$\Sigma C_\ell = C_{\ell 1} + C_{\ell 2} \tag{5.7}$$

enters the training of the multivariate classifier. The distinct VBF topology is also reflected in the sum of the four combinations of lepton-jet invariant mass,

$$\Sigma m_{\ell j} = m_{\ell 1,j1} + m_{\ell 1,j2} + m_{\ell 2,j1} + m_{\ell 2,j2} \tag{5.8}$$

and thus used as an input variable to the training of the multivariate classifier.

The background from top-quark pair production is reduced by vetoing any event containing a jet with $p_{\mathrm{T}} > 20\,\mathrm{GeV}$ tagged as containing a b-quark, $n_b = 0$. The magnitude of the summed vector $\boldsymbol{p}_{\mathrm{T}}$ of the final-state objects,

$$\boldsymbol{p}_{\mathrm{T}}^{\mathrm{sum}} = \boldsymbol{p}_{\mathrm{T}}^{\ell\ell} + \boldsymbol{p}_{\mathrm{T}}^{\mathrm{miss}} + \sum_{\mathrm{jets}} \boldsymbol{p}_{\mathrm{T}}^{j}, \tag{5.9}$$

is exploiting the topology of the dominant top quark pair production mechanism contributing to this category: gluon-gluon annihilation accompanied by QCD radiation. The $H \to WW^* \to \ell\nu\ell\nu$ decay topology enters the multivariate analysis through the variables $m_{\ell\ell}$, $\Delta\phi_{\ell\ell}$, and m_{T}. The distributions of the eight variables used by the multivariate classifier to distinguish the VBF Higgs signal from other processes can be found in Ref. [30].

The final discriminant, O_{BDT}, is shown in Fig. 5.6. It uses four bins, numbered from 0 to 3, with the boundaries $[-1, -0.48, 0.3, 0.78, 1]$. These have been optimized to maximize the expected significance to the VBF process, considering limited template statistics, and the statistics in BDT-binned control regions, which are used to estimate the rate of background processes, c.f. Sec. 5.3. The first bin is enriched in background processes and not used for measuring VBF production. For a summary of the expected and observed event yields after each selection requirement and after the classification in bins of the BDT discriminant, the reader is referred to Ref. [30].

The ggF-enriched $n_j \geq 2$ category

Events failing at least one of the VBF-specific selection criteria that define the VBF-enriched $n_j \geq 2$ category, are used to measure ggF production. The ggF-enriched $n_j \geq 2$ sample is obtained by inverting at least one of the requirements $C_{j3} > 1$, $C_\ell < 1$, or $O_{\mathrm{BDT}} > -0.48$. Due to the large $Z/\gamma^* \to ee$, $\mu\mu$ background, events with $ee/\mu\mu$ final states are not considered in this category.

The top-quark and DY backgrounds are reduced by requiring $n_b = 0$ and $m_{\tau\tau} < m_Z - 25\,\mathrm{GeV}$ respectively. Events in the region of $\Delta\eta_{jj} \leq 1.2$ and $|m_{jj} - 85| < 15\,\mathrm{GeV}$ originate from VH production with a hadronically decaying W or Z boson and thus are rejected. The contamination from top quark production is further reduced by exploiting the decay topology of the SM Higgs boson decay to W bosons, $m_{\ell\ell} < 55\,\mathrm{GeV}$ and $\Delta\phi_{\ell\ell} < 1.8$. For a summary of the expected and observed event yields after each selection requirement for $e\mu$ final states, the reader is referred to Ref. [30].

Summary and categorization

The inclusive signal selection efficiency for $H \to WW^* \to \ell\nu\ell\nu$ events in final states with $\ell = e, \mu$ is 10.2% for the 8 TeV sample, assuming a Higgs boson mass of 125.36 GeV. In the $n_j = 0$, $n_j = 1$ and ggF-enriched $n_j \geq 2$ $e\mu$ and $ee/\mu\mu$ categories the shape of the m_{T} distribution is used to discriminate between the signal and background processes, and eventually to simultaneously measure the Higgs boson production in the n_j and lepton-flavor categories.

Table 5.5: Summary of kinematic selections dividing the signal region (SR) categories into samples with different background composition. The fit variable is used in the statistical analysis to discriminate signal and background processes in a given category. All energy-related quantities are given in units of GeV.

SR category				Fit var.
n_j, flavor	$\otimes\, m_{\ell\ell}$	$\otimes\, p_{\mathrm{T}}^{\ell 2}$	$\otimes\, \ell_2$	
$n_j = 0$				
$e\mu$	$\otimes\,[10, 30, 55]$	$\otimes\,[10, 15, 20, \infty]$	$\otimes\,[e, \mu]$	m_{T}
$ee/\mu\mu$	$\otimes\,[12, 55]$	$\otimes\,[10, \infty]$		m_{T}
$n_j = 1$				
$e\mu$	$\otimes\,[10, 30, 55]$	$\otimes\,[10, 15, 20, \infty]$	$\otimes\,[e, \mu]$	m_{T}
$ee/\mu\mu$	$\otimes\,[12, 55]$	$\otimes\,[10, \infty]$		m_{T}
$n_j \geq 2$ ggF				
$e\mu$	$\otimes\,[10, 55]$	$\otimes\,[10, \infty]$		m_{T}
$n_j \geq 2$ VBF				
$e\mu$	$\otimes\,[10, 50]$	$\otimes\,[10, \infty]$		O_{BDT}
$ee/\mu\mu$	$\otimes\,[12, 50]$	$\otimes\,[10, \infty]$		O_{BDT}

Figure 5.5 shows the m_{T} distributions in these categories. In the VBF-enriched $n_j \geq 2$ category, a BDT multivariate output distribution used to separate Higgs production via VBF from other processes, c.f. Fig. 5.6. The corresponding distributions for the 7 TeV data sample can be found in Ref. [30].

The size of the selected $e\mu$ samples in the $n_j \leq 1$ categories allows exploiting distinct kinematic topologies of the background processes. The rate of the background due to misidentified lepton and the VV background varies across the $p_{\mathrm{T}}^{\ell 2}$ distribution. Figure 5.7 motivates analyzing the $e\mu$ samples in three regions in $p_{\mathrm{T}}^{\ell 2}$. Similarly, the signal-to-background ratio is correlated to the dilepton invariant mass, as illustrated in Fig. 5.8. Thus, the data samples are further split into two bins of $m_{\ell\ell}$. Misidentified electrons and muons contribute with different rates to the total background, c.f. Sec. 5.3.3, motivating a separation of the samples by the flavor of the lepton with the higher p_{T}. In total, twelve kinematic regions are exploited for the $e\mu$ samples with $n_j \leq 1$, each. Due to the limited sensitivity of the $ee/\mu\mu$ samples in the $n_j \leq 1$ categories, the analysis does not benefit from exploiting different ranges of $m_{\ell\ell}$ and $p_{\mathrm{T}}^{\ell 2}$. Table 5.5 summarizes the categorization.

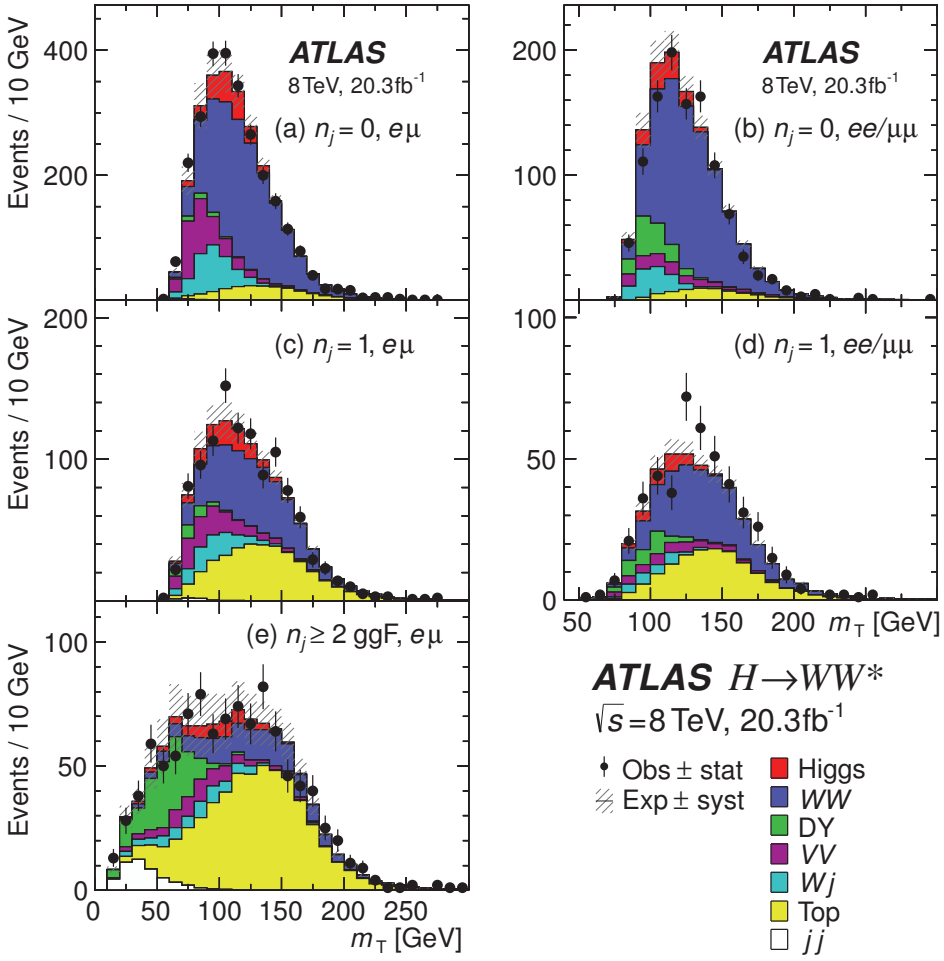

Figure 5.5: Distributions of m_{T} for events in the $n_j \leq 1$ and $n_j \geq 2$ ggF-enriched categories of the 8 TeV data set, satisfying all selection criteria up to m_{T}. See Fig. 5.2 for plotting details.

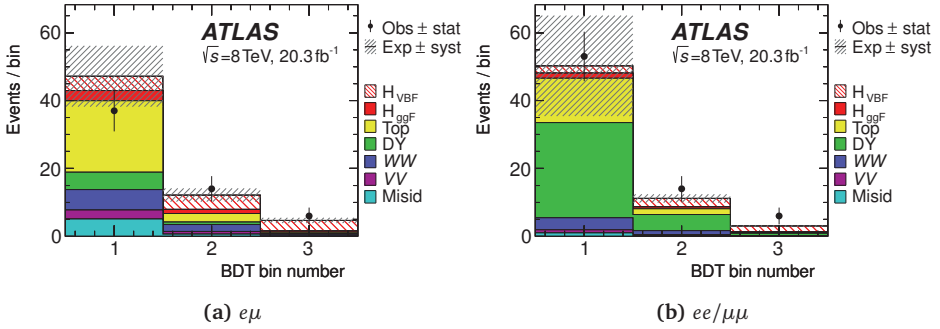

(a) $e\mu$ **(b)** $ee/\mu\mu$

Figure 5.6: BDT output distributions for events with (a) $e\mu$, and (b) $ee/\mu\mu$ final state in the VBF-enriched $n_j \geq 2$ category of the 8 TeV data set, satisfying all selection criteria summarized in Tab. 5.4. See Fig. 5.2 for plotting details.

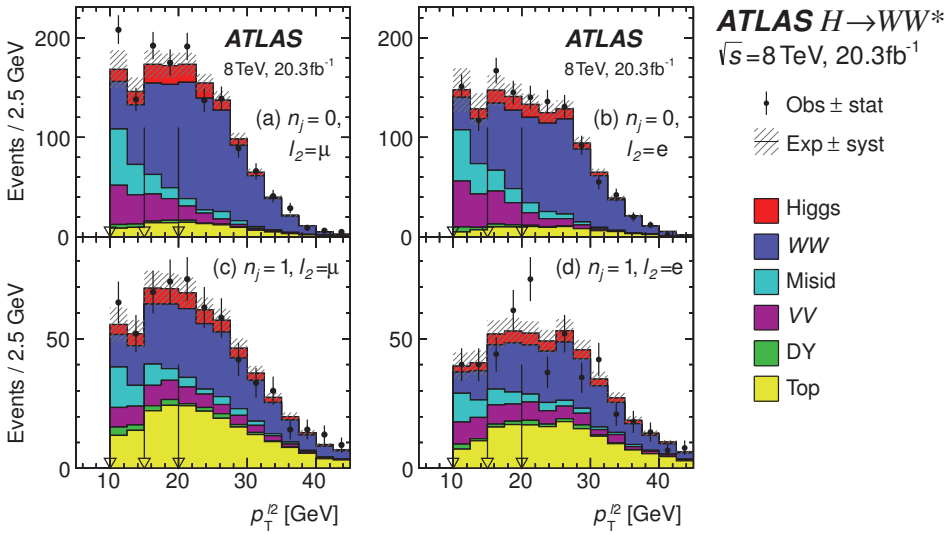

Figure 5.7: Distributions of $p_{\mathrm{T}}^{\ell 2}$ for events with $e\mu$ final state in the $n_j \leq 1$ categories of the 8 TeV data set, satisfying all selection criteria up to m_{T}. The distributions are shown for different flavor of the lower-p_{T} lepton ℓ_2. The arrows indicate boundaries, c.f. Tab. 5.5, dividing the sample into three regions in $p_{\mathrm{T}}^{\ell 2}$ with different background composition. See Fig. 5.2 for plotting details.

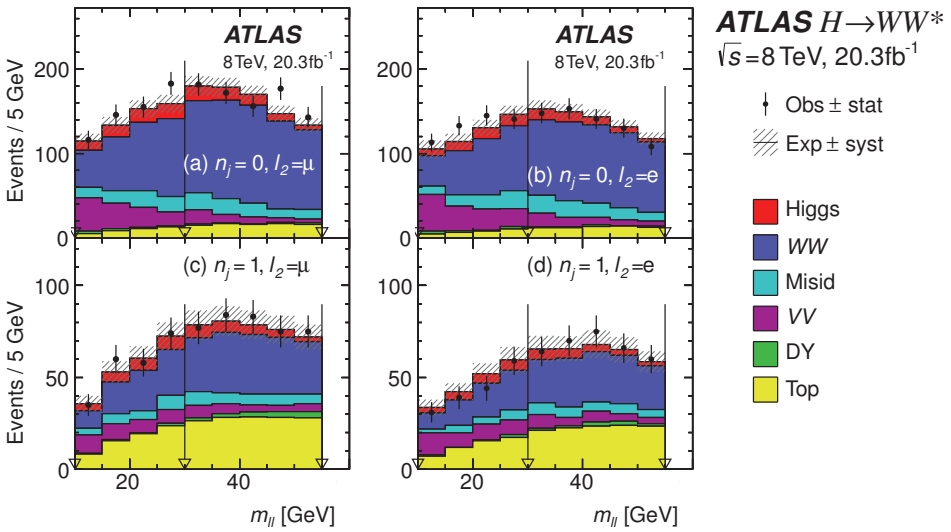

Figure 5.8: Distributions of $m_{\ell\ell}$ for events with $e\mu$ final state in the $n_j \leq 1$ categories of the 8 TeV data set, satisfying all selection criteria up to m_{T}. The distributions are shown for different flavor of the lower-p_{T} lepton ℓ_2. The arrows indicate boundaries, c.f. Tab. 5.5, dividing the sample into two regions in $m_{\ell\ell}$ with different background composition. See Fig. 5.2 for plotting details.

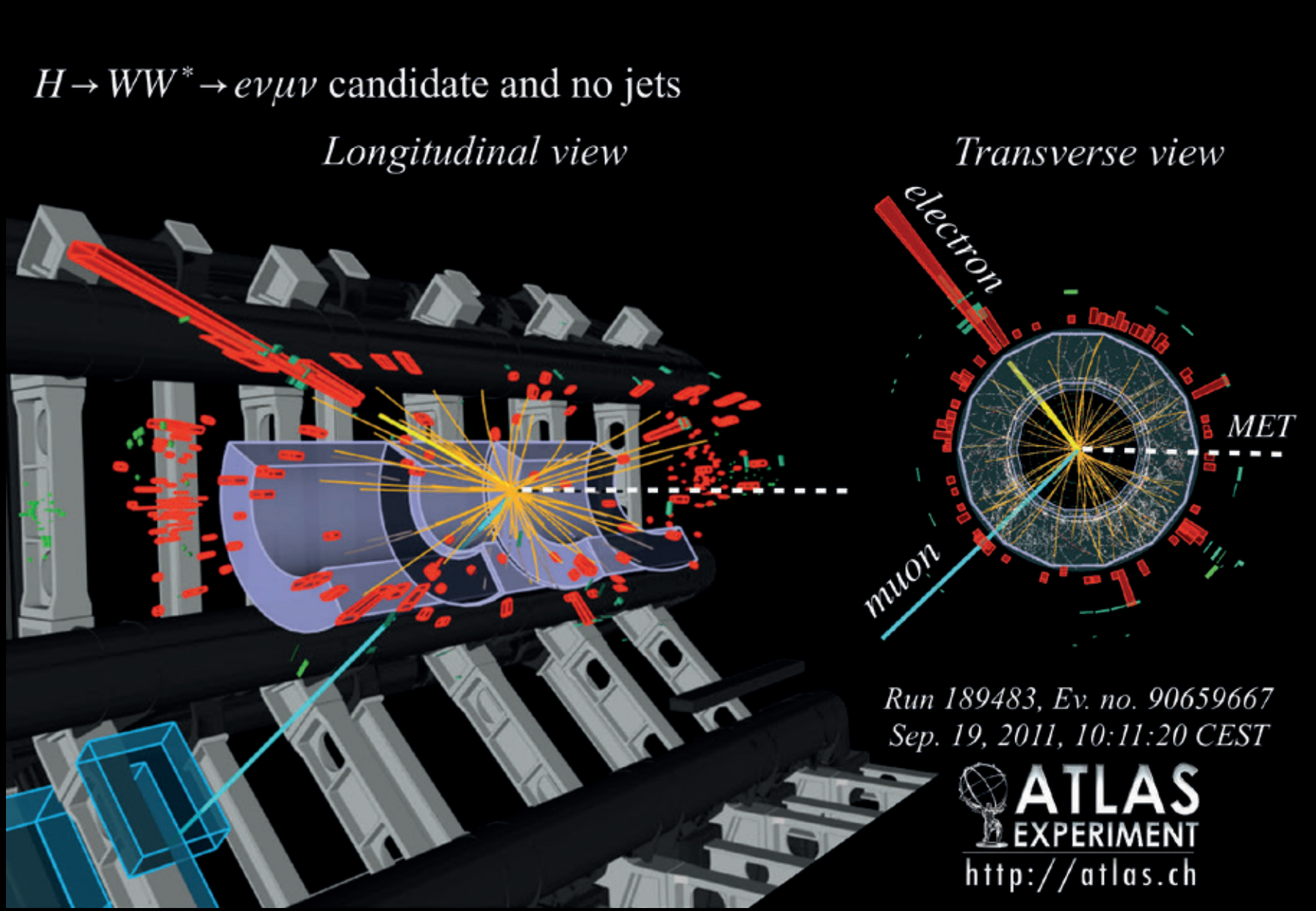
$H \to WW^* \to e\nu\mu\nu$ candidate and no jets
Longitudinal view
Transverse view
electron
MET
muon
Run 189483, Ev. no. 90659667
Sep. 19, 2011, 10:11:20 CEST
ATLAS
EXPERIMENT
http://atlas.ch

$H \to WW^* \to e\nu\mu\nu$ candidate and two jets with VBF topology

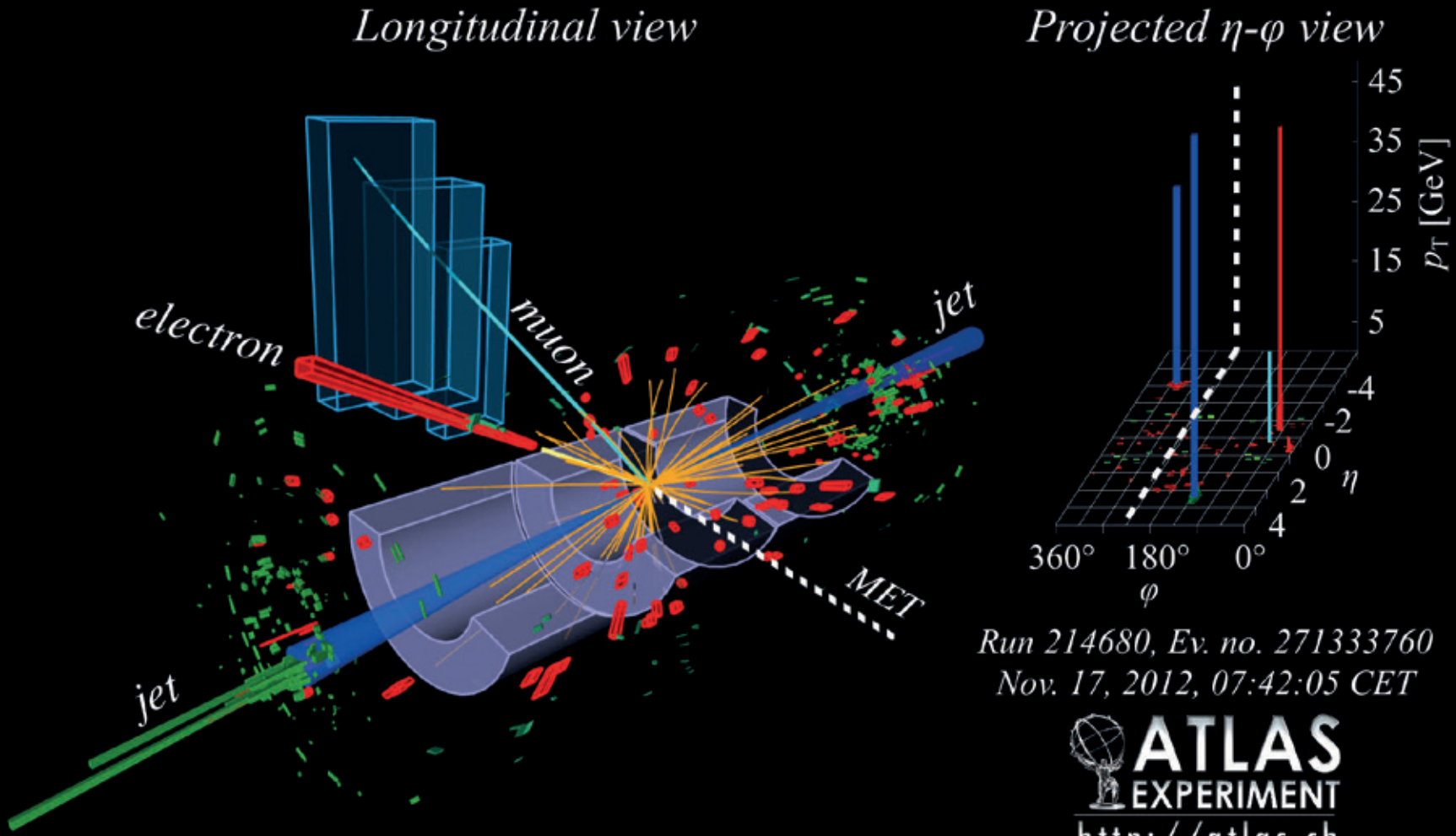

Run 214680, Ev. no. 271333760
Nov. 17, 2012, 07:42:05 CET

ATLAS EXPERIMENT
http://atlas.ch

5.3 Data-driven background estimates

The physics processes contributing to the background to the $H \to WW^* \to \ell\nu\ell\nu$ measurements have been summarized in the introduction to this chapter. An overview is provided in Tab. 5.1. The modeling of the processes is predicted by MC simulation, cf. Tab. 5.2, but it is refined by exploiting the recorded collision data. This section gives an overview of the techniques used to estimate the rates, templates, and associated uncertainties for the various background processes in the studied categories.

Background rates and templates are determined using data-driven techniques, or are derived directly from MC simulation for less dominant processes. A data-driven estimate of a background process is performed in a sample with sufficiently large statistics enriched in the given process. These events are required to pass a set of kinematic selection criteria, orthogonal to the ones used to define other samples entering the likelihood.

Under the assumption that the so constructed control region (CR) is pure in one background process, its rate in another category, e.g. the SR, can be written as

$$B_{\mathrm{SR}}^{\mathrm{est}} = B_{\mathrm{SR}} \cdot \underbrace{N_{\mathrm{CR}}/B_{\mathrm{CR}}}_{\text{Normalization } \beta} = N_{\mathrm{CR}} \cdot \underbrace{B_{\mathrm{SR}}/B_{\mathrm{CR}}}_{\text{Extrapolation } \alpha} . \tag{5.10}$$

N_{CR} denotes the observed event yield in the CR, while B_{CR} and B_{SR} are the predictions from MC simulation in the CR and SR, respectively. β is the data-to-MC normalization factor estimated in the CR, defined as the ratio of observed to expected rate. The yield N_{CR} is extrapolated to the SR using a transfer factor α, predicted by the MC simulation. Ignoring systematic uncertainties, the relevant terms of a simplified likelihood for a counting experiment with i_{SR} and j_{CR} profiled signal and control regions and k normalized background processes, read

$$L = \underbrace{\prod_{i=1}^{i_{\mathrm{SR}}} \left[\mathrm{Poisson}(N_i | \mu \cdot S_i + \sum_k \beta_k \cdot B_{ik}) \right]}_{\substack{\text{Poisson for SRs; signal strength } \mu\text{; predictions } S,\, B}} \times \underbrace{\prod_{j=1}^{j_{\mathrm{CR}}} \left[\mathrm{Poisson}(N_j | \sum_k \beta_k \cdot B_{jk}) \right]}_{\substack{\text{Poisson for profiled CRs; background normalizations } \beta_k}} \tag{5.11}$$

where μ denotes the signal strength, i.e a normalization factor assigned to the signal processes and defined as the ratio of the measured signal yield to the predicted SM value.

Uncertainties on the background estimate in the SR only enter due to the systematic uncertainty on the extrapolation, e.g. due to different event topologies in SR and CR, and due to the statistical uncertainty on the observed event yield in the CR. Thus, employing a data-driven technique for estimating the cross section of a background process greatly reduces the impact of experimental systematic uncertainties on the background rates due to detector response and event simulation models by absorbing them in the normalization factor, and hence leads to more accurate physics measurements.

The method can be extended to determine the extrapolation factor α and the background template from data. The observed and expected event yields in the control samples used to estimate the cross section of the background processes in the phase space selected by the $H \to WW^* \to \ell\nu\ell\nu$ analysis are summarized in Tab. 5.6. The normalization factors themselves are presented in Tab. 5.7.

5.3.1 Non-resonant WW diboson production

In the $n_j = 0$ and $n_j = 1$ bins, the cross section of the non-resonant WW background in the selected phase space is determined from data in a range of the invariant mass of the charged leptons enriched in $(q\bar{q}$ or $qg) \to WW$ and $gg \to WW$ events, c.f. Fig. 5.3. The templates for these processes are derived from MC simulation using the POWHEG+PYTHIA6 and GG2VV+HERWIG generators, respectively.

The selection criteria defining the control sample must ensure selecting events with similar kinematic properties as the ones passing the signal selection requirements. Furthermore, the control sample has to be sufficiently pure in WW events and must be statistically powerful to constrain the rate of the targeted processes. Thus, the CRs for the $n_j = 0$ and $n_j = 1$ categories are defined by selecting events that pass the signal selection requirement including the $p_{\mathrm{T}}^{\ell\ell} > 30\,\mathrm{GeV}$ and $m_{\mathrm{T}}^{\ell} > 50\,\mathrm{GeV}$ requirements, respectively. Several selection criteria are employed to suppress the contamination from other physics processes in these samples. The $Z/\gamma^* \to \tau\tau$ background in the $n_j = 0$ and $n_j = 1$ $e\mu$ categories is controlled by rejecting events with $\Delta\phi_{\ell\ell} > 2.6$ and $|m_{\tau\tau} - m_Z| < 25\,\mathrm{GeV}$, respectively. The contamination of the $ee/\mu\mu$ categories arising from $Z/\gamma^* \to ee$, $\mu\mu$ production is substantial, and therefore these events are dropped. Similarly, the W+jets background below $p_{\mathrm{T}}^{\ell 2} = 15\,\mathrm{GeV}$ is sizable such that these events have to be rejected. Finally, events have to enter a window of $55 < m_{\ell\ell} < 110\,\mathrm{GeV}$ and $m_{\ell\ell} > 80\,\mathrm{GeV}$, enriched in non-resonant WW diboson production, for the $n_j = 0$ and $n_j = 1$ categories, respectively.

The ranges in $m_{\ell\ell}$ are selected orthogonal to the SR definitions and have been optimized simultaneously to minimize the statistical uncertainty on the WW normalization and the systematic uncertainties on the extrapolation to the low $m_{\ell\ell}$ regions. These uncertainties arise predominantly from limitations in the MC modeling and are summarized in Tab. 5.8. In particular, the uncertainties reflect missing higher-order perturbative QCD and EW corrections in the MC simulation and differences in the matching schemes of the hard-scatter process to the PS in selected NLO generators. Additional uncertainties are due to the choice of the nominal PDF set and differences in the PS model, i.e. differences between string fragmentation and cluster fragmentation models. All uncertainties directly affect the rate of the WW background in the SRs, but also induce an uncertainty on the distribution of the reconstructed transverse mass.

Table 5.6: Summary of the event yields and their composition in the various control samples used in the analysis of the 8 TeV data set. The entries corresponding to the targeted processes are given in a bold font and define the purity of the control sample. The event yields are normalized using the data-driven techniques described in the text. The quoted uncertainties are due to the size of the selected control samples and do not include experimental and theoretical uncertainties on the modeling of the corresponding physics processes.

Control regions	Summary			Composition of N_{bkg}						Purity
	N_{obs}	N_{bkg}	N_{sig}	N_{WW}	N_{top}	N_{misid}	N_{VV}	N_{DY}		$N_{\text{bold}}/N_{\text{bkg}}$ (%)
								$N_{ee/\mu\mu}$	$N_{\tau\tau}$	
$n_j = 0$										
CR for WW	2713	2680 ± 9	28	**1950**	335	184	97	8.7	106	73
CR for top quarks	76013	75730 ± 50	618	8120	**56210**	2730	1330	138	7200	74
CR for VV	533	531 ± 8	2.2	2.5	1.1	180	**327**	19	2.7	62
CR for $Z/\gamma^* \to \tau\tau$	4557	4530 ± 30	23	117	16.5	239	33	28	**4100**	91
$n_j = 1$										
CR for WW	2647	2640 ± 12	4.3	**1148**	1114	165	127	17	81	43
CR for top quarks	6722	6680 ± 12	17	244	**6070**	102	50	6	204	91
CR for VV	194	192 ± 4	1.9	1	3.1	65	**117**	4.7	0.8	61
CR for $Z/\gamma^* \to \tau\tau$	1540	1520 ± 14	18	100	75	84	27	7	**1220**	80
$n_j \geq 2$ ggF										
CR for top quarks	2664	2660 ± 10	4.9	561	**1821**	129	101	10	44	68
CR for $Z/\gamma^* \to \tau\tau$	266	263 ± 6	2.6	13	34	18	4.1	0.1	**194**	74
$n_j \geq 2$ VBF										
CR for top quarks, bin 1	143	142 ± 2	2.1	1.9	**130**	2.1	0.8	6.3	1.1	92
CR for top quarks, bin 2–3	14	14.3 ± 0.5	1.8	0.6	**11.6**	0.2	0.2	0.9	0.2	81
CR for $Z/\gamma^* \to \tau\tau$	24	20.7 ± 0.9	2.4	0.9	1.2	0.6	0.2	0.8	**17**	82

Table 5.7: Summary of the data-to-MC normalization factors β estimated in the CRs for the 8 TeV sample. The quoted uncertainties are due to the size of the selected control samples and do not include experimental and theoretical uncertainties on the modeling of the corresponding physics processes.

Category	WW	Top quarks	VV	$Z/\gamma^* \to \tau\tau$
$n_j = 0$	1.22 ± 0.03	1.08 ± 0.02	0.92 ± 0.07	1.00 ± 0.02
$n_j = 1$	1.05 ± 0.05	1.06 ± 0.03	0.96 ± 0.12	1.05 ± 0.04
$n_j \geq 2$, ggF	-	1.05 ± 0.03	-	1.00 ± 0.09
$n_j \geq 2$, VBF bin 1	-	1.58 ± 0.15	-	0.90 ± 0.30
$n_j \geq 2$, VBF bins 2–3	-	0.95 ± 0.31	-	

The expected and observed event yields in the control samples, i.e. after all selection criteria described above, are summarized in Tab. 5.6. Figure 5.9 shows the m_{T} distribution of the selected events in the WW CRs. The estimated normalization factors for non-resonant WW production are summarized in Tab. 5.7. The normalization estimated from the $n_j = 0$ CR is consistent with the prediction obtained from a validation region (VR) with $m_{\ell\ell} > 110$ GeV at 1.1 standard deviations, considering all systematic uncertainties.

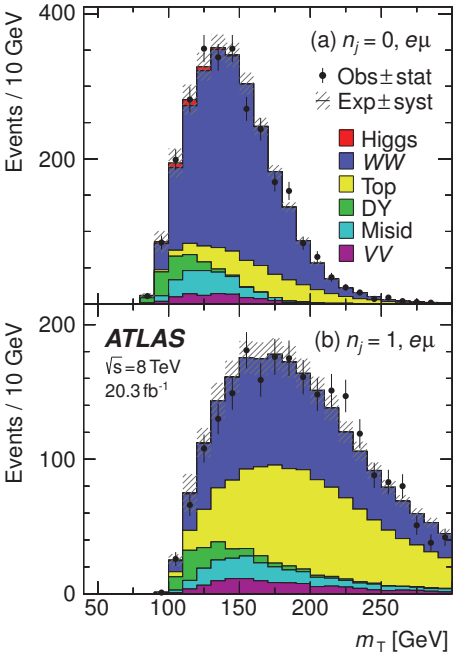

Figure 5.9: Distribution of m_{T} for events entering the (a) $n_j = 0$, and (b) $n_j = 1$, 8 TeV WW CR. See Fig. 5.2 for plotting details.

The WW background created in double parton interactions (DPIs) is modest. It is estimated using PYTHIA8 MC simulation and normalized to the predicted cross section, assigning an uncertainty of 60% [30, 450, 451]. Contributions from two $pp \to W$ collisions in the same bunch crossing to the total WW background are negligible.

In the ggF-enriched and VBF-enriched $n_j \geq 2$ categories, the non-resonant WW background is estimated using simulated events from SHERPA. The analysis considers several systematic uncertainties on the yields and distributions, with a typical size of approximately 10% to 25%: the interference between diagrams with jets originating from QCD or EW vertices; missing higher order terms in

Table 5.8: Systematic uncertainties (in %) on the WW extrapolation factor in the $n_j \leq 1$ categories from missing higher-order perturbative QCD and EW corrections in the MC simulation (assessed by varying the renormalization and factorization scales), the choice of the CT10 as the nominal PDF set (evaluated by comparing to the MSTW2008 [114] and the NNPDF2.3 [119] PDF sets, following the PDF4LHC recommendations), the matching between hard-scatter process and UE, hadronization, and PS models (estimated from a comparison of POWHEG+HERWIG and aMC@NLO+HERWIG), and the modeling of those (evaluated by comparing POWHEG+PYTHIA6 and POWHEG+HERWIG). Total is the sum in quadrature of these uncertainties. The sign indicates the sign of the correlation coefficient with respect to the SR categories in the same column. All energy-related quantities are given in units of GeV.

SR category	$n_j = 0$						$= 1$
	Scale	PDF	Gen	EW	UE/PS	Tot	Tot
SR $e\mu$, $10 < m_{\ell\ell} < 30$							
$p_{\mathrm{T}}^{\ell 2} > 20$	0.7	0.6	3.1	−0.3	−1.9	3.8	7.1
$15 < p_{\mathrm{T}}^{\ell 2} \leq 20$	1.2	0.8	0.9	0.7	1.7	2.6	3.9
$10 < p_{\mathrm{T}}^{\ell 2} \leq 15$	0.7	1.0	0.4	1.2	2.2	2.8	5.4
SR $e\mu$, $30 < m_{\ell\ell} < 55$							
$p_{\mathrm{T}}^{\ell 2} > 20$	0.8	0.7	3.9	−0.4	−2.4	4.8	7.1
$15 < p_{\mathrm{T}}^{\ell 2} \leq 20$	0.8	0.7	1.0	0.5	1.0	2.0	4.5
$10 < p_{\mathrm{T}}^{\ell 2} \leq 15$	0.7	0.8	0.5	0.8	1.5	2.1	4.5
SR $ee/\mu\mu$, $12 < m_{\ell\ell} < 55$							
$p_{\mathrm{T}}^{\ell 2} > 10$	0.8	1.1	2.4	0.1	−1.2	2.9	5.1

the calculation of the production process; the choice of matrix element and PS generators. The MC prediction is validated in a category enriched in $WW + 2$-jet events, showing that predicted and observed rates are well compatible within statistical uncertainties [30].

5.3.2 Top quark processes

The cross section for the production of top quarks in pairs or in association with a W boson, or quarks, in the selected phase space is estimated from data in dedicated CRs for all jet multiplicities, assuming that the rates of the various top quark processes scale in a fully correlated manner. The predicted and observed event yields for these control samples, i.e. after all selection criteria, are given in Tab. 5.6. The estimated normalization factors are presented in Tab. 5.7. The nominal templates used in the likelihood are determined from MC simulation using the POWHEG+PYTHIA6 and ACERMC+PYTHIA6 generators.

In the $n_j = 0$ category, the CR that is used is constructed from $e\mu$ events satisfying the preselection MET requirement, but dropping the jet-veto. Thus, a negligible subset of the control sample overlaps with the category enriched in signal events. The selection of only $e\mu$ events is motivated by the large contribution of the $Z/\gamma^* \to ee, \mu\mu$ background to $ee/\mu\mu$ final states. To reduce the contamination from the $Z/\gamma^* \to \tau\tau$ background in the $e\mu$ sample, and thus to increase its purity, selected events have to satisfy $\Delta\phi_{\ell\ell} < 2.8$.

The extrapolation from this inclusive sample to a sample with jet-veto is corrected for the probability for an event to contain one and only one b-tagged jet but no additional reconstructed jets, considering that $t\bar{t}$ production results in two final state jets at the Born-level. An additional correction exploits differences between collision data and the simulation. The estimate of the top-quark background in the $n_j = 0$ category is then given by

$$B^{\text{est}}_{\text{top},0j} = N_{\text{CR}} \cdot \underbrace{B_{\text{SR}}/B_{\text{CR}}}_{\alpha^{0j}_{\text{MC}}} \cdot \Big(\underbrace{\alpha^{1b}_{\text{data}}/\alpha^{1b}_{\text{MC}}}_{\gamma_{1b}}\Big)^2. \tag{5.12}$$

Kinematic differences between the b-tagged and the inclusive sample, e.g. due to missing higher-order QCD corrections, the choice of the nominal PDFs set, or the UE and PS models, are considered in the estimate. The contamination of the CR from single top quark processes as well as their interference with the top-quark pair production affects the estimate and induced uncertainties on the estimated rates. The efficiency of the remaining selection requirements and their impact on the measured top quark production cross section is evaluated in MC simulation. The full set of systematic uncertainties on the estimate is summarized in Tab. 5.9a.

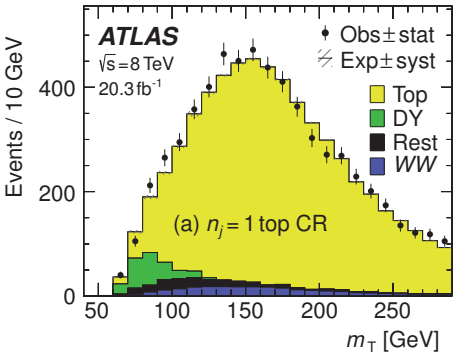

Figure 5.10: Distribution of m_T for events entering the $n_j = 1$ 8 TeV CR for top quark processes. See Fig. 5.2 for plotting details.

In the $n_j = 1$ category a statistically powerful CR for measuring the top quark production is constructed from events satisfying the preselection criteria, except that the reconstructed jet in the events is required to be b-tagged. By selecting only events with $e\mu$ final states satisfying $m_T^{\ell} > 50\,\text{GeV}$, the Z/γ^* and multijet contamination is reduced significantly. Figure 5.10 shows the m_T distribution for events entering this CR.

The b-tagging efficiency is measured in situ using a control sample selected similar to the SR, but enriched in di-leptonic top quark events. This is achieved by selecting events

comprising exactly two reconstructed jets, at least one of which is tagged to contain a b-quark.

The probability to observe N_{2j}^{1b} (N_{2j}^{2b}) events with one (two) b-jets given the corresponding estimates B_{top}^{1b} (B_{top}^{2b}) from MC simulation, is given by Poisson terms,

$$\begin{aligned} L = &\text{Poisson}\left(N_{2j}^{2b} \middle| \beta_{\text{top}}^{2j} \cdot \beta_{b\text{-tag}}^{2} \cdot B_{\text{top}}^{2b} + B_{\text{other}}\right) \\ &\times \text{Poisson}\left(N_{2j}^{1b} \middle| \beta_{\text{top}}^{2j} \cdot \beta_{b\text{-tag}} \cdot B_{\text{top}}^{1b} + \beta_{\text{top}}^{2j} \cdot \beta_{b\text{-tag}} \cdot (1-\beta_{b\text{-tag}}) \cdot B_{\text{top}}^{2b} + B_{\text{other}}\right), \end{aligned} \tag{5.13}$$

where β_{top}^{2j} normalizes the top-quark cross section in the $n_j = 2$ control sample and $\beta_{b\text{-tag}} = \epsilon_{2j}^{\text{data}}/\epsilon_{2j}$ is the normalization of the probability of tagging a jet as containing a b-quark in $n_j = 2$ top-quark events, i.e. it is the normalization of the b-tagging efficiency.

The rate of the top-quark background in the $n_j = 1$ categories is given by

$$B_{\text{top},1j}^{\text{est}} = N_{\text{CR}} \cdot \underbrace{\left(\frac{1-\epsilon_{1j}^{\text{est}}}{\epsilon_{1j}^{\text{est}}}\right)}_{\alpha_{\text{data}}^{1j}} \quad \text{with} \quad \epsilon_{1j}^{\text{est}} = \gamma_{1j} \cdot \epsilon_{2j}^{\text{data}} \quad \text{and} \quad \gamma_{1j} = \epsilon_{1j}/\epsilon_{2j}, \tag{5.14}$$

where $\epsilon_{1j}^{\text{est}}$ is the estimated b-tagging efficiency for the $n_j = 1$ sample, corrected by γ_{1j} for kinematic differences between the $n_j = 2$ and $n_j = 1$ samples, derived using MC simulation. In practice, the relevant terms of the likelihood in the $n_j = 1$ categories are expressed as

$$\begin{aligned} L = &\text{Poisson}\left(N_{1j}^{0b} \middle| \mu \cdot S + \beta_{\text{top}}^{1j} \cdot B_{\text{top}}^{0b} + \beta_{\text{top}}^{1j} \cdot (1-\beta_{b\text{-tag}}) \cdot B_{\text{top}}^{1b} + B_{\text{other}}\right) \\ &\times \text{Poisson}\left(N_{1j}^{1b} \middle| \beta_{\text{top}}^{1j} \cdot \beta_{b\text{-tag}} \cdot B_{\text{top}}^{1b} + B_{\text{other}}\right) \end{aligned} \tag{5.15}$$

Systematic uncertainties arise from similar effects as discussed in the context of the top background estimate in the $n_j = 0$ category. They are summarized in Tab. 5.9b.

The majority of top-quark events entering the VBF-enriched $n_j \geq 2$ category comprise one light-quark jet from ISR in addition to a non-tagged b-quark jet. The kinematics of these events changes as function of the BDT discriminant, since the classifier is trained on variables exploiting the jet kinematics, e.g. m_{jj}. As a consequence, the simulated cross section for the top quark processes in this category is corrected bin-by-bin for differences between the recorded collision data and the prediction. To this end, a CR that mimics this specific event topology is designed. For the control sample both $e\mu$ and $ee/\mu\mu$ events are selected and the two bins with the highest O_{BDT} score are merged in order to reduce the statistical uncertainty on the background estimate. All events are required to contain one jet that was tagged as including a heavy flavor. The theoretical uncertainties on the extrapolation of the estimated rates from the control sample to different O_{BDT} bins in the SR range from 4% to 21%. They are dominated by differences in the modeling of the top quark background,

Table 5.9: Systematic uncertainties (in %) on the top quark extrapolation factor in the (a) $n_j = 0$, and (b) $n_j = 1$ categories. All energy-related quantities are given in units of GeV. See Tab. 5.8 for nomenclature.

Uncertainty source	$\alpha_{\mathrm{MC}}^{0j}/\left(\alpha_{\mathrm{MC}}^{1b}\right)^2$	ϵ_{rest}	Total
Experimental	4.4	1.2	4.6
Non-top-quark subtraction	2.7	-	2.7
Theoretical	3.9	4.5	4.9
Statistical	2.2	0.7	2.3
Total	6.8	4.7	7.6

(a) $n_j = 0$

Regions		Scale	PDF	Gen	UE/PS	Tot
Signal region						
$e\mu$	$(10 < m_{\ell\ell} < 55)$	−1.1	−0.12	−2.4	2.4	3.6
$ee/\mu\mu$	$(12 < m_{\ell\ell} < 55)$	−1.0	−0.12	−2.0	3.0	3.7
WW control region						
$e\mu$	$(m_{\ell\ell} > 80)$	0.6	0.08	2.0	1.8	2.8

(b) $n_j = 1$

evaluated by comparing the predictions from POWHEG+HERWIG, ALPGEN+HERWIG and MC@NLO [452]+HERWIG.

The top-quark background in the ggF-enriched $n_j \geq 2$ category is estimated in a high $m_{\ell\ell}$ control sample ($m_{\ell\ell} > 80\,\mathrm{GeV}$) of $e\mu$ events, vetoing any number of b-tagged jets. Uncertainties on the extrapolation from this phase space to the SR are due to the modeling of the top-quark background (3.2%), the UE and PS model (1.2%), missing higher order contributions (1%), and the PDF sets (0.3%).

5.3.3 Misidentified leptons

Both the rate and the template of the background from W+jets production is determined from data in a CR. Events entering this sample are required to meet all selection criteria except that one of the lepton candidates should be anti-identified i.e. it fails the identification and isolation criteria for the SR, described in Sec. 5.2.1, but satisfies less restrictive requirements.

The estimate is extrapolated to the SR using a transfer factor, which is measured as a function of the p_{T} and η of the anti-identified lepton in a data sample enriched in jets produced in

association with a Z boson. The estimate takes into account the contamination from other production processes in this category, e.g. $WZ \to \ell\nu\ell\ell$, Z/γ^*, or $Z\gamma$. The transfer factor is corrected for differences in the composition of the jets produced in association with W and Z bosons based on the comparison of ALPGEN+PYTHIA6, ALPGEN+HERWIG and POWHEG+PYTHIA8. This correction is derived individually for anti-identified electrons and muons, as well as for opposite-charge and same-charge candidates. The systematic uncertainty on the former correction is uncorrelated between the anti-identified lepton flavors. For the latter correction, the correlation between the assigned uncertainties reflects the composition of the jets producing objects misidentified as leptons. The total systematic uncertaintiy on the corrected extrapolation factor ranges from 29% to 63% (25% to 53%) for anti-identified electrons (muons) as function of the candidate's E_{T} (p_{T}).

The background due to multijet production is estimated in a similar manner. The rate and template of this background process are determined from a control sample of events with two anti-identified lepton candidates, indicated by a topology of two misidentified leptons in the event. A extrapolation factor is measured in a multijet sample and applied for every object misidentified as lepton. The extrapolation is corrected event-by-event for the presence of an additional identified or anti-identified lepton candidate.

5.3.4 Other diboson processes

The templates for the diboson backgrounds other than WW, i.e. $W\gamma$, $W\gamma^*$, WZ, and ZZ production, collectively referred to as VV, are determined from MC simulation, c.f. Tab. 5.2, and validated in dedicated control samples.

A sample of $e\mu$ events with non-prompt electrons from photon conversions mimics the topology of the $W\gamma$ background entering the $n_j \leq 1$ SRs and serves as VR [30]. The rejection of non-prompt electrons from photon conversions has been validated in a sample enriched in $Z \to \mu\mu\gamma$ events, suggesting the inclusion of a p_{T}-dependent systematic uncertainty ranging from 25% for $10 < p_{\mathrm{T}} < 15\,\mathrm{GeV}$ to 5% for $p_{\mathrm{T}} > 20\,\mathrm{GeV}$. The modeling of the $W\gamma^*$ background is validated in a sample enriched in $W\gamma^* \to e\nu\mu\mu$ events [30].

In the $n_j \leq 1$ categories, the rate of the VV background is obtained from a sample of same-charge events, i.e. events where the second lepton produced in the $W\gamma$, $W\gamma^*$, and WZ processes has the same charge as the lepton from the W boson decay. Non-charge-symmetric contributions from ZZ production are negligible both in the control and signal samples. The selected events are required to pass the signal selection criteria described in Sec. 5.2.3, except the lepton charge requirement. The predicted and observed event yields in the same-charge CRs are summarized in Tab. 5.6. Figure 5.11 shows the m_{T} distributions of the selected same-charge events in the $n_j = 0$ and $n_j = 1$ categories. Due to the limited sample size, the normalization for the targeted diboson processes is treated correlated, c.f. Tab. 5.7.

Since the probability for observing same-charge and opposite-charge $W\gamma$, $W\gamma^*$, and WZ is equal, no uncertainty due to the extrapolation of the estimate from same-charge to opposite-

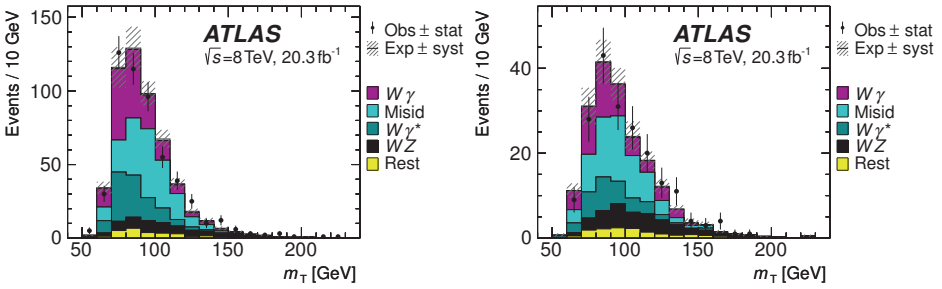

Figure 5.11: Distribution of m_{T} for events entering the (a) $n_j = 0$, and (b) $n_j = 1$, 8 TeV same-charge CR. See Fig. 5.2 for plotting details.

charge events. However, the total cross section of the $W\gamma$ and $W\gamma^*$ processes is known only with an accuracy of 6% and 7%, respectively. Uncertainties of 9% (7%), 53% (30%), and 100% (26%) arise due to jet binning or veto for the $W\gamma$ ($W\gamma^*$) process in the $n_j = 0$, $n_j = 1$, and $n_j \geq 2$ categories.

5.3.5 The Drell-Yan process

Even after applying the selection requirements described in Sec. 5.2.3, the contamination of the SRs by the residual Z/γ^* background is significant in all jet bins. The DY process enters the $e\mu$ signal-enriched categories due to neutrinos produced in $Z/\gamma^* \to \tau\tau$ decays, i.e. due to real MET. The templates for this background process are derived from events simulated by the ALPGEN+HERWIG generator. The simulation is corrected in the data for the mismodeling of the PS of soft jets balancing $p_{\mathrm{T}}^{\ell\ell}$ in the $n_j = 0$ category.

The rate of the $Z/\gamma^* \to \tau\tau$ background in the ggF-enriched $e\mu$ categories is corrected in control samples populated by $e\mu$ events passing the selection criteria $m_{\ell\ell} < 80\,\mathrm{GeV}$ and $\Delta\phi_{\ell\ell} > 2.8$, $m_{\ell\ell} < 80\,\mathrm{GeV}$ and $m_{\tau\tau} > (m_Z - 25\,\mathrm{GeV})$, $m_{\ell\ell} < 70\,\mathrm{GeV}$ and $\Delta\phi_{\ell\ell} > 2.8$ in the $n_j = 0$, $n_j = 1$, $n_j \geq 2$ categories, respectively. Figure 5.12 shows the m_{T} distributions of the selected events in the CRs in the $n_j = 0$ and $n_j = 1$ jet bins. The control sample designed for estimating the $Z/\gamma^* \to \tau\tau$ rate in the $n_j \geq 2$ VBF-enriched category includes $ee/\mu\mu$ events and merges the O_{BDT} bins to increase the statistical precision of the estimate. To enter this sample, the events have to satisfy requirements on the dilepton invariant mass, $m_{\ell\ell} < 80\,\mathrm{GeV}$ ($e\mu$) or $m_{\ell\ell} < 75\,\mathrm{GeV}$ ($ee/\mu\mu$), and on the reconstructed mass of τ-lepton pair, $|\, m_{\tau\tau} - m_Z \,| < 25\,\mathrm{GeV}$.

Uncertainties on the extrapolation to the SRs and other control samples are parametrized in terms of several sources, c.f. Tab. 5.10. Missing higher order terms in the calculation of the $Z/\gamma^* \to \tau\tau$ cross section have been evaluated by varying the renormalization and factorization scales of the MC generator. The uncertainty due to the PS model is evaluated by comparing the default matrix element generator interfaced with different showering and fragmentation

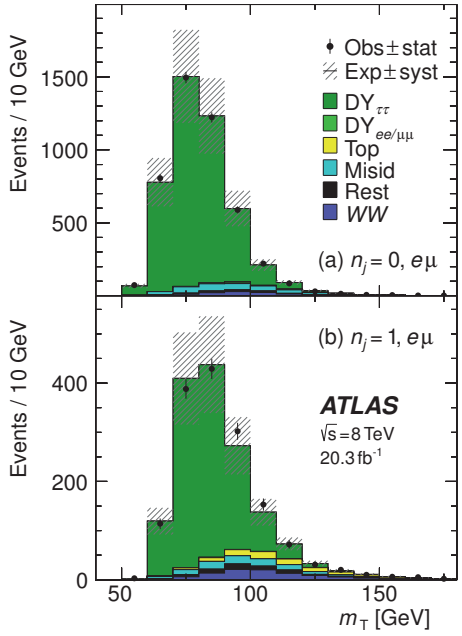

Figure 5.12: Distribution of m_T for events entering the (a) $n_j = 0$, and (b) $n_j = 1$, 8 TeV $Z/\gamma^* \to \tau\tau$ CR. See Fig. 5.2 for plotting details.

Table 5.10: Systematic uncertainties (in %) on the $Z/\gamma^* \to \tau\tau$ extrapolation factor for the categories in signal and WW events. For the $n_j = 0$ category, the uncertainty due to p_T^{Z/γ^*} reweighting is shown, too. See Tab. 5.8 for nomenclature.

Regions	Scale	PDF	Gen	p_T^{Z/γ^*}
Signal regions				
$n_j = 0$	−1.6	1.4	5.7	19
$n_j = 1$	4.7	1.8	−2.0	-
$n_j \geq 2$ ggF	−10.3	1.1	10.4	-
WW control regions				
$n_j = 0$	−5.5	1.0	−8.0	16
$n_j = 1$	−7.2	2.1	3.2	-

algorithms, i.e. by comparing ALPGEN+HERWIG and ALPGEN+PYTHIA. In addition, the effect of using different PDF sets is considered in the extrapolation.

For $ee/\mu\mu$ final states, the $Z/\gamma^* \to \tau\tau$ background is negligible compared to the $Z/\gamma^* \to ee, \mu\mu$ rate, and thus is determined entirely from MC simulation. The rate of the latter is estimated from data for the phase-space selected by the $n_j \leq 1$ requirements. To this end, the analysis exploits the selection efficiencies $\varepsilon = N_{\text{pass}}/(N_{\text{pass}} + N_{\text{fail}})$ of the f_{recoil} requirement for DY and non-DY events:

$$\begin{pmatrix} N_{\text{pass}} \\ N_{\text{pass}} + N_{\text{fail}} \end{pmatrix} = \begin{pmatrix} 1 & 1 \\ 1/\varepsilon_{\text{DY}} & 1/\varepsilon_{\text{non-DY}} \end{pmatrix} \cdot \begin{pmatrix} B_{\text{DY}} \\ B_{\text{non-DY}} \end{pmatrix} \tag{5.16}$$

$$\Leftrightarrow \qquad B_{\text{DY}} = \varepsilon_{\text{DY}} \cdot \frac{N_{\text{pass}} - \varepsilon_{\text{non-DY}} \cdot (N_{\text{pass}} + N_{\text{fail}})}{\varepsilon_{\text{DY}} - \varepsilon_{\text{non-DY}}}. \tag{5.17}$$

The efficiency for DY events satisfying the f_{recoil} requirement, ε_{DY}, is measured in a $ee/\mu\mu$ control sample in the Z mass window, $|m_{\ell\ell} - m_Z| < 15$ GeV. The probability of observing

N events passing or failing the f_{recoil} selection given the predicted rates of DY and non-DY events, B_{DY} and $B_{\text{non-DY}}$, is given by the Poisson terms

$$\begin{aligned} L = &\text{Poisson}\left(N^{ZCR}_{\text{pass}} \middle| \beta'_{\text{DY}} \cdot \varepsilon_{\text{DY}} \cdot B^{ZCR}_{\text{DY}} + \varepsilon'_{\text{non-DY}} \cdot B^{ZCR}_{\text{non-DY}}\right) \\ &\times \text{Poisson}\left(N^{ZCR}_{\text{fail}} \middle| \beta'_{\text{DY}} \cdot \left(1-\varepsilon_{\text{DY}}\right) \cdot B^{ZCR}_{\text{DY}} + \left(1-\varepsilon'_{\text{non-DY}}\right) \cdot B^{ZCR}_{\text{non-DY}}\right), \end{aligned} \tag{5.18}$$

where the cross section of the DY process is normalized by β'_{DY}. The efficiency for selecting non-DY events contaminating the Z mass peak, $\varepsilon'_{\text{non-DY}}$, is measured in the same $m_{\ell\ell}$ window, but using $e\mu$ events, depleted in $Z/\gamma^* \to ee$, $\mu\mu$ decays,

$$\begin{aligned} L = &\text{Poisson}\left(N^{ZCR,e\mu}_{\text{pass}} \middle| \varepsilon'_{\text{non-DY}} \cdot B^{ZCR,e\mu}_{\text{non-DY}}\right) \\ &\times \text{Poisson}\left(N^{ZCR,e\mu}_{\text{fail}} \middle| (1-\varepsilon'_{\text{non-DY}}) \cdot B^{ZCR,e\mu}_{\text{non-DY}}\right). \end{aligned} \tag{5.19}$$

The selection efficiency for DY events, normalized by β_{DY}, is extrapolated to the SR,

$$\begin{aligned} L = &\text{Poisson}\left(N^{SR}_{\text{pass}} \middle| \beta_{\text{DY}} \cdot \varepsilon_{\text{DY}} \cdot B^{SR}_{\text{DY}} + \varepsilon_{\text{non-DY}} \cdot B^{SR}_{\text{non-DY}}\right) \\ &\times \text{Poisson}\left(N^{SR}_{\text{fail}} \middle| \beta_{\text{DY}} \cdot \left(1-\varepsilon_{\text{DY}}\right) \cdot B^{SR}_{\text{DY}} + \left(1-\varepsilon_{\text{non-DY}}\right) \cdot B^{SR}_{\text{non-DY}}\right). \end{aligned} \tag{5.20}$$

Similar to the Z mass range, the selection efficiency for non-DY events is measured in a control sample from $e\mu$ events, passing the $ee/\mu\mu$ selection requirements,

$$\begin{aligned} L = &\text{Poisson}\left(N^{SR,e\mu}_{\text{pass}} \middle| \varepsilon_{\text{non-DY}} \cdot B^{SR,e\mu}_{\text{non-DY}}\right) \\ &\times \text{Poisson}\left(N^{SR,e\mu}_{\text{fail}} \middle| \left(1-\varepsilon_{\text{non-DY}}\right) \cdot B^{SR,e\mu}_{\text{non-DY}}\right). \end{aligned} \tag{5.21}$$

The selection efficiency for Higgs decays is generally lower than for the non-DY background, and thus has to be corrected for this difference,

$$\varepsilon^{\text{signal}}_{\text{non-DY}}(\varepsilon_{\text{non-DY}}) = \underbrace{\left(1-(1-f_0)\frac{\varepsilon_{\text{non-DY}} \cdot \left(1-\varepsilon_{\text{non-DY}}\right)}{\varepsilon^0_{\text{non-DY}} \cdot \left(1-\varepsilon^0_{\text{non-DY}}\right)}\right)}_{\text{Correction } \gamma_{\text{signal}}} \cdot \varepsilon_{\text{non-DY}}, \tag{5.22}$$

with $f_0 = 0.91$ (0.93) being the ratio of the selection efficiencies between signal and other non-DY processes.

The ratio is determined from data and defined at a reference efficiency, indicated by the superscript "0". The difference with unity, $\delta = 1 - f_0$, is assigned as uncertainty on the parametrization of the difference. In the likelihood function, it is implemented using a modified log-normal response function for the nuisance parameter θ,

$$\nu(\theta) = \kappa^{\theta}_{\text{signal}}(\varepsilon_{\text{non-DY}}) \quad \text{with} \quad \kappa_{\text{signal}}(\varepsilon_{\text{non-DY}}) = 1 + \delta \cdot \frac{\varepsilon_{\text{non-DY}} \cdot \left(1-\varepsilon_{\text{non-DY}}\right)}{\varepsilon^0_{\text{non-DY}} \cdot \left(1-\varepsilon^0_{\text{non-DY}}\right)}. \tag{5.23}$$

Table 5.11: Estimated f_{recoil} selection efficiencies (in %) for DY and non-DY events including systematic uncertainties from the statistics in the control sample and due to the extrapolation from control samples.

Efficiency type		$n_j = 0$	$n_j = 1$
$\varepsilon_{\text{non-DY}}$,	efficiency for non-DY events	69 ± 1	64 ± 2
ε_{DY},	efficiency for DY events	14 ± 5	13 ± 4
$\varepsilon'_{\text{non-DY}}$,	efficiency for non-DY when determining the prev. row	68 ± 2	66 ± 3

The chosen parametrization, a quadratic form, is the simplest expression, which ensures that a set of natural boundary conditions is fulfilled, $\gamma_{\text{signal}}(0) = \gamma_{\text{signal}}(1) = 1$, $\kappa_{\text{signal}}(0) = \kappa_{\text{signal}}(1) = 1$, $\gamma_{\text{signal}}(\varepsilon^0_{\text{non-DY}}) = f_0$, and $\kappa_{\text{signal}}(\varepsilon^0_{\text{non-DY}}) = 1 + \delta$. The measured f_{recoil} selection efficiencies are summarized in Tab. 5.11.

No additional uncertainties due to the non-DY sample composition are assigned. Systematic uncertainties on the f_{recoil} selection efficiencies arise from extrapolating $\varepsilon_{\text{non-DY}}$ and $\varepsilon'_{\text{non-DY}}$ from $e\mu$ control samples to $ee/\mu\mu$ categories, and from extrapolating ε_{DY} from the Z mass window to the low $m_{\ell\ell}$ signal enriched samples, c.f. Tab. 5.12. The estimated selection efficiencies and uncertainties have been validated using alternate MC generators and collision data.

The analysis presented in this chapter relies on an accurate modeling of the shapes of the $Z/\gamma^* \to ee, \mu\mu$ process other than the soft hadronic recoil in the MC simulation. However, in future iterations of the analysis, the simplified estimate presented in this section, can be extended to simultaneously extract the f_{recoil} templates and other distributions of the DY and non-DY processes from data.

In the VBF-enriched $n_j \geq 2$ category, the $Z/\gamma^* \to ee, \mu\mu$ background is estimated using an ABCD method. Under the implicit assumption that the O_{BDT} and $p_{\text{T}}^{\text{miss}}$ distributions for DY events are uncorrelated, the background template is derived from data in a low $m_{\ell\ell}$ ($m_{\ell\ell} \leq 75\,\text{GeV}$) and low $p_{\text{T}}^{\text{miss}}$ ($25 < p_{\text{T}}^{\text{miss}} < 45\,\text{GeV}$) control sample. The uncertainties arising from this assumption are 4%, 10%, and 60% in the bins with increasing O_{BDT} score. The cross section is obtained from a $p_{\text{T}}^{\text{miss}}$ cut efficiency measured in a 15 GeV window in $m_{\ell\ell}$ around the Z mass peak, and corrected for a 17% non-closure of the method. The normalization applied to the highest O_{BDT} score bins is fully correlated, and thus introduces a dependence on the prediction from MC simulation due to higher order corrections, the PDF sets, and differences in the PS model. The consequence is a 11% uncertainty on the background estimate in the most signal-like O_{BDT} bin.

Table 5.12: Systematic uncertainties (in %) associated with the f_{recoil} selection efficiencies for DY and non-DY events, listed in Tab. 5.11.

Source	$n_j = 0$	$n_j = 1$
Uncertainty on $\varepsilon_{\text{non-DY}}$	1.9	3.2
From statistical	1.8	3.0
From using $e\mu$ CR to extrapolate to the SR ($ee/\mu\mu$ category)	0.8	1.2
Uncertainty on ε_{DY}	38	32
From statistical	9.4	16
From using Z-peak to extrapolate to the SR ($12 < m_{\ell\ell} < 55\,\text{GeV}$)	32	16
Uncertainty on $\varepsilon'_{\text{non-DY}}$	3.1	4.5
From statistical	1.9	3.9
From using $e\mu$ CR to extrapolate to the SR ($ee/\mu\mu$ category)	2.5	2.4
Total uncertainty on yield estimate B_{DY}	49	45

5.4 Results and interpretations

Following the discussion in Cha. 4, all information about the selected samples and background estimates are encoded in a likelihood function. It simultaneously models the m_{T} or O_{BDT} distribution of the physics processes in all profiled kinematic regions, i.e. in all samples that are used to extract a cross section, efficiency, or template. The likelihood function is maximized with respect to its arguments, i.e. parameters of interest as well as nuisance parameters, in order to estimated their true values, c.f. Sec. 4.2.1.

The analysis at hand uses piece-wise constant p.d.f.s derived from the m_{T} and O_{BDT} distributions, respectively. Hence, the likelihood simplifies to a product of Poisson terms, one for each bin of the observables in the SR categories listed in Tab. 5.5. The binning is optimized independently for each of the kinematic regions using the expected significance for observing a SM Higgs boson as metric, while mitigating effects due to limited template statistics. For the $e\mu$ and $ee/\mu\mu$ samples in the $n_j = 0$ ($n_j = 1$) category this is accomplished by specifying a variable binning scheme for the m_{T} distribution. The signal population is approximately constant across all bins. In the $n_j = 0$ category the width of each of the ten bins in the kinematically favored range is approximately 5 GeV. For the $n_j = 1$ category six bins with a width of approximately 10 GeV each, are chosen. The $e\mu$ events in the ggF-enriched $n_j \geq 2$ sample are arranged in four bins of m_{T}. The bin boundaries are $[0, 50, 80, 130, \infty]$ GeV. The binning for the VBF-enriched $n_j \geq 2$ category has already been discussed in Sec. 5.2.3. The likelihood models the three bins of the O_{BDT} distribution with highest signal purity, i.e. the bins with boundaries at a O_{BDT} score of $[-0.48, 0.3, 0.78, 1]$. In most cases the CR categories are explicitly included in the likelihood function as a single Poisson term to constrain the

rate of a given background process, while not introducing spurious tensions due to multiple measurements. Exceptions are the CRs for the W+jets and QCD multijet backgrounds, whose estimates are virtually independent of the rates of other processes.

The results presented in the remainder of this section are obtained from simultaneously maximizing the likelihood function of the 7 and 8 TeV data samples, accounting for the correlations between the analyses, in particular due to calibrations, c.f. Cha. 3. Theoretical uncertainties are assumed to be fully correlated across the data sets, though their response function may be different. The statistical component of systematic uncertainties is treated uncorrelated between the data samples.

5.4.1 Systematic uncertainties

Section 4.1.2 describes the modeling of systematic uncertainties in the likelihood of a physics measurement using nuisance parameters and advocates their implementation as subsidiary measurements. These measurements reflect uncertainties due to limitations in the modeling of the physics processes, c.f. Sec. 5.2.2 and 5.3, but also parametrize unknown effects in the calibration of the physics objects used in the physics measurement, c.f. Cha. 3. The analysis tries to mitigate the effects of systematic uncertainties on the measurement whenever it is feasible and beneficial by exploiting data-driven estimates of the cross sections and distributions of background processes and in situ measurements of selection efficiencies.

It is important to recognize that measuring the response of a small uncertainty, which is hindered by limited template statistics, in the physics likelihood may lead to instabilities in the maximization of the likelihood function. Thus, the effect of every systematic uncertainty on the predicted yields is checked individually for every template, i.e. for every physics process in every kinematic selection. If the relative change is found to be below 0.1%, this particular response is excluded from the statistical analysis. The effect on the template is checked separately. Owing to the employed binning, it is sufficient to model variations of the shape by vertical bin-by-bin morphing. If and only if, the variation in every bin is below 1%, the effect on the studied template is deemed negligible. These thresholds are estimated empirically based on the expected performance of the measurement.

Jet energy scale and resolution

The largest uncertainty on the signal and background yields induced by the calibration of physics objects, arises from the JES and jet energy resolution (JER) measurement. The calibration scheme for calorimeter jets has been outlined in Sec. 3.3.1. The complexity of the analysis, in particular exploiting the n_j distribution, requires careful modeling of the uncertainties associated with jets. The analysis uses a sufficiently flexible, yet accurate, parameterization of the uncertainties to capture possible variations in the calibration due to physics effects and detector effects over the entire phase space, while maintaining the statistical power to constrain the subsidiary measurements in the analyzed area of the phase space.

The following categories are considered: uncertainties on the pseudorapidity dependence of the jet response (η intercalibration), e.g. due to the response modeling, statistical effects, or additional soft objects produced outside the jet cone; the high-p_{T} jet behavior assessed in a multijet balance measurement [362, 363]; MC non-closure uncertainties; the dependence of the calorimeter response and calibration on the flavor composition of a jet, in particular the difference between jets originating from light quarks or gluons; jets with heavy-flavor content, i.e. jets tagged as containing a b-quark; systematic uncertainties on corrections for in-time and out-of-time pile-up interactions; and uncertainties due to residual *in situ* jet energy corrections [30]. In the studied area of the phase space, the relative uncertainty on the JES (JER) calibration ranges from 1% to 7% (2% to 40%), as a function of the jet p_{T} and η.

Flavor tagging

In particular the top quark background is subject to uncertainties related to the b-jet identification. The calibration of the b-jet tagging algorithm is described in Sec. 3.1.5. The associated uncertainties, e.g. due to MC modeling, hadronization, the PS model, in-time and out-of-time pile-up interactions, and others, are decomposed into six diagonal eigenvectors, one for each p_{T} bin used in the calibration. The uncertainties associated with these components range from less than 1% to 7.8%. The uncertainty due to spuriously reconstructing jets originating from c-quarks as b-jets, ranges from 6% to 14%, depending on the p_{T}. For light-flavor jets, the misidentification rate amounts to an uncertainty of 9% to 19% as function of the jet p_{T} and η.

Lepton identification

The reconstruction, identification, and calibration of leptons has been outlined in Sec. 3.2. In the selected area of phase space, the associated uncertainties are typically less than 1%, except for the uncertainty on the electron identification efficiency, which shows a variation of up to 2.7%, depending on the reconstructed p_{T} and η. The uncertainties on the trigger efficiencies, c.f. Sec. 5.2.1, are small. The uncertainties on the isolation efficiency for electrons (muons) can be as large as 1.6% (2.7%) at low p_{T}.

Missing transverse momentum

The concept of MET has been introduced in Sec. 3.3.3. In particular the modeling of the calibrated calorimeter clusters not associated with reconstructed physics objects and the track-based soft terms contribute to the uncertainties on the $E_{\mathrm{T}}^{\mathrm{miss}}$ and $p_{\mathrm{T}}^{\mathrm{miss}}$, respectively. Jet energy and lepton momentum scale uncertainties are varied in the MET calculation and naively propagated, assuming a Gaussian regime. In future iterations of the analysis, the correlation between these uncertainties can be modeled in the likelihood, e.g. using the approach outlined in Sec. 4.3. The mean of the longitudinal component of the soft terms

entering the $E_{\mathrm{T}}^{\mathrm{miss}}$ ($p_{\mathrm{T}}^{\mathrm{miss}}$) calculation picks up an uncertainty of 0.2 GeV to 0.3 GeV (0.3 GeV to 1.4 GeV), depending on the transverse momenta of the hard objects and the average number of interactions per bunch crossing. The resolution of the longitudinal and perpendicular components is found to be between 1% and 4% (calorimeter-based) and 1.5 GeV to 3.3 GeV (track-based).

Summary

Table 5.13 shows the leading systematic uncertainties on the cumulative signal and background yields integrated over all the lepton-flavor final states in each n_j category for the 8 TeV sample after maximizing the likelihood function. These uncertainties can be classified according to their origin, namely statistical uncertainties due to the finite observed event yields in the CRs; experimental uncertainties related to the understanding of the detector, calibrations, and the limited template statistics; and uncertainties due to the theoretical model of the physics processes, including uncertainties on the signal acceptance and cross sections, and due to theoretical uncertainties on the background extrapolation from control samples. Table 5.14 summarizes the uncertainties on the total signal, total background, and individual backgrounds yields integrated over all SRs in each n_j category for the 8 TeV sample after maximizing the likelihood function. The total uncertainty on the sum of all background processes is smaller than the naive sum in quadrature of the individual process uncertainties due to negative correlations introduced by impure control samples populated by multiple physics processes. One prominent example of this "cross-talk" are the WW and top quark backgrounds in the $n_j = 1$ category.

5.4.2 Yields and distributions

Following the discussion on statistical modeling in Cha. 4, both rates and distributions of the background processes are subject to changes in the nuisance parameters when finding their MLEs. This section summarizes the post-fit yields and shows some of the discriminant distributions for the MLEs.

Table 5.15 shows the observed rate as well as the measured signal and backgrounds yields for all signal-enriched categories in the n_j categories of the 8 TeV data set integrated over all values of the $p_{\mathrm{T}}^{\ell 2}$ and $m_{\ell\ell}$. The predicted rates reflect the MLEs for all profiled parameters, i.e. normalization parameters as well as nuisance parameters. The associated uncertainties include both the statistical and systematic components, propagated from subsidiary measurements using the nuisance parameter approach outlined in Sec. 4.1.

The deviations from the predicted yields are well below one standard deviation, except for the multijet background in the $e\mu$ $n_j = 0$ category and the $Z/\gamma^* \to ee, \mu\mu$ background in the $ee/\mu\mu$ $n_j = 0$ category. The rate of the multijet background increases by 1.3 with respect to the expected predictions due to corrections to the extrapolation from the sample

Table 5.13: Propagated systematic uncertainties (in %), i.e. after profiling all nuisance parameters, on (a) the predicted signal yield (N_{sig}), and (b) the total background yield (N_{bkg}) integrated over all lepton-flavor channels in the signal-enriched n_j categories of the 8 TeV data set. Entries marked with a dash (-) indicate that the corresponding uncertainties either do not apply or are less than 0.1%.

	$n_j = 0$	$n_j = 1$	$n_j \geq 2$ ggF	$n_j \geq 2$ VBF
ggF H, jet veto for $n_j = 0$, ϵ_0	8.1	14	12	-
ggF H, jet veto for $n_j = 1$, ϵ_1	-	12	15	-
ggF H, $n_j \geq 2$ cross section	-	-	-	6.9
ggF H, $n_j \geq 3$ cross section	-	-	-	3.1
ggF H, total cross section	10	9.1	7.9	2.0
ggF H acceptance model	4.8	4.5	4.2	4.0
VBF H, total cross section	-	0.4	0.8	2.9
VBF H acceptance model	-	0.3	0.6	5.5
$H \to WW^*$ branch. fraction	4.3	4.3	4.3	4.3
Integrated luminosity	2.8	2.8	2.8	2.8
Jet energy scale & reso.	5.1	2.3	7.1	5.4
$p_{\text{T}}^{\text{miss}}$ scale & resolution	0.6	1.4	0.1	1.2
f_{recoil} efficiency	2.5	2.1	-	-
Trigger efficiency	0.8	0.7	-	0.4
Electron id., iso., reco. eff.	1.4	1.6	1.2	1.0
Muon id., isolation, reco. eff.	1.1	1.6	0.8	0.9
Pile-up model	1.2	0.8	0.8	1.7

(a) Signal

	$n_j = 0$	$n_j = 1$	$n_j \geq 2$ ggF	$n_j \geq 2$ VBF
WW theoretical model	1.4	1.6	0.7	3.0
Top theoretical model	-	1.2	1.7	3.0
VV theoretical model	-	0.4	1.1	0.5
$Z/\gamma^* \to \tau\tau$ estimate	0.6	0.3	1.6	1.6
$Z/\gamma^* \to ee$, $\mu\mu$ est. in VBF	-	-	-	4.8
Wj estimate	1.0	0.8	1.6	1.3
jj estimate	0.1	0.1	1.8	0.9
Integrated luminosity	-	-	0.1	0.4
Jet energy scale & reso.	0.4	0.7	0.9	2.7
$p_{\text{T}}^{\text{miss}}$ scale & resolution	0.1	0.3	0.5	1.6
b-tagging efficiency	-	0.2	0.4	2.0
Light- and c-jet mistag	-	0.2	0.4	2.0
f_{recoil} efficiency	0.5	0.5	-	-
Trigger efficiency	0.3	0.3	0.1	-
Electron id., iso., reco. eff.	0.3	0.3	0.2	0.3
Muon id., isolation, reco. eff.	0.2	0.2	0.3	0.2
Pile-up model	0.4	0.5	0.2	0.8

(b) Background

Table 5.14: Composition of the systematic uncertainties (in %) after profiling all nuisance parameters on the total signal (N_{sig}), total background (N_{bkg}), and individual background yields integrated over all lepton-flavor final states in the ggF-enriched (a) $n_j = 0$, (b) $n_j = 1$, and (c) $n_j \geq 2$ categories, and (d) in the VBF-enriched $n_j \geq 2$ category of the 8 TeV data set. Entries marked with a dash (-) indicate that the corresponding uncertainties either do not apply or are less than 1%.

Sample	Total error	Stat. error	Expt. syst. err.	Theo. syst. err.
N_{sig}	16	-	6.7	15
N_{bkg}	2.5	1.5	1.2	1.7
N_{WW}	4.2	2.4	2.3	2.6
N_{top}	7.4	2.3	4.2	5.6
N_{misid}	17	-	9.9	14
N_{VV}	9.9	4.8	4.6	7.4
$N_{\tau\tau}$	34	1.7	33	7.2
$N_{ee/\mu\mu}$	30	14	26	5.5

(a) $n_j = 0$

Sample	Total error	Stat. error	Expt. syst. err.	Theo. syst. err.
N_{sig}	22	-	5.3	22
N_{bkg}	3	1.7	1.4	2.1
N_{WW}	7.7	5.5	2.7	4.6
N_{top}	5	3.4	2.9	2.3
N_{misid}	18	-	11	14
N_{VV}	14	8.9	6.1	8.5
$N_{\tau\tau}$	27	3.3	26	6.3
$N_{ee/\mu\mu}$	39	27	26	7.4

(b) $n_j = 1$

Sample	Total error	Stat. error	Expt. syst. err.	Theo. syst. err.
N_{sig}	23	-	8.6	22
N_{bkg}	4.2	1.5	2.2	3.2
N_{WW}	20	-	8.7	18
N_{top}	7.9	2.6	3.4	6.7
N_{misid}	29	-	16	24
N_{VV}	32	-	9.6	31
$N_{\tau\tau}$	18	8	13	10
$N_{ee/\mu\mu}$	15	-	14	4

(c) $n_j \geq 2$ ggF-enriched

Sample	Total error	Stat. error	Expt. syst. err.	Theo. syst. err.
N_{sig}	13	-	6.8	12
N_{bkg}	9.2	4.7	6.4	4.5
N_{WW}	32	-	14	28
N_{top}	15	9.6	7.6	8.5
N_{misid}	22	-	12	19
N_{VV}	20	-	12	15
$N_{\tau\tau}$	40	25	31	2.9
$N_{ee/\mu\mu}$	19	11	15	-

(d) $n_j \geq 2$ VBF-enriched

of anti-identified leptons. The f_{recoil} selection efficiency for DY events is estimated to be lower than its prediction, leading to a decrease of 1.6 standard deviations of the DY contribution in the aforementioned category.

The estimated m_{T} distribution shows a remarkable agreement with the recorded collision data across all $m_{\ell\ell}$ and $p_{\text{T}}^{\ell 2}$ bins in the $n_j \leq 1$ categories. Figure 5.13 shows the combined m_{T} distribution integrated over the lepton-flavor samples and the $n_j \leq 1$ categories and summed for the 7 and 8 TeV data sets. The significance of the excess of events observed in data with respect to the total background is illustrated in the bottom panel of the same figure. It shows the background-subtracted data, i.e. the residuals of the data with respect to the total estimated background, compared to the predicted m_{T} distribution of a SM Higgs boson with a hypothesized mass of 125 GeV and scaled by the measured inclusive production strength, c.f. Sec. 5.4.4. The m_{T} and O_{BDT} distributions in the ggF-enriched and VBF-enriched $n_j \geq 2$ categories for the 8 TeV sample are shown in Fig. 5.14 and Fig. 5.15, respectively.

Table 5.15: (a) Summary of the event yields including propagated systematic uncertainties, i.e. after profiling all nuisance parameters, in the various signal-enriched n_j and lepton-flavor categories of the 8 TeV sample. The signal yield is scaled to the observed inclusive production strength. (b) Composition of the total background yield. Values less than 0.1 (0.01) events are written as 0.0 (-).

Channel	Summary			
	N_{obs}	N_{bkg}	N_{signal}	
			N_{ggF}	N_{VBF}
$n_j = 0$	3750	3430 ± 90	300 ± 50	8 ± 4
$e\mu$, $\ell_2 = \mu$	1430	1280 ± 40	129 ± 20	3.0 ± 2.1
$e\mu$, $\ell_2 = e$	1212	1106 ± 35	97 ± 15	2.5 ± 0.6
$ee/\mu\mu$	1108	1040 ± 40	77 ± 15	2.4 ± 1.7
$n_j = 1$	1596	1470 ± 40	102 ± 26	17 ± 5
$e\mu$, $\ell_2 = \mu$	621	569 ± 19	45 ± 11	7.4 ± 2
$e\mu$, $\ell_2 = e$	508	475 ± 18	35 ± 9	6.1 ± 1.4
$ee/\mu\mu$	467	427 ± 21	22 ± 6	3.6 ± 1.8
$n_j \geq 2$, ggF $e\mu$	1017	960 ± 40	37 ± 11	13 ± 1.4
$n_j \geq 2$, VBF	130	99 ± 9	7.7 ± 2.6	21 ± 3
$e\mu$ bin 1	37	36 ± 4	3.3 ± 1.2	4.9 ± 0.5
$e\mu$ bin 2	14	6.5 ± 1.3	1.4 ± 0.5	4.9 ± 0.5
$e\mu$ bin 3	6	1.2 ± 0.3	0.4 ± 0.3	3.8 ± 0.7
$ee/\mu\mu$ bin 1	53	46 ± 6	1.7 ± 0.6	2.6 ± 0.3
$ee/\mu\mu$ bin 2	14	8.4 ± 1.8	0.7 ± 0.3	3.0 ± 0.4
$ee/\mu\mu$ bin 3	6	1.1 ± 0.4	0.2 ± 0.2	2.1 ± 0.4

(a)

Channel	Composition of N_{bkg}						
	N_{WW}	N_{top}		N_{misid}		N_{VV}	N_{DY}
		N_t	$N_{t\bar{t}}$	N_{Wj}	N_{jj}		
$n_j = 0$	2250 ± 95	112 ± 9	195 ± 15	360 ± 60	16 ± 5	420 ± 40	78 ± 21
$e\mu$, $\ell_2 = \mu$	830 ± 34	41 ± 3	73 ± 6	149 ± 29	10.1 ± 3.6	167 ± 21	14 ± 2.4
$e\mu$, $\ell_2 = e$	686 ± 29	33 ± 3	57 ± 5	128 ± 31	3.8 ± 1.5	184 ± 23	14 ± 2.4
$ee/\mu\mu$	740 ± 40	39 ± 3	65 ± 5	82 ± 16	2 ± 0.5	68 ± 7	50 ± 21
$n_j = 1$	630 ± 50	150 ± 10	385 ± 20	108 ± 20	8.2 ± 3.0	143 ± 20	51 ± 13
$e\mu$, $\ell_2 = \mu$	241 ± 20	58 ± 4	147 ± 7	51 ± 11	5.7 ± 2.0	53 ± 10	13.8 ± 3.3
$e\mu$, $\ell_2 = e$	202 ± 17	45 ± 3	119 ± 6	37 ± 9	2.3 ± 0.9	60 ± 10	9.3 ± 2.5
$ee/\mu\mu$	184 ± 15	46 ± 4	119 ± 10	19 ± 4	0.2 ± 0.1	31 ± 4	28 ± 12
$n_j \geq 2$, ggF $e\mu$	138 ± 28	56 ± 5	480 ± 40	54 ± 25	62 ± 22	56 ± 18	117 ± 21
$n_j \geq 2$, VBF	11 ± 3.5	5.5 ± 0.7	29 ± 5	4.7 ± 1.4	2.8 ± 1.0	4.4 ± 0.9	38 ± 7
$e\mu$ bin 1	5.0 ± 1.5	3.0 ± 0.6	15.6 ± 2.6	3.2 ± 1.0	2.3 ± 0.8	2.3 ± 0.7	3.6 ± 1.5
$e\mu$ bin 2	1.7 ± 0.7	0.3 ± 0.4	2.0 ± 1.0	0.4 ± 0.1	0.3 ± 0.1	0.7 ± 0.2	0.6 ± 0.2
$e\mu$ bin 3	0.3 ± 0.1	0.1 ± 0.0	0.3 ± 0.1	-	-	0.1 ± 0.0	0.2 ± 0.1
$ee/\mu\mu$ bin 1	3.1 ± 1.0	1.7 ± 0.3	10.1 ± 1.6	0.9 ± 0.2	0.2 ± 0.1	1.0 ± 0.3	28 ± 5
$ee/\mu\mu$ bin 2	0.9 ± 0.3	0.3 ± 0.2	1.2 ± 0.5	0.2 ± 0.1	-	0.3 ± 0.1	5.2 ± 1.7
$ee/\mu\mu$ bin 3	0.1 ± 0.1	0.1 ± 0.0	0.2 ± 0.1	-	-	-	0.5 ± 0.3

(b)

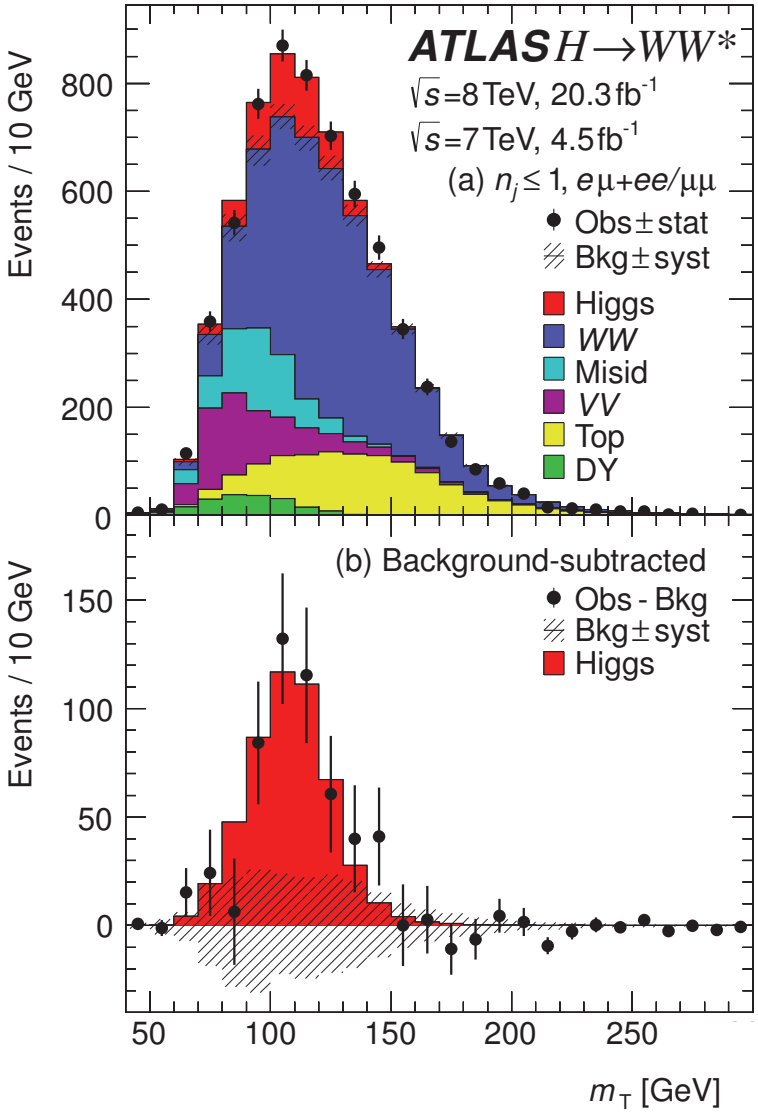

Figure 5.13: (a) Cumulative m_{T} distribution integrated over all lepton-flavor final states and $n_j \leq 1$ categories of the 7 and 8 TeV data sets after profiling all nuisance parameters. (b) Residuals of the data with respect to the total estimated background, compared to the predicted m_{T} distribution of a SM Higgs boson with a hypothesized mass of 125 GeV and scaled by the measured inclusive production strength. Although the reconstructed transverse mass m_{T} is not identical to the invariant mass m_H of the Higgs boson due to the unknown longitudinal momenta of the neutrinos in the final state, it has a kinematic bound at the true Higgs boson mass, smeared by the detector resolution. See Fig. 5.2 for plotting details.

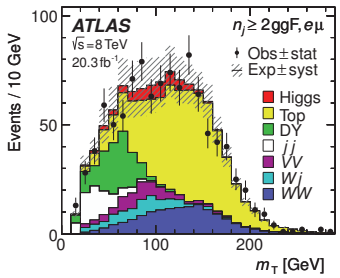

Figure 5.14: Distributions of m_{T} for events in the $n_j \geq 2$ ggF-enriched category of the 8 TeV data set after profiling all nuisance parameters. See Fig. 5.2 for plotting details.

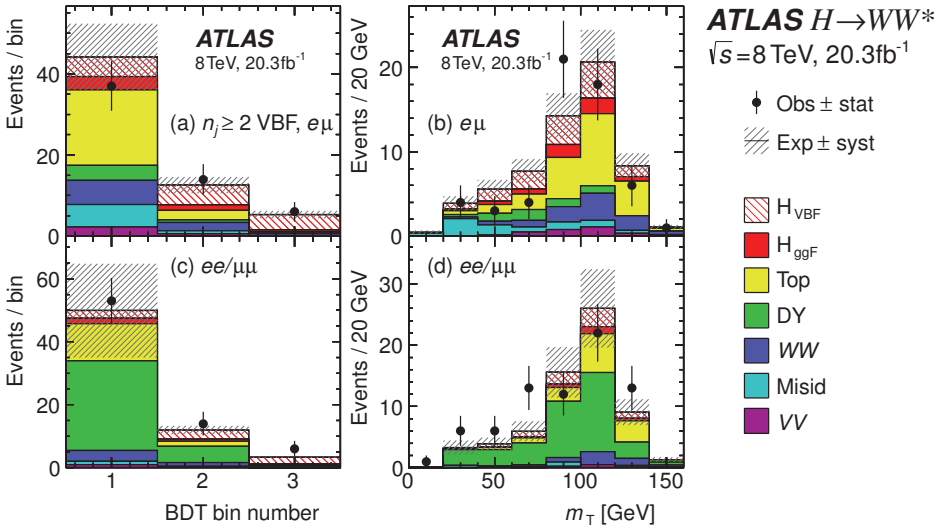

Figure 5.15: BDT output distributions for events in the (a) $e\mu$, and (c) $ee/\mu\mu$ VBF-enriched $n_j \geq 2$ categories. Distributions of m_{T} for events with (b) $e\mu$, and (d) $ee/\mu\mu$ final states in the VBF-enriched $n_j \geq 2$ categories, integrated over the three O_{BDT} bins with the highest score. The distributions are shown after profiling all nuisance parameters for the 8 TeV data set. See Fig. 5.2 for plotting details.

5.4.3 Observation of Higgs boson decays to *WW**

The results presented in the following sections combine the 7 and 8 TeV data sets and are obtained following the procedures explained in Cha. 4.

To establish the $H \to WW^*$ decay mode, the significance of the observed excess of events in data with respect to the background is quantified. The discovery test statistic q_0 is used to test the null hypothesis $\mu = 0$, i.e. the hypothesis that the background can fluctuate to produce an excess at least as large as the one observed in the previous section. Figure 5.16 shows both the median expected and the observed p-values for finding data that is less

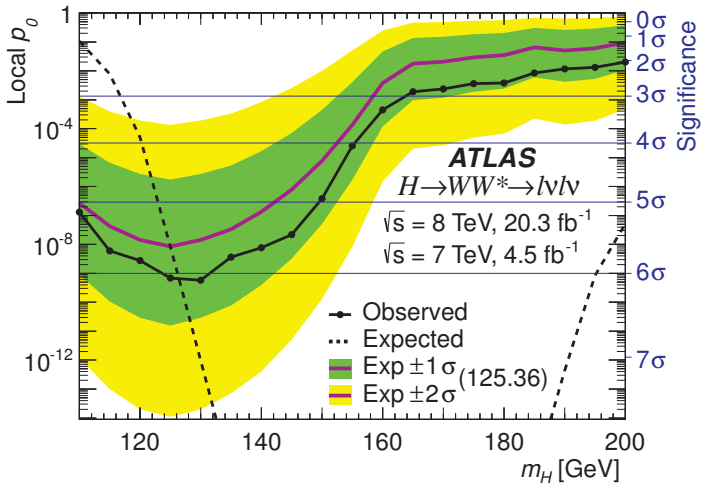

Figure 5.16: The local p_0 as a function of m_H observed in collision data (solid, with markers), expected (dashed) for a SM Higgs boson signal hypothesis ($\mu = 1$) at the given mass m_H, and expected for a SM Higgs boson with $m_H = 125.36\,\text{GeV}$ (solid, without markers). The shaded bands indicate the approximate 68% and 95% CL intervals.

compatible with the prediction of the null hypothesis as function of m_H. The local p_0 has been computed in the range from $m_H = 110\,\text{GeV}$ to $m_H = 200\,\text{GeV}$ in 5 GeV intervals, corresponding to the mass points for which fully simulated and reconstructed MC samples are available.

The minimum p_0-value is observed at $m_H = 130\,\text{GeV}$ and corresponds to a local significance of 6.1 standard deviations. The null hypothesis is rejected with approximately the same significance for $m_H = 125.36\,\text{GeV}$, i.e. for the mass measured by the ATLAS collaboration using the $\gamma\gamma$ and 4ℓ final states. This result establishes the observation of Higgs boson decays to WW^* in dilepton final states. The median expected significance for a SM Higgs boson with the same mass corresponds to 5.8 standard deviations.

5.4.4 Production strength measurements

This section summarizes the measurements of the inclusive Higgs boson signal strength and the relative contributions of the different production mechanisms, in particular the production via VBF.

The inclusive production strength

The inclusive Higgs boson signal strength is characterized by the parameter μ. It is defined as a normalization of the observed Higgs boson rate with respect to the SM prediction,

$$\mu = \frac{(\sigma \times \mathrm{BR})_{\mathrm{obs}}}{\sigma_{\mathrm{SM}} \times \mathrm{BR}_{\mathrm{SM}}}, \tag{5.24}$$

assuming that all production modes and decay channels scale in the same way. In particular, results in this section consider events from $H \to \tau\tau$ decays entering the $n_j \geq 2$ categories as signal, assuming the branching fractions as predicted by the SM. The compatibility of the measured production strength with the SM expectation for a Higgs boson of mass m_H is illustrated in Fig. 5.17. It shows the MLE of μ with its 68% confidence interval determined from collision data as a function of m_H. The curve is compared to the expected $\hat{\mu}$ values in the presence of a SM Higgs boson with $m_H = 125.36\,\mathrm{GeV}$. The indicated confidence intervals are constructed under the assumption that the test statistic $t_\mu = -2\ln\Lambda(\mu)$ asymptotically is distributed as a χ^2 distribution with one degree of freedom.

Figure 5.18a shows confidence intervals containing the values of μ and m_H, which are simultaneously consistent with the $H \to WW^* \to \ell\nu\ell\nu$ data set. Moment morphing is used to construct a continuous parametric model of the Higgs boson mass by non-linearly interpolating the signal templates as a function of m_H, given the templates available in 5 GeV intervals in m_H, c.f. Sec. 4.3. The confidence intervals are constructed under the assumption that the test statistic $-2\ln\Lambda(\mu, m_H)$ asymptotically is distributed as a χ^2 distribution with two degrees of freedom. The minimum of the likelihood function is at

$$\begin{array}{llllll} \mu & = 0.94 & {}^{+0.22}_{-0.18}\,(\mathrm{stat.}) & {}^{+0.18}_{-0.13}\,(\mathrm{syst.}) & = 0.94 & {}^{+0.28}_{-0.23} \\ m_H & = 127.9 & {}^{+2.8}_{-2.7}\,(\mathrm{stat.}) & \pm 1.3\,(\mathrm{syst.})\,\mathrm{GeV} & = 127.9 & \pm 3.0\,\mathrm{GeV}. \end{array} \tag{5.25}$$

The SM hypothesis ($\mu = 1$, $m_H = 125.36\,\mathrm{GeV}$) lies well within the 68% confidence interval. The two-dimensional compatibility of this hypothesis with the data is approximately 60%, derived from the p-value obtained from the PLR evaluated at the SM values.

The inclusive signal strength μ is correlated with the measured mass m_H via the Higgs boson production cross sections and the $H \to WW^*$ branching fraction. In order to remove these dependencies, the test statistic is modified to become a function of m_H and the normalized signal yield S, defined by fixing the denominator to the best estimate of the Higgs mass obtained from the high-resolution channels,

$$S = \frac{(\sigma \times \mathrm{BR})_{\mathrm{obs}}}{\sigma_{125.36} \times \mathrm{BR}_{125.36}}. \tag{5.26}$$

Figure 5.18b shows that the residual dependence of the fitted signal yield arises from a decrease of the signal selection efficiency at low m_H, driven by a softening of the lepton p_{T} distributions.

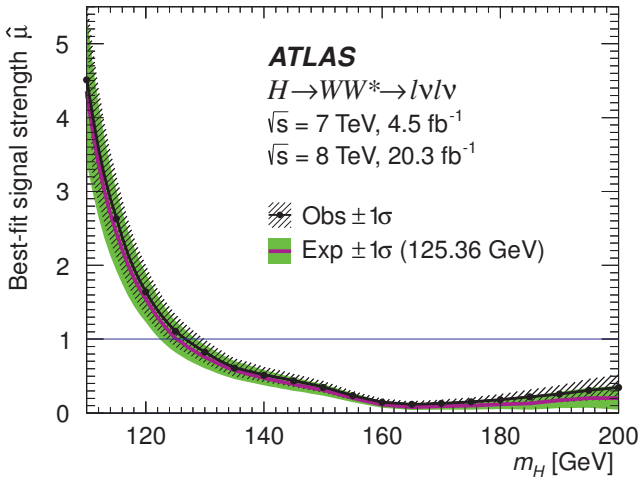

Figure 5.17: MLE of the inclusive production strength μ as a function of m_H observed in collision data (solid, with markers), and expected for a SM Higgs boson with $m_H = 125.36\,\text{GeV}$ (solid, without markers). The hashed (solid) band indicates the approximate 68% CL interval around the observed (expected) values.

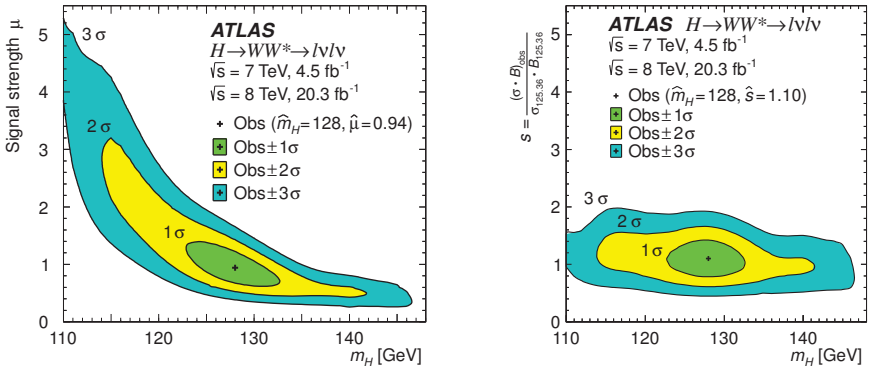

(a) **(b)**

Figure 5.18: Confidence intervals as function of (a) the inclusive production strength μ and m_H, and (b) the normalized signal yield $S = (\sigma \cdot \text{BR})_{\text{obs}} / (\sigma_{125.36} \cdot \text{BR}_{125.36})$ and m_H. The markers indicate the MLEs observed in the collision data. The normalized signal yield S is equivalent to the inclusive signal strength μ with the dependence on m_H, both of the branching fraction and of the cross section, removed. The non-ellipsoidal structures appearing in the contours reflect the continuous, but non-monotonic behaviour of the test statistic introduced by the higher-order polynomial interpolation used for constructing the parametric model of the Higgs boson mass.

The combined inclusive signal strength for a Higgs boson with $m_H = 125.36\,\text{GeV}$ obtained from a fit to the 7 and 8 TeV data sets, is

$$\begin{aligned}\mu &= 1.09 \;{}^{+0.16}_{-0.15}\,(\text{stat.}) \;{}^{+0.08}_{-0.07}\left(\begin{smallmatrix}\text{expt.}\\ \text{syst.}\end{smallmatrix}\right) \;{}^{+0.15}_{-0.12}\left(\begin{smallmatrix}\text{theo.}\\ \text{syst.}\end{smallmatrix}\right) \;\pm 0.03\left(\begin{smallmatrix}\text{lumi.}\\ \text{syst.}\end{smallmatrix}\right) \\ &= 1.09 \;{}^{+0.16}_{-0.15}\,(\text{stat.}) \;{}^{+0.17}_{-0.14}\,(\text{syst.}) \\ &= 1.09 \;{}^{+0.23}_{-0.21}.\end{aligned} \tag{5.27}$$

The expected precision for a measurement of μ is

$$\mu = 1\,{}^{+0.16}_{-0.15}\,(\text{stat.})\,{}^{+0.17}_{-0.13}\,(\text{syst.}). \tag{5.28}$$

The uncertainties are classified according to their source, following the discussion in Sec. 5.4.1. A detailed summary of the uncertainties on the inclusive production strength is provided in Tab. 5.16. The largest single source of uncertainty arises from the statistics in the signal-enriched categories, which is being reduced naturally in future iterations of the analysis using a larger data sample. Theoretical uncertainties, in particular associated with the ggF production mechanism, are substantially larger than the ones with experimental origin.

Table 5.17 summarizes the inclusive production strength as well as the significance of the excess of the data over the predicted background observed in the individual signal-enriched categories. In all cases, the estimate of the background processes follows the nominal approach outlined in Sec. 5.3, e.g. even when measuring the Higgs production rate in $ee/\mu\mu$ final stats, some background estimates may be extrapolated from $e\mu$ control samples. The measurements are consistent with each other and with unity, i.e. with the SM prediction, within the assigned uncertainties.

Evidence for Higgs production via vector boson fusion

The measurement of the inclusive production strength does not account for the relative contributions of the different production mechanism to the total Higgs production rate. Differences between data and theory can be exploited by releasing the constraint that the ratios of the production cross sections for the various processes are as the ones predicted by the SM. In particular the VBF-enriched $n_j \geq 2$ category is optimized to measure the rate of Higgs bosons produced via VBF. It then is compared to the rate from ggF production, determined in the other categories, to test that a fraction of the observed Higgs bosons is produced through vector boson mediated processes. This approach achieves a consistent parametrization of production and decay modes without imposing the assumptions needed for a measurement of the Higgs boson couplings, as it is done in the following chapter.

Figure 5.19a shows the two dimensional confidence intervals for a simultaneous measurement of vector boson mediated processes, VBF and Higgs strahlung, and gluon-initiated processes, ggF and associated Higgs production with heavy quarks, assuming the SM values for the ratios $\sigma_{\text{VBF}}/\sigma_{VH}$ and $\sigma_{\text{ggF}}/\sigma_{qqH}$, respectively, i.e. $\mu_{\text{VBF+}VH} = \mu_{\text{VBF}} = \mu_{VH}$ and

Table 5.16: Uncertainties on the measurement of inclusive Higgs production (left), production via gluon fusion (middle), and production via VBF (right). The uncertainties are classified according to their source: data statistics, template statistics, theoretical systematics, experimental systematics, and integrated luminosity. The uncertainties are estimated for a SM Higgs boson with $m_H = 125.36\,\text{GeV}$. Entries marked with a dash (-) indicate that the corresponding uncertainties either do not apply or are less than 0.01.

Source	Observed $\mu = 1.09$ Error +	Error −	Plot of error (scaled by 100)	Observed $\mu_{\text{ggF}} = 1.02$ Error +	Error −	Plot of error (scaled by 100)	Observed $\mu_{\text{VBF}} = 1.27$ Error +	Error −	Plot of error (scaled by 100)
Data statistics	0.16	0.15		0.19	0.19		0.44	0.40	
Signal regions	0.12	0.12		0.14	0.14		0.38	0.35	
Profiled control regions	0.10	0.10		0.12	0.12		0.21	0.18	
Profiled signal regions	-	-		0.03	0.03		0.09	0.08	
MC statistics	0.04	0.04		0.06	0.06		0.05	0.05	
Theoretical systematics	0.15	0.12		0.19	0.16		0.22	0.15	
Signal $H \to WW^*$ BR	0.05	0.04		0.05	0.03		0.07	0.04	
Signal ggF cross section	0.09	0.07		0.13	0.09		0.03	0.03	
Signal ggF acceptance	0.05	0.04		0.06	0.05		0.07	0.07	
Signal VBF cross section	0.01	0.01		-	-		0.07	0.04	
Signal VBF acceptance	0.02	0.01		-	-		0.15	0.08	
Background WW	0.06	0.06		0.08	0.08		0.07	0.07	
Background top quark	0.03	0.03		0.04	0.04		0.06	0.06	
Background misid. factor	0.05	0.05		0.06	0.06		0.02	0.02	
Others	0.02	0.02		0.02	0.02		0.03	0.03	
Experimental systematics	0.07	0.06		0.08	0.08		0.18	0.14	
Background misid. factor	0.03	0.03		0.04	0.04		0.02	0.01	
Bkg. $Z/\gamma^* \to ee, \mu\mu$	0.02	0.02		0.03	0.03		0.01	0.01	
Muons and electrons	0.04	0.04		0.05	0.04		0.03	0.02	
Missing transv. momentum	0.02	0.02		0.02	0.01		0.05	0.05	
Jets	0.03	0.02		0.03	0.03		0.15	0.11	
Others	0.03	0.02		0.03	0.03		0.06	0.06	
Integrated luminosity	0.03	0.03		0.03	0.02		0.05	0.03	
Total	0.23	0.21		0.29	0.26		0.53	0.45	

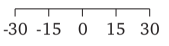

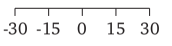

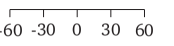

Table 5.17: Measurement of the production strength and expected precision for various signal-enriched categories, assuming a SM Higgs boson with $m_H = 125.36\,\text{GeV}$. The total uncertainty as well as the statistical and systematic error on the signal strength are quoted. The local significance of an excess of events in data with respect to the background is shown, too.

	Signal significance			Expected		Observed uncertainty						Observed central value	
				Tot. err.		Tot. err.		Stat. err.		Syst. err.			
Sample	Exp. Z_0	Obs. Z_0	Bar graph of observed Z_0	+	−	+	−	+	−	+	−	μ_{obs}	$\mu_{\text{obs}} \pm$ stat. (thick) $\pm$ total (thin)
$n_j = 0$	3.70	4.08		0.35	0.30	0.37	0.32	0.22	0.22	0.30	0.23	1.15	
$e\mu$, $\ell_2 = \mu$	2.89	3.07		0.41	0.36	0.43	0.38	0.30	0.29	0.32	0.24	1.08	
$e\mu$, $\ell_2 = e$	2.36	3.12		0.49	0.44	0.54	0.48	0.38	0.37	0.39	0.30	1.40	
$ee/\mu\mu$ category	1.43	0.71		0.74	0.70	0.68	0.66	0.45	0.44	0.51	0.50	0.47	
$n_j = 1$	2.60	2.49		0.51	0.41	0.50	0.41	0.33	0.32	0.38	0.26	0.96	
$e\mu$ category	2.56	2.83		0.51	0.42	0.56	0.45	0.35	0.35	0.43	0.29	1.16	
$ee/\mu\mu$ category	1.02	0.21		1.12	0.98	1.02	0.97	0.80	0.76	0.63	0.61	0.19	
$n_j \geq 2$, ggF, $e\mu$	1.21	1.44		0.96	0.83	0.91	0.84	0.70	0.68	0.70	0.49	1.20	
$n_j \geq 2$, VBF-enr.	3.38	3.84		0.42	0.36	0.45	0.38	0.36	0.33	0.27	0.19	1.20	
$e\mu$ category	3.01	3.02		0.48	0.40	0.47	0.39	0.40	0.35	0.24	0.16	0.98	
$ee/\mu\mu$ category	1.58	2.96		0.84	0.67	0.97	0.78	0.83	0.71	0.51	0.33	1.98	
All n_j, all signal	5.76	6.06		0.23	0.20	0.23	0.21	0.16	0.15	0.17	0.14	1.09	
ggF as signal	4.34	4.28		0.30	0.24	0.29	0.26	0.19	0.19	0.22	0.18	1.02	
VBF as signal	2.67	3.24		0.50	0.43	0.53	0.45	0.44	0.40	0.30	0.21	1.27	

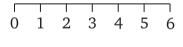

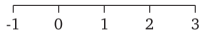

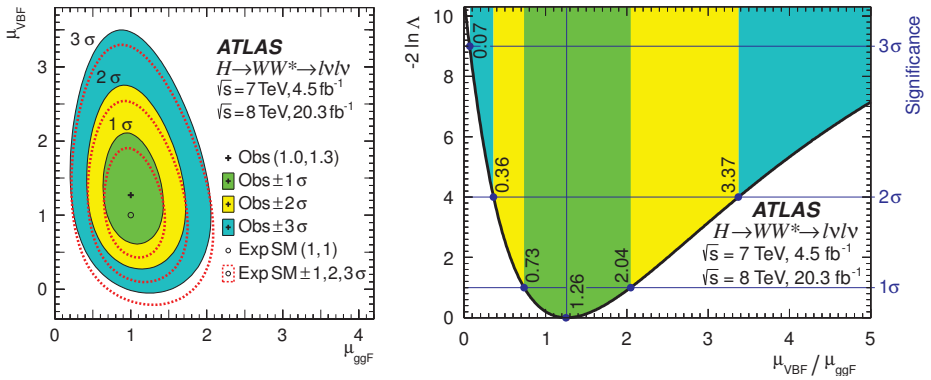

Figure 5.19: (a) Confidence intervals as function of the production strengths for gluon initiated and vector boson mediated processes, $\mu_{ggF+qqH}$ and μ_{VBF+VH}, observed in collision data (solid), and expected for a SM Higgs boson with $m_H = 125.36\,\text{GeV}$ (dashed). The MLEs are indicated by markers. (b) Measurement of the $\mu_{VBF+VH}/\mu_{ggF+qqH}$ ratio for a SM Higgs boson with mass $m_H = 125.36\,\text{GeV}$. The indicated confidence intervals are constructed under the assumption that the test statistic $t_\mu = -2\ln\Lambda(\mu)$ asymptotically is distributed as a χ^2 distribution with one degree of freedom. Under the same assumption, the hypothesis $\mu_{VBF+VH}/\mu_{ggF+qqH} = 0$ is rejected at 3.2 standard deviations.

$\mu_{ggF+qqH} = \mu_{ggF} = \mu_{qqH}$. The contributions from VH and qqH production are small, at most 1% of the total signal yield, and therefore the measurement effectively probes the correlation of ggF and VBF production. The two-dimensional compatibility of the SM hypothesis, $\mu_{ggF+qqH} = \mu_{VBF+VH} = 1$, with the best-fit point is approximately 85%. The measurement of the individual signal strengths yields

$$\begin{aligned} \mu_{ggF} &= 1.02 \pm 0.19\,(\text{stat.})\ ^{+0.22}_{-0.18}\,(\text{syst.}) &&= 1.02\ ^{+0.29}_{-0.26} \\ \mu_{VBF} &= 1.27\ ^{+0.44}_{-0.40}\,(\text{stat.})\ ^{+0.29}_{-0.21}\,(\text{syst.}) &&= 1.27\ ^{+0.53}_{-0.45}. \end{aligned} \tag{5.29}$$

The composition of the uncertainties is presented in detail in Tab. 5.16.

Figure 5.19b shows the measurement of the ratio $\mu_{VBF+VH}/\mu_{ggF+qqH}$, independent of the SM branching fraction,

$$\frac{\mu_{VBF+VH}}{\mu_{ggF+qqH}} = 1.26\ ^{+0.61}_{-0.45}\,(\text{stat.})\ ^{+0.50}_{-0.26}\,(\text{syst.}) = 1.26\ ^{+0.79}_{-0.53}. \tag{5.30}$$

Testing the hypothesis $\mu_{VBF+VH}/\mu_{ggF+qqH} = 0$ provides evidence at a level of 3.2 standard deviations that indeed a fraction of the observed Higgs bosons is produced through vector boson mediated processes, notably VBF. The expected sensitivity corresponds to a median significance of 2.7 standard deviations, using the asymptotic approximation outlined in Sec. 4.2.

5.4.5 Correlations between the inclusive signal strength and nuisance parameters

The correlation of a nuisance parameter to the POI of a measurement can be used to assess the importance of a systematic uncertainty for a measurement. The correlation is by construction identical to the quadratic change in the total error when fixing the nuisance parameter under consideration. However, a large number of pseudo experiments is typically required to determine the correlation coefficient, frustrating the metric, in particular in light of models growing in sensitivity and complexity[1].

A more efficient way of estimating the impact of a single nuisance parameter θ is by evaluating the change of the POI's MLE, $\hat{\mu}$, when varying θ within its confidence interval, i.e.,

$$\Delta_{\hat{\mu},\pm} = \hat{\mu}(\hat{\theta} \pm \Delta_\theta) - \hat{\mu}(\hat{\theta}). \tag{5.31}$$

Under the approximation that uncertainties can be described by a normal distribution, the metric is identical to the correlation coefficient of μ and θ. Thus, (5.31) is identical to the uncertainty of μ due to the nuisance parameter of interest, taken as the quadratic difference of the total uncertainty and the uncertainty excluding all components but θ. The effect of constraining a systematic uncertainty in the physics measurement can be evaluated by comparing the change of $\hat{\mu}$ for a variation of θ within the confidence interval set by the subsidiary measurement (pre-fit) and the one obtained from the physics measurement (post-fit).

Table 5.18 gives an overview of the twenty single largest systematic uncertainties considered in the measurement of the inclusive signal strength in the $H \to WW^* \to \ell\nu\ell\nu$ decay channel. The m_{T} shape of the WW background is estimated more precisely in the analyzed phase space than it is expected from a subsidiary measurement, driven by the high-m_{T} tail of the SR, c.f. Fig. 5.13, which contains a significant fraction of WW events. No other systematic uncertainty is reduced significantly compared to the subsidiary measurements.

The metric can be used to reduce the complexity of statistical models and thus stabilize the minimization of the likelihood. Although the performance is greatly improved compared to methods that require generating a large number of pseudo experiments, the required number of likelihood minimizations can become substantial, since the impact of the remaining parameters should be evaluated again after removing θ to account for correlations between the nuisance parameters.

An improved, fully analytic, algorithm exploits the variance-covariance matrix, i.e. the curvature of the space spanned by all parameters entering the likelihood function. The variance

[1] The analysis presented in this chapter considers more than 200 subsidiary measurements, estimates approximately 50 background normalization factors and efficiencies, using information of the data distributed over almost 400 bins.

of a POI approximates its true confidence interval, accounting for two-point correlations between μ and $\boldsymbol{\theta}$. When removing one θ, i.e. reducing the Hessian matrix by one column and one row, the curvature, and thus the variance, is reduced. The effect is proportional to the component of the total uncertainty due to a single source. The Hessian matrix, and thus the complexity of the statistical model, can be reduced up to a threshold that retains the size of the confidence interval within the quoted precision. It has been shown, that even with imposing a conservative threshold, the complexity of benchmark models can safely be reduced up to tenfold. The main benefits of this algorithm are its computational performance and numeric stability owing to an analytic approach without the need to compute quadratic differences of small numbers.

5.4.6 Inclusive Higgs production cross sections

The measurement of the Higgs production strength in Sec 5.4.4 can be interpreted as a measurement of the inclusive cross section,

$$\begin{aligned}\left(\sigma \cdot \mathrm{BR}_{H\to WW^*}\right)_{\mathrm{obs}} &= \frac{(N_{\mathrm{sig}})_{\mathrm{obs}}}{\mathscr{A}\times\mathscr{C}\cdot \mathrm{BR}_{WW\to\ell\nu\ell\nu}}\cdot\frac{1}{\int L\,\mathrm{d}t} \\ &= \hat{\mu}\cdot(\sigma\cdot\mathrm{BR}_{H\to WW^*})_{\mathrm{exp}}.\end{aligned} \tag{5.32}$$

Here, the product $\mathscr{A}\times\mathscr{C}$ is the total acceptance for reconstructed events, defined as the kinematic and geometric acceptance of the analysis ($\mathscr{A}$) corrected for the fraction of events produced in the fiducial phase space of the detector ($\mathscr{C}$). The acceptance is evaluated determined from MC simulation.

The analysis presented in this section is sensitive to the inclusive cross section of the ggF process both at 7 and 8 TeV and the inclusive cross section of the VBF process at 8 TeV. The measurement of the VBF cross section at a collision energy of 7 TeV is statistically limited. The contributions from other production mechanisms are typically small, and thus can be neglected. Their fractional yields have been added linearly to the total error of the measurement.

The Higgs production strengths that are used to extract the corresponding inclusive cross sections are

$$\begin{aligned}
\mu_{\mathrm{ggF}}^{7\mathrm{TeV}} &= 0.57 \quad {}^{+0.52}_{-0.51}\mathrm{stat} \quad {}^{+0.36}_{-0.34}\mathrm{syst} \quad {}^{+0.14}_{-0.004}\ (\mathrm{sig.}) \\
\mu_{\mathrm{ggF}}^{8\mathrm{TeV}} &= 1.09 \quad \pm 0.20\mathrm{stat} \quad {}^{+0.19}_{-0.17}\mathrm{syst} \quad {}^{+0.14}_{-0.09}\ (\mathrm{sig.}) \\
\mu_{\mathrm{VBF}}^{8\mathrm{TeV}} &= 1.45 \quad {}^{+0.48}_{-0.44}\mathrm{stat} \quad {}^{+0.38}_{-0.24}\mathrm{syst} \quad {}^{+0.11}_{-0.06}\ (\mathrm{sig.})
\end{aligned} \tag{5.33}$$

The cross section measurement is not affected by the systematic uncertainty on the total signal yield for the measured process, denoted as "(sig.)". However, the uncertainty on the signal yield of other production processes enters as a systematic uncertainty.

Table 5.18: Correlations between the measured inclusive production strength and nuisance parameters. The impact is evaluated by monitoring the MLE of the inclusive signal strength under variations of a nuisance parameter. A positive (negative) variation of the θ is indicated by the column header, + (−). The sign of the correlation coefficient can be inferred from the sign of the resulting change in $\hat{\mu}$. The MLE of each nuisance parameter ($\hat{\theta}$) is quoted along with its confidence interval (Δ_θ), given in units of standard deviations (σ).

Systematic source	Impact on $\hat{\mu}$					Impact on $\hat{\theta}$	
	Pre-fit $\Delta_{\hat{\mu}}$		Post-fit $\Delta_{\hat{\mu}}$		Plot of post-fit $\pm\Delta_{\hat{\mu}}$	Pull, $\hat{\theta}$ (σ)	Constr., Δ_θ
	+	−	+	−			
ggF H, PDF variations on cross section	−0.06	+0.06	−0.06	+0.06		−0.06	±1
ggF H, QCD scale on total cross section	−0.05	+0.06	−0.05	+0.06		−0.05	±1
WW, generator modeling	−0.07	+0.06	−0.05	+0.05		0	±0.7
Top quarks, generator modeling on α_{top} in ggF cat.	+0.03	−0.03	+0.03	−0.03		−0.40	±0.9
Misid. of μ, OC uncorrelated corr. factor α_{misid}, 2012	−0.03	+0.03	−0.03	+0.03		0.48	±0.8
Integrated luminosity, 2012	−0.03	+0.03	−0.03	+0.03		0.08	±1
Misid. of e, OC uncorrelated corr. factor α_{misid}, 2012	−0.03	+0.03	−0.02	+0.03		−0.06	±0.9
ggF H, PDF variations on acceptance	−0.02	+0.02	−0.02	+0.02		−0.03	±1
Jet energy scale, η intercalibration	−0.02	+0.02	−0.02	+0.02		0.45	±0.95
VBF H, UE/PS	−0.02	+0.02	−0.02	+0.02		0.26	±1
ggF H, QCD scale on ϵ_1	−0.01	+0.03	−0.01	+0.03		−0.10	±0.95
Muon isolation efficiency	−0.02	+0.02	−0.02	+0.02		0.13	±1
VV, QCD scale on acceptance	−0.02	+0.02	−0.02	+0.02		0.09	±1
ggF H, UE/PS	-	−0.02	-	−0.02		0	±0.9
ggF H, QCD scale on acceptance	−0.02	+0.02	−0.02	+0.02		0	±1
Light jets, tagging efficiency	+0.02	−0.02	+0.02	−0.02		0.21	±1
ggF H, generator modeling on acceptance	+0.01	−0.02	+0.01	−0.02		0.10	±1
ggF H, QCD scale on $n_j \geq 2$ cross section	−0.01	+0.02	−0.01	+0.02		−0.04	±1
Top quarks, generator modeling on α_{top} in VBF cat.	−0.01	+0.02	−0.01	+0.02		−0.16	±1
Electron isolation efficiency	−0.02	+0.02	−0.02	+0.02		−0.14	±1

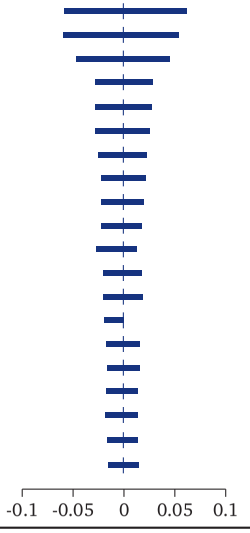

The estimated production cross sections,

$$\begin{aligned}
\sigma^{7\text{TeV}}_{\text{ggF}} \cdot \text{BR}_{H\to WW^*} &= 2.0 \pm 1.7\ (\text{stat.})\ ^{+1.2}_{-1.1}\ (\text{syst.}) = 2.0\ ^{+2.1}_{-2.0}\ \text{pb} \\
\sigma^{8\text{TeV}}_{\text{ggF}} \cdot \text{BR}_{H\to WW^*} &= 4.6 \pm 0.9\ (\text{stat.})\ ^{+0.8}_{-0.7}\ (\text{syst.}) = 4.6\ ^{+1.2}_{-1.1}\ \text{pb} \\
\sigma^{8\text{TeV}}_{\text{VBF}} \cdot \text{BR}_{H\to WW^*} &= 0.51\ ^{+0.17}_{-0.15}\ (\text{stat.})\ ^{+0.13}_{-0.08}\ (\text{syst.}) = 0.51\ ^{+0.22}_{-0.17}\ \text{pb.}
\end{aligned} \tag{5.34}$$

compare well with the theoretical predictions for a SM Higgs boson, 3.3 ± 0.4 pb, 4.2 ± 0.5 pb, and 0.35 ± 0.02 pb, respectively.

Higgs boson production and decay rates and coupling strengths

6

Chapter 1 and in particular Sec. 1.4 summarize the phenomenology of Higgs boson production and decays at the LHC, building on the state-of-the-art theoretical calculations of the Higgs boson production cross sections and its decay BRs, which have been compiled in Refs. [135, 205, 453].

The discovery of the Higgs boson is made through the analyses of its bosonic decay modes in $H \to \gamma\gamma$, $H \to ZZ^* \to 4\ell$ and $H \to WW^* \to \ell\nu\ell\nu$ ($\ell = e, \mu$) events [4–6]. Since the discovery, these analyses have been improved and updated with more data [23, 24, 30]. The $H \to WW^* \to \ell\nu\ell\nu$ analysis has been supplemented with a dedicated VH analysis targeting $H \to WW^*$ [454]. The ATLAS collaboration has measured the Higgs boson mass from the $H \to \gamma\gamma$ and $H \to ZZ^* \to 4\ell$ decays to be $m_H = 125.36 \pm 0.41$ GeV [21], reported results in the $H \to \tau\tau$ [25] and $H \to b\bar{b}$ [26] fermionic decay modes, and published upper limits on the rare decays of $H \to Z\gamma$ [455] and $H \to \mu\mu$ [456]. Furthermore, constraints have been set on the ttH production rate [27, 28, 457] and on the off-shell coupling strengths of the Higgs boson [458]. These results are based on the full proton-proton collision data with integrated luminosities of up to 4.7 fb^{-1} at a centre-of-mass energy of 7 TeV recorded in 2011 and 20.3 fb^{-1} at $\sqrt{s} = 8$ TeV recorded in 2012 by the ATLAS detector at the LHC.

This chapter presents the combined results of the analyses mentioned above. These analyses are designed for maximum sensitivities to the Higgs boson production from different processes, exploiting in particular the differences in kinematics through categorisation of the selected events. Thus the yields of different Higgs boson production processes and decays can be extracted. The Higgs boson coupling strengths to SM vector bosons and fermions in different benchmark models are probed for the measured Higgs boson mass of $m_H = 125.36$ GeV. A similar combination has been published by the CMS collaboration [221].

6.1 Input analyses to the combinations

The combinations take inputs from the analyses of $H \to \gamma\gamma$, ZZ^*, WW^*, $\tau\tau$, $b\bar{b}$, $\mu\mu$ and $Z\gamma$ Higgs boson decay modes, and of the constraints on the ttH and off-shell Higgs boson production. These analyses and changes made for the combinations are briefly discussed in this section. The ATLAS Collaboration has also performed a search for the rare $H \to J/\psi\gamma$ decay [459] which has the potential to constrain the Higgs boson coupling strength to the

charm quark. However, the current result does not add sensitivity and is therefore omitted from the combinations. Furthermore, the inclusion of the results from direct searches for Higgs boson decays to invisible particles, such as that reported in Ref. [460], is beyond the scope of the combinations presented in this chapter.

All analyses use MC Higgs boson samples to model signal acceptances and efficiencies. Table 6.1 summarises the event generators and PDFs used. The ggF and VBF production of Higgs bosons is simulated with the NLO ME POWHEG-BOX program [407, 408, 410, 461, 462] interfaced to either PYTHIA [315] or PYTHIA8 [341] for the simulation of UE, PS and hadronization (referred as showering program). The Higgs boson p_T distribution of the ggF production is reweighted to match the calculation of HRES2.1 [434, 463], which includes QCD corrections up to the NNLO and NNLL in perturbative expansions. The WH and ZH ($q\bar{q} \to ZH$) production is simulated with the LO PYTHIA8 program. The $gg \to ZH$ production contributes approximately 8% to the total ZH production cross section in the SM. For most of the analyses, the process is modelled using $q\bar{q} \to ZH$ of PYTHIA8. Only the VH analysis in the $H \to b\bar{b}$ decay specifically models the $gg \to ZH$ production using POWHEG [407, 408, 461] interfaced to PYTHIA8. The ttH process is modelled using the NLO calculation of HELAC-Oneloop package [464] interfaced to POWHEG-BOX for the subsequent simulation, the chain is referred as POWHEL in the table. The tH production is simulated using MADGRAPH [465] interfaced to PYTHIA8 for $qg \to tHq'b$ and using MADGRAPH5_aMC@NLO [206] interfaced to HERWIG++ [466] for $gb \to WtH$. The bbH production is not explicitly simulated and its detection efficiency is assumed to be the same as for ggF. PDFs used in the event generations are CT10 [116] and CTEQL6L1 [115]. All Higgs boson decays are simulated by the showering programs. The predicted Higgs boson yields in the SM are calculated using the cross sections and BRs shown in Tab. 1.2.

Table 6.1: Summary of event generators, showering programs and PDF sets used to model the Higgs boson production and decays.

Production process	Event generator	Showering program	PDF set
ggF	POWHEG-BOX	PYTHIA/PYTHIA8	CT10
VBF	POWHEG-BOX	PYTHIA/PYTHIA8	CT10
WH	PYTHIA8	PYTHIA8	CTEQL6L1
ZH	PYTHIA8	PYTHIA8	CTEQL6L1
$ZH: gg \to ZH$	POWHEG	PYTHIA8	CT10
ttH	POWHEL	PYTHIA8	CT10
$tH: qg \to tHq'b$	MADGRAPH	PYTHIA8	CT10
$tH: gb \to WtH$	MADGRAPH5_aMC@NLO	HERWIG++	CT10

Table 6.2 gives an overview of the analyses that are inputs to the combinations and their main results, as published. An essential feature of these analyses is the extensive application of

exclusive categorisation, i. e., classifying candidate events based on the expected kinematics of the different Higgs boson production processes. The categorisation not only improves the analysis sensitivity, but also allows for the discrimination among different production processes. Figure 6.1 summarises the signal-strength measurements of different production processes that are used as inputs to the combinations.

Throughout this chapter, the signal-strength parameter μ is defined as the ratio between the measured Higgs boson rate and its SM expectation:

$$\mu = \frac{\sigma \times \mathrm{BR}}{(\sigma \times \mathrm{BR})_{\mathrm{SM}}}. \tag{6.1}$$

Here σ and BR are the production cross section and decay BR of the Higgs boson. For a specific production process i and decay channel f, i. e., $i \to H \to f$, the signal-strength parameter is labelled as μ_i^f.

Leptons (ℓ) refer to electrons or muons unless specified otherwise; the symbols τ_{lep} and τ_{had} refer to tau leptons identified through their decays to leptons or hadrons; and variables p_{T}, E_{T} and $E_{\mathrm{T}}^{\mathrm{miss}}$ refer to transverse momentum, transverse energy and missing transverse momentum, respectively. Notation indicating particle charges or antiparticles are generally omitted.

6.1.1 $H \to \gamma\gamma$

In the $H \to \gamma\gamma$ analysis, described in detail in Ref. [23], the Higgs boson signal is measured in events with at least two isolated and well identified photon candidates. The leading and subleading photon candidates are required to have $E_{\mathrm{T}}/m_{\gamma\gamma} > 0.35$ and 0.25, respectively, where $m_{\gamma\gamma}$ is the invariant mass of the two selected photons. The diphoton candidate events are grouped into twelve exclusive categories separately for the $\sqrt{s} = 7$ and 8 TeV datasets: the order of categorisation is chosen to give precedence to production modes with the most distinct signatures. Each category is optimised by adjusting the event selection criteria to minimise the expected uncertainty on the signal yield of the targeted production mode.

The first two categories are designed for ttH production based on the topology of leptonic and hadronic decays of the associated $t\bar{t}$ pair. They are described in Sec. 6.1.8 on the ttH production. The next four categories are optimised for VH production, targeting one-lepton, dilepton, missing transverse momentum, and hadronic signatures of both W and Z boson decays. Events from VBF production are identified by requiring two well-separated and high p_{T} jets and little hadronic activity between them. A BDT [444, 448] is employed to maximise the VBF signal and background separation. Events are sorted into two categories with different VBF purities according to the output value of the BDT. Finally, the remaining events are separated into four categories based on the pseudorapidities of the photons and the p_{Tt} of the diphoton system [23], the diphoton momentum transverse to its thrust axis in the transverse plane.

Table 6.2: Overview of the individual analyses that are included in the combinations described in this chapter. The signal strengths, the statistical significances of a Higgs boson signal, or the 95% CL upper limits on the Higgs boson production rates or properties are also shown wherever appropriate. A range is quoted for the upper limit on the off-shell signal strength, depending on the assumption of the continuum $gg \to WW/ZZ$ cross section. These results are taken directly from individual publications. Results of the on-shell analyses are quoted for $m_H = 125.36$ GeV except that $m_H = 125.5$ GeV is assumed for the $H \to Z\gamma$ and $H \to \mu\mu$ analyses and that $m_H = 125$ GeV is used for the ttH searches with $H \to b\bar{b}$ and $ttH \to$ multileptons. The luminosity used for the $\sqrt{s} = 7$ TeV $VH \to Vb\bar{b}$ analysis differs slightly from the other analyses because a previous version of the luminosity calibration was applied. The significance is given in units of standard deviations (σ). The numbers in parentheses are the expected values from the SM Higgs boson. The ttH analysis in the $H \to \gamma\gamma$ decay is part of the $H \to \gamma\gamma$ analysis and is also included separately under the ttH production for completeness. The checkmark (✓) indicates whether the analysis is performed for the respective $\sqrt{s} = 7$ and 8 TeV dataset.

Analysis	Signal		$\int \mathcal{L}dt$ (fb^{-1})	
Categorisation or final states	Strength μ	Significance [σ]	7 TeV	8 TeV
$H \to \gamma\gamma$ [23]	1.17 ± 0.27	5.2 (4.6)	4.5	20.3
ttH: leptonic, hadronic			✓	✓
VH: one-lepton, dilepton, missing transverse momentum, hadronic			✓	✓
VBF: tight, loose			✓	✓
ggF: 4 p_{Tt} categories			✓	✓
$H \to ZZ^* \to 4\ell$ [24]	$1.44^{+0.40}_{-0.33}$	8.1 (6.2)	4.5	20.3
VBF			✓	✓
VH: hadronic, leptonic			✓	✓
ggF			✓	✓
$H \to WW^*$ [30, 454]	$1.16^{+0.24}_{-0.21}$	6.5 (5.9)	4.5	20.3
ggF: (0-jet, 1-jet) $\otimes$ $(ee + \mu\mu,\ e\mu)$			✓	✓
ggF: $\geq$ 2-jet and $e\mu$				✓
VBF: $\geq$ 2-jet $\otimes$ $(ee + \mu\mu,\ e\mu)$			✓	✓
VH: opposite-charge dilepton, three-lepton, four-lepton			✓	✓
VH: same-charge dilepton				✓
$H \to \tau\tau$ [25]	$1.43^{+0.43}_{-0.37}$	4.5 (3.4)	4.5	20.3
Boosted: $\tau_{\mathrm{lep}}\tau_{\mathrm{lep}}, \tau_{\mathrm{lep}}\tau_{\mathrm{had}}, \tau_{\mathrm{had}}\tau_{\mathrm{had}}$			✓	✓
VBF: $\tau_{\mathrm{lep}}\tau_{\mathrm{lep}}, \tau_{\mathrm{lep}}\tau_{\mathrm{had}}, \tau_{\mathrm{had}}\tau_{\mathrm{had}}$			✓	✓
$VH \to Vb\bar{b}$ [26]	0.52 ± 0.40	1.4 (2.6)	4.7	20.3
0ℓ ($ZH \to \nu\nu bb$): $n_j = 2,3$, $n_b = 1,2$, $p_{\mathrm{T}}^V >$ and < 120 GeV			✓	✓
1ℓ ($WH \to \ell\nu bb$): $n_j = 2,3$, $n_b = 1,2$, $p_{\mathrm{T}}^V >$ and < 120 GeV			✓	✓
2ℓ ($ZH \to \ell\ell bb$): $n_j = 2,3$, $n_b = 1,2$, $p_{\mathrm{T}}^V >$ and < 120 GeV			✓	✓
		95% CL limit		
$H \to Z\gamma$ [455]		$\mu < 11$ (9)	4.5	20.3
10 categories based on $\Delta\eta_{Z\gamma}$ and p_{Tt}			✓	✓
$H \to \mu\mu$ [456]		$\mu < 7.0$ (7.2)	4.5	20.3
VBF and 6 other categories based on η_μ and $p_{\mathrm{T}}^{\mu\mu}$			✓	✓
ttH production [27, 28, 457]			4.5	20.3
$H \to b\bar{b}$: single-lepton, dilepton		$\mu < 3.4$ (2.2)		✓
$ttH \to$multileptons: categories on lepton multiplicity		$\mu < 4.7$ (2.4)		✓
$H \to \gamma\gamma$: leptonic, hadronic		$\mu < 6.7$ (4.9)	✓	✓
Off-shell H^* production [458]		$\mu < 5.1 - 8.6$ (6.7 − 11.0)		20.3
$H^* \to ZZ \to 4\ell$				✓
$H^* \to ZZ \to 2\ell 2\nu$				✓
$H^* \to WW \to e\nu\mu\nu$				✓

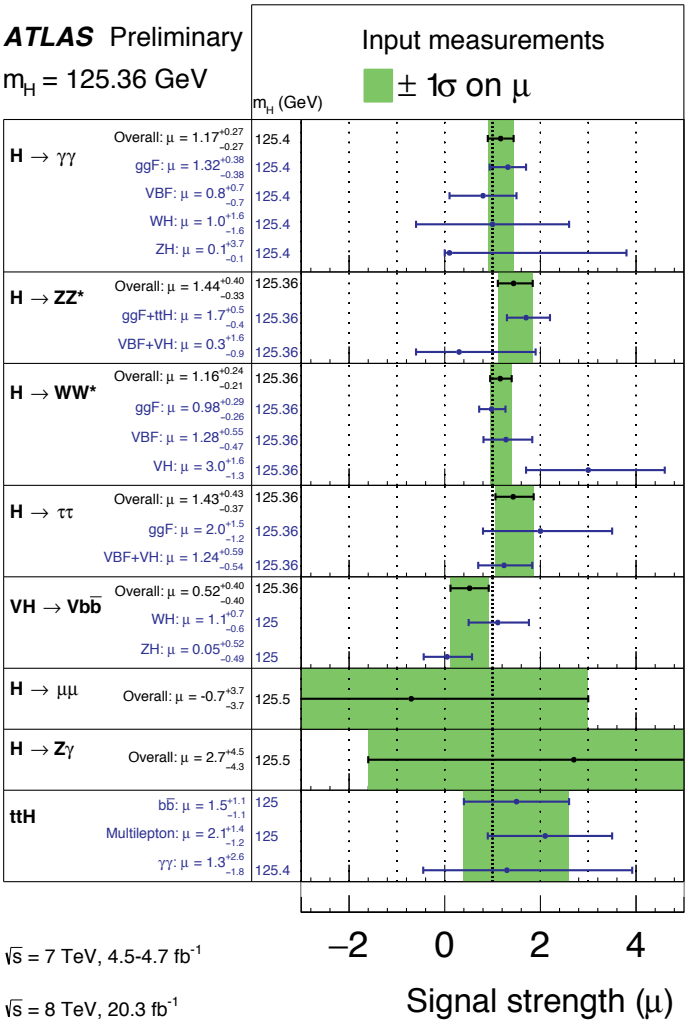

Figure 6.1: Summary of the signal-strength measurements, as published, from individual analyses that are inputs to the combinations. The Higgs boson mass column indicates the m_H value at which the result is quoted. The overall signal strength of each analysis (black) is the combined result of the measurements for different production processes (blue). The error bars represent $\pm 1\sigma$ total uncertainties, combining statistical and systematic contributions. The green shaded bands indicate the uncertainty of the overall signal strength of its respective analysis. The combined signal strength of the $H \to \gamma\gamma$ analysis also includes the ttH contribution which is listed separately under the ttH production.

For most of the categories, the background is composed of a mixture of $\gamma\gamma$, γ-jet and jet-jet events where one or two jets are misidentified as photons. In particular the $\gamma\gamma$ background is dominant and irreducible. The Higgs boson signal is extracted from maximum likelihood fits of a narrow resonance plus continuum background models to unbinned diphoton invariant mass distributions observed in the different event categories. In the fit, the signal is modelled by the sum of a Crystal Ball function [467] and a smaller but wider Gaussian component while the backgrounds are modelled by category-dependent exponential functions of first- or second-order polynomials.

6.1.2 $H \to ZZ^* \to 4\ell$

The $H \to ZZ^* \to 4\ell$ analysis, described in detail in Ref. [24], has a high signal-to-background ratio, which is about two for each of the four final states considered: 4μ, $2e2\mu$, $2\mu2e$, and $4e$, where the first lepton pair has an invariant mass closest to the Z boson mass. The analysis selects Higgs boson candidates by requiring two pairs of isolated, same flavor and opposite charge leptons with one of the two pairs having a dilepton invariant mass in the range of $50-106$ GeV.

To measure the rates of different production processes, each $H \to ZZ^* \to 4\ell$ candidate is assigned to one of four categories depending on event characteristics beyond the four selected leptons. The VBF category consists of candidates with two additional jets of dijet mass $m_{jj} > 130$ GeV. The events failing this selection are considered for the VH-hadronic category, where the dijet mass is required to be $40 < m_{jj} < 130$ GeV. Events failing the VH-hadronic category criteria are considered for the VH-leptonic category with the requirement of an additional lepton. Finally, the remaining events are assigned to the ggF category. The separation of VBF and VH production from the dominant ggF production mode is improved by exploiting two BDT discriminants trained on the jet kinematics, one for the VBF and the other for the VH-hadronic categories. A third BDT discriminant based on the four lepton kinematics is used to improve the separation between the ggF signal and its main background.

The largest background comes from continuum ZZ^* production and is estimated using simulation normalised to the SM next-to-leading-order cross section calculation. For the four-lepton events with an invariant mass, $m_{4\ell}$, below about 160 GeV, there are also important background contributions from Z+jets and $t\bar{t}$ production with two prompt leptons, where the additional charged lepton candidates arise from decays of hadrons with b- or c-quark content, from photon conversions or from misidentified jets. Their contributions are estimated with data-driven methods.

For each category, the signal is extracted from a maximum likelihood fit to either the $m_{4\ell}$ distribution (VH categories) or the combined two-dimensional distributions of $m_{4\ell}$ and a BDT discriminant (ggF and VBF categories). The four-lepton mass range of $110 < m_{4\ell} < 140$ GeV is included in the fits.

6.1.3 $H \to WW^*$

Analyses targeting the ggF, VBF, and VH production modes [30, 454] are performed for the $H \to WW^*$ decay channel. The ggF and VBF production processes are explored through the $H \to WW^* \to \ell\nu\ell\nu$ decay while the VH process is studied in final states with two or more leptons. A detailed description of analyses targeting the ggF and VBF production modes is given in Cha. 5.

The analysis of the ggF and VBF production processes [30] selects the signal candidate events by requiring two oppositely charged leptons. Candidates are categorised according to the number of jets (n_j) and lepton flavors. The n_j categorisation separates the large background of the top-quark production from the ggF signal while the categorisation by lepton flavors isolates the most challenging DY background in the same flavor categories. The categories targeting the ggF production include $n_j = 0$, 1 and ≥ 2 and are further divided into the same- and different-flavor leptons for $n_j = 0$, 1. Only the different-flavor leptons are considered for $n_j \geq 2$. The category targeting the VBF analysis requires $n_j \geq 2$ with same- or different-flavor leptons. The primary background processes are WW, top quark ($t\bar{t}$ and Wt), W+jets, DY, and other diboson (WZ, $W\gamma$, $W\gamma^*$, and ZZ) production. Most of the background contributions are estimated using data. For the ggF categories, the final SR is selected by $m_{\ell\ell} < 55$ GeV and $\Delta\phi_{\ell\ell} < 1.8$ and the signal is extracted through a combined fit to the transverse mass distributions of the dilepton plus missing transverse momentum system. For the VBF categories, a BDT combining information such as rapidity separation and mass of the two leading jets and the dilepton angular separation, is used as the final discriminant, from which the signal is extracted.

The VH analysis [454] is optimised for different lepton multiplicities: opposite-charge dileptons, same-charge dileptons, three- and four-leptons. Most final states are required to have missing transverse momentum and events with a b-tagged jet are vetoed. Dilepton final states target $VH \to VWW^*$ production with two bosons decaying leptonically and the other hadronically. The opposite-charge dilepton final state selects events with two or more jets, with the value of m_{jj} required to be close to the W and Z boson masses. Similar to the ggF $n_j \geq 2$ category, the dominant background is from top quark production. The same-charge dilepton category accepts events with either one or two jets. The dominant backgrounds are from WZ, $W\gamma^{(*)}$, and W+jets production. The three-lepton final state targets $WH \to WWW^*$ and has the highest sensitivity of the four final states. The three leptons are required to have a net charge of ± 1 and the event can have at most one jet. The dominant background process is WZ production and is reduced with a $Z \to \ell\ell$ veto. The four-lepton category is designed to accept events from $ZH \to ZWW^*$ production. The net charge of the leptons is required to be zero and at least one pair of leptons is required to have the same flavor, opposite sign, and an invariant mass close to the Z boson mass. The dominant background is SM ZZ^* production. In the three-lepton category, the signal yield is extracted through fits to distributions of a BDT or the minimum ΔR between opposite-charged leptons depending on lepton flavors.

For other categories, the event yields are used, without exploiting information on the shapes of distributions.

6.1.4 $H \to \tau\tau$

The $H \to \tau\tau$ analysis [25] considers both leptonic (τ_{lep}) and hadronic (τ_{had}) decays of the tau lepton. Three sub-channels ($\tau_{\text{lep}}\tau_{\text{lep}}$, $\tau_{\text{lep}}\tau_{\text{had}}$ and $\tau_{\text{had}}\tau_{\text{had}}$) are defined by orthogonal requirements on the number of reconstructed hadronic tau decays and leptons (electrons or muons) in the event[1].

Candidate events are divided into boosted and VBF categories. The boosted category targets signal events where the Higgs boson has been produced with a large boost, primarily from the ggF process, and requires the transverse momentum of the reconstructed Higgs boson candidate to be greater than 100 GeV. The VBF category contains events with two jets separated in pseudorapidity and targets signal events produced through the vector boson fusion process. A separate BDT is then employed in each category and sub-channel to discriminate signal from background, utilising between five and nine input variables, chosen in order to exploit discriminating features such as Higgs boson decay properties, event activity, and the VBF topology in the corresponding category. One of the most important input variables is the mass of the ditau system, which is quite challenging to reconstruct due to the presence of at least two neutrinos in the final state; the Missing Mass Calculator (MMC) [468] is used for this purpose.

In all three sub-channels, the most important backgrounds are irreducible $Z \to \tau\tau$ events, and events with one or two jets misidentified as tau lepton decay products (primarily from multijet and W+jets production). To estimate the former, the embedding technique [25] is used, where $Z \to \mu\mu$ events are selected in data and the reconstructed muons are replaced by simulated tau lepton decays. Fully data-driven techniques are used for the estimation of backgrounds from misidentified tau decay products, while MC corrected to data is used for other backgrounds, such as the top quark and $Z \to \ell\ell$ production.

The signal is extracted by fitting the shape of the BDT discriminant with signal and background templates simultaneously in all SRs. The fit also includes dedicated control regions enriched with top quark, $Z \to \ell\ell$ and multijet events. These control regions are used to constrain normalisations of the corresponding backgrounds.

[1] For events with two leptons, a requirement on the invariant mass of the ditau system reconstructed via the collinear approximation also ensures orthogonality with the $H \to WW^* \to \ell\nu\ell\nu$ analysis.

6.1.5 *VH* with $H \to b\bar{b}$

The $H \to b\bar{b}$ decay mode is predicted in the SM to have the largest BR (see Tab. 1.2b). In spite of this large BR, an inclusive search for $H \to b\bar{b}$ is not feasible because of the overwhelming background from multijet production. Associated production of a Higgs boson with a vector boson V (W or Z), offers a viable alternative because leptonic decays of the vector boson, $W \to \ell\nu$, $Z \to \ell\ell$, and $Z \to \nu\nu$, can be efficiently used for triggering and background reduction.

The search for associated VH production with $H \to b\bar{b}$ [26] is performed for events containing zero, one, or two charged leptons. Contributions from $W \to \tau\nu$ and $Z \to \tau\tau$ decays in which the tau leptons subsequently decay to electrons or muons are also included. A b-tagging algorithm is used to identify jets from $H \to b\bar{b}$ decays. To improve the sensitivity, the three channels are each split into categories according to the vector-boson transverse momentum, p_{T}^{V}, the number of jets, and the number and quality of b-tagged jets. Topological and kinematic selection criteria are applied within each of the resulting categories. The categories providing most of the sensitivity are those requiring two b-tagged jets and large p_{T}^{V}. The categories with low sensitivity are used to constrain the contributions of the dominant background processes.

A binned profile maximum likelihood fit to all categories simultaneously is used to extract the signal yield and the background normalisations. The most significant background sources are V+heavy-flavor-jet production and $t\bar{t}$ production. The normalisations of these backgrounds are fully determined by the likelihood fit. Other significant background sources are single-top-quark and diboson (WZ and ZZ) production, with normalisations from theory, as well as multijet events. The shapes of all backgrounds are estimated from simulation, except for the multijet background for which the shape and normalisation are obtained using multijet-enriched control samples.

Two versions of the analysis are performed. In the dijet-mass analysis, the mass of the dijet system of b-tagged jets is the final discriminating variable used in the statistical analysis. In the multivariate analysis (MVA), which incorporates various kinematic variables in addition to the dijet mass as well as b-tagging information, the outputs of BDTs provide the final discriminating variable. Since the MVA has higher expected sensitivity, it is chosen as the nominal analysis for the $\sqrt{s} = 8$ TeV dataset to extract the final results. For the $\sqrt{s} = 7$ TeV dataset, only a dijet-mass analysis is performed.

6.1.6 $H \to Z\gamma$

The $H \to Z\gamma$ analysis [455] with $Z \to \ell\ell$ searches for a narrow peak in the reconstructed $\ell\ell\gamma$ invariant-mass distribution around 125 GeV over a smooth background. The Z+γ production, $Z \to \ell\ell\gamma$ radiative decays and Z+jets events where a jet is misidentified as a photon dominate the background contributions.

The analysis selects two isolated leptons of same flavor and opposite charge and one isolated photon. Due to the kinematics of the decay, low p_{T} thresholds are applied to the leptons and the photon. The invariant mass of the dilepton system should satisfy $m_{\ell\ell} > m_Z - 10$ GeV and the three-body invariant mass should be consistent with the mass of the Higgs boson. To enhance the sensitivity of the analysis, events are classified into categories with different signal-to-background ratios and invariant-mass resolutions, based on the pseudorapidity difference $\Delta\eta_{Z\gamma}$ between the photon and the Z boson and p_{Tt}, the component of the Higgs boson candidate p_{T} that is orthogonal to the $Z\gamma$ thrust axis in the transverse plane.

The final discrimination between signal and background events is based on a simultaneous likelihood fit to the $m_{\ell\ell\gamma}$ spectra in each category, separately for the $\sqrt{s} = 7$ and 8 TeV datasets. Similar to the $H \to \gamma\gamma$ analysis (cf. Sec. 6.1.1), the signal is modelled with the sum of a Crystal Ball function and a smaller but wider Gaussian component while the backgrounds are modelled with polynomials, or exponentiated polynomials depending on categories.

6.1.7 $H \to \mu\mu$

The $H \to \mu\mu$ analysis [456] searches for a narrow peak in the dimuon invariant mass $m_{\mu\mu}$ distribution over a smooth background, where the width of the signal is dominated by the experimental resolution. The mass spectrum is dominated by the continuously falling background due to the Z/γ^* production, with smaller contributions from top quark and diboson production.

The selected events containing a pair of oppositely charged muons are separated into seven mutually exclusive categories based on the VBF dijet signature, the muon pseudorapidity η_μ, and the transverse momentum of the dimuon system $p_T^{\mu\mu}$. The events with two or more jets that match selections designed for the VBF process are accepted in the VBF SR. All other selected events are split up into six categories based on η_μ and $p_T^{\mu\mu}$. This categorisation takes advantage of the higher momentum resolution of muons reconstructed in the central part of the detector, and high $p_T^{\mu\mu}$ for the expected SM signal.

The $m_{\mu\mu}$ distribution in the $110-160$ GeV region is fitted with an analytic signal plus background model separately for the $\sqrt{s} = 7$ and 8 TeV datasets, setting a limit on the dimuon decay of the SM Higgs boson with a mass of 125.5 GeV. In the fit, the signal is modelled as the sum of a Crystal Ball and a Gaussian function in all regions while the backgrounds are modelled using exponentials or polynomials.

6.1.8 *ttH* production

Searches for $q\bar{q}/gg \to t\bar{t}H$ production have been performed with three analyses targeting the Higgs boson decays of $H \to b\bar{b}$; $H \to (WW^*, \tau\tau, ZZ^*) \to$ leptons; and $H \to \gamma\gamma$. The search in the $H \to \gamma\gamma$ decay mode uses both $\sqrt{s} = 7$ and 8 TeV data, while the other two use only the $\sqrt{s} = 8$ TeV data.

The search for ttH production with $H \to b\bar{b}$ [27] considers two separate selections optimised for single-lepton and dilepton final states of $t\bar{t}$ decays. In the single-lepton channel, events are required to have one isolated electron or muon and at least four jets. In the dilepton channel, events are required to have two opposite-charged leptons (ee, $\mu\mu$ or $e\mu$) and at least two jets; events consistent with originating from a $Z \to \ell\ell$ decay are rejected. In both cases at least two b-tagged jets are required. Candidate events are categorised according to the jet and b-jet multiplicities with a total of 9 (6) categories for the single-lepton (dilepton) final states. The background is dominated by $t\bar{t}$+jets events, with increasing fractions of $t\bar{t}b\bar{b}$ and $t\bar{t}c\bar{c}$ at the higher b-jet multiplicities characteristic of signal events. The analysis uses a NN to discriminate signal from background in the most signal-like categories. Simpler kinematic discriminants are used in background-like categories.

The ttH search with $H \to WW^*$, $\tau\tau$ and ZZ^* decays [28] exploits several multilepton signatures resulting from leptonic decays of vector bosons and/or the presence of tau leptons. The events are categorised by the number of reconstructed electrons or muons and hadronic tau candidates. The five channels used in this combination are: one lepton with two hadronic tau candidates, two same-charge leptons with zero or one hadronic tau candidates, three leptons, and four leptons. The largest backgrounds to the analysis are non-prompt leptons, primarily arising from semileptonic B-hadron decays in $t\bar{t}$ events; electron charge misreconstruction in events where opposite-sign leptons are produced and the production of $t\bar{t}W$ and $t\bar{t}Z$ ($t\bar{t}V$). The potential signal is determined from the numbers of observed events in data and of the estimated background events.

The ttH search in the $H \to \gamma\gamma$ channel [457] is part of the $H \to \gamma\gamma$ analysis (cf. Sec. 6.1.1) and employs the same diphoton selection. The leptonic as well as fully-hadronic decay signatures of the $t\bar{t}$ system are considered. The leptonic selection requires at least one lepton and one b-tagged jet as well as missing transverse momentum. In the hadronic selection, different combinations of jet and b-tagging multiplicities are applied to improve the signal sensitivity. The small contribution from ggF, VBF and VH productions is estimated from MC simulation. The ttH signal is extracted from a fit to the observed diphoton mass distribution.

6.1.9 Off-shell Higgs boson production

Measurements of the $H^* \to ZZ$ and $H^* \to WW$ final states in the mass range above the $2m_Z$ and $2m_W$ thresholds (off-shell region) provide a unique opportunity to measure the

off-shell coupling strengths of the observed Higgs boson, as discussed in Refs. [469–472]. The $ZZ \to 4\ell$, $ZZ \to 2\ell 2\nu$ and $WW \to e\nu\mu\nu$ final states of the $\sqrt{s} = 8$ TeV dataset are used in these measurements, detailed in Ref. [458]. Assuming the relevant Higgs boson coupling strengths are independent of the energy scale of the Higgs boson production, a combination with the on-shell measurements can be interpreted as a constraint on the total width of the Higgs boson.

The analysis in the $ZZ \to 4\ell$ final state follows closely the Higgs boson measurements in the same final state, described in Sec. 6.1.2, with the same object definitions, event selections and background estimation methods. The off-peak region is defined to include the range $220 < m_{4\ell} < 1000$ GeV. Like the $H \to ZZ^* \to 4\ell$ analysis, the background is dominated by the $q\bar{q}/gg \to ZZ$ production. A matrix element based discriminant [458] is constructed to enhance the $gg \to H^* \to ZZ$ signal and is used in a binned maximum likelihood fit for the final result.

The analysis in the $ZZ \to 2\ell 2\nu$ channel follows closely the ZH analysis with the Higgs boson decaying to weakly interacting particles [460], with the same object definitions. As the analysis is performed inclusively in the number of jets in the final states, kinematic cuts are optimised accordingly. SM ZZ and WZ production are the major backgrounds. The transverse mass (m_{T}^{ZZ}) [458], reconstructed from the momentum of the dilepton system and the missing transverse momentum, is chosen as the discriminating variable. Events in the range of $380 < m_{\mathrm{T}}^{ZZ} < 1000$ GeV are used in a binned maximum likelihood fit for the final result.

The analysis in the $WW \to e\nu\mu\nu$ channel follows closely the Higgs boson measurements in the oppositely charged electron-muon pair final state, described in Sec. 6.1.3, with the same object definitions. The analysis is performed inclusively in the number of jets in the final state, and selections are optimised for the off-shell region with revised background estimation methods. Top quark pairs and WW events constitute the major backgrounds. In order to isolate the off-shell Higgs boson production while minimising sensitivity to higher-order QCD effects on $gg \to WW$ kinematics, a new variable R_8 [454], defined as the weighted combination of the dilepton mass and the transverse mass of the dilepton and missing transverse momentum system, is constructed to select the SR. Events in the SR, $\mathrm{R}_8 > 450$ GeV, are used in a counting experiment for the final results.

6.1.10 Modifications of analyses

To ensure a consistent interpretation of all inputs in terms of Higgs boson coupling strengths, several minor modifications were made to the inputs of these combinations with respect to their previously published versions:

- The upper limits on the $H \to Z\gamma$ and $H \to \mu\mu$ decays and the results of the ttH searches in $H \to b\bar{b}$ and $ttH \to$ multileptons have been updated to assume a Higgs boson mass of 125.36 GeV.

- In some individual analyses, cross-feed of other Higgs boson decays occurs: in the $VH \to WW^*$ selection cross-feed of $H \to \tau\tau$ and $H \to ZZ^*$ occurs (whereas this cross-feed is negligible in the ggF and VBF $H \to WW^*$ analyses where a veto on the reconstructed $\tau\tau$ mass has been applied). Similarly, there is cross-feed from $H \to WW^*$ in the $H \to \tau\tau$ analysis. In such cases, this cross-feed was treated as background in the relevant individual channel analyses. For the coupling strength combination, such events are interpreted as signal from the corresponding Higgs boson decay.

- The rate of $gg \to ZH$ events in the VH channels has been parameterised in terms of Higgs boson coupling strengths to Z bosons and top quarks, following the calculations of Ref. [159] for $\sqrt{s} = 7$ and 8 TeV.

- The rate of tH events in all the ttH channels has been parameterised in terms of Higgs boson coupling strengths to W bosons and top quarks.

- In the standalone analysis of the ttH channels small contributions of Higgs decay to cc and gg are explicitly modeled. To avoid spurious sensitivity due to these very small components in the combined analyses presented in this chapter, both aforementioned decays are treated like $H \to b\bar{b}$ in the fits for the Higgs signal strength. In fits for Higgs coupling strenghts, $H \to cc$ is also treated like $H \to b\bar{b}$, but $H \to gg$ is implemented as an expression in terms of the Higgs gluon coupling strength scale factor.

- Theoretical uncertainties on QCD scales in Higgs boson signal processes have consistently been updated to the latest recommendations [135] for $H \to WW^*$, $H \to b\bar{b}$, $H \to \tau\tau$ and $H \to Z\gamma$. No modifications were needed for the $H \to \gamma\gamma$ and $H \to ZZ^*$ channels.

- In channels where bbH production was not explicitly modeled, the signal strength of ggF is redefined to include this process. In channels where bbH was modelled explicitly ($H \to \gamma\gamma, ZZ^*$), ggF and bbH production are correlated with their ratio fixed to the SM value, allowing a consistent treatment of bbH production across all channels. The impact of this average scaling on the results is negligible since, as can be seen in Tab. 6.2, the bbH production process has a cross section which is only 1% of the ggF production in the SM.

- The off-shell analysis depends on the unknown K-factor, $R^B_{H^*}$, for the $gg \to H^* \to VV$ background process. In the case of the very similar Higgs boson signal production process, a K-factor between 0.5 and 2 is expected, as discussed in Ref. [458], and the full range from these calculations is used as a systematic uncertainty on $R^B_{H^*}$.

6.2 Signal strength measurements

This section discusses the measurements of the signal-strength parameter μ of different production modes and decay channels as well as their ratios for a fixed Higgs boson mass hypothesis of $m_H = 125.36\,\text{GeV}$ [440]. The signal-strength parameter is a measure of potential deviations from the SM prediction under the assumption that the Higgs boson production and decay kinematics do not change appreciably from the SM expectations. In particular, the transverse momentum and rapidity distributions of the Higgs boson are assumed to be those predicted for the SM Higgs boson by state-of-the-art event generators and calculations of each production process. This assumption is corroborated by studies such as the measurements of differential production cross sections [473, 474] and tests of spin and CP properties of the Higgs boson [32, 222].

For the signal-strength discussion below, bbH is included in ggF, tH in ttH and $gg \to ZH$ in VH unless noted otherwise. The ggF and bbH processes lead to similar event signatures and no attempt is made to separate them in the analyses. The ttH and tH events have similar topologies. The $gg \to ZH$ process leads to the same final state as the $q\bar{q} \to ZH$ process via VH production.

6.2.1 Global signal strength

In Sec. 6.1, the published ATLAS measurements on Higgs boson production and decay modes as well as the changes since their publications are summarised. Figure 6.2 shows the updated measurements of the signal-strength parameter μ from a simultaneous fit to all decay channels analysed. Most of these results are similar to the separate measurements shown in Fig. 6.1. A few noticeable changes can be attributed to the assignment of the Higgs boson yield of the ttH searches to appropriate Higgs boson decay channels. For example, the result of the ttH search in $H \to b\bar{b}$ is combined with that of the VH analysis of the $H \to b\bar{b}$ decay. The measurements are consistent and compatible with a single value with a p-value of 76%. Assuming a common multiplier to all signal yields, they can be combined to give a global, more precise measurement of the signal-strength parameter, providing the simplest consistency test with the SM expectation. Combining all measurements using the profile likelihood ratio (PLR) $\Lambda(\mu)$ results in a global signal-strength value of

$$\mu = 1.18^{+0.15}_{-0.14} = 1.18 \pm 0.10\,(\text{stat.}) \pm 0.07\,(\text{expt.})^{+0.08}_{-0.07}\,(\text{theo.})\,^{2}, \tag{6.2}$$

consistent with the SM expectation of $\mu = 1$ with a p-value of 18%. The uncertainty of the combination has comparable statistical and systematic components and is notably reduced compared with individual measurements as illustrated in Fig. 6.2. Here the theoretical uncertainty includes contributions from those on SM cross sections and BRs as well as on the modellings of the production and decays of the Higgs boson. The theoretical uncertainties on background processes are included in the uncertainty labelled as experimental systematic

[2] In this chapter, stat., expt. and theo. refer to statistical, experimental and theoretical systematic uncertainties.

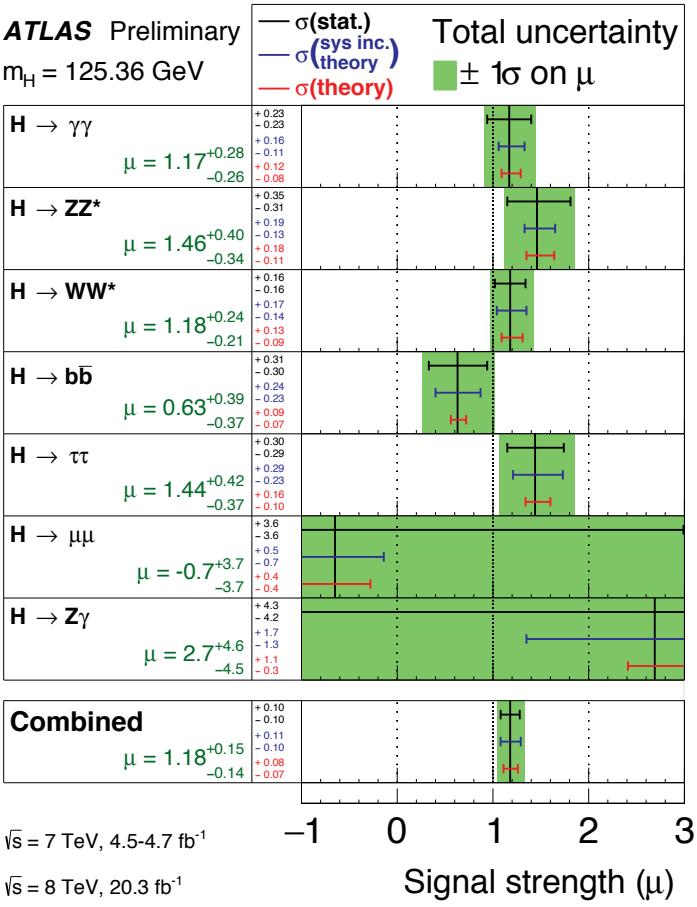

Figure 6.2: The observed signal strengths and uncertainties for different Higgs boson decay channels and their combination for $m_H = 125.36$ GeV. Higgs boson signals corresponding to the same decay channel are combined together for all analyses. The best-fit values are shown by the solid vertical lines. The total $\pm 1\sigma$ uncertainties are indicated by green shaded bands, with the individual contributions from the statistical uncertainty (top), the total (experimental and theoretical) systematic uncertainty (middle), and the theory systematic uncertainty (bottom) on the signal strength shown as horizontal error bars.

uncertainty. The relative theoretical uncertainty of the measured μ value is smaller than that of the total SM cross section (Tab. 1.2a) as μ is effectively a weighted average of the signal strength measurements in all categories: the contributions from VBF and VH production, which have comparatively small theoretical uncertainties, have a larger weight in this

average than in the total cross section. Combinations of measurements at $\sqrt{s} = 7$ and 8 TeV independently lead to signal-strength values of

$$\mu(7\,\text{TeV}) = 0.75\,^{+0.32}_{-0.29} = 0.75\,^{+0.28}_{-0.26}\,(\text{stat.})\,^{+0.13}_{-0.11}\,(\text{expt.})\,^{+0.08}_{-0.05}\,(\text{theo.}), \quad \text{and} \tag{6.3}$$

$$\mu(8\,\text{TeV}) = 1.28\,^{+0.17}_{-0.15} = 1.28 \pm 0.11\,(\text{stat.})\,^{+0.08}_{-0.07}\,(\text{expt.})\,^{+0.10}_{-0.08}\,(\text{theo.}) \tag{6.4}$$

at these two energies.

A significant component of the theoretical uncertainty is associated with the SM predictions of the Higgs boson production cross sections and decay BRs. Advances in theoretical calculations are required to improve the precision of future measurements.

6.2.2 Boson and fermion-mediated production processes

The measurements of the signal strengths described above assume the SM predictions of the relative contributions of different Higgs boson production processes and/or decay channels. Thus they may conceal differences between data and theoretical predictions. Therefore, in addition to the signal strengths of different decay channels, the signal strengths of different production modes are determined, exploiting the sensitivity offered by the use of event categories in the analyses of all channels.

The Higgs boson production processes can be categorised into two groups according to the Higgs boson couplings to fermions (ggF and ttH) or vector bosons (VBF and VH). Potential deviations from the SM can be tested with two signal-strength parameters, $\mu^f_{\text{ggF}+ttH} \equiv (\mu^f_{\text{ggF}} = \mu^f_{ttH})$ and $\mu^f_{\text{VBF}+VH} \equiv (\mu^f_{\text{VBF}} = \mu^f_{VH})$ for each decay channel f. The 68% and 95% CL two-dimensional contours of $\mu^f_{\text{ggF}+ttH}$ and $\mu^f_{\text{VBF}+VH}$ of the five main decay channels are shown in Fig. 6.3. The cutoff in the contours of the $H \to \gamma\gamma$ and $H \to ZZ^*$ decays is caused by the expected sum of signal and backgrounds yield in one of the contributing measurements going below zero in selected regions of the parameter space shown in Fig. 6.3. The SM expectation of $\mu^f_{\text{ggF}+ttH} = 1$ and $\mu^f_{\text{VBF}+VH} = 1$ is within the 68% CL contour of most of these measurements.

The relative production cross sections of the vector boson and fermion-mediated processes can be tested using the ratio of $\mu^f_{\text{VBF}+VH}/\mu^f_{\text{ggF}+ttH}$. When measured separately for each decay channel, this ratio (shown in Fig. 6.4) reduces to the ratio of production cross sections as the Higgs boson decay BRs cancel, i. e.,

$$\mu^f_{\text{VBF}+VH}/\mu^f_{\text{ggF}+ttH} = \frac{\sigma_{\text{VBF}+VH}/\sigma_{\text{ggF}+ttH}}{\left[\sigma_{\text{VBF}+VH}/\sigma_{\text{ggF}+ttH}\right]_{\text{SM}}} \equiv R_{ff}\,. \tag{6.5}$$

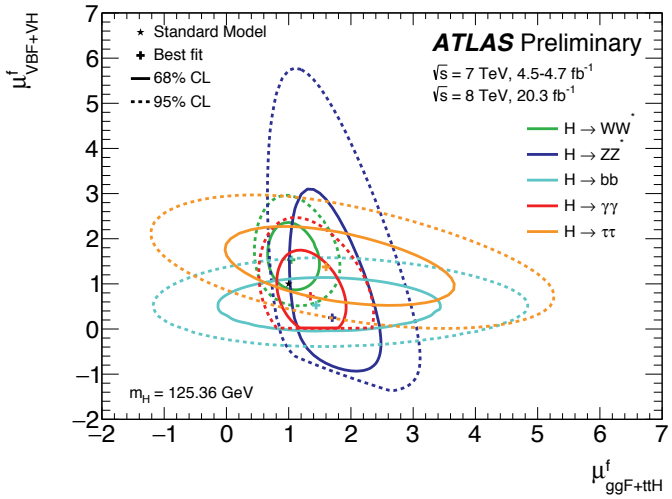

Figure 6.3: Likelihood contours in the $(\mu^{f}_{\mathrm{ggF}+ttH}, \mu^{f}_{\mathrm{VBF}+VH})$ plane for a Higgs boson mass $m_H = 125.36$ GeV measured separately for $H \to WW^*$, ZZ^*, $b\bar{b}$, $\gamma\gamma$ and $\tau\tau$ decays. The sharp lower edges of the $H \to \gamma\gamma$ and $H \to ZZ^* \to 4\ell$ contours are due to the small numbers of events in these channels and the requirement of a positive probability density function. The best-fit values to the data (+) and the 68% (full) and 95% (dashed) CL contours are indicated, as well as the SM expectation ($\star$).

The combination of these measurements yields an overall value of the cross section ratio between the boson- and fermion-mediated processes (relative to its SM prediction):

$$R_{\mathrm{Combined}} = 0.96^{+0.43}_{-0.31} = 0.96^{+0.34}_{-0.26}\,(\mathrm{stat.})^{+0.19}_{-0.13}\,(\mathrm{expt.})^{+0.18}_{-0.10}\,(\mathrm{theo.}). \tag{6.6}$$

consistent with the SM expectation of one.

6.2.3 Individual production processes

The Higgs boson production modes can be probed with four signal-strength parameters: μ_{ggF}, μ_{VBF}, μ_{VH} and μ_{ttH}, one for each main production mode, assuming the SM values of the Higgs boson decay BRs. The SM predictions of the signal yields are scaled by these four production-dependent parameters. The best-fit values of these parameters for the $\sqrt{s} = 8$ TeV data separately and the combination with the $\sqrt{s} = 7$ TeV data are shown in Tab. 6.3. Uncertainties are broken down into statistical, experimental and theoretical systematic components. The theoretical components include both theory uncertainties on the SM cross sections and branching ratios and on the signal modelling. The $\sqrt{s} = 7$ and 8 TeV combined values with their total uncertainties are also illustrated in Fig. 6.5. The $\sqrt{s} = 7$ TeV data are included in the combinations only as they have limited statistical power to distinguish between different production modes. The signal-strength measurements are in reasonable agreement with the SM predictions of unity. Though the results indicate evidence for ttH production (see

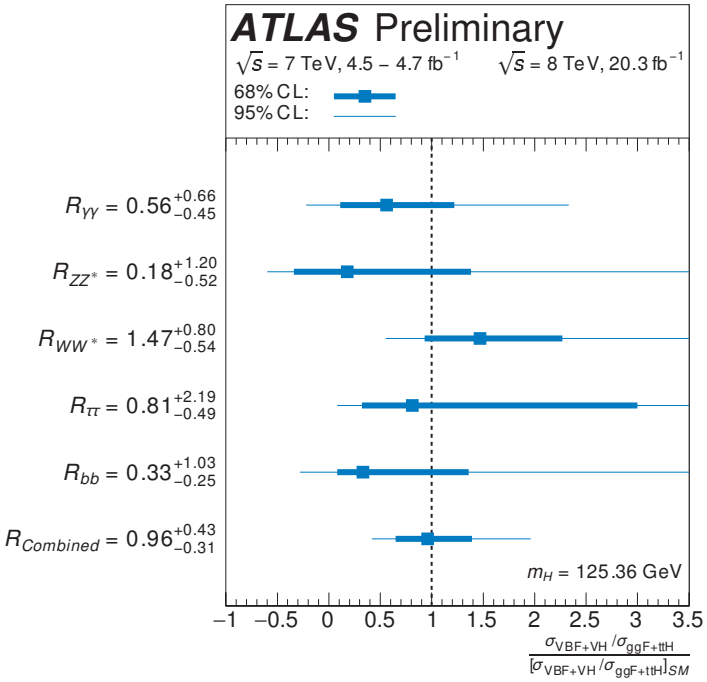

Figure 6.4: The cross section ratios between vector boson and fermion-mediated processes relative to their SM values at $m_H = 125.36$ GeV, measured in the individual Higgs boson decay final states and their combination, R_{Combined} (see text). The inner and outer error bars represent 68% CL and 95% CL intervals, combining statistical and systematic uncertainties. These measurements are independent on the assumptions of Higgs boson decay BRs.

Sec. 6.2.4), this production process remains to be firmly established in future LHC runs. Thus, a 95% upper limit on its signal strengths is also derived. Combining the results from various analyses with sensitivity to ttH production, the observed and expected limits are $\mu_{ttH} < 3.2$ and 1.4, respectively.

The signal-strength measurements shown in Tab. 6.3 are extrapolated to total cross section measurements for each production process, as shown in Tab. 6.4 for $\sqrt{s} = 8$ TeV. The theoretical uncertainties on the SM Higgs production cross sections are thereby removed, but significant theoretical uncertainties remain, related in particular to the modelling of the Higgs boson production and of the limited acceptance of the event selection in some analyses. One can sum the different cross sections to obtain an overall extrapolated cross section for Higgs boson production. Despite its limited statistical power, the $\sqrt{s} = 7$ TeV data neverthe-

Table 6.3: Measured signal strengths μ at $m_H = 125.36$ GeV and their total $\pm1\sigma$ uncertainties for different production modes for the $\sqrt{s} = 8$ TeV data and the combination with the $\sqrt{s} = 7$ TeV data. The $\sqrt{s} = 7$ TeV data do not have sufficient statistical power to yield meaningful measurements for individual production modes, but are included in the combination. Shown in the square brackets are uncertainty components: statistical (first), experimental (second) and theoretical (third) systematic uncertainties. These results are derived using the SM values of the Higgs boson decay BRs.

Production process	Signal strength μ at $m_H = 125.36$ GeV	
	$\sqrt{s} = 8$ TeV	Combined $\sqrt{s} = 7$ and 8 TeV
ggF	$1.23^{+0.25}_{-0.21}$ $\left[^{+0.16\ +0.10\ +0.16}_{-0.16\ -0.08\ -0.11}\right]$	$1.23^{+0.23}_{-0.20}$ $\left[^{+0.14\ +0.09\ +0.16}_{-0.14\ -0.08\ -0.12}\right]$
VBF	$1.55^{+0.39}_{-0.35}$ $\left[^{+0.32\ +0.17\ +0.13}_{-0.31\ -0.13\ -0.11}\right]$	1.23 ± 0.32 $\left[^{+0.28\ +0.13\ +0.11}_{-0.27\ -0.12\ -0.09}\right]$
VH	0.93 ± 0.39 $\left[^{+0.37\ +0.20\ +0.12}_{-0.33\ -0.18\ -0.06}\right]$	0.80 ± 0.36 $\left[^{+0.31\ +0.17\ +0.10}_{-0.30\ -0.17\ -0.05}\right]$
ttH	1.62 ± 0.78 $\left[^{+0.51\ +0.58\ +0.28}_{-0.50\ -0.54\ -0.10}\right]$	1.81 ± 0.80 $\left[^{+0.52\ +0.58\ +0.31}_{-0.50\ -0.55\ -0.12}\right]$

Table 6.4: Measured cross sections of different Higgs boson production modes at $\sqrt{s} = 8$ TeV for $m_H = 125.36$ GeV obtained from the signal-strength values of Table 6.3. Uncertainty breakdowns are shown in the square brackets. These results are derived using the SM values of the Higgs boson decay BRs.

Production process	Cross section (pb) at $\sqrt{s} = 8$ TeV
ggF	23.9 ± 3.6 $\left[^{+3.1}_{-3.1}\,(\text{stat.})\,^{+1.9}_{-1.6}\,(\text{expt.})\,^{+1.0}_{-1.0}\,(\text{theo.})\right]$
VBF	2.43 ± 0.58 $\left[^{+0.50}_{-0.49}\,(\text{stat.})\,^{+0.27}_{-0.20}\,(\text{expt.})\,^{+0.19}_{-0.16}\,(\text{theo.})\right]$
VH	1.03 ± 0.53 $\left[^{+0.37}_{-0.36}\,(\text{stat.})\,^{+0.22}_{-0.20}\,(\text{expt.})\,^{+0.13}_{-0.06}\,(\text{theo.})\right]$
ttH	0.24 ± 0.11 $\left[^{+0.07}_{-0.07}\,(\text{stat.})\,^{+0.08}_{-0.08}\,(\text{expt.})\,^{+0.01}_{-0.01}\,(\text{theo.})\right]$

less yield a reasonable measurement for the total cross section. The resulting total Higgs boson production cross sections at the two energies are

$$\sigma_H(7\,\text{TeV}) = 22.1\,^{+7.4}_{-6.0}\,\text{pb} \quad = 22.1\,^{+6.7}_{-5.3}\,(\text{stat})\,^{+2.7}_{-2.3}\,(\text{expt.})\,^{+1.9}_{-1.4}\,(\text{theo.})\,\text{pb} \quad \text{and} \tag{6.7}$$

$$\sigma_H(8\,\text{TeV}) = 27.7 \pm 3.7\,\text{pb} = 27.7 \pm 3.0\,(\text{stat.})\,^{+2.0}_{-1.7}\,(\text{expt.})\,^{+1.2}_{-0.9}\,(\text{theo.})\,\text{pb}, \tag{6.8}$$

to be compared with the theoretical predictions of (17.4 ± 1.6) pb at $\sqrt{s} = 7$ TeV and (22.3 ± 2.0) pb at $\sqrt{s} = 8$ TeV, as shown in Tab. 1.2a.

These cross sections are different from what one would naively expect from the global signal-strength values discussed in Sec. 6.2.1, particularly for $\sqrt{s} = 7$ TeV. The differences are largely the result of analysis categorisation. Categories often explore production processes or phase space regions with distinct signal-event topologies. The resulting good signal-to-background

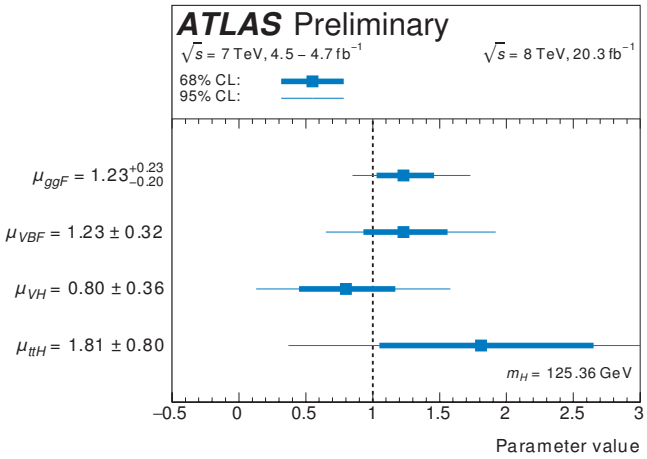

Figure 6.5: The best-fit signal-strength values of different production modes determined from the combined fit to the $\sqrt{s} = 7$ and 8 TeV data. The inner and outer error bars correspond to 68% CL and 95% CL intervals. Total uncertainties combining statistical, experimental and theoretical systematic uncertainties are shown. The fit assumes the SM values of the Higgs boson decay BRs for $m_H = 125.36$ GeV.

ratios can significantly improve the precision of the signal-strength measurements. However, these categories often account for small fractions of the production cross section and thus have limited impact on the total cross section measurement which is dominated by processes with larger expected cross sections. One good example is the VBF category. It contributes significantly to the global signal-strength measurement, but has a relatively minor impact on the total cross section measurement.

6.2.4 Ratios of production cross sections and decay branching ratios

At the LHC, the Higgs boson production cross sections and decay BRs cannot be separately determined in a model-independent way as only their products are measured. However, the ratios of cross sections and ratios of BRs can be factorised model-independently and thus the decays can be decoupled from the production. A parameterisation using these ratios also benefits from cancellations of many theoretical and experimental systematic uncertainties.

By normalising the production yields to the signal strength of the $gg \to H \to WW^*$ production, $\mu_{\mathrm{ggF}}^{WW^*}$, the yields of other Higgs boson production modes and decay channels can be

Table 6.5: Best-fit values of $gg \to H \to WW^*$ signal strength $\mu_{\text{ggF}}^{WW^*}$, ratios of cross sections $R_{i/\text{ggF}}$ and of BRs ρ_{f/WW^*}. All $R_{i/\text{ggF}}$ and ρ_{f/WW^*} are measured relative to their SM values for $m_H = 125.36$ GeV from the combined analysis of the $\sqrt{s} = 7$ and 8 TeV data. The observed and expected significances of the VBF, VH and ttH production with respect to the background-only hypothesis, i. e. $R_{i/\text{ggF}} = 0$, are also shown.

$\mu_{\text{ggF}}^{WW^*}$	$1.15^{+0.28}_{-0.24}$			Ratio of branching ratios	Best-fit value
Ratio of cross sections	Best-fit value	Significance (σ)			
		Observed	Expected		
$R_{\text{VBF/ggF}}$	$1.00^{+0.46}_{-0.34}$	4.3	3.8	$\rho_{\gamma\gamma/WW^*}$	$0.95^{+0.31}_{-0.24}$
$R_{VH/\text{ggF}}$	$1.33^{+0.94}_{-0.68}$	2.6	3.1	ρ_{ZZ^*/WW^*}	$1.23^{+0.41}_{-0.31}$
$R_{ttH/\text{ggF}}$	$1.90^{+1.12}_{-0.86}$	2.4	1.5	$\rho_{\tau\tau/WW^*}$	$1.19^{+0.51}_{-0.37}$
				ρ_{bb/WW^*}	$0.41^{+0.47}_{-0.25}$

parameterised using the ratios of cross sections and ratios of BRs. The $gg \to H \to WW^*$ process is chosen as reference as it has the largest rate after event selection and is well measured (see for example Fig. 6.3). For example, for the production and decay $i \to H \to f$, the yield is then

$$\sigma_i \cdot \text{BR}_f = \mu_i^f \times \left[\sigma_i \cdot \text{BR}_f\right]_{\text{SM}} = \left(\mu_{\text{ggF}}^{WW^*} \cdot R_{i/\text{ggF}} \cdot \rho_{f/WW^*}\right) \times \left[\sigma_i \cdot \text{BR}_f\right]_{\text{SM}}. \tag{6.9}$$

Here R and ρ are ratios of cross sections and BRs, respectively:

$$R_{i/\text{ggF}} = \frac{\sigma_i/\sigma_{\text{ggF}}}{\left[\sigma_i/\sigma_{\text{ggF}}\right]_{\text{SM}}} \quad \text{and} \quad \rho_{f/WW^*} = \frac{\text{BR}_f/\text{BR}_{WW^*}}{\left[\text{BR}_f/\text{BR}_{WW^*}\right]_{\text{SM}}}. \tag{6.10}$$

The data are fitted with $\mu_{\text{ggF}}^{WW^*}$, three cross section ratios and one ratio of BRs for each decay channel other than the $H \to WW^*$ decay. The results are shown in Tab. 6.5 and illustrated in Fig. 6.6. Results from the searches of $H \to \mu\mu$ and $H \to Z\gamma$ decays are included in the fit, but the current datasets do not result in sensitive measurements of $\rho_{\mu\mu/WW^*}$ and $\rho_{Z\gamma/WW^*}$. Therefore only 95% CL upper limits are derived for these two ratios. The respective upper limit is 5.9 for $\rho_{\mu\mu/WW^*}$ and 11.0 for $\rho_{Z\gamma/WW^*}$.

The results exhibit a few noticeable features. As a common multiplicative factor to all rates in this parameterisation, the $gg \to H \to WW^*$ signal strength $\mu_{\text{ggF}}^{WW^*}$ is pulled up from $0.98^{+0.29}_{-0.26}$ of its standalone measurement in the $H \to WW^*$ decay (see Fig. 6.1) to $1.15^{+0.28}_{-0.24}$ to accommodate the observed large global signal-strength value (cf. Sec. 6.2.1). Another important feature is the anticorrelation between $R_{i/\text{ggF}}$ and ρ_{f/WW^*}, see Eqn. (6.9). One evident case is that the fit yields a $R_{VH/\text{ggF}}$ value above the SM prediction, but it is compensated by a small value of ρ_{bb/WW^*} to account for the small observed signal strength in the $VH \to Vb\bar{b}$ analysis.

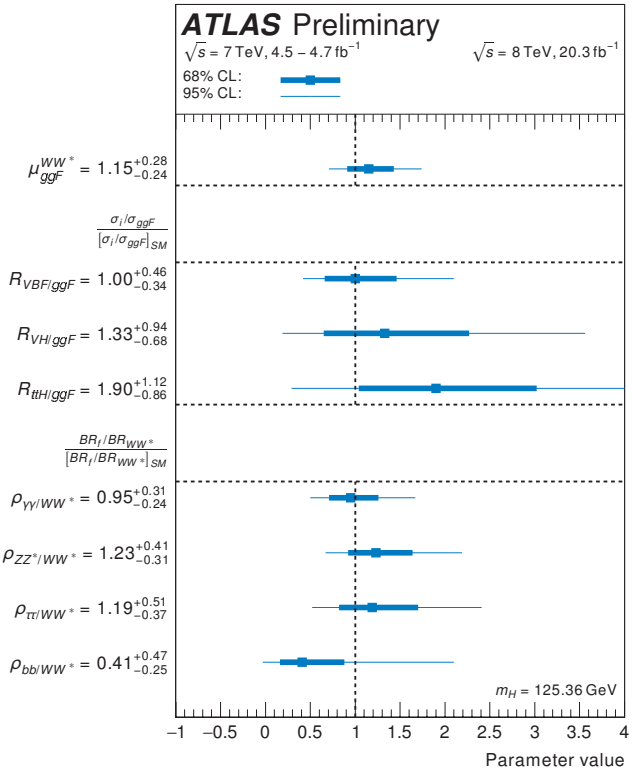

Figure 6.6: The $gg \to H \to WW^*$ signal strength, ratios of cross sections and of BRs from the combined analyses of the $\sqrt{s} = 7$ and 8 TeV data. All ratios are normalised to their SM values at $m_H = 125.36$ GeV. The inner and outer error bars represent 68% CL and 95% CL intervals.

Table 6.5 also includes the observed and expected significances in units of standard deviations (σ) of the VBF, VH and ttH processes for the background-only hypothesis. The significance for each process is calculated from a likelihood scan while contributions from other processes are profiled. The result provides strong evidence at the 4.3σ level of the VBF production of the Higgs boson and supports the SM assumptions of production in association with vector bosons or a pair of top quarks.

6.3 Coupling strength fits

In the previous section signal strength scale factors μ_i^f for given Higgs boson production or decay modes are discussed. However, for a measurement of Higgs boson coupling strengths, production and decay modes cannot be treated independently, as each observed process involves at least two Higgs boson coupling strengths.

Scenarios with a consistent treatment of coupling strengths in production and decay modes are studied in this section. All uncertainties on the best-fit values shown take into account both experimental and theoretical systematic uncertainties.

6.3.1 Framework for coupling strength measurements

Following the LO tree level motivated framework and benchmark models recommended in Ref. [135], measurements of coupling strength scale factors κ_j are implemented for the combination of all analyses and channels summarised in Tab. 6.2.

Assumptions of the framework for benchmark models

The framework is based on the following assumptions:

- The signals observed in the different channels originate from a single narrow resonance with a mass near 125.36 GeV. The case of several, possibly overlapping, resonances in this mass region is not considered.
- Unless otherwise noted, the Higgs boson production and decay kinematics are assumed to be compatible with those expected for a SM Higgs boson, similar to what was assumed for the signal strength measurements of Sec. 6.2.
- The width of the assumed Higgs boson near 125.36 GeV is neglected, i. e. the zero-width approximation is used. Due to the zero-width assumption in the Higgs boson propagator, the product $[\sigma \times \mathrm{BR}](i \to H \to f)$ for on-shell measurements can always be decomposed in the following way for all channels:

$$\sigma(i \to H \to f) = \frac{\sigma_i(\kappa_j) \cdot \Gamma_f(\kappa_j)}{\Gamma_\mathrm{H}(\kappa_j)} \tag{6.11}$$

  where σ_i is the production cross section through the initial state i, Γ_f the partial decay width into the final state f and Γ_H the total width of the Higgs boson. The components of σ_i, Γ_f, and Γ_H of Eqn. 6.11 are expressed in terms of LO-motivated scale factors κ_j of the Higgs boson coupling strengths to other particles j, where a value of $\kappa_j = 1$

corresponds to the SM expectation. In particular, the total width Γ_H relates to the Higgs boson coupling strengths as

$$\Gamma_H(\kappa_j, \mathrm{BR}_{\mathrm{i.,u.}}) = \frac{\kappa_H^2(\kappa_j)}{(1-\mathrm{BR}_{\mathrm{i.,u.}})}\Gamma_H^{\mathrm{SM}}, \tag{6.12}$$

where $\kappa_H^2(\kappa_j)$ is the sum of the κ_j^2 weighted by the corresponding SM BRs, Γ_H^{SM} is the SM width of the Higgs boson, and $\mathrm{BR}_{\mathrm{i.,u.}}$ is the Higgs boson BR to invisible or undetected decays[3].

Only modifications of coupling strengths, i. e. of absolute values of coupling strengths, are taken into account, while the tensor structure of the couplings is assumed to be the same as in the SM. This means in particular that the observed state is assumed to be a CP-even scalar as in the SM (this assumption was tested by both the ATLAS [32] and CMS [222] Collaborations).

- The signal strength of off-shell measurements is assumed to only depend on the coupling strengths and not on the total width [469, 470], i.e.

$$\sigma^{\mathrm{off}}(i \to H^* \to f) \sim \kappa_{i,\mathrm{off}}^2 \cdot \kappa_{f,\mathrm{off}}^2 \tag{6.13}$$

where the additional assumption of non-running coupling strengths

$$\kappa_{j,\mathrm{off}} = \kappa_{j,\mathrm{on}} \tag{6.14}$$

allows to constrain Γ_H from a simultaneous measurement of on-shell and off-shell measurements. While this assumption of non-running coupling strengths cannot hold universally for the ggF and VBF production without violating unitarity, it is assumed to hold in the region of phase space of the off-shell $H^* \to WW$ and $H^* \to ZZ$ measurements described in Sec. 6.1.9 that is relatively close to the on-shell regime.

Characterisation of the input measurements in terms of coupling strengths

The combined input channels described in Tab. 6.2 probe eight different production processes: $\sigma(\mathrm{ggF})$, $\sigma(\mathrm{VBF})$, $\sigma(WH)$, $\sigma(q\bar{q} \to ZH)$, $\sigma(gg \to ZH)$, $\sigma(bbH)$, $\sigma(ttH)$, and $\sigma(tH)$ whose SM cross sections are listed in Tab. 1.2a. Table 6.6 summarises the Higgs boson coupling strength characteristics of all production processes and lists the rate scaling behavior in terms of Higgs boson coupling strength scale factors.

The ggF production process involves a loop process at lowest order, with contributions from top-quark and b-quark loops and a small interference between them. The VBF production

[3] Invisible final states can be directly searched for through the missing transverse momentum signature [460]. An example of an undetected mode would be a decay mode to multiple light jets, which presently cannot be distinguished from multijet backgrounds.

process probes a combination of κ_W and κ_Z coupling strengths, with a negligible amount ($\ll 0.1\%$) of interference between these tree-level contributions.

The WH and $q\bar{q} \to ZH$ processes each probe a single coupling strength, κ_W and κ_Z, respectively. The gluon-initiated associated production of a Higgs boson with a Z boson, $\sigma(gg \to ZH)$, is characterised by gluon-fusion-style production involving t, b-quark loops where the Z boson is radiated off the fermion loop and the Higgs boson is either also radiated directly off the fermion loop or is radiated off the outgoing Z boson. The cross section of $gg \to ZH$ production is sensitive to the relative sign between κ_t and κ_Z due to interference between these contributions and depends on the kinematics of the process.

The ttH production process directly probes the Higgs boson coupling strength to t-quarks, κ_t. The tree-level tH production process is included as background to events in all reconstructed ttH categories, and has for SM Higgs boson coupling strengths a large destructive interference between contributions where the Higgs boson is radiated from the W boson and from the top quark. Its SM cross section is consequently small, about 14% of the ttH cross section. However, for negative κ_t the interference becomes constructive and, following Tab. 6.6, the cross section increases by a factor of 6 (13) for $|\kappa_t| = |\kappa_W| = 1$ for the $gb \to WtH$ ($qg \to tHq'b$) process, making the tH process a sensitive probe to the relative sign of the W and top-quark coupling strength, despite its small SM cross section.

The bbH production process directly probes the Higgs boson coupling strength to b-quarks, κ_b. As no MC simulation is available to model the small bbH contribution in various input channels, and it is in most kinematic regions experimentally indistinguishable from ggF production, the bbH production mode is modeled using simulated ggF events (cf. Sec. 6.1.10).

The combined input channels probe seven Higgs boson decay modes. Each of the first five of these decay modes $\Gamma_{b\bar{b}}$, Γ_{WW}, Γ_{ZZ}, $\Gamma_{\tau\tau}$, and $\Gamma_{\mu\mu}$ probes a single coupling strength scale factor. The remaining two decay modes, $\Gamma_{\gamma\gamma}$ and $\Gamma_{Z\gamma}$ are characterised by the interference between W boson or top-quark loop diagrams. These modes probe the W and t coupling strengths as well as their relative sign through interference effects.

For completeness it should be noted also that the $gg \to H$, tH and $gg \to ZH$ cross sections expressed in Higgs boson coupling strengths depend on the kinematic selection criteria used. The $b-t$ interference expression quoted in Tab. 6.6 for ggF is valid for the inclusive cross section, but in events with additional jets the top-quark loop dominates, and the observed interference is somewhat smaller. Neither this ggF phase-space dependence, nor that of $gg \to ZH$ are considered in this chapter. For the tH process on the other hand, which features a comparatively large $W-t$ interference term, the effect of phase-space dependence is taken into account, even though Tab. 6.6 only lists the inclusive expression.

Effective coupling strength scale factors

In some of the fits, effective scale factors κ_g, κ_γ, $\kappa_{Z\gamma}$ are introduced to describe the processes $gg \to H$, $H \to \gamma\gamma$, and $H \to Z\gamma$, which are loop-induced in the SM. In other fits they are treated as a function of the more fundamental coupling strength scale factors κ_t, κ_b, κ_W, and similarly for all other particles that contribute to these SM loop processes. In these cases, the loop contributions are expressed in terms of the fundamental coupling strengths, including all interference effects, as listed for the SM in Tab. 6.6. The loop process $gg \to ZH$ is never treated as an effective scale factor, as unlike in the other loop processes, tree-level contributions from new physics are expected to be highly suppressed [159]. What then remains are BSM contributions to κ_Z and κ_t, which are best taken into account within the limitation of the framework by resolving the loop.

Strategies for measurements of absolute coupling strengths

As all observed Higgs boson cross sections in the LO framework are inversely proportional to the Higgs boson width (Eqn. (6.11)), which is not experimentally constrained to a meaningful precision at the LHC, only ratios of coupling strengths can be measured at the LHC without assumptions on the Higgs boson width. To make measurements of absolute coupling strengths, an assumption on the Higgs boson width must be introduced.

The simplest assumption is that there are no invisible or undetected Higgs boson decays, i.e. $BR_{i.,u.} = 0$ is assumed in Eqn. (6.12). An alternative, less strong assumption, is that $\kappa_W \leq 1$ and $\kappa_Z \leq 1$[135]. This assumption is theoretically motivated by the premise that the Higgs boson should solve the unitarity problem in vector boson scattering and also holds in a wide class of BSM models. In particular, it is valid in any model with an arbitrary number of Higgs doublets, with and without additional Higgs singlets. The assumption is also justified in certain classes of composite Higgs boson models. A second alternative is to assume that the coupling strengths in off-shell Higgs boson production are identical to those for on-shell Higgs boson production. Under the assumption that the off-shell signal strength and coupling strength scale factors are independent of the energy scale of the Higgs boson production, the total Higgs boson decay width can be determined from the ratio of off-shell to on-shell signal strengths [458]. The boundary $BR_{i.,u.} \geq 0$, motivated by the basic assumption that the total width of the Higgs boson must be greater or equal to the sum of the partial widths, always introduces a lower bound on the Higgs boson width. The difference in effect of these assumptions is therefore mostly in the resulting upper limit on the Higgs boson width. The assumptions made for the various measurements are summarised in Tab. 6.7 and discussed in the next sections together with the results.

Table 6.6: Overview of Higgs boson production cross sections σ_i and Higgs boson partial decay widths Γ_f. For each production or decay mode the scaling of the corresponding rate in terms of Higgs boson coupling strength scale factors is given. For processes where multiple amplitudes contribute, the rate may depend on multiple Higgs boson coupling strength scale factors, and interference terms may give rise to scalar product terms $\kappa_i \kappa_j$ that allow the relative sign of the coupling strengths κ_i and κ_j to be determined. Expressions originate from Ref. [135], except for $\sigma(gg \to ZH)$ (from Ref. [159]) and $\sigma(gb \to WtH)$ and $\sigma(qg \to tHq'b)$ (calculated using Ref. [206]). The expressions are given for $\sqrt{s} = 8\,\text{TeV}$ and $m_H = 125.36\,\text{GeV}$ and are similar for $\sqrt{s} = 7\,\text{TeV}$. Interference contributions with negligible magnitudes have been been omitted in this table.

Production	Loops	Interference	Expression in terms of fundamental coupling strengths	
$\sigma(\text{ggF})$	✓	$b-t$	$\kappa^2_{\text{g}} \sim$	$1.06 \cdot \kappa^2_{\text{t}} + 0.01 \cdot \kappa^2_{\text{b}} - 0.07 \cdot \kappa_{\text{t}} \kappa_{\text{b}}$
$\sigma(\text{VBF})$	-	-	$\sim$	$0.74 \cdot \kappa^2_{\text{W}} + 0.26 \cdot \kappa^2_{\text{Z}}$
$\sigma(WH)$	-	-	$\sim$	κ^2_{W}
$\sigma(q\bar{q} \to ZH)$	-	-	$\sim$	κ^2_{Z}
$\sigma(gg \to ZH)$	✓	$Z-t$	$\kappa^2_{\text{ggZH}} \sim$	$2.27 \cdot \kappa^2_{\text{Z}} + 0.37 \cdot \kappa^2_{\text{t}} - 1.64 \cdot \kappa_{\text{Z}} \kappa_{\text{t}}$
$\sigma(bbH)$	-	-	$\sim$	κ^2_{b}
$\sigma(ttH)$	-	-	$\sim$	κ^2_{t}
$\sigma(gb \to WtH)$	-	$W-t$	$\sim$	$1.84 \cdot \kappa^2_{\text{t}} + 1.57 \cdot \kappa^2_{\text{W}} - 2.41 \cdot \kappa_{\text{t}} \kappa_{\text{W}}$
$\sigma(qg \to tHq'b)$	-	$W-t$	$\sim$	$3.4 \cdot \kappa^2_{\text{t}} + 3.56 \cdot \kappa^2_{\text{W}} - 5.96 \cdot \kappa_{\text{t}} \kappa_{\text{W}}$
Partial decay width				
$\Gamma_{b\bar{b}}$	-	-	$\sim$	κ^2_{b}
Γ_{WW}	-	-	$\sim$	κ^2_{W}
Γ_{ZZ}	-	-	$\sim$	κ^2_{Z}
$\Gamma_{\tau\tau}$	-	-	$\sim$	κ^2_{τ}
$\Gamma_{\mu\mu}$	-	-	$\sim$	κ^2_{μ}
$\Gamma_{\gamma\gamma}$	✓	$W-t$	$\kappa^2_{\gamma} \sim$	$1.59 \cdot \kappa^2_{\text{W}} + 0.07 \cdot \kappa^2_{\text{t}} - 0.66 \cdot \kappa_{\text{W}} \kappa_{\text{t}}$
$\Gamma_{Z\gamma}$	✓	$W-t$	$\kappa^2_{Z\gamma} \sim$	$1.12 \cdot \kappa^2_{\text{W}} + 0.00035 \cdot \kappa^2_{\text{t}} - 0.12 \cdot \kappa_{\text{W}} \kappa_{\text{t}}$
Total decay width				
Γ_{H}	✓	$W-t$ $b-t$	$\kappa^2_{\text{H}} \sim$	$0.57 \cdot \kappa^2_{\text{b}} + 0.22 \cdot \kappa^2_{\text{W}} + 0.09 \cdot \kappa^2_{\text{g}} +$ $0.06 \cdot \kappa^2_{\tau} + 0.03 \cdot \kappa^2_{\text{Z}} + 0.03 \cdot \kappa^2_{\text{c}} +$ $0.0023 \cdot \kappa^2_{\gamma} + 0.0016 \cdot \kappa^2_{Z\gamma} + 0.00022 \cdot \kappa^2_{\mu}$

6.3.2 Fermion versus vector (gauge) coupling strengths

The benchmark model considered is a minimal extension of the fit for the global signal strength μ, where now different strengths for the fermion and vector couplings are allowed. It assumes that only SM particles contribute to the $gg \to H$, $H \to \gamma\gamma$, $H \to Z\gamma$ and $gg \to ZH$ vertex loops, and modifications of the coupling strength factors for fermions and vector bosons are propagated through the loop calculations. The fit is performed in two variants, with and without the assumption that the total width of the Higgs boson is given by the sum of the known SM Higgs boson decay modes (modified in strength by the appropriate fermion and vector coupling strength scale factors, see for example the last column of Tab. 6.7).

Table 6.7: Summary of coupling benchmark models considered in this chapter, where $\lambda_{ij} \equiv \kappa_i/\kappa_j$, $\kappa_{ii} \equiv \kappa_i\kappa_i/\kappa_{\mathrm{H}}$, and the functional dependence assumptions are: $\kappa_V = \kappa_{\mathrm{W}} = \kappa_{\mathrm{Z}}$, $\kappa_F = \kappa_{\mathrm{t}} = \kappa_{\mathrm{b}} = \kappa_{\tau} = \kappa_{\mu}$ (and similarly for the other fermions), $\kappa_{\mathrm{g}} = \kappa_{\mathrm{g}}(\kappa_{\mathrm{b}}, \kappa_{\mathrm{t}})$, $\kappa_{\gamma} = \kappa_{\gamma}(\kappa_{\mathrm{b}}, \kappa_{\mathrm{t}}, \kappa_{\tau}, \kappa_{\mathrm{W}})$, and $\kappa_{\mathrm{H}} = \kappa_{\mathrm{H}}(\kappa_i)$. The tick marks indicate which assumptions are made in each case. The last column shows, as an example, the relative coupling strengths involved in the $gg \to H \to \gamma\gamma$ process.

Section in this chapter	Corresponding table in [135]	Probed couplings	Parameters of interest	Functional assumptions κ_V	κ_F	κ_{g}	κ_{γ}	κ_{H}	Example: $gg \to H \to \gamma\gamma$
6.3.2	43.1	Couplings to fermions and bosons	κ_V, κ_F	✓	✓	✓	✓	✓	$\kappa_F^2 \cdot \kappa_{\gamma}^2(\kappa_F, \kappa_V)/\kappa_{\mathrm{H}}^2(\kappa_F, \kappa_V)$
6.3.2	43.3		λ_{FV}, κ_{VV}	✓	✓	✓	✓	–	$\kappa_{VV}^2 \cdot \lambda_{FV}^2 \cdot \kappa_{\gamma}^2(\lambda_{FV}, \lambda_{FV}, 1)$
6.3.3	48.1	Vertex loops + H →invisible/undetected decays	$\kappa_{\mathrm{g}}, \kappa_{\gamma}, \kappa_{\mathrm{Z}\gamma}$	=1	=1	–	–	✓	$\kappa_{\mathrm{g}}^2 \cdot \kappa_{\gamma}^2/\kappa_{\mathrm{H}}^2(\kappa_{\mathrm{g}}, \kappa_{\gamma})$
6.3.3	48.2		$\kappa_{\mathrm{g}}, \kappa_{\gamma}, \kappa_{\mathrm{Z}\gamma}, \mathrm{BR}_{\mathrm{i,u.}}$	=1	=1	–	–	✓	$\kappa_{\mathrm{g}}^2 \cdot \kappa_{\gamma}^2/\kappa_{\mathrm{H}}^2(\kappa_{\mathrm{g}}, \kappa_{\gamma}) \cdot (1 - \mathrm{BR}_{\mathrm{i,u.}})$
6.3.4	43.2		κ_F, κ_V, $\mathrm{BR}_{\mathrm{i,u.}}$	≤ 1 –	– –	✓ ✓	✓ ✓	✓ μ_{off}	$\frac{\kappa_F^2 \cdot \kappa_{\gamma}(\kappa_F, \kappa_V)^2}{\kappa_{\mathrm{H}}^2(\kappa_F, \kappa_V)} \cdot (1 - \mathrm{BR}_{\mathrm{i,u.}})$
6.3.4	49		$\kappa_F, \kappa_V, \kappa_{\mathrm{g}}, \kappa_{\gamma}, \kappa_{\mathrm{Z}\gamma}, \mathrm{BR}_{\mathrm{i,u.}}$	≤ 1 –	– –	– –	– –	✓ μ_{off}	$\frac{\kappa_F^2 \cdot \kappa_{\gamma}(\kappa_F, \kappa_V)^2}{\kappa_{\mathrm{H}}^2(\kappa_F, \kappa_V, \kappa_{\mathrm{g}}, \kappa_{\gamma})} \cdot (1 - \mathrm{BR}_{\mathrm{i,u.}})$
6.3.5	46	Up-/down-type fermions	λ_{du}, λ_{Vu}, κ_{uu}	✓	κ_u, κ_d	✓	✓	–	$\kappa_{uu}^2 \cdot \kappa_{\mathrm{g}}^2(\lambda_{du}, 1) \cdot \kappa_{\gamma}^2(\lambda_{du}, 1, \lambda_{du}, \lambda_{Vu})$
6.3.5	47	Leptons/quarks	λ_{lq}, λ_{Vq}, κ_{qq}	✓	κ_l, κ_q	✓	✓	–	$\kappa_{qq}^2 \cdot \kappa_{\gamma}^2(1, 1, \lambda_{lq}, \lambda_{Vq})$
6.3.6	51	Generic models with and without assumptions on vertex loops and Γ_{H}	$\kappa_{\mathrm{W}}, \kappa_{\mathrm{Z}}, \kappa_{\mathrm{t}}, \kappa_{\mathrm{b}}, \kappa_{\tau}, \kappa_{\mu}$	–	–	✓	✓	✓	$\frac{\kappa_{\mathrm{g}}^2(\kappa_{\mathrm{b}}, \kappa_{\mathrm{t}}) \cdot \kappa_{\gamma}^2(\kappa_{\mathrm{b}}, \kappa_{\mathrm{t}}, \kappa_{\tau}, \kappa_{\mu}, \kappa_{\mathrm{W}})}{\kappa_{\mathrm{H}}^2(\kappa_{\mathrm{b}}, \kappa_{\mathrm{t}}, \kappa_{\tau}, \kappa_{\mu}, \kappa_{\mathrm{W}}, \kappa_{\mathrm{Z}})}$
6.3.6	50.2		$\kappa_{\mathrm{W}}, \kappa_{\mathrm{Z}}, \kappa_{\mathrm{t}}, \kappa_{\mathrm{b}}, \kappa_{\tau}, \kappa_{\mu}, \kappa_{\mathrm{g}}, \kappa_{\gamma}, \kappa_{\mathrm{Z}\gamma}, \mathrm{BR}_{\mathrm{i,u.}}$	≤ 1 – –	– – –	– – –	– – –	✓ ✓ μ_{off}	$\frac{\kappa_{\mathrm{g}}^2 \cdot \kappa_{\gamma}^2}{\kappa_{\mathrm{H}}^2(\kappa_{\mathrm{b}}, \kappa_{\mathrm{t}}, \kappa_{\tau}, \kappa_{\mu}, \kappa_{\mathrm{W}}, \kappa_{\mathrm{Z}})} \cdot (1 - \mathrm{BR}_{\mathrm{i,u.}})$
6.3.6	50.3		$\lambda_{\mathrm{WZ}}, \lambda_{\mathrm{tg}}, \lambda_{\mathrm{bZ}}, \lambda_{\tau\mathrm{Z}}, \lambda_{\mathrm{gZ}}, \lambda_{\gamma\mathrm{Z}}, \lambda_{(\mathrm{Z}\gamma)\mathrm{Z}}, \kappa_{\mathrm{gZ}}$	–	–	–	–	–	$\kappa_{\mathrm{gZ}}^2 \cdot \lambda_{\gamma\mathrm{Z}}^2$

Only SM contributions to the total width

The fit parameters are the coupling strength scale factors κ_F for all fermions and κ_V for all vector bosons:

$$\kappa_V = \kappa_W = \kappa_Z \tag{6.15}$$

$$\kappa_F = \kappa_t = \kappa_b = \kappa_\tau = \kappa_g = \kappa_\mu. \tag{6.16}$$

As only SM particles are assumed to contribute to the $gg \to H$ loop in this benchmark model, the ggF process depends directly on the fermion scale factor κ_F^2. Only the relative sign between κ_F and κ_V is physical and hence in the following only $\kappa_V > 0$ is considered, without loss of generality. Sensitivity to this relative sign is gained from the negative interference between the loop contributions of the W boson and the t quark in $H \to \gamma\gamma$ and $H \to Z\gamma$ decays and in $gg \to ZH$ production, as well as from the tH processes (cf. Tab. 6.6).

Figure 6.7 shows the results of the fits for this benchmark model. Figure 6.7a illustrates how the $H \to \gamma\gamma$, $H \to ZZ^*$, $H \to WW^*$, $H \to \tau\tau$ and $H \to b\bar{b}$ channels contribute to the combined measurement. The slight asymmetry in κ_F for the $H \to WW^*$ and $H \to b\bar{b}$ is introduced by the small contributions of the tH and $gg \to ZH$ production processes for these decay modes. The strong constraint on κ_F from $H \to WW^*$ decays is related to the 3.2σ observation of the $qq' \to qq'H$ production process in this channel. Outside the range shown in Fig. 6.7a there are two additional minima for $H \to \gamma\gamma$. The long tails in the $H \to b\bar{b}$ contour towards high values of κ_V are the result of an asymptotically disappearing sensitivity of the observed signal strength in the bb final states to κ_V at large values of κ_V.

Figure 6.7b shows only the combined measurement with the SM-like minimum with a positive relative sign, as the local minimum with negative relative sign is disfavoured at the $\sim 4.0\sigma$ level, which can be seen in the wider scan of κ_F, where κ_V is profiled, shown in Fig. 6.7c. The likelihood as a function of κ_V, profiling κ_F, is given in Fig. 6.7d. Around $\kappa_V = 0.8$ the sign of the chosen profiled solution for κ_F changes, causing a kink in the likelihood. The profile likelihood curves restricting κ_F to be either positive or negative are also shown in Fig. 6.7d as thin curves to illustrate that this sign change in the unrestricted profile likelihood is the origin of the kink.

The best-fit values and uncertainties, when the other parameter is profiled, are:

$$\kappa_V = 1.09 \pm 0.07 \tag{6.17}$$

$$\kappa_F = 1.11 \pm 0.16. \tag{6.18}$$

The two-dimensional compatibility of the SM hypothesis with the best-fit point is 41%.

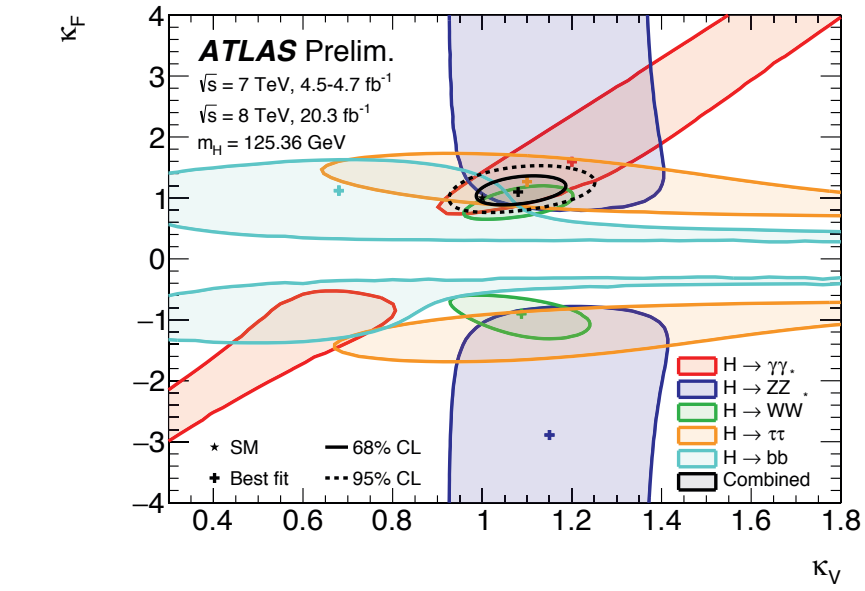

(a)

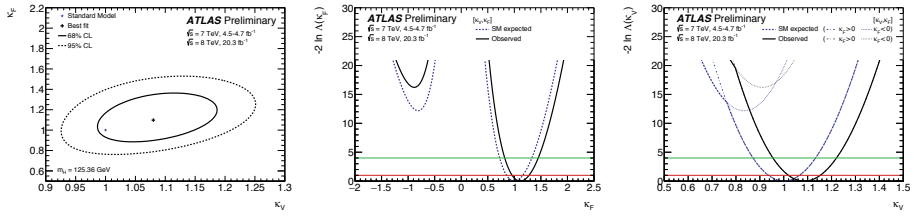

(b) (c) (d)

Figure 6.7: Results of fits for the two-parameter benchmark model defined in Sec. 6.3.2 that probes different coupling strength scale factors for fermions and vector bosons, assuming only SM contributions to the total width: (a) Results of the two-dimensional fit to κ_F and κ_V, including 68% and 95% CL contours; overlaying the 68% CL contours derived from the individual channels and their combination; (b) the same measurement, without the overlays of the individual channels, (c) PLRs as a function of the coupling strength scale factors κ_F (κ_V is profiled) and (d) as a function of κ_V (κ_F is profiled). The dashed curves in (c) and (d) show the SM expectations. In (d) the sign of the chosen profiled solution for κ_F changes at $\kappa_V \approx 0.8$, causing a kink in the likelihood. The profile likelihood curves restricting κ_F to be either positive or negative are also shown to illustrate that this sign change in the unrestricted profile likelihood is the origin of the kink. The red (green) horizontal lines indicates the cutoff values on the PLR corresponding to a 68% (95%) confidence interval on the POI, assuming the asymptotic χ^2 distribution for the test statistic.

No assumption on the total width

The assumption on the total width gives a strong constraint on the fermion coupling strength scale factor κ_F in the previous benchmark model, as the total width is dominated in the SM by the sum of the fermion-induced b, τ and gluon-decay widths. The fit is therefore repeated without the assumption on the total width.

In this case only ratios of coupling strength scale factors can be measured. Hence there are the following free parameters:

$$\lambda_{FV} = \kappa_F / \kappa_V \tag{6.19}$$

$$\kappa_{VV} = \kappa_V \cdot \kappa_V / \kappa_{\mathrm{H}}, \tag{6.20}$$

where λ_{FV} is the ratio of the fermion and vector boson coupling strength scale factors, κ_{VV} is an overall scale that includes the total width and applies to all rates, and κ_{H} is defined in Tab. 6.6.

Figure 6.8 shows the results of this fit. The best-fit values and uncertainties, when profiling the other parameter, are:

$$\lambda_{FV} = 1.02^{+0.15}_{-0.13} \tag{6.21}$$

$$\kappa_{VV} = 1.07^{+0.14}_{-0.13}. \tag{6.22}$$

Similar to the model described in Sec. 6.3.2, Fig. 6.8a shows the determination of the sign of λ_{FV} disfavouring $\lambda_{FV} = -1$ at approximately $\sim 4.0\sigma$, while Fig. 6.8b shows the two-dimensional likelihood contour. The two variables are anticorrelated because only their product appears in the model. The two-dimensional compatibility of the SM hypothesis with the best-fit point is 41%.

6.3.3 Probing beyond the SM contributions assuming unmodified coupling strengths of SM particles

In this section, contributions from new particles either in loops or in new final states are considered. All coupling strength scale factors of known SM particles are assumed to be as predicted by the SM, i. e. $\kappa_i = 1$. For the $H \to \gamma\gamma$, $H \to Z\gamma$ and $gg \to H$ vertices, effective scale factors κ_γ, $\kappa_{Z\gamma}$ and κ_g are introduced that allow for extra contributions from new particles. These effective scale factors are defined to be positive as there is no sensitivity to the sign of these coupling strengths. The potential new particles contributing to the $H \to \gamma\gamma$, $H \to Z\gamma$, $gg \to ZH$ and $gg \to H$ loops may or may not contribute to the total width of the observed state through direct invisible decays or decays into final states that cannot be distinguished from the background. In these cases the resulting variation in the total width is parameterised in terms of the additional BR into invisible or undetected particles $\mathrm{BR}_{\mathrm{i.,u.}}$ of Eqn. (6.12).

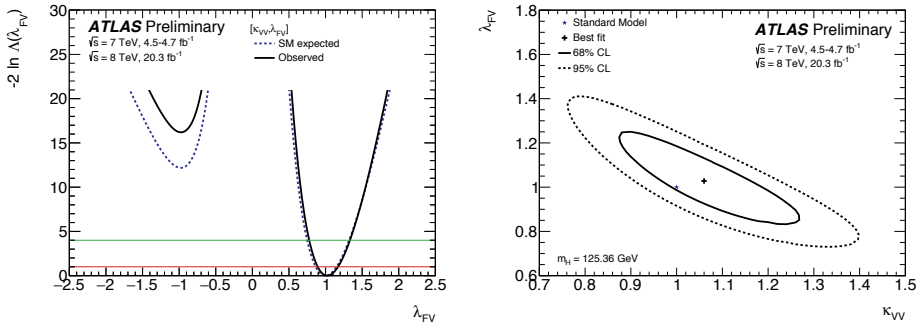

(a) **(b)**

Figure 6.8: Results of fits for the two-parameter benchmark model defined in Sec. 6.3.2 that probes different coupling strength scale factors for fermions and vector bosons without assumptions on the total width: (a) PLR as function of the coupling strength scale factor ratio λ_{FV} (κ_{VV} is profiled). The dashed curve shows the SM expectation. (b) Results of the two-dimensional fit to κ_{VV} and λ_{FV}, including 68% and 95% CL contours. The red (green) horizontal lines indicates the cutoff values on the PLR corresponding to a 68% (95%) confidence interval on the POI, assuming the asymptotic χ^2 distribution for the test statistic.

SM coupling strengths to all known particles and no BSM contributions to the total width

In the first benchmark model it is assumed that there are no extra contributions to the total width caused by non-SM particles, but that BSM contributions can modify the loop coupling strengths from their SM prediction. The free parameters are κ_g, κ_γ, $\kappa_{Z\gamma}$.

Figure 6.9 shows the results of fits for this benchmark scenario and the best-fit values and uncertainties, when profiling the other parameters. The effective coupling strengths κ_g and κ_γ are measured to be consistent with the SM expectation, whereas a limit is set on the effective coupling strength $\kappa_{Z\gamma}$.

Also shown in Fig. 6.9 is the uncertainty on the total width that this model allows, expressed as the ratio Γ_H/Γ_H^{SM}. The estimate for the width is obtained from an alternative parameterisation of this benchmark model where the effective coupling strength κ_g is replaced by the expression that results from solving Eqn. (6.12) for κ_g, introducing Γ_H/Γ_H^{SM} as a parameter of the model. As the effective loop couplings only contribute a small fraction to the total width of the Higgs boson, the allowed uncertainty in the Higgs boson width in this benchmark model is highly constrained by its model assumptions. The three-dimensional compatibility of the SM hypothesis with the best-fit point is 69%.

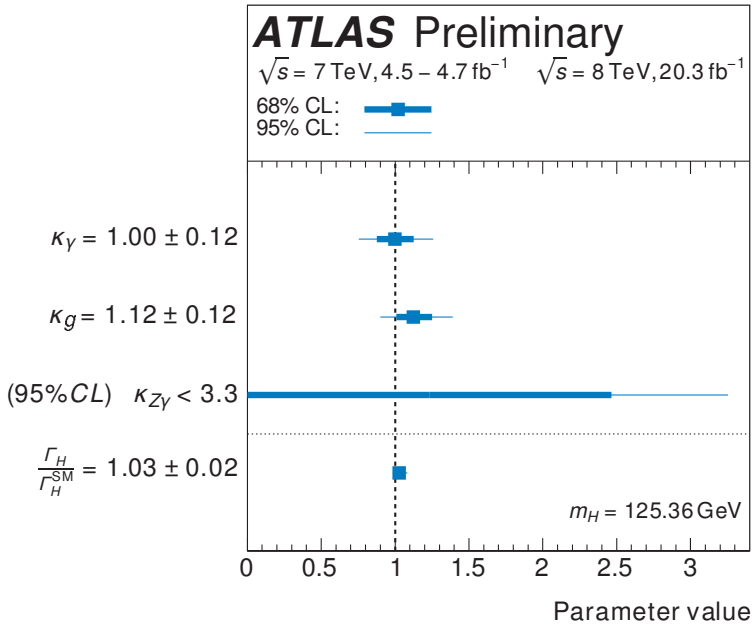

(a)

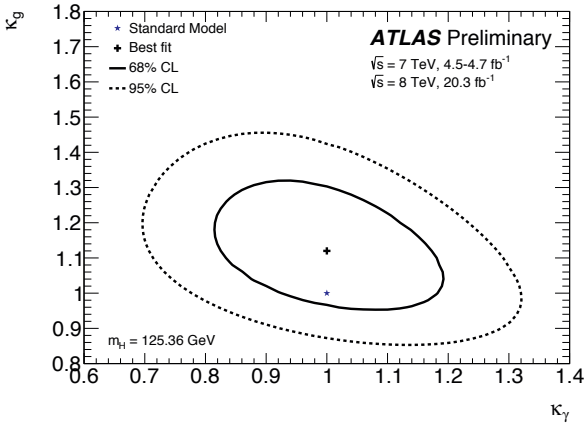

(b)

Figure 6.9: Results of fits for the benchmark model that probes for contributions from non-SM particles in the $H \to \gamma\gamma$, $H \to Z\gamma$ and $gg \to H$ loops, assuming no extra contributions to the total width: (a) overview of fitted parameters, where the inner and outer bars correspond to 68% CL and 95% CL intervals, and (b) results of the two-dimensional fit to κ_γ and κ_g, including 68% and 95% CL contours ($\kappa_{Z\gamma}$ is profiled).

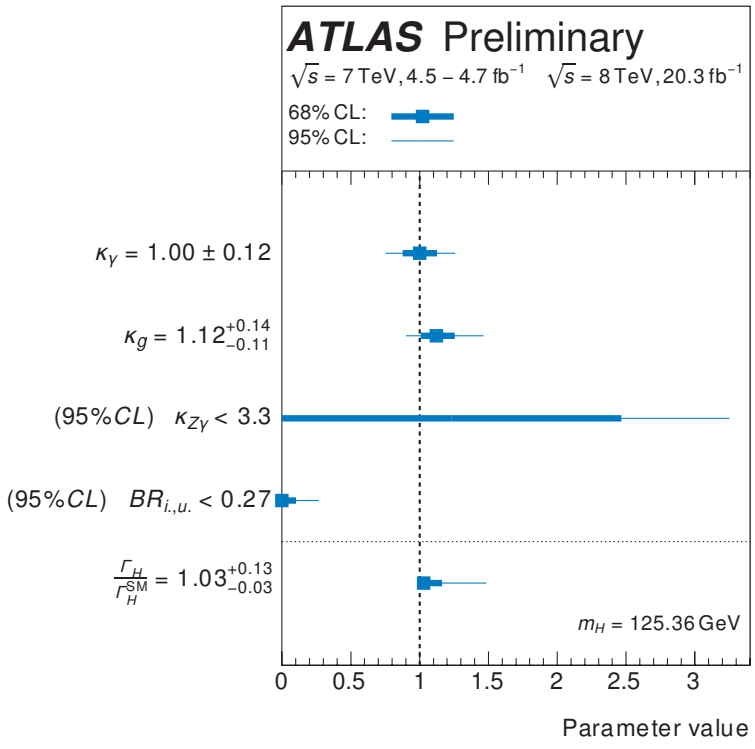

(a)

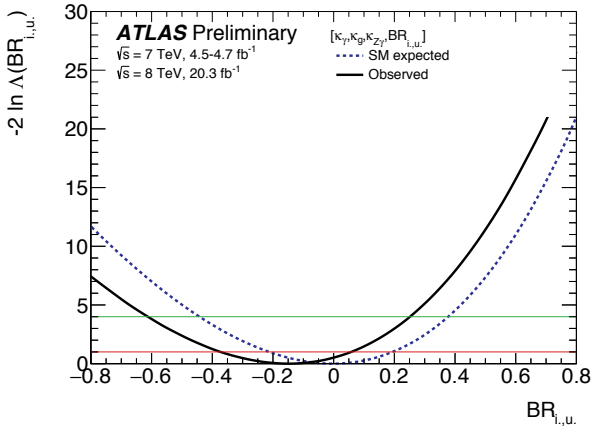

(b)

Figure 6.10: Results of fits for benchmark models that probe for contributions from non-SM particles in the $H \to \gamma\gamma$, $H \to Z\gamma$ and $gg \to H$ loops, while allowing for potential extra contributions to the total width: (a) overview of fitted parameters. The inner and outer bars correspond to 68% CL and 95% CL intervals The confidence intervals for $BR_{i.,u.}$ are estimated with respect to the physical boundary as described in the text. (b) PLR as function of the branching fraction $BR_{i.,u.}$ to invisible or undetected decay modes (κ_γ, κ_g and $\kappa_{Z\gamma}$ are profiled). The dashed curve shows the SM expectation. The red (green) horizontal lines indicates the cutoff values on the PLR corresponding to a 68% (95%) confidence interval on the POI, assuming the asymptotic χ^2 distribution for the test statistic.

SM coupling strengths to all known particles and no assumption on the total width

When all coupling strength scale factors of known SM particles are assumed to be as predicted by the SM, i. e. $\kappa_i = 1$, the total width Γ_H as expressed as function of κ_H^2 in Eqn. (6.12) is sufficiently constrained that it is possible to probe for invisible and undetected Higgs boson decays with the BR $BR_{i.,u.}$ as free parameter, without further constraints on the total width. The free parameters in this case are κ_g, κ_γ, $\kappa_{Z\gamma}$ and $BR_{i.,u.}$. Figure 6.10 shows the best-fit values and their uncertainties, when profiling the other parameters. Also shown in Fig. 6.10 is the uncertainty on the total width that this model allows, obtained in the same fashion as for the previous benchmark model. The upward uncertainty on Γ_H/Γ_H^{SM} is notably increased due the released constraint on $BR_{i.,u.}$, whereas the downward uncertainty is identical to that of the previous benchmark model due to the imposed condition that $BR_{i.,u.} \geq 0$.

The four-dimensional compatibility of the SM hypothesis with the best-fit point is 74%. By using the physical constraint $BR_{i.,u.} \geq 0$, the 95% CL upper limit is $BR_{i.,u.} < 0.27$ (the expected limit in case of the SM hypothesis is $BR_{i.,u.} < 0.37$). The 95% confidence interval is based on the PLR restricted to the allowed region of parameter space; however, the confidence interval is defined by the standard χ^2 cutoff, which leads to some over coverage near the boundaries.

As the choice of free parameters in this model gives extra degrees of freedom to the $gg \to H$ production and $H \to \gamma\gamma$ and $H \to Z\gamma$ decays, the most precise measurements based on the $gg \to H$ production or the $H \to \gamma\gamma$ decays (cf. Fig. 6.2) do not give a sizable contribution to the determination of $BR_{i.,u.}$. Instead $BR_{i.,u.}$ is mostly constrained from channels sensitive to VBF and VH production, as the tree level couplings involved in these production modes are fixed to their SM values within this model.

6.3.4 Probing beyond the SM contributions allowing for modified coupling strengths of SM particles

In this section, benchmark models similar to those of Sec. 6.3.3 are considered, but now releasing the assumption that $\kappa_i = 1$ and allowing couplings to fermions and boson to be modified according to coupling strengths κ_F and κ_V. With these additional parameters these benchmark models are underconstrained, and a constraint on the Higgs boson width must be introduced to resolve the degeneracy. All three choices of the total width constraint discussed in the introduction of this section are studied: $\kappa_V < 1$, $\kappa_{on} = \kappa_{off}$, $BR_{i.,u.} = 0$. These choices of constraints complement each other, as the present limit of $\mu_{off} < 5.1$ in the combined off-shell measurement in the $H \to WW^*$ and $H \to ZZ^*$ channels effectively constrains κ_V to be greater than 1 in the combined fit when exploiting the assumption $\kappa_{on} = \kappa_{off}$.

Probing BSM contributions to the total width assuming SM loop couplings

This benchmark model is a straightforward extension of the model of Sec. 6.3.2 by introducing the branching fraction of Higgs boson decays to invisible or undetected states $BR_{i.,u.}$ as free parameter. The free parameters of the model thus are κ_F, κ_V and $BR_{i.,u.}$. Loop processes are assumed to have only SM content, as was also the case in the model of Sec. 6.3.2.

Figure 6.11 shows the results of fits from this benchmark scenario. Also shown in Fig. 6.11 is the uncertainty that this benchmark model allows on the total width ratio Γ_H/Γ_H^{SM}, obtained in similar fashion as for the previous benchmark models, now solving Eqn. (6.12) for κ_F instead of κ_g. Unlike the benchmark models of Sec. 6.3.3, the measured width ratio is now allowed to go substantially below 1 as the free parameters κ_F and κ_V allow the dominant terms in κ_H to be reduced with respect to their SM expectation (cf. Tab. 6.6). For comparison the results of the benchmark model of Sec. 6.3.2 are included, corresponding to the condition $BR_{i.,u.} = 0$ in this model. Figure 6.11 shows that the upper bound on the Higgs width from the assumption $\kappa_{off} = \kappa_{on}$ is substantially weaker than the bound from the assumption $\kappa_V < 1$.

The implicit boundary $\sigma_{off} \geq 0$ in the parametrization of the off-shell signal strength of Eqn. 6.13, detailed in Ref. [458], causes the distribution of the test statistic to deviate from its asymptotic form for low values of σ_{off}, with deviations in p-values of up to 10% for $\sigma_{off} \approx 2.5$, corresponding to the upper end of the 68% asymptotic confidence interval of Γ_H/Γ_H^{SM} for the scenario $\kappa_{off} = \kappa_{on}$. The deviation of the asymptotic distribution is shown to be negligible for off-shell signal strengths corresponding to the upper end of the 95% asymptotic confidence interval. The upper bound of the 68% C.L. interval for the scenario $\kappa_{off} = \kappa_{on}$ should therefore considered to be only approximate. As the lower boundary on Γ_H/Γ_H^{SM} is always dominated by the constraint $BR_{i.,u.} \geq 0$, the lower bounds are not affected by these deviations from asymptotic behavior.

The three-dimensional compatibility of the SM hypothesis with the best-fit point is 99% (29%), when applying the $\kappa_V < 1$(off-shell) constraint, respectively. By using the physical constraint $BR_{i.,u.} \geq 0$, the 95% CL upper limit is $BR_{i.,u.} < 0.13$, when applying $\kappa_V < 1$ (the expected limit in case of the SM hypothesis is $BR_{i.,u.} < 0.24$), and is $BR_{i.,u.} < 0.52$ when applying the off-shell constraint (the expected limit in case of the SM hypothesis is $BR_{i.,u.} < 0.71$). The 95% confidence interval is based on the PLR restricted to the allowed region of parameter space; the confidence interval is defined by the standard χ^2 cutoff, which leads to some over coverage near the boundaries.

Probing BSM contributions in loops and to the total width

This next benchmark model releases the assumption of SM particle content in loop processes of the previous benchmark by introducing the effective loop coupling parameters

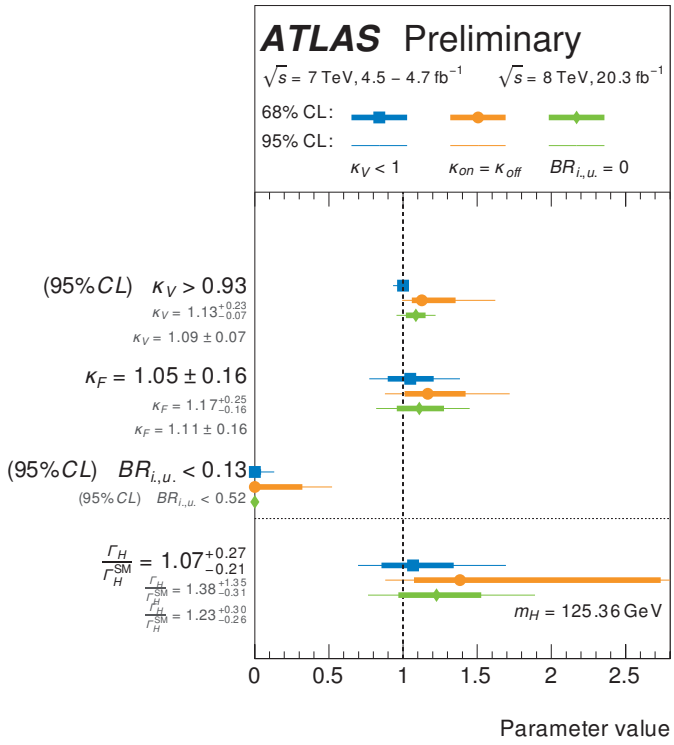

Figure 6.11: Results of fits for benchmark models that probe for potential extra contributions to the total width, but do not allow contributions from non-SM particles in the $H \to \gamma\gamma$, $gg \to H$ and $H \to Z\gamma$ loops, with free gauge and fermion coupling strengths κ_V, κ_F. The result for each parameter marked by a full box corresponds to the model with the constraint $\kappa_V < 1$ imposed. The result for each parameter marked by a full circle corresponds to the model with a constraint on the total width from μ_{off}. The result for each parameter marked by a full diamond corresponds to the model where the total Higgs boson decay width is not modified with respect to the SM. The the inner and outer bars correspond to 68% CL and 95% CL intervals. The confidence intervals of $\text{BR}_{\text{i.,u.}}$ and, in the benchmark model with the constraint $\kappa_V < 1$, also κ_V, are estimated with respect to their physical boundaries as described in the text.

used in the benchmark models of Sec. 6.3.3. The free parameters of this model are thus κ_F, κ_V, κ_g, κ_γ, $\kappa_{Z\gamma}$ and $\text{BR}_{\text{i.,u.}}$. Figure 6.12 shows the best-fit values and their uncertainties.

The six-dimensional compatibility of the SM hypothesis with the best-fit point is 96% (64%) when applying the $\kappa_V < 1$(off-shell) constraint, respectively. By using the physical constraint $\text{BR}_{\text{i.,u.}} \geq 0$, the 95% CL upper limit is $\text{BR}_{\text{i.,u.}} < 0.27$ when applying $\kappa_V < 1$ (the expected limit in case of the SM hypothesis is $\text{BR}_{\text{i.,u.}} < 0.39$), and is $\text{BR}_{\text{i.,u.}} < 0.54$, when applying the off-shell constraint (the expected limit in case of the SM hypothesis is $\text{BR}_{\text{i.,u.}} < 0.72$).

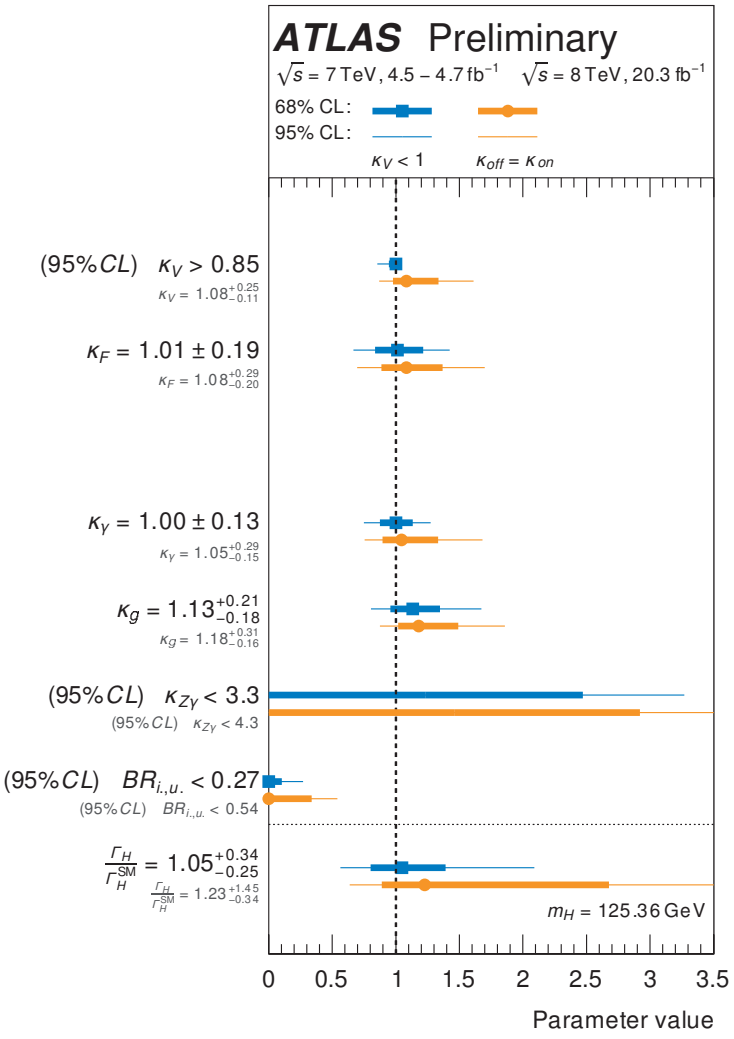

Figure 6.12: Results of fits for benchmark models that probe for contributions from non-SM particles in the $H \to \gamma\gamma$, $gg \to H$ and $H \to Z\gamma$ loops, with free gauge and fermion coupling strengths κ_V, κ_F, while allowing for potential extra contributions to the total width. The result for each parameter marked by a full box corresponds to the model with the constraint $\kappa_V < 1$ imposed. The result for each parameter marked by a full circle corresponds to the model with a constraint on the total width from μ_{off}. The the inner and outer bars correspond to 68% CL and 95% CL intervals. The confidence intervals of $\text{BR}_{\text{i.,u.}}$ and, in the benchmark model with the constraint $\kappa_V < 1$, also κ_V, are estimated with respect to their physical boundaries as described in the text.

6.3.5 Probing relations within the fermion coupling sector

The previous sections assumed universal coupling strength scale factors for all fermions, while many extensions of the SM predict deviations within the fermion sector [135]. The currently accessible channels, in particular $H \to b\bar{b}$, $H \to \tau\tau$, $H \to \mu\mu$ and $q\bar{q}/gg \to t\bar{t}H$, allow the relations between the up- and down-type fermions and between the lepton and quark sectors to be probed.

Probing the up- and down-type fermion symmetry

Many extensions of the SM contain different coupling strengths of the Higgs boson to up-type and down-type fermions. This is for instance the case for certain 2HDMs [244–246]. In this benchmark model the ratio λ_{du} between down- and up-type fermions is probed, while vector boson coupling strengths are assumed to be unified and equal to κ_V. The indices u, d stand for all up- and down-type fermions, respectively. The free parameters are:

$$\lambda_{du} = \kappa_d/\kappa_u \tag{6.23}$$
$$\lambda_{Vu} = \kappa_V/\kappa_u \tag{6.24}$$
$$\kappa_{uu} = \kappa_u \cdot \kappa_u/\kappa_{\mathrm{H}}. \tag{6.25}$$

The up-type quark coupling strength scale factor is mostly indirectly constrained through the $gg \to H$ production channel, from the Higgs boson to top-quark coupling strength, with an additional weak direct constraint from the $q\bar{q}/gg \to t\bar{t}H$ production channel, while the down-type coupling strength is constrained through the $H \to b\bar{b}$, $H \to \tau\tau$ and $H \to \mu\mu$ decays as well as weakly through the $q\bar{q}/gg \to b\bar{b}H$ production mode and the b-loop in the $gg \to H$ production mode.

Figure 6.13 shows the results of the fits for this benchmark model. The likelihood curve is nearly symmetric around $\lambda_{du} = 0$ as the model is almost insensitive to the relative sign of κ_u and κ_d. The interference of contributions from the b and t loops in the $gg \to H$ production induces an observed asymmetry of about 0.6σ (no significant asymmetry is expected with the present sensitivity). The fit results for the parameters of interest are:

$$\lambda_{du} \in [-1.08, -0.81] \cup [0.75, 1.04] \text{ (68\% CL)} \tag{6.26}$$
$$\lambda_{Vu} = 0.92^{+0.18}_{-0.16} \tag{6.27}$$
$$\kappa_{uu} = 1.25^{+0.33}_{-0.33}. \tag{6.28}$$

The value of λ_{du} around the SM-like minimum at 1 is $\lambda_{du} = 0.90 \pm 0.15$. This fit provides a $\sim 4.5\sigma$ level evidence of the coupling of the Higgs boson to down-type fermions, mostly coming predominantly from the $H \to \tau\tau$ measurement and to a lesser extent from the $H \to b\bar{b}$ measurements. The three-dimensional compatibility of the SM hypothesis with the best-fit point is 51%.

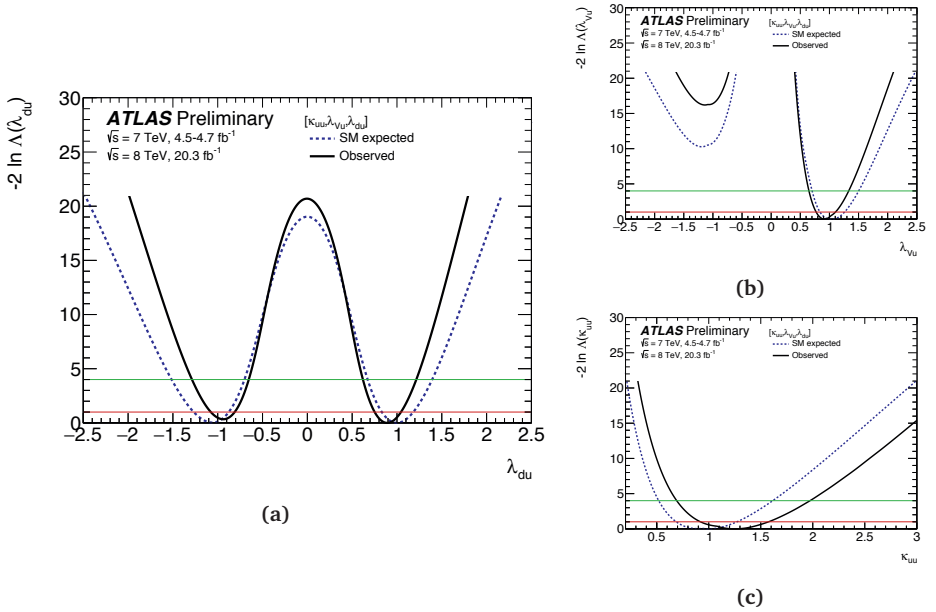

Figure 6.13: Results of fits for the benchmark model described in Sec. 6.3.5 that probes the ratio of scale factors between down- and up-type fermions: PLRs as functions of the coupling strength scale factor ratios (a) λ_{du} (λ_{Vu} and κ_{uu} are profiled), (b) λ_{Vu} (λ_{du} and κ_{uu} are profiled), and (c) the overall scale factor κ_{uu} (λ_{du} and λ_{Vu} are profiled). The dashed curves show the SM expectations. The red (green) horizontal lines indicates the cutoff values on the PLR corresponding to a 68% (95%) confidence interval on the POI, assuming the asymptotic χ^2 distribution for the test statistic.

Probing the quark and lepton symmetry

Extensions of the SM can also contain different coupling strengths of the Higgs boson to leptons and quarks, notably some variants of 2HDMs. In this benchmark model the ratio λ_{lq} of coupling strength scale factors to leptons and quarks is probed, while vector boson coupling scale factors are assumed to be unified and equal to κ_V. The indices l, q stand for all leptons and quarks, respectively. The free parameters are:

$$\lambda_{lq} = \kappa_l / \kappa_q \tag{6.29}$$

$$\lambda_{Vq} = \kappa_V / \kappa_q \tag{6.30}$$

$$\kappa_{qq} = \kappa_q \cdot \kappa_q / \kappa_{\mathrm{H}}. \tag{6.31}$$

The lepton coupling strength is constrained through the $H \to \tau\tau$ and $H \to \mu\mu$ decays.

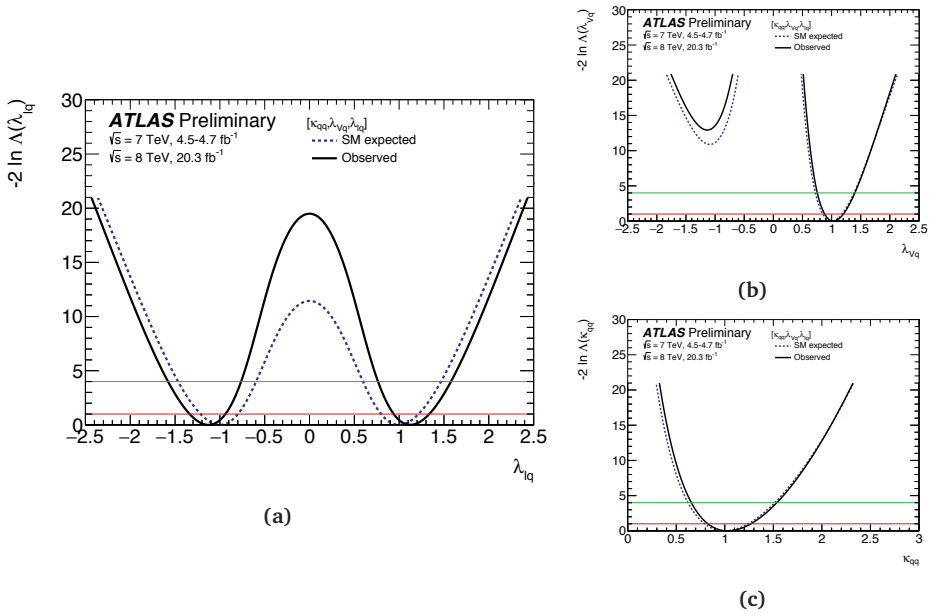

Figure 6.14: Results of fits for the benchmark model described in Sec. 6.3.5 that probes the symmetry between quarks and leptons: PLRs as functions of the coupling strength scale factor ratios (a) λ_{lq} (λ_{Vq} and κ_{qq} are profiled), (b) λ_{Vq} (λ_{lq} and κ_{qq} are profiled), and (c) the overall scale factor κ_{qq} (λ_{lq} and λ_{Vq} are profiled). The dashed curves show the SM expectations. The red (green) horizontal lines indicates the cutoff values on the PLR corresponding to a 68% (95%) confidence interval on the POI, assuming the asymptotic χ^2 distribution for the test statistic.

Figure 6.14 shows the results of the fits for this benchmark. Similar to the case above, the likelihood curve is nearly symmetric around $\lambda_{lq} = 0$. The fit results for the POIs are:

$$\lambda_{lq} \in [-1.34, -0.94] \cup [0.94, 1.34] \text{ (68\% CL)} \tag{6.32}$$

$$\lambda_{Vq} = 1.03^{+0.18}_{-0.15} \tag{6.33}$$

$$\kappa_{qq} = 1.03^{+0.24}_{-0.20}. \tag{6.34}$$

The value of λ_{lq} around the SM-like minimum at 1 is $\lambda_{lq} = 1.12^{+0.22}_{-0.18}$. A vanishing coupling strength of the Higgs boson to leptons is excluded at the $\sim 4.4\sigma$ level due to the $H \to \tau\tau$ measurement. The three-dimensional compatibility of the SM hypothesis with the best-fit point is 53%.

6.3.6 Generic models

In the benchmark models studied in Sec 6.3.2 to 6.3.5, specific aspects of the scalar sector are tested by combining under certain assumptions coupling strength scale factors into a minimum number of parameters, thereby maximizing the sensitivity to the scenarios under study. In the case of the generic models evaluated in this section the scale factors for the coupling strenghts to W, Z, t, b, τ and μ are treated independently, while for the $gg \to H$ production, $H \to \gamma\gamma$ decay, $H \to Z\gamma$ decay and the total width Γ_H, either the SM particle content is assumed or no such assumptions are made.

Generic model 1: only SM particles in loops, no invisible or undetected Higgs boson decays

In this benchmark scenario, all coupling strengths to SM particles, relevant to the measured modes, are fitted independently. The free parameters are: κ_W, κ_Z, κ_t, κ_b, κ_τ, and κ_μ, while the vertex loop factors and the total width are calculated as a function of these parameters, as listed in Tab. 6.6. Without loss of generality the W coupling strength scale factor is assumed to be positive. Due to the interference terms, the fit is sensitive to the relative sign between the W and t couplings (through the tH, $H \to \gamma\gamma$, $H \to Z\gamma$ processes) and the relative sign between the Z and t coupling (through the $gg \to ZH$ process), providing indirect sensitivity to the relative sign between the W- and Z-coupling. Furthermore, the model has some sensitivity to the relative sign between the top- and bottom-coupling ($gg \to H$).

Figure 6.15 shows the results of the fits for this benchmark scenario. All measured coupling strengths are found to be compatible with the SM expectation within 1σ. As shown in Figs. 6.16a and 6.16b, the negative solution of κ_t is strongly disfavoured at 3.1σ (2.9σ expected), while the negative minimum of κ_b is slightly disfavoured at 0.5σ (no sensitivity expected). The six-dimensional compatibility of the SM hypothesis with the best-fit point is 57%. Figure 6.17 shows the results of the fit for generic model 1 as reduced coupling strength scale factors

$$y_{V,i} = \sqrt{\kappa_{V,i} \frac{g_{V,i}}{2v}} = \sqrt{\kappa_{V,i}} \frac{m_{V,i}}{v} \tag{6.35}$$

for weak bosons with a mass m_V, where $g_{V,i}$ is the absolute Higgs boson coupling strength, v is the vacuum expectation value of the Higgs field and

$$y_{F,i} = \kappa_{F,i} \frac{g_{F,i}}{\sqrt{2}} = \kappa_{F,i} \frac{m_{F,i}}{v} \tag{6.36}$$

for fermions as a function of the particle mass m_F, assuming a SM Higgs boson with a mass of 125.36 GeV. For the b quark mass in Fig. 6.17 the $\overline{MS}$ running mass evaluated at 125.36 GeV is assumed.

For the interpretations in this generic model, it should be noted that the low fitted value of κ_b causes a reduction of the total width Γ_H by about 30% compared to the SM expectation (cf. Tab. 6.6), which in turn induces a reduction of all other κ-values by about 20%.

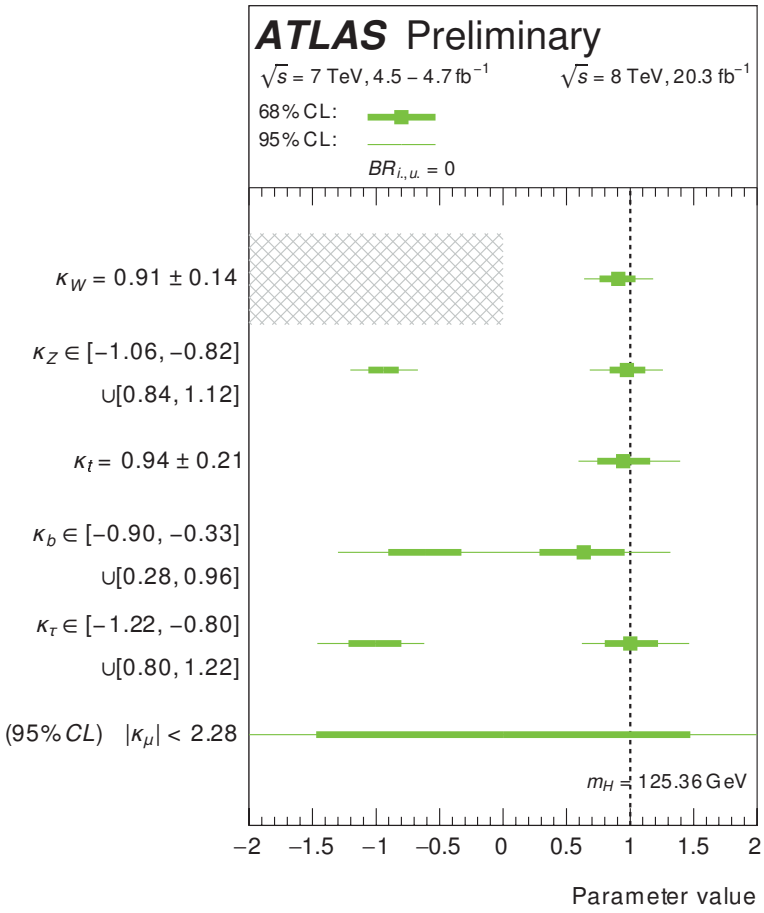

Figure 6.15: Overview of best-fit values of parameters with 68% and 95% CL intervals for the generic model 1 (see text). In this model only SM particles are considered in loops and no invisible or undetected Higgs boson decay are allowed. The sign of κ_W is assumed to be positive, as indicated by the hatched area, without loss of generality. The inner and outer bars correspond to 68% CL and 95% CL intervals.

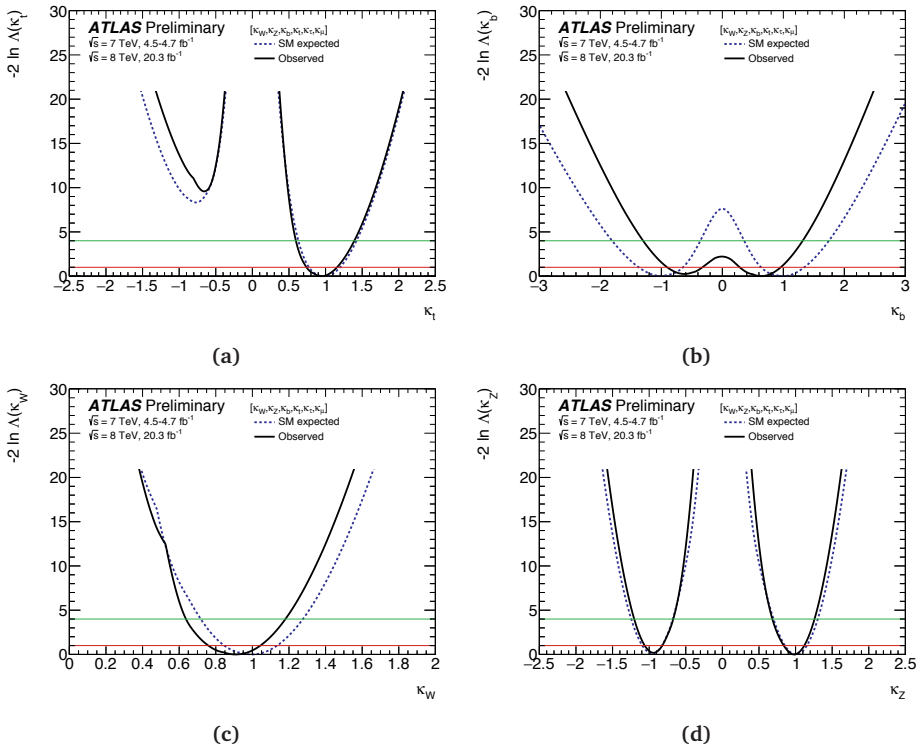

Figure 6.16: Results of fits for the generic model 1 (see text): only SM particles in loops, no invisible or undetected Higgs boson decays. PLRs as a functions of the coupling strength scale factors (a) κ_t, (b) κ_b, (c) κ_W, and (d) κ_Z. For each measurement, the other coupling strength scale factors are profiled. The kinks in the curves of (a) and (c) are caused by transitions in solutions chosen by the profile likelihood for the relative sign between profiled couplings. The dashed curves show the SM expectations. The red (green) horizontal lines indicates the cutoff values on the PLR corresponding to a 68% (95%) confidence interval on the POI, assuming the asymptotic χ^2 distribution for the test statistic.

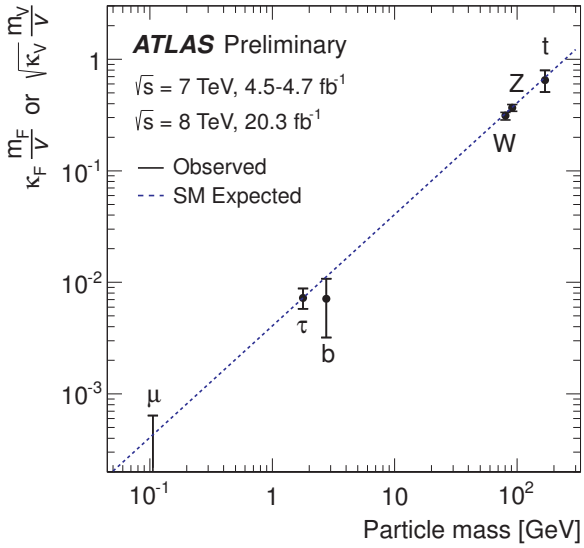

Figure 6.17: Fit results for the reduced coupling strength scale factors $y_{V,i} = \sqrt{\kappa_{V,i}\frac{g_{V,i}}{2v}} = \sqrt{\kappa_{V,i}}\frac{m_{V,i}}{v}$ for weak bosons and $y_{F,i} = \kappa_{F,i}\frac{g_{F,i}}{\sqrt{2}} = \kappa_{F,i}\frac{m_{F,i}}{v}$ for fermions as a function of the particle mass, assuming a SM Higgs boson with a mass of 125.36 GeV. The dashed line indicates the predicted mass dependence for the SM Higgs boson.

Generic model 2: allowing deviations in vertex loop couplings and invisible or undetected Higgs boson decays

In this case the six free parameters from model 1 are retained but the assumptions about which particles contribute to the loops and the total width are dropped. Effective coupling strength scale factors for the $gg \to H$, $H \to \gamma\gamma$, and $H \to Z\gamma$ vertices are introduced, and optionally also a BR $\mathrm{BR}_{\mathrm{i.,u.}}$ to new non-SM decays that might yield invisible or undetected final states, resulting in a total of nine (ten) free parameters. In the variant where $\mathrm{BR}_{\mathrm{i.,u.}}$ is not fixed to zero, either the constraint $\kappa_V < 1$ is imposed, or the constraint on the total width from off-shell measurements is included.

Figure 6.19 illustrates the results of the fits for this benchmark scenario. The numerical results are shown in Tab. 6.8. The nine-dimensional compatibility of the SM hypothesis with the best-fit point is 73% when $\mathrm{BR}_{\mathrm{i.,u.}}$ is fixed to zero. The compatibilities for the fits with the conditions $\kappa_V < 1$ and $\kappa_{\mathrm{on}} = \kappa_{\mathrm{off}}$ imposed are 80% and 57%, respectively.

The implicit boundary $\sigma_{\mathrm{off}} \geq 0$ in the parametrization of the off-shell signal strength of Eqn. 6.13, detailed in Ref. [458], causes the distribution of the test statistic to deviate from

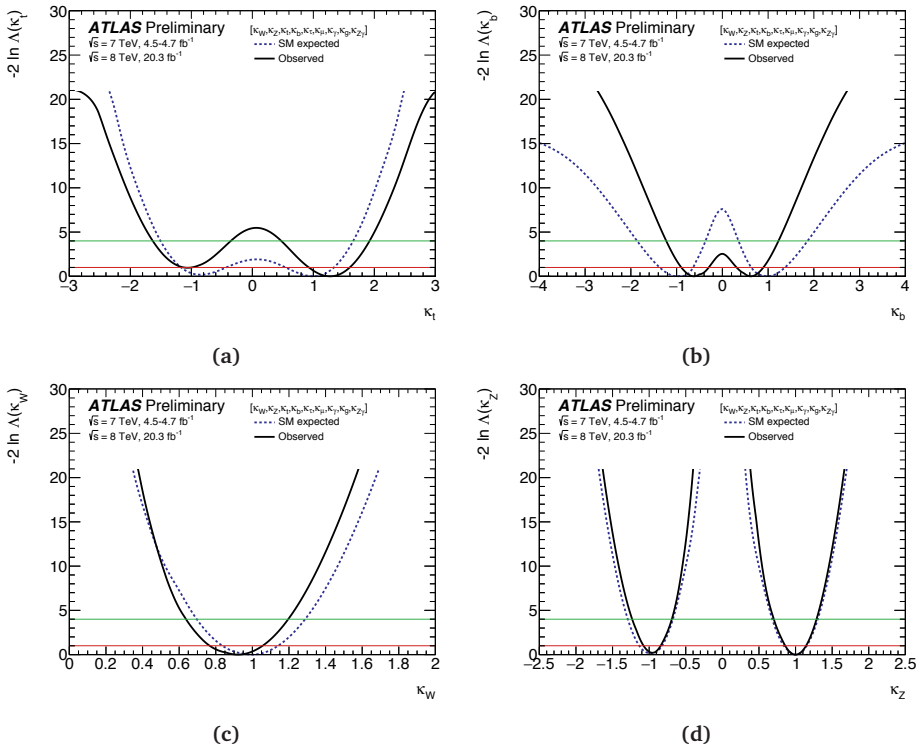

Figure 6.18: Results of fits for the generic model 2 (see text): effective coupling strengths for loop processes allowing non-SM contributions, but assuming that the total Higgs boson decay width is not modified with respect to the SM ($BR_{i.,u.} = 0$). PLRs as functions of the coupling strength scale factors (a) κ_t, (b) κ_b, (c) κ_W, and (d) κ_Z. For each measurement, the other coupling strength scale factors are profiled. The dashed curves show the SM expectations. The red (green) horizontal lines indicates the cutoff values on the PLR corresponding to a 68% (95%) confidence interval on the POI, assuming the asymptotic χ^2 distribution for the test statistic.

Table 6.8: Numerical results of the fits to generic model 2 (see text): effective coupling strengths for loop processes allowing non-SM contributions with various assumptions on the total Higgs boson width. The confidence interval of $BR_{i.,u.}$ in the benchmark model with the constraints $\kappa_W < 1$ and $|\kappa_Z| < 1$, and the confidence intervals κ_W and κ_Z, are estimated with respect to their physical boundaries as described in the text. These results are also shown in Fig. 6.19.

Parameter		$\kappa_V < 1$	$\kappa_{off} = \kappa_{on}$	$BR_{i.,u.} = 0$
κ_W		> 0.64 (95% CL)	$= 0.96^{0.35}_{0.16}$	$= 0.92^{+0.14}_{-0.15}$
κ_Z		> 0.71 (95% CL)	$= 1.05^{0.38}_{0.17}$	$\in [-1.08,-0.84] \cup [0.86, 1.14]$
κ_t		$= 1.28 \pm 0.35$	$= 1.35^{+0.61}_{-0.39}$	$\in [-1.12,-1.00] \cup [0.93, 1.60]$
$\lvert\kappa_b\rvert$	$=$	0.62 ± 0.28	$0.64^{+0.34}_{-0.28}$	$0.62^{+0.31}_{-0.27}$
$\lvert\kappa_\tau\rvert$	$=$	$0.99^{+0.22}_{-0.18}$	$1.03^{+0.21}_{-0.40}$	1.00 ± 0.20
$\lvert\kappa_\mu\rvert$	$<$	2.3 (95% CL)	< 2.8 (95% CL)	2.3 (95% CL)
κ_γ	$=$	$0.90^{+0.16}_{-0.14}$	$0.93^{0.36}_{0.17}$	0.90 ± 0.15
κ_g	$=$	$0.92^{+0.23}_{-0.16}$	$1.02^{0.37}_{0.19}$	0.92 ± 0.17
$\kappa_{Z\gamma}$	$<$	3.15 (95% CL)	4.03 (95% CL)	3.18 (95% CL)
$BR_{i.,u.}$	$<$	0.49 (95% CL)	0.68 (95% CL)	-
Γ_H/Γ_H^{SM}	$=$	$0.64^{+0.40}_{-0.25}$	$0.74^{+1.57}_{-0.21}$ [< 4.9 (95% CL)]	$0.64^{+0.31}_{-0.25}$

its asymptotic form for low values of σ_{off}, with deviations in p-values of up to 10% for $\sigma_{off} \approx 2.5$, corresponding to the upper end of the 68% asymptotic confidence interval of Γ_H/Γ_H^{SM} for the scenario $\kappa_{off} = \kappa_{on}$. The deviation of the asymptotic distribution is shown to be negligible for off-shell signal strengths corresponding to the upper end of the 95% asymptotic confidence interval. The upper bound of the 68% C.L. interval for the scenario $\kappa_{off} = \kappa_{on}$ should therefore considered to be only approximate. As the lower boundary on Γ_H/Γ_H^{SM} is always dominated by the constraint $BR_{i.,u.} > 0$, the lower bounds are not affected by these deviations from asymptotic behavior.

Figure 6.18 shows PLRs as a function of selected coupling strength scale factors. In Fig. 6.18a, the negative minimum of κ_t is disfavoured at 1.0σ. The sensitivity to disfavour the negative minimum of κ_t is reduced with respect to generic model 1 as the interference in loop couplings can no longer be exploited as effective coupling strengths are introduced. The observed residual sensitivity to the sign of κ_t is exclusively due to the tree-level interference effect of the tH background of the ttH channel. The minimum corresponding to the positive solution is given by $\kappa_t = 1.28^{+0.32}_{-0.35}$.

Figure 6.20 illustrates the influence of individual loop processes on the precision of the κ_t measurement as well as their ability to determine the sign of κ_t relative to κ_W. As a starting point the red curve shows the sensitivity of generic model 2, as also shown in Fig. 6.18a. In this benchmark the sensitivity to the $W-t$ relative sign originates only from the non-loop tH process and from the resolved $gg \to ZH$ loop process. The observed 1σ sensitivity to the sign

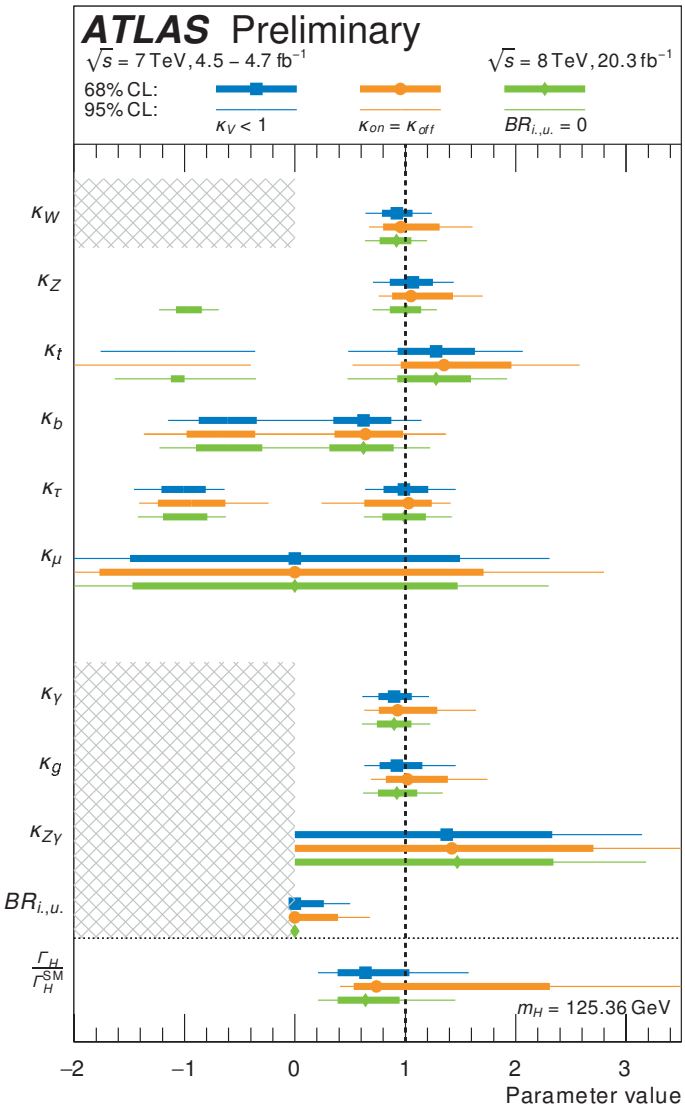

Figure 6.19: Results of fits for the generic model 2 (see text): the results indicated by a full box are obtained for a benchmark model with effective coupling strengths for loop processes allowing non-SM contributions, and a floating $BR_{i.,u.}$ allowing non-SM contributions to the total decay width. The result for each parameter marked by a full box corresponds to the model with the constraint $\kappa_V < 1$ imposed. The result for each parameter marked by a full circle corresponds to the model with a constraint on the total width from μ_{off}. The result for each parameter marked by a full diamond corresponds to the model where the total Higgs boson decay width is not modified with respect to the SM. The hatched area indicates regions that are outside the defined parameter boundaries. The inner and outer bars correspond to 68% CL and 95% CL intervals. The confidence intervals of $BR_{i.,u.}$ and, in the benchmark model with the constraints $\kappa_W < 1$ and $|\kappa_Z| < 1$, also κ_W and κ_Z, are estimated with respect to their physical boundaries as described in the text. Numerical results are shown in Tab. 6.8.

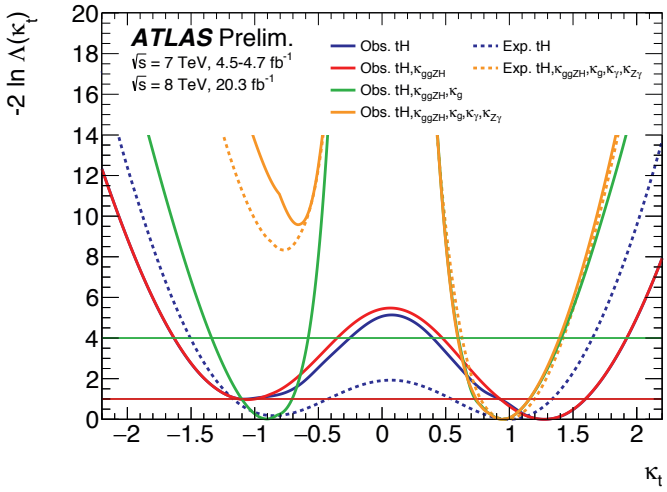

Figure 6.20: Comparison of measurements of κ_t with and without resolved loop processes: shown are models with no loop processes resolved (blue), only $gg \to ZH$ resolved (red, generic model 2), $gg \to H$ additionally resolved (green), and $H \to \gamma\gamma$ and $H \to Z\gamma$ additionally resolved (orange, generic model 1). The dashed blue and orange curves correspond to the expected sensitivity for the no-loop and all-loop models. The red (green) horizontal lines indicates the cutoff values on the PLR corresponding to a 68% (95%) confidence interval on the POI, assuming the asymptotic χ^2 distribution for the test statistic.

of κ_t is exclusively due to the tH process contribution, as is demonstrated by a model variant (blue curve) in which the $gg \to ZH$ contribution is described with an effective coupling strength: this results in a nearly identical sensitivity to the relative sign, in addition to a slightly reduced sensitivity to reject $\kappa_t = 0$. Incorporating information from the $gg \to H$ loop process in generic model 2 by expressing the loop content in terms of its SM contributions, greatly improves the precision on κ_t (green curve), but reduces the sensitivity to the sign of κ_t relative to κ_W. This reduction happens because on one hand the $gg \to H$ process yields no new information on this relative sign as it is dominated by a $t - b$ interference, and on the other hand because it decreases the observed magnitude of κ_t to a level more compatible with the SM, thereby reducing the sensitivity of the tH process to the relative sign. Further resolving the $H \to \gamma\gamma$ and $H \to Z\gamma$ loop processes, which are dominated by a $W - t$ interference results in the configuration of generic model 1 and greatly improves the measurement of the relative sign of κ_W and κ_t (orange curve), but does not significantly contribute to the precision of the magnitude of κ_t.

Generic model 3: allowing deviations in vertex loop coupling strengths, no assumption on the total width

In this benchmark model, the six absolute coupling strengths and three effective loop coupling strengths of generic model 2 are retained, and expressed in ratios of scale factor that can be measured independent of any assumptions on the Higgs boson total width. The free parameters are:

$$\kappa_{gZ} = \kappa_g \cdot \kappa_Z / \kappa_H \quad (6.37)$$
$$\lambda_{Zg} = \kappa_Z / \kappa_g \quad (6.38)$$
$$\lambda_{WZ} = \kappa_W / \kappa_Z \quad (6.39)$$
$$\lambda_{tg} = \kappa_t / \kappa_g \quad (6.40)$$
$$\lambda_{bZ} = \kappa_b / \kappa_Z \quad (6.41)$$
$$\lambda_{\tau Z} = \kappa_\tau / \kappa_Z \quad (6.42)$$
$$\lambda_{\mu Z} = \kappa_\mu / \kappa_Z \quad (6.43)$$
$$\lambda_{\gamma Z} = \kappa_\gamma / \kappa_Z \quad (6.44)$$
$$\lambda_{(Z\gamma)Z} = \kappa_{Z\gamma} / \kappa_Z . \quad (6.45)$$

Figure 6.21 shows the full set of results obtained from the fit to this benchmark. The fitted values and their uncertainties are also shown in Tab. 6.9.

This model allows custodial symmetry to be probed: identical coupling strength scale factors for the W and Z boson are required within tight bounds by the $SU(2)$ custodial symmetry and the ρ parameter measurements at LEP and at the Tevatron [3]. To test this constraint directly in the scalar sector, the ratio $\lambda_{WZ} = \kappa_W / \kappa_Z$ is probed.

The ratio λ_{WZ} is in part directly constrained by the decays in the $H \to WW^* \to \ell\nu\ell\nu$ and $H \to ZZ^* \to 4\ell$ channels and the WH and ZH production processes. It is also indirectly constrained by the VBF production process, which in the SM is 74% W fusion and 26% Z fusion-mediated (cf. Tab. 6.6). Fig. 6.22a shows the PLR as a function of the coupling strength scale factor ratio λ_{WZ}. Due to the interference terms, the fit is sensitive to the relative sign between the W and top-coupling (tH) and the relative sign between the Z and top-coupling ($gg \to ZH$), providing indirect sensitivity to the sign of λ_{WZ}. The negative solution is disfavoured at 0.5σ (0.3σ expected). The minimum corresponding to the positive solution is given by $\lambda_{WZ} = 0.92^{+0.14}_{-0.12}$. Also shown in Figs. 6.22b and 6.22c are the ratios $\lambda_{\gamma Z}$ and λ_{tg}. The ratio $\lambda_{\gamma Z}$ is sensitive to new charged particles contributing to the $H \to \gamma\gamma$ loop in comparison to $H \to ZZ^*$ decays. Similarly, the ratio λ_{tg} is sensitive to new coloured particles contributing through the $gg \to H$ loop as compared to ttH. The minimum corresponding to the positive solution is given by $\lambda_{tg} = 1.38 \pm 0.35$. Both are observed to be compatible with the SM expectation.

As the loop-induced processes are expressed by effective coupling strength scale factors, there is little sensitivity to the relative sign between coupling strength scale factors due to tH and $gg \to ZH$ processes only. Hence only positive values for all κ-factors except κ_t are shown without loss of generality. The nine-dimensional compatibility of the SM hypothesis with the

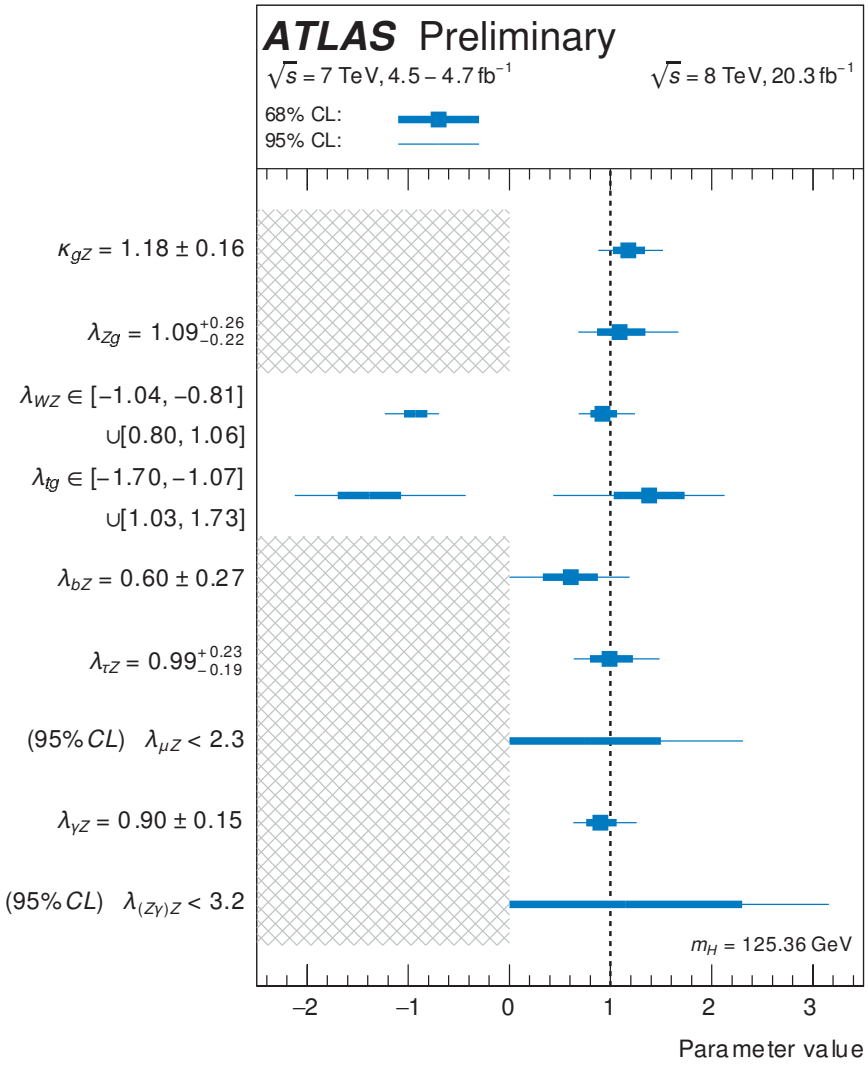

Figure 6.21: Results of fits for the generic model 3 (see text): allowing deviations in vertex loop coupling strengths and in the total width. Overview of best-fit values of parameters, where the inner and outer bars correspond to 68% CL and 95% CL intervals. The hatched area indicates regions that are outside the defined parameter boundaries.

Table 6.9: Numerical results of the fits for generic model 3 (see text). These results are also shown in Fig. 6.21.

Parameter		Measurement
κ_{gZ}	$=$	1.18 ± 0.16
λ_{Zg}	$=$	$1.09^{+0.26}_{-0.22}$
λ_{WZ}	$\in$	$[-1.04, -0.81] \cup [0.80, 1.06]$
λ_{tg}	$\in$	$[-1.70, -1.07] \cup [1.03, 1.73]$
λ_{bZ}	$=$	0.60 ± 0.27
$\lambda_{\tau Z}$	$=$	$0.99^{+0.23}_{-0.19}$
$\lvert\lambda_{\mu Z}\rvert$	$<$	2.3 (95% CL)
$\lambda_{\gamma Z}$	$=$	0.90 ± 0.15
$\lvert\lambda_{(Z\gamma)Z}\rvert$	$<$	3.2 (95% CL)

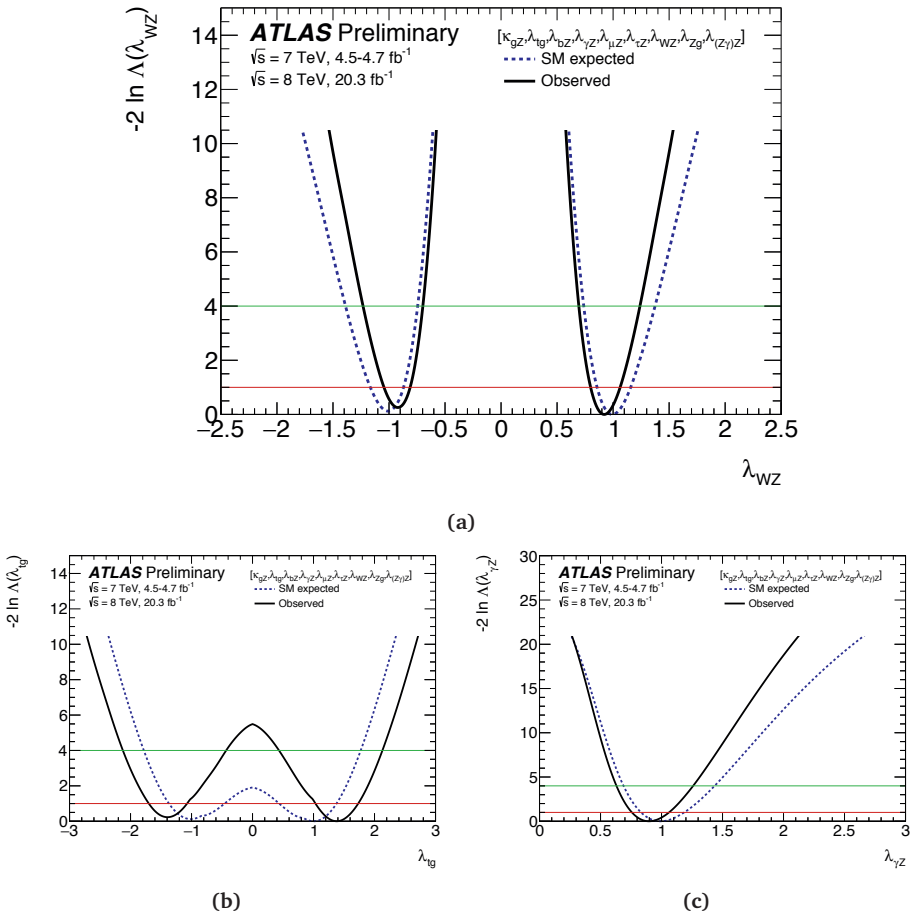

Figure 6.22: Results of fits for the generic model 3 (see text): allowing deviations in vertex loop coupling strengths and in the total width. PLRs as a functions of the coupling strength scale factor ratios (a) λ_{WZ}, (b) λ_{tg}, and (c) $\lambda_{\gamma\mathrm{Z}}$. For each measurement, the other coupling strength scale factor ratios are profiled. The dashed curves show the SM expectations. The red (green) horizontal lines indicates the cutoff values on the PLR corresponding to a 68% (95%) confidence interval on the POI, assuming the asymptotic χ^2 distribution for the test statistic.

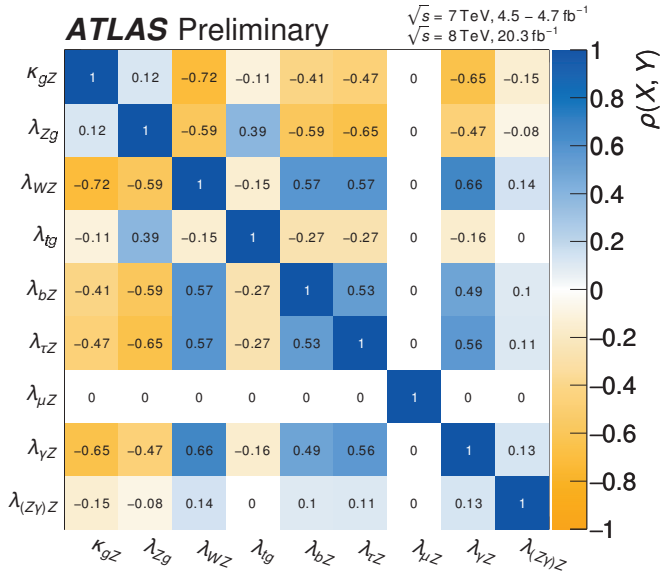

Figure 6.23: Correlation matrix of the coupling strength ratio parameters of generic model 3, detailed in Sec. 6.3.6.

best-fit point is 73%. Figure 6.23 shows the correlation matrix of the coupling strength ratio parameters of generic model 3.

The fit in the third generic benchmark model uses only the basic assumptions as stated at the beginning of this section and hence represents the most model-independent determination of coupling strength scale factors that is currently possible.

New Physics in Higgs couplings

7

Section 1.5 alludes to the open questions the SM currently faces, and fails to answer satisfactorily, e. g. regarding the naturalness of the Higgs boson mass, or the nature of DM. Many ideas have been proposed to address these shortcomings, yet no evidence for any BSM scenario has been found.

Typically, BSM models predict extensions or modifications of the minimal scalar sector that is embedded in the SM. For all interpretations presented in this chapter, it is assumed that any modification of the Higgs couplings does not change the Higgs boson decay kinematics appreciably. If this holds, the rate of any given process, in particular the production and decay of a BSM Higgs boson, can be expressed as an analytic function of the measured SM couplings and the parameters of the BSM theory. Within this framework, the observed Higgs boson serves as a probe of NP and constrains the parameter space of extended scalar sectors to guide future searches towards a discovery. Throughout this chapter, h denotes a light, CP-even Higgs boson with a mass of approximately 125.5 GeV.

The results discussed in this chapter have previously been presented in Ref. [38]. The interpretations are *not* based on the combined Higgs boson coupling strength measurements discussed in Cha. 6, but on an earlier iteration of the same analysis using 2014 input measurements [36]. In particular, these exploit the full 7 and 8 TeV pp collision data sample recorded by the ATLAS experiment for the decay modes $h \to \gamma\gamma$, $h \to ZZ^* \to 4\ell$, $h \to WW^* \to \ell\nu\ell\nu$ [440], and $h \to b\bar{b}$ [475], and the full 8 TeV pp collision data sample for the $h \to \tau\tau$ [476] channel. An additional constraint on the branching fraction of Higgs boson decays to invisible final states emanates from the measured rate of the process $Zh \to \ell\ell + E_{\mathrm{T}}^{\mathrm{miss}}$ [460]. Table 7.1 reports the measured couplings and the upper limit on the invisible branching fraction in various benchmark models, along with representative classes of BSM models that can be probed by the SM measurements.

In this chapter, the dependence of the Higgs boson couplings on particle masses is probed explicitly. It further is checked whether the Higgs boson is an elementary particle, or could be a composite state. For several BSM scenarios, e. g. MSSM, it is shown how the parameter space can be constrained through Higgs boson coupling measurements. Finally, a limit on the WIMP-nucleon scattering cross section via Higgs boson exchange, is derived. The interpretations presented in this chapter are complementary to direct searches for additional Higgs bosons and other NP scenarios. The statistical treatment of the data follows the common procedures outlined in Cha. 4. Peculiarities arise from physical boundaries being present in the studied models. An example is the branching fraction of Higgs boson decays into invisible final states, which, by definition, must be a positive quantity.

Table 7.1: Measurements of the Higgs boson coupling scale factors in different benchmark models, as reported in Ref. [36], along with BSM models that can be probed. For all models, the production modes are assumed to be the SM ones. Model 1, 2, and 5, assume the decay modes to be identical to the SM ones. Models 3 and 4 make no assumption on the total Higgs decay width. However, the decay modes are assumed to be identical to the SM ones, when setting limits on the underlying parameters of these BSM models. Models 6 and 7 allow for new decay modes, and thus do not make an assumption about the total Higgs decay width.

Model		Coupling Parameter	Description	Measurement
1	MCHM4, EW singlet	μ	Inclusive signal strength	$1.30\ ^{+0.18}_{-0.17}$
		$\kappa = \sqrt{\mu}$	Universal coupling	$1.14\ ^{+0.09}_{-0.08}$
2	MCHM5, 2HDM Type I	κ_V	Vector boson coupling	1.15 ± 0.08
		κ_F	Fermion coupling	$0.99\ ^{+0.17}_{-0.15}$
3	2HDM Type II, MSSM	$\lambda_{Vu} = \kappa_V/\kappa_u$	Ratio of vector boson and up-type fermion couplings	$1.21\ ^{+0.24}_{-0.26}$
		$\kappa_{uu} = \kappa_u^2/\kappa_h$	Ratio of squared up-type fermion coupling and total width scale factor	$0.86\ ^{+0.41}_{-0.21}$
		$\lambda_{du} = \kappa_d/\kappa_u$	Ratio of down-type fermion and up-type fermion couplings	$[-1.24, -0.81]$ $\cup [0.78, 1.15]$
4	2HDM Type III	$\lambda_{Vq} = \kappa_V/\kappa_q$	Ratio of vector boson and quark couplings	$1.27\ ^{+0.23}_{-0.20}$
		$\kappa_{qq} = \kappa_q^2/\kappa_h$	Ratio of squared quark coupling and total width scale factor	$0.82\ ^{+0.23}_{-0.19}$
		$\lambda_{lq} = \kappa_l/\kappa_q$	Ratio of lepton and quark couplings	$[-1.48, -0.99]$ $\cup [0.99, 1.50]$
5	Mass scaling parametrization	κ_Z	Z boson coupling	$0.95\ ^{+0.24}_{-0.19}$
		κ_W	W boson coupling	$0.68\ ^{+0.30}_{-0.14}$
		κ_t	t quark coupling	$[-0.80, -0.50]$ $\cup [0.61, 0.80]$
		κ_b	b quark coupling	$[-0.7, 0.7]$
		κ_τ	τ-lepton coupling	$[-1.15, -0.67]$ $\cup [0.67, 1.14]$
6	Higgs portal without $Zh \to \ell\ell + E_{\mathrm{T}}^{\mathrm{miss}}$	κ_g	Gluon effective coupling	$1.00\ ^{+0.23}_{-0.16}$
		κ_γ	Photon effective coupling	$1.17\ ^{+0.16}_{-0.13}$
		$\mathrm{BR}_{\mathrm{i.,u.}}$	Invisible branching ratio	$-0.16\ ^{+0.29}_{-0.30}$
7	Higgs portal with $Zh \to \ell\ell + E_{\mathrm{T}}^{\mathrm{miss}}$	κ_g	Gluon effective coupling	-
		κ_γ	Photon effective coupling	-
		$\mathrm{BR}_{\mathrm{i.,u.}}$	Invisible branching ratio	-0.02 ± 0.20

7.1 Mass scaling of couplings

The SM suggests that the couplings of the Higgs boson to other particles are directly proportional to their (pole) masses, cf. Cha. 1,

$$g_{hVV} \propto \frac{m_V^2}{v} \quad \text{and} \quad g_{hff} \propto \frac{m_f}{v}. \tag{7.1}$$

The framework for measuring coupling scale factors has been described in Sec. 6.3.1. Within this framework, the flavor structure of Higgs couplings is determined by the rates measured for the different production and decay modes, listed in the introduction of this chapter. Model 5 of Tab. 7.1 summarizes the measured coupling scale factors κ_x with $x = Z, W, t, b, \tau$, defined as the ratios between the measured couplings and their corresponding SM prediction.

The mass scaling hypothesized in the SM is tested using a purely phenomenological parametrization of the Higgs couplings to fermions and bosons, proposed in Ref. [477, 478],

$$\kappa_{f,i} = v \frac{m_{f,i}^{\epsilon}}{M^{1+\epsilon}} \quad \text{and} \quad \kappa_{V,j} = v \frac{m_{V,j}^{2\epsilon}}{M^{1+2\epsilon}}. \tag{7.2}$$

Here, $v \approx 246\,\text{GeV}$ is the canonical Higgs VEV in the SM, and $m_{f,i}$ ($m_{V,j}$) denotes the (pole) mass of each fermion (massive gauge boson) flavor, indexed i (j). The parameter ϵ explicitly probes the mass dependence of the couplings, and M is a "VEV parameter".

This parametrization assumes no additional production mechanisms and decay modes beyond the ones predicted in the SM. Higgs production or decay loops, e.g. $gg \to H$ or $h \to \gamma\gamma$, are resolved in terms of the running particles, assuming the same relative contributions as in the SM, and taking into account interference effects. In the double limit $\epsilon \to 0$ and $M \to v$ the SM is recovered, i. e. the VEV of the SM Higgs field, and the couplings of the Higgs boson ($\kappa_{F,i} = \kappa_{V,j} = 1$) are as predicted by the SM,

Figure 7.1 displays the observed and expected 68% and 95% CL intervals for a simultaneous measurement of the mass scaling factor ϵ and the VEV parameter M. The maximum of the likelihood function is obtained for

$$\epsilon = 0.01 \pm 0.04 \quad \text{and} \quad M = 215^{+15}_{-14}\,\text{GeV}. \tag{7.3}$$

The measurement is compatible with the expectation for a SM Higgs boson at the level of approximately 1.5 standard deviations, assuming that the test statistic $-2\ln\Lambda(\epsilon, M)$ asymptotically is distributed as a χ^2 distribution with two degrees of freedom.

The measurement of ϵ indicates that, within a few percent, the couplings to fermions and gauge bosons scale linearly and quadratic with their (pole) mass, respectively, as predicted in

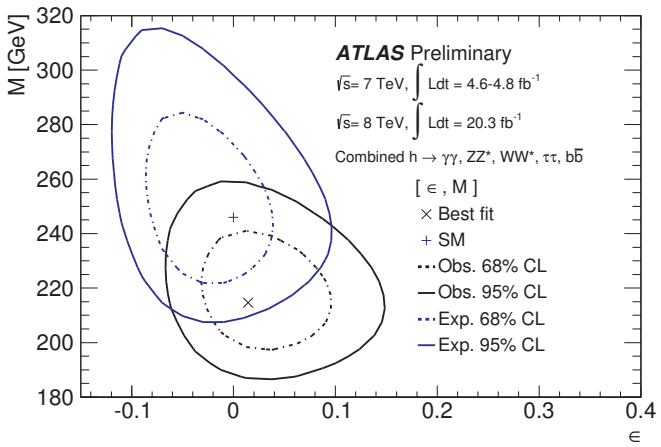

Figure 7.1: Confidence intervals as function of the mass scaling factor, ϵ, and the VEV parameter, M. The intervals are constructed at 68% and 95% CL for the recorded pp collision data, and compared to the prediction for a SM Higgs boson, under the assumption that the test statistic $-2\ln\Lambda(\epsilon, M)$ asymptotically is distributed as a χ^2 distribution with two degrees of freedom. The MLEs are indicated by markers.

the SM. The sensitivity is primarily owing to the relatively large mass of the W and Z bosons compared to the bulk of the fermions, and the precise measurement of their couplings to the Higgs boson. The deviation of the MLE of M from the SM VEV v is driven by the inclusive production strength exceeding the SM prediction. Nevertheless, this measurement suggests that the Higgs boson indeed resembles a quantum excitation of the Higgs field, cf. Cha. 1.

7.2 Minimal Composite Higgs model

Section 1.5.2 introduced a scenario wherein the Higgs boson is a composite pNG boson, rather than an elementary particle. Composite Higgs models are particularly appealing as they provide means to explain the relatively light Higgs boson mass, i. e. they may solve the scalar naturalness problem, and above all, they present a dynamical origin of EWSB. The (partial) compositeness paradigm can be tested through its implications for the Higgs boson couplings to the massive EW gauge bosons and the fermions, respectively. Deviations from the couplings of an elementary SM Higgs boson can be expressed as a function of the compositeness scale, f. The ratio of the predicted couplings to vector bosons relative to their SM expectation takes the form

$$\kappa_V = \sqrt{1-\xi}, \tag{7.4}$$

where $\xi = v^2/f^2$. However, the exact parametrization of the predicted Higgs couplings to the fermions depends on the representation which the SM quarks and leptons are embedded into. Popular choices are the spinorial or the fundamental representation of $SO(5)$. They have in common that in the limit $\xi \to 0$ the SM couplings are recovered and the resonances of the CFT decouple, $f \to \infty$.

Figure 7.2 shows the 68% and 95% CL intervals as function of the coupling scale factors for Higgs couplings to vector bosons and fermions, respectively. Overlaid are the predictions in the MCHM_4 and MCHM_5 as parametric functions of ξ. The results presented in this section neglect corrections due to new heavy resonances such as vector-like quarks [479]. Furthermore, the interpretations assume the same production and decay modes as in the SM. Higgs production or decay loops are resolved in terms of the running SM particles.

7.2.1 MCHM_4: fermions in the spinorial representation of *SO(5)*

When embedding the SM fermions into the spinorial representation of the $SO(5)$ bulk, the ratio of the predicted Higgs fermion couplings relative to the corresponding SM predictions, is given by

$$\kappa_F = \sqrt{1-\xi}. \tag{7.5}$$

Thus, in the MCHM_4, all Higgs couplings can be expressed in terms of a universal coupling scale factor, $\kappa = \kappa_V = \kappa_F$, which is equivalent to the inclusive production strength, $\kappa = \sqrt{\mu}$, cf. Model 1 of Tab. 7.1.

In order to confront the recorded collision data with the model, the measured rates in the different production and decay modes are expressed in terms of coupling scale factors. But these are a function of the underlying model parameter, ξ. The large inclusive production strength drives the MLE of ξ negative, cf. Fig. 7.3a,

$$\xi = 1 - \mu = -0.30^{+0.17}_{-0.18}, \tag{7.6}$$

which should be compared to the expectation for a elementary SM Higgs boson, $0.00^{+0.15}_{-0.17}$.

The model exhibits a lower physical boundary, $\xi \geq 0$, which has to be taken into account by the statistical interpretation of the data. The boundary is imposed on the PLR, restricting it to the allowed region of parameter space. In other words, the confidence interval is based on the test statistic $\tilde{t}_\mu$, as it is outlined in Sec. 4.2.4. The 95% CL upper limit is defined by a standard χ^2 cutoff of approximately 3.84. This is equivalent to the assumption that the test statistic used for performing the measurement (7.6), t_μ, asymptotically is distributed as a χ^2 distribution with one degree of freedom, which leads to some overcoverage near the boundaries. The observed 95% CL upper limit is $\xi < 0.12$. Transforming the boundaries of the confidence interval according to $f = v/\sqrt{\xi}$, yields the 95% CL lower limit on the compositeness scale,

$$f > 710\,\text{GeV}. \tag{7.7}$$

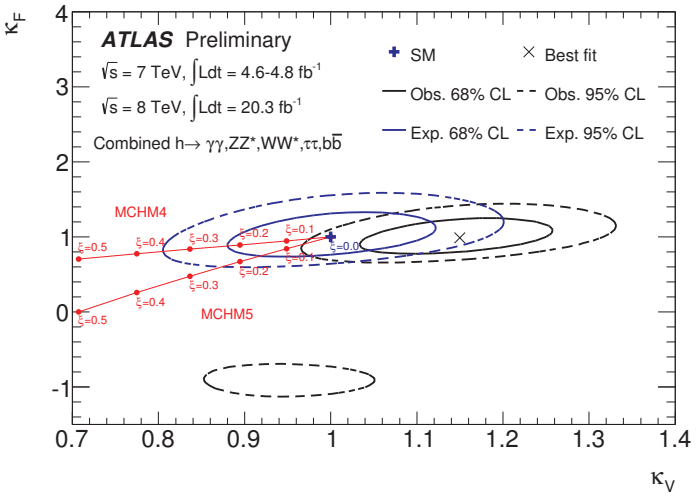

Figure 7.2: Confidence intervals as function of the coupling scale factors for Higgs couplings to vector bosons, κ_V, and fermions, κ_F, respectively. The intervals are constructed at 68% and 95% CL for the recorded pp collision data, and compared to the prediction for an elementary SM Higgs boson, under the assumption that the test statistic $-2\ln\Lambda(\kappa_V, \kappa_F)$ asymptotically is distributed as a χ^2 distribution with two degrees of freedom. A secondary minimum for $\kappa_F < 0$ is primarily due to the large rate measured for $h \to \gamma\gamma$ decays [36]. The MLEs are indicated by markers. The coupling predictions in the MCHM_4 and MCHM_5 are shown as parametric functions of the Higgs boson compositeness parameter, $\xi = v^2/f^2$. The two-dimensional likelihood contours are shown for reference only, i. e. the lower limit on the compositeness scale should not be determined from this illustration.

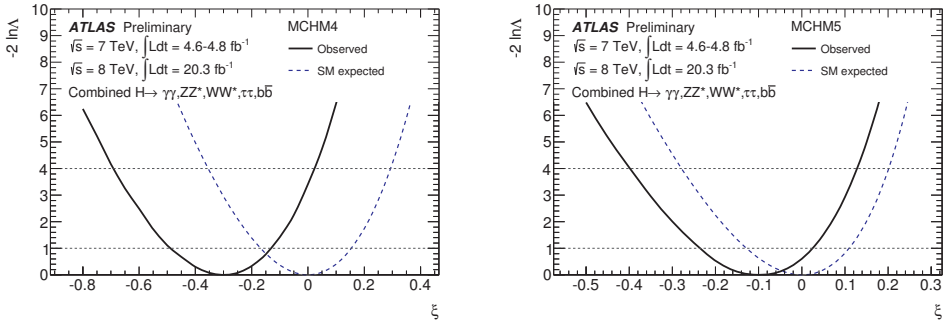

(a) **(b)**

Figure 7.3: Measurement of the Higgs boson compositeness parameter, $\xi = v^2/f^2$, in (a) the MCHM_4 and (b) MCHM_5. The profile likelihood functions are shown for collision data and for an elementary SM Higgs boson. The indicated confidence intervals are constructed under the assumption that the test statistic $-2\ln\Lambda(\xi)$ asymptotically is distributed as a χ^2 distribution with one degree of freedom.

The expected limits are $\xi < 0.29$, or $f > 460\,\text{GeV}$. The strong observed limit is driven by the large inclusive production strength measured in the combination of all studied channels.

7.2.2 MCHM$_5$: fermions in the fundamental representation of *SO(5)*

In the MCHM$_5$, i. e. when exploiting the fundamental representation of $SO(5)$, the Higgs couplings to vector bosons and fermions are not universal. Instead, the latter take the form

$$\kappa_F = \frac{1-2\xi}{\sqrt{1-\xi}}. \tag{7.8}$$

Model 2 of Tab. 7.1 summarizes the result of a measurement of κ_V and κ_F in the SM. The MLE of ξ is, cf. Fig. 7.3b,

$$\xi = -0.08^{+0.11}_{-0.16}, \tag{7.9}$$

to be compared to the expected precision, $0.00^{+0.11}_{-0.13}$, assuming an elementary SM Higgs boson. The measured value is negative because of the large production strengths observed throughout almost all channels.

As with the MCHM$_4$, the 95% CL upper limit must respect the physical boundary $\xi \geq 0$. Using the collision data, the limit is set to be $\xi < 0.15$, or equivalently in terms of the compositeness scale

$$f > 640\,\text{GeV}. \tag{7.10}$$

The expected limits are $\xi < 0.20$, or $f > 550\,\text{GeV}$. Again, the strong observed limit is driven by the large production strengths.

7.3 Additional electroweak singlet

Section 1.5.3 introduced the reader to a category of models with one additional scalar EW singlet field, serving as a viable DM candidate. One realization recently attracting attention, is a supersymmetric model with minimally extended scalar sector, namely the Next-to-Minimal Supersymmetric Standard Model (NMSSM) [480–483].

For a pair of non-degenerate CP-even states, h and H, the inclusive production strengths, i. e. the ratio of the observed production and decay rates relative to the prediction for a SM Higgs boson of the same mass, are

$$\mu_h = \frac{\sigma_h \times \text{BR}_h}{\left(\sigma_h \times \text{BR}_h\right)_{\text{SM}}} = \kappa^2 \quad \text{and} \quad \mu_H = \frac{\sigma_H \times \text{BR}_H}{\left(\sigma_H \times \text{BR}_H\right)_{\text{SM}}} = \kappa'^2\left(1 - \text{BR}_{H,\text{new}}\right), \tag{7.11}$$

respectively. The lighter state h and the heavier state H fully unitarize the high-energy scattering amplitudes for longitudinal gauge boson scattering, i. e. $\kappa^2 + \kappa'^2 = 1$. Thus, the

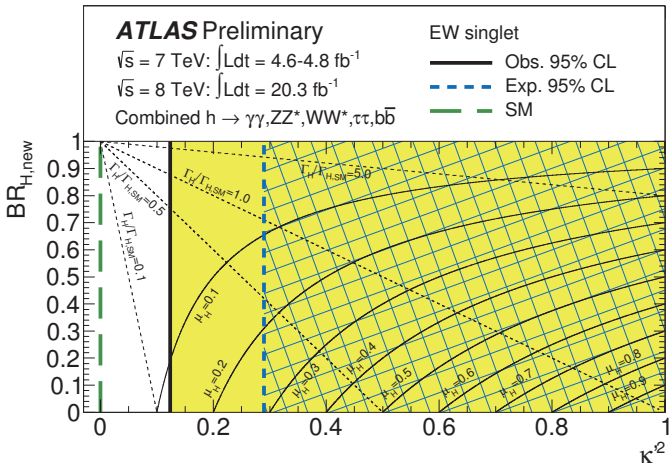

Figure 7.4: Observed (solid) and expected (dashed) 95% CL upper limits on the squared coupling, κ'^2, of a heavy Higgs boson arising from an additional real field transforming as an EW singlet. The limits are shown in the $(\kappa'^2, \mathrm{BR}_{H,\mathrm{new}})$ plane of the heavy Higgs boson along with selected contours of the scale factor for the total width, $\Gamma_H/\Gamma_{H,\mathrm{SM}}$, and the inclusive production strength, μ_H. The light shaded and hashed regions indicate the observed and expected exclusions, respectively. The results are independent of the mass of the heavy Higgs boson and potentially accessible invisible and di-Higgs final states, e.g. from $H \to hh$ decays.

squared universal coupling of the heavy Higgs boson can be inferred from the signal strength of the light Higgs boson,

$$\kappa'^2 = 1 - \mu_h. \tag{7.12}$$

It is important to note that this relation holds independent of the mass of the heavy Higgs boson. It also is independent of invisible or di-Higgs final states, e.g. from $H \to hh$ decays, that could potentially be accessible.

The combined measurement of the inclusive production strength of the light Higgs boson in the SM is given in Model 1 of Tab. 7.1. Thus, from this measurement follows the squared universal coupling of the heavy Higgs boson,

$$\kappa'^2 = 1 - \mu_h = -0.30^{+0.17}_{-0.18}. \tag{7.13}$$

The expected precision for a minimal scalar sector is $0.00^{+0.15}_{-0.17}$.

As with the MCHM, the EWS model contains a lower physical boundary, $\kappa'^2 \geq 0$. Since the measured Higgs boson rate exceeds the expectation for a SM Higgs boson, the MLE of κ'^2 is found to be approximately 1.5 standard deviations below the boundary. Taking into account

the physical constraint in the usual way, the 95% CL upper limit on the squared universal coupling of the heavy Higgs boson is

$$\kappa'^2 < 0.12. \tag{7.14}$$

The expected limit is $\kappa'^2 < 0.29$. Figure 7.4 shows the observed and expected upper limits on κ'^2 in the $(\kappa'^2, \mathrm{BR}_{H,\mathrm{new}})$ plane of the heavy Higgs boson along with selected contours of the scale factor for the total width, $\Gamma_H/\Gamma_{H,\mathrm{SM}}$, and the inclusive production strength, μ_H.

7.4 The Two Higgs Doublet Model

The symmetries of many BSM scenarios, e. g. the MSSM, require a second Higgs doublet in addition to the one present in the SM. Section 1.5.4 introduced the reader to the theoretical foundations of generic 2HDMs. The scalar sector of the Lagrangian is described by only six parameters: the mixing angle of the light (h) and the heavy (H) scalar, α, the mixing angle of the charged scalars ($H^\pm$) and the pseudoscalar (A), β, and the masses of the five physical Higgs bosons, m_h, m_H, m_A, and $m_{H^\pm}$. The tangent of β is defined as the ratio of the VEVs of the Higgs doublets, $\tan\beta \equiv v_2/v_1$, cf. Sec. 1.5.4.

The interpretations presented in this section assume that the discovered particle is the light CP-even neutral scalar h with $m_h = 125.5\,\mathrm{GeV}$. Its couplings to massive gauge bosons, up-type and down-type quarks, and leptons, relative to the ones of a SM Higgs boson, are fully determined by the mixing angles α and β. The parametrizations have been summarized for four types of 2HDMs by Eqn. (1.67) and in Tab. 1.3. In data, the measured production and decay rates scale as functions of the couplings κ_V, κ_u, κ_d, and κ_l. The exact benchmark depends on the type of the studied 2HDM. Model 3 and 4 of Tab. 7.1 show measurements of ratios of these couplings, assuming no production modes beyond the SM ones, but do not make any assumption about the total decay width. However, in order to facilitate a measurement of the absolute couplings, in the remainder of this section the decay modes are restricted to the ones of a SM Higgs boson.

The coupling-rescaled production and decay rates have been validated against predictions from SusHi [484] and 2hdmc [485], respectively. These programs implement the calculation of (neutral) Higgs production rates and the BRs within the 2HDMs, respectively. The agreement of the two approaches is found to be within one percent. For certain regions of the 2HDM parameter space, in particular for small or large values of $\tan\beta$, the Yukawa coupling to the b-quark is enhanced. Thus, Higgs production through bottom quark annihilation, $q\bar{q}/gg \to b\bar{b}h$, can become the dominant production mechanism for the neutral Higgs bosons, cf. Fig. 7.5. In the regions of the parameter space that are compatible with the data at 95% CL, the rate can be as large as 10% of the total production rate. Within the scope of the combined SM coupling measurements, summarized in Tab. 7.1, this production mode is deemed to be negligible. No MC simulation is available for the $q\bar{q}/gg \to b\bar{b}h$ process.

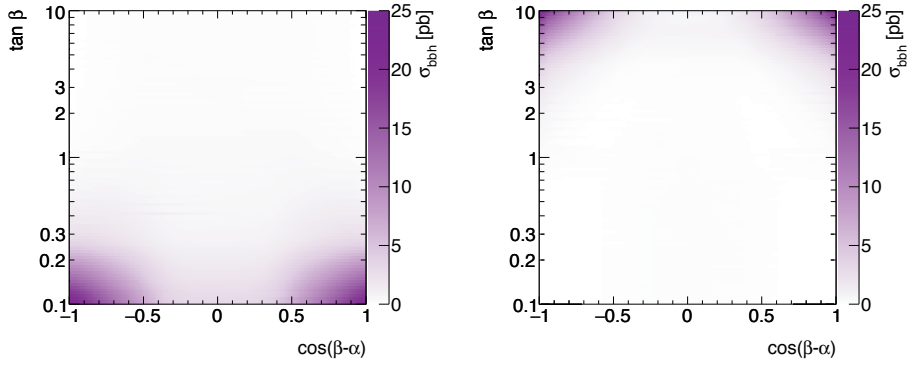

Figure 7.5: Cross section for the production of a light scalar with $m_h = 125.5\,\text{GeV}$ through bottom quark annihilation, $q\bar{q}/gg \to b\bar{b}h$, at $\sqrt{s} = 8\,\text{TeV}$, as a function of the mixing angles α and β. The rates are computed using the SusHi program in case the b-quark couples (a) to the second or (b) to the first Higgs doublet. In the SM, the cross section for producing a Higgs boson is approximately 0.2 pb.

However, the results presented in this section include the bbh production mode through a correction. The implementation is such that the $q\bar{q}/gg \to b\bar{b}h$ rate scales with the square of the Yukawa coupling to the b-quark, under the assumption that it produces differential distributions that are the same as those in gluon fusion [38].

Figure 7.6 shows for four types of 2HDMs the regions of the $(\cos(\beta-\alpha), \tan\beta)$ space that are (indirectly) excluded at 95% CL or more via Higgs coupling measurements, independent of the masses of the five physical Higgs bosons. The regions expected to be excluded in case the scalar sector would be as predicted by the SM, are overlaid. All considered models exhibit a physical boundary, $\kappa_V \leq 1$. To account for it, the PLR is restricted to the allowed region of the parameter space, namely $|\sin(\beta-\alpha)| \leq 1$. In the SM alignment limit, $\cos(\beta-\alpha) = 0$, the likelihood function is independent of β. Thus, the number of POIs is locally reduced to one, leading to some over-coverage in that region of the parameter space. Eventually, the data are consistent with the SM alignment limit at a level of approximately 1 or 2 standard deviations in each of the tested models.

The shape of the excluded regions can be understood by explicitly transforming the confidence intervals for all coupling scale factors according to the functional dependence on the mixing angles α and β for each of the four types of models. The reader is referred to Sec. 9.3.4, in particular Fig. 9.11, which shows the transformed confidence intervals based on the projections for measurements of the Higgs boson couplings at the HL-LHC.

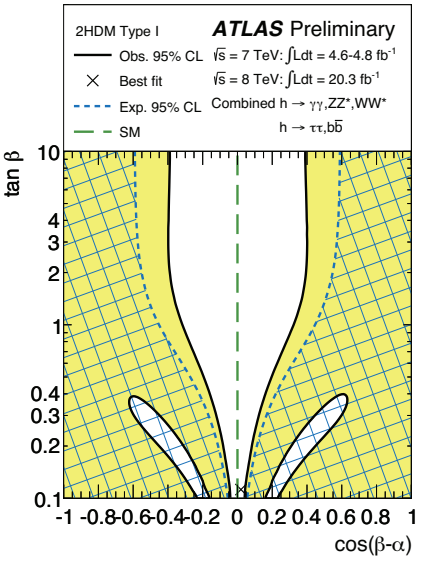

(a) Type I

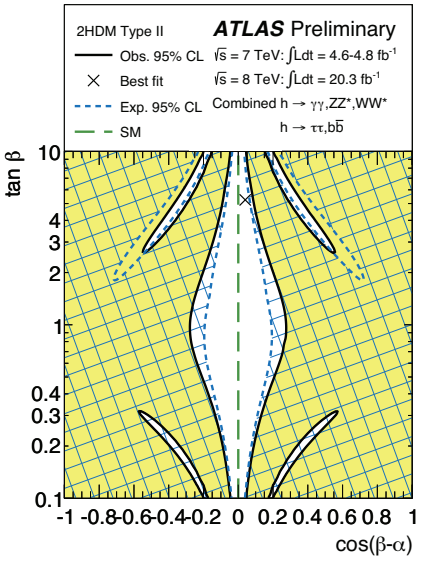

(b) Type II

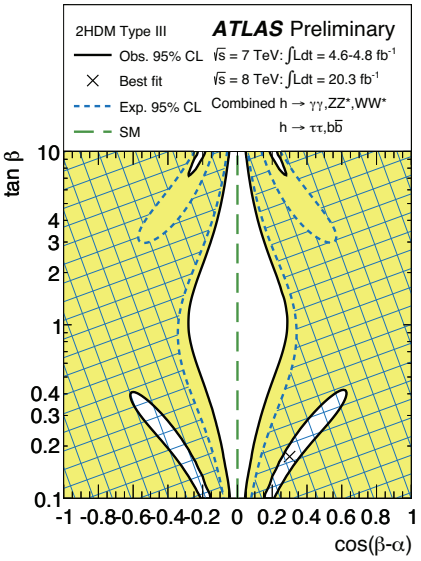

(c) Lepton specific

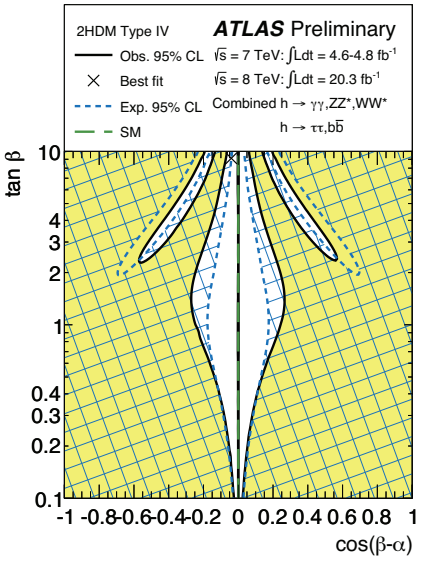

(d) Flipped

Figure 7.6: Regions of the $(\cos(\beta-\alpha), \tan\beta)$ space of four types of 2HDMs that are indirectly excluded at 95% CL or more from a combined measurement of the Higgs boson production and decay rates, independent of the masses of the five physical Higgs bosons. The regions expected to be excluded in case the scalar sector would be as predicted by the SM, are overlaid. The light shaded and hashed regions indicate the observed and expected exclusions, respectively. The indicated confidence intervals are constructed under the assumption that the test statistic $-2\ln\Lambda(\cos(\beta-\alpha), \tan\beta)$ asymptotically is distributed as a χ^2 distribution with two degrees of freedom.

7.5 The Minimal Supersymmetric Standard Model

The generic MSSM presents a concrete, but rather involved, realization of a 2HDM of Type II. Focusing on the scalar sector, notably the radiative corrections involving SUSY parameters complicate the model. Examples of such BSM model parameters are the SUSY breaking scale, the top and bottom squark trilinear couplings, or the higgsino mass. These parameters explicitly enter the mass squared mixing matrix of the neutral, CP-even scalars in the MSSM, Eqn. (1.68). This picture is manifest at the TeV scale, but assumed to also hold for higher scales. Further assuming that the dominant radiative corrections only involve top quark and top squark loops, their size can be inferred from the measured Higgs boson mass, m_h. This simplified model is termed hMSSM, cf. Sec. 1.5.5, where the letter "h" indicates that the discovered Higgs boson is identified with the light CP-even state h of the full MSSM.

In light of the current experimental results, direct corrections to the couplings of the Higgs boson can be neglected. Then, the ratios of the couplings to vector bosons (κ_V), up-type fermions (κ_u) and down-type fermions (κ_d), relative to the corresponding SM predictions, can be expressed in terms of just three parameters: the mixing angle of the charged scalars ($H^\pm$) and the pseudoscalar (A), β, and the masses of the pseudoscalar and the Z boson, m_A and m_Z, respectively. For convenience, the exact parametric expressions are reproduced in this section,

$$\kappa_V = s_d(m_A, \tan\beta)\frac{1}{\sqrt{1+\tan^2\beta}} + s_u(m_A, \tan\beta)\frac{\tan\beta}{\sqrt{1+\tan^2\beta}}, \tag{7.15}$$

$$\kappa_u = s_u(m_A, \tan\beta)\frac{\sqrt{1+\tan^2\beta}}{\tan\beta} \quad \text{and} \quad \kappa_d = s_d(m_A, \tan\beta)\sqrt{1+\tan^2\beta}. \tag{7.16}$$

The functions $s_u = \sin\alpha$ and $s_d = \cos\alpha$ diagonalize the CP-even neutral states,

$$s_u = \frac{1}{\sqrt{1+\frac{\left(m_A^2+m_Z^2\right)^2\tan^2\beta}{\left(m_Z^2+m_A^2\tan^2\beta-m_h^2\left(1+\tan^2\beta\right)\right)^2}}} \quad \text{and} \quad s_d = \frac{\left(m_A^2+m_Z^2\right)\tan\beta}{m_Z^2+m_A^2\tan^2\beta-m_h^2\left(1+\tan^2\beta\right)}s_u. \tag{7.17}$$

The Z boson mass has been measured to a high precision, $m_Z = 91.1876 \pm 0.0021\,\text{GeV}$ [486], leaving only two fundamental parameters to be determined, namely m_A and $\tan\beta$. It is important to point out, that this can be done remarkably economically and independent of assumptions on the SUSY parameters, i. e. without explicitly probing a grid of benchmark points.

Model 3 of Tab. 7.1 shows the results of a combined measurement of the Higgs production and decay rates, interpreted in terms of ratios of the scale factors for Higgs couplings to vector bosons, up-type fermions and down-type fermions. The measurement only considers production modes identical to the SM ones, but does not make any assumption about the Higgs boson total decay width. However, in order to facilitate a measurement of the

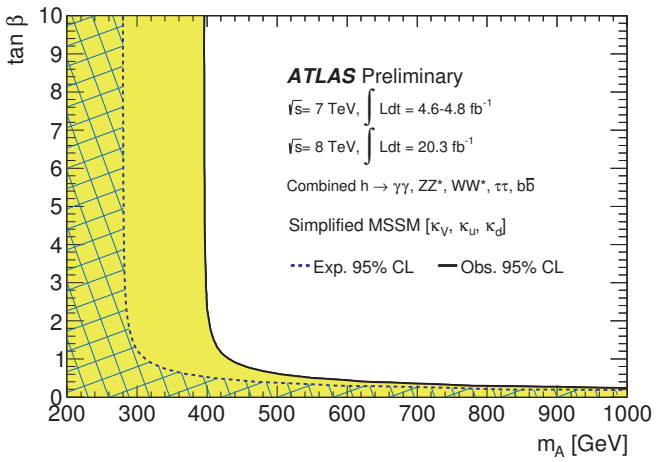

Figure 7.7: Regions of the hMSSM parameter space that are indirectly excluded at 95% CL or greater from a combined measurement of the Higgs boson production and decay rates. The regions expected to be excluded in case the scalar sector would be as predicted by the SM, are overlaid. The light shaded and hashed regions indicate the observed and expected exclusions, respectively. The indicated confidence intervals are constructed under the assumption that the test statistic $-2\ln\Lambda(m_A, \tan\beta)$ asymptotically is distributed as a χ^2 distribution with two degrees of freedom. The SM decoupling limit is at large m_A.

absolute couplings, in the remainder of this section the decay modes are restricted to the ones of a SM Higgs boson. These are parametrized according to the functional dependence on m_A and $\tan\beta$ in the hMSSM. As with the generic 2HDMs, the cross section must be corrected for Higgs production through bottom quark annihilation. Again, this is implemented as a function of the Yukawa coupling to the b-quark, following the procedure outlined in Sec. 7.4.

Figure 7.7 shows the regions of the hMSSM parameter space that are indirectly excluded by the pp collision data recorded by the ATLAS experiment. The data are consistent with the SM decoupling limit at large m_A. The observed (expected) lower limit at 95% CL on the CP-odd Higgs boson mass is

$$m_A > 400\,\text{GeV}\ (m_A > 280\,\text{GeV}) \quad \text{for} \quad 2 \leq \tan\beta \leq 10. \tag{7.18}$$

The limit increases to larger masses for $\tan\beta < 2$. The low $\tan\beta$ regime is explicitly excluded by this measurement. Variations of m_H within the measured uncertainties have a negligible impact on the derived limits. This also implies that the estimated size of the radiative corrections is stable.

Just as the underlying 2HDM, the hMSSM exhibits a physical boundary, restricting the coupling to the massive gauge bosons to not exceeding the SM value, $\kappa_V \leq 1$. Hence, the test statistic is constructed with respect to the maximum likelihood value obtained within the physical region of the parameter space, $m_A > 0$ and $\tan\beta > 0$. However, the rates measured for the $h \to \gamma\gamma$ and $h \to ZZ^* \to 4\ell$ decay modes, exceed the SM prediction. Since they are interpreted either through a resolved loop (dominated by a W boson), or directly in terms of the coupling scale factor κ_V, the limits on the hMSSM parameters are stronger than expected. The shape of the excluded regions can be understood by explicitly visualizing the confidence intervals for all coupling scale factors in the m_A-$\tan\beta$ parameter space. The reader is referred to Sec. 9.3.5, in particular Fig. 9.13, which shows the projected confidence intervals for the Higgs boson couplings at the HL-LHC transformed according to functional dependence on the hMSSM model parameters.

7.6 Dark Matter and the Higgs portal model

In Higgs portal models, the branching fraction for Higgs boson decays into invisible final states, $\mathrm{BR}_{\mathrm{i.,u.}}$, can be interpreted as the coupling of the Higgs boson to a DM candidate, i. e. a WIMP. $\mathrm{BR}_{\mathrm{i.,u.}}$ is determined indirectly from measuring the rates of the SM production and decay modes in a benchmark model that allows for extra contributions from new particles to the total width,

$$\Gamma_h = \frac{\sum_i \kappa_i^2}{(1-\mathrm{BR}_{\mathrm{i.,u.}})}\Gamma_h^{\mathrm{SM}} \quad \text{with} \quad \sum_i \kappa_i^2 = \mathrm{BR}(h \to \gamma\gamma)\cdot\kappa_\gamma^2 + \mathrm{BR}(h \to gg)\cdot\kappa_g^2 + \mathrm{BR}(h \to \text{other}), \tag{7.19}$$

as well as for enhancements of loop induced processes, e. g. $gg \to h$ or $h \to \gamma\gamma$. Thus, loops are not resolved in terms of the contributing SM particles, but rather parametrized by effective coupling scale factors, κ_g and κ_γ, to absorb the additional contributions. The couplings of the Higgs boson to the known massive SM particles other than the WIMP are assumed to be as predicted by the SM, i. e. $\kappa_i = 1$. Hence, the corresponding partial decay widths can be inferred, implying the form of $\sum_i \kappa_i^2$ given in Eqn. (7.19). In the remainder of this section, no new Higgs boson production modes beyond the SM ones are considered. Including $Zh \to \ell\ell + E_{\mathrm{T}}^{\mathrm{miss}}$ decays allows distinguishing direct invisible decays with a true MET signature from undetected modes, i. e. decays into final states resembling background processes. An example for such an undetected decay mode would be a final state with multiple light jets, which is typically identified as QCD multijet production.

The indirect measurement of $\mathrm{BR}_{\mathrm{i.,u.}}$ using SM final states only, and the measurement with additional constraint from the search for invisible decays of a Higgs boson produced in association with a Z boson, corresponding to Model 6 and 7 of Tab. 7.1, respectively, are

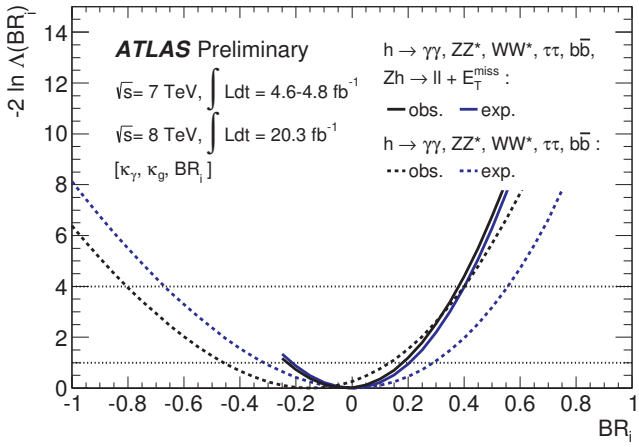

Figure 7.8: Indirect measurement of the branching fraction of Higgs boson decays into invisible final states, $\mathrm{BR}_{\mathrm{i.,u.}}$, using SM final states only, and the measurement with additional constraint from the search for invisible decays of a Higgs boson produced in association with a Z boson. Effective loop-induced coupling scale factors absorb contributions from new particles to the respective production and decay modes. The indicated confidence intervals are constructed under the assumption that the test statistic $-2\ln\Lambda(\mathrm{BR}_{\mathrm{i.,u.}})$ asymptotically is distributed as a χ^2 distribution with one degree of freedom, ignoring the physical boundary, $\mathrm{BR}_{\mathrm{i.,u.}} \geq 0$. At low values of $\mathrm{BR}_{\mathrm{i.,u.}}$, approximately one standard deviation below the MLE, the $Zh \to \ell\ell + E_{\mathrm{T}}^{\mathrm{miss}}$ p.d.f. for some categories becomes ill-defined (negative).

shown in Fig. 7.8. The branching fraction of the Higgs boson to invisible final states is estimated to be

$$\mathrm{BR}_{\mathrm{i.,u.}} = -0.16^{+0.29}_{-0.30} \quad \text{and} \quad \mathrm{BR}_{\mathrm{i.,u.}} = -0.02 \pm 0.20 \tag{7.20}$$

in the two scenarios, respectively. The expected precision for the measurement of $\mathrm{BR}_{\mathrm{i.,u.}}$ assuming that the SM holds, is $0.00^{+0.29}_{-0.32}$ and 0.00 ± 0.21, respectively. This demonstrates the increase in sensitivity when including the data from the $Zh \to \ell\ell + E_{\mathrm{T}}^{\mathrm{miss}}$ search. No evidence is found for invisible final states in Higgs boson decays. Thus, in the following an upper limit is constructed.

The negative estimate of $\mathrm{BR}_{\mathrm{i.,u.}}$ reflects an inclusive production strength, which is larger than the one predicted by the SM. It can be interpreted as a decrease in the Higgs boson total decay width. However, in a physical context, a branching fraction must be defined strictly positive, $\mathrm{BR}_{\mathrm{i.,u.}} \geq 0$. Hence, to account for the boundary, the PLR must be restricted to the allowed region of the parameter space when constructing the confidence interval around $\mathrm{BR}_{\mathrm{i.,u.}}$. The 95% CL upper limit then is defined under the assumption that the test statistic

asymptotically is distributed as a χ^2 distribution with one degree of freedom, which leads to some overcoverage near the boundaries. The result is

$$\mathrm{BR}_{\mathrm{i.,u.}} < 0.41 \quad \text{and} \quad \mathrm{BR}_{\mathrm{i.,u.}} < 0.37 \tag{7.21}$$

without including the $Zh \to \ell\ell + E_{\mathrm{T}}^{\mathrm{miss}}$ data, or explicitly exploiting it. The expected upper limits are $\mathrm{BR}_{\mathrm{i.,u.}} < 0.55$ and $\mathrm{BR}_{\mathrm{i.,u.}} < 0.39$, respectively.

As it is outlined in Sec. 1.5.6, the observed upper limit ($\mathrm{BR}_{\mathrm{i.,u.}} < 0.37$) can be used to deduce an upper limit on the coupling of the Higgs boson to a WIMP. The Higgs partial decay widths into a pair of DM candidates depends on the WIMP mass, m_χ, and its spin, $\chi = S$, V, or f. For the results presented in this section, scalar (S), Majorana fermion (f), e. g. neutralinos or gluinos in the MSSM, or vector (V) DM candidates are considered, cf. Eqns. (1.76)-(1.78). The most conservative limits are obtained under the assumption that Higgs boson decays to WIMP pairs account entirely for the partial width for decays to invisible states. Any contribution beyond this, would reduce the branching fraction for Higgs boson decays to WIMP pairs, and thus produces more stringent constraints.

To ease the comparison with results from direct searches for DM through nuclei recoils from elastic scattering of WIMPs [284–290], the cross section for scattering between the WIMP and nucleons, $\sigma_{\chi-N}$, is computed, assuming that the process is mediated via exchanging a Higgs boson. In other words, a Higgs portal model is probed. The calculations have been summarized in Sec. 1.5.6.

The results derived in this section take $m_N \approx 0.94\,\mathrm{GeV}$ as the nucleon mass, and the form factor associated with the Higgs-nucleon coupling has been computed on the lattice, $f_N = 0.33^{+0.30}_{-0.07}$ [280]. Figure 7.9 shows the 95% CL upper limit on the WIMP-nucleon scattering cross section as a function of the WIMP mass. The indirect constraints are complementary to the generic searches of direct detection experiments, presented for comparison on the same canvas at the confidence levels indicated. In the Higgs portal model at low WIMP masses, $m_\chi \leq m_h/2$, the Higgs coupling measurements produce considerably more stringent limits than the direct searches. At higher masses, $m_\chi > m_h/2$, the sensitivity of the indirect measurements degrades due to kinematic reasons.

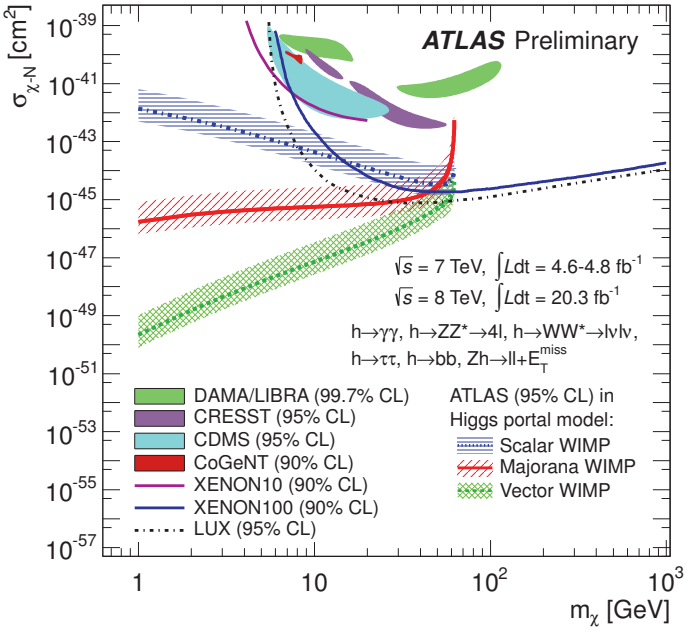

Figure 7.9: Upper limit at 95% CL on the WIMP-nucleon scattering cross section, $\sigma_{\chi-N}$, as a function of the mass of the DM particle, m_χ, for a scalar, Majorana fermion, or vector boson DM candidate. The hashed bands indicate the (theoretical) uncertainty associated with the calculation of the form factor describing the Higgs-nucleon coupling, f_N. The upper limit from ATLAS is indirectly inferred from Higgs boson exchange in a Higgs portal model. The coupling of the Higgs boson to the WIMP is determined indirectly from Higgs coupling measurements in combination with a search for invisible decays of a Higgs boson produced in association with a Z boson. Spin-independent results from direct searches for DM through nuclei recoils from elastic scattering of WIMPs, are shown for comparison [284–290].

The Higgs boson mass

8

The ATLAS and CMS Collaborations have independently measured m_H using the samples of proton-proton collision data collected in 2011 and 2012, commonly referred to as LHC Run 1. The analyzed samples correspond to approximately 5 fb^{-1} of integrated luminosity at $\sqrt{s} = 7$ TeV, and 20 fb^{-1} at $\sqrt{s} = 8$ TeV, for each experiment. Combined results in the context of the separate experiments, as well as those in the individual channels, are presented in Refs. [21, 221, 487, 488].

This chapter describes a combination of the Run 1 data from the two experiments, leading to improved precision for m_H. Besides its intrinsic importance as a fundamental parameter, improved knowledge of m_H yields more precise predictions for the other Higgs boson properties. Furthermore, the combined mass measurement provides a first step towards combinations of other quantities, such as the couplings. In the SM, m_H is related to the values of the masses of the W boson and top quark through loop-induced effects. Taking into account other measured SM quantities, the comparison of the measurements of the Higgs boson, W boson, and top quark masses can be used to directly test the consistency of the SM [489] and thus to search for evidence of physics beyond the SM.

8.1 Input analyses to the combination

The combination is performed using only the $H \to \gamma\gamma$ and $H \to ZZ^* \to 4\ell$ decay channels, because these two channels offer the best mass resolution. Interference between the Higgs boson signal and the continuum background is expected to produce a downward shift of the signal peak relative to the true value of m_H. The overall effect in the $H \to \gamma\gamma$ channel [490–492] is expected to be a few tens of MeV for a Higgs boson with a width near the SM value, which is small compared to the current precision. The effect in the $H \to ZZ^* \to 4\ell$ channel is expected to be much smaller [469]. The effects of the interference on the mass spectra are neglected in this chapter.

The ATLAS and CMS detectors, cf. Cha. 2 are designed to precisely reconstruct charged leptons, photons, hadronic jets, and the imbalance of momentum transverse to the direction of the beams. The two detectors are based on different technologies requiring different reconstruction and calibration methods. Consequently they are subject to different sources of systematic uncertainty.

The $H \to \gamma\gamma$ channel is characterized by a narrow resonant signal peak containing several hundred events per experiment above a large falling continuum background. The overall signal-to-background ratio is a few percent. Both experiments divide the $H \to \gamma\gamma$ events into different categories depending on the signal purity and mass resolution, as a means to improve sensitivity. While CMS uses the same analysis procedure for the measurement of the Higgs boson mass and couplings [487], ATLAS implements separate analyses for the couplings [23] and for the mass [21]; the latter analysis classifies events in a manner that reduces the expected systematic uncertainties in m_H.

The $H \to ZZ^* \to 4\ell$ channel yields only a few tens of signal events per experiment, but has very little background, resulting in a signal-to-background ratio larger than 1. The events are analyzed separately depending on the flavor of the lepton pairs. To extract m_H, ATLAS employs a two-dimensional (2D) fit to the distribution of the four-lepton mass and a kinematic discriminant introduced to reject the main background, which arises from ZZ continuum production. The CMS procedure is based on a three-dimensional fit, utilizing the four-lepton mass distribution, a kinematic discriminant, and the estimated event-by-event uncertainty in the four-lepton mass. Both analyses are optimized for the mass measurement and neither attempts to distinguish between different Higgs boson production mechanisms.

8.2 Measurement parametrization and combination methodology

There are only minor differences in the parameterizations used for the present combination compared to those used for the combination of the two channels by the individual experiments. These differences have almost no effect on the results.

The measurement of m_H, along with its uncertainty, is based on the maximization of PLRs $\Lambda(\boldsymbol{\alpha})$ in the asymptotic regime [392, 396], cf. Cha. 4:

$$\Lambda(\boldsymbol{\alpha}) = \frac{L\big(\boldsymbol{\alpha}\,,\,\hat{\hat{\boldsymbol{\theta}}}(\boldsymbol{\alpha})\big)}{L(\hat{\boldsymbol{\alpha}},\hat{\boldsymbol{\theta}})}, \tag{8.1}$$

where L represents the likelihood function, $\boldsymbol{\alpha}$ the POI, and $\boldsymbol{\theta}$ the nuisance parameters. There are three types of nuisance parameters: those corresponding to systematic uncertainties, the fitted parameters of the background models, and any unconstrained signal model parameters not relevant to the particular hypothesis under test. Systematic uncertainties are discussed below. The other two types of nuisance parameters are incorporated into the statistical uncertainty. The $\boldsymbol{\theta}$ terms are profiled, i.e., for each possible value of a POI (e.g., m_H), all nuisance parameters are refitted to maximize L. The $\hat{\boldsymbol{\alpha}}$ and $\hat{\boldsymbol{\theta}}$ terms denote the unconditional MLEs of the best-fit values for the parameters, while $\hat{\hat{\boldsymbol{\theta}}}(\boldsymbol{\alpha})$ is the CMLE for given parameter values $\boldsymbol{\alpha}$.

The likelihood functions L are constructed using signal and background p.d.f.s that depend on the discriminating variables: for the $H \to \gamma\gamma$ channel, the diphoton mass and, for the $H \to ZZ^* \to 4\ell$ channel, the four-lepton mass (for CMS, also its uncertainty) and the kinematic discriminant. The signal p.d.f.s are derived from samples of MC simulated events. For the $H \to ZZ^* \to 4\ell$ channel, the background p.d.f.s are determined using a combination of simulation and data control regions. For the $H \to \gamma\gamma$ channel, the background p.d.f.s are obtained directly from the fit to the data. The profile-likelihood fits to the data are performed as a function of m_H and the signal-strength scale factors defined below. The fitting framework is implemented independently by ATLAS and CMS, using the RooFit [388], RooStats [397], and HistFactory [390] data modeling and handling packages.

Despite the current agreement between the measured Higgs boson properties and the SM predictions, it is pertinent to perform a mass measurement that is as independent as possible of SM assumptions. For this purpose, three signal-strength scale factors are introduced and profiled in the fit, thus reducing the dependence of the results on assumptions about the Higgs boson couplings and about the variation of the production cross section times branching fraction with the mass. The signal strengths are defined as $\mu = (\sigma_{\text{expt}} \times \text{BR}_{\text{expt}})/(\sigma_{\text{SM}} \times \text{BR}_{\text{SM}})$, representing the ratio of the cross section times branching fraction in the experiment to the corresponding SM expectation for the different production and decay modes. Two factors, $\mu^{\gamma\gamma}_{\text{ggF}+ttH}$ and $\mu^{\gamma\gamma}_{\text{VBF}+VH}$, are used to scale the signal strength in the $H \to \gamma\gamma$ channel. The production processes involving Higgs boson couplings to fermions, namely ggF and associated production with a top quark-antiquark pair (ttH), are scaled with the $\mu^{\gamma\gamma}_{\text{ggF}+ttH}$ factor. The production processes involving couplings to vector bosons, namely VBF and associated production with a vector boson (VH), are scaled with the $\mu^{\gamma\gamma}_{\text{VBF}+VH}$ factor. The third factor, $\mu^{4\ell}$, is used to scale the signal strength in the $H \to ZZ^* \to 4\ell$ channel. Only a single signal-strength parameter is used for $H \to ZZ^* \to 4\ell$ events because the m_H measurement in this case is found to exhibit almost no sensitivity to the different production mechanisms.

The procedure based on the two scale factors $\mu^{\gamma\gamma}_{\text{ggF}+ttH}$ and $\mu^{\gamma\gamma}_{\text{VBF}+VH}$ for the $H \to \gamma\gamma$ channel was previously employed by CMS [487] but not by ATLAS. Instead, ATLAS relied on a single $H \to \gamma\gamma$ signal-strength scale factor. The additional degree-of-freedom introduced by ATLAS for the present study results in a shift of about 40 MeV in the ATLAS $H \to \gamma\gamma$ result, leading to a shift of 20 MeV in the ATLAS combined mass measurement.

The individual signal strengths $\mu^{\gamma\gamma}_{\text{ggF}+ttH}$, $\mu^{\gamma\gamma}_{\text{VBF}+VH}$, and $\mu^{4\ell}$ are assumed to be the same for ATLAS and CMS, and are profiled in the combined fit for m_H. The corresponding PLR is

$$\Lambda(m_H) = \frac{L\big(m_H, \hat{\hat{\mu}}^{\gamma\gamma}_{\text{ggF}+ttH}(m_H), \hat{\hat{\mu}}^{\gamma\gamma}_{\text{VBF}+VH}(m_H), \hat{\hat{\mu}}^{4\ell}(m_H), \hat{\hat{\boldsymbol{\theta}}}(m_H)\big)}{L(\hat{m}_H, \hat{\mu}^{\gamma\gamma}_{\text{ggF}+ttH}, \hat{\mu}^{\gamma\gamma}_{\text{VBF}+VH}, \hat{\mu}^{4\ell}, \hat{\boldsymbol{\theta}})} \,. \tag{8.2}$$

Slightly more complex fit models are used, as described below, to perform additional compatibility tests between the different decay channels and between the results from ATLAS and CMS.

8.3 Results

Combining the ATLAS and CMS data for the $H \to \gamma\gamma$ and $H \to ZZ^* \to 4\ell$ channels according to the above procedure, the mass of the Higgs boson is determined to be

$$\begin{aligned} m_H &= 125.09 \pm 0.24 \text{ GeV} \\ &= 125.09 \pm 0.21\,(\text{stat.}) \pm 0.11\,(\text{syst.}) \text{ GeV}, \end{aligned} \tag{8.3}$$

where the total uncertainty is obtained from the width of a negative log-likelihood ratio scan with all parameters profiled. The statistical uncertainty is determined by fixing all nuisance parameters to their best-fit values, except for the three signal-strength scale factors and the $H \to \gamma\gamma$ background function parameters, which are profiled. The systematic uncertainty is determined by subtracting in quadrature the statistical uncertainty from the total uncertainty. Equation (8.3) shows that the uncertainties in the m_H measurement are dominated by the statistical term, even when the Run 1 data sets of ATLAS and CMS are combined. Figure 8.1 shows the negative log-likelihood ratio scans as a function of m_H, with all nuisance parameters profiled (solid curves), and with the nuisance parameters fixed to their best-fit values (dashed curves).

The signal strengths at the measured value of m_H are found to be $\mu^{\gamma\gamma}_{\text{ggF}+ttH} = 1.15^{+0.28}_{-0.25}$, $\mu^{\gamma\gamma}_{\text{VBF}+VH} = 1.17^{+0.58}_{-0.53}$, and $\mu^{4\ell} = 1.40^{+0.30}_{-0.25}$. The combined overall signal strength μ (with $\mu^{\gamma\gamma}_{\text{ggF}+ttH} = \mu^{\gamma\gamma}_{\text{VBF}+VH} = \mu^{4\ell} \equiv \mu$) is $\mu = 1.24^{+0.18}_{-0.16}$. The results reported here for the signal strengths are not expected to have the same sensitivity, nor exactly the same values, as those that would be extracted from a combined analysis optimized for the coupling measurements.

The combined ATLAS and CMS results for m_H in the separate $H \to \gamma\gamma$ and $H \to ZZ^* \to 4\ell$ channels are

$$\begin{aligned} m_H^{\gamma\gamma} &= 125.07 \pm 0.29 \text{ GeV} \\ &= 125.07 \pm 0.25\,(\text{stat.}) \pm 0.14\,(\text{syst.}) \text{ GeV} \end{aligned} \tag{8.4}$$

and

$$\begin{aligned} m_H^{4\ell} &= 125.15 \pm 0.40 \text{ GeV} \\ &= 125.15 \pm 0.37\,(\text{stat.}) \pm 0.15\,(\text{syst.}) \text{ GeV}. \end{aligned} \tag{8.5}$$

The corresponding likelihood ratio scans are shown in Fig. 8.1.

A summary of the results from the individual analyses and their combination is presented in Fig. 8.2.

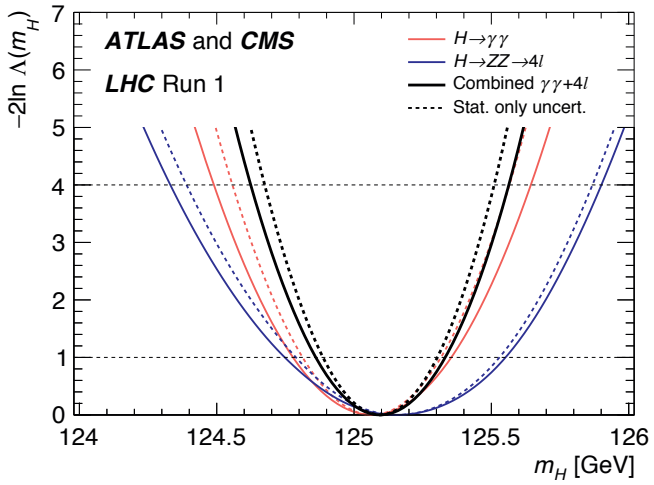

Figure 8.1: Scans of twice the negative log-likelihood ratio $-2\ln\Lambda(m_H)$ as functions of the Higgs boson mass m_H for the ATLAS and CMS combination of the $H\to\gamma\gamma$ (red), $H\to ZZ^*\to 4\ell$ (blue), and combined (black) channels. The dashed curves show the results accounting for statistical uncertainties only, with all nuisance parameters associated with systematic uncertainties fixed to their best-fit values. The 1 and 2 standard deviation limits are indicated by the intersections of the horizontal lines at 1 and 4, respectively, with the log-likelihood scan curves.

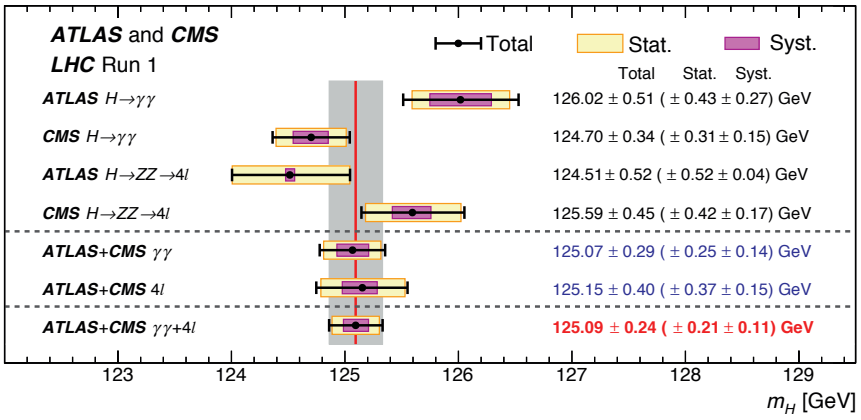

Figure 8.2: Summary of Higgs boson mass measurements from the individual analyses of ATLAS and CMS and from the combined analysis presented here. The systematic (narrower, magenta-shaded bands), statistical (wider, yellow-shaded bands), and total (black error bars) uncertainties are indicated. The (red) vertical line and corresponding (gray) shaded column indicate the central value and the total uncertainty of the combined measurement, respectively.

Expected sensitivity

The observed uncertainties in the combined measurement can be compared with expectations. The latter are evaluated by generating two Asimov data sets [396], where an Asimov data set is a representative event sample that provides both the median expectation for an experimental result and its expected statistical variation, in the asymptotic approximation, without the need for an extensive MC-based calculation, cf. Cha. 4. The first Asimov data set is a "prefit" sample, generated using $m_H = 125.0$ GeV and the SM predictions for the couplings, with all nuisance parameters fixed to their nominal values. The second Asimov data set is a "postfit" sample, in which m_H, the three signal strengths $\mu^{\gamma\gamma}_{\mathrm{ggF}+ttH}$, $\mu^{\gamma\gamma}_{\mathrm{VBF}+VH}$, and $\mu^{4\ell}$, and all nuisance parameters are fixed to their best-fit estimates from the data. The expected uncertainties for the combined mass are

$$\delta m_{H\,\mathrm{prefit}} = \pm 0.24\ \mathrm{GeV} = \pm 0.22\,(\mathrm{stat.}) \pm 0.10\,(\mathrm{syst.})\ \mathrm{GeV} \tag{8.6}$$

for the prefit case and

$$\delta m_{H\,\mathrm{postfit}} = \pm 0.22\ \mathrm{GeV} = \pm 0.19\,(\mathrm{stat.}) \pm 0.10(\mathrm{syst.})\ \mathrm{GeV} \tag{8.7}$$

for the postfit case, which are both very similar to the observed uncertainties reported in Eqn. (8.3).

Constraining all signal yields to their SM predictions results in an m_H value that is about 70 MeV larger than the nominal result with a comparable uncertainty. The increase in the central value reflects the combined effect of the higher-than-expected $H \to ZZ^* \to 4\ell$ measured signal strength and the increase of the $H \to ZZ$ branching fraction with m_H. Thus, the fit assuming SM couplings forces the mass to a higher value in order to accommodate the value $\mu = 1$ expected in the SM.

8.3.1 Systematic uncertainties

Since the discovery, both experiments have improved their understanding of the electron, photon, and muon measurements [352, 357, 488, 493–495], leading to a significant reduction of the systematic uncertainties in the mass measurement. Nevertheless, the treatment and understanding of systematic uncertainties is an important aspect of the individual measurements and their combination. The combined analysis incorporates approximately 300 nuisance parameters. Among these, approximately 100 are fitted parameters describing the shapes and normalizations of the background models in the $H \to \gamma\gamma$ channel, including a number of discrete parameters that allow the functional form in each of the CMS $H \to \gamma\gamma$ analysis categories to be changed [496]. Of the remaining almost 200 nuisance parameters, most correspond to experimental or theoretical systematic uncertainties.

Based on the results from the individual experiments, the dominant systematic uncertainties for the combined m_H result are expected to be those associated with the energy or momentum scale and its resolution: for the photons in the $H \to \gamma\gamma$ channel and for the electrons and muons in the $H \to ZZ^* \to 4\ell$ channel [21, 487, 488]. These uncertainties are assumed to be uncorrelated between the two experiments since they are related to the specific characteristics of the detectors as well as to the calibration procedures, which are fully independent except for negligible effects due to the use of the common Z boson mass [497] to specify the absolute energy and momentum scales. Other experimental systematic uncertainties [21, 487, 488] are similarly assumed to be uncorrelated between the two experiments. Uncertainties in the theoretical predictions and in the measured integrated luminosities are treated as fully and partially correlated, respectively.

To evaluate the relative importance of the different sources of systematic uncertainty, the nuisance parameters are grouped according to their correspondence to three broad classes of systematic uncertainty:

- uncertainties in the energy or momentum scale and resolution for photons, electrons, and muons ("scale"),
- theoretical uncertainties, e.g., uncertainties in the Higgs boson cross section and branching fractions, and in the normalization of SM background processes ("theory"),
- other experimental uncertainties ("other").

First, the total uncertainty is obtained from the full profile-likelihood scan, as explained above. Next, parameters associated with the "scale" terms are fixed and a new scan is performed. Then, in addition to the scale terms, the parameters associated with the "theory" terms are fixed and a scan performed. Finally, in addition, the "other" parameters are fixed and a scan performed. Thus the fits are performed iteratively, with the different classes of nuisance parameters cumulatively held fixed to their best-fit values. The uncertainties associated with the different classes of nuisance parameters are defined by the difference in quadrature between the uncertainties resulting from consecutive scans. The statistical uncertainty is determined from the final scan, with all nuisance parameters associated with systematic terms held fixed, as explained above. The result is

$$m_H = 125.09 \pm 0.21\,(\text{stat.}) \pm 0.11\,(\text{scale}) \pm 0.02\,(\text{other}) \pm 0.01\,(\text{theory})\ \text{GeV}, \tag{8.8}$$

from which it is seen that the systematic uncertainty is indeed dominated by the energy and momentum scale terms.

The relative importance of the various sources of systematic uncertainty is further investigated by dividing the nuisance parameters into yet-finer groups, with each group associated with a specific underlying effect, and evaluating the impact of each group on the overall mass uncertainty. The matching of nuisance parameters to an effect is not strictly rigorous because nuisance parameters in the two experiments do not always represent exactly the same effect

Table 8.1: Systematic uncertainties δm_H (see text) associated with the indicated effects for each of the four input channels, and the corresponding contributions of ATLAS and CMS to the systematic uncertainties of the combined result. "ECAL" refers to the electromagnetic calorimeters. The numbers in parentheses indicate expected values obtained from the prefit Asimov data set discussed in the text. The uncertainties for the combined result are related to the values of the individual channels through the relative weight of the individual channel in the combination, which is proportional to the inverse of the respective uncertainty squared. The top section of the table divides the sources of systematic uncertainty into three classes, which are discussed in the text. The bottom section of the table shows the total systematic uncertainties estimated by adding the individual contributions in quadrature, the total systematic uncertainties evaluated using the nominal method discussed in the text, the statistical uncertainties, the total uncertainties, and the analysis weights, illustrative of the relative weight of each channel in the combined m_H measurement.

	Uncertainty in ATLAS results [GeV]: observed (expected)		Uncertainty in CMS results [GeV]: observed (expected)		Uncertainty in combined result [GeV]: observed (expected)	
	$H \to \gamma\gamma$	$H \to ZZ^* \to 4\ell$	$H \to \gamma\gamma$	$H \to ZZ^* \to 4\ell$	ATLAS	CMS
Scale uncertainties:						
ATLAS ECAL non-linearity / CMS photon non-linearity	0.14 (0.16)	–	0.10 (0.13)	–	0.02 (0.04)	0.05 (0.06)
Material in front of ECAL	0.15 (0.13)	–	0.07 (0.07)	–	0.03 (0.03)	0.04 (0.03)
ECAL longitudinal response	0.12 (0.13)	–	0.02 (0.01)	–	0.02 (0.03)	0.01 (0.01)
ECAL lateral shower shape	0.09 (0.08)	–	0.06 (0.06)	–	0.02 (0.02)	0.03 (0.03)
Photon energy resolution	0.03 (0.01)	–	0.01 (<0.01)	–	0.02 (<0.01)	<0.01 (<0.01)
ATLAS $H \to \gamma\gamma$ vertex & conversion reconstruction	0.05 (0.05)	–	–	–	0.01 (0.01)	–
$Z \to ee$ calibration	0.05 (0.04)	0.03 (0.02)	0.05 (0.05)	–	0.02 (0.01)	0.02 (0.02)
CMS electron energy scale & resolution	–	–	–	0.12 (0.09)	–	0.03 (0.02)
Muon momentum scale & resolution	–	0.03 (0.04)	–	0.11 (0.10)	<0.01 (0.01)	0.05 (0.02)
Other uncertainties:						
ATLAS $H \to \gamma\gamma$ background modeling	0.04 (0.03)	–	–	–	0.01 (0.01)	–
Integrated luminosity	0.01 (<0.01)	<0.01 (<0.01)	0.01 (<0.01)	<0.01 (<0.01)	0.01 (<0.01)	
Additional experimental systematic uncertainties	0.03 (<0.01)	<0.01 (<0.01)	0.02 (<0.01)	0.01 (<0.01)	0.01 (<0.01)	0.01 (<0.01)
Theory uncertainties	<0.01 (<0.01)	<0.01 (<0.01)	0.02 (<0.01)	<0.01 (<0.01)	0.01 (<0.01)	
Systematic uncertainty (sum in quadrature)	0.27 (0.27)	0.04 (0.04)	0.15 (0.17)	0.16 (0.13)	0.11 (0.10)	
Systematic uncertainty (nominal)	0.27 (0.27)	0.04 (0.05)	0.15 (0.17)	0.17 (0.14)	0.11 (0.10)	
Statistical uncertainty	0.43 (0.45)	0.52 (0.66)	0.31 (0.32)	0.42 (0.57)	0.21 (0.22)	
Total uncertainty	0.51 (0.52)	0.52 (0.66)	0.34 (0.36)	0.45 (0.59)	0.24 (0.24)	
Analysis weights	19% (22%)	18% (14%)	40% (46%)	23% (17%)	–	

and in some cases multiple effects are related to the same nuisance parameter. Nevertheless the relative impact of the different effects can be explored. A few experiment-specific groups of nuisance parameters are defined. For example, ATLAS includes a group of nuisance parameters to account for the inaccuracy of the background modeling for the $H \to \gamma\gamma$ channel. To model this background, ATLAS uses specific analytic functions in each category [21] while CMS simultaneously considers different background parameterizations [496]. The systematic uncertainty in m_H related to the background modeling in CMS is estimated to be negligible [487].

The impact of groups of nuisance parameters is evaluated starting from the contribution of each individual nuisance parameter to the total uncertainty. This contribution is defined as the mass shift δm_H observed when re-evaluating the PLR after fixing the nuisance parameter in question to its best-fit value increased or decreased by 1 standard deviation (σ) in its distribution. For a nuisance parameter whose p.d.f. is a Gaussian distribution, this shift corresponds to the contribution of that particular nuisance parameter to the final uncertainty. The impact of a group of nuisance parameters is estimated by summing in quadrature the contributions from the individual parameters.

The impacts δm_H due to each of the considered effects are listed in Tab. 8.1. The results are reported for the four individual channels, both for the data and (in parentheses) the prefit Asimov data set. The row labeled "Systematic uncertainty (sum in quadrature)" shows the total sums in quadrature of the individual terms in the table. The row labeled "Systematic uncertainty (nominal)" shows the corresponding total systematic uncertainties derived using the subtraction in quadrature method discussed in connection with Eqn. (8.3). The two methods to evaluate the total systematic uncertainty are seen to agree within 10 MeV, which is comparable with the precision of the estimates. The two rightmost columns of Tab. 8.1 list the contribution of each group of nuisance parameters to the uncertainties in the combined mass measurement, for ATLAS and CMS separately.

The statistical and total uncertainties are summarized in the bottom section of Tab. 8.1. Since the weight of a channel in the final combination is determined by the inverse of the squared uncertainty, the approximate relative weights for the combined result are 19% ($H \to \gamma\gamma$) and 18% ($H \to ZZ^* \to 4\ell$) for ATLAS, and 40% ($H \to \gamma\gamma$) and 23% ($H \to ZZ^* \to 4\ell$) for CMS. These weights are reported in the last row of Tab. 8.1, along with the expected values.

Figure 8.3 presents the impact of each group of nuisance parameters on the total systematic uncertainty in the mass measurement of ATLAS, CMS, and the combination. For the individual ATLAS and CMS measurements, the results in Fig. 8.3 are approximately equivalent to the sum in quadrature of the respective δm_H terms in Tab. 8.1 multiplied by their analysis weights, after normalizing these weights to correspond to either ATLAS only or CMS only. The ATLAS and CMS combined results in Fig. 8.3 are the sum in quadrature of the combined results in Tab. 8.1.

The results in Tab. 8.1 and Fig. 8.3 establish that the largest systematic effects for the mass uncertainty are those related to the determination of the energy scale of the photons, followed

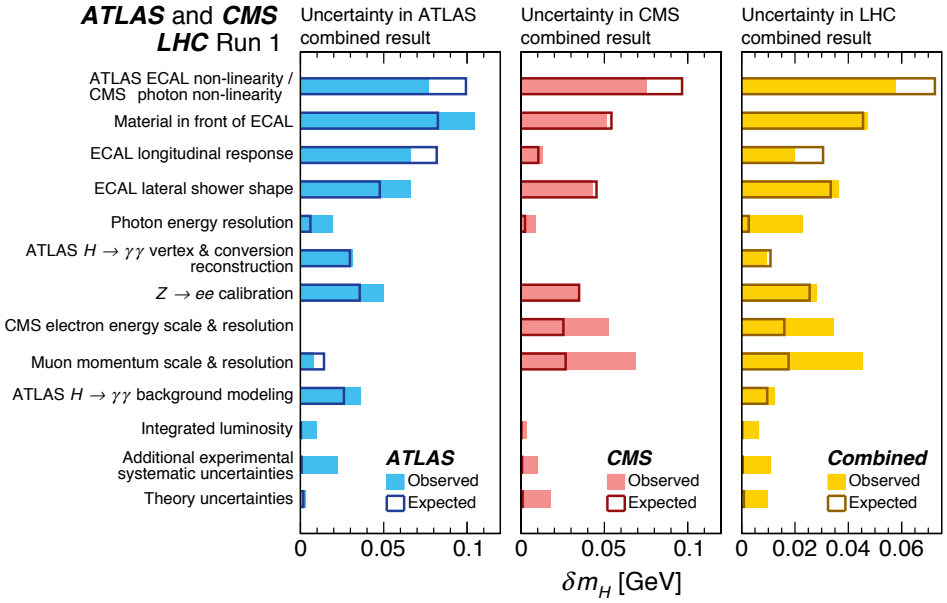

Figure 8.3: The impacts δm_H (see text) of the nuisance parameter groups in Tab. 8.1 on the ATLAS (left), CMS (center), and combined (right) mass measurement uncertainty. The observed (expected) results are shown by the solid (empty) bars.

by those associated with the determination of the electron and muon momentum scales. Since the CMS $H \to \gamma\gamma$ channel has the largest weight in the combination, its impact on the systematic uncertainty of the combined result is largest.

8.3.2 Compatibility tests

The mutual compatibility of the m_H results from the four individual channels is tested using a likelihood ratio with four masses in the numerator and a common mass in the denominator, and thus three degrees of freedom. The three signal strengths are profiled in both the numerator and denominator as in Eqn. (8.1). The resulting compatibility, defined as the asymptotic p-value of the fit, is 10%. Allowing the ATLAS and CMS signal strengths to vary independently yields a compatibility of 7%. This latter fit results in an m_H value that is 40 MeV larger than the nominal result.

The compatibility of the combined ATLAS and CMS mass measurement in the $H \to \gamma\gamma$ channel with the combined measurement in the $H \to ZZ^* \to 4\ell$ channel is evaluated using the variable $\Delta m_{\gamma Z} \equiv m_H^{\gamma\gamma} - m_H^{4\ell}$ as the POI, with all other parameters, including m_H, profiled. Similarly,

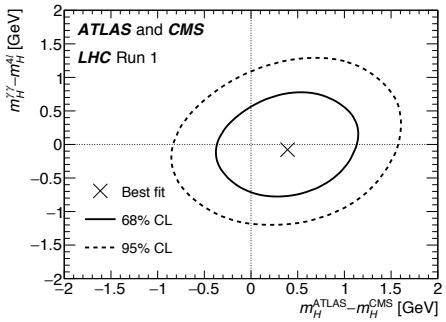

Figure 8.4: Summary of likelihood scan in the 2D plane of the mass differences between two experiments, $\Delta m^{\text{expt}} \equiv m_H^{\text{ATLAS}} - m_H^{\text{CMS}}$, and between two channels, $\Delta m_{\gamma Z} \equiv m_H^{\gamma\gamma} - m_H^{4\ell}$. The 68% and 95% CL confidence regions are shown by the solid and dashed curves, respectively. The marker indicates the best-fit values.

the compatibility of the ATLAS combined mass measurement in the two channels with the CMS combined measurement in the two channels is evaluated using the variable $\Delta m^{\text{expt}} \equiv m_H^{\text{ATLAS}} - m_H^{\text{CMS}}$. The observed results, $\Delta m_{\gamma Z} = -0.1 \pm 0.5$ GeV and $\Delta m^{\text{expt}} = 0.4 \pm 0.5$ GeV, are both consistent with zero within $1\,\sigma$. The difference between the mass values in the two experiments is $\Delta m_{\gamma\gamma}^{\text{expt}} = 1.3 \pm 0.6$ GeV $(2.1\,\sigma)$ for the $H \to \gamma\gamma$ channel and $\Delta m_{4\ell}^{\text{expt}} = -0.9 \pm 0.7$ GeV $(1.3\,\sigma)$ for the $H \to ZZ^* \to 4\ell$ channel. The combined results exhibit a greater degree of compatibility than the results from the individual decay channels because the Δm^{expt} value has opposite signs in the two channels, cf. Fig. 8.4

The compatibility of the signal strengths from ATLAS and CMS is evaluated through the ratios $\lambda^{\text{expt}} = \mu^{\text{ATLAS}}/\mu^{\text{CMS}}$, $\lambda_F^{\text{expt}} = \mu_{\text{ggF+}ttH}^{\gamma\gamma\ \text{ATLAS}}/\mu_{\text{ggF+}ttH}^{\gamma\gamma\ \text{CMS}}$, and $\lambda_{4\ell}^{\text{expt}} = \mu^{4\ell\ \text{ATLAS}}/\mu^{4\ell\ \text{CMS}}$. For this purpose, each ratio is individually taken to be the POI, with all other nuisance parameters profiled, including the remaining two ratios for the first two tests. We find $\lambda^{\text{expt}} = 1.21^{+0.30}_{-0.24}$, $\lambda_F^{\text{expt}} = 1.3^{+0.8}_{-0.5}$, and $\lambda_{4\ell}^{\text{expt}} = 1.3^{+0.5}_{-0.4}$, all of which are consistent with unity within $1\,\sigma$. The ratio $\lambda_V^{\text{expt}} = \mu_{\text{VBF+}VH}^{\gamma\gamma\ \text{ATLAS}}/\mu_{\text{VBF+}VH}^{\gamma\gamma\ \text{CMS}}$ is omitted because the ATLAS mass measurement in the $H \to \gamma\gamma$ channel is not sensitive to $\mu_{\text{VBF+}VH}^{\gamma\gamma}/\mu_{\text{ggF+}ttH}^{\gamma\gamma}$.

The correlation between the signal strength and the measured mass is explored with 2D likelihood scans as functions of μ and m_H. The three signal strengths are assumed to be the same: $\mu_{\text{ggF+}ttH}^{\gamma\gamma} = \mu_{\text{VBF+}VH}^{\gamma\gamma} = \mu^{4\ell} \equiv \mu$, and thus the ratios of the production cross sections times branching fractions are constrained to the SM predictions. Assuming that the negative log-likelihood ratio $-2\ln\Lambda(\mu, m_H)$ is distributed as a χ^2 variable with two degrees of freedom, the 68% CL confidence regions are shown in Fig. 8.5a for each individual measurement, as well as for the combined result. Similarly, Fig. 8.5b shows the 68% CL confidence regions in the 2D plane of normalized signal yield $S \equiv \sigma/\sigma_{\text{SM}}(m_h = 125.09\ \text{GeV})$ versus Higgs boson mass m_H for the ATLAS and CMS experiments. The fitted signal yield is observed to be independent of the measured mass.

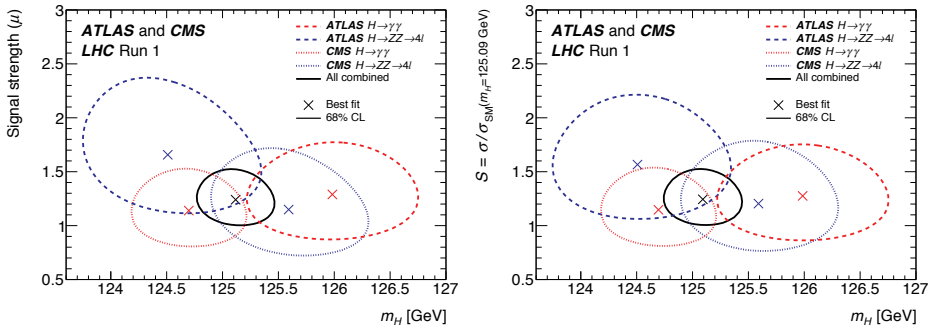

(a) **(b)**

Figure 8.5: Summary of likelihood scans in the 2D plane of (a) signal strength μ versus Higgs boson mass m_H, and (b) normalized signal yield $S \equiv \sigma/\sigma_{\rm SM}(m_h = 125.09\ \text{GeV})$ versus Higgs boson mass m_H for the ATLAS and CMS experiments. S is similar to the signal strength $\mu \equiv \sigma/\sigma_{\rm SM}(\mathrm{m_H})$, except the m_H-dependence of the expected SM event yield that enters into the denominator, principally for the $H \to ZZ^* \to 4\ell$ channel, is removed by fixing m_H to the combined best-fit mass. The 68% CL confidence regions of the individual measurements are shown by the dashed curves and of the overall combination by the solid curve. The markers indicate the respective best-fit values. The fitted signal yield is observed to be independent of the measured mass.

Higgs physics at future facilities

9

The results presented in the previous chapters exploit the full data sample recorded by the ATLAS and CMS experiments in LHC Run 1. During the first years of operation, the LHC delivered pp collisions at centre-of-mass energies of up to 8 TeV, i. e. just more than half of the design energy, cf. Cha. 2. The machine was operated at a peak instantaneous luminosity below the design specification and a conservative bunch spacing of 50 ns. Nevertheless, the physics potential of the machine has been enormous, reflected by the discovery of the long sought-for Higgs boson. In order to benefit even more from this unique facility and increase its discovery potential, upgrades of the accelerator and the physics experiments are necessary to reach the nominal performance, and to even exceed it in the long-term future.

This chapter sketches a road map for the ambitious upgrade program the LHC is following over the next decades. In a first step (Phase 0), the current center-of-mass energy and peak instantaneous luminosity are increased towards the machine's design values, establishing the basis for producing and discovering physics beyond the SM. By reducing the bunch spacing to 25 ns, the average number of inelastic interactions per bunch crossing can be kept at a level of approximately 20. The expected integrated luminosity for the data set collected during this run, is approximately 150 fb^{-1}. After further upgrades (Phase 1), the LHC can be operated at a peak instantaneous luminosity of approximately twice the nominal value, $2\text{-}3 \cdot 10^{34}\,\text{cm}^{-2}\text{s}^{-1}$, with the pile-up interactions increasing to approximately 50-60. By the year 2022, the integrated luminosity of the data set collected by ATLAS will be approximately 300 fb^{-1}. The so-called Phase 2 upgrade supports operating the LHC at a nominal leveled instantaneous luminosity of $5 \cdot 10^{34}\,\text{cm}^{-2}\text{s}^{-1}$ with a pile-up rate of approximately 140. Referring to these conditions, the machine goes under the name HL-LHC [39]. The machine is expected to deliver approximately 3000 fb^{-1} of data by approximately 2035, i. e. about ten times the integrated luminosity recorded prior to the Phase 2 upgrade.

The HL-LHC enables the direct and indirect observation of phenomena that current experiments are not sensitive to, or could not be accessed in the laboratory, yet. An example of the former are rare processes with an exiguous cross section relative to dominating background processes. As an example for the latter scenario, the reader should think about heavy particles, whose production is limited by the centre-of-mass energy. Owing to the increased statistics, precision measurements of the particles' properties become feasible. This chapter summarizes the projected precision for measuring the Higgs boson signal strengths and its coupling strengths with the ATLAS detector at the HL-LHC. Later, the results are interpreted

in various BSM scenarios, yielding limits on the corresponding model parameters. The presentation of the results proceeds along the lines of Cha. 6 and Ref. 7. The prospects for Higgs physics with the ATLAS experiment at the HL-LHC shown in this chapter, have previously been released as Refs. [52, 54], respectively. Thus, only a concise summary is presented here, and the reader is referred to Cha. 6 and 7 for a review of the probed models, and to the original analysis documentation for a more detailed discussion of the results.

By the time the results for the full HL-LHC data sample are being finalized, it is assumed that the earliest stages of the ILC program [47–51] could become operational. The ILC is a high-luminosity linear electron-positron collider, providing collisions at a centre-of-mass energy of 200-500 GeV, extendable to 1 TeV. The machine facilitates EW precision measurements within a wide range of energies at the TeV scale. Owing to a reduced rate of high-energy collisions and generally easier event topologies, the ILC provides a better handle on signatures that are dominated by background processes at a pp collider. As an example of possible measurements, the prospects for measuring the properties of the Higgs boson have been summarized in Ref. [53]. It is interesting to investigate to which extent the (coupling strength) measurements performed at the HL-LHC and the ILC are complementary. Such a combination of measurements is already available in the literature [498–500], but lacks detailed information about the statistical model and the full likelihood function used for the HL-LHC projections.

9.1 Future facilities

This section provides a brief overview of selected future accelerators for which in the remainder of this chapter projected sensitivities are presented. A detailed description is beyond the scope of this work. Thus, the reader is referred to the literature [11–13, 16, 39, 47–51] for a more comprehensive presentation. The section also comprises information about the planned upgrades of the ATLAS detector for Phase 0, 1, and 2. Again, the reader is referred to the literature [40–46] for a more detailed description.

9.1.1 Towards the High-Luminosity LHC

The LHC road map for the coming years is shaped by major shutdowns, termed Long Shutdown (LS), interleaving the data taking periods. A schematic time line is presented in Fig. 9.1. The shutdowns are required for upgrades of the machine. Details on the required work will be provided in the following paragraphs.

Run 1 has been very fruitful both in terms of operations and physics output. The expected performance has been matched or even exceeded. The LHC provided pp collisions at centre-of-mass energies of up to 8 TeV, with a peak instantaneous luminosity of $7.73 \cdot 10^{33}\,\mathrm{cm}^{-2}\mathrm{s}^{-1}$. At a bunch spacing of 50 ns, the average number of inelastic interactions per bunch crossing

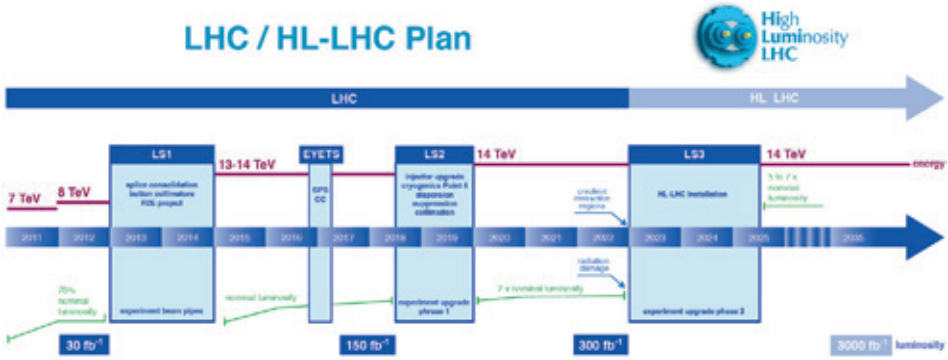

Figure 9.1: Road map for the LHC upgrades. Details are provided in the body text. Figure taken from Ref. [501].

was approximately 21. The recorded pp collision data, up to $25\,\text{fb}^{-1}$, has been exploited by many physics analyses, leading to remarkable results, e. g. the discovery of the Higgs boson [4–6], or evidence for the decay $B_s^0 \to \mu^+\mu^-$ [502].

During LS1, from Winter 2013 until Spring 2015, the Phase 0 upgrade of the machine has been performed. At this stage, the splice at the magnet interconnections are consolidated, electrically weak magnets are replaced, the collimator system is equipped with Beam Position Monitors (BPMs) (the so called "button" collimator), and many more updates, e. g. to remove the limits to the beam intensity. The changes will enable operating the accelerator near the nominal design specifications. In particular it will be possible to safely operate the magnets near the design value of 8.3 T. This is necessary to control the beam energies of up to 6.5 TeV and obtain a peak instantaneous luminosity of $10 \cdot 10^{33}\,\text{cm}^{-2}\text{s}^{-1}$ at a bunch spacing of 25 ns. During Run 2, the LHC is expected to deliver approximately $150\,\text{fb}^{-1}$ of pp collision data at a collision energy of up to 13 TeV. The pile-up conditions are expected to be similar to the ones faced during Run 1.

The experiment upgrade Phase 1 will take place during LS2 in 2018 and 2019. The upgrade is planned considering future upgrades that are needed for the HL-LHC, and aims at eliminating technical limitations. The time will be used to upgrade the LHC injector complex, in particular the straight segments of the accelerator chain (LINAC4), and to improve the beam characteristics (PSB, PS, SPS). The addition of a new helium refrigerator at Point 4 improves the cryogenics and allows decoupling the cooling of the four LHC superconducting RF modules from the magnet cooling circuit. The upgrade of the cryogenics will allow a more flexible, yet more stable, operation of the machine. Furthermore, it might be necessary to revisit the collimator system, in particular the Dispersion Suppressor (DS), suffering from wear out through aging, and install low impedance collimators. After these upgrades, the LHC is expected to reach its ultimate peak instantaneous luminosity, $2\text{-}3 \cdot 10^{34}\,\text{cm}^{-2}\text{s}^{-1}$, with the pile-

Table 9.1: Main beam and machine parameters for the LHC and the HL-LHC. The comparison is extracted from the HL-LHC project accelerator physics package resources [503].

Parameter	Nominal LHC	HL-LHC @ 25 ns
Centre-of-mass energy $\sqrt{s}$ [TeV]	14	14
Delivered integrated luminosity per year $\left[\text{fb}^{-1}\right]$	30	250 to 300
Minimum bunch spacing for physics [ns]	25	25
Maximum number of bunch pairs colliding	2808	2748
Typical bunch population N_b $\left[10^{11}\text{ protons}\right]$	1.15	2.2
Beam current [A]	0.58	1.09
Crossing angle θ_c [rad]	285	590
Beam separation [standard deviations]	9.4	12.5
β^* [m]	0.55	0.15
Norm. transverse beam emittance ε_n [m]	3.75	2.50
Longitudinal beam emittance ε_l [eVs]	2.50	2.50
RMS energy spread	1.13×10^{-4}	1.13×10^{-4}
RMS bunch length σ_z [m]	7.55×10^{-2}	7.55×10^{-2}
Intrabeam scattering (horizontal) [h]	80 → 106	18.5
Intrabeam scattering (longitudinal) [h]	61 → 60	20.4
Transverse RMS beam size σ^* [m]	16.6	7.1
Piwinski angle $\theta_c \sigma_z / 2\sigma^*$	0.65	3.14
Geo. lumi. reduction factor F (w/o Crab Cavity)	0.836	0.305
Geo. lumi. reduction factor F (w/ Crab Cavity)	0.981	0.829
Peak inst. lumi. (w/o Crab Cavity) $\left[10^{34}\,\text{cm}^{-2}\,\text{s}^{-1}\right]$	1.00	7.18
Virtual peak inst. lumi. (w/ Crab Cavity) $\left[10^{34}\,\text{cm}^{-2}\,\text{s}^{-1}\right]$	1.18	19.54
Levelled luminosity $\left[10^{34}\,\text{cm}^{-2}\,\text{s}^{-1}\right]$	-	5.00
Leveling time (no emittance growth) [h]	-	8.3
Nominal pile-up w/o leveling and w/o Crab Cavity	27	198
Nominal pile-up w/ leveling and w/ Crab Cavity for HL-LHC	27	138

up increasing to approximately 50-60. The bunch spacing will be unchanged with respect to Run 2 and the centre-of-mass energy could reach 14 TeV. By the year 2022, an integrated luminosity of approximately 300 fb^{-1} is estimated to be delivered to the high-luminosity experiments.

At this point, many components of the accelerator will be damaged by the high radiation. Also, it will not be economical to continue operating the accelerator without further increasing its instantaneous luminosity. A statistical gain can only be achieved with an integrated luminosity that is approximately ten times higher than the data that will have been delivered by the end of Run 3, i. e. $10 \cdot 300\,\text{fb}^{-1}$. This goal can be achieved efficiently only in case the machine provides an integrated luminosity of approximately 250-300 fb^{-1} per year. At an average number of inelastic interactions per bunch crossing of approximately 140 (peaking at approximately 280 pile-up interactions), the collider must be operated with a constant ("leveled") instantaneous luminosity of $5 \cdot 10^{34}\,\text{cm}^{-2}\text{s}^{-1}$, corresponding to a virtual peak instantaneous luminosity of more than $10 \cdot 10^{34}\,\text{cm}^{-2}\text{s}^{-1}$. The technical challenges for exploring

higher beam energies are enormous. Thus, the HL-LHC will be operated at the same collision energy that can be achieved in Run 3.

In order to reach this performance, almost all parameters affecting the instantaneous luminosity have to be tuned. The intensity of each bunch must be maximized, while minimizing the beam emittance and the beam size. It would be helpful to increase the number of bunches as well, but it is technically limited to a bunch spacing of 25 ns. Furthermore, the geometric luminosity reduction factor due to the crossing angle at the interaction points must be compensated. Naturally, the machine must be operated at a maximum efficiency, including a minimal turnaround time. Research and development of the hardware has started to successfully complete the upgrade for the HL-LHC, though the definite technical design is not yet finalized. As one of the key components emerges the development of superconducting RF Crab Cavities that rotate each bunch by half of the crossing angle at the interaction point, providing perfect head-on collisions. Among others, further technical challenges involve the construction of large aperture superconducting triplet magnets with niobium-tin technology and tungsten shielding, and of large aperture superconducting insertion magnets with niobium-titanium technology. Table 9.1 compares the LHC design specifications and the HL-LHC main beam and machine parameters.

9.1.2 Upgrades of the ATLAS detector

The ATLAS detector in its current form is described in Sec. 2.2. Over the next years, the LHC will undergo major upgrades to push its performance to a maximum. These changes express themselves through harsh radiation levels and imply high detector occupancies, in particular for the inner tracking devices. To not only cope with this environment, but eventually benefit from it, the experiments must be adapted accordingly. The schedule for the detector upgrades follows the road map set by the accelerator upgrade, cf. Fig. 9.1.

The Phase 0 upgrade of the ATLAS detector during LS1 is devoted to completing the experiment's initial technical design for the nominal luminosity. A new (fourth) layer of silicon pixels, the so-called Insertable B-layer (IBL), is installed between a new beryllium beam pipe and the (currently) innermost layer of the Pixel detector in the central region of the detector [40]. Beyond this, a topological trigger system will be implemented at Level 1. Furthermore, minor repairs will be carried out, e. g. of optical readout links. These upgrades will help to mitigate pile-up effects and increase the robustness and precision of the tracking and vertexing at higher luminosities during Run 2 and Run 3.

The environment set by the LHC for Run 3, requires further major upgrades of the trigger and data acquisition system [45] to cope with the high instantaneous luminosity and collision rates. For successful physics operations with high signal acceptance rates, the low p_{T} thresholds for single leptons must be maintained without the need for pre-scaling, while sharpening the trigger threshold turn-on curves. To control the total rate, it is necessary to improve the discrimination against background processes. In order to achieve these requirements, it

is necessary to digitally incorporate higher granularity data from the LAr calorimeter [44]. The fraction of fake triggers can be reduced significantly owing to the new first station of the muon end-cap system, the New Small Wheel (NSW) [42]. The new Fast Tracker (FTK) [43] enables full track reconstruction at the Level 1 trigger rate (approximately 100 kHz) with full coverage in pseudorapidity, which can be used for example for real-time heavy flavor tagging. Track reconstruction consists of a coarse hit pattern matching, followed by linear track fitting in field-programmable gate arrays (FPGAs). Naturally, the upgrades are designed such that physics objects can be reconstructed with high resolution. It should be noted explicitly, that the upgrades involve most notably the ID, and the forward calorimeters and muon spectrometer. At low pseudorapidity, the latter detector sub-systems suffer less from the more challenging conditions.

To fully exploit the highest luminosity run of the HL-LHC (Run 3, 2025 to 2035), further major upgrades of the ATLAS detector are necessary, in particular of the ID, the trigger, and calorimeters. However, the definite technical design is still in the research and development phase and has not yet been finalized. The specifications of the new detector must be such that its performance in the high pile-up environment will not be worse than the one of the current detector at approximately 20 inelastic interactions per bunch crossing. To achieve this goal and to cope with the vast detector occupancy and radiation close to the interaction point, the ID must be replaced by a new, radiation hard tracking device. Currently, the most promising design involves several all-silicon pixel and strip layers with a four times larger overall granularity, smaller material budget, and carbon dioxide based cooling. The trigger system and read out electronics must be upgraded to operate at 1 MHz at the new Level 0 (former Level 1) and at 400 kHz at Level 1. These rates can only be achieved without compromising the p_{T} thresholds for single leptons, e. g. through pre-scaling, when the tracking information is already used at Level 1, i. e. through the FTK. Furthermore, it is planned to upgrade the calorimeters' read out architecture and the front-end electronics of the muon system. Enhancements regarding the large-η region are being considered.

9.1.3 The International Linear Collider

The technical design of the ILC is presented in great detail in [47–51]. This section comprises only a brief summary. A more detailed description is beyond the scope of this work.

The ILC is a high-luminosity linear electron-positron collider with a footprint of approximately 31 km, cf. Fig. 9.2. The electron source is based on a strained gallium arsenide photocathode in a direct current (DC) gun. The primary electron beam traverses a superconducting helical undulator, forcing the radiation of high-energy photons. The photon beam produces electron-positron pairs in a spinning titanium alloy target, from which the positron beam is extracted. The design provides electron and positron bunch trains with 80 % and 30 % polarization, respectively. The polarization of the positron beam depends on the undulator and can be increased through future upgrades.

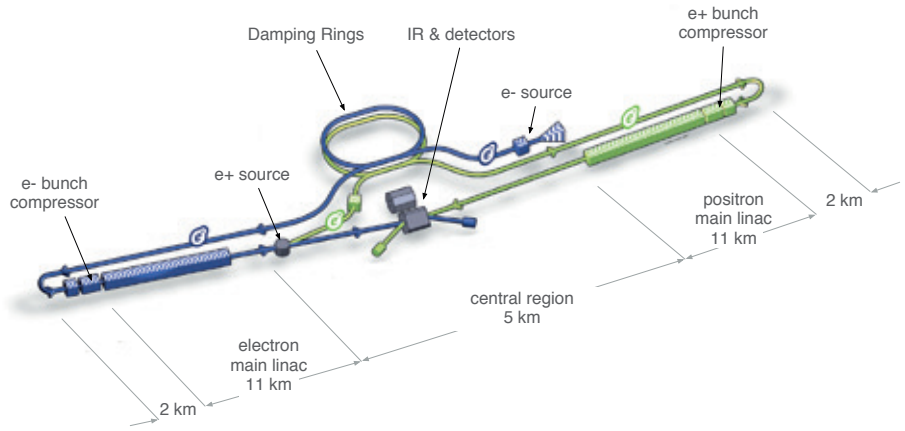

Figure 9.2: Blueprint of the ILC. Figure taken from Ref. [47].

At an energy of 5 GeV, the electron and positron beams have large transverse and longitudinal emittances. In order to increase the instantaneous luminosity, the emittances are reduced by superferric wigglers in dedicated damping rings with a circumference of 3.2 km. For each beam, the damped emittance must be preserved by the transport line between the damping ring and the main linear accelerator, while stabilizing the beam (using feed-forward synchronization), orienting its polarization, and compressing the bunch length. The heart of the machine are the two 11 km long main linear accelerators. In the baseline design, 1.3 GHz superconducting niobium RF cavities accelerate each beam to an energy of up to 250 GeV, corresponding to a average accelerating gradient of 31.5 MV m^{-1}. Operating in this configuration, with a nominal pulse current of 5.8 mA, the accelerators' total RF pulse lengths are 1.65 ms. The beam delivery systems are designed such that the beams collide with a 14 mrad crossing angle at a single interaction point. A fast push-pull configuration allows to equip the interaction region with two complementary experiments cross-checking each other. While one of the detectors takes data, the other one is being kept in a close-by maintenance position. Figure 9.3 shows the proposed experiments, Silicon Detector (SiD) and International Large Detector (ILD), respectively. A description of the detector concepts is beyond the scope of this work. Therefore, the interested reader is referred to Ref. [51].

The remainder of this chapter puts the focus on the ILC as a light Higgs factory, though the physics case for a linear e^+e^- collider is considerably more diverse [48]. In this configuration the ILC provides an instantaneous luminosity of 0.75×10^{34} cm^{-2} s^{-1} at a centre-of-mass energy of 250 GeV, corresponding to an average accelerating gradient of 14.7 MV m^{-1}.

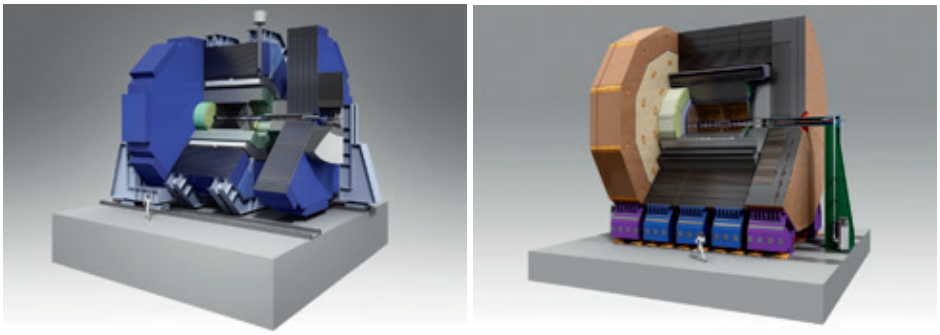

(a) SiD **(b)** ILD

Figure 9.3: Cut-away view of the (a) SiD and (b) ILD detector concepts. The humans shown next to the detectors indicate the size of the apparatuses. Figures taken from Ref. [51], updated by the Liner Collider Collaboration

9.2 Higgs boson coupling strengths

The beginning of this section is devoted to projections for Higgs boson signal strength and coupling strength measurements with ATLAS at the HL-LHC. A second part comprises combined coupling strength measurements at the HL-LHC and the ILC, aiming at identifying synergies of the Higgs physics programs at the two facilities. The statistical treatment of the (Asimov) data is outlined in Cha. 4. It is assumed that the Higgs boson has a mass of approximately 125 GeV, and that its width is narrow. Then, the coupling scale factors can be extracted from a combined fit to all production and decay modes in the leading-order tree-level motivated κ-framework, introduced in Sec. 6.3.1. The methodology and notation of the analysis is as outlined in Cha. 6.

9.2.1 Sensitivity at the HL-LHC

This section summarizes the prospects for measuring the coupling strengths of the Higgs boson, exploiting the full pp collision data sample delivered by the present LHC program and recorded with the ATLAS detector. This data set corresponds to a total integrated luminosity of 300 fb^{-1} in an environment with approximately 50-60 pile-up interactions per bunch crossing. The results are compared to the expected sensitivity obtained from exploiting 3000 fb^{-1} of data expected to be delivered by the HL-LHC. The conditions at the HL-LHC are considerably more harsh than they are at the LHC. As a benchmark, an environment with an average of 140 inelastic interactions per bunch crossing is studied. The uncertainty on the total integrated luminosity is assumed to be 3 % for both the 300 fb^{-1} and 3000 fb^{-1} scenarios.

The prospects for measuring the coupling strengths of the Higgs boson with ATLAS at the HL-LHC have previously been released as Ref. [52], superseding an earlier iteration of the analysis [504]. Major updates include revised projections for the $H \to Z\gamma$ [505] and $VH/t\bar{t}H \to \gamma\gamma$ [506] measurements. The addition of a $VH \to b\bar{b}$ rate measurement [507] provides a direct handle on the Yukawa coupling to the b-quark.

As it was alluded to in Sec. 9.1.2, the definite technical design of the ATLAS detector for the high-luminosity run is still in the research and development phase and has not yet been finalized. Thus, the performance of the detector can only be approximated using the knowledge obtained during Run 1 of data taking. The ambition is to match the performance of the current detector also in the high-occupancy environment. The assumption relies on future improvements of the reconstruction algorithms, mitigating the degradation due to the operating conditions. The ATLAS detector acceptances and object selection efficiencies and resolutions are modeled according to parametrized response functions. These are derived from a full simulation of the upgraded inner tracker, embedded into a model of the current calorimeters and MS, and extrapolated to large instantaneous luminosities accompanied by high pile-up [508, 509]. The systematic uncertainties associated with an experimental origin are considered to be analysis-specific, and thus treated as uncorrelated between the different rate measurements.

Signal theory uncertainties with a common source are treated as fully correlated across all categories. The uncertainty on the Higgs production cross sections due to missing higher-order perturbative corrections, is assessed by varying the renormalization and factorization scales in the MC simulation, following the recommendations of Ref. [135]. Similarly, the uncertainties due to the chosen PDF parametrisations and models and due to theoretical uncertainties on the branching fractions, are included [135]. The sum of the branching fractions is one, leading to correlations in the uncertainties on the BRs beyond the ones induced by the parameter uncertainties (strong coupling constant and quark masses), and by the theory calculation. The projections for the HL-LHC presented in this section, account for these correlations. The uncertainty on the branching fractions induced by the uncertainty on the Higgs boson mass in future precision measurements, is deemed to be negligible. The uncertainties arising from jet binning and the Higgs p_{T} in the ggF and $VH \to b\bar{b}$ processes, emanate from the current Run 1 analyses [26, 30, 135]. The theory calculations are expected to evolve over time, reducing the theoretical component of the uncertainty on the measured rates and couplings. Thus, as the two extreme cases, results are quoted for the current theory uncertainties, and for a scenario without theory uncertainties, identifying the expected experimental limits for the measurements.

Production strengths and decay rates

The Higgs boson decay rates are measured for seven decay modes as well as for their combination, assuming that the BRs are as predicted by the SM for a Higgs boson with

Table 9.2: Expected sensitivity (in %) for measuring the decay rates for a SM Higgs boson with a mass of 125 GeV in the different experimental categories used in the combination of all channels at the HL-LHC using 300 fb^{-1} and 3000 fb^{-1} of data at a collision energy of $\sqrt{s} = 14$ TeV. The measurement assumes the production cross sections to be as predicted by the SM. The results are reported for a scenario assuming the current theoretical systematic uncertainties and for a scenario, which takes into account only the statistical and experimental systematic uncertainties.

$\Delta\mu/\mu$	300 fb^{-1}		3000 fb^{-1}	
	All unc.	No theory unc.	All unc.	No theory unc.
$H \to \gamma\gamma$ (comb.)	0.13	0.09	0.09	0.04
(0j)	0.19	0.12	0.16	0.05
(1j)	0.27	0.14	0.23	0.05
(VBF-like)	0.47	0.43	0.22	0.15
(WH-like)	0.48	0.48	0.19	0.17
(ZH-like)	0.85	0.85	0.28	0.27
(ttH-like)	0.38	0.36	0.17	0.12
$H \to ZZ$ (comb.)	0.11	0.07	0.09	0.04
(VH-like)	0.35	0.34	0.13	0.12
(ttH-like)	0.49	0.48	0.20	0.16
(VBF-like)	0.36	0.33	0.21	0.16
(ggF-like)	0.12	0.07	0.11	0.04
$H \to WW$ (comb.)	0.13	0.08	0.11	0.05
(0j)	0.18	0.09	0.16	0.05
(1j)	0.30	0.18	0.26	0.10
(VBF-like)	0.21	0.20	0.15	0.09
$H \to Z\gamma$ (incl.)	0.46	0.44	0.30	0.27
$H \to b\bar{b}$ (comb.)	0.26	0.26	0.14	0.12
(WH-like)	0.57	0.56	0.37	0.36
(ZH-like)	0.29	0.29	0.14	0.13
$H \to \tau\tau$ (VBF-like)	0.21	0.18	0.19	0.15
$H \to \mu\mu$ (comb.)	0.39	0.38	0.16	0.12
(incl.)	0.47	0.45	0.18	0.14
(ttH-like)	0.74	0.72	0.27	0.23

a mass of approximately 125 GeV. The analyses feature categories with final state topologies that are characteristic for the different production modes of the Higgs boson in the SM.

The $H \to \gamma\gamma$ rate measurement is performed in final states with an enhanced sensitivity to ggF production, i. e. zero and one jet final states, and in two jet final states with a VBF

selection [504]. As previously advertised, dedicated one and two lepton selections allow measuring the production in association with t-quarks, W or Z bosons [506]. Similarly, the $H \to ZZ^* \to 4\ell$ analysis considers categories sensitive to ggF, VBF, VH, and ttH production [504]. The $H \to WW^* \to \ell\nu\ell\nu$ analysis is streamlined with respect to the Run 1 measurement presented in Cha. 5. It exploits final states with zero and one jet, as well as two jet final states with a VBF topology [504]. For the $H \to Z\gamma$ decay, final states with electrons and muons originating from the decay of the Z boson are considered. The events are classified according to the pseudorapidity difference between the photon and the Z boson, and the component of the Higgs boson candidate's transverse momentum orthogonal to the $Z\gamma$ thrust axis in the transverse plane [505]. The included $H \to \tau\tau$ analysis covers the VBF production mode [504]. The search for the rare process $H \to \mu\mu$ comprises a category enhanced in ttH production in addition to an inclusive event selection [504]. The $VH \to b\bar{b}$ analysis features one and two lepton selections to identify Higgs boson production in association with W and Z bosons, respectively [507].

Table 9.2 summarizes the precision on the decay rates expected to be obtained for each of the categories and their combination exploiting the full data set of the current LHC program, and using the full HL-LHC data set, respectively. The results are visualized in Fig. 9.4. Using $3000\,\text{fb}^{-1}$ of data, the experimental uncertainties on the rates of Higgs boson decays to diboson final states, can be as low as 5 %.

The inclusive production strength can be measured from a combination of the different final states under the assumption that the branching fractions of the different decay modes do not deviate from the predicted ones. Considering all systematic uncertainties, the combined measurement results in an accuracy of 8.5 % using a total integrated luminosity of $300\,\text{fb}^{-1}$, and 6.5 % when using the $3000\,\text{fb}^{-1}$ data set. Neglecting theoretical uncertainties, the precision is expected to be as good as 4.8 % and 3.4 %, for the two runs, respectively. Table 9.3 provides detailed projections of the precision reachable for the individual production modes.

The experimental precision for measuring the cross section of the ggF process is approximately 4 % at the HL-LHC. Ultimately, the measurement is limited by the uncertainty on the luminosity. In the SM, Higgs production via ggF is mediated by a heavy quark loop. NP scenarios predict modifications through BSM contributions to the process. However, in order to constrain these contributions and simultaneously measure the Yukawa coupling to the top quark, the cross section of the ttH production mode needs to be measured to a high precision. The latter is expected to be measured to an accuracy of better than 10 %, in particular when including a dedicated search for Higgs bosons produced in association with top quarks and decaying to bottom quarks, providing excellent prospects for the HL-LHC upgrade.

$gg \to ZH$ production becomes relevant at high p_{T} in the $VH \to b\bar{b}$ channel, cf. Sec. 1.4. The production loop provides a window on BSM contributions that modify the predicted rate.

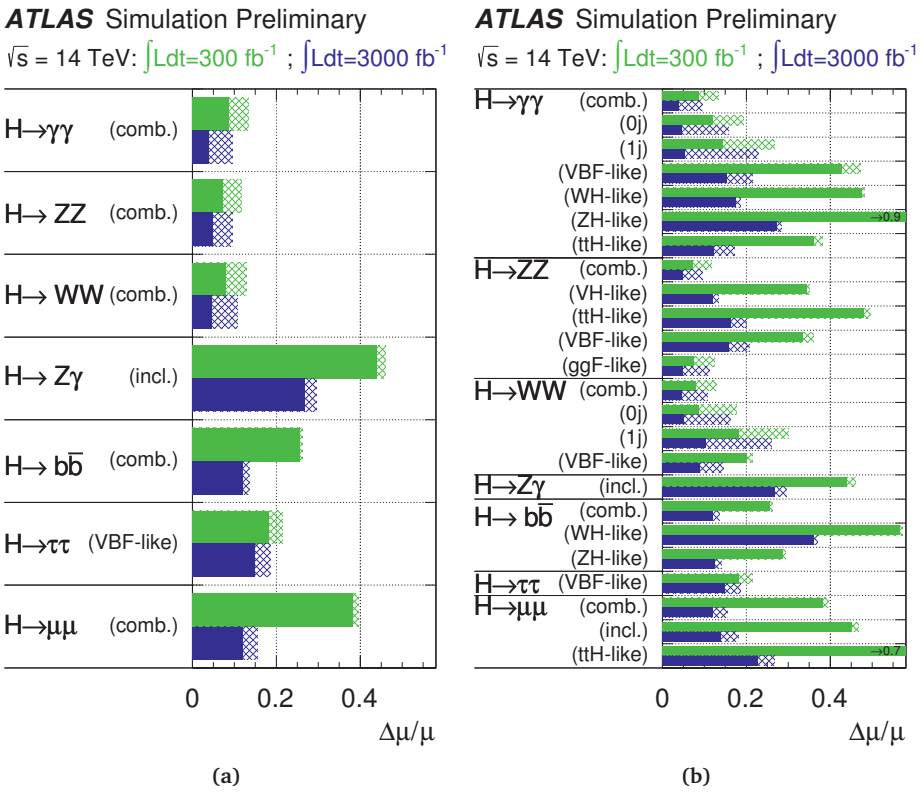

Figure 9.4: Expected sensitivity (in %) for measuring the decay rates for a SM Higgs boson with a mass of 125 GeV at the HL-LHC using 300 fb^{-1} and 3000 fb^{-1} of data at a collision energy of $\sqrt{s} = 14$ TeV. The measurement assumes the production cross sections to be as predicted by the SM. The hashed areas indicate the increase of the estimated uncertainty due to current theory systematic uncertainties included in the projections. The combined signal strength in the considered final states is shown in (a), while (b) shows the expected precision for the different experimental categories used in the combination of all channels.

However, without a dedicated analysis, the expected sensitivity to this mode is limited, even with a total integrated luminosity of 3000 fb^{-1}.

It should be noted explicitly that the sensitivity to the total Higgs decay width can be significantly enhanced beyond the combined analysis presented in this section by incorporating additional measurements. Examples of analyses to be included in future iterations, are the direct searches for invisible Higgs decays [460, 504, 510, 511], or measurements of the off-shell Higgs production rate in WW and ZZ final states at invariant masses above the corresponding on-shell production thresholds [469–472]. However, in the region of phase space of the off-shell measurements probed at the HL-LHC it is expected that the assumption

Table 9.3: Expected sensitivity (in %) for measuring the production strengths for a SM Higgs boson with a mass of 125 GeV at the HL-LHC using 300 fb^{-1} and 3000 fb^{-1} of data at a collision energy of $\sqrt{s} = 14$ TeV. The measurement assumes the branching fractions to be as predicted by the SM. The results are reported for a scenario assuming the current theoretical systematic uncertainties and for a scenario, which takes into account only the statistical and experimental systematic uncertainties.

$\Delta\mu/\mu$	300 fb^{-1}		3000 fb^{-1}	
	All unc.	No theory unc.	All unc.	No theory unc.
$gg \to H$	0.12	0.06	0.11	0.04
VBF	0.18	0.15	0.15	0.09
WH	0.41	0.41	0.18	0.18
$qqZH$	0.80	0.79	0.28	0.27
$ggZH$	3.71	3.62	1.47	1.38
ttH	0.32	0.30	0.16	0.10

of non-running coupling strengths does not hold universally for ggF and VBF production without violating unitarity. Thus, the inclusion of off-shell measurements requires advances in the calculation of the running coupling strengths.

Coupling strength measurements

The previous section explored the prospects for measuring Higgs production cross sections and decay rates at the HL-LHC, respectively. Within the κ-framework, cf. 6.3.1, the production and decay rates are coherently interpreted in terms of coupling scale factors. The analysis does not incorporate differential measurements of the Higgs boson production cross sections, for example as a function of the Higgs p_{T} or rapidity [473, 474]. Following the recommendations in Ref. [135], the prospects for measuring the Higgs boson coupling strengths at the HL-LHC are studied for two classes of benchmark models: parametric extensions of the SM *with* or *without* assumptions on the Higgs total decay width. The experimental mass resolution at the LHC is not sufficient to directly observe a total width as narrow as the one of a light (SM) Higgs boson [453]. Conceding the possibility of BSM Higgs decay modes, the extra degree of freedom introduces a degeneracy that prevents constraining the total width indirectly from measurements of the detectable partial decay widths. Thus, without further assumptions on the total width canceling at least one degree of freedom, only ratios of coupling scale factors can be determined, cf. Sec. 6.3.

The absence of invisible or undetected decay modes, i. e. the assumption that the Higgs boson couples only to SM particles, presents a viable scenario for measuring absolute Higgs boson coupling strengths. Naturally, if one or more coupling scale factors are measured externally,

e. g. at another experiment, or if they can be determined from theoretical considerations, the degrees of freedom reduce and enable determining the absolute couplings even in the presence of NP. De facto, it is sufficient to impose an upper boundary on the couplings to gauge bosons to fix the Higgs width [135, 512–514], and has been studied for selected benchmark models in Sec. 6.3 for the current collision data set. Although this scenario is theoretically well motivated, it has not yet been investigated for the HL-LHC upgrade. It should be emphasized that the precision on any coupling scale factor or coupling scale factor ratio, is specific to the benchmark model in which the measurement is performed. Generally, reducing the degrees of freedom, implies an increase in the statistical precision.

Table 9.4 summarizes the precision on the absolute Higgs boson coupling strengths expected to be reached in various benchmark models by the current LHC program and at the HL-LHC, under the assumption that all decay modes are detected. Some of the models are interpreted in BSM scenarios, as discussed in Sec. 9.3. In the most elementary scenario, a universal Higgs coupling scale factor is probed, cf. Model 1. Subsequently, constraints on the couplings are released to probe symmetries in different sectors of the SM. Model 2 tests fundamental differences between the gauge coupling and Yukawa coupling sectors by releasing the assumption on identical scaling of the couplings to massive vector bosons and fermions. The results for this benchmark model for the current collision data set are reported in Sec. 6.3.2. Custodial symmetry requires the couplings of the SM Higgs boson to the W and Z bosons to scale identically, cf. Model 3. The following models probe symmetries in the fermion sector, namely through distinct modifications of the couplings to up-type and down-type fermions (Model 4), differences between the lepton and quark couplings to the Higgs boson (Model 5), and between different fermion generations (Model 6). Model 7 presents a generic parametrization, which treats the coupling scale factors to SM particles independently, but does not allow for NP in vertex loops, cf. Sec. 6.3.6. This restriction is dropped for Model 8, when introducing effective coupling scale factors for the loop-induced couplings to photons, gluons, and $Z\gamma$, cf. Sec. 6.3.6.

Generally, the prospects for measuring the coupling strengths to vector bosons and the loop-induced couplings to photons and gluons exceed the expected precision on the Yukawa coupling strengths. Typically, the precision on the Higgs boson coupling strengths at the HL-LHC is expected to improve by a factor of two with respect to the current LHC program in the experimental limit. This is an indication for experimental systematic uncertainties not scaling according to the integrated luminosity. The measurement of the coupling strength to muons presents an exception from this statement. Being statistically limited, its precision is expected to improve by a factor of three. The effective coupling to $Z\gamma$ can only be determined with limited experimental accuracy. Thus, the benefit from the increased integrated luminosity is modest in comparison with the other measurements.

The expected precision for a simultaneous measurement of BSM contributions to the loop-induced Higgs couplings to photons, gluons, and $Z\gamma$, and the branching fraction for invisible or undetectable Higgs decays, is given in Tab. 9.5. The benchmark model assumes that the

Table 9.4: Expected sensitivity (in %) for measuring the coupling strengths for a SM Higgs boson with a mass of 125 GeV at the HL-LHC using 300 fb^{-1} and 3000 fb^{-1} of data at a collision energy of $\sqrt{s} = 14$ TeV. The observed and expected results for an integrated luminosity of up to 4.7 fb^{-1} at $\sqrt{s} = 7$ TeV and 20.3 fb^{-1} at $\sqrt{s} = 8$ TeV are shown for comparison. A dash (-) indicates a insignificant sensitivity to the corresponding coupling strength. The benchmark models assume no decay modes beyond those predicted by the SM. The results are reported for scenarios assuming the current theoretical systematic uncertainties or half of those, and for a scenario, which takes into account only the statistical and experimental systematic uncertainties.

Model		Coupling Parameter	25 fb^{-1}		300 fb^{-1}			3000 fb^{-1}		
			All theory unc.		Theory unc.:			Theory unc.:		
			Obs.	Exp.	All	Half	None	All	Half	None
1	MCHM4 EW singlet	κ	5.7	6.2	4.2	3.0	2.4	3.2	2.2	1.7
2	MCHM5 2HDM Type I	κ_V	6.4	6.5	4.3	3.0	2.5	3.3	2.2	1.7
		κ_F	14	15	8.8	7.5	7.1	5.1	3.8	3.2
3		κ_Z			4.7	3.7	3.3	3.3	2.3	1.9
		κ_W			4.9	3.6	3.1	3.6	2.4	1.8
		κ_F			9.3	7.9	7.3	5.4	4.0	3.4
4	2HDM Type II MSSM	κ_V			5.9	5.4	5.3	3.7	3.2	3.0
		κ_u			8.9	7.7	7.2	5.4	4.0	3.4
		κ_d			12	12	12	6.7	6.2	6.1
5	2HDM Type III	κ_V			4.3	3.1	2.5	3.3	2.2	1.7
		κ_q			11	8.7	7.8	6.6	4.5	3.6
		κ_l			10	9.6	9.3	6.0	5.3	5.1
6		κ_V			4.3	3.1	2.5	3.3	2.2	1.7
		κ_q			11	9.0	8.1	6.7	4.7	3.8
		κ_τ			12	11	11	9.2	8.4	8.1
		κ_μ			20	20	19	6.9	6.3	6.1
7	Mass scaling parametrization	κ_Z	14	15	8.1	7.9	7.8	4.3	3.9	3.8
		κ_W	16	14	8.5	8.2	8.1	4.8	4.1	3.9
		κ_t	22	21	14	12	11	8.2	6.1	5.3
		κ_b	53	33	23	22	22	12	11	10
		κ_τ	21	23	14	13	13	9.8	9.0	8.7
		κ_μ	-	-	21	21	21	7.3	7.1	7.0
8		κ_Z	14	16	8.1	7.9	7.9	4.4	4.0	3.8
		κ_W	16	15	9.0	8.7	8.6	5.1	4.5	4.2
		κ_t	26	40	22	21	20	11	8.5	7.6
		κ_b	47	37	23	22	22	12	11	10
		κ_τ	20	24	14	14	13	9.7	9.0	8.8
		κ_μ	-	-	21	21	21	7.5	7.2	7.1
		κ_g	19	21	14	12	11	9.1	6.5	5.3
		κ_γ	17	19	9.3	9.0	8.9	4.9	4.3	4.1
		$\kappa_{Z\gamma}$	-	-	24	24	24	14	14	14

Table 9.5: Expected sensitivity (in %) for measuring the effective loop induced coupling strengths for a SM Higgs boson with a mass of 125 GeV at the HL-LHC using 300 fb^{-1} and 3000 fb^{-1} of data at a collision energy of $\sqrt{s} = 14$ TeV. The benchmark model accommodates BSM contributions to the total width through a branching fraction for invisible or undetectable Higgs decays. The 95 % CL upper limit on $BR_{i.,u.}$ is reported. The observed and expected results for an integrated luminosity of up to 4.7 fb^{-1} at $\sqrt{s} = 7$ TeV and 20.3 fb^{-1} at $\sqrt{s} = 8$ TeV are shown for comparison. A dash (-) indicates a insignificant sensitivity to the corresponding coupling strength. The benchmark model assumes the couplings to massive particles to be as predicted by the SM. The results are reported for scenarios assuming the current theoretical systematic uncertainties or half of those, and for a scenario, which takes into account only the statistical and experimental systematic uncertainties.

Model	Coupling Parameter	25 fb^{-1}		300 fb^{-1}			3000 fb^{-1}		
		All theory unc.		Theory unc.:			Theory unc.:		
		Obs.	Exp.	All	Half	None	All	Half	None
9 Higgs portal	κ_g	11	14	8.9	7.1	6.3	6.7	4.1	2.8
	κ_γ	12	13	4.9	4.8	4.7	2.1	1.8	1.7
	$\kappa_{Z\gamma}$	-	-	23	23	23	14	14	14
	$BR_{i.,u.}$	<27	<37	<22	<20	<20	<14	<11	<10

couplings to massive particles not proceeding through vertex loops at the lowest order, are not modified with respect to the SM prediction. Similar to the previously studied parametrizations, at the HL-LHC, the sensitivity to most model parameters improves by up to a factor of two.

Table 9.6 summarizes the expected precision on ratios of Higgs coupling scale factors in selected benchmark models without assumption on the total decay width. Models 10 to 14 are designed to probe the same symmetries as Models 2 to 6 did in absolute Higgs coupling strength measurements. Many experimental and theoretical systematic uncertainties, e. g. the uncertainty on the integrated luminosity, cancel in the ratio. Thus, by exploiting ratios of couplings, the SM symmetries can be probed to a higher precision, than it would be possible from measuring the absolute couplings.

Figure 9.5 visualizes the prospects for measuring coupling scale factor ratios in a fully generic benchmark model, accommodating BSM contributions to loop-induced vertices and to the total width. The parametrization corresponds to Model 15 in Tab. 9.6. In the experimental limit of the HL-LHC, the precision on the ratio of the coupling strengths to the EW gauge bosons is approximately 2 %. The sensitivity degrades for ratios involving fermions, gluons, or $Z\gamma$, in accordance with previous findings. New charged particles contributing through the $H \to \gamma\gamma$ decay loop as compared to the $H \to ZZ^*$ decay mode, would modify the ratio of the effective photon coupling and the Z boson coupling, $\lambda_{\gamma Z}$. Similarly, modifications of the ratio of the top quark Yukawa coupling and the effective gluon coupling, λ_{tg}, reflect contributions from colored BSM particles to the ggF production loop, which is dominated by a running

Table 9.6: Expected sensitivity (in %) for measuring ratios coupling strengths for a SM Higgs boson with a mass of 125 GeV at the HL-LHC using 300 fb^{-1} and 3000 fb^{-1} of data at a collision energy of $\sqrt{s} = 14$ TeV. The observed and expected results for an integrated luminosity of up to 4.7 fb^{-1} at $\sqrt{s} = 7$ TeV and 20.3 fb^{-1} at $\sqrt{s} = 8$ TeV are shown for comparison. A dash (-) indicates a insignificant sensitivity to the corresponding coupling strength. The benchmark models make no assumption the Higgs boson total decay width. The results are reported for scenarios assuming the current theoretical systematic uncertainties or half of those, and for a scenario, which takes into account only the statistical and experimental systematic uncertainties.

Model	Coupling Parameter	25 fb^{-1}		300 fb^{-1}			3000 fb^{-1}		
		All theory unc.		Theory unc.:			Theory unc.:		
		Obs.	Exp.	All	Half	None	All	Half	None
10	κ_{VV}	12	13	7.3	6.7	6.5	4.0	3.2	2.9
	λ_{FV}	14	14	7.8	7.4	7.2	3.6	3.1	2.9
11	κ_{ZZ}	25	28	9.8	9.1	8.9	5.1	4.3	3.9
	λ_{WZ}	13	14	4.3	4.0	3.9	2.3	1.8	1.6
	λ_{FZ}	19	20	9.2	8.5	8.3	4.4	3.7	3.5
12	κ_{uu}	26	29	14	11	9.7	8.7	5.7	4.2
	λ_{Vu}	18	21	9.4	8.3	7.9	5.1	3.8	3.2
	λ_{du}	16	18	9.7	8.2	7.7	6.0	4.6	4.0
13	κ_{qq}	22	22	14	11	9.9	8.1	5.6	4.5
	λ_{Vq}	16	17	9.6	8.5	8.1	5.2	3.9	3.4
	λ_{lq}	18	21	12	10	9.4	7.3	6.0	5.4
14	$\kappa_{\tau\tau}$			21	19	19	17	15	15
	$\lambda_{V\tau}$			11	11	11	8.5	7.8	7.6
	$\lambda_{q\tau}$			12	10	9.8	9.3	7.9	7.4
	$\lambda_{\mu\tau}$			22	22	22	11	9.8	9.6
15	κ_{gZ}	13	14	6.4	4.4	3.5	5.7	3.3	2.0
	λ_{WZ}	14	15	5.2	4.8	4.6	3.1	2.4	2.1
	λ_{tg}	25	47	17	16	15	9.4	6.4	5.0
	λ_{bZ}	45	32	18	17	17	9.8	8.1	7.4
	$\lambda_{\tau Z}$	21	24	12	12	11	8.9	8.1	7.8
	$\lambda_{\mu Z}$	-	-	20	20	20	6.3	6.2	6.1
	λ_{gZ}	22	24	13	11	10	8.7	5.8	4.5
	$\lambda_{\gamma Z}$	17	18	5.5	5.2	5.1	2.6	2.0	1.8
	$\lambda_{(Z\gamma)Z}$	-	-	23	23	23	14	14	14
16	$\kappa_{\gamma\gamma}$			14	13	12	6.8	5.5	5.0
	$\lambda_{Z\gamma}$			5.5	5.2	5.1	2.5	2.0	1.8
	$\lambda_{W\gamma}$			5.9	5.7	5.6	2.7	2.4	2.2
	$\lambda_{t\gamma}$			21	20	20	10	8.0	7.0
	$\lambda_{b\gamma}$			18	17	17	9.5	8.0	7.4
	$\lambda_{\tau\gamma}$			13	12	12	8.7	8.1	7.9
	$\lambda_{\mu\gamma}$			20	20	20	6.5	6.2	6.1
	$\lambda_{g\gamma}$			13	12	11	8.5	5.9	4.6
	$\lambda_{(Z\gamma)\gamma}$			23	23	23	14	14	14

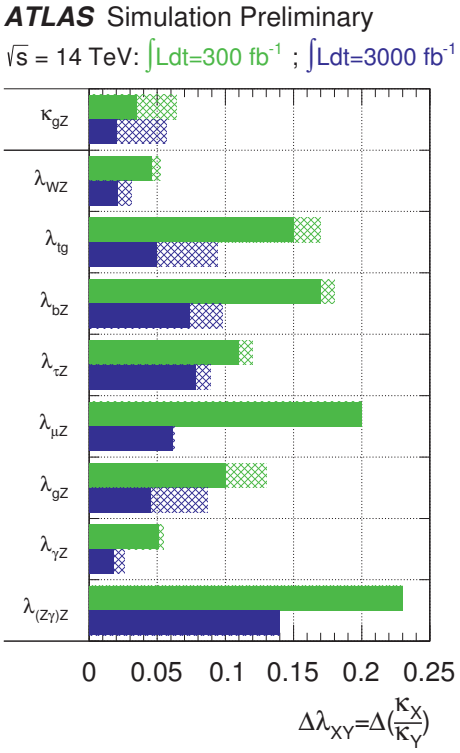

Figure 9.5: Expected sensitivity (in %) for measuring ratios coupling strengths in a generic model for a SM Higgs boson with a mass of 125 GeV at the HL-LHC using 300 fb^{-1} and 3000 fb^{-1} of data at a collision energy of $\sqrt{s}$ = 14 TeV. The benchmark model makes no assumption the Higgs boson total decay width and accommodates BSM contributions to the loop-induced vertices. The hashed areas indicate the increase of the estimated uncertainty due to current theory systematic uncertainties included in the projections.

top quark in the SM. Model 16 presents a complementary parametrization, choosing $\kappa_{\gamma\gamma}$ as a common overall scale factor.

9.2.2 Combined measurements at the HL-LHC and the ILC

The ILC is expected to start operations at a collision energy of 250 GeV towards the end of the HL-LHC program. Higgs precision measurements, in particular of its coupling properties, are among the key motivations driving the technical design for both the HL-LHC upgrade and the ILC. However, their approach towards precision measurements is fundamentally different. The HL-LHC provides the experiments with a unique total integrated luminosity at the cost of a high occupancy environment. The ILC on the other hand, allows the experiments operating in extraordinarily clean conditions enabling excellent control over all physics processes. The prospects for measuring the Higgs boson couplings at the HL-LHC and the ILC have been reviewed in great detail in the previous section and in Ref. [53], respectively. Based on these results, the prospects for a combined measurement of the Higgs boson couplings at the two facilities are presented.

Phenomenology of Higgs physics at the ILC

At a collision energy of 250 GeV, SM Higgs boson production at the ILC occurs predominantly via Higgs-strahlung, $e^+e^- \to ZH$. The W boson fusion process, $e^+e^- \to H\nu_e\bar{\nu}_e$, becomes dominant only at larger centre-of-mass energies. The cross section for Z boson fusion, $e^+e^- \to He^+e^-$, is approximately one order of magnitude smaller. In addition, the Higgs boson is also produced in association with fermions, notably top quarks, $e^+e^- \to t\bar{t}H$. However, the kinematic threshold for this particular production mode is approximately 480 GeV, and thus not accessible at the start of the ILC operations. Figure 9.6 shows the Feynman diagrams for these processs and their cross sections as a function of the collision energy for the ILC. The decay modes of a SM Higgs boson have been reviewed in Sec. 1.4.2.

Colliding leptons, the four-momenta of the initial state particles are known at the ILC. Thus, a unique feature of such a machine is the ability for measuring the absolute Higgs-strahlung cross section independently of the Higgs decay mode. The invariant mass recoiling against the reconstructed Z boson is identified with the mass of Higgs boson produced in association,

$$m_H^2 = m_{\text{recoil}}^2 = s + m_Z^2 - 2E_Z\sqrt{s}. \tag{9.1}$$

Here, m_Z and E_Z denote the invariant mass of the Z boson and its energy in the laboratory frame, respectively, and $\sqrt{s}$ is the nominal collision energy. As such, the ILC enables measuring the absolute Higgs boson branching fraction and the total width without model assumptions, even if the Higgs boson decays to invisible final states. The expected precision on the Higgs-strahlung cross section and the cross section times BR for the dominant decay modes of a 125 GeV SM Higgs boson is given in Tab. 9.7.

Combination methodology

The absolute coupling strengths of the Higgs boson and its total decay width can be determined at the ILC independent of model assumptions. However, to facilitate a combined measurement of the Higgs boson coupling strengths exploiting the benefits of the HL-LHC and the ILC, a generic benchmark parametrization is employed [135]. Hence, the measurements of the cross section times BR at the ILC (cf. Tab. 9.7) are incorporated into the likelihood function of the corresponding HL-LHC measurements as uncorrelated subsidiary measurements. In the same way the measurement of the Higgs-strahlung cross section and the direct limit on the branching fraction of Higgs boson decays into invisible final states is included. Consequently, the production and decay rates are coherently interpreted in terms of coupling scale factors.

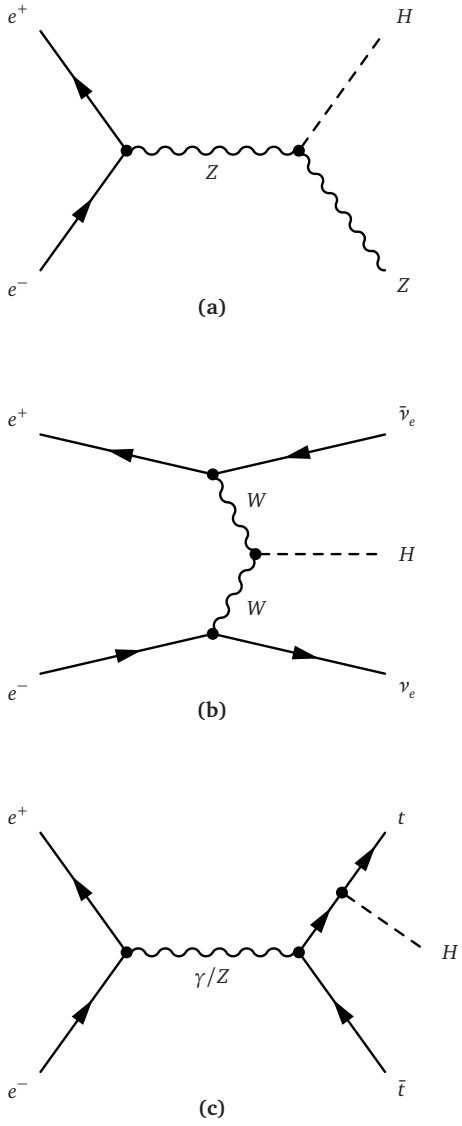

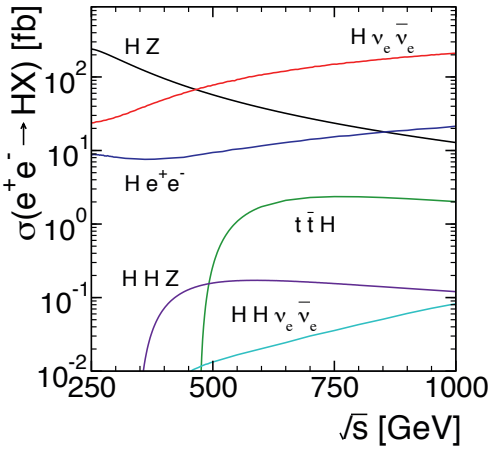

(d)

Figure 9.6: Feynman diagrams showing the main production mechanisms of the SM Higgs boson at electron-positron colliders: (a) Higgs-strahlung (b) W boson fusion, (c) associated production with top quarks. The cross sections for different production processes at the ILC are shown in (d) as a function of the centre-of-mass energy for a SM Higgs boson with a mass of 125 GeV. Figure (d) taken from Ref. [53].

Table 9.7: Expected precision on the Higgs-strahlung cross section and the cross section times BR for the dominant decay modes of a 125 GeV SM Higgs boson. The sensitivities are given for a collision energy of 250 GeV and an integrated luminosity of 250 fb^{-1}. Table adapted from Ref. [53].

	$e^+e^- \to ZH$
$\Delta\sigma/\sigma$	2.6%
$\text{BR}_{\text{i.,u.}}$	$< 0.9\%$
Decay mode	$\Delta(\sigma \times \text{BR})/(\sigma \times \text{BR})$
$H \to b\bar{b}$	1.2%
$H \to c\bar{c}$	8.3%
$H \to gg$	7.0%
$H \to WW^*$	6.4%
$H \to \tau\tau$	4.2%
$H \to ZZ^*$	18 %
$H \to \gamma\gamma$	34 %
$H \to \mu\mu$	100 %

Combined results

The combined results presented in the remainder of this section are based on the sensitivity to the Higgs boson coupling strengths expected for 3000 fb^{-1} of data provided by the HL-LHC at $\sqrt{s} = 14\,\text{TeV}$, and 250 fb^{-1} of data provided by the ILC during its first run at $\sqrt{s} = 250\,\text{GeV}$.

The scenario studied in this section, probes the absolute Higgs boson coupling strengths to the SM particles that are relevant to the accessible decay modes, i. e. κ_W, κ_Z, κ_t, κ_b, κ_τ, and κ_μ. In addition, the model accommodates modifications of the loop induced couplings κ_g, κ_γ, and $\kappa_{Z\gamma}$ with respect to the SM prediction. In this benchmark model, new decay modes with a branching fraction $\text{BR}_{\text{i.,u.}}$ leading to invisible or undetected final states can only be constrained by exploiting the invariant mass recoiling against the Z boson that is produced in association with the Higgs boson at the ILC. Using only measurements at the HL-LHC, the model is underconstrained by one degree of freedom. Thus, it has to be assumed that there is no NP in Higgs boson decays, i. e. the Higgs boson total decay width is as predicted by the SM. The latter configuration corresponds to Model 8 in Tab. 9.4.

Figure 9.7 visualizes the prospects for measuring the Higgs boson coupling scale factors in this fully generic benchmark model. The numerical values are given in Tab. 9.8. For comparison, the projections for ILC operations at $\sqrt{s} = 1\,\text{TeV}$ are shown as well. The Yukawa coupling to the top quark is only accessible at the HL-LHC and become accessible at the ILC only at higher collision energies, to be reached after future upgrades. The precision on its strength improves indirectly through a more precise determination of the Higgs boson total decay width. Typically, the precision for combined coupling strength measurements is expected to improve by approximately 5 % or more compared to the individual measurements. Incorporating the direct limit on the branching fraction of Higgs boson decays into invisible final states, reduces the uncertainty on the coupling to Z bosons beyond the preci-

sion expected from the Higgs-strahlung process. It should be noted, that the correlation of the measurements of the Higgs-strahlung cross section and the branching fraction of Higgs boson decays into invisible final states, is not modeled. The results indicate that the HL-LHC and the ILC are complementary facilities.

The ILC provides a precise measurement of the absolute coupling to Z bosons independently of the Higgs decay mode through measuring the Higgs-strahlung cross section. It excels at determining the Higgs boson coupling strengths associated to decay modes with a high rate, e. g. $H \to b\bar{b}$. Once more it should be emphasized that the absolute Higgs boson branching fraction and the total width are measured at the ILC without model assumptions, even in case the Higgs boson decays to invisible final states. However, the performance of the HL-LHC for studying decay modes with a low rate and other rare processes, e. g. $H \to \mu\mu$, is unmatched.

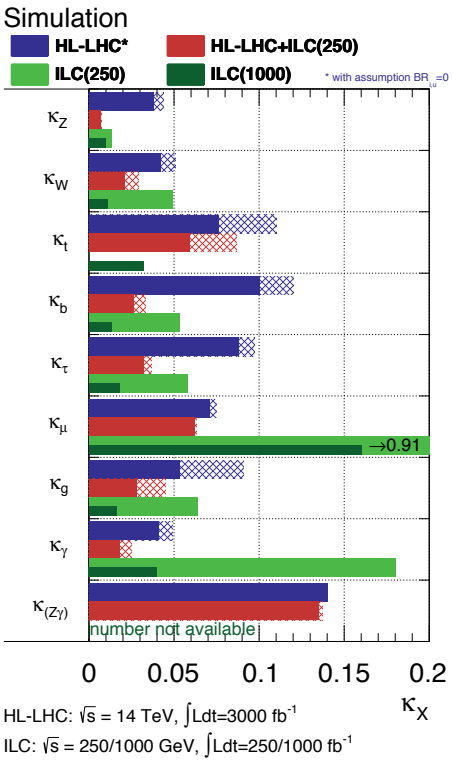

Figure 9.7: Relative uncertainty expected for the measurement of the Higgs boson coupling strengths assuming a Higgs boson mass of 125 GeV in a generic benchmark model for 3000 fb^{-1} of $\sqrt{s} = 14$ TeV HL-LHC data, from a model independent fit using 250 fb^{-1} of $\sqrt{s} = 250$ GeV ILC data, and for their combination in a generic benchmark model. For comparison, the model independent projections for ILC operations at $\sqrt{s} = 1$ TeV are overlayed. The Yukawa coupling to the top quark becomes accessible at the ILC only at higher collision energies. The precision on its strength improves indirectly through a more precise determination of the Higgs boson total decay width. The hashed areas indicate the increase of the estimated uncertainty due to current theory systematic uncertainties included in the projections for the HL-LHC. The projections for the ILC assume theory uncertainties of 0.5 %. The results for the HL-LHC have been described in Sec. 9.2.1. The results for the ILC are taken from Ref. [53].

Table 9.8: Relative uncertainty expected for the measurement of the Higgs boson coupling strengths assuming a Higgs boson mass of 125 GeV in a generic benchmark model for 3000 fb^{-1} of $\sqrt{s} = 14$ TeV HL-LHC data, from a model independent fit using 250 fb^{-1} of $\sqrt{s} = 250$ GeV ILC data, and for their combination in a generic benchmark model. For comparison, the model independent projections for ILC operations at $\sqrt{s} = 1$ TeV are shown. The Yukawa coupling to the top quark becomes accessible at the ILC only at higher collision energies. The precision on its strength improves indirectly through a more precise determination of the Higgs boson total decay width. The results for the HL-LHC are reported using the current theory uncertainties, or assuming no theory uncertainties. The projections for the ILC assume theory uncertainties of 0.5 %. The results for the HL-LHC have been described in Sec. 9.2.1. The results for the ILC are taken from Ref. [53]. A dash (-) indicates that the corresponding coupling strength measurement is not available.

Coupling Parameter	HL-LHC (3000 fb^{-1})		ILC(250) 250 GeV 250 fb^{-1}	ILC(1000) 1 TeV 1000 fb^{-1}	HL-LHC+ILC(250)	
	Theory unc.:				Theory unc.:	
	All	None			All	None
κ_Z	4.4	3.8	1.3	1.0	0.7	0.7
κ_W	5.1	4.2	4.9	1.1	2.9	2.1
κ_t	11	7.6	-	3.2	8.7	5.9
κ_b	12	10	5.3	1.3	3.3	2.6
κ_τ	9.7	8.8	5.8	1.8	3.7	3.2
κ_μ	7.5	7.1	91	16	6.3	6.2
κ_g	9.1	5.3	6.4	1.6	4.5	2.8
κ_γ	4.9	4.1	18	4.0	2.5	1.8
$\kappa_{Z\gamma}$	14	14	-	-	14	14

9.3 Prospects for New Physics in Higgs couplings

The precision on the Higgs boson coupling scale factors translates directly into constraints on the model parameters for BSM extensions of the SM, cf. Sec. 1.5 and Cha. 7. This section summarizes the sensitivity to new phenomena in Higgs boson couplings at the HL-LHC in selected BSM models, building on the projections presented in the previous section. For a detailed discussion of the benchmark models, the reader is referred to Sec. 1.5, Cha. 7, and the public literature featured in those sections. The results discussed in this chapter have previously been reported in Ref. [54]. The interpretations presented in this section imply that any modification of the Higgs boson coupling strengths does not change the Higgs boson decay kinematics appreciably. Throughout this section, h denotes a light, CP-even Higgs boson with a mass of approximately 125 GeV.

9.3.1 Mass scaling of couplings

In the SM the couplings of the Higgs boson to other particles are expected to be directly proportional to their (pole) masses, cf. Cha. 1,

$$g_{hVV} \propto \frac{m_V^2}{v} \quad \text{and} \quad g_{hff} \propto \frac{m_f}{v}. \tag{9.2}$$

Starting from Model 7 in Tab. 9.4, the deviation of the Higgs boson couplings from this scaling behaviour, is empirically parametrized by a mass scaling factor ϵ and a VEV parameter M [477, 478],

$$\kappa_{f,i} = v\frac{m_{f,i}^{\epsilon}}{M^{1+\epsilon}} \quad \text{and} \quad \kappa_{V,j} = v\frac{m_{V,j}^{2\epsilon}}{M^{1+2\epsilon}}. \tag{9.3}$$

Here, $v \approx 246\,\text{GeV}$ denotes the canonical Higgs VEV in the SM, and $m_{f,i}$ ($m_{V,j}$) is the (pole) mass of each fermion (massive gauge boson) flavor, indexed i (j).

Figure 9.8 displays the expected 68% and 95% CL regions for a simultaneous measurement of the parameters ϵ and M. The precision on the model parameters is expected to improve by a factor two to three, compared to the precision obtained for an integrated luminosity of up to $4.7\,\text{fb}^{-1}$ at $\sqrt{s} = 7\,\text{TeV}$ and $20.3\,\text{fb}^{-1}$ at $\sqrt{s} = 8\,\text{TeV}$. Using $300\,\text{fb}^{-1}$ ($3000\,\text{fb}^{-1}$) of data and taking into account only the statistical and experimental systematic uncertainties, parameter values $|\epsilon| > 0.04$ ($|\epsilon| > 0.02$) are expected to be excluded at 95 % CL. The relative improvement from $300\,\text{fb}^{-1}$ to $3000\,\text{fb}^{-1}$ is expected to be similar in case current theory systematic uncertainties are considered in the projection. The VEV parameter is expected to be measured with a precision of 15 GeV (10 GeV) at 95 % CL using $300\,\text{fb}^{-1}$ ($3000\,\text{fb}^{-1}$) of data and taking into account only the statistical and experimental systematic uncertainties. The expected relative improvement with a higher integrated luminosity is expected to degrade when considering theoretical uncertainties. Furthermore, the impact of the theoretical uncertainties on the Higgs boson decay modes varies, leading to a change in the correlation between ϵ and M.

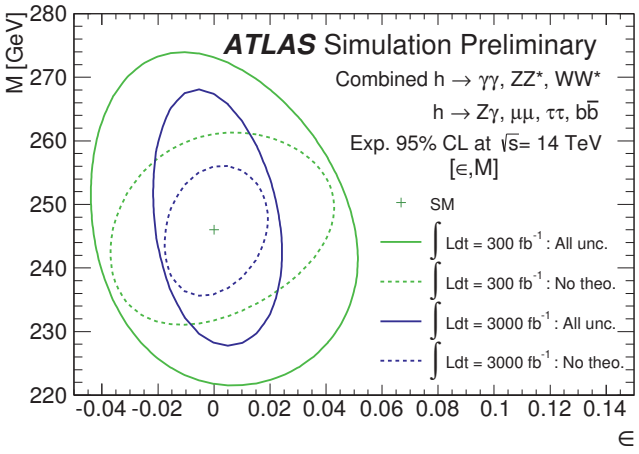

Figure 9.8: Confidence regions as a function of the mass scaling factor, ϵ, and the VEV parameter, M. The intervals are constructed at 68% and 95% CL for a SM Higgs boson under the assumption that the test statistic $-2\ln\Lambda(\epsilon, M)$ asymptotically is distributed as a χ^2 distribution with two degrees of freedom, exploiting $300\,\text{fb}^{-1}$ and $3000\,\text{fb}^{-1}$ of data at a collision energy of $\sqrt{s} = 14\,\text{TeV}$. The solid likelihood contours indicate the increase of the estimated uncertainty due to including current theory systematic uncertainties in the projections.

9.3.2 Minimal Composite Higgs Model

The theoretical aspects of MCHM models have been introduced in Sec. 1.5.2, while Sec. 7.2 reports on an indirect experimental search for this extension of the SM. The prospects for determining the Higgs boson compositeness scale f are studied starting from Model 1 and 2 in Tab. 9.4 for MCHM_4 and MCHM_5, respectively. In the MCHM_4, the ratio of the coupling strengths of the pNG boson to vector bosons and fermions relative to the corresponding SM predictions is given by

$$\kappa = \kappa_V = \kappa_F = \sqrt{1-\xi}, \tag{9.4}$$

where $\xi = v^2/f^2$. Similarly, in the MCHM_5 the coupling scale factors take the form

$$\kappa_V = \sqrt{1-\xi} \quad \text{and} \quad \kappa_F = \frac{1-2\xi}{\sqrt{1-\xi}}. \tag{9.5}$$

In both scenarios, the SM is recovered in the limit $\xi \to 0$, namely $f \to \infty$. Figure 9.9 shows the expected two-dimensional confidence intervals as a function of the coupling scale factors κ_V and κ_F, overlaid with the coupling strengths predicted by MCHM_4 and MCHM_5 as a function of ξ. Table 9.9 summarizes the expected 95 % CL lower limit on the Higgs boson compositeness scale at the HL-LHC using $300\,\text{fb}^{-1}$ and $3000\,\text{fb}^{-1}$ of data at a collision energy of $\sqrt{s} = 14\,\text{TeV}$. The results are limited by the theoretical uncertainties on the Higgs boson production rates through ggF and VBF [52, 54].

Table 9.9: Expected 95% CL lower limit on the Higgs boson compositeness scale, f, in the MCHM$_4$ and MCHM$_5$ models, exploiting 300 fb^{-1} and 3000 fb^{-1} of data at a collision energy of $\sqrt{s} = 14$ TeV. The results are reported for scenarios assuming the current theoretical systematic uncertainties, and for a scenario, which takes into account only the statistical and experimental systematic uncertainties. The observed and expected limits for an integrated luminosity of up to 4.7 fb^{-1} at $\sqrt{s} = 7$ TeV and 20.3 fb^{-1} at $\sqrt{s} = 8$ TeV are shown for comparison.

Model	25 fb^{-1}		300 fb^{-1}		3000 fb^{-1}	
	Obs.	Exp.	All unc.	No theory unc.	All unc.	No theory unc.
MCHM$_4$	710 GeV	460 GeV	620 GeV	810 GeV	710 GeV	980 GeV
MCHM$_5$	640 GeV	550 GeV	780 GeV	950 GeV	1000 GeV	1200 GeV

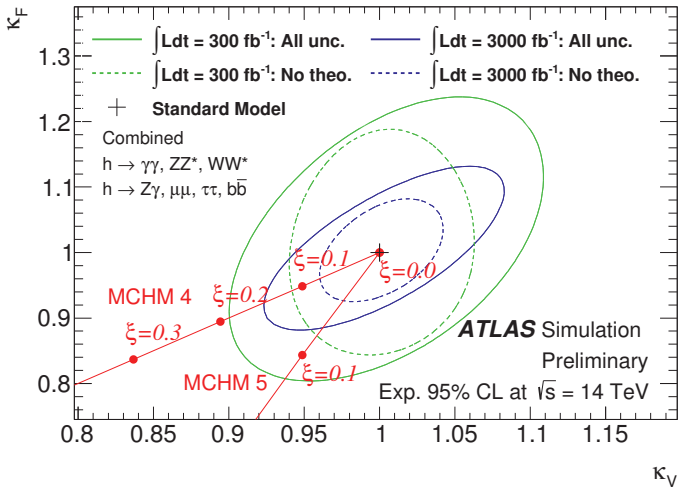

Figure 9.9: Confidence regions as a function of the coupling scale factors for Higgs couplings to vector bosons, κ_V, and fermions, κ_F, respectively. The regions are constructed at 68% and 95% CL for a SM Higgs boson under the assumption that the test statistic $-2\ln\Lambda(\kappa_V, \kappa_F)$ asymptotically is distributed as a χ^2 distribution with two degrees of freedom, exploiting 300 fb^{-1} and 3000 fb^{-1} of data at a collision energy of $\sqrt{s} = 14$ TeV. The solid likelihood contours indicate the increase of the estimated uncertainty due to including current theory systematic uncertainties in the projections. The coupling predictions in the MCHM$_4$ and MCHM$_5$ models are shown as parametric functions of the Higgs boson compositeness parameter, $\xi = v^2/f^2$. The two-dimensional likelihood contours are shown for reference only, i. e. the upper limit on the compositeness scale should not be determined from this illustration.

9.3.3 Additional electroweak singlet

The motivation for introducing an extra real field transforming as an EW singlet in addition to the Higgs doublet of the SM is discussed along with the theoretical background of such BSM models in Sec. 1.5.3. The current limits on the squared universal coupling of the emanating heavy Higgs boson,

$$\kappa'^2 = 1 - \mu_h, \tag{9.6}$$

are presented in Sec. 7.3. Table 9.10 summarizes the expected 95 % CL upper limit on κ'^2 at the HL-LHC using 300 fb^{-1} and 3000 fb^{-1} of data at a collision energy of $\sqrt{s} = 14$ TeV. Figure 9.10 shows a graphical representation of the results. In particular the high precision coupling measurements in $h \to \gamma\gamma$, $h \to ZZ^* \to 4\ell$, and $h \to WW^* \to \ell\nu\ell\nu$ lead to more stringent expected limits as a function of the integrated luminosity. The expected limits are dominated by the theoretical uncertainties on the Higgs boson production rates through ggF and VBF [52, 54].

9.3.4 The Two Higgs Doublet Model

2HDMs present a theoretically appealing class of extensions of the SM scalar sector. The phenomenology of four types of these models is discussed in Sec. 1.5.4. In the following, the established Higgs boson is identified as the light CP-even neutral scalar h with a mass of approximately 125 GeV. Similar to the indirect search presented in Sec. 7.4, the decay modes of the scalar h are restricted to the ones of a SM Higgs boson. Higgs boson production through bottom quark annihilation is incorporated through a correction that scales with the square of the Yukawa coupling to the b-quark, assuming that its differential distributions are the same as those in gluon fusion [54]. The deviations of the couplings of the scalar h to massive gauge bosons, up-type and down-type quarks, and leptons, as compared to the ones predicted for a SM Higgs boson, are fully determined by the mixing of the two

Table 9.10: Expected 95 % CL upper limit on the squared universal coupling strength, κ'^2, of a heavy Higgs boson arising from an additional real field transforming as an EW singlet, exploiting 300 fb^{-1} and 3000 fb^{-1} of data at a collision energy of $\sqrt{s} = 14$ TeV. The results are reported for scenarios assuming the current theoretical systematic uncertainties, and for a scenario, which takes into account only the statistical and experimental systematic uncertainties. The results are independent of the mass of the heavy Higgs boson and potentially accessible invisible and di-Higgs final states, e.g. from $H \to hh$ decays. The observed and expected limits for an integrated luminosity of up to 4.7 fb^{-1} at $\sqrt{s} = 7$ TeV and 20.3 fb^{-1} at $\sqrt{s} = 8$ TeV are shown for comparison.

Coupling	25 fb^{-1}		300 fb^{-1}		3000 fb^{-1}	
	Obs.	Exp.	All unc.	No theory unc.	All unc.	No theory unc.
κ'^2	0.12	0.29	0.17	0.10	0.13	0.06

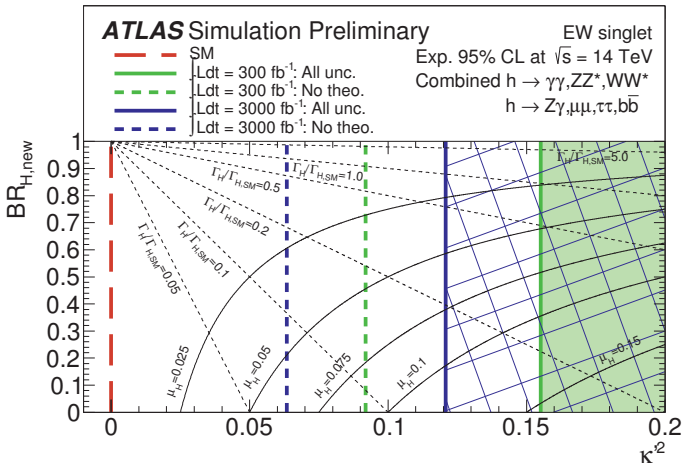

Figure 9.10: Expected 95% CL upper limit on the squared universal coupling strength, κ'^2, of a heavy Higgs boson arising from an additional real field transforming as an EW singlet, exploiting 300 fb^{-1} and 3000 fb^{-1} of data at a collision energy of $\sqrt{s} = 14$ TeV. The limits are shown in the $(\kappa'^2, \mathrm{BR}_{H,\mathrm{new}})$ plane of the heavy Higgs boson along with selected contours of the scale factor for the total width, $\Gamma_H/\Gamma_{H,\mathrm{SM}}$, and the inclusive production strength, μ_H. The light shaded and hashed regions indicate the increase of the estimated uncertainty due to including current theory systematic uncertainties in the projections. The results are independent of the mass of the heavy Higgs boson and potentially accessible invisible and di-Higgs final states, e.g. from $H \to hh$ decays.

neutral, CP-even Higgs states, and the mixing of the charged scalars and the pseudoscalars. The explicit functional forms have been summarized for the studied types of 2HDMs by Eqn. (1.67) and Tab. 1.3. The underlying benchmark models correspond to Model 2, 4, and 5 in Tab. 9.4.

Figure 9.11 shows the regions of the $(\cos(\beta-\alpha), \tan\beta)$ space for four types of 2HDMs that are expected to be compatible with the SM prediction at 95% CL at the HL-LHC using 3000 fb^{-1} of data. The confidence regions are constructed from the measurements of the Higgs boson couplings in the underlying benchmark models under the assumption that the test statistic $-2\ln\Lambda(\kappa_x)$ $(x = V, u, d, \ell)$ asymptotically is distributed as a χ^2 distribution with two degrees of freedom, corresponding to the dimensionality of the probed 2HDM parameter space. The upper and lower limits on the coupling scale factors are mapped to the 2HDM parameter space according to the parametrizations previously alluded to. The combined confidence region is constructed using the test statistic $-2\ln\Lambda(\cos(\beta-\alpha), \tan\beta)$, employing the same χ^2 cutoff. Figure 9.12 compares in a narrow window around the SM alignment limit for different integrated luminosities the regions of the $(\cos(\beta-\alpha), \tan\beta)$ space that are expected to be indirectly excluded at 95% CL or more from a combined measurement of the Higgs boson production and decay rates at the HL-LHC.

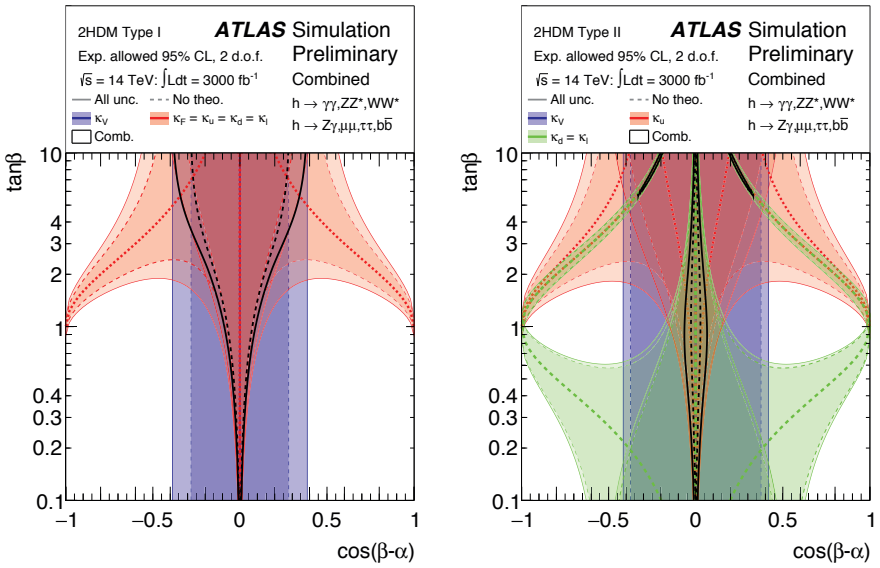

(a) Type I

(b) Type II

(c) Lepton specific

(d) Flipped

Figure 9.11: Confidence regions as a function of the Higgs boson coupling strengths to massive gauge bosons, up-type and down-type quarks, and leptons mapped to the $(\cos(\beta-\alpha), \tan\beta)$ space of four types of 2HDMs. The regions are constructed at 95% CL under the assumption that the test statistic $-2\ln\Lambda(\kappa_x)$ $(x = V, u, d, \ell)$ asymptotically is distributed as a χ^2 distribution with two degrees of freedom, corresponding to the dimensionality of the probed 2HDM parameter space. The combined confidence region is defined using the test statistic $-2\ln\Lambda(\cos(\beta-\alpha), \tan\beta)$. The results are shown for an integrated luminosity of $3000\,\text{fb}^{-1}$ of data at a collision energy of $\sqrt{s} = 14\,\text{TeV}$. The light shaded regions indicate the increase of the estimated uncertainty due to including current theory systematic uncertainties in the projections. The narrow green regions at large $\tan\beta$ correspond to a negative coupling sign relative to the profiled fermion coupling.

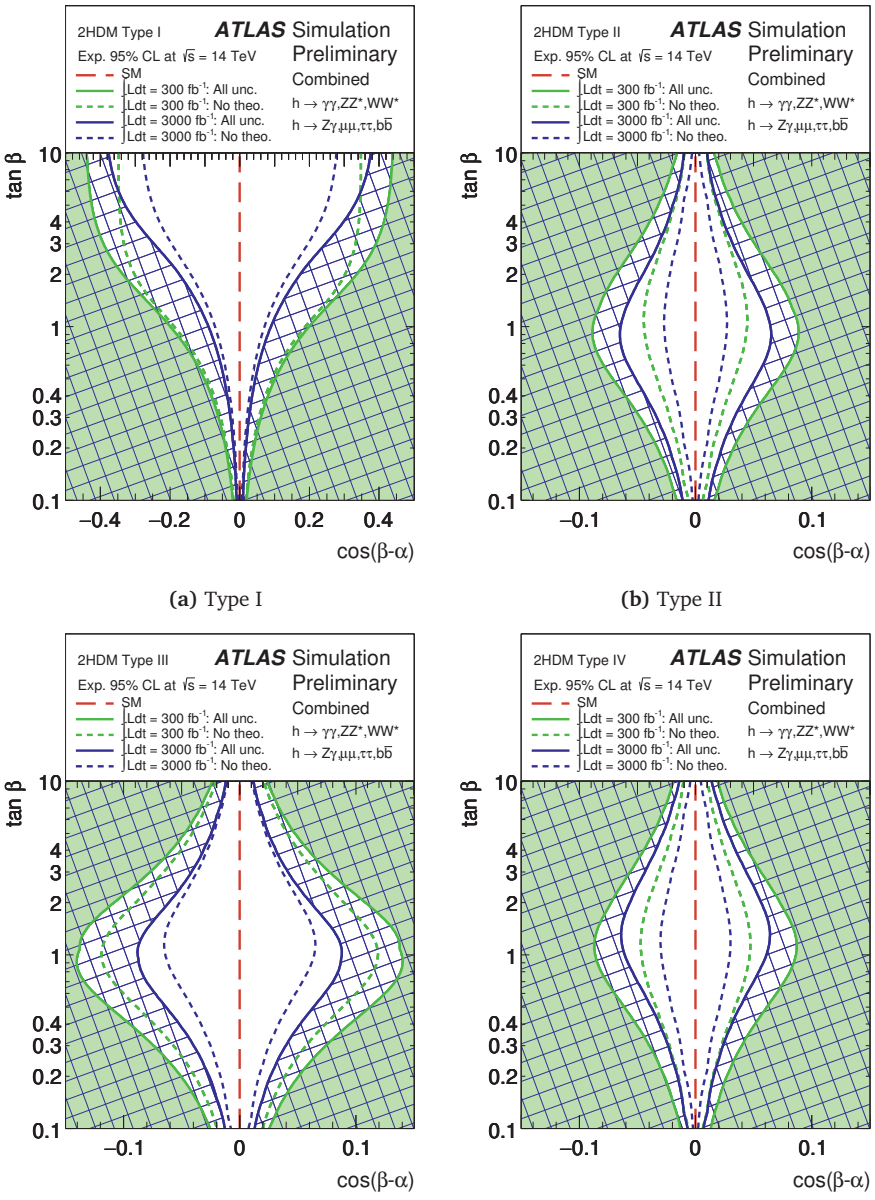

(a) Type I

(b) Type II

(c) Lepton specific

(d) Flipped

Figure 9.12: Regions of the $(\cos(\beta-\alpha), \tan\beta)$ space of four types of 2HDMs that are expected to be indirectly excluded at 95% CL or greater from a combined measurement of the Higgs boson production and decay rates at the HL-LHC, independent of the masses of the five physical Higgs bosons. The results are shown for an integrated luminosity of 300 fb^{-1} and 3000 fb^{-1} at a collision energy of $\sqrt{s} = 14\,\text{TeV}$. The solid and dashed contours indicate the expected exclusions with current theory systematics and in the experimental limit, respectively. The indicated confidence intervals are constructed under the assumption that the test statistic $-2\ln\Lambda(\cos(\beta-\alpha), \tan\beta)$ asymptotically is distributed as a χ^2 distribution with two degrees of freedom.

9.3.5 The Minimal Supersymmetric Standard Model

The hMSSM presents a simplified MSSM model, and as such is a specific realization of a generic 2HDM, cf. Sec. 1.5.5 and Sec. 7.5. In this model, the radiative corrections to the mass squared mixing matrix of the neutral, CP even Higgs bosons are fixed by the value of $\tan\beta$ at the mass of the established Higgs boson (identified as the light CP-even neutral scalar h), the mass of the Z boson, and the mass of the CP odd boson A. Hence, only two fundamental parameters associated with SUSY determine the modifications of the Higgs boson coupling strengths to massive gauge bosons, up-type fermions, and down-type fermions relative to the SM ones. The underlying benchmark model corresponds to Model 4 in Tab. 9.4, but is corrected for Higgs boson production through bottom quark annihilation as described in Sec. 7.5.

Figure 9.13 shows the regions of the $(m_A, \tan\beta)$ space of the hMSSM that are expected to be compatible with the measured production and decay rates of a SM Higgs boson at 95% CL with an integrated luminosity of $3000\,\text{fb}^{-1}$ at a collision energy of $\sqrt{s} = 14\,\text{TeV}$. The confidence regions are constructed from the measurements of the Higgs boson coupling

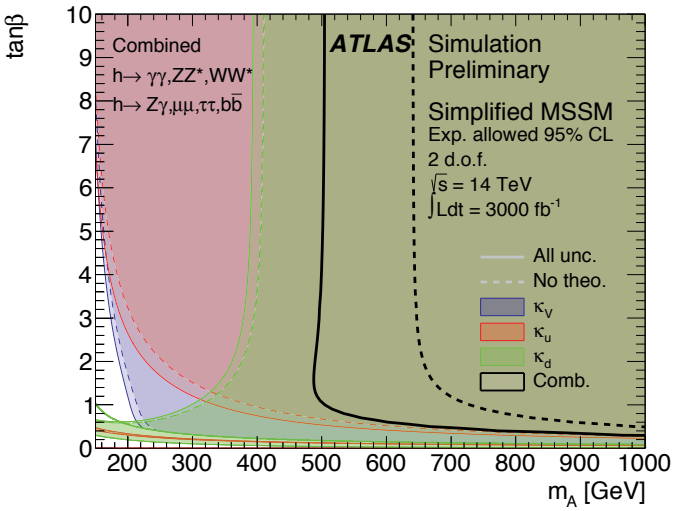

Figure 9.13: Confidence regions as a function of the Higgs boson coupling strengths to massive gauge bosons, up-type fermions, and down-type fermions mapped to the $(m_A, \tan\beta)$ space of the hMSSM. The regions are constructed at 95% CL under the assumption that the test statistic $-2\ln\Lambda(\kappa_x)$ $(x = V, u, d)$ asymptotically is distributed as a χ^2 distribution with two degrees of freedom, corresponding to the dimensionality of the probed hMSSM parameter space. The combined confidence region is defined using the test statistic $-2\ln\Lambda(m_A, \tan\beta)$. The results are shown for an integrated luminosity of $3000\,\text{fb}^{-1}$ of data at a collision energy of $\sqrt{s} = 14\,\text{TeV}$. The light shaded regions indicate the increase of the estimated uncertainty due to including current theory systematic uncertainties in the projections. The confidence region of κ_d at large (low) $\tan\beta$ corresponds to a positive (negative) sign relative to κ_u. The confidence region of κ_u at low $\tan\beta$ corresponds to a second solution of Eqn. (1.71). The SM decoupling limit is at large m_A.

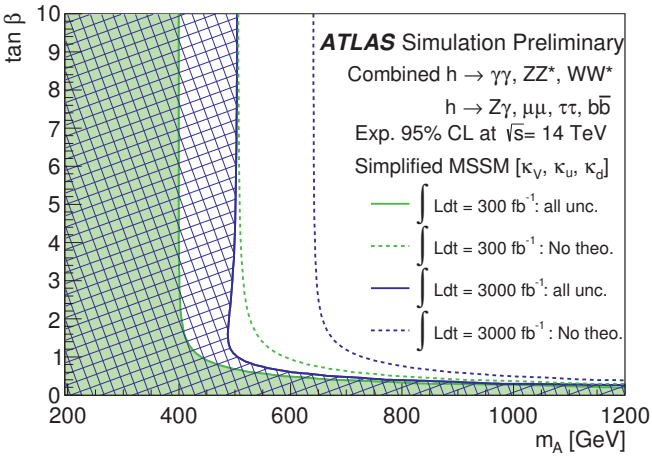

Figure 9.14: Regions of the hMSSM parameter space that are expected to be indirectly excluded at 95% CL or greater from a combined measurement of the Higgs boson production and decay rates at the HL-LHC. The results are shown for an integrated luminosity of $300\,\text{fb}^{-1}$ and $3000\,\text{fb}^{-1}$ at a collision energy of $\sqrt{s} = 14\,\text{TeV}$. The solid and dashed contours indicate the expected exclusions with current theory systematics and in the experimental limit, respectively. The indicated confidence intervals are constructed under the assumption that the test statistic $-2\ln\Lambda(m_A, \tan\beta)$ asymptotically is distributed as a χ^2 distribution with two degrees of freedom. The SM decoupling limit is at large m_A.

strengths in the underlying benchmark model under the assumption that the test statistic $-2\ln\Lambda(\kappa_x)$ $(x = V, u, d)$ asymptotically is distributed as a χ^2 distribution with two degrees of freedom, corresponding to the dimensionality of the probed hMSSM parameter space. The upper and lower limits on the coupling scale factors are mapped to the hMSSM parameter space according to their functional dependence on m_A and $\tan\beta$. The combined confidence region is constructed using the test statistic $-2\ln\Lambda(m_A, \tan\beta)$, employing the same χ^2 cutoff. Figure 9.14 compares the regions of the hMSSM parameter space that are expected to be indirectly excluded at 95% CL or greater from a combined measurement of the Higgs boson production and decay rates at the HL-LHC as a function of the integrated luminosity. With $300\,\text{fb}^{-1}$ of data and with (without) the inclusion of theoretical uncertainties, the expected lower limit on the CP-odd Higgs boson mass is

$$m_A > 390\,\text{GeV}\ (m_A > 490\,\text{GeV}) \quad \text{for} \quad 2 \leq \tan\beta \leq 10 \tag{9.7}$$

at 95% CL. With an increased integrated luminosity of $3000\,\text{fb}^{-1}$ more stringent limits on m_A are expected,

$$m_A > 480\,\text{GeV}\ (m_A > 640\,\text{GeV}) \quad \text{for} \quad 2 \leq \tan\beta \leq 10. \tag{9.8}$$

The expected limits increase to larger masses for $\tan\beta < 2$. The low $\tan\beta$ regime is explicitly excluded by this measurement. Variations of m_h within the measured uncertainties have a negligible impact on the derived limits. The improvement with respect to the lower limit on the CP-odd Higgs boson mass observed (expected) for an integrated luminosity of up to $4.7\,\text{fb}^{-1}$ at $\sqrt{s} = 7\,\text{TeV}$ and $20.3\,\text{fb}^{-1}$ at $\sqrt{s} = 8\,\text{TeV}$, $m_A > 400\,\text{GeV}$ ($m_A > 280\,\text{GeV}$) for $2 \leq \tan\beta \leq 10$, is limited by the precision on the coupling strength to down type fermions. In particular the measurement of the Yukawa coupling to the b quark is dominated by systematic uncertainties.

9.3.6 Dark Matter and the Higgs portal model

In Higgs portal models, WIMP DM candidates are assumed to only couple appreciably to the Higgs boson, and to fully account for extra contributions from new particles to the Higgs boson total decay width, resulting in a branching fraction for invisible Higgs boson decays. Furthermore, the underlying benchmark coupling model accommodates enhancements of loop induced processes from heavy new particles, cf. Tab. 9.5. The results presented in this section do not incorporate the constraints from direct searches for invisible Higgs decays [460, 504, 510, 511], which are statistically limited and expected to significantly improve the limit on $\text{BR}_{\text{i.,u.}}$ with an increasing integrated luminosity.

With $300\,\text{fb}^{-1}$ of data and with (without) the inclusion of theoretical uncertainties, the expected indirect upper limit on the branching fraction for invisible Higgs boson decays is

$$\text{BR}_{\text{i.,u.}} < 0.22 \quad (\text{BR}_{\text{i.,u.}} < 0.19) \tag{9.9}$$

at 95% CL. With an increased integrated luminosity of $3000\,\text{fb}^{-1}$ more stringent limits on $\text{BR}_{\text{i.,u.}}$ are expected,

$$\text{BR}_{\text{i.,u.}} < 0.13 \quad (\text{BR}_{\text{i.,u.}} < 0.09). \tag{9.10}$$

These results should be compared to the observed (expected) limits on $\text{BR}_{\text{i.,u.}}$ for an integrated luminosity of up to $4.7\,\text{fb}^{-1}$ at $\sqrt{s} = 7\,\text{TeV}$ and $20.3\,\text{fb}^{-1}$ at $\sqrt{s} = 8\,\text{TeV}$, measured as $\text{BR}_{\text{i.,u.}} < 0.27$ ($\text{BR}_{\text{i.,u.}} < 0.37$). An earlier version of that analysis reported $\text{BR}_{\text{i.,u.}} < 0.41$ ($\text{BR}_{\text{i.,u.}} < 0.55$) for an indirect measurement using SM final states only. Including an additional constraint from the search for invisible decays of a Higgs boson produced in association with a Z boson, yielded $\text{BR}_{\text{i.,u.}} < 0.37$ ($\text{BR}_{\text{i.,u.}} < 0.39$).

Following Sec. 1.5.6 and Sec. 7.6, the upper limit on $\text{BR}_{\text{i.,u.}}$ is translated into an upper limit on the coupling of the Higgs boson to a WIMP as a function of its mass, m_χ, and spin, $\chi = S$, V, or f. Figure 9.15 shows for an integrated luminosity of $3000\,\text{fb}^{-1}$ and including all systematic uncertainties the expected indirect 95% CL upper limit on the WIMP-nucleon scattering cross section, $\sigma_{\chi-N}$, assuming that the process is mediated via the exchange of a Higgs boson. The indirect exclusions are presented for scalar (S), Majorana fermion (f), or vector (V) DM candidates, as compared to the model independent searches of direct detection experiments. The results are directly proportional to the expected upper limit on the branching fraction for invisible Higgs boson decays.

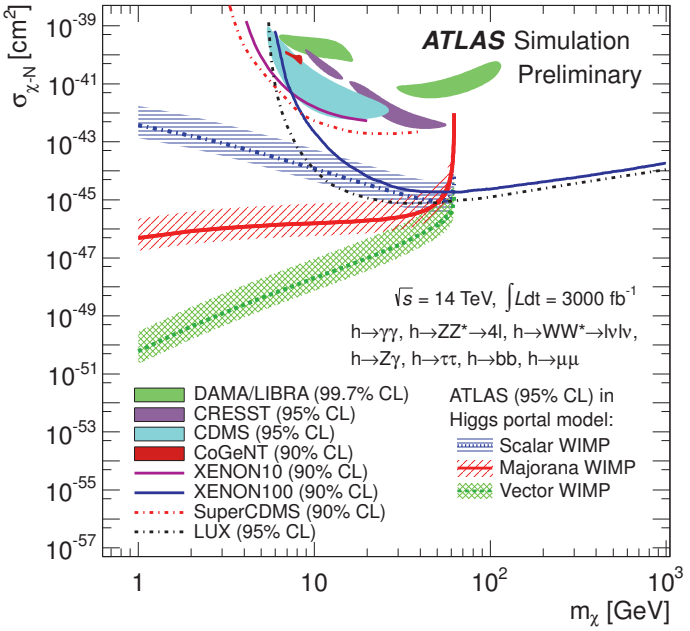

Figure 9.15: Expected upper limit at 95% CL on the WIMP-nucleon scattering cross section, $\sigma_{\chi-N}$, as a function of the mass of the DM particle, m_χ, for a scalar, Majorana fermion, or vector boson DM candidate. The results include all experimental systematic uncertainties and are shown for an integrated luminosity of 3000 fb^{-1} at a collision energy of $\sqrt{s} = 14$ TeV at the HL-LHC. The hashed bands indicate the (theoretical) uncertainty associated with the calculation of the form factor describing the Higgs-nucleon coupling, f_N. The upper limit from ATLAS is indirectly inferred from Higgs boson exchange in a Higgs portal model. The coupling of the Higgs boson to the WIMP is determined indirectly from Higgs coupling measurements. Spin-independent results from direct searches for DM through nuclei recoils from elastic scattering of WIMPs, are shown for comparison [284–290].

Conclusions

C

Since its discovery in 2012, precision measurements of the Higgs boson properties have been performed by the ATLAS and CMS collaborations using the experiments' full LHC Run 1 proton-proton collision data sets. The Higgs boson mass is determined to a great accuracy [21, 22, 221], spin and parity of the Higgs boson are found to be zero and even, respectively [33, 222], and the Higgs boson coupling strengths are constrained by the data to a precision of approximately 10 % to 50 %, depending on the degrees of freedom allowed in the benchmark model [31, 221]. No significant deviations of the Higgs boson properties from the SM predictions are found within the precision of the measurements performed at the LHC in Run 1. Under a wide range of benchmark scenarios, and for a variety of (physics-motivated) assumptions on the Higgs boson total decay width, the data is very compatible with the SM hypothesis. Current results thus support the SM hypothesis and indicate that EWSB and the origin of elementary particle masses are indeed described by the Brout-Englert-Higgs mechanism.

Nevertheless Higgs boson properties are still sensitive probes of new physics that may reveal a scenario more complex than the one envisioned by the original Brout-Englert-Higgs mechanism and which predicts Higgs properties different from the SM. Within the current experimental accuracy, anticipated new physics can be excluded indirectly up to energy scales of several hundred GeV. The results are so far consistent with the outcome of direct searches for so far unobserved new heavy particles, predicted by such BSM theories, and probe new physics on a similar energy scale, using the same data sample. As an increasing new physics energy scale results in smaller predicted deviations of Higgs coupling strengths, future higher precision measurements can probe deviations of Higgs coupling strengths that correspond to new physics energy scales that are not yet in reach of current experiments. Of interest is here that the energy scale of new physics probed by Higgs property studies only depends on the size of the Higgs boson sample and on the control of the systematic uncertainties in these measurements. Thus, the reach of these indirect probes for physics beyond the SM may eventually outperform direct search strategies that depend more strongly on the centre-of-mass energy. If such deviations would be found in future measurements, the pattern of coupling deviations will give guidance on the type of new physics as well as on its energy scale. This information may help the design of future facilities to perform direct searches for new heavy particles that may manifest themselves at high energy scales. Such measurements could become feasible in the intermediate future at facilities like the HL-LHC or the ILC. Independent of what future data will reveal, the Higgs boson is a unique tool to test the SM and many of its extensions to highest precision.

Acronyms

A

2HDM	Two Higgs Doublet Model.
AdS	anti-de Sitter.
APD	avalanche photodiode.
BDT	Boosted Decision Tree.
BNL	Brookhaven National Laboratory.
BPM	Beam Position Monitor.
BR	branching ratio.
BSM	beyond Standard Model.
C/A algorithm	Camebridge/Aachen algorithm.
CDF	Collider Detector at Fermilab.
c.d.f.	cumulative distribution function.
ΛCDM model	Lambda Cold Dark Matter model.
CFT	Conformal Field Theory.
CKF	Combinatorial Kalman filter.
CKM matrix	Cabibbo-Kobayashi-Maskawa matrix.
CL	confidence level.
CLT	central limit theorem.
CMB	cosmic microwave background.
CMLE	conditional maximum likelihood estimator.
CR	control region.
CSC	Cathode Strip Chambers.
CTEQ	Coordinated Theoretical-Experimental Project on QCD.
DC	direct current.
DGLAP equation	Dokshitzer-Gribov-Lipatov-Altarelli-Parisi equation.
DIS	deep inelastic scattering.
DM	Dark Matter.
DPI	double parton interaction.
DS	Dispersion Suppressor.
DT	drift tube.
DY	Drell-Yan.

ECAL	electromangnetic calorimeter.
EM	electromagnetic.
e.o.m.	equations of motion.
EVBA	equivalent vector boson approximation.
EW	electroweak.
EWS	electroweak singlet.
EWSB	electroweak symmetry breaking.
FCal	forward calorimeter.
FCNC	flavor changing neutral current.
Fermilab	Fermi National Accelerator Laboratory.
FPGA	field-programmable gate array.
FSR	final state radiation.
FTK	Fast Tracker.
ggF	gluon fusion.
GIM mechanism	Glashow-Iliopoulos-Maiani mechanism.
GR	General Relativity.
GSF	Gaussian-sum filter.
GSW model	Glashow-Salam-Weinberg model.
HCAL	hadronic calorimeter.
HEC	hadronic end-cap calorimeter.
HEP	High Energy Physics.
HL-LHC	High-Luminosity LHC.
HLT	High-Level Trigger.
HPD	hybrid photodiode.
HQET	heavy quark effective theory.
IBL	Insertable B-layer.
ID	Inner Detector.
ILC	International Linear Collider.
ILD	International Large Detector.
IR	infrared.
ISR	initial state radiation.
JER	jet energy resolution.
JES	jet energy scale.
JVE method	jet-veto-efficiency method.
JVF	jet vertex fraction.

KK	Kaluza-Klein.
KS	Kolmogorov-Smirnov.
LAr	liquid-argon.
LCW	local cell signal weighting.
LEP	Large Electron-Positron Collider.
LH	Little Higgs.
LHC	Large Hadron Collider.
LINAC2	Linear accelerator 2.
LO	leading order.
LS	Long Shutdown.
MC	Monte Carlo.
MCHM	Minimal Composite Higgs Model.
MDT	Monitored Drift Tube.
ME	matrix element.
MET	missing transverse energy.
MLE	maximum likelihood estimator.
MMC	Missing Mass Calculator.
MPI	multiple parton interaction.
MS	muon spectrometer.
MSSM	Minimal Supersymmetric Standard Model.
MVA	multivariate analysis.
N^3LO	next-to-NNLO.
NEWT	New Tracking.
NLL	next-to-leading logarithm.
NLO	next-to-leading order.
NMSSM	Next-to-Minimal Supersymmetric Standard Model.
NN	neural network.
NNLL	next-to-next-to-leading logarithm.
NNLO	next-to-next-to-leading order.
NP	New Physics.
NSW	New Small Wheel.
PDF	parton distribution function.
p.d.f.	probability density function.
PLR	profile likelihood ratio.
pNG	pseudo Nambu-Goldstone.
POI	parameter of interest.
PS	parton shower.

PSB	Proton Synchrotron Booster.
QCD	Quantum Chromodynamics.
QED	Quantum Electrodynamics.
QFT	Quantum Field Theory.
res. NNLO	NNLO matched with resummed next-to-leading logs.
RF	Radio Frequency.
RGE	renormalization group equation.
RMS	root mean square.
RoI	Region-of-Interest.
RPC	Resistive Plate Chamber.
SCT	Semiconductor Tracker.
SiD	Silicon Detector.
SM	Standard Model of Elementary Particle Physics.
SPS	Super Proton Synchrotron.
SR	signal region.
ST method	Stewart-Tackmann method.
STVF	soft term vertex fraction.
SUSY	Supersymmetry.
SV	Secondary Vertex.
TC	technicolor.
TDR	Technical Design Report.
TGC	Thin Gap Chamber.
TRT	Transition Radiation Tracker.
UE	underlying event.
UV	ultraviolet.
VBF	vector boson fusion.
VEV	vacuum expectation value.
VPT	vacuum phototriode.
VR	validation region.
WIMP	weakly interacting massive particle.

Bibliography

B

[1] The LEP Working Group for Higgs boson searches, ALEPH, DELPHI, L3, and OPAL Collaborations, *Search for the Standard Model Higgs boson at LEP*, Phys.Lett. **B565** (2003) pp. 61–75, arXiv: hep-ex/0306033 [hep-ex].

[2] The CDF and DØ Collaborations, *Combined CDF and DØ Upper Limits on Standard Model Higgs-Boson Production with up to 6.7 fb^{-1} of Data* (2010), arXiv: 1007.4587 [hep-ex].

[3] The ALEPH, CDF, DØ, DELPHI, L3, OPAL and SLD Collaborations; LEP and Tevatron Electroweak Working Group; SLD Electroweak and Heavy Flavour Groups, *Precision Electroweak Measurements and Constraints on the Standard Model* (2010), arXiv: 1012.2367 [hep-ex].

[4] The ATLAS Collaboration, *Observation of a new particle in the search for the Standard Model Higgs boson with the ATLAS detector at the LHC*, Phys.Lett. **B716** (2012) pp. 1–29, arXiv: 1207.7214 [hep-ex].

[5] The CMS Collaboration, *Observation of a new boson at a mass of 125 GeV with the CMS experiment at the LHC*, Phys.Lett. **B716** (2012) pp. 30–61, arXiv: 1207.7235 [hep-ex].

[6] The CMS Collaboration, *Observation of a new boson with mass near 125 GeV in pp collisions at $\sqrt{s}$ = 7 and 8 TeV*, JHEP **1306** (2013) p. 081, arXiv: 1303.4571 [hep-ex].

[7] M. E. Peskin and D. V. Schroeder, *An Introduction to Quantum Field Theory*, Westview Press, 1995.

[8] M. Böhm, A. Denner, and H. Joos, *Gauge Theories of the Strong and Electroweak Interaction*, 3rd ed., Stuttgart/Leipzig/Wiesbaden: B. G. Teubner, 2001.

[9] J. F. Donoghue, E. Golowich, and B. R. Holstein, *Dynamics of the Standard Model*, 2nd ed., Cambridge University Press, 1994.

[10] A. Djouadi, *The Anatomy of electro-weak symmetry breaking. I: The Higgs boson in the standard model*, Phys.Rept. **457** (2008) pp. 1–216, arXiv: hep-ph/0503172 [hep-ph].

[11] O. S. Bruning, P. Collier, P. Lebrun, S. Myers, R. Ostojic, et al., *LHC Design Report. 1. The LHC Main Ring* (2004), ed. by O. S. Bruning.

[12] O. Buning, P. Collier, P. Lebrun, S. Myers, R. Ostojic, et al., *LHC Design Report. 2. The LHC infrastructure and general services* (2004), ed. by O. Buning.

[13] M. Benedikt, P. Collier, V. Mertens, J. Poole, and K. Schindl, *LHC Design Report. 3. The LHC injector chain* (2004), ed. by M. Benedikt.

[14] The ATLAS Collaboration, *ATLAS: Technical proposal for a general-purpose p p experiment at the Large Hadron Collider at CERN* (1994).

[15] The CMS Collaboration, *CMS, the Compact Muon Solenoid: Technical proposal* (1994).

[16] L. Evans and P. Bryant, *LHC Machine*, JINST **3** (2008) S08001, ed. by L. Evans.

[17] The ATLAS Collaboration, *The ATLAS Experiment at the CERN Large Hadron Collider*, JINST **3** (2008) S08003.

[18] The CMS Collaboration, *The CMS experiment at the CERN LHC*, JINST **3** (2008) S08004.

[19] The ATLAS Collaboration, *Performance of the ATLAS Inner Detector Track and Vertex Reconstruction in the High Pile-Up LHC Environment*, ATLAS-CONF-2012-042 (2012).

[20] M. Baak, S. Gadatsch, R. Harrington, and W. Verkerke, *Interpolation between multi-dimensional histograms using a new non-linear moment morphing method* (2014), arXiv: 1410.7388 [physics.data-an].

[21] The ATLAS Collaboration, *Measurement of the Higgs boson mass from the $H \to \gamma\gamma$ and $H \to ZZ^* \to 4\ell$ channels with the ATLAS detector using 25 fb^{-1} of pp collision data*, Phys.Rev. **D90**.5 (2014) p. 052004, arXiv: 1406.3827 [hep-ex].

[22] The ATLAS and CMS Collaborations, *Combined Measurement of the Higgs Boson Mass in pp Collisions at $\sqrt{s} = 7$ and 8 TeV with the ATLAS and CMS Experiments* (2015), arXiv: 1503.07589 [hep-ex].

[23] The ATLAS Collaboration, *Measurement of Higgs boson production in the diphoton decay channel in pp collisions at center-of-mass energies of 7 and 8 TeV with the ATLAS detector*, Phys.Rev. **D90**.11 (2014) p. 112015, arXiv: 1408.7084 [hep-ex].

[24] The ATLAS Collaboration, *Measurements of Higgs boson production and couplings in the four-lepton channel in pp collisions at center-of-mass energies of 7 and 8 TeV with the ATLAS detector*, Phys.Rev. **D91**.1 (2015) p. 012006, arXiv: 1408.5191 [hep-ex].

[25] The ATLAS Collaboration, *Evidence for the Higgs-boson Yukawa coupling to tau leptons with the ATLAS detector* (2015), arXiv: 1501.04943 [hep-ex].

[26] The ATLAS Collaboration, *Search for the $b\bar{b}$ decay of the Standard Model Higgs boson in associated $(W/Z)H$ production with the ATLAS detector* (2014), arXiv: 1409.6212 [hep-ex].

[27] The ATLAS Collaboration, *Search for the Standard Model Higgs boson produced in association with top quarks and decaying into $b\bar{b}$ in pp collisions at $\sqrt{s} = 8$ TeV with the ATLAS detector* (2015), arXiv: 1503.05066 [hep-ex].

[28] The ATLAS Collaboration, *Search for the associated production of the Higgs boson with a top quark pair in multi-lepton final states with the ATLAS detector*, ATLAS-CONF-2015-006 (2015).

[29] The ATLAS Collaboration, *Search for charged Higgs bosons decaying via $H^\pm \to \tau^\pm \nu$ in fully hadronic final states using pp collision data at $\sqrt{s} = 8$ TeV with the ATLAS detector*, JHEP **1503** (2015) p. 088, arXiv: 1412.6663 [hep-ex].

[30] The ATLAS Collaboration, *Observation and measurement of Higgs boson decays to WW^* with the ATLAS detector* (2014), arXiv: 1412.2641 [hep-ex].

[31] The ATLAS Collaboration, *Measurements of the Higgs boson production and decay rates and coupling strengths using pp collision data at $\sqrt{s} = 7$ and 8 TeV in the ATLAS experiment*, ATLAS-CONF-2015-007 (2015).

[32] The ATLAS Collaboration, *Evidence for the spin-0 nature of the Higgs boson using ATLAS data*, Phys.Lett. **B726** (2013) pp. 120–144, arXiv: 1307.1432 [hep-ex].

[33] The ATLAS Collaboration, *Study of the spin and parity of the Higgs boson in HVV decays with the ATLAS detector*, ATLAS-CONF-2015-008 (2015).

[34] The ATLAS Collaboration, *Search for squarks and gluinos in events with isolated leptons, jets and missing transverse momentum at $\sqrt{s} = 8$ TeV with the ATLAS detector* (2015), arXiv: 1501.03555 [hep-ex].

[35] The ATLAS Collaboration, *Summary of the inclusive searches for squarks and gluinos with Run I LHC data at ATLAS* (In preparation).

[36] The ATLAS Collaboration, *Updated coupling measurements of the Higgs boson with the ATLAS detector using up to 25 fb^{-1} of proton-proton collision data*, ATLAS-CONF-2014-009 (2014).

[37] The ATLAS Collaboration, *Higgs Boson Coupling Measurements from the Combination of All Decay Channels*, ATL-COM-PHYS-2015-072 (2015).

[38] The ATLAS Collaboration, *Constraints on New Phenomena via Higgs Coupling Measurements with the ATLAS Detector*, ATLAS-CONF-2014-010 (2014).

[39] L. Rossi, O. Brüning, et al., *High Luminosity Large Hadron Collider; A description for the European Strategy Preparatory Group*, CERN-ATS-2012-236 (2012).

[40] The ATLAS Collaboration, *ATLAS Insertable B-Layer Technical Design Report*, CERN-LHCC-2010-013. ATLAS-TDR-19 (2010).

[41] The ATLAS Collaboration, *Letter of Intent for the Phase-I Upgrade of the ATLAS Experiment*, CERN-LHCC-2011-012. LHCC-I-020 (2011).

[42] The ATLAS Collaboration, *ATLAS New Small Wheel Technical Design Report*, CERN-LHCC-2013-006. ATLAS-TDR-020 (2013).

[43] The ATLAS Collaboration, *ATLAS Fast TracKer Technical Design Report*, CERN-LHCC-2013-007. ATLAS-TDR-021 (2013).

[44] The ATLAS Collaboration, *ATLAS Liquid Argon Calorimeter Phase-I Upgrade Technical Design Report*, CERN-LHCC-2013-017. ATLAS-TDR-022 (2013).

[45] The ATLAS Collaboration, *Technical Design Report for the Phase-I Upgrade of the ATLAS TDAQ System*, CERN-LHCC-2013-018. ATLAS-TDR-023 (2013).

[46] The ATLAS Collaboration, *Letter of Intent for the Phase-II Upgrade of the ATLAS Experiment*, CERN-LHCC-2012-022. LHCC-I-023 (2012).

[47] T. Behnke, J. E. Brau, B. Foster, J. Fuster, M. Harrison, et al., *The International Linear Collider Technical Design Report - Volume 1: Executive Summary* (2013), ed. by T. Behnke, arXiv: 1306.6327 [physics.acc-ph].

[48] H. Baer, T. Barklow, K. Fujii, Y. Gao, A. Hoang, et al., *The International Linear Collider Technical Design Report - Volume 2: Physics* (2013), ed. by H. Baer, arXiv: 1306.6352 [hep-ph].

[49] C. Adolphsen, M. Barone, B. Barish, K. Buesser, P. Burrows, et al., *The International Linear Collider Technical Design Report - Volume 3.I: Accelerator & in the Technical Design Phase* (2013), ed. by C. Adolphsen, arXiv: 1306.6353 [physics.acc-ph].

[50] C. Adolphsen, M. Barone, B. Barish, K. Buesser, P. Burrows, et al., *The International Linear Collider Technical Design Report - Volume 3.II: Accelerator Baseline Design* (2013), ed. by C. Adolphsen, arXiv: 1306.6328 [physics.acc-ph].

[51] T. Behnke, J. E. Brau, P. N. Burrows, J. Fuster, M. Peskin, et al., *The International Linear Collider Technical Design Report - Volume 4: Detectors* (2013), ed. by T. Behnke, arXiv: 1306.6329 [physics.ins-det].

[52] The ATLAS Collaboration, *Projections for measurements of Higgs boson signal strengths and coupling parameters with the ATLAS detector at the HL-LHC*, ATL-PHYS-PUB-2014-016 (2014).

[53] D. Asner, T. Barklow, C. Calancha, K. Fujii, N. Graf, et al., *ILC Higgs White Paper* (2013), arXiv: 1310.0763 [hep-ph].

[54] The ATLAS Collaboration, *Prospects for New Physics in Higgs Couplings Studies with the ATLAS Detector at the HL-LHC*, ATL-PHYS-PUB-2014-017 (2014).

[55] C.-N. Yang and R. L. Mills, *Conservation of Isotopic Spin and Isotopic Gauge Invariance*, Phys.Rev. **96** (1954) pp. 191–195.

[56] A. Einstein, *Die Grundlage der allgemeinen Relativitätstheorie*, Annalen der Physik **354**.7 (1916) pp. 769–822.

[57] A. Purcell, *Go on a particle quest at the first CERN webfest. Le premier webfest du CERN se lance à la conquête des particules*, BUL-NA-2012-269. 35/2012 (2012) p. 10.

[58] The Particle Data Group Collaboration, *Review of Particle Physics (RPP)*, Phys.Rev. **D86** (2012) p. 010001.

[59] S. L. Glashow, *Partial Symmetries of Weak Interactions*, Nucl. Phys. **22** (1961) pp. 579–588.

[60] A. Salam, *Weak and Electromagnetic Interactions* (1968), Originally printed in *Svartholm: Elementary Particle Theory, Proceedings Of The Nobel Symposium Held 1968 At Lerum, Sweden*, Stockholm 1968, 367-377.

[61] S. Weinberg, *A Model of Leptons*, Phys. Rev. Lett. **19** (1967) pp. 1264–1266.

[62] H. Fritzsch, M. Gell-Mann, and H. Leutwyler, *Advantages of the Color Octet Gluon Picture*, Phys. Lett. **B47** (1973) pp. 365–368.

[63] S. Weinberg, *Nonabelian Gauge Theories of the Strong Interactions*, Phys. Rev. Lett. **31** (1973) pp. 494–497.

[64] D. J. Gross and F. Wilczek, *Ultraviolet Behavior of Non-Abelian Gauge Theorie*, Phys. Rev. Lett. **30** (1973) pp. 1343–1346.

[65] P. W. Higgs, *Broken Symmetries and the Masses of Gauge Bosons*, Phys. Rev. Lett. **13** (1964) pp. 508–509.

[66] P. W. Higgs, *Broken Symmetries, Massless Particles and Gauge Fields*, Phys. Lett. **12** (1964) pp. 132–133.

[67] P. W. Higgs, *Spontaneous Symmetry Breakdown without Massless Bosons*, Phys. Rev. **145** (1966) pp. 1156–1163.

[68] F. Englert and R. Brout, *Broken Symmetry and the Mass of Gauge Vector Mesons*, Phys. Rev. Lett. **13** (1964) pp. 321–322.

[69] G. S. Guralnik, C. R. Hagen, and T. W. B. Kibble, *Global Conservation Laws and Massless Particles*, Phys. Rev. Lett. **13** (1964) pp. 585–587.

[70] T. W. B. Kibble, *Symmetry breaking in non-Abelian gauge theories*, Phys. Rev. **155** (1967) pp. 1554–1561.

[71] J. Bernstein, *Spontaneous symmetry breaking, gauge theories, the higgs mechanism and all that*, Rev. Mod. Phys. **46** (1974) pp. 7–48.

[72] M. Veltman, *Limit on Mass Differences in the Weinberg Model*, Nucl.Phys. **B123** (1977) p. 89.

[73] P. Sikivie, L. Susskind, M. B. Voloshin, and V. I. Zakharov, *Isospin Breaking in Technicolor Models*, Nucl.Phys. **B173** (1980) p. 189.

[74] M. Veltman, *Second Threshold in Weak Interactions*, Acta Phys.Polon. **B8** (1977) p. 475.

[75] W. J. Marciano, *The Weak Mixing Angle and Grand Unified Gauge Theories*, Phys.Rev. **D20** (1979) p. 274.

[76] A. C. Longhitano, *Heavy Higgs Bosons in the Weinberg-Salam Model*, Phys.Rev. **D22** (1980) p. 1166.

[77] R. Boughezal, J. Tausk, and J. van der Bij, *Three-loop electroweak correction to the Rho parameter in the large Higgs mass limit*, Nucl.Phys. **B713** (2005) pp. 278–290, arXiv: hep-ph/0410216 [hep-ph].

[78] J. van der Bij, K. Chetyrkin, M. Faisst, G. Jikia, and T. Seidensticker, *Three loop leading top mass contributions to the rho parameter*, Phys.Lett. **B498** (2001) pp. 156–162, arXiv: hep-ph/0011373 [hep-ph].

[79] M. Faisst, J. H. Kuhn, T. Seidensticker, and O. Veretin, *Three loop top quark contributions to the rho parameter*, Nucl.Phys. **B665** (2003) pp. 649–662, arXiv: hep-ph/0302275 [hep-ph].

[80] M. Einhorn, D. Jones, and M. Veltman, *Heavy Particles and the rho Parameter in the Standard Model*, Nucl.Phys. **B191** (1981) p. 146.

[81] The CDF Collaboration, *Observation of top quark production in $\bar{p}p$ collisions*, Phys. Rev. Lett. **74** (1995) pp. 2626–2631, arXiv: hep-ex/9503002.

[82] The DØ Collaboration, *Observation of the top quark*, Phys. Rev. Lett. **74** (1995) pp. 2632–2637, arXiv: hep-ex/9503003.

[83] The Super-Kamiokande Collaboration, *Evidence for oscillation of atmospheric neutrinos*, Phys.Rev.Lett. **81** (1998) pp. 1562–1567, arXiv: hep-ex/9807003 [hep-ex].

[84] N. Cabibbo, *Unitary Symmetry and Leptonic Decays*, Phys. Rev. Lett. **10** (1963) pp. 531–533.

[85] M. Kobayashi and T. Maskawa, *CP Violation in the Renormalizable Theory of Weak Interaction*, Prog. Theor. Phys. **49** (1973) pp. 652–657.

[86] S. L. Glashow, J. Iliopoulos, and L. Maiani, *Weak Interactions with Lepton-Hadron Symmetry*, Phys. Rev. **D2** (1970) pp. 1285–1292.

[87] T. Muta, *Foundations of quantum chromodynamics. Second edition*, World Sci. Lect. Notes Phys. **57** (1998) pp. 1–409.

[88] P. Skands, *Introduction to QCD* (2013) pp. 341–420, arXiv: 1207.2389 [hep-ph].

[89] A. Khodjamirian, *Quantum chromodynamics and hadrons: An elementary introduction* (2004), arXiv: hep-ph/0403145.

[90] A. Buckley, J. Butterworth, S. Gieseke, D. Grellscheid, S. Hoche, et al., *General-purpose event generators for LHC physics*, Phys.Rept. **504** (2011) pp. 145–233, arXiv: 1101.2599 [hep-ph].

[91] R. D. Peccei, *The strong CP problem and axions*, Lect. Notes Phys. **741** (2008) pp. 3–17, arXiv: hep-ph/0607268.

[92] R. D. Peccei and H. R. Quinn, *Constraints Imposed by CP Conservation in the Presence of Instantons*, Phys. Rev. **D16** (1977) pp. 1791–1797.

[93] R. D. Peccei and H. R. Quinn, *CP Conservation in the Presence of Instantons*, Phys. Rev. Lett. **38** (1977) pp. 1440–1443.

[94] R. P. Feynman, *The Theory of Positrons*, Phys. Rev. **76** (6 1949) pp. 749–759.

[95] C. G. Bollini and J. J. Giambiagi, *Dimensional Renormalization: The Number of Dimensions as a Regularizing Parameter*, Nuovo Cim. **B12** (1972) pp. 20–25.

[96] C. G. Bollini and J. J. Giambiagi, *Lowest order divergent graphs in nu-dimensional space*, Phys. Lett. **B40** (1972) pp. 566–568.

[97] G. 't Hooft and M. J. G. Veltman, *Regularization and Renormalization of Gauge Fields*, Nucl. Phys. **B44** (1972) pp. 189–213.

[98] J. F. Ashmore, *A Method of Gauge Invariant Regularization*, Lett. Nuovo Cim. **4** (1972) pp. 289–290.

[99] G. M. Cicuta and E. Montaldi, *Analytic renormalization via continuous space dimension*, Nuovo Cim. Lett. **4** (1972) pp. 329–332.

[100] G. 't Hooft, *Dimensional regularization and the renormalization group*, Nucl. Phys. **B61** (1973) pp. 455–468.

[101] W. A. Bardeen, A. J. Buras, D. W. Duke, and T. Muta, *Deep Inelastic Scattering Beyond the Leading Order in Asymptotically Free Gauge Theories*, Phys. Rev. **D18** (1978) p. 3998.

[102] D. J. Gross, *Applications of the Renormalization Group to High-Energy Physics* (), In *Les Houches 1975, Proceedings, Methods In Field Theory*, Amsterdam 1976, 141-250.

[103] K. Symanzik, *Small distance behavior in field theory and power counting*, Commun. Math. Phys. **18** (1970) pp. 227–246.

[104] C. G. Callan Jr., *Broken scale invariance in scalar field theory*, Phys. Rev. **D2** (1970) pp. 1541–1547.

[105] H. D. Politzer, *Reliable Perturbative Results for Strong Interactions?*, Phys.Rev.Lett. **30** (1973) pp. 1346–1349.

[106] J. C. Collins and D. E. Soper, *Parton Distribution and Decay Functions*, Nucl.Phys. **B194** (1982) p. 445.

[107] The NuTeV Collaboration, *Measurement of the Nucleon Strange-Antistrange Asymmetry at Next-to-Leading Order in QCD from NuTeV Dimuon Data*, Phys.Rev.Lett. **99** (2007) p. 192001.

[108] A. Cooper-Sarkar, *What did HERA teach us about the structure of the proton?*, J.Phys. **G39** (2012) p. 093001, arXiv: 1206.0894 [hep-ph].

[109] S. Alekhin, K. Melnikov, and F. Petriello, *Fixed target Drell-Yan data and NNLO QCD fits of parton distribution functions*, Phys.Rev. **D74** (2006) p. 054033, arXiv: hep-ph/0606237 [hep-ph].

[110] S. Alekhin, S. Alioli, R. D. Ball, V. Bertone, J. Blumlein, et al., *The PDF4LHC Working Group Interim Report* (2011), arXiv: 1101.0536 [hep-ph].

[111] G. Altarelli and G. Parisi, *Asymptotic Freedom in Parton Language*, Nucl.Phys. **B126** (1977) p. 298.

[112] V. N. Gribov and L. N. Lipatov, *Deep inelastic e p scattering in perturbation theory*, Sov. J. Nucl. Phys. **15** (1972) pp. 438–450.

[113] Y. L. Dokshitzer, *Calculation of the Structure Functions for Deep Inelastic Scattering and e+ e- Annihilation by Perturbation Theory in Quantum Chromodynamics.*, Sov.Phys.JETP **46** (1977) pp. 641–653.

[114] A. Martin, W. Stirling, R. Thorne, and G. Watt, *Parton distributions for the LHC*, Eur.Phys.J. **C63** (2009) pp. 189–285, arXiv: 0901.0002 [hep-ph].

[115] P. M. Nadolsky, H.-L. Lai, Q.-H. Cao, J. Huston, J. Pumplin, et al., *Implications of CTEQ global analysis for collider observables*, Phys.Rev. **D78** (2008) p. 013004, arXiv: 0802.0007 [hep-ph].

[116] H.-L. Lai, M. Guzzi, J. Huston, Z. Li, P. M. Nadolsky, et al., *New parton distributions for collider physics*, Phys.Rev. **D82** (2010) p. 074024, arXiv: 1007.2241 [hep-ph].

[117] The H1 and ZEUS Collaborations, *Combined Measurement and QCD Analysis of the Inclusive e+-p Scattering Cross Sections at HERA*, JHEP **1001** (2010) p. 109, arXiv: 0911.0884 [hep-ex].

[118] R. D. Ball, L. Del Debbio, S. Forte, A. Guffanti, J. I. Latorre, et al., *A first unbiased global NLO determination of parton distributions and their uncertainties*, Nucl.Phys. **B838** (2010) pp. 136–206, arXiv: 1002.4407 [hep-ph].

[119] R. D. Ball, V. Bertone, S. Carrazza, C. S. Deans, L. Del Debbio, et al., *Parton distributions with LHC data*, Nucl.Phys. **B867** (2013) pp. 244–289, arXiv: 1207.1303 [hep-ph].

[120] M. Botje, J. Butterworth, A. Cooper-Sarkar, A. de Roeck, J. Feltesse, et al., *The PDF4LHC Working Group Interim Recommendations* (2011), arXiv: 1101.0538 [hep-ph].

[121] A. Buckley and M. Whalley, *HepData reloaded: Reinventing the HEP data archive*, PoS **ACAT2010** (2010) p. 067, arXiv: 1006.0517 [hep-ex].

[122] G. F. Sterman and S. Weinberg, *Jets from Quantum Chromodynamics*, Phys.Rev.Lett. **39** (1977) p. 1436.

[123] B. Andersson, G. Gustafson, G. Ingelman, and T. Sjostrand, *Parton Fragmentation and String Dynamics*, Phys.Rept. **97** (1983) pp. 31–145.

[124] B. Webber, *A QCD Model for Jet Fragmentation Including Soft Gluon Interference*, Nucl.Phys. **B238** (1984) p. 492.

[125] J.-C. Winter, F. Krauss, and G. Soff, *A Modified cluster hadronization model*, Eur.Phys.J. **C36** (2004) pp. 381–395, arXiv: hep-ph/0311085 [hep-ph].

[126] G. P. Salam, *Towards Jetography*, Eur.Phys.J. **C67** (2010) pp. 637–686, arXiv: 0906.1833 [hep-ph].

[127] S. Catani, Y. L. Dokshitzer, M. Olsson, G. Turnock, and B. Webber, *New clustering algorithm for multi - jet cross-sections in e+ e- annihilation*, Phys.Lett. **B269** (1991) pp. 432–438.

[128] S. Catani, Y. L. Dokshitzer, M. Seymour, and B. Webber, *Longitudinally invariant K_t clustering algorithms for hadron hadron collisions*, Nucl.Phys. **B406** (1993) pp. 187–224.

[129] S. D. Ellis and D. E. Soper, *Successive combination jet algorithm for hadron collisions*, Phys.Rev. **D48** (1993) pp. 3160–3166, arXiv: hep-ph/9305266 [hep-ph].

[130] M. Cacciari, G. P. Salam, and G. Soyez, *The Anti-k(t) jet clustering algorithm*, JHEP **0804** (2008) p. 063, arXiv: 0802.1189 [hep-ph].

[131] Y. L. Dokshitzer, G. Leder, S. Moretti, and B. Webber, *Better jet clustering algorithms*, JHEP **9708** (1997) p. 001, arXiv: hep-ph/9707323 [hep-ph].

[132] M. Wobisch and T. Wengler, *Hadronization corrections to jet cross-sections in deep inelastic scattering* (1998), arXiv: hep-ph/9907280 [hep-ph].

[133] The TOTEM Collaboration, *Luminosity-Independent Measurement of the Proton-Proton Total Cross Section at $\sqrt{s} = 8$ TeV*, Phys.Rev.Lett. **111**.1 (2013) p. 012001.

[134] T. Sjostrand and M. van Zijl, *A Multiple Interaction Model for the Event Structure in Hadron Collisions*, Phys.Rev. **D36** (1987) p. 2019.

[135] The LHC Higgs Cross Section Working Group Collaboration, *Handbook of LHC Higgs Cross Sections: 3. Higgs Properties* (2013), ed. by S. Heinemeyer, arXiv: 1307.1347 [hep-ph].

[136] H. Georgi, S. Glashow, M. Machacek, and D. V. Nanopoulos, *Higgs Bosons from Two Gluon Annihilation in Proton Proton Collisions*, Phys.Rev.Lett. **40** (1978) p. 692.

[137] D. Jones and S. Petcov, *Heavy Higgs Bosons at LEP*, Phys.Lett. **B84** (1979) p. 440.

[138] R. Cahn and S. Dawson, *Production of Very Massive Higgs Bosons*, Phys.Lett. **B136** (1984) p. 196.

[139] D. A. Dicus and S. S. Willenbrock, *Higgs Bosons From Vector Boson Fusion in e^+e^-, ep and pp Collisions*, Phys.Rev. **D32** (1985) p. 1642.

[140] G. Altarelli, B. Mele, and F. Pitolli, *Heavy Higgs Production at Future Colliders*, Nucl.Phys. **B287** (1987) pp. 205–224.

[141] W. Kilian, M. Kramer, and P. Zerwas, *Higgsstrahlung and W W fusion in e+ e- collisions*, Phys.Lett. **B373** (1996) pp. 135–140, arXiv: hep-ph/9512355 [hep-ph].

[142] S. Glashow, D. V. Nanopoulos, and A. Yildiz, *Associated Production of Higgs Bosons and Z Particles*, Phys.Rev. **D18** (1978) pp. 1724–1727.

[143] E. Eichten, I. Hinchliffe, K. D. Lane, and C. Quigg, *Super Collider Physics*, Rev.Mod.Phys. **56** (1984) pp. 579–707.

[144] R. Raitio and W. W. Wada, *Higgs Boson Production at Large Transverse Momentum in QCD*, Phys.Rev. **D19** (1979) p. 941.

[145] Z. Kunszt, *Associated Production of Heavy Higgs Boson with Top Quarks*, Nucl.Phys. **B247** (1984) p. 339.

[146] J. N. Ng and P. Zakarauskas, *A QCD Parton Calculation of Conjoined Production of Higgs Bosons and Heavy Flavors in $p\bar{p}$ Collision*, Phys.Rev. **D29** (1984) p. 876.

[147] R. M. Barnett, H. E. Haber, and D. E. Soper, *Ultraheavy Particle Production from Heavy Partons at Hadron Colliders*, Nucl.Phys. **B306** (1988) p. 697.

[148] F. I. Olness and W.-K. Tung, *When Is a Heavy Quark Not a Parton? Charged Higgs Production and Heavy Quark Mass Effects in the QCD Based Parton Model*, Nucl.Phys. **B308** (1988) p. 813.

[149] D. A. Dicus and S. Willenbrock, *Higgs Boson Production from Heavy Quark Fusion*, Phys.Rev. **D39** (1989) p. 751.

[150] F. Maltoni, K. Paul, T. Stelzer, and S. Willenbrock, *Associated production of Higgs and single top at hadron colliders*, Phys.Rev. **D64** (2001) p. 094023, arXiv: hep-ph/0106293 [hep-ph].

[151] V. Barger, M. McCaskey, and G. Shaughnessy, *Single top and Higgs associated production at the LHC*, Phys.Rev. **D81** (2010) p. 034020, arXiv: 0911.1556 [hep-ph].

[152] M. Farina, C. Grojean, F. Maltoni, E. Salvioni, and A. Thamm, *Lifting degeneracies in Higgs couplings using single top production in association with a Higgs boson*, JHEP **1305** (2013) p. 022, arXiv: 1211.3736 [hep-ph].

[153] S. Biswas, E. Gabrielli, and B. Mele, *Single top and Higgs associated production as a probe of the Htt coupling sign at the LHC*, JHEP **1301** (2013) p. 088, arXiv: 1211.0499 [hep-ph].

[154] P. Agrawal, S. Mitra, and A. Shivaji, *Effect of Anomalous Couplings on the Associated Production of a Single Top Quark and a Higgs Boson at the LHC*, JHEP **1312** (2013) p. 077, arXiv: 1211.4362 [hep-ph].

[155] D. A. Dicus and C. Kao, *Higgs Boson - Z^0 Production From Gluon Fusion*, Phys.Rev. **D38** (1988) p. 1008.

[156] B. A. Kniehl, *Associated Production of Higgs and Z Bosons From Gluon Fusion in Hadron Collisions*, Phys.Rev. **D42** (1990) pp. 2253–2258.

[157] T. Matsuura, R. Hamberg, and W. van Neerven, *The Contribution of the Gluon-gluon Subprocess to the Drell-Yan K Factor*, Nucl.Phys. **B345** (1990) pp. 331–368.

[158] B. A. Kniehl and C. P. Palisoc, *Associated production of Z and neutral Higgs bosons at the CERN Large Hadron Collider*, Phys.Rev. **D85** (2012) p. 075027, arXiv: 1112.1575 [hep-ph].

[159] C. Englert, M. McCullough, and M. Spannowsky, *Gluon-initiated associated production boosts Higgs physics*, Phys.Rev. **D89**.1 (2014) p. 013013, arXiv: 1310.4828 [hep-ph].

[160] E. N. Glover and J. van der Bij, *Higgs boson pair production via gluon fusion*, Nucl.Phys. **B309** (1988) p. 282.

[161] D. A. Dicus, C. Kao, and S. S. Willenbrock, *Higgs Boson Pair Production From Gluon Fusion*, Phys.Lett. **B203** (1988) p. 457.

[162] T. Plehn, M. Spira, and P. Zerwas, *Pair production of neutral Higgs particles in gluon-gluon collisions*, Nucl.Phys. **B479** (1996) pp. 46–64, arXiv: hep-ph/9603205 [hep-ph].

[163] V. D. Barger, T. Han, and R. Phillips, *Double Higgs Boson Bremsstrahlung From W and Z Bosons at Supercolliders*, Phys.Rev. **D38** (1988) p. 2766.

[164] A. Djouadi, W. Kilian, M. Muhlleitner, and P. Zerwas, *Production of neutral Higgs boson pairs at LHC*, Eur.Phys.J. **C10** (1999) pp. 45–49, arXiv: hep-ph/9904287 [hep-ph].

[165] R. Frederix, E. Re, and P. Torrielli, *Single-top t-channel hadroproduction in the four-flavour scheme with POWHEG and aMC@NLO*, JHEP **1209** (2012) p. 130, arXiv: 1207.5391 [hep-ph].

[166] S. Dawson, *Radiative corrections to Higgs boson production*, Nucl.Phys. **B359** (1991) pp. 283–300.

[167] A. Djouadi, M. Spira, and P. Zerwas, *Production of Higgs bosons in proton colliders: QCD corrections*, Phys.Lett. **B264** (1991) pp. 440–446.

[168] M. Spira, A. Djouadi, D. Graudenz, and P. Zerwas, *Higgs boson production at the LHC*, Nucl.Phys. **B453** (1995) pp. 17–82, arXiv: hep-ph/9504378 [hep-ph].

[169] R. V. Harlander and W. B. Kilgore, *Next-to-next-to-leading order Higgs production at hadron colliders*, Phys.Rev.Lett. **88** (2002) p. 201801, arXiv: hep-ph/0201206 [hep-ph].

[170] C. Anastasiou and K. Melnikov, *Higgs boson production at hadron colliders in NNLO QCD*, Nucl.Phys. **B646** (2002) pp. 220–256, arXiv: hep-ph/0207004 [hep-ph].

[171] V. Ravindran, J. Smith, and W. L. van Neerven, *NNLO corrections to the total cross-section for Higgs boson production in hadron hadron collisions*, Nucl.Phys. **B665** (2003) pp. 325–366, arXiv: hep-ph/0302135 [hep-ph].

[172] E. Eichten and B. R. Hill, *An Effective Field Theory for the Calculation of Matrix Elements Involving Heavy Quarks*, Phys.Lett. **B234** (1990) p. 511.

[173] H. Georgi, *An Effective Field Theory for Heavy Quarks at Low-energies*, Phys.Lett. **B240** (1990) pp. 447–450.

[174] B. Grinstein, *The Static Quark Effective Theory*, Nucl.Phys. **B339** (1990) pp. 253–268.

[175] T. Mannel, W. Roberts, and Z. Ryzak, *A Derivation of the heavy quark effective Lagrangian from QCD*, Nucl.Phys. **B368** (1992) pp. 204–220.

[176] M. Kramer, E. Laenen, and M. Spira, *Soft gluon radiation in Higgs boson production at the LHC*, Nucl.Phys. **B511** (1998) pp. 523–549, arXiv: hep-ph/9611272 [hep-ph].

[177] S. Catani, D. de Florian, M. Grazzini, and P. Nason, *Soft gluon resummation for Higgs boson production at hadron colliders*, JHEP **0307** (2003) p. 028, arXiv: hep-ph/0306211 [hep-ph].

[178] U. Aglietti, R. Bonciani, G. Degrassi, and A. Vicini, *Two loop light fermion contribution to Higgs production and decays*, Phys.Lett. **B595** (2004) pp. 432–441, arXiv: hep-ph/0404071 [hep-ph].

[179] S. Actis, G. Passarino, C. Sturm, and S. Uccirati, *NLO Electroweak Corrections to Higgs Boson Production at Hadron Colliders*, Phys.Lett. **B670** (2008) pp. 12–17, arXiv: 0809.1301 [hep-ph].

[180] C. Anastasiou, R. Boughezal, and F. Petriello, *Mixed QCD-electroweak corrections to Higgs boson production in gluon fusion*, JHEP **0904** (2009) p. 003, arXiv: 0811.3458 [hep-ph].

[181] D. de Florian and M. Grazzini, *Higgs production at the LHC: updated cross sections at* $\sqrt{s} = 8$ *TeV*, Phys.Lett. **B718** (2012) pp. 117–120, arXiv: 1206.4133 [hep-ph].

[182] C. Anastasiou, S. Buehler, F. Herzog, and A. Lazopoulos, *Inclusive Higgs boson cross-section for the LHC at 8 TeV*, JHEP **1204** (2012) p. 004, arXiv: 1202.3638 [hep-ph].

[183] J. Baglio and A. Djouadi, *Higgs production at the lHC*, JHEP **1103** (2011) p. 055, arXiv: 1012.0530 [hep-ph].

[184] D. L. Rainwater, *Intermediate mass Higgs searches in weak boson fusion* (1999), arXiv: hep-ph/9908378 [hep-ph].

[185] S. Dawson, *The Effective W Approximation*, Nucl.Phys. **B249** (1985) pp. 42–60.

[186] G. L. Kane, W. Repko, and W. Rolnick, *The Effective $W^{\pm}$, Z^0 Approximation for High-Energy Collisions*, Phys.Lett. **B148** (1984) pp. 367–372.

[187] J. Lindfors, *Distribution Functions for Heavy Vector Bosons Inside Colliding Particle Beams*, Z.Phys. **C28** (1985) p. 427.

[188] M. Ciccolini, A. Denner, and S. Dittmaier, *Strong and electroweak corrections to the production of Higgs + 2jets via weak interactions at the LHC*, Phys.Rev.Lett. **99** (2007) p. 161803, arXiv: 0707.0381 [hep-ph].

[189] M. Ciccolini, A. Denner, and S. Dittmaier, *Electroweak and QCD corrections to Higgs production via vector-boson fusion at the LHC*, Phys.Rev. **D77** (2008) p. 013002, arXiv: 0710.4749 [hep-ph].

[190] K. Arnold, M. Bahr, G. Bozzi, F. Campanario, C. Englert, et al., *VBFNLO: A Parton level Monte Carlo for processes with electroweak bosons*, Comput.Phys.Commun. **180** (2009) pp. 1661–1670, arXiv: 0811.4559 [hep-ph].

[191] P. Bolzoni, F. Maltoni, S.-O. Moch, and M. Zaro, *Higgs production via vector-boson fusion at NNLO in QCD*, Phys.Rev.Lett. **105** (2010) p. 011801, arXiv: 1003.4451 [hep-ph].

[192] S. Drell and T.-M. Yan, *Massive Lepton Pair Production in Hadron-Hadron Collisions at High-Energies*, Phys.Rev.Lett. **25** (1970) pp. 316–320.

[193] T. Han and S. Willenbrock, *QCD correction to the $pp \to WH$ and ZH total cross-sections*, Phys.Lett. **B273** (1991) pp. 167–172.

[194] O. Brein, A. Djouadi, and R. Harlander, *NNLO QCD corrections to the Higgs-strahlung processes at hadron colliders*, Phys.Lett. **B579** (2004) pp. 149–156, arXiv: hep-ph/0307206 [hep-ph].

[195] G. Altarelli, R. K. Ellis, and G. Martinelli, *Large Perturbative Corrections to the Drell-Yan Process in QCD*, Nucl.Phys. **B157** (1979) p. 461.

[196] J. Kubar-Andre and F. E. Paige, *Gluon Corrections to the Drell-Yan Model*, Phys.Rev. **D19** (1979) p. 221.

[197] M. Ciccolini, S. Dittmaier, and M. Kramer, *Electroweak radiative corrections to associated WH and ZH production at hadron colliders*, Phys.Rev. **D68** (2003) p. 073003, arXiv: hep-ph/0306234 [hep-ph].

[198] W. Beenakker, S. Dittmaier, M. Kramer, B. Plumper, M. Spira, et al., *Higgs radiation off top quarks at the Tevatron and the LHC*, Phys.Rev.Lett. **87** (2001) p. 201805, arXiv: hep-ph/0107081 [hep-ph].

[199] W. Beenakker, S. Dittmaier, M. Kramer, B. Plumper, M. Spira, et al., *NLO QCD corrections to t anti-t H production in hadron collisions*, Nucl.Phys. **B653** (2003) pp. 151–203, arXiv: hep-ph/0211352 [hep-ph].

[200] S. Dawson, L. Orr, L. Reina, and D. Wackeroth, *Associated top quark Higgs boson production at the LHC*, Phys.Rev. **D67** (2003) p. 071503, arXiv: hep-ph/0211438 [hep-ph].

[201] S. Dawson, C. Jackson, L. Orr, L. Reina, and D. Wackeroth, *Associated Higgs production with top quarks at the large hadron collider: NLO QCD corrections*, Phys.Rev. **D68** (2003) p. 034022, arXiv: hep-ph/0305087 [hep-ph].

[202] R. V. Harlander and W. B. Kilgore, *Higgs boson production in bottom quark fusion at next-to-next-to leading order*, Phys.Rev. **D68** (2003) p. 013001, arXiv: hep-ph/0304035 [hep-ph].

[203] S. Dittmaier, 1. Kramer Michael, and M. Spira, *Higgs radiation off bottom quarks at the Tevatron and the CERN LHC*, Phys.Rev. **D70** (2004) p. 074010, arXiv: hep-ph/0309204 [hep-ph].

[204] S. Dawson, C. Jackson, L. Reina, and D. Wackeroth, *Exclusive Higgs boson production with bottom quarks at hadron colliders*, Phys.Rev. **D69** (2004) p. 074027, arXiv: hep-ph/0311067 [hep-ph].

[205] S. Dittmaier, S. Dittmaier, C. Mariotti, G. Passarino, R. Tanaka, et al., *Handbook of LHC Higgs Cross Sections: 2. Differential Distributions* (2012), arXiv: 1201.3084 [hep-ph].

[206] J. Alwall, R. Frederix, S. Frixione, V. Hirschi, F. Maltoni, et al., *The automated computation of tree-level and next-to-leading order differential cross sections, and their matching to parton shower simulations*, JHEP **1407** (2014) p. 079, arXiv: 1405.0301 [hep-ph].

[207] The ATLAS Collaboration, *Summary plots from the ATLAS Standard Model physics group*, 2015, URL: https://atlas.web.cern.ch/Atlas/GROUPS/PHYSICS/CombinedSummaryPlots/SM/.

[208] J. R. Ellis, M. K. Gaillard, and D. V. Nanopoulos, *A Phenomenological Profile of the Higgs Boson*, Nucl.Phys. **B106** (1976) p. 292.

[209] E. Braaten and J. Leveille, *Higgs Boson Decay and the Running Mass*, Phys.Rev. **D22** (1980) p. 715.

[210] N. Sakai, *Perturbative QCD Corrections to the Hadronic Decay Width of the Higgs Boson*, Phys.Rev. **D22** (1980) p. 2220.

[211] T. Inami and T. Kubota, *Renormalization Group Estimate of the Hadronic Decay Width of the Higgs Boson*, Nucl.Phys. **B179** (1981) p. 171.

[212] M. Drees and K.-i. Hikasa, *NOTE ON QCD CORRECTIONS TO HADRONIC HIGGS DECAY*, Phys.Lett. **B240** (1990) p. 455.

[213] K. Chetyrkin, *Correlator of the quark scalar currents and $\Gamma_{tot}(H \to hadrons)$ at $\mathcal{O}(\alpha_s^3)$ in pQCD*, Phys.Lett. **B390** (1997) pp. 309–317, arXiv: hep-ph/9608318 [hep-ph].

[214] T. G. Rizzo, *Decays of Heavy Higgs Bosons*, Phys.Rev. **D22** (1980) p. 722.

[215] W.-Y. Keung and W. J. Marciano, *HIGGS SCALAR DECAYS: $H \to W^{\pm} + X$*, Phys.Rev. **D30** (1984) p. 248.

[216] R. N. Cahn, *The Higgs Boson*, Rept.Prog.Phys. **52** (1989) p. 389.

[217] E. Gross, G. Wolf, and B. A. Kniehl, *Production and decay of the Standard Model Higgs boson LEP-200*, Z.Phys. **C63** (1994) pp. 417–426, arXiv: hep-ph/9404220 [hep-ph].

[218] A. Djouadi, M. Spira, J. van der Bij, and P. Zerwas, *QCD corrections to gamma gamma decays of Higgs particles in the intermediate mass range*, Phys.Lett. **B257** (1991) pp. 187–190.

[219] S. Dawson and R. Kauffman, *QCD corrections to $H \to \gamma\gamma$*, Phys.Rev. **D47** (1993) pp. 1264–1267.

[220] A. Djouadi, M. Spira, and P. Zerwas, *Two photon decay widths of Higgs particles*, Phys.Lett. **B311** (1993) pp. 255–260, arXiv: hep-ph/9305335 [hep-ph].

[221] The CMS Collaboration, *Precise determination of the mass of the Higgs boson and tests of compatibility of its couplings with the standard model predictions using proton collisions at 7 and 8 TeV* (2014), arXiv: 1412.8662 [hep-ex].

[222] The CMS Collaboration, *Constraints on the spin-parity and anomalous HVV couplings of the Higgs boson in proton collisions at 7 and 8 TeV* (2014), arXiv: 1411.3441 [hep-ex].

[223] S. Weinberg, *Implications of Dynamical Symmetry Breaking*, Phys. Rev. **D13** (1976) pp. 974–996.

[224] E. Gildener, *Gauge Symmetry Hierarchies*, Phys. Rev. **D14** (1976) p. 1667.

[225] S. Weinberg, *Implications of Dynamical Symmetry Breaking: An Addendum*, Phys. Rev. **D19** (1979) pp. 1277–1280.

[226] L. Susskind, *Dynamics of Spontaneous Symmetry Breaking in the Weinberg- Salam Theory*, Phys. Rev. **D20** (1979) pp. 2619–2625.

[227] R. Barbieri, *Electroweak theory after the first Large Hadron Collider phase*, Phys.Scripta **T158** (2013) p. 014006, arXiv: 1309.3473 [hep-ph].

[228] The Planck Collaboration, *Planck 2013 results. XVI. Cosmological parameters* (2013), arXiv: 1303.5076 [astro-ph.CO].

[229] Y. Gershtein, M. Luty, M. Narain, L.-T. Wang, D. Whiteson, et al., *Working Group Report: New Particles, Forces, and Dimensions* (2013), arXiv: 1311.0299 [hep-ex].

[230] R. Contino, *The Higgs as a Composite Nambu-Goldstone Boson* (2010), arXiv: 1005.4269 [hep-ph].

[231] K. Agashe, R. Contino, and A. Pomarol, *The Minimal composite Higgs model*, Nucl.Phys. **B719** (2005) pp. 165–187, arXiv: hep-ph/0412089 [hep-ph].

[232] R. Contino, L. Da Rold, and A. Pomarol, *Light custodians in natural composite Higgs models*, Phys.Rev. **D75** (2007) p. 055014, arXiv: hep-ph/0612048 [hep-ph].

[233] M. S. Carena, E. Ponton, J. Santiago, and C. Wagner, *Electroweak constraints on warped models with custodial symmetry*, Phys.Rev. **D76** (2007) p. 035006, arXiv: hep-ph/0701055 [hep-ph].

[234] M. Schmaltz and D. Tucker-Smith, *Little Higgs review*, Ann.Rev.Nucl.Part.Sci. **55** (2005) pp. 229–270, arXiv: hep-ph/0502182 [hep-ph].

[235] N. Arkani-Hamed, S. Dimopoulos, and G. Dvali, *The Hierarchy problem and new dimensions at a millimeter*, Phys.Lett. **B429** (1998) pp. 263–272, arXiv: hep-ph/9803315 [hep-ph].

[236] C. T. Hill and E. H. Simmons, *Strong dynamics and electroweak symmetry breaking*, Phys.Rept. **381** (2003) pp. 235–402, arXiv: hep-ph/0203079 [hep-ph].

[237] L. Randall and R. Sundrum, *A Large mass hierarchy from a small extra dimension*, Phys.Rev.Lett. **83** (1999) pp. 3370–3373, arXiv: hep-ph/9905221 [hep-ph].

[238] M. Gell-Mann and M. Levy, *The axial vector current in beta decay*, Nuovo Cim. **16** (1960) p. 705.

[239] A. Hill and J. van der Bij, *Strongly interacting singlet - doublet Higgs model*, Phys.Rev. **D36** (1987) pp. 3463–3473.

[240] M. Veltman and F. Yndurain, *Radiative corrections to WW scattering*, Nucl.Phys. **B325** (1989) p. 1.

[241] T. Binoth and J. van der Bij, *Influence of strongly coupled, hidden scalars on Higgs signals*, Z.Phys. **C75** (1997) pp. 17–25, arXiv: hep-ph/9608245 [hep-ph].

[242] R. Schabinger and J. D. Wells, *A Minimal spontaneously broken hidden sector and its impact on Higgs boson physics at the large hadron collider*, Phys.Rev. **D72** (2005) p. 093007, arXiv: hep-ph/0509209 [hep-ph].

[243] B. Patt and F. Wilczek, *Higgs-field portal into hidden sectors* (2006), arXiv: hep-ph/0605188 [hep-ph].

[244] T. Lee, *A Theory of Spontaneous T Violation*, Phys.Rev. **D8** (1973) pp. 1226–1239.

[245] J. F. Gunion and H. E. Haber, *The CP conserving two Higgs doublet model: The Approach to the decoupling limit*, Phys.Rev. **D67** (2003) p. 075019, arXiv: hep-ph/0207010 [hep-ph].

[246] G. Branco, P. Ferreira, L. Lavoura, M. Rebelo, M. Sher, et al., *Theory and phenomenology of two-Higgs-doublet models*, Phys.Rept. **516** (2012) pp. 1–102, arXiv: 1106.0034 [hep-ph].

[247] S. L. Glashow and S. Weinberg, *Natural Conservation Laws for Neutral Currents*, Phys.Rev. **D15** (1977) p. 1958.

[248] E. Paschos, *Diagonal Neutral Currents*, Phys.Rev. **D15** (1977) p. 1966.

[249] H. Miyazawa, *Baryon Number Changing Currents*, Prog. Theor. Phys. **36 (6)** (1966) pp. 1266–1276.

[250] P. Ramond, *Dual Theory for Free Fermions*, Phys. Rev. **D3** (1971) pp. 2415–2418.

[251] Y. A. Gol'fand and E. P. Likhtman, *Extension of the Algebra of Poincare Group Generators and Violation of p Invariance*, JETP Lett. **13** (1971) pp. 323–326, [Pisma Zh.Eksp.Teor.Fiz.13:452-455,1971].

[252] A. Neveu and J. H. Schwarz, *Factorizable dual model of pions*, Nucl. Phys. **B31** (1971) pp. 86–112.

[253] A. Neveu and J. H. Schwarz, *Quark Model of Dual Pions*, Phys. Rev. **D4** (1971) pp. 1109–1111.

[254] J. Gervais and B. Sakita, *Field theory interpretation of supergauges in dual models*, Nucl. Phys. **B34** (1971) pp. 632–639.

[255] D. V. Volkov and V. P. Akulov, *Is the Neutrino a Goldstone Particle?*, Phys. Lett. **B46** (1973) pp. 109–110.

[256] J. Wess and B. Zumino, *A Lagrangian Model Invariant Under Supergauge Transformations*, Phys. Lett. **B49** (1974) p. 52.

[257] J. Wess and B. Zumino, *Supergauge Transformations in Four-Dimensions*, Nucl. Phys. **B70** (1974) pp. 39–50.

[258] S. Dimopoulos and H. Georgi, *Softly Broken Supersymmetry and SU(5)*, Nucl. Phys. **B193** (1981) p. 150.

[259] E. Witten, *Dynamical Breaking of Supersymmetry*, Nucl. Phys. **B188** (1981) p. 513.

[260] M. Dine, W. Fischler, and M. Srednicki, *Supersymmetric Technicolor*, Nucl. Phys. **B189** (1981) pp. 575–593.

[261] S. Dimopoulos and S. Raby, *Supercolor*, Nucl. Phys. **B192** (1981) p. 353.

[262] N. Sakai, *Naturalness in Supersymmetric Guts*, Zeit. Phys. **C11** (1981) p. 153.

[263] R. Kaul and P. Majumdar, *Cancellation of Quadratically Divergent Mass Corrections in Globally Supersymmetric Spontaneously Broken Gauge Theories*, Nucl. Phys. **B199** (1982) p. 36.

[264] H. Goldberg, *Constraint on the photino mass from cosmology*, Phys. Rev. Lett. **50** (1983) p. 1419.

[265] J. Ellis, J. Hagelin, D. Nanopoulos, K. Olive, and M. Srednicki, *Supersymmetric relics from the big bang*, Nucl. Phys. **B238** (1984) pp. 453–476.

[266] P. Fayet, *Supersymmetry and Weak, Electromagnetic and Strong Interactions*, Phys. Lett. **B64** (1976) p. 159.

[267] P. Fayet, *Spontaneously Broken Supersymmetric Theories of Weak, Electromagnetic and Strong Interactions*, Phys. Lett. **B69** (1977) p. 489.

[268] G. R. Farrar and P. Fayet, *Phenomenology of the Production, Decay, and Detection of New Hadronic States Associated with Supersymmetry*, Phys. Lett. **B76** (1978) pp. 575–579.

[269] P. Fayet, *Relations Between the Masses of the Superpartners of Leptons and Quarks, the Goldstino Couplings and the Neutral Currents*, Phys. Lett. **B84** (1979) p. 416.

[270] A. Djouadi, *The Anatomy of electro-weak symmetry breaking. II. The Higgs bosons in the minimal supersymmetric model*, Phys.Rept. **459** (2008) pp. 1–241, arXiv: hep-ph/0503173 [hep-ph].

[271] L. Maiani, A. Polosa, and V. Riquer, *Bounds to the Higgs Sector Masses in Minimal Supersymmetry from LHC Data*, Phys.Lett. **B724** (2013) pp. 274–277, arXiv: 1305.2172 [hep-ph].

[272] A. Djouadi, L. Maiani, G. Moreau, A. Polosa, J. Quevillon, et al., *The post-Higgs MSSM scenario: Habemus MSSM?*, Eur.Phys.J. **C73** (2013) p. 2650, arXiv: 1307.5205 [hep-ph].

[273] M. S. Carena, M. Quiros, and C. Wagner, *Effective potential methods and the Higgs mass spectrum in the MSSM*, Nucl.Phys. **B461** (1996) pp. 407–436, arXiv: hep-ph/9508343 [hep-ph].

[274] A. Djouadi, *Squark effects on Higgs boson production and decay at the LHC*, Phys.Lett. **B435** (1998) pp. 101–108, arXiv: hep-ph/9806315 [hep-ph].

[275] A. Arvanitaki and G. Villadoro, *A Non Standard Model Higgs at the LHC as a Sign of Naturalness*, JHEP **1202** (2012) p. 144, arXiv: 1112.4835 [hep-ph].

[276] A. Delgado, G. F. Giudice, G. Isidori, M. Pierini, and A. Strumia, *The light stop window*, Eur.Phys.J. **C73** (2013) p. 2370, arXiv: 1212.6847 [hep-ph].

[277] M. Carena, S. Heinemeyer, O. Stal, C. Wagner, and G. Weiglein, *MSSM Higgs Boson Searches at the LHC: Benchmark Scenarios after the Discovery of a Higgs-like Particle*, Eur. Phys. J. **C73** (2013) p. 2552, arXiv: 1302.7033 [hep-ph].

[278] S. Kanemura, S. Matsumoto, T. Nabeshima, and N. Okada, *Can WIMP Dark Matter overcome the Nightmare Scenario?*, Phys.Rev. **D82** (2010) p. 055026, arXiv: 1005.5651 [hep-ph].

[279] P. J. Fox, R. Harnik, J. Kopp, and Y. Tsai, *Missing Energy Signatures of Dark Matter at the LHC*, Phys.Rev. **D85** (2012) p. 056011, arXiv: 1109.4398 [hep-ph].

[280] A. Djouadi, O. Lebedev, Y. Mambrini, and J. Quevillon, *Implications of LHC searches for Higgs–portal dark matter*, Phys.Lett. **B709** (2012) pp. 65–69, arXiv: 1112.3299 [hep-ph].

[281] L. Lopez-Honorez, T. Schwetz, and J. Zupan, *Higgs portal, fermionic dark matter, and a Standard Model like Higgs at 125 GeV*, Phys.Lett. **B716** (2012) pp. 179–185, arXiv: 1203.2064 [hep-ph].

[282] C. Englert, T. Plehn, D. Zerwas, and P. M. Zerwas, *Exploring the Higgs portal*, Phys.Lett. **B703** (2011) pp. 298–305, arXiv: 1106.3097 [hep-ph].

[283] R. E. Shrock and M. Suzuki, *Invisible Decays of Higgs Bosons*, Phys.Lett. **B110** (1982) p. 250.

[284] The XENON10 Collaboration, *A search for light dark matter in XENON10 data*, Phys.Rev.Lett. **107** (2011) p. 051301, arXiv: 1104.3088 [astro-ph.CO].

[285] The XENON100 Collaboration, *Dark Matter Results from 225 Live Days of XENON100 Data*, Phys.Rev.Lett. **109** (2012) p. 181301, arXiv: 1207.5988 [astro-ph.CO].

[286] P. Belli, R. Bernabei, A. Bottino, F. Cappella, R. Cerulli, et al., *Observations of annual modulation in direct detection of relic particles and light neutralinos*, Phys.Rev. **D84** (2011) p. 055014, arXiv: 1106.4667 [hep-ph].

[287] G. Angloher, M. Bauer, I. Bavykina, A. Bento, C. Bucci, et al., *Results from 730 kg days of the CRESST-II Dark Matter Search*, Eur.Phys.J. **C72** (2012) p. 1971, arXiv: 1109.0702 [astro-ph.CO].

[288] The CDMS Collaboration, *Silicon Detector Dark Matter Results from the Final Exposure of CDMS II*, Phys.Rev.Lett. **111** (2013) p. 251301, arXiv: 1304.4279 [hep-ex].

[289] C. Aalseth, P. Barbeau, J. Colaresi, J. Collar, J. Diaz Leon, et al., *Search for an Annual Modulation in a P-type Point Contact Germanium Dark Matter Detector*, Phys.Rev.Lett. **107** (2011) p. 141301, arXiv: 1106.0650 [astro-ph.CO].

[290] The LUX Collaboration, *First results from the LUX dark matter experiment at the Sanford Underground Research Facility*, Phys.Rev.Lett. **112** (2014) p. 091303, arXiv: 1310.8214 [astro-ph.CO].

[291] R. Young and A. Thomas, *Octet baryon masses and sigma terms from an SU(3) chiral extrapolation*, Phys.Rev. **D81** (2010) p. 014503, arXiv: 0901.3310 [hep-lat].

[292] The MILC Collaboration, *The Strange quark condensate in the nucleon in 2+1 flavor QCD*, Phys.Rev.Lett. **103** (2009) p. 122002, arXiv: 0905.2432 [hep-lat].

[293] T. Appelquist and J. Carazzone, *Infrared Singularities and Massive Fields*, Phys.Rev. **D11** (1975) p. 2856.

[294] S. Weinberg, *Effective Gauge Theories*, Phys.Lett. **B91** (1980) p. 51.

[295] J. Polchinski, *Renormalization and Effective Lagrangians*, Nucl.Phys. **B231** (1984) pp. 269–295.

[296] H. Georgi, *Effective field theory*, Ann.Rev.Nucl.Part.Sci. **43** (1993) pp. 209–252.

[297] A. V. Manohar, *Effective field theories*, Lect.Notes Phys. **479** (1997) pp. 311–362, arXiv: hep-ph/9606222 [hep-ph].

[298] G. Buchalla, A. J. Buras, and M. E. Lautenbacher, *Weak decays beyond leading logarithms*, Rev.Mod.Phys. **68** (1996) pp. 1125–1144, arXiv: hep-ph/9512380 [hep-ph].

[299] M. Neubert, *Heavy quark symmetry*, Phys.Rept. **245** (1994) pp. 259–396, arXiv: hep-ph/9306320 [hep-ph].

[300] T. Mannel, *Effective Field Theories in Flavor Physics*, Springer Tracts Mod.Phys. **203** (2004) pp. 1–175.

[301] W. Buchmuller and D. Wyler, *Effective Lagrangian Analysis of New Interactions and Flavor Conservation*, Nucl.Phys. **B268** (1986) pp. 621–653.

[302] B. Grzadkowski, M. Iskrzynski, M. Misiak, and J. Rosiek, *Dimension-Six Terms in the Standard Model Lagrangian*, JHEP **1010** (2010) p. 085, arXiv: 1008.4884 [hep-ph].

[303] G. Giudice, C. Grojean, A. Pomarol, and R. Rattazzi, *The Strongly-Interacting Light Higgs*, JHEP **0706** (2007) p. 045, arXiv: hep-ph/0703164 [hep-ph].

[304] R. Contino, M. Ghezzi, C. Grojean, M. Muhlleitner, and M. Spira, *Effective Lagrangian for a light Higgs-like scalar*, JHEP **1307** (2013) p. 035, arXiv: 1303.3876 [hep-ph].

[305] *ATLAS: letter of intent for a general-purpose pp experiment at the large hadron collider at CERN*, CERN-LHCC-92-004 ().

[306] The CMS Collaboration, "Letter of intent: by the CMS Collaboration for a general purpose detector at LHC", tech. rep. CERN-LHCC-92-003. LHCC-I-1, Open presentation to the LHCC 5 November 1992, M. Della Negra/CERN, CMS Spokesman: CERN, 1992.

[307] The ALICE Collaboration, *The ALICE experiment at the CERN LHC*, JINST **3** (2008) S08002.

[308] The LHCb Collaboration, *The LHCb Detector at the LHC*, JINST **3** (2008) S08005.

[309] The LHCf Collaboration, *The LHCf detector at the CERN Large Hadron Collider*, JINST **3** (2008) S08006.

[310] The MoEDAL Collaboration, *Technical Design Report of the MoEDAL Experiment* (2009).

[311] The TOTEM Collaboration, *The TOTEM experiment at the CERN Large Hadron Collider*, JINST **3** (2008) S08007.

[312] J. Haffner, *The CERN accelerator complex. Complexe des accélérateurs du CERN* (2013), General Photo.

[313] S. Myers and E. Picasso, *The Design, construction and commissioning of the CERN Large Electron Positron collider*, Contemp.Phys. **31** (1990) pp. 387–403.

[314] D. Brandt, H. Burkhardt, M. Lamont, S. Myers, and J. Wenninger, *Accelerator physics at LEP*, Rept.Prog.Phys. **63** (2000) pp. 939–1000.

[315] T. Sjostrand, S. Mrenna, and P. Z. Skands, *PYTHIA 6.4 Physics and Manual*, JHEP **0605** (2006) p. 026, arXiv: `hep-ph/0603175 [hep-ph]`.

[316] The ATLAS Collaboration, *Improved luminosity determination in pp collisions at $\sqrt{s} = 7$ TeV using the ATLAS detector at the LHC*, Eur.Phys.J. **C73** (2013) p. 2518, arXiv: `1302.4393 [hep-ex]`.

[317] The TOTEM Collaboration, *Luminosity-independent measurements of total, elastic and inelastic cross-sections at $\sqrt{s} = 7$ TeV*, Europhys.Lett. **101** (2013) p. 21004.

[318] The ATLAS Collaboration, *Measurement of the Inelastic Proton-Proton Cross-Section at $\sqrt{s} = 7$ TeV with the ATLAS Detector*, Nature Commun. **2** (2011) p. 463, arXiv: `1104.0326 [hep-ex]`.

[319] The CMS Collaboration, "Absolute Calibration of the Luminosity Measurement at CMS: Winter 2012 Update", tech. rep. CMS-PAS-SMP-12-008, CERN, 2012.

[320] The CMS Collaboration, "CMS Luminosity Based on Pixel Cluster Counting - Summer 2013 Update", tech. rep. CMS-PAS-LUM-13-001, CERN, 2013.

[321] The ATLAS Collaboration, *ATLAS Data Summary*, 2014, URL: `https://atlas.web.cern.ch/Atlas/GROUPS/DATAPREPARATION/DataSummary`.

[322] C. Grupen and B. Schwartz, *Particle detectors*, 2008.

[323] J. Pequenao and P. Schaffner, *An computer generated image representing how ATLAS detects particles*, 2013, URL: `https://cds.cern.ch/record/1505342`.

[324] The ATLAS Collaboration, *Performance of the ATLAS muon trigger in pp collisions at $\sqrt{s} = 8$ TeV*, Eur.Phys.J. **C75**.3 (2015) p. 120, arXiv: `1408.3179 [hep-ex]`.

[325] H. Dekker, H. d. Graaf, H. Groenstege, F. Linde, S. Sman, et al., *The RASNIK/CCD 3-Dimensional Alignment System*, eConf **C930928** (1993) p. 017.

[326] H. van der Graaf, H. Groenstege, F. Linde, and P. Rewiersma, "RasNiK, an Alignment System for the ATLAS MDT Barrel Muon Chambers: Technical System Description; Revised Version 2.0", tech. rep., NIKHEF, 2000.

[327] The ATLAS Collaboration, *Trigger Operation Public Results*, URL: `https://twiki.cern.ch/twiki/bin/view/AtlasPublic/TriggerOperationPublicResults`.

[328] The CMS Collaboration, *CMS detector design*, 2014, URL: http://cms.web.cern.ch/news/cms-detector-design.

[329] The CMS Collaboration, *Particle-Flow Event Reconstruction in CMS and Performance for Jets, Taus, and MET*, CMS-PAS-PFT-09-001 (2009).

[330] The CMS Collaboration, *Commissioning of the Particle-flow Event Reconstruction with the first LHC collisions recorded in the CMS detector*, CMS-PAS-PFT-10-001 (2010).

[331] The ATLAS Collaboration, *ATLAS Inner Detector: Technical design report. Vol. 1* (1997).

[332] P. F. Åkesson, T. Atkinson, M. J. Costa, M. Elsing, S. Fleischmann, A. N. Gaponenko, W. Liebig, E. Moyse, A. Salzburger, and M. Siebel, *ATLAS Tracking Event Data Model*, ATL-SOFT-PUB-2006-004 (2006).

[333] T. Cornelissen, M. Elsing, S. Fleischmann, W. Liebig, E. Moyse, and A. Salzburger, *Concepts, Design and Implementation of the ATLAS New Tracking (NEWT)*, ATL-SOFT-PUB-2007-007 (2007).

[334] R. E. Kalman, *A New Approach to Linear Filtering and Prediction Problems*, Transactions of the ASME–Journal of Basic Engineering **82**.Series D (1960) pp. 35–45.

[335] R. Fruhwirth, *Application of Kalman filtering to track and vertex fitting*, Nucl.Instrum.Meth. **A262** (1987) pp. 444–450.

[336] D. Wicke, *A New algorithm for solving tracking ambiguities* (1998).

[337] The ATLAS Collaboration, *A neural network clustering algorithm for the ATLAS silicon pixel detector* (2014), arXiv: 1406.7690 [hep-ex].

[338] R. O. Duda and P. E. Hart, *Use of the Hough Transformation to Detect Lines and Curves in Pictures*, Commun. ACM **15**.1 (1972) pp. 11–15.

[339] The ATLAS Collaboration, *Charged-particle multiplicities in pp interactions measured with the ATLAS detector at the LHC*, New J.Phys. **13** (2011) p. 053033, arXiv: 1012.5104 [hep-ex].

[340] A. Salzburger, personal communication, 2011.

[341] T. Sjostrand, S. Mrenna, and P. Z. Skands, *A Brief Introduction to PYTHIA 8.1*, Comput.Phys.Commun. **178** (2008) pp. 852–867, arXiv: 0710.3820 [hep-ph].

[342] The ATLAS Collaboration, *Further ATLAS tunes of PYTHIA6 and Pythia 8*, ATL-PHYS-PUB-2011-014 (2011).

[343] The ATLAS Collaboration, *Alignment of the ATLAS Inner Detector and its Performance in 2012*, ATLAS-CONF-2014-047 (2014).

[344] The ATLAS Collaboration, *Performance of primary vertex reconstruction in proton-proton collisions at $\sqrt{s}$ =7 TeV in the ATLAS experiment*, ATLAS-CONF-2010-069 (2010).

[345] R. Fruhwirth, W. Waltenberger, and P. Vanlaer, *Adaptive vertex fitting*, J.Phys. **G34** (2007) N343.

[346] K. Rose, *Deterministic annealing for clustering, compression, classification, regression, and related optimization problems*, Proceedings of the IEEE **86**.11 (1998) pp. 2210–2239.

[347] The ATLAS Collaboration, *Vertex reconstruction plots*, 2012, URL: http://atlas.web.cern.ch/Atlas/GROUPS/PHYSICS/IDTRACKING/PublicPlots/ATL-COM-PHYS-2012-474/.

[348] H. Gray, personal communication, 2011.

[349] The ATLAS Collaboration, *Calibration of b-tagging using dileptonic top pair events in a combinatorial likelihood approach with the ATLAS experiment*, ATLAS-CONF-2014-004 (2014).

[350] The ATLAS Collaboration, *Calibration of the performance of b-tagging for c and light-flavour jets in the 2012 ATLAS data*, ATLAS-CONF-2014-046 (2014).

[351] The ATLAS Collaboration, *Commissioning of the ATLAS high-performance b-tagging algorithms in the 7 TeV collision data*, ATLAS-CONF-2011-102 (2011).

[352] The ATLAS Collaboration, *Measurement of the muon reconstruction performance of the ATLAS detector using 2011 and 2012 LHC proton-proton collision data* (2014), arXiv: 1407.3935 [hep-ex].

[353] S. Hassani, L. Chevalier, E. Lancon, J. Laporte, R. Nicolaidou, et al., *A muon identification and combined reconstruction procedure for the ATLAS detector at the LHC using the (MUONBOY, STACO, MuTag) reconstruction packages*, Nucl.Instrum.Meth. **A572** (2007) pp. 77–79.

[354] T. Lagouri, D. Adams, K. Assamagan, M. Biglietti, G. Carlino, et al., *A Muon Identification and Combined Reconstruction Procedure for the ATLAS Detector at the LHC at CERN*, IEEE Trans.Nucl.Sci. **51** (2004) pp. 3030–3033.

[355] The ATLAS Collaboration, *Electron reconstruction and identification efficiency measurements with the ATLAS detector using the 2011 LHC proton-proton collision data*, Eur.Phys.J. **C74** (2014) p. 2941, arXiv: 1404.2240 [hep-ex].

[356] The ATLAS Collaboration, *Electron efficiency measurements with the ATLAS detector using the 2012 LHC proton-proton collision data*, ATLAS-CONF-2014-032 (2014).

[357] The ATLAS Collaboration, *Electron and photon energy calibration with the ATLAS detector using LHC Run 1 data* (2014), arXiv: 1407.5063 [hep-ex].

[358] The ATLAS Collaboration, *Calorimeter Clustering Algorithms: Description and Performance*, ATL-LARG-PUB-2008-002 (2008).

[359] The ATLAS Collaboration, *Improved electron reconstruction in ATLAS using the Gaussian Sum Filter-based model for bremsstrahlung*, ATLAS-CONF-2012-047 (2012).

[360] The ATLAS Collaboration, *Expected photon performance in the ATLAS experiment*, ATL-PHYS-PUB-2011-007 (2011).

[361] The ATLAS Collaboration, *Measurements of the photon identification efficiency with the ATLAS detector using 4.9 fb-1 of pp collision data collected in 2011*, ATLAS-CONF-2012-123 (2012).

[362] The ATLAS Collaboration, *Jet energy measurement with the ATLAS detector in proton-proton collisions at* $\sqrt{s} = 7$ *TeV*, Eur.Phys.J. **C73** (2013) p. 2304, arXiv: 1112.6426 [hep-ex].

[363] The ATLAS Collaboration, *Jet energy measurement and its systematic uncertainty in proton-proton collisions at* $\sqrt{s} = 7$ *TeV with the ATLAS detector* (2014), arXiv: 1406.0076 [hep-ex].

[364] The ATLAS Liquid Argon EMEC/HEC Collaboration, *Hadronic calibration of the ATLAS liquid argon end-cap calorimeter in the pseudorapidity region* $1.6 < |\eta| < 1.8$ *in beam tests*, Nucl.Instrum.Meth. **A531** (2004) pp. 481–514, arXiv: physics/0407009 [physics].

[365] W. Lampl, S. Laplace, D. Lelas, P. Loch, H. Ma, et al., *Calorimeter clustering algorithms: Description and performance*, ATL-LARG-PUB-2008-002, ATL-COM-LARG-2008-003 (2008).

[366] The ATLAS Collaboration, *Approved 2012 jet energy scal uncertainty*, URL: https://twiki.cern.ch/twiki/bin/view/AtlasPublic/JetEtmissApproved2013JESUncertainty.

[367] M. Cacciari and G. P. Salam, *Dispelling the* N^3 *myth for the* k_t *jet-finder*, Phys.Lett. **B641** (2006) pp. 57–61, arXiv: hep-ph/0512210 [hep-ph].

[368] M. Cacciari, G. P. Salam, and G. Soyez, *FastJet User Manual*, Eur.Phys.J. **C72** (2012) p. 1896, arXiv: 1111.6097 [hep-ph].

[369] The ATLAS Collaboration, *Pile-up subtraction and suppression for jets in ATLAS*, ATLAS-CONF-2013-083 (2013).

[370] The ATLAS Collaboration, *Identification of the Hadronic Decays of Tau Leptons in 2012 Data with the ATLAS Detector*, ATLAS-CONF-2013-064 (2013).

[371] The ATLAS Collaboration, *Determination of the tau energy scale and the associated systematic uncertainty in proton-proton collisions at $\sqrt{s} = 8$ TeV with the ATLAS detector at the LHC in 2012*, ATLAS-CONF-2013-044 (2013).

[372] The Super-Kamiokande Collaboration, *The Super-Kamiokande detector*, Nucl.Instrum.Meth. **A501** (2003) pp. 418–462.

[373] The ANTARES Collaboration, *ANTARES: the first undersea neutrino telescope*, Nucl.Instrum.Meth. **A656** (2011) pp. 11–38, arXiv: 1104.1607 [astro-ph.IM].

[374] The KM3NeT Consortium, *Technical Design Report for a Deep-Sea Research Infrastructure in the Mediterranean Sea Incorporating a Very Large Volume Neutrino Telescope* (2011).

[375] The IceCube Collaboration, *First Year Performance of The IceCube Neutrino Telescope*, Astropart.Phys. **26** (2006) pp. 155–173, arXiv: astro-ph/0604450 [astro-ph].

[376] J. Sander, Z. Ahmed, A. Anderson, S. Arrenberg, D. Balakishiyeva, et al., *SuperCDMS status from Soudan and plans for SNOLab*, AIP Conf.Proc. **1534** (2012) pp. 129–135.

[377] The XENON Collaboration, *Design and Performance of the XENON10 Dark Matter Experiment*, Astropart.Phys. **34** (2011) pp. 679–698, arXiv: 1001.2834 [astro-ph.IM].

[378] The XENON100 Collaboration, *The XENON100 Dark Matter Experiment*, Astropart.Phys. **35** (2012) pp. 573–590, arXiv: 1107.2155 [astro-ph.IM].

[379] The XENON1T collaboration Collaboration, *The XENON1T Dark Matter Search Experiment*, Springer Proc.Phys. **C12-02-22** (2013) pp. 93–96, arXiv: 1206.6288 [astro-ph.IM].

[380] The LUX Collaboration, *The Large Underground Xenon (LUX) Experiment*, Nucl.Instrum.Meth. **A704** (2013) pp. 111–126, arXiv: 1211.3788 [physics.ins-det].

[381] The ATLAS Collaboration, *Performance of Missing Transverse Momentum Reconstruction in Proton-Proton Collisions at 7 TeV with ATLAS*, Eur.Phys.J. **C72** (2012) p. 1844, arXiv: 1108.5602 [hep-ex].

[382] The ATLAS Collaboration, *Performance of Missing Transverse Momentum Reconstruction in ATLAS studied in Proton-Proton Collisions recorded in 2012 at 8 TeV*, ATLAS-CONF-2013-082 (2013).

[383] M. Cacciari, G. P. Salam, and G. Soyez, *The Catchment Area of Jets*, JHEP **0804** (2008) p. 005, arXiv: 0802.1188 [hep-ph].

[384] G. Cowan, *Statistical Data Analysis*, Oxford University Press, Oxford, 1998.

[385] F. James, *Statistical methods in experimental physics*, 2006.

[386] The ATLAS Collaboration, *Combined search for the Standard Model Higgs boson in pp collisions at $\sqrt{s} = 7$ TeV with the ATLAS detector*, Phys.Rev. **D86** (2012) p. 032003, arXiv: 1207.0319 [hep-ex].

[387] R. Brun and F. Rademakers, *ROOT: An object oriented data analysis framework*, Nucl.Instrum.Meth. **A389** (1997) pp. 81–86.

[388] W. Verkerke and D. P. Kirkby, *The RooFit toolkit for data modeling*, eConf **C0303241** (2003) MOLT007, arXiv: physics/0306116 [physics].

[389] R. J. Barlow and C. Beeston, *Fitting using finite Monte Carlo samples*, Comput.Phys.Commun. **77** (1993) pp. 219–228.

[390] K. Cranmer, G. Lewis, L. Moneta, A. Shibata, and W. Verkerke, *HistFactory: A tool for creating statistical models for use with RooFit and RooStats*, CERN-OPEN-2012-016 (2012).

[391] A. L. Read, *Linear interpolation of histograms*, Nucl.Instrum.Meth. **A425** (1999) pp. 357–360.

[392] *Procedure for the LHC Higgs boson search combination in Summer 2011*, ATL-PHYS-PUB-2011-011, CERN-CMS-NOTE-2011-005 (2011).

[393] F. James and M. Roos, *Minuit: A System for Function Minimization and Analysis of the Parameter Errors and Correlations*, Comput.Phys.Commun. **10** (1975) pp. 343–367.

[394] W. Davidon, *Variable Metric Method for Minimization*, SIAM Journal on Optimization **1**.1 (1991) pp. 1–17.

[395] R. Fletcher and M. J. D. Powell, *A Rapidly Convergent Descent Method for Minimization*, The Computer Journal **6**.2 (1963) pp. 163–168.

[396] G. Cowan, K. Cranmer, E. Gross, and O. Vitells, *Asymptotic formulae for likelihood-based tests of new physics*, Eur.Phys.J. **C71** (2011) p. 1554, arXiv: 1007.1727 [physics.data-an]. *Erratum to: Asymptotic formulae for likelihood-based tests of new physics*, Eur.Phys.J. **C73** (2013) p. 2501.

[397] L. Moneta, K. Belasco, K. S. Cranmer, S. Kreiss, A. Lazzaro, et al., *The RooStats Project*, PoS **ACAT2010** (2010) p. 057, arXiv: 1009.1003 [physics.data-an].

[398] J. Neyman and E. S. Pearson, *On the Problem of the Most Efficient Tests of Statistical Hypotheses*, Philosophical Transactions of the Royal Society of London. Series A, Containing Papers of a Mathematical or Physical Character **231**.694-706 (1933) pp. 289–337.

[399] K. Cranmer, A. Read, and W. Verkerke, *Extensions to the Frequentist Recommendation*, 2014, URL: https://twiki.cern.ch/twiki/pub/AtlasProtected/StatisticsTools/ExtendedStatForumRecommendations.pdf.

[400] A. Wald, *Tests of Statistical Hypotheses Concerning Several Parameters When the Number of Observations is Large*, Transactions of the American Mathematical Society **54**.3 (1943) pp. 426–482.

[401] S. Wilks, *The Large-Sample Distribution of the Likelihood Ratio for Testing Composite Hypotheses*, Annals Math.Statist. **9**.1 (1938) pp. 60–62.

[402] J. Neyman, *Outline of a Theory of Statistical Estimation Based on the Classical Theory of Probability*, Philosophical Transactions of the Royal Society of London. Series A, Mathematical and Physical Sciences **236**.767 (1937) pp. 333–380.

[403] G. J. Feldman and R. D. Cousins, *A Unified approach to the classical statistical analysis of small signals*, Phys.Rev. **D57** (1998) pp. 3873–3889, arXiv: physics/9711021 [physics.data-an].

[404] G. Cowan, K. Cranmer, E. Gross, and O. Vitells, *Asymptotic distribution for two-sided tests with lower and upper boundaries on the parameter of interest* (2012), arXiv: 1210.6948 [physics.data-an].

[405] A. L. Read, *Presentation of search results: The CL(s) technique*, J.Phys. **G28** (2002) pp. 2693–2704.

[406] The PGS Group, 2012, URL: http://www.physics.ucdavis.edu/~conway/research/software/pgs/pgs4-general.htm.

[407] P. Nason, *A New method for combining NLO QCD with shower Monte Carlo algorithms*, JHEP **0411** (2004) p. 040, arXiv: hep-ph/0409146 [hep-ph].

[408] S. Alioli, P. Nason, C. Oleari, and E. Re, *NLO Higgs boson production via gluon fusion matched with shower in POWHEG*, JHEP **0904** (2009) p. 002, arXiv: 0812.0578 [hep-ph].

[409] P. Nason and C. Oleari, *NLO Higgs boson production via vector-boson fusion matched with shower in POWHEG*, JHEP **1002** (2010) p. 037, arXiv: 0911.5299 [hep-ph].

[410] E. Bagnaschi, G. Degrassi, P. Slavich, and A. Vicini, *Higgs production via gluon fusion in the POWHEG approach in the SM and in the MSSM*, JHEP **1202** (2012) p. 088, arXiv: 1111.2854 [hep-ph].

[411] T. Melia, P. Nason, R. Rontsch, and G. Zanderighi, *W+W-, WZ and ZZ production in the POWHEG BOX*, JHEP **1111** (2011) p. 078, arXiv: 1107.5051 [hep-ph].

[412] M. L. Mangano, M. Moretti, F. Piccinini, R. Pittau, and A. D. Polosa, *ALPGEN, a generator for hard multiparton processes in hadronic collisions*, JHEP **0307** (2003) p. 001, arXiv: hep-ph/0206293 [hep-ph].

[413] T. Gleisberg, S. Hoeche, F. Krauss, M. Schonherr, S. Schumann, et al., *Event generation with SHERPA 1.1*, JHEP **0902** (2009) p. 007, arXiv: 0811.4622 [hep-ph].

[414] B. P. Kersevan and E. Richter-Was, *The Monte Carlo event generator AcerMC versions 2.0 to 3.8 with interfaces to PYTHIA 6.4, HERWIG 6.5 and ARIADNE 4.1*, Comput.Phys.Commun. **184** (2013) pp. 919–985, arXiv: hep-ph/0405247 [hep-ph].

[415] N. Kauer, *Interference effects for $H \to WW/ZZ \to \ell\bar{\nu}_\ell\bar{\ell}\nu_\ell$ searches in gluon fusion at the LHC*, JHEP **1312** (2013) p. 082, arXiv: 1310.7011 [hep-ph].

[416] J. Pumplin, D. Stump, J. Huston, H. Lai, P. M. Nadolsky, et al., *New generation of parton distributions with uncertainties from global QCD analysis*, JHEP **0207** (2002) p. 012, arXiv: hep-ph/0201195 [hep-ph].

[417] A. Sherstnev and R. Thorne, *Parton Distributions for LO Generators*, Eur.Phys.J. **C55** (2008) pp. 553–575, arXiv: 0711.2473 [hep-ph].

[418] G. Corcella, I. Knowles, G. Marchesini, S. Moretti, K. Odagiri, et al., *HERWIG 6: An Event generator for hadron emission reactions with interfering gluons (including supersymmetric processes)*, JHEP **0101** (2001) p. 010, arXiv: hep-ph/0011363 [hep-ph].

[419] J. Butterworth, J. R. Forshaw, and M. Seymour, *Multiparton interactions in photoproduction at HERA*, Z.Phys. **C72** (1996) pp. 637–646, arXiv: hep-ph/9601371 [hep-ph].

[420] The ATLAS Collaboration, *The ATLAS Simulation Infrastructure*, Eur.Phys.J. **C70** (2010) pp. 823–874, arXiv: 1005.4568 [physics.ins-det].

[421] The GEANT4 Collaboration, *GEANT4: A Simulation toolkit*, Nucl.Instrum.Meth. **A506** (2003) pp. 250–303.

[422] The ATLAS Collaboration, *The simulation principle and performance of the ATLAS fast calorimeter simulation FastCaloSim*, ATL-PHYS-PUB-2010-013 (2010).

[423] J. M. Campbell, R. K. Ellis, and C. Williams, *Vector boson pair production at the LHC*, JHEP **1107** (2011) p. 018, arXiv: 1105.0020 [hep-ph].

[424] M. Czakon and A. Mitov, *Top++: A Program for the Calculation of the Top-Pair Cross-Section at Hadron Colliders*, Comput.Phys.Commun. **185** (2014) p. 2930, arXiv: 1112.5675 [hep-ph].

[425] S. Catani, L. Cieri, G. Ferrera, D. de Florian, and M. Grazzini, *Vector boson production at hadron colliders: a fully exclusive QCD calculation at NNLO*, Phys.Rev.Lett. **103** (2009) p. 082001, arXiv: 0903.2120 [hep-ph].

[426] S. Catani and M. Grazzini, *An NNLO subtraction formalism in hadron collisions and its application to Higgs boson production at the LHC*, Phys.Rev.Lett. **98** (2007) p. 222002, arXiv: hep-ph/0703012 [hep-ph].

[427] C. A. Nelson, *Correlation Between Decay Planes in Higgs Boson Decays Into W Pair (Into Z Pair)*, Phys.Rev. **D37** (1988) p. 1220.

[428] V. D. Barger, G. Bhattacharya, T. Han, and B. A. Kniehl, *Intermediate mass Higgs boson at hadron supercolliders*, Phys.Rev. **D43** (1991) pp. 779–788.

[429] M. Dittmar and H. K. Dreiner, *How to find a Higgs boson with a mass between 155-GeV - 180-GeV at the LHC*, Phys.Rev. **D55** (1997) pp. 167–172, arXiv: hep-ph/9608317 [hep-ph].

[430] A. J. Barr, B. Gripaios, and C. G. Lester, *Measuring the Higgs boson mass in dileptonic W-boson decays at hadron colliders*, JHEP **0907** (2009) p. 072, arXiv: 0902.4864 [hep-ph].

[431] M. Cacciari and G. P. Salam, *Pileup subtraction using jet areas*, Phys.Lett. **B659** (2008) pp. 119–126, arXiv: 0707.1378 [hep-ph].

[432] A. Bredenstein, A. Denner, S. Dittmaier, and M. Weber, *Precise predictions for the Higgs-boson decay $H \to WW/ZZ \to 4leptons$*, Phys.Rev. **D74** (2006) p. 013004, arXiv: hep-ph/0604011 [hep-ph].

[433] A. Djouadi, J. Kalinowski, and M. Spira, *HDECAY: A Program for Higgs boson decays in the standard model and its supersymmetric extension*, Comput.Phys.Commun. **108** (1998) pp. 56–74, arXiv: hep-ph/9704448 [hep-ph].

[434] M. Grazzini and H. Sargsyan, *Heavy-quark mass effects in Higgs boson production at the LHC*, JHEP **1309** (2013) p. 129, arXiv: 1306.4581 [hep-ph].

[435] K. Hamilton, P. Nason, and G. Zanderighi, *MINLO: Multi-Scale Improved NLO*, JHEP **1210** (2012) p. 155, arXiv: 1206.3572 [hep-ph].

[436] A. Banfi, G. P. Salam, and G. Zanderighi, *NLL+NNLO predictions for jet-veto efficiencies in Higgs-boson and Drell-Yan production*, JHEP **1206** (2012) p. 159, arXiv: 1203.5773 [hep-ph].

[437] A. Banfi, P. F. Monni, G. P. Salam, and G. Zanderighi, *Higgs and Z-boson production with a jet veto*, Phys.Rev.Lett. **109** (2012) p. 202001, arXiv: 1206.4998 [hep-ph].

[438] J. Butterworth, G. Dissertori, S. Dittmaier, D. de Florian, N. Glover, et al., *Les Houches 2013: Physics at TeV Colliders: Standard Model Working Group Report* (2014), arXiv: 1405.1067 [hep-ph].

[439] I. W. Stewart and F. J. Tackmann, *Theory Uncertainties for Higgs and Other Searches Using Jet Bins*, Phys.Rev. **D85** (2012) p. 034011, arXiv: 1107.2117 [hep-ph].

[440] The ATLAS Collaboration, *Measurements of Higgs boson production and couplings in diboson final states with the ATLAS detector at the LHC*, Phys.Lett. **B726** (2013) pp. 88–119, arXiv: 1307.1427 [hep-ex].

[441] R. K. Ellis, I. Hinchliffe, M. Soldate, and J. van der Bij, *Higgs Decay to tau+ tau-: A Possible Signature of Intermediate Mass Higgs Bosons at the SSC*, Nucl.Phys. **B297** (1988) p. 221.

[442] T. Plehn, D. L. Rainwater, and D. Zeppenfeld, *A Method for identifying $H \to \tau^+\tau^- \to e^\pm\mu^\mp p_T$ at the CERN LHC*, Phys.Rev. **D61** (2000) p. 093005, arXiv: hep-ph/9911385 [hep-ph].

[443] The ATLAS Collaboration, *Expected Performance of the ATLAS Experiment - Detector, Trigger and Physics* (2009), arXiv: 0901.0512 [hep-ex].

[444] L. Breiman, J. H. Friedman, R. A. Olshen, and C. J. Stone, *Classification and Regression Trees*, New York: Chapman and Hall, 1984.

[445] Y. Freund and R. E. Schapire, *A Decision-Theoretic Generalization of On-Line Learning and an Application to Boosting*, Journal of Computer and System Sciences **55**.1 (1997) pp. 119–139.

[446] J. H. Friedman, *Stochastic gradient boosting*, Computational Statistics & Data Analysis **38**.4 (2002) pp. 367–378, Nonlinear Methods and Data Mining.

[447] A. Hocker, J. Stelzer, F. Tegenfeldt, H. Voss, K. Voss, et al., *TMVA - Toolkit for Multivariate Data Analysis*, PoS **ACAT** (2007) p. 040, arXiv: physics/0703039 [PHYSICS].

[448] P. Speckmayer, A. Hocker, J. Stelzer, and H. Voss, *The toolkit for multivariate data analysis, TMVA 4*, J.Phys.Conf.Ser. **219** (2010) p. 032057.

[449] V. D. Barger, R. Phillips, and D. Zeppenfeld, *Mini - jet veto: A Tool for the heavy Higgs search at the LHC*, Phys.Lett. **B346** (1995) pp. 106–114, arXiv: hep-ph/9412276 [hep-ph].

[450] The ATLAS Collaboration, *Measurement of hard double-parton interactions in $W(\rightarrow l\nu)+2$ jet events at $\sqrt{s}=7$ TeV with the ATLAS detector*, New J.Phys. **15** (2013) p. 033038, arXiv: 1301.6872 [hep-ex].

[451] B. Blok, Y. Dokshitzer, L. Frankfurt, and M. Strikman, *Perturbative QCD correlations in multi-parton collisions*, Eur.Phys.J. **C74** (2014) p. 2926, arXiv: 1306.3763 [hep-ph].

[452] S. Frixione and B. R. Webber, *Matching NLO QCD computations and parton shower simulations*, JHEP **0206** (2002) p. 029, arXiv: hep-ph/0204244 [hep-ph].

[453] The LHC Higgs Cross Section Working Group Collaboration, *Handbook of LHC Higgs Cross Sections: 1. Inclusive Observables* (2011), arXiv: 1101.0593 [hep-ph].

[454] The ATLAS Collaboration, *Study of the Higgs boson decaying to WW^* produced in association with a weak boson with the ATLAS detector at the LHC*, ATLAS-CONF-2015-005 (2015).

[455] The ATLAS Collaboration, *Search for Higgs boson decays to a photon and a Z boson in pp collisions at $\sqrt{s}=7$ and 8 TeV with the ATLAS detector*, Phys.Lett. **B732** (2014) pp. 8–27, arXiv: 1402.3051 [hep-ex].

[456] The ATLAS Collaboration, *Search for the Standard Model Higgs boson decay to $\mu^+\mu^-$ with the ATLAS detector*, Phys.Lett. **B738** (2014) pp. 68–86, arXiv: 1406.7663 [hep-ex].

[457] The ATLAS Collaboration, *Search for $H \rightarrow \gamma\gamma$ produced in association with top quarks and constraints on the Yukawa coupling between the top quark and the Higgs boson using data taken at 7 TeV and 8 TeV with the ATLAS detector*, Phys.Lett. **B740** (2015) pp. 222–242, arXiv: 1409.3122 [hep-ex].

[458] The ATLAS Collaboration, *Determination of the off-shell Higgs boson signal strength in the high-mass ZZ and WW final states with the ATLAS detector* (2015), arXiv: 1503.01060 [hep-ex].

[459] The ATLAS Collaboration, *Search for Higgs and Z Boson Decays to $J/\psi\gamma$ and $\Upsilon(nS)\gamma$ with the ATLAS Detector* (2015), arXiv: 1501.03276 [hep-ex].

[460] The ATLAS Collaboration, *Search for Invisible Decays of a Higgs Boson Produced in Association with a Z Boson in ATLAS*, Phys.Rev.Lett. **112** (2014) p. 201802, arXiv: 1402.3244 [hep-ex].

[461] S. Frixione, P. Nason, and C. Oleari, *Matching NLO QCD computations with Parton Shower simulations: the POWHEG method*, JHEP **0711** (2007) p. 070, arXiv: 0709.2092 [hep-ph].

[462] S. Alioli, P. Nason, C. Oleari, and E. Re, *A general framework for implementing NLO calculations in shower Monte Carlo programs: the POWHEG BOX*, JHEP **1006** (2010) p. 043, arXiv: 1002.2581 [hep-ph].

[463] D. de Florian, G. Ferrera, M. Grazzini, and D. Tommasini, *Higgs boson production at the LHC: transverse momentum resummation effects in the $H \rightarrow 2gamma$, $H \rightarrow WW \rightarrow l\nu l\nu$ and $H \rightarrow ZZ \rightarrow 4l$ decay modes*, JHEP **1206** (2012) p. 132, arXiv: 1203.6321 [hep-ph].

[464] G. Bevilacqua, M. Czakon, M. Garzelli, A. van Hameren, A. Kardos, et al., *HELAC-NLO*, Comput.Phys.Commun. **184** (2013) pp. 986–997, arXiv: 1110.1499 [hep-ph].

[465] F. Maltoni and T. Stelzer, *MadEvent: Automatic event generation with MadGraph*, JHEP **0302** (2003) p. 027, arXiv: hep-ph/0208156 [hep-ph].

[466] M. Bahr, S. Gieseke, M. Gigg, D. Grellscheid, K. Hamilton, et al., *Herwig++ Physics and Manual*, Eur.Phys.J. **C58** (2008) pp. 639–707, arXiv: 0803.0883 [hep-ph].

[467] M. Oreglia, *A Study of the Reactions $\psi' \to \gamma\gamma\psi$*, SLAC-R-0236 (1980).

[468] A. Elagin, P. Murat, A. Pranko, and A. Safonov, *A New Mass Reconstruction Technique for Resonances Decaying to di-tau*, Nucl.Instrum.Meth. **A654** (2011) pp. 481–489, arXiv: 1012.4686 [hep-ex].

[469] N. Kauer and G. Passarino, *Inadequacy of zero-width approximation for a light Higgs boson signal*, JHEP **1208** (2012) p. 116, arXiv: 1206.4803 [hep-ph].

[470] F. Caola and K. Melnikov, *Constraining the Higgs boson width with ZZ production at the LHC*, Phys.Rev. **D88** (2013) p. 054024, arXiv: 1307.4935 [hep-ph].

[471] J. M. Campbell, R. K. Ellis, and C. Williams, *Bounding the Higgs width at the LHC using full analytic results for $gg \to e^- e^+ \mu^- \mu^+$*, JHEP **1404** (2014) p. 060, arXiv: 1311.3589 [hep-ph].

[472] J. M. Campbell, R. K. Ellis, and C. Williams, *Bounding the Higgs width at the LHC: complementary results from $H \to WW$*, Phys.Rev. **D89** (2014) p. 053011, arXiv: 1312.1628 [hep-ph].

[473] The ATLAS Collaboration, *Measurements of fiducial and differential cross sections for Higgs boson production in the diphoton decay channel at $\sqrt{s} = 8$ TeV with ATLAS*, JHEP **1409** (2014) p. 112, arXiv: 1407.4222 [hep-ex].

[474] The ATLAS Collaboration, *Fiducial and differential cross sections of Higgs boson production measured in the four-lepton decay channel in pp collisions at $\sqrt{s}$=8 TeV with the ATLAS detector*, Phys.Lett. **B738** (2014) pp. 234–253, arXiv: 1408.3226 [hep-ex].

[475] The ATLAS Collaboration, *Search for the bb decay of the Standard Model Higgs boson in associated W/ZH production with the ATLAS detector*, ATLAS-CONF-2013-079 (2013).

[476] The ATLAS Collaboration, *Evidence for Higgs Boson Decays to the $\tau^+\tau^-$ Final State with the ATLAS Detector*, ATLAS-CONF-2013-108 (2013).

[477] J. Ellis and T. You, *Global Analysis of the Higgs Candidate with Mass 125 GeV*, JHEP **1209** (2012) p. 123, arXiv: 1207.1693 [hep-ph].

[478] J. Ellis and T. You, *Updated Global Analysis of Higgs Couplings*, JHEP **1306** (2013) p. 103, arXiv: 1303.3879 [hep-ph].

[479] J. Aguilar-Saavedra, R. Benbrik, S. Heinemeyer, and M. Pérez-Victoria, *Handbook of vectorlike quarks: Mixing and single production*, Phys.Rev. **D88**.9 (2013) p. 094010, arXiv: 1306.0572 [hep-ph].

[480] J. R. Ellis, J. Gunion, H. E. Haber, L. Roszkowski, and F. Zwirner, *Higgs Bosons in a Nonminimal Supersymmetric Model*, Phys.Rev. **D39** (1989) p. 844.

[481] M. Drees, *Supersymmetric Models with Extended Higgs Sector*, Int.J.Mod.Phys. **A4** (1989) p. 3635.

[482] M. Maniatis, *The Next-to-Minimal Supersymmetric extension of the Standard Model reviewed*, Int.J.Mod.Phys. **A25** (2010) pp. 3505–3602, arXiv: 0906.0777 [hep-ph].

[483] U. Ellwanger, C. Hugonie, and A. M. Teixeira, *The Next-to-Minimal Supersymmetric Standard Model*, Phys.Rept. **496** (2010) pp. 1–77, arXiv: 0910.1785 [hep-ph].

[484] R. V. Harlander, S. Liebler, and H. Mantler, *SusHi: A program for the calculation of Higgs production in gluon fusion and bottom-quark annihilation in the Standard Model and the MSSM*, Computer Physics Communications **184** (2013) pp. 1605–1617, arXiv: 1212.3249 [hep-ph].

[485] D. Eriksson, J. Rathsman, and O. Stal, *2HDMC: Two-Higgs-Doublet Model Calculator Physics and Manual*, Comput.Phys.Commun. **181** (2010) pp. 189–205, arXiv: 0902.0851 [hep-ph].

[486] The Particle Data Group Collaboration, *Review of Particle Physics*, Chin.Phys. **C38** (2014) p. 090001.

[487] The CMS Collaboration, *Observation of the diphoton decay of the Higgs boson and measurement of its properties*, Eur.Phys.J. **C74**.10 (2014) p. 3076, arXiv: 1407.0558 [hep-ex].

[488] The CMS Collaboration, *Measurement of the properties of a Higgs boson in the four-lepton final state*, Phys.Rev. **D89**.9 (2014) p. 092007, arXiv: 1312.5353 [hep-ex].

[489] The Gfitter Collaboration, *The global electroweak fit at NNLO and prospects for the LHC and ILC*, Eur.Phys.J. **C74** (2014) p. 3046, arXiv: 1407.3792 [hep-ph].

[490] L. J. Dixon and M. S. Siu, *Resonance continuum interference in the diphoton Higgs signal at the LHC*, Phys.Rev.Lett. **90** (2003) p. 252001, arXiv: hep-ph/0302233 [hep-ph].

[491] S. P. Martin, *Shift in the LHC Higgs diphoton mass peak from interference with background*, Phys.Rev. **D86** (2012) p. 073016, arXiv: 1208.1533 [hep-ph].

[492] L. J. Dixon and Y. Li, *Bounding the Higgs Boson Width Through Interferometry*, Phys.Rev.Lett. **111** (2013) p. 111802, arXiv: 1305.3854 [hep-ph].

[493] The CMS Collaboration, *Performance of CMS muon reconstruction in pp collision events at $\sqrt{s} = 7$ TeV*, JINST **7** (2012) P10002, arXiv: 1206.4071 [physics.ins-det].

[494] The CMS Collaboration, *Performance of electron reconstruction and selection with the CMS detector in proton-proton collisions at sqrt(s)=8 TeV* (2015), arXiv: 1502.02701 [physics.ins-det].

[495] The CMS Collaboration, *Performance of photon reconstruction and identification with the CMS detector in proton-proton collisions at sqrt(s) = 8 TeV* (2015), arXiv: 1502.02702 [physics.ins-det].

[496] P. Dauncey, M. Kenzie, N. Wardle, and G. Davies, *Handling uncertainties in background shapes: the discrete profiling method* (2014), arXiv: 1408.6865 [physics.data-an].

[497] The ALEPH, DELPHI, L3, OPAL, SLD Collaborations; LEP Electroweak Working Group; SLD Electroweak and Heavy Flavour Groups, *Precision Electroweak Measurements on the Z Resonance*, Phys. Rept. **427** (2006) p. 257, eprint: hep-ex/0509008.

[498] M. E. Peskin, *Comparison of LHC and ILC Capabilities for Higgs Boson Coupling Measurements* (2012), arXiv: 1207.2516 [hep-ph].

[499] M. E. Peskin, *Estimation of LHC and ILC Capabilities for Precision Higgs Boson Coupling Measurements* (2013), arXiv: 1312.4974 [hep-ph].

[500] T. Han, Z. Liu, and J. Sayre, *Potential Precision on Higgs Couplings and Total Width at the ILC*, Phys.Rev. **D89** (2014) p. 113006, arXiv: 1311.7155 [hep-ph].

[501] A. D. Rosso, *HL-LHC updates in Japan*, CERN Bulletin BUL-NA-2014-272. 51/2014 (2014).

[502] The LHCb Collaboration, *First Evidence for the Decay $B_s^0 \to \mu^+\mu^-$*, Phys.Rev.Lett. **110** (2013) p. 021801, arXiv: 1211.2674 [hep-ex].

[503] H.-L. P. team, *High Luminosity upgrade for the LHC*, URL: http://hilumilhc.web.cern.ch/ (visited on 01/01/2015).

[504] The ATLAS Collaboration, *Projections for measurements of Higgs boson cross sections, branching ratios and coupling parameters with the ATLAS detector at a HL-LHC*, ATL-PHYS-PUB-2013-014 (2013).

[505] The ATLAS Collaboration, *Update of the prospects for the H Z search at the High-Luminosity LHC*, ATL-PHYS-PUB-2014-006 (2014).

[506] The ATLAS Collaboration, *HL-LHC projections for signal and background yield measurements of the $H \to \gamma\gamma$ when the Higgs boson is produced in association with t quarks, W or Z bosons*, ATL-PHYS-PUB-2014-012 (2014).

[507] The ATLAS Collaboration, *Prospects for the study of the Higgs boson in the VH(bb) channel at HL-LHC*, ATL-PHYS-PUB-2014-011 (2014).

[508] The ATLAS Collaboration, *Performance assumptions based on full simulation for an upgraded ATLAS detector at a High-Luminosity LHC*, ATL-PHYS-PUB-2013-009 (2013).

[509] The ATLAS Collaboration, *Performance assumptions for an upgraded ATLAS detector at a High-Luminosity LHC*, ATL-PHYS-PUB-2013-004 (2013).

[510] The ATLAS Collaboration, *Search for new phenomena in final states with an energetic jet and large missing transverse momentum in pp collisions at $\sqrt{s} = 8$ TeV with the ATLAS detector* (2015), arXiv: 1502.01518 [hep-ex].

[511] The ATLAS Collaboration, *Search for an Invisibly Decaying Higgs Boson Produced via Vector Boson Fusion in pp Collisions at $\sqrt{s} = 8$ TeV using the ATLAS Detector at the LHC*, ATLAS-CONF-2015-004 (2015).

[512] D. Zeppenfeld, R. Kinnunen, A. Nikitenko, and E. Richter-Was, *Measuring Higgs boson couplings at the CERN LHC*, Phys.Rev. **D62** (2000) p. 013009, arXiv: hep-ph/0002036 [hep-ph].

[513] M. Duhrssen, S. Heinemeyer, H. Logan, D. Rainwater, G. Weiglein, et al., *Extracting Higgs boson couplings from CERN LHC data*, Phys.Rev. **D70** (2004) p. 113009, arXiv: hep-ph/0406323 [hep-ph].

[514] B. A. Dobrescu and J. D. Lykken, *Coupling spans of the Higgs-like boson*, JHEP **1302** (2013) p. 073, arXiv: 1210.3342 [hep-ph].

Summary

The Standard Model of Elementary Particle Physics (SM) provides a fundamental description of all established elementary particles, their dynamics and interactions, except gravity. Fermions of half-integer spin form all matter in nature. The interactions between the fermions are interpreted as exchange of force-mediating bosons of integer spin. Symmetries play an essential role in constructing the SM, making it an remarkably elegant theory. However, the particles embedded into the theory are a priori massless, unlike the observed particles. Thus, a mechanism must be introduced to give the particles mass in the theory.

The W and Z gauge bosons can acquire their mass through breaking of the electroweak symmetry, referred to as electroweak symmetry breaking (EWSB). In the SM, the complex Higgs scalar field induces a spontaneous breaking of the electroweak gauge group when it acquires a non-vanishing vacuum expectation value. The mechanism is commonly referred to as the Brout-Englert-Higgs mechanism. The Higgs field picked up its vacuum expectation value through the so-called electroweak phase transition when the early universe cooled down and expanded after the Big Bang. The underlying dynamics of this process are not known. Spontaneous symmetry breaking also gives mass to the fermions, yet the concept differs from the mechanism gauge bosons acquire their mass. The fermion mass terms are generated in the SM by gauge invariant Yukawa interactions between the Higgs field and the fermion fields. The Brout-Englert-Higgs mechanism postulates the existence of one real scalar field, identified as the Higgs boson. In 2012, the discovery of a new particle with a mass near 125 GeV in the search for the SM Higgs boson [4–6] provided the first hint at the mechanism of EWSB. Elucidating the mechanism of EWSB and the origin of elementary particle masses is among the principal quests of the CERN LHC physics program.

This manuscript presents comprehensive precision measurements of the Higgs particle's properties, in particular of its mass, production and decay rates, and coupling strengths. The results are based on the samples of proton-proton collision data recorded by the ATLAS and CMS detectors at the LHC in Run 1. The analyzed samples correspond to an integrated luminosity of approximately 5 fb^{-1} and 20 fb^{-1} at a collision energy of 7 TeV and 8 TeV, respectively, for each experiment.

At the LHC, multiple inelastic proton-proton interactions may occur at the same time. Understanding this complex environment is essential for any analysis at the LHC. The event reconstruction algorithms, in particular those associated with the ATLAS Inner Detector (ID),

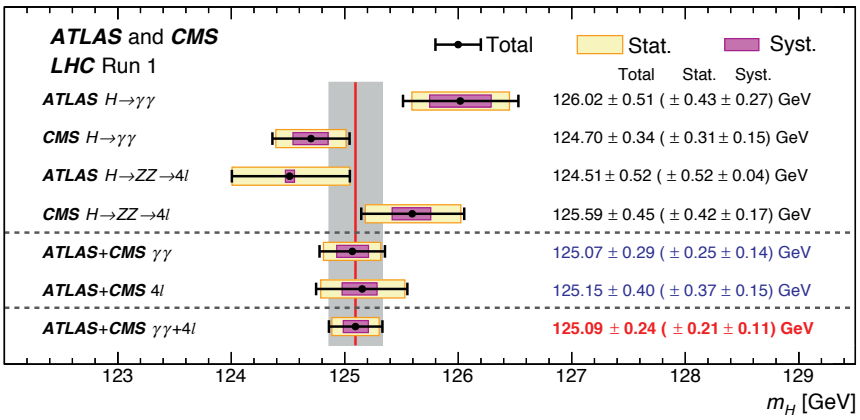

Figure 1: Summary of Higgs boson mass measurements from the individual analyses of ATLAS and CMS and from the combined analysis presented here. The systematic (narrower, magenta-shaded bands), statistical (wider, yellow-shaded bands), and total (black error bars) uncertainties are indicated. The (red) vertical line and corresponding (gray) shaded column indicate the central value and the total uncertainty of the combined measurement, respectively.

are studied in terms of physics and detector performance and computational efficiency. Optimizing the early stages of the pattern recognition yields a 30 % faster ID reconstruction, while maintaining the reconstruction efficiencies and resolutions for all physics objects in a high occupancy environment [19].

In the SM, the Higgs boson mass is not predicted by the theory. Instead, it must be determined experimentally from data. Prior to the turn-on of the LHC, Higgs boson masses below 114 GeV and in the range of 158 GeV to 175 GeV have been excluded by direct searches at LEP [1] and Tevatron [2], respectively. Global fits to precision EW data implied an upper limit on the Higgs boson mass of 158 GeV [3]. Combining the $H \to \gamma\gamma$ and $H \to ZZ^* \to 4\ell$ channels, in which the mass of the Higgs boson can be explicitly reconstructed from its decay products, and using the full LHC Run 1 collision data sets of the ATLAS and CMS experiments, the mass is now – virtually independent of SM assumptions – determined to an accuracy of 0.2 %. The measurement is summarized in Fig. 1. The total uncertainty is dominated by the sample statistics of the analyzed data set. The systematic uncertainty is dominated by effects related to the photon, electron, and muon energy or momentum scales and resolutions [22].

Having established the Higgs boson mass, all properties of the SM Higgs boson, such as its production cross section and partial decay widths, are predicted by the SM. This then allows to test the predictions against the recorded collision data. As an example, the sequential Higgs boson decay $H \to WW^* \to \ell\nu\ell\nu$, with the Higgs boson produced through gluon fusion

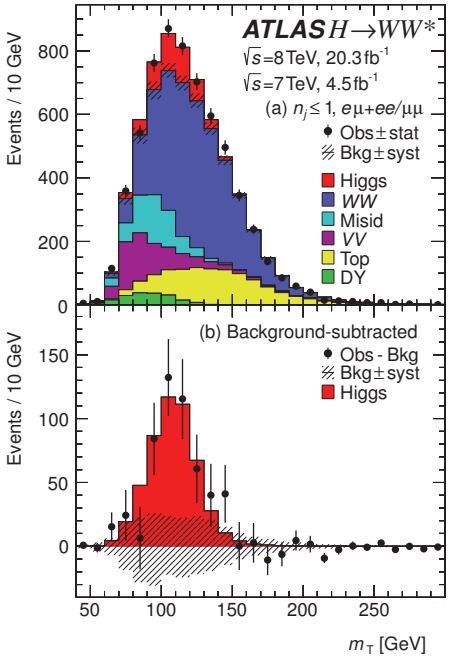

Figure 2: (a) Cumulative m_{T} distribution integrated over all lepton-flavor final states and $n_j \leq 1$ categories of the 7 and 8 TeV data sets after profiling all nuisance parameters. (b) Residuals of the data with respect to the total estimated background, compared to the predicted m_{T} distribution of a SM Higgs boson with a hypothesized mass of 125 GeV and scaled by the measured inclusive production strength. Although the reconstructed transverse mass m_{T} is not identical to the invariant mass m_H of the Higgs boson due to the unknown longitudinal momenta of the neutrinos in the final state, it has a kinematic bound at the true Higgs boson mass, smeared by the detector resolution.

(ggF) or vector boson fusion (VBF), is studied. For a Higgs boson with a mass of approximately 125 GeV, the decay mode is relatively abundant in the SM. The neutrinos produced in the signal process escape detection so that the final state can not be reconstructed fully, unlike $H \to \gamma\gamma$ and $H \to ZZ^* \to 4\ell$. To extract the Higgs boson properties, the categories enriched in signal events from gluon fusion employ a three-dimensional discriminant. The categories enriched in Higgs boson candidates produced through vector boson fusion make use of a Boosted Decision Tree (BDT), combining information about background rejection, the VBF topology, and the $H \to WW^* \to \ell\nu\ell\nu$ decay topology. To reduce the influence of simulation uncertainties of the many background processes on the signal estimate, the signal selections are augmented with control samples. The statistical data analysis is designed to estimate (almost) all background processes from data in regions that are kinematically close to the phase space enriched in signal events. These control selections have been optimized to simultaneously minimize the statistical uncertainty on the background estimate and the systematic uncertainties associated with the extrapolation of the background rates in the control samples to the signal regions. Figure 2 illustrates the results of the analysis. The local significance of the observed excess of events in data with respect to the background hypothesis is 6.1 standard deviations. The reported signal strength, $\mu = 1.09^{+0.23}_{-0.21}$, is the most precise measurement of its kind in a single decay channel, to date [30], despite the inability to explicitly reconstruct the Higgs boson invariant mass from its decay products.

Statistical data analysis is an important element of all physics analyses. In this context, a key part of the effort is the construction of probability models that can be fit to the data, where predictions are based on simulated data. Possible deformations of these distributions associated to known systematic uncertainties are introduced in these models through a technical procedure called template morphing. In this thesis a new non-linear moment morphing method is presented. It is fast, numerically stable, allows for the morphing of both binned histogram and continuous templates, has proper handling of both horizontal as well as vertical shifting distributions, and is not restricted in the number of input templates, the number of model parameters, or the number of input observables [20]. These features are of increasing importance for complex probability models with many systematic uncertainties. Moment morphing is applicable to many problems in modern particle physics and beyond because modeling of systematic uncertainties on distributions is a common issue in statistical analyses. The statistical analysis of the $H \to WW^* \to \ell\nu\ell\nu$ channel is among the first ones exploiting this new interpolation technique: in the absence of an analytical prediction of the probability density functions (p.d.f.s) used in the statistical data analysis at the LHC, the dependence on the Higgs boson mass is modeled continuously through moment morphing. The analysis of Higgs boson decays to four leptons ($H \to ZZ^* \to 4\ell$) by the ATLAS collaboration is an example for the use of moment morphing to model the variations of systematic uncertainties [24]. Moment morphing of n-dimensional distributions is also used in the context of Higgs boson spin and parity measurements in diboson final states by the ATLAS collaboration [33].

To shed light on the mechanism responsible for EWSB in the SM, precise measurements of all Higgs boson properties are required. Every theoretical extension of the SM alters the scalar sector of nature and exhibits distinct features that probe specific aspects of the SM. For the best possible analysis, a joint likelihood model is built. It comprises the detailed likelihood models of each of the individual channels, taking into account all systematic correlations. The statistical interpretation of the data combines knowledge of the phenomenology of Higgs boson production and decays, state-of-the-art advances in theoretical calculations, as well as a detailed understanding of all reconstructed physics objects used by the experiment.

The simplest model to describe the joint data is a variant of the SM that allows a different global signal strength of Higgs boson production, while keeping all other properties identical to the SM. The global signal strength relative to the SM expectation is measured to be $\mu = 1.18^{+0.15}_{-0.14}$, compatible with the SM hypothesis, and asymptotically corresponding to a significance of more than 10 standard deviations. Other interpretations of the data that allow different signal strengths for all known production mechanisms result in a strong evidence for Higgs boson production through vector boson fusion with a significance of 4.3 standard deviations. The analysis also supports the SM predictions of the Higgs boson production in association with a vector boson or a pair of top quark with a significance of 2.6 and 2.4 standard deviations, respectively [31].

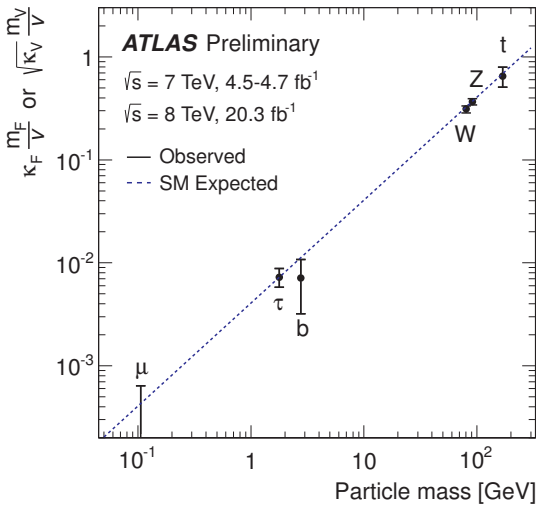

Figure 3: Fit results for the reduced coupling strength scale factors $y_{V,i} = \sqrt{\kappa_{V,i}\frac{g_{V,i}}{2v}} = \sqrt{\kappa_{V,i}}\frac{m_{V,i}}{v}$ for weak bosons and $y_{F,i} = \kappa_{F,i}\frac{g_{F,i}}{\sqrt{2}} = \kappa_{F,i}\frac{m_{F,i}}{v}$ for fermions as a function of the particle mass, assuming a SM Higgs boson with a mass of 125.36 GeV. The dashed line indicates the predicted mass dependence for the SM Higgs boson.

Beyond rate measurements of Higgs boson production modes, the observed production and decay rates are also interpreted in terms of modified Higgs boson coupling strengths, where the allowed modifications are parametrized following the degrees of freedom allowed in the leading order processes for Higgs boson production and decay [31]. This treatment allows to disentangle the effects of modified couplings in the production and decay, which occur in varying admixtures in the probed channels. The compatibility of the Higgs boson coupling strengths with the SM expectation is tested for a wide range of benchmark scenarios, building up on symmetries of SM. A variety of (physics-motivated) assumptions on the Higgs boson total decay width is studied. Depending on the choice of assumptions, the upper limit at 95 % confidence level (CL) on the branching fraction for invisible or undetected Higgs boson decays varies from 13 % to 68 %. Loop induced processes are used to indirectly search for new charged or colored particles. The effective coupling strengths associated with these processes are determined to an accuracy of approximately 10 % to 20 %, depending on the benchmark scenario. No significant deviations from the SM predictions are found. Under the considered benchmark models and for a wide range of assumptions, the compatibility of the data with the SM hypothesis is 29 % to 99 %. As an example, Fig. 3 shows the Higgs boson coupling strengths to μ and τ leptons, b and t quarks, and W and Z-bosons as function of the respective particle mass and illustrate the salient feature of the Brout-Englert-Higgs mechanism: the measured coupling strengths of particles to the Higgs boson are proportional to the observed masses of these particles.

Although the measured properties of the Higgs boson support the SM, and the SM is a viable perturbative description of physics phenomena up to the Planck scale, several fundamental questions are not answered satisfyingly. Among these are for example the hierarchy problem regarding the naturalness of the Higgs boson mass, the nature of dark matter, or the

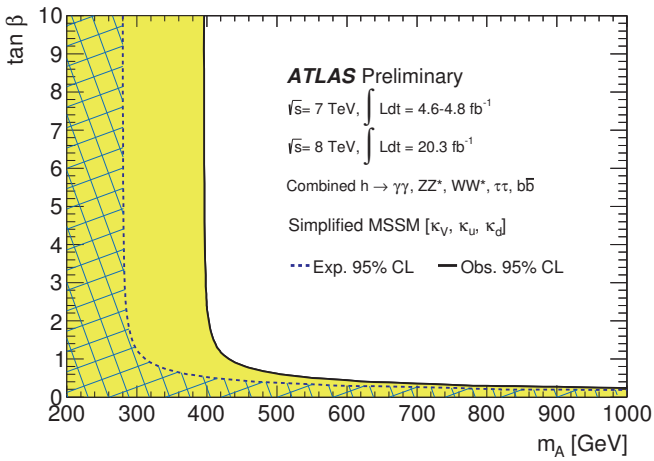

Figure 4: Regions of the hMSSM parameter space that are indirectly excluded at 95% CL or greater from a combined measurement of the Higgs boson production and decay rates. The regions expected to be excluded in case the scalar sector would be as predicted by the SM, are overlaid. The light shaded and hashed regions indicate the observed and expected exclusions, respectively. The indicated confidence intervals are constructed under the assumption that the test statistic $-2\ln\Lambda(m_A, \tan\beta)$ asymptotically is distributed as a χ^2 distribution with two degrees of freedom. The SM decoupling limit is at large m_A.

dynamical origin of EWSB. Many of the proposed solutions for these open questions have implications at the current energy frontier and predict modifications or extensions of the minimal scalar sector that is embedded in the SM. Some of the promising scenarios with fundamental physics beyond the SM are composite Higgs models, theories with two Higgs doublets, supersymmetry, and other models with a dark matter candidate. All these models make explicit predictions how the couplings of the observed 125 GeV Higgs boson deviate from the SM expectation. Tests with these model specific parametrizations are performed. Under certain assumptions, stringent limits on the model parameters associated with new phenomena are set [38]. These results possibly guide future direct searches for fundamental physics beyond the SM towards a discovery.

An example of a new physics theory that is constrained by measurements of properties of the observed Higgs boson is the Minimal Supersymmetric extension of the Standard Model. In this extension of the SM the scalar sector is represented by two doublet fields rather than one, which manifest themselves as five scalar particles: h, H, A, and $H^{\pm}$. In a simplified version of the theory [271, 272] the coupling properties of the light h boson depend only on two parameters: the mass of the heavy A boson and the mixing angle β of the light h and heavy H fields. Assuming the observed Higgs boson is the light state h of this theory, Fig. 4 shows the constraints on m_A and $\tan\beta$ that follow from the observed coupling properties of the Higgs boson in this simplified model.

Finally, the physics potential of the ATLAS experiment at the HL-LHC for measuring the Higgs boson production and decay rates and coupling strengths is studied. By the year 2022 the data sample recorded by the ATLAS detector is expected to correspond to an integrated luminosity of $300\,\text{fb}^{-1}$ at a collision energy of 14 TeV and increases to $3000\,\text{fb}^{-1}$ by 2035. The precision on the measured parameters is expected to significantly improve with increasing integrated luminosity, though advances both in the theoretical calculations and in the understanding of the detector are required to fully benefit from the upgrade program [52]. The possible synergies of the Higgs physics programs at the HL-LHC and the ILC are also studied. The two facilities are expected to complement each other with the HL-LHC having advantages in measuring decay modes with a low rate and other rare processes, and the ILC being ideally suited for determining the absolute Higgs boson coupling strengths.

Samenvatting

S

Het Standaard Model voor Elementaire Deeltjes (SM) geeft een fundamentele beschrijving van alle bekende elementaire deeltjes, hun dynamica en interacties, uitgezonderd zwaartekracht. Materie is opgebouwd uit fermionen met spin $1/2$. Interacties tussen de fermionen worden beschreven door de uitwisseling van boodschapperdeeltjes van krachten met een heeltallige spin. Symmetrieën spelen een belangijke rol bij de formulering van het SM, en leiden tot een elegante formulering. De deeltjes die voorkomen in de theorie zijn echter *a priori* massaloos, in tegenstelling tot de waargenomen deeltjes. Een mechanisme om deeltjes massa te geven in de theorie moet dus worden toegevoegd.

De W en Z ijkbosonen kunnen een massa verkrijgen door de elektrozwakke symmetrie te breken, gebruikelijk aangeduid als ElektroZwakke Symmetrie Breking (EZSB). In het SM kan het complexe scalaire higgsveld de symmetrie van de elektrozwakke ijkgroep spontaan breken als het veld een vacuümverwachtingswaarde krijgt die niet nul is. Dit mechanisme is algemeen bekend als het Brout-Englert-Higgs mechanisme. Het higgsveld verkrijgt een eindige vacuümverwachtingswaarde door de elektrozwakke fasetransitie die plaats vindt tijdens het afkoelen en uitdijen van het vroege heelal. De onderliggende dynamica van dit proces is onbekend. Spontane symmetriebreking geeft ook massa aan de fermionen, maar het concept is anders dan voor de ijkbosonen. De fermionmassa wordt gegenereerd in het SM door ijkinvariante Yukawa interacties tussen het higgsveld en de fermionvelden. Het Brout-Englert-Higgs mechanisme postuleert het bestaan van een één reëel scalair veld dat wordt geïdentificeerd als het higgsboson. De ontdekking van een nieuw deeltje in 2012 met een massa rond de 125 GeV in de zoektocht naar het SM higgsboson [4–6] gaf een eerste hint voor het mechanisme van EZSB. Opheldering van het mechanisme van EZSB en de oorsprong van de massa van elementaire deeltjes is een van de belangrijkste doelen van het CERN LHC fysica programma.

Dit manuscript presenteert een breed programma aan precisiemetingen van eigenschappen van het higgsdeeltje, in het bijzonder van de massa, productie- en vervalswaarschijnlijkheden, en koppelingssterktes. De resultaten zijn gebaseerd op een verzameling van proton-proton botsingen waargenomen door de ATLAS en CMS detectoren bij de LHC in Run-1. De geanalyseerde verzamelingen komen overeen met een geïntegreerde luminositeit van ongeveer $5\,\text{fb}^{-1}$ en $20\,\text{fb}^{-1}$ bij een respectievelijke botsingsenergie van 7 TeV and 8 TeV voor beide experimenten.

Bij de LHC kunnen gelijktijdig meerdere inelastische proton-proton botsingen plaatsvinden. Voor elke analyse van LHC data is het essentieel deze complexe omgeving te begrijpen.

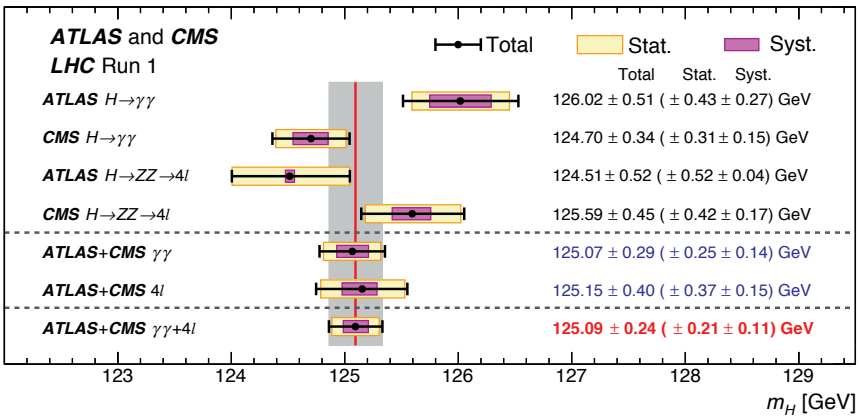

Figuur 1: Samenvatting van higgsbosonmassametingen van de individuele analyses van ATLAS en CMS, en van de combineerde meting die hier gepresenteerd wordt. De systematische (smalle magenta banden), statistische (brede gele banden) en totale onzekerheden (zwarte lijnen) zijn apart aangegeven. De (rode) verticale lijn en de bijbehorende grijze band geven respectievelijk de centrale waarde en de totale onzekerheid van de gecombineerde meting weer.

De reconstructie-algoritmes van botsingen, in het bijzonder die van de ATLAS Inner Detector (ID), zijn bestudeerd op natuurkundige aspecten, op het functioneren van de detectoren en op de efficiëntie van de berekeningen. Een optimalisatie van de vroege stadia van patroonherkenning geeft een 30% snellere ID reconstructie, met behoud van de efficiëntie en resolutie voor gereconstueerde objecten in een drukke omgeving [19].

In het SM wordt de massa van het higgsboson niet voorspeld door de theorie, maar kan alleen experimenteel worden vastgesteld. Voor de inbedrijfstelling van de LHC waren massawaardes van het higgsdeeltje kleiner dan 114 GeV en tussen 158 GeV en 175 GeV uitgesloten door eerdere resultaten bij de LEP [1] en Tevatron [2] versnellers. Globale fits aan elektrozwakke precisiemetingen impliceren een bovenlimiet op de higgsbosonmassa van 158 GeV. Door een combinatie van de metingen in de $H \to \gamma\gamma$ en $H \to ZZ^* \to 4\ell$ vervalskanalen, waar de massa van het boson expliciet gereconstrueerd kan worden uit de vervalsproducten, is massa nu – vrijwel onafhankelijk van SM aannames – vastgesteld met een precisie van 0.2 %. De meting is samengevat in Fig. 1. De totale onzekerheid wordt gedomineerd door de statistische onzekerheid op de geanalyseerde data. De systematische component van de onzekerheid wordt gedomineerd door effecten gerelateerd aan de calibratie van en de resolutie op de energie of impuls van elektronen, fotonen en muonen.

Met het vaststellen van de massa van het higgsboson kunnen alle eigenschappen van het SM higgsboson, zoals de werkzame doorsnede voor productie en de partiële vervalsbreedtes, worden voorspeld door het SM. Deze voorspellingen kunnen dan getest worden aan de

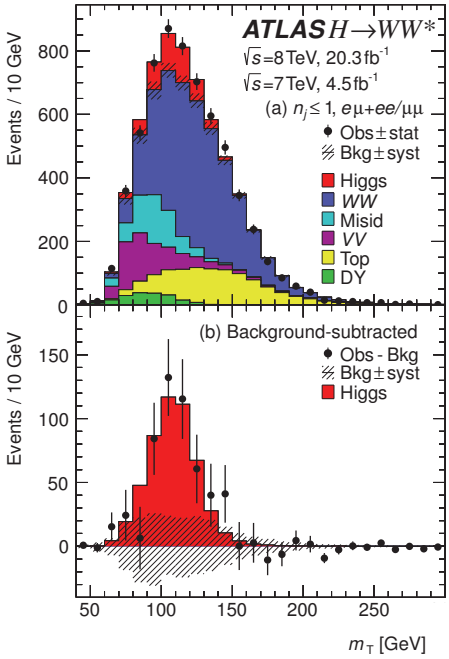

Figuur 2: (a) Cumulatieve verdeling van de transversale massa m_{T} van $H \to WW^* \to \ell\nu\ell\nu$ vervallen in de 7 TeV and 8 TeV data, geïntegreerd over alle leptonvervalskanalen met maximaal één jet, na het fitten van alle modelparameters. (b) Verschil tussen de data en de afschatting van de achtergrond, vergeleken met de voorspelling voor de m_{T} verdeling van een SM higgsboson met een massa van 125 GeV, geschaald naar de gemeten signaalsterkte. Alhoewel de gereconstueerde transversale massa m_{T} niet identiek is aan de invariante mass m_H van het higgsboson vanwege de ongemeten impuls van neutrinos in de longitudinale richting, heeft de verdeling van m_{T} een kinematische limiet bij de ware higgsbosonmassa en is gesmeerd door de detectorresolutie.

waargenomen data. Als voorbeeld is het sequentieële higgsbosonverval $H \to WW^* \to \ell\nu\ell\nu$ bestudeerd, waar het higgsboson geproduceerd wordt door gluonfusie (ggF) of vectorbosonfusie (VBF). Voor een higgsboson met een massa van ongeveer 125 GeV is deze vervalsmodus relatief veel voorkomend. De neutrinos die vrijkomen in dit higgsbosonvervalssignaal kunnen niet waargenomen worden, waardoor de verzameling waargenomen eindproducten van het verval van het higgsdeeltje incompleet is, dit in tegenstelling tot de vervalskanalen $H \to \gamma\gamma$ en $H \to ZZ^* \to 4\ell$. Om de eigenschappen van het higgsboson te bepalen wordt gebruik gemaakt van een drie-dimensionale discriminant in categoriën van de data die relatief rijk zijn in signaal geproduceerd door gluonfusie. In categoriën die relatief rijk zijn aan signaal produceerd door vectorbosonfusie wordt gebruikt gemaakt van een *Boosted Decision Tree* (BDT) die informatie over achtergronddiscriminatie combineert met informatie over de VBF productietopologie en de $H \to WW^* \to \ell\nu\ell\nu$ vervalstopologie. Om de invloed van simulatieonzekerheden in de vele achtergrondprocessen op de signaalafschatting te verminderen wordt de selectie van signaalbotsingen uitgebreid met controleverzamelingen. De statistische analyse is ontworpen om bijna alle achtergrondprocessen af te schatten uit data in controlegebieden die kinematisch dicht bij de faseruimte van de signaalselectie liggen. Deze controlegebieden zijn geoptimaliseerd om tegelijktijdig de statistische onzekerheid op de achtgrondafschatting en de systematische onzekerheiden op de extrapolatie van achtergrondmetingen in controlegebieden naar het signaalgebied te minimaliseren. Figuur 2 geeft het

resultaat van deze analyse weer. De lokale significantie van de geobserveerde hoeveelheid extra data boven de achtergrondverwachting is 6.1 standaardafwijking. De gemeten signaalsterkte, $\mu = 1.09^{+0.23}_{-0.21}$, is momenteel de meest nauwkeurige meting van dit type in een enkel vervalskanaal [30], ondanks de onmogelijkheid om het gehele higgsverval te reconstrueren in dit kanaal.

Statistische analyse vormt een belangrijk aspect van de interpretatie van de data. In deze context is het construeren van een parametrisch waarschijnlijkheidsmodel dat de data kan beschrijven op basis van voorspellingen van gesimuleerde data een belangrijk onderdeel. Mogelijke vervormingen van deze kansverdelingen die geassocieerd zijn met systematische onzekerheden in de simulatie worden in deze modellen geïntroduceerd door een technische procedure die bekend staat als *template morphing*. In dit proefschrift wordt een nieuwe niet-lineare methode van *moment morphing* geïntroduceerd. Deze techniek is snel, numeriek stabiel, kan zowel continue als discrete distributies behandelen, modelleert zowel horizontale als verticale verschuivingen in distributies, en kent geen beperkingen in het aantal sjablonen, in het aantal modelparameters, en in het aantal observabelen [20]. Deze eigenschappen worden steeds belangrijker voor het construeren van complexe waarschijnlijkheidsmodellen met veel systematische onzekerheden. *Moment morphing* heeft veel mogelijke toepassingen in de moderne elementaire deeltjesfysica en daarbuiten omdat het modelleren van systematische onzekerheden op kansverdelingen een algemeen probleem is in statistische analyse. De analyse van het $H \to WW^* \to \ell\nu\ell\nu$ kanaal is een van de eerste analyses die gebruik heeft gemaakt van deze nieuwe interpolatietechniek: door de afwezigheid van analytische uitdrukkingen voor kansverdelingen voor analyse van LHC botsingen, wordt de afhankelijkheid van kansverdelingen voor de geobserveerde data van de higgsbosonmassa beschreven door *moment morphing*. De analyse van higgsbosonverval naar vier leptonen ($H \to ZZ^* \to 4\ell$) door ATLAS is een voorbeeld van een analyse die *moment morphing* gebruikt voor het beschrijven van systematische onzekerheden [24]. *Moment morphing* van n-dimensionale verdelingen is gebruikt in de context van de meting van de spin en pariteit van het higgsboson gemeten in vervalskanalen met bosonen door ATLAS [33].

Om het mechanisme dat verantwoordelijk is voor de electrozwakke symmetriebreking in het SM te verhelderen, zijn precisiemetingen van alle higgsbosoneigenschappen vereist. Elke theoretische uitbreiding van het SM verandert de scalaire sector van de natuur en heeft onderscheidende eigenschappen die specifieke aspecten van het SM uitbreiden. Voor de best mogelijke analyse is een gezamenlijk kansmodel opgesteld voor alle data. Dit model bevat gedetailleerde kansverdelingen van alle individuele higgsvervalskanalen en neemt alle correlaties van systematische onzekerheden mee. De statistische interpretatie van de data combineert kennis van de fenomenologie van higgsbosonproductie en -verval, *state-of-the-art* theoretische berekeningen, en een gedetailleerde beschrijving van alle gereconstueerde objecten die zijn gebruikt in het experiment.

Het eenvoudigste model om alle data te beschrijven is een variant van het SM die een andere globale signaalsterkte van higgsbosonproductie toestaat, terwijl alle andere eigenschappen

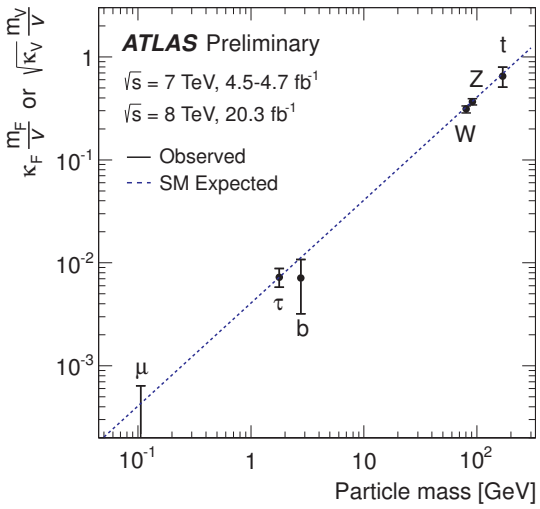

Figuur 3: Fit resultaat voor de gereduceerde schaalfactoren voor de koppelingsstertkte $y_{V,i} = \sqrt{\kappa_{V,i}\frac{g_{V,i}}{2v}} = \sqrt{\kappa_{V,i}}\frac{m_{V,i}}{v}$ voor vectorbosonen en $y_{F,i} = \kappa_{F,i}\frac{g_{F,i}}{\sqrt{2}} = \kappa_{F,i}\frac{m_{F,i}}{v}$ voor fermionen als functie van de massa van de corresponderende deeltjes, onder de aanname van een SM higgsboson met een massa van 125.36 GeV. De gestippelde lijn geeft de voorspelde massa-afhankelijkheid weer voor een SM higgsboson.

gelijkblijven aan die van het SM. De gemeten globale signaalsterkte is $\mu = 1.18^{+0.15}_{-0.14}$ maal de verwachte signaalsterke in het SM. Deze gemeten waarde is consistent met de SM verwachting en komt asymptotisch overeen met een significantie van meer dan 10 standaardafwijking. Een andere interpretatie van de data die verschillende afwijkingen in signaalsterkte toestaat voor alle bekende productiemechanismen resulteert in sterk bewijs voor higgsbosonproductie door vectorbosonfusie met een significantie van 4.3 standaardafwijking. Deze analyse ondersteunt ook de SM voorspellingen voor higgsbosonproductie gezamenlijk met een vectorboson, of met een paar topquarks met een respectievelijke significantie van 2.6 en 2.4 standaardafwijking [31].

De observeerde productie- en vervalswaarschijnlijkheden zijn ook geïnterpreteerd in termen van gewijzigde sterktes van higgskoppelingen, waar de toegestane wijzigingen in vervalswaarschijnlijkheden zijn geparametriseerd volgens de vrijheidsgraden die zijn toegestaan in de laagste orde processen voor higgsbosonproductie en -verval [31]. Met deze behandeling is het mogelijk het effect van gewijzigde koppelingen in productie en verval van elkaar te scheiden, die in verschillende verhoudingen in de gemeten kanalen voorkomen. De compatibiliteit van de sterkte van de higgsbosonkoppelingen met hun SM verwachtingen is getest voor een brede verzameling van *benchmark* scenarios die zijn gebouwd op symmetrieën van het SM. Een verscheidenheid aan (natuurkundig gemotiveerde) aannames over de totale vervalsbreedte van het higgsboson is bestudeerd. Afhankelijk van de verkozen aannames variëert de 95% C.L. bovenlimiet op de fractie higgsbosonvervallen naar onzichtbare of ongedetecteerde vervalsmogelijkheden tussen de 13% en 68%. Lusprocessen zijn gebruikt om indirect te zoeken naar nieuwe deeltjes met elektrische lading of kleurlading. De effectieve

koppelingssterkte die geassocieerd is met deze lusprocessen is gemeten met een precisie van 10% tot 20%, afhankelijk van het gekozen benchmark model. Er zijn geen significante afwijkingen ten opzicht van het SM waargenomen. Onder de beschouwde benchmark modellen, en onder een brede reeks aannames, is de compatibiliteit van de data met de SM hypothese tussen de 29% en 99%. Als voorbeeld geeft Fig. 3 een overzicht van de koppelingssterkte van het higgsboson aan μ en τ leptonen, b— en t-quarks, en W- en Z-bosonen als functie van de massa van deze deeltjes en illustreert het de karakteristieke eigenschap van het Brout-Englert-Higgs mechanisme: de gemeten sterkte van de koppelingen van deze deeltjes aan het higgsboson is proportioneel met hun massa.

Alhoewel de gemeten eigenschappen van het higgsboson het SM ondersteunen en het SM een bruikbare perturbatieve beschrijving geeft van natuurkundige verschijnselen tot aan de Planck schaal, zijn diverse fundamentele vragen niet bevredigend beantwoord. Deze vragen omvatten onder andere het hierarchieprobleem betreffende de natuurlijkheid van de higgsbosonmassa, het karakter van donkere materie, en de dynamische oorsprong van EZSB. Veel van de voorgestelde oplossingen voor deze open vragen hebben implicaties voor natuurkunde bij de huidige energiegrens, en voorspellen wijzigingen of een uitbreiding van de minimale scalaire sector van de natuur die is beschreven in het SM. Onder de veelbelovende scenarios met fundamentele natuurkunde buiten het SM bevinden zich modellen met een samengesteld higgsboson, theorieën met twee higgsdoubletten, supersymmetrie, en andere modellen met kandidaten voor donkere materie. Deze modelen doen specifieke voorspellingen over hoe de koppelingen van het waargenomen 125 GeV higgsboson afwijken van die van het SM. Tests met modellen met specifieke parameterisaties voor deze theorieën zijn uitgevoerd. Met bepaalde aannames zijn scherpe limieten gezet op modelparameters die geassocieerd zijn met deze nieuwe natuurkunde [38]. Deze resultaten kunnen toekomstige directe zoektochten naar fundamentale natuurkunde buiten het SM in de richting van een ontdekking wijzen.

Een voorbeeld van een theorie met nieuwe natuurkunde die is ingeperkt door een meting van eigenschappen van het waargenomen higgsboson is de minimale supersymmetrische uitbreiding van het Standaard Model. In deze uitbreiding van het SM is de scalaire sector gerepresenteerd door twee doubletvelden in plaats van een, die zich manifesteren als vijf scalaire deeltjes: h, H, A en $H^{\pm}$. In een versimpelde versie van de theorie [271, 272] zijn de koppelingseigenschappen van het lichte h boson slechts afhankelijk van twee parameters: de massa van het zware A boson en de mixingshoek β tussen de lichte h en zware H velden. Figuur 4 geeft de limieten op m_A en $\tan\beta$ weer die volgen uit de geobserveerde koppelingseigenschappen van het higgsboson in dit versimpelde model, onder de aanname dat het waargenomen higgsboson het lichte h deeltje uit deze theorie is.

Tenslotte is het fysicapotentieel van het ATLAS experiment bij de HL-LHC bestudeerd voor metingen van higgsbosonproductie, -verval en -koppelingssterktes. In het jaar 2022 wordt verwacht dat waargenomen data door de ATLAS detector correspondeert met een geïntegreerde luminositeit van 300 fb^{-1} bij een botsingsenergie van 14 TeV, en verder toeneemt

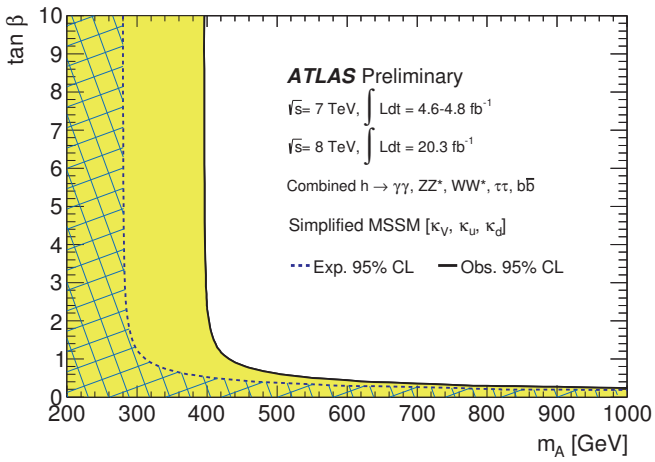

Figuur 4: Gebied in de hMSSM parameterruimte dat indirect is uitgesloten met 95% CL of groter, door een gecombineerde meting van higgsbosonproductie en -vervallen (geel). De gebieden waarvan verwacht wordt dat ze uitgesloten kunnen worden, onder de hypothese dat de scalaire sector die van het SM is, is met een ruitpatroon aangegeven. De betrouwbaarheidsintervallen zijn geconstrueerd onder de aanname dat de toetsingsgrootheid $-2\ln\Lambda(m_A, \tan\beta)$ asymptotisch verdeeld is volgens een χ^2 verdeling met twee vrijheidsgraden. De ontkoppelingslimiet van het SM bevindt zich bij grote waardes van m_A.

tot 3000 fb^{-1} in 2035. Het is de verwachting dat de precisie van de gemeten parameters significant zal verbeteren met toenemende geïntegreerde luminositeit, maar dat vooruitgang in zowel theoretische berekeningen als in het begrip van de detector nodig zijn om volledig te kunnen profiteren van het upgradeprogramma [52]. De mogelijke synergie tussen het Higgs fysicaprogramma van de HL-LHC en de ILC is ook onderzocht. Van deze twee faciliteiten wordt verwacht dat zij elkaar complementeren, waar de HL-LHC een voordeel heeft in het meten van vervalsprocessen met een kleine waarschijnlijkheid en in metingen van andere zeldzame processen en de ILC ideaal is voor het bepalen van de absolute sterkte van higgskoppelingen.

Acknowledgements

A

It would not have been possible to finalize this manuscript without receiving the support of many people I met on the four-year journey, some whom I would like to thank explicitly.

First and foremost I would like to thank my advisor, Wouter Verkerke. His guidance in combination with constant support and the freedom to follow new ideas shaped me as a researcher and physicist. The conversations on physics and statistics have been highly enlightening and were a great motivation to learn and think about the details as well as the big picture of our research. I was fortunate for having Stan Bentvelsen as a promoter. His enthusiasm towards high energy physics in general and my research in particular has been truly inspiring.

I am indebted to Wim Beenakker, Auke-Pieter Colijn, Jos Engelen, Paul de Jong, Sijbrand de Jong, Marumi Kado, and Gerhard Raven for accepting to be in the dissertation committee.

Many people, both at Nikhef and at CERN, have taken a big part in my life over the past years, became close friends, and played and invaluable role in completing this manuscript. I feel lucky to have been part of Nikhef and wish to thank my colleagues for the unique atmosphere at the institute. Thanks go to Max Baak: I would not have joined Nikhef without you. Within the Nikhef ATLAS group Lydia Brenner, Ingrid Deigaard, Pamela Ferrari, Peter Kluit, Jörn Mahlstedt, and Priscilla Pani have always made the office a great place to be and offered their time and help with any problem that I encountered. Ingrid and Jörn, thank you for being my paranymphs. For the help with all administrative matters I have to thank Joan Berger, Pieter van Braam van Vloten, Teus van Egdom, and Ed van Willigen.

Doing the first steps in experimental particle physics and when performing my first analysis, I immensely benefitted from the knowledge and experience of Pamela Ferrari, Tatjana Lenz, Duc Bao Ta, and Marcel Vreeswijk. I would like to thank Heather Gray and Simone Pagan Griso for introducing me to the ATLAS software framework and event reconstruction algorithms. It was a joy to work with and learn from the many students, post-docs, and research fellows being part of the ATLAS Higgs working group. Representative for all those who have been part of the journey from the Higgs boson discovery to first property measurements, I would like to express my gratitude to the coordinators of the analysis efforts I took part in, Olivier Arnaez, German Carrillo-Montoya, Fabio Cerutti, Michael Dührssen-Debling, Erez Etzion, Eilam Gross, Marumi Kado, Bruno Mansoulié, Tatsuya Masubuchi, Biagio Di Micco, Corrinne Mills, Aleandro Nisati, Richard Polifka, Kirill Prokofiev, Jianming Qian, Nikolaos Rompotis, Pierre Savard, Christian Schmitt, and Wouter Verkerke.

Within the analysis teams, I am especially grateful for the excellent collaboration with Tim Adye, Aaron Armbruster, Olivier Arnaez, Max Baak, Lydia Brenner, Magda Chelstowska, David Delgove, Michael Dührssen-Debling, Eric Feng, Andrea Gabrielli, Robert Harrington, Sven Kreiss, Jonathan Long, Joana Machado Miguéns, Corrinne Mills, Richard Mudd, Richard Polifka, Joe Taenzer, Hongtao Yang, and Fangzhou Zhang. I do not want to miss the insightful discussions, support, and work with you – my research would certainly have been different without you. I owe gratitude to Eilam Gross and Marco Pieri for have given me the opportunity to contribute to the first combined ATLAS and CMS Higgs boson measurements. My analyses would not have been possible without the support from the computing departments of Nikhef and CERN: thanks to Alessandro Di Girolamo, Ronald Starink, and Jeff Templon for the help and patience with my jobs.

Finally, I would like to thank my family and friends outside of the physics community. Their support and encouragement have been essential for helping me through the busy and sometimes also difficult times.